DESIGN OF SUSTAINABLE REFRIGERANTS BY MULTI-SCALE MODELING

Carlos Albà I Garriga

DOCTORAL THESIS

UNIVERSITAT ROVIRA i VIRGILI
Escola Tècnica Superior
d'Enginyeria Química

Design of Sustainable Refrigerants by Multi-Scale Modeling

Carlos Albà I Garriga

Carlos Albà I Garriga

Design of Sustainable Refrigerants by Multi-Scale Modeling

PhD Thesis

Universitat Rovira i Virgili

Doctoral Programme in Nanoscience, Materials, and Chemical Engineering

Supervised by: Prof. Fèlix Llovell Ferret

Prof. Lourdes Vega Fernández

2024

"An expert is a person who has made all the mistakes that can be made in a very narrow field."

Niels Bohr, 1922 Nobel Laureate in Physics

Acknowledgments

From a personal perspective, supportive and helpful discussions with Fareeha Shadab, Kalppana Chelvam (also known as K), Seba AlAreeqi and Daniel Bahamon from Khalifa University of Science and Technology; as well as my dear friends Luan Alencar and Merve Gözdenur from URV are appreciatively acknowledged. I would also like to express my deepest gratitude to my parents, my sister, my beloved dog Bart, family members, my grandmother, and friends, as well as my beloved partner in life Fabri, all of whom have been by my side throughout this journey. Furthermore, I extend my heartfelt thanks to Prof. Gonzalo Guillén and his entire team in ETH Zurich.

Though, this project would have been impossible to accomplish without the commitment and constant dedication of Dr. Belén Rodríguez, Dr. Ismail I.I. Alkhatib, Dr. Fèlix Llovell and Professor Lourdes Vega. Special gratitude to the entire Abu Dhabi team for their hospitality and kindness throughout my stay, which led to unforgettable experiences at COP28 Dubai, celebrating the Emirates Day, running in the Abu Dhabi marathon, and the forging of lasting friendships with K and Fareeha. Both professors truly deserve a special mention in this section for the spirit of excellence and continuous improvement in professional performance that they have transmitted throughout these years as well as their contagious devotion for science.

This thesis has been carried out under the support of a FI-SDUR fellowship from the Catalan Government, which is gratefully acknowledged. Additionally, the work has been performed under the framework of projects STOP-F-Gas (ref: PID2019-108014RB-C21), and NEW-F-TECH (Ref. TED2021-130959B-I00), funded by MCIN/AEI/10.13039/501100011033, project KET4F-Gas−SOE2/P1/P0823, cofinanced by the European Regional Development Fund within the framework of the Interreg SUDOE Program, and project RC2-2019-007 to the Research and Innovation Center on CO_2 and Hydrogen (RICH Center) at Khalifa University (KU). Finally, a visiting scholar grant from the RICH Center at KU for developing part of this thesis is much appreciated.

شكراً جزيلاً,
Merci vielmal,
Thank you very much,
Muchas gracias,
Moltes gràcies.

Abstract

As Europe enforces mandates to substantially phase down the emission of high global warming potential refrigerants, a pressing challenge emerges in the refrigeration and air conditioning industry: the development of environmentally sustainable alternatives to hydrofluorocarbons. In response, this thesis focuses on the implementation of multiscale modelling tools for the development of a consistent methodology to identify new refrigerants with lower emissions. The proposed approach relies on the robust polar soft-SAFT equation of state to predict thermodynamic properties required for their technical evaluation at conditions relevant for cooling applications, in combination with artificial intelligence neural networks integrated using molecular descriptors through COSMO-RS. Overall, the strength of this methodology lies in the development of accurate coarse-grain models that provide the required data for the rational design of new refrigerants, without the need of further experiments. Based on these data, an energy, exergy, economic and environmental (4E) analysis is conducted to minimize retrofitting costs of existing systems, in order to address data gaps and enhance the accuracy of predictions for thermodynamic properties and system performance. This framework is applied across a wide range of operating conditions and system configurations to ensure robustness and accuracy in the context of waste-heat recovery, finding a potential blend [(60/40) *wt.*% R1243zf + R1234ze(E)] that can effectively replace R134a. A multi-objective optimization method using statistical tools has been developed to assess the impact of design factors on potential enhancements in cooling cycle performance, finding annual cost savings and reduction in CO_2 emissions. Additional analysis of environmental impact and projected cost is included to quantify the impact associated with their use and emissions, aiding in the identification of appropriate drop-ins from a holistic techno-environmental-economic perspective. Further studies on lubricant leaks and their impact on cycle efficiency have revealed minimal effects, with the balance between solubility, miscibility, and viscosity as of main concern. Finally, this thesis explores promising retrofitting alternatives to CO_2, overcoming its safety limitation in sub-critical cascade cycles, extending the methodology presented to non-fluorinated compounds. Overall, the results indicate the capability of the approach, based on molecular modelling tools in providing an adequate framework to address the challenge of reducing emissions in the refrigeration industry, following guidelines by the European Commission.

Resum

A mesura que Europa imposa mandats per reduir l'emissió de gasos refrigerants amb un potencial d'escalfament global alt, sorgeix un desafiament urgent per a la indústria de la refrigeració i l'aire condicionat: el desenvolupament d'alternatives mediambientalment sostenibles als fluorocarbonis hidrogenats. En resposta, aquesta tesi se centra en el desenvolupament d'eines de modelatge multiescalar per a una descripció precisa de la captura, ús i emmagatzematge de gasos d'efecte hivernacle, amb especial atenció als gasos fluorats. L'enfocament proposat es basa en l'equació d'estat soft-SAFT, en la seva versió polar, per tal de predir les propietats termodinàmiques idònies que permetin una avaluació tècnica precisa en condicions rellevants per a la indústria de la refrigeració i l'aire condicionat, en combinació amb xarxes neuronals mitjançant descriptors moleculars COSMO. En termes generals, la fortalesa d'aquesta metodologia rau en el desenvolupament de models predictius per al disseny de nous fluids de refrigeració. D'ençà, s'efectua una anàlisi 4E (energètic, exergètic, econòmic i ambiental) per tal de minimitzar costos operacionals, i així donar resposta mitjançant un modelatge computacional a la necessitat imperiosa de nous refrigerants amb propietats termodinàmiques i de rendiment òptimes. Aquest marc és aplicable a una àmplia gamma de condicions de treball i configuracions del sistema, garantint així la seva versatilitat i robustesa, procedint a identificar una mescla [(60/40) *wt.*% R1243zf + R1234ze(E)] potencial substituta al refrigerant d'ampli ús social R134a. Mètodes d'optimització amb ús d'eines d'anàlisi estadística van avaluar l'impacte dels factors de disseny en la millora del rendiment, resultant en estalvis anuals de caire considerable i en reduccions de les emissions base CO_2. S'hi inclou una anàlisi de l'impacte del cicle de vida per quantificar l'impacte associat al seu ús i emissions, amb l'objectiu d'identificar substituts des d'una perspectiva tecno-ambiental-econòmica integral. Estudis posteriors sobre possibles fuites de material lubrificant i el seu impacte en l'eficiència del cicle no revelaren efectes considerables, destacant un balanç multifactorial entre solubilitat, miscibilitat i viscositat. Per acabar, aquesta tesi explora alternatives al diòxid de carboni per a sistemes subcrítics en cascada. En resum, l'objectiu d'aquesta tesi és doble: en primer lloc, millorar la recuperació, i utilització de gasos fluorats, així com identificar mescles de gasos amb propietats fisicoquímiques òptimes per al seu ús en cicles de refrigeració, complint amb els estàndards de seguretat i mediambientals dictats per la Comissió Europea.

Resumen

A medida que Europa impone mandatos para reducir la emisión de gases refrigerantes con alto potencial de calentamiento global, surge un desafío apremiante para la industria de la refrigeración y el aire acondicionado: el desarrollo de alternativas medioambientalmente sostenibles a los hidrofluorocarbonos. En respuesta, esta tesis se centra en el desarrollo de herramientas de modelado multiescalar para describir con precisión la captura, utilización y almacenamiento de gases de efecto invernadero, con especial énfasis en los gases fluorados. El enfoque propuesto se basa en la ecuación de estado soft-SAFT, en su versión polar, para predecir las propiedades termodinámicas necesarias para su evaluación técnica en condiciones relevantes para las aplicaciones de refrigeración, en combinación con redes neuronales mediante descriptores moleculares COSMO. En términos generales, la fortaleza de esta metodología radica en el desarrollo de modelos predictivos para el diseño de nuevos fluidos de refrigeración. A partir de estos datos, se realiza un análisis 4E (energético, exergético, económico y ambiental) para minimizar los costes operacionales, con el fin de dar respuesta mediante modelado computacional a la necesidad imperiosa de nuevos refrigerantes con propiedades termodinámicas y de rendimiento óptimas. Este marco es aplicable a una amplia gama de condiciones de trabajo y configuraciones para así garantizar la solidez y la precisión en el contexto de la recuperación de calor residual, procediendo a identificar una mezcla [(60/40) *wt.*% R1243zf + R1234ze(E)] potencial sustituta al refrigerante R134a. Métodos de optimización con uso de herramientas de análisis estadístico evaluaron el impacto de los factores de diseño en la mejora del rendimiento, resultando en ahorros anuales y en reducciones de las emisiones de CO_2 equivalente. Se incluye un análisis adicional del impacto de vida para cuantificar el impacto asociado a su uso y emisiones, proyectando la identificación de sustitutos desde una perspectiva integral tecno-ambiental-económica. Nuevos estudios sobre fugas de lubricante y su impacto en la eficiencia del ciclo no revelaron efectos considerables, destacando un balance multifactorial entre solubilidad, miscibilidad y viscosidad. Por último, se exploran alternativas al CO_2 para sistemas subcríticos en cascada. En resumen, esta tesis tiene como objetivo mejorar la utilización de gases de efecto invernadero asociados con compuestos fluorados, así como identificar mezclas de gases con propiedades fisicoquímicas óptimas para su uso en ciclos de refrigeración, cumpliendo con los estándares dictados por la Comisión Europea.

Content

List of Figures

List of Tables

List of Abbreviations

Latin symbols

4E	Energy, Exergy, Environmental, Economic
$A_{2/3}$	Second - and Third-Order Perturbation Terms
AAD	Absolute Average Deviation
AARD	Absolute Average Relative Deviation
AB	Activity Browser Software
AC	Air-Conditioning
Act	Actual Data
AD	Applicability Domain
AF	Activation Function
AI	Artificial Intelligence
A_k	Van der Waals Surface Area
ANN	Artificial Neural Networks
ANOVA	Analysis of Variance
AOT	Annual Operational Time
ASHRAE	American Society of Heating, Refrigerating and AC Engineers
Assoc	Association Term
b	Bias
BMs	Binary Mixtures
BO	Boundary Outliers
BRO	Response Outliers
BSO	Structural Outliers
CAPEX, $\sum \dot{C}_k$	Capital Cost
CC	Cooling Capacity
c_{CO_2}	Costs of CO_2 Emission Avoidance
CCUS	Carbon Capture, Utilization and Storage
CFCs	Chlorofluorocarbons
CFD	Complete Factorial Design

CG	Coarse-Grain Model
C_i	Relative Closeness
C_k	Cost Function Related to CAPEX
Comb	Combinatorial Term
Cond	Condenser
CoC	Commercial Air Conditioning Applications
COP	Coefficient of Performance
C_p	Isobaric Heat Capacity
COSMO-RS	Conductor-like Screening Model for Real Solvents
C_{set-up}	Set-up Cost
CW	Cooling Water
d^*	Number of Descriptors
DES	Deep Eutectic Solvents
D_i^+	Distance from the Ideal Solution
D_i^+	Distance from the Anti-Ideal Solution
DLT	Discharge Line Temperature
DoE	Design of Experiments
E	Electricity
E_a	System Energy Consumption
EEV	Electronic Expansion Valve
Enviro, $\dot{C_{env}}$	Environmental Cost
EoS	Equation of State
EU-27	European Union as of January 1, 2024
Evap	Evaporator
Exp	Experimental Data
$\frac{F}{F+H}$	Degree of Fluorination
FFD	Fractional Factorial Design
FU	Funtional Unit
GHG	Greenhouse Gases
GLO	Global

GRA	Grey Relational Analysis
GWP	Global Warming Potential
h^*	Leverage Threshold
h_i	Leverage Value
HBA	Hydrogen Bond Acceptor
HBD	Hydrogen Bond Donor
HCs	Hydrocarbons
HCFCs	Hydrochlorofluorocarbons
HCFOs	Hydrochlorofluoroolefins
HFCs	Hydrofluorocarbons
HFEs	HydroFluoroEthers
HFOs	Hydrofluoroolefins
HL	Hidden Layer
HNPP	Half-Normal Probability Plot
HOC	Heat of Combustion
HX	Internal Heat Exchanger or Intercooler
I	Input Descriptors
i	Annual Interest Rate
I_n	Identity Matrix
IL	Ionic Liquids
J	Angular Pair Correlation Function for the LJ Fluid
J_f	Jacobian Matrix
K	Angular Triplet Correlation Function for the LJ Fluid
k_B	Boltzmann Constant
k_H	Henry's Constant
KPIs	Key Performance Indicators
L	Annual Leakage Rate
LCA	Life Cycle Assessment
LCI	Life Cycle Inventory
LFL	Lower Flammability Level
LLE	Liquid-Liquid Equilibria

LL/SL-HX	Liquid-to-Suction Line Heat Exchanger Cycle
$LMTD$	Logarithmic Mean Temperature Difference
$logsig$	Logistic Sigmoid
m	Refrigerant Charge Load
$\dot{m}$	Mass Flow
MAC	Mobile Air-Conditioner
$m_{CO_2,e}$	CO_2 Penalty Cost Rate
m_i	*C*hain Length
ML	Machine Learning
MP	Material Production
MSE	Mean Squared Error
M_w	Molecular Weight
n	System Operating Life
NBP	Normal Boiling Point
NFI	Normalized Flammability Index
NMAD	Normalized Median Absolute Deviation
O	Output
OA	Orthogonal Array
OCR	Oil Circulation Ratio
ODP	Ozone Depletion Potential
OPEX, $\dot{C_{op}}$	Operational Cost
P	Vapor Pressure
PaD	Partial Derivatives Method
P_c	Critical Pressure
P_{comp}	Compressor Pressure
PECs	Pentaerythritol Esters
PEGDMEs	Polyethylene Glycol Dimethyl Ethers
PH	Pressure-Enthalpy Diagram
POEs	Polyol Esters
$PPTR$	Power Per Ton of Refrigeration

P_R	Pressure Ratio
P_i	Probability
PRC	People's Republic of China
Pred	Predicted Data
PSR	Polynomial Surface Regression
purelin	Linear
Q_i	Quadrupole Moment
R^2	Coefficient of Determination
RAC	Refrigeration and Air Conditioning
radbas	Radial Basis
RC	Relative Contribution
RE	Refrigeration Effect or Enthalpy of Vaporization
ReC	Residential Air Conditioning Applications
ReE	Refrigerant Emissions
Ref	Reference Term
REFPROP	Reference Fluid Thermodynamic and Transport Properties
ReLU	Rectified Linear Unit
Res	Residual Term
RMSE	Root Mean Square Error
RO	Response Outliers
RP	Retail Price of Raw Materials
ReP	Refrigerant Production
RSM	Response Surface Methodology
S_σ	COSMO σ Descriptor
SAFT	Statistical Associating Fluid Theory
SD_{av}	Average Standard Deviation
SDR	Standardized Residuals
SMILES	Simplified Molecular Input Line Entry System
S/N	Signal-to-Noise Ratios
SO	Structural Outliers
SS-VCRC	Basic Vapor Compression Refrigeration Cycle

T_0	Dead-State Temperature
TAC, $\dot{C}$	Total Annual Cost
T_{ad}	Adiabatic Flame Temperature
tansig	Hyperbolic Tangent
T_b	Bubble Temperature
TC	Total Costs
T_c	Critical Temperature
$\bar{T}_C$	Entropy-Averaged Temperature for the Cold Stream
T_d	Dew Temperature
TEWI	Total Equivalent Warming Impact
T_G	Glide Temperature
$\bar{T}_H$	Entropy-Averaged Temperature for the Hot Stream
Th	Thickness
TOPSIS	Technique for Order of Preference by Similarity to Ideal Solution
T_{PP}	Pinch Point Temperature Difference
TQ	Pinch Temperature-Heat Duty Diagram
TS	Temperature-Entropy Diagram
TS-VCRC	Multi-compression Vapor Compression Refrigeration Cycle
UA	Heat Transfer Coefficient and Area of Exchange Product
USA	United States of America
Var	Variance
VCC	Volumetric Cooling Capacity
VCRC	Vapor Compression Refrigeration Cycle
V_k	Van der Waals Volume
VLE	Vapor-Liquid Equilibria
$\dot{W}$	Compressor Work
wt.	Weight
x_i	Mole Fraction in Liquid Phase
$x_{p,i}$	Dipolar Molecular Fraction
y_i	Mole Fraction in Vapor Phase

Greek symbols

α	Recovery Factor
α_{el}	Electricity Unit Cost
β	Indirect Emission Factor
γ	Grey Relational Grade
$\Delta_f H$	Enthalpy of Formation
ΔT_{SC}	Subcooling Degree
ΔT_{SH}	Superheating Degree
ΔH_{vap}	Refrigeration Effect or Enthalpy of Vaporization
ε_i	LJ Dispersive Energy Between Segments
ε^{HX}	Intercooler Effectiveness
η	Efficiency
η_{II}	Exergy Efficiency
η_s	Isentropic Efficiency
η_{ij}	Size Binary Parameter
μ_i	Dipole Moment
ξ_{ij}	Energy Binary Parameter
$\overline{\Pi}$	Normalized Flammability Index
ρ	Density
ρ_v	Suction Density
τ_i	Total Activity Coefficient
$\sum \dot{\chi}_d$	Total Exergy Destruction Rate
σ	Specific Charge Density
σ_i	Segment Diameter
τ_p	Stoichiometric Coefficients
ϕ	Maintenance Factor
ψ_i	Availability or Specific Exergy of Stream i
ω	Speed of Sound
ω_c	Net Cycle Compressor's Work
ω_i	Weight Factor

Chapter 1. Introduction

This chapter begins by exploring the evolving landscape of F-gas refrigerants, focusing on current trends and regulatory frameworks that shape their use. The main goals of the work are outlined as follows, highlighting the research aims that guide this PhD thesis. The introduction chapter concludes with an overview of the thesis structure, providing a roadmap for the content and progression of the subsequent chapters.

1.1. Current trends and regulation on F-gas refrigerants

The persistent effects of global warming have consistently increased average global surface temperatures, recording a 1.36 ℃ above the 20th century average as of date, predicting the year 2024 to be the warmest on record [1]. In face of these warming trends, the global population has increased its demand for domestic and industrial space cooling to counter act the increasing temperatures and extreme heat waves. As of 2022, approximately 2 billion air-conditioning (AC) units are in operation worldwide, mainly owned by 37% of global population, and projected to nearly double by 2050, with expected growth in population, income and living standards, and more importantly, global raising temperatures [2,3]. By 2050, nearly 75% of global households will own an AC unit, with leading economies in developing countries including India, Indonesia, and People's Republic of China (PRC) accounting for 50% of total owned AC units.

The associated energy consumption for AC units is absent from the energy debate, though accounting for nearly 20% of total building electricity consumption, marking 10% of global electricity use [2,3]. This is a rapidly growing energy consumption segment, increasing by nearly 5% annually, and expected to reach 40% of global electricity usage by 2030, and triple by 2050, making space cooling the fastest growing energy use in buildings and one of the top drivers for global electricity utilization. This might impact peak electricity demand, leading to more frequent power outages, especially during hot seasons, requiring additional power plants to meet required electricity demand [4]. Even though electricity production is shifting towards low-carbon resources such as natural gas, renewable energy, and others, still, indirect CO_2 emissions from space cooling are growing, reaching 1 gigatons (Gt) in 2022, and projected to triple by 2050, further aggravating the increasing warming trends [2–5].

To deal with this phenomena, refrigeration and air conditioning technologies have experienced a transformative evolution [6], driven primarily by the changing landscape of fluorinated gases (F-gases), a subgroup of greenhouse gases (GHGs) primarily used for cooling applications. Investing in more efficient ACs is another key factor in developing sustainable cooling infrastructure, reducing the current electricity demand and CO_2 equivalent emissions nearly by half, while drastically cutting overall emissions if coupled to a low-carbon grid electrification. Hence, the energy efficiency of the cooling

cycle can be directly enhanced through either optimization of operating conditions [7–10] or the deployment of novel cycle configurations and designs [11–20].

Emerging in the era of industrialization, F-gases have played a crucial role in altering Earth's climate, though, with hydrofluorocarbons (HFCs) role in refrigeration, [21,22] being a notable example due to their high global warming potential (GWP). This aligns with the key findings presented in **Figure 1.1**, which highlight a notable acceleration in global warming since the final years of the 20th century, with some regions experiencing temperature increases of 1 degree or more per decade. According to the latest report from the National Oceanic and Atmospheric Administration (NOAA), although atmospheric levels of HFCs are significantly lower compared to CO_2, (*i.e.,* 237 ppt for HFCs *vs.* 410 ppm for CO_2) [23], the substantial emissions of these since the early 1990s have undeniably impacted the average surface temperature, due to their higher GWP, outpacing the long-term average trend from 1901 up to date.

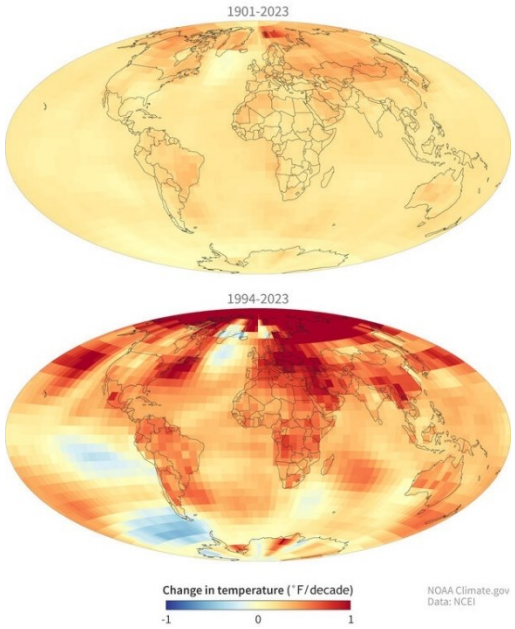

Figure 1.1. *Trends in annual surface temperature in the past few decades (1994-2023, bottom) compared to the trend since the start of the 20th century (1901-2023, top). Refer to NOAA at [24].*

The evolution of refrigerants traces a path through various generations [25], leading to the adoption of simple yet functional compounds like water, ammonia, carbon dioxide, and methyl chloride (CH_3Cl) in early applications [26]. Initially revolutionary [27], these first-generation refrigerants were eventually replaced due to safety concerns including ammonia's high toxicity, carbon dioxide's high pressure requirements, and

CH_3Cl's flammable and toxic nature. This quest for safer alternatives [28] paved the way for the development of next generation of refrigerants [29,30], transitioning from chlorofluorocarbons (CFCs) as with Freon (R12) in the 1930s, valued for non-flammability, to hydrochlorofluorocarbons (HCFCs) such as R22 in the 1980s, with lesser ozone impact but still highly pollutant, and finally to HFCs as with 1,1,1,2-Tetrafluoroethane (R134a) in the 1990s, which, while ozone-safe, is currently targeted due to high-GWP standards.

Each stage of this evolution, defined by distinct environmental impacts and regulatory measures [31], has propelled the advancement of sustainable cooling technologies, furthering global initiatives to adopt more environmentally friendly solutions. This transition to a new generation of refrigerants, along with global long-term initiatives, is outlined in **Figure 1.2**, summarizing the main collective global goals in the fight against climate change [32], primarily driven by the introduction and later approval of the 2016 Kigali Amendment [33] on the original Montreal protocol. As of September 2024, the Kigali Amendment has been ratified by 160 countries, representing approximately 88% of the global population and accounting for 98% of global HFCs consumption. Among these, top HFC-producing nations—China, the United States, India, the European Union, and Japan—all ratified the Kigali Amendment no sooner than 2021, with the exceptions of the European Union and Japan, as appreciated in **Figure 1.3**. Indeed, the United States Senate ratified the final passage of the treaty in late October 2022, while China and India finalized theirs between June and September 2021.

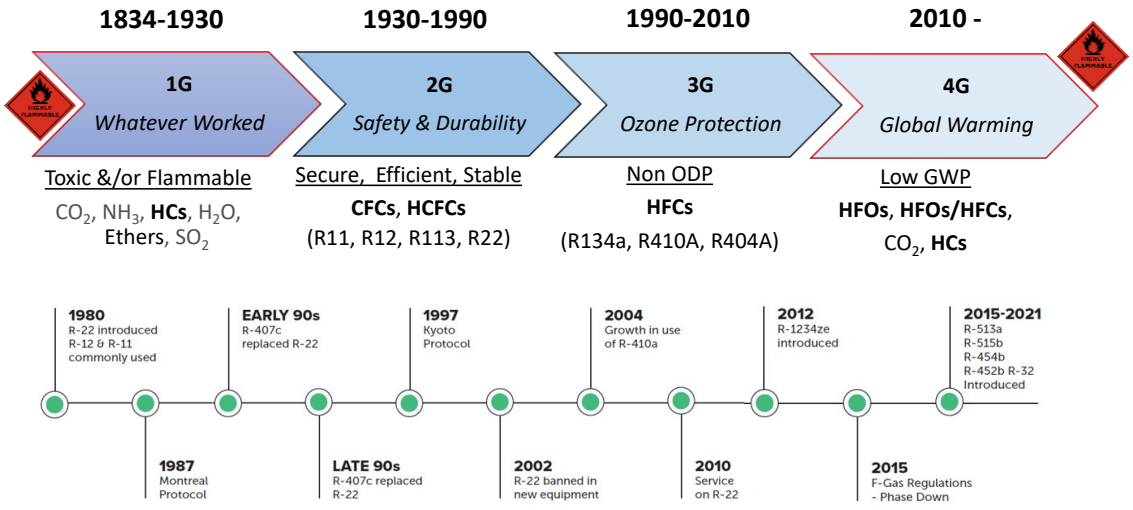

Figure 1.2. *Generation of refrigerants (G), and enacted regulations over time.*

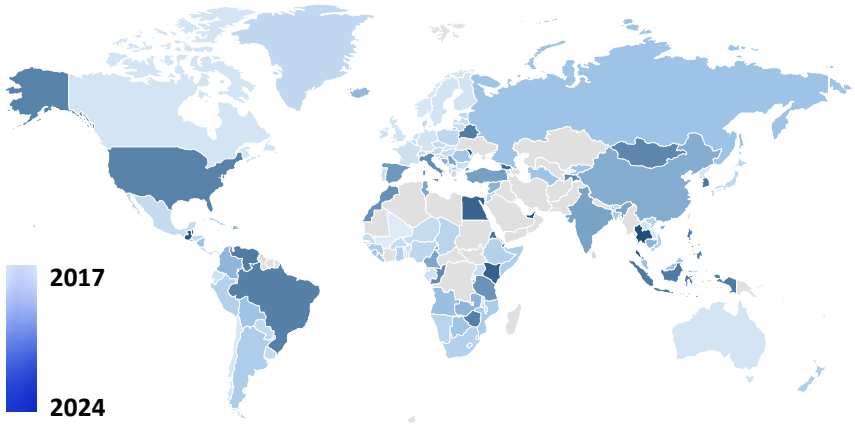

Figure 1.3. *Worldwide ratification of the Kigali Amendment to the Montreal Protocol, tracking progress from early 2017 (light blue) to September 2024 (intense blue).*

Figure 1.4 presents hypothetical scenarios [34] for global HFC production and emissions over a 25-year period, relative to the Kigali Amendment and current baselines, while considering unabated growth in HFC use and emissions [35]. Therefore, without intervention from major emitting countries such as PRC, USA, and India, HFC emissions could reach 3 to 5 Gt of CO_2-equivalent per year, potentially contributing an additional 0.2°C to 0.4°C of global warming by 2050. Conversely, full implementation of the Kigali Amendment by 2050 could lead to a reduction in surface temperatures of approximately 0.5°C compared to current levels, primarily due to a severe phase-out of HFCs. Evidence from scenarios where HFC production or emissions (from both new and existing stocks) cease in 2023 further illustrates the significant impact of HFCs on global warming, reinforcing the urgent need for effective regulation. Notably, this is due to global warming potentials of up to 10,000 times greater than pure CO_2 for certain HFCs, such as R23.

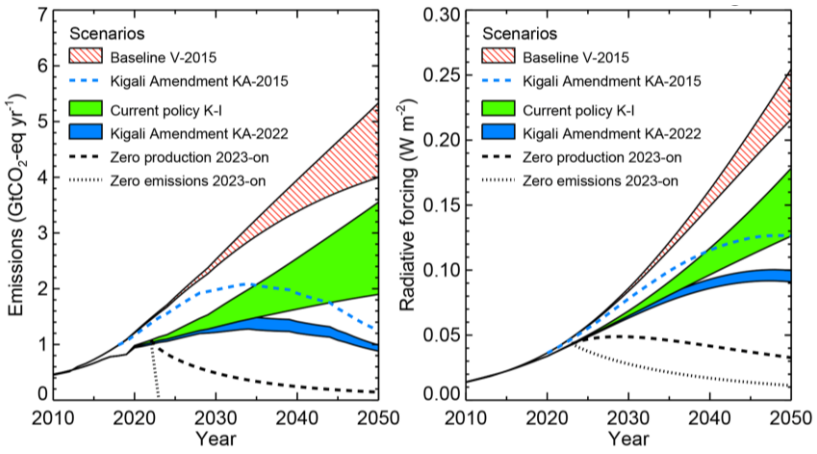

Figure 1.4. *Global HFC emissions (left panel) and radiative forcing (right panel) shown for V-2015 baseline [35], and updated scenarios from Velders et al. [34].*

In addition to Kigali's environmental protection agreement, regional and national regulations have also emerged as competent legal basis to attend the environmental drawback related to HFCs disproportioned emissions. European directive 2006/40/EC [36] came into effect on January 2017 and is consistent with the steady replacement of R134a (GWP=1360) in new air conditioning vehicles equipment, while (EU) legislation No 517/2014 [37] states a manufacture and consumption total veto on HFCs with a GWP greater than 2500 since the beginning of 2020, reducing up to 150 by 2022. This is projected to target a 80 – 95% reduction of HFCs emissions by 2050 [38,39], with a recent proposal [40] for an even more ambitious phase-down, thus aligning with the European Green Deal and the European Climate Law. This would lead to a consumption reduction of 102.5 megatons of CO_2 equivalent by 2030, with a further annual decrease of 20.1 Mt thereafter.

Furthermore, nationwide legislation has been passed in the United States to both incentive the production of low GWP refrigerants [41] and restrict the usage of 3rd generation commercial coolers [42]. Building upon these efforts, the American Innovation and Manufacturing (AIM) Act [43], enacted in December 2020, represents a significant advancement in U.S. climate policy. This landmark legislation aims to drastically reduce HFC production and consumption, targeting a 40% decrease by 2024 and 85% by 2036, thereby addressing their substantial contribution to global warming. The Environmental Protection Agency's (EPA) phasedown plan of HFCs further restricts the manufacture, import, and sale of non-compliant products with GWP superior to 700 in new air-conditioning and refrigeration equipment. It also actively promotes the development and adoption of low-GWP refrigerants, while establishing regulations for the recovery, recycling, and safe disposal of HFCs, aiming to minimize their environmental impact and ensure a gradual shift towards more sustainable alternatives.

Alongside, Japan has enacted the *Fluorocarbons Emission Reduction Law*, revised in 2020, which imposes stringent reduction targets for fluorocarbons, including HFCs, and encourages investment in energy-efficient, low-GWP alternatives. It is crucial to acknowledge similar efforts in other countries and regions [44,45] like Canada, Australia, Norway, and Switzerland, in order to actively implementing policies to reduce the use of high-GWP F-gases, aligning with global commitments like the Kigali Amendment to the Montreal Protocol. In China, the *13th Five-Year Plan for Ecological*

and Environmental Protection, along with the *Measures for the Administration of Fluorinated Gas Management* established in 2015, have set clear targets and regulations for reducing HFC consumption and promoting low-GWP technologies. Similarly, India's National Cooling Action Plan (NCAP), launched in 2019, outlines strategies for enhancing energy efficiency and transitioning to low-GWP refrigerants, supported by the *Draft Refrigerant Management Regulation* of 2020, which includes controls on HFCs and incentives for alternatives. Such international regulatory efforts are not only responding to environmental imperatives, but are actively shaping the landscape of refrigerant technology, promoting the emergence of innovative, low-GWP formulas, in addition to spotlighting the growing importance of CO_2 in this transition. This goes in line with the Global Cooling Pledge for COP28 [46], committing national and regional governments to advance sustainable cooling practices as a strategy for both climate mitigation and adaptation. Consequently, governments from 71 countries worldwide committed to reducing cooling-related emissions by at least 68% by 2050, advancing cooling action plans, and actively promoting the development and deployment of highly efficient cooling technologies based on low-GWP refrigerants.

Thus far, seeing that the complete removal of HFCs from market circulation is imminently close, it is necessary to find an answer to the elusive question *"what are the alternative sustainable refrigerants replacing the technically efficient HFCs?"*. The National Institute of Standards and Technology (NIST) developed a framework to investigate new classes of potential refrigerants meeting imposed environmental and safety regulations, while maintaining the technical efficiencies of widely used high-GWP HFCs such as 1,1,1,2-tetrafluoroethane (R134a) and R410A (blend of difluoromethane (R32) + pentafluoroethane (R125)) [47].

From a pool of 56000 single-component refrigerants, limited options for low GWP refrigerants existed, with merely 27 potential candidates balancing environmental, safety, and technical trade-offs, mainly from hydrofluoroolefins (HFOs) [48], commonly called 4th generation refrigerants. Refer to **Figure 1.5** for a visual representation of refrigerant trade-offs and intrinsic characteristics, with optimal selections clustered in regions neither toxic, flammable, nor fully halogenated. Additional investigations on the operational compatibility of pure HFOs and hydrochlorofluoroolefins (HCFOs) as drop-in replacements (*i.e.,* having the capacity to substitute current HFCs to existing systems

with minimal modifications) identified their potential to only replace a small pool of commercial single-component HFCs (*e.g.,* R134a, 1,1-difluoroethane (R152a), and 1,1,1,3,3-pentafluoropropane (R245fa)), with no viable replacements for the majority of widely used HFCs [49]. Moreover, the most promising HFOs such as, 2,3,3,3-tetrafluoroprop-1-ene (R1234yf) and trans-1,3,3,3-tetrafluoroprop-1-ene (R1234ze(E)), are mildly-flammable (A2L ASHRAE classification) [50] compared to non-flammable HFCs in use (1 class) [50] R134a and R410A, which might be reflected on the costs required for additional safety layers [51,52].

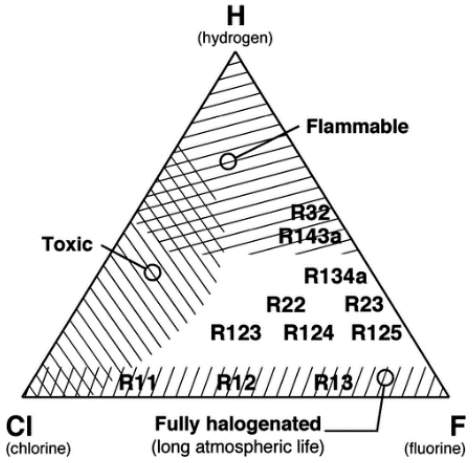

Figure 1.5. *Ternary diagram on refrigerants based on chlorine (Cl), fluorine (F), and hydrogen (H). As seen for selected CFCs, HCFCs, and HFCs, hydrogen increases flammability, fluorine raises GWP and atmospheric lifetime, while chlorine boosts toxicity. Figure taken from reference [6].*

Though several low GWP refrigerants have been recently identified [27,38,52,53], their market deployment is constrained by several barriers in global and country-specific contexts, spanning across (1) technical barriers of safety-related properties and limited range of applications, (2) technological barriers related to high investment costs either for retrofitting existing systems or deploying newly designed systems with low GWP refrigerants, and (3) commercial barriers associated with misaligned commercial interests of industrial sectors with imposed regulations [31,54–56]. Among these, RE170, R1132a, R1336mzz(E/Z), R13I1, and notably CO_2, are beginning to surface as viable low-GWP options, although their presence remains limited. Particularly, CO_2 is distinguished by its potential [57–59], owed to non-flammability and environmental friendliness compared to fluorinated compounds, despite facing challenges from high critical pressure to low critical temperature that limits its applications compared to standard F-fluids.

As seen from the evolution depicted in **Figure 1.2**, refrigerant blends offer a promising alternative to currently adopted 3rd generation refrigerants, potentially overcoming existing barriers towards deployment of low GWP refrigerants, with a summary of promising replacements listed in **Table 1.1**.

Table 1.1. *Summary of alternative drop-in replacement blends, specifying their proportion, GWP, normal boiling point (NBP) and glide temperature (T_G).*

Blend	*wt.%*	GWP	ASHRAE	*NBP* / °C	T_G / K	Baseline	Ref.
R1234ze(E) + R152a	10/90	112.2	A2	-24.41	0.013	R134a/R410A	[60,61]
R600a + R1234ze(Z)	90/10	18.6	A3	-11.77	0.001	R134a/R410A	[60]
R600a + R1233zd(E)	90/10	31.4	A3	-11.92	0.031	R134a/R410A	[60]
R450A (R1234ze(E) + R134a)	58/42	547	A1	-23.36	0.640	R134a	[60,62–64]
R513A (R1234yf + R134a)	56/44	573	A1	-29.58	0.000	R134a	[62]
R1234ze + R134a	90/10	150	A2L	-21.40	0.930	R134a	[65,66]
R430A (R152a + R600a)	76/24	107	A3	-27.60	0.200	R134a	[67]
R431A (R290 + R152a)	71/29	43	A3	-43.20	0.000	R134a	[67]
R435A (RE170 +R152a)	80/20	30	A3	-26.00	0.200	R134a	[67]
R436A (R290 + R600a)	56/44	<3	A3	-34.30	8.200	R134a	[67]
R600a + R1224yd(Z)	90/10	18.1	A2L – A3	-12.03	0.081	R134a/R410A	[60]
R1243zf + R152a	10/90	111.7	A2	-24.88	0.103	R134a/R410A	[60]
R600a + R236ea	90/10	138	A2L – A3	-12.18	0.217	R134a/R410A	[60]
R1234yf + R152a	10/90	112	A2L – A2	-25.13	0.236	R134a/R410A	[60,66]
R600a + R245fa	90/10	121	A3	-12.97	0.756	R134a/R410A	[60]
R152a + R600	90/10	99.8	A2	-25.92	0.194	R134a/R410A	[60]
R454A (R32 + R1234yf)	35/65	238	A2L	-47.80	5.000	R404A	[68,69]
R454C (R32 + R1234yf)	21.5/78.5	146	A2L	-45.50	6.000	R404A	[68–70]
R32 + R1234yf + R744	22/72/6	149	A2L	-57.50	14.120	R410A	[71]
R455A (R744 + R32 +R1234yf)	3/21.5/75.5	146	A2L	-52.00	9.860	R404A	[69,70]
R457A (R32 + R1234yf + R152a)	18/70/12	139	A2L	-42.60	6.140	R404A	[70]
R459B (R32 +R1234yf +R1234ze(E))	21/69/10	143	A2L	-45.00	7.040	R404A	[70]

R600 (*n*-butane), R600a (*i*-butane), R774 (CO_2) and RE170 (Dimethyl ether).

This is attributed to the additional degrees of freedom during blend design, facilitating a targeted fine-tuning of blend properties within environmental/safety constraints and technical requirements. The use of refrigerant blends is not uncommon, as seen with the release of R410A with the phase-out of chlorodifluoromethane (R22) and dichlorodifluoromethane (R12) [72,73]. Similarly, synthetic medium-GWP blends (*i.e.,* GWP ≈ 500 – 750) exploiting low-GWP HFOs and non-flammable HFCs [74] such as R513A and R450A, have been proposed as mid-term replacements for R134a (GWP = 1300), given their high technical performance [75,76]. Nonetheless, their adequacy has

to be re-evaluated with the realigned GWP constraints [37], hence, the need for alternative low-GWP synthetic blends. Zeotropic blends can lead to operational issues, and with the market's limited supply (see **Table 1.1**) of fully azeotropic blends—many of which have high ODP or GWP—near-azeotropic alternatives are becoming a preferred choice.

In this regard, hydrocarbons are re-emerging [77] as promising solutions following setbacks in past efforts, and a reevaluation [78,79] of their potential has brought them back into focus. Known for their very low GWP and zero ODP, light hydrocarbons are both environmentally benign and efficient conductors of heat [67]. Nevertheless, their use is not without challenges; their flammability has always led to concerns and rigorous safety standards, being typically classified in the high flammability class [80]. In this sense, the re-introduction of aliphatic hydrocarbon gases in new mixtures of refrigerants aligns with global sustainability goals, but faces intricate challenges linked to intrinsic flammability concerns.

In summary, this apparent progress toward environmental compliance has unfolded an unexpected challenge [6,29]; as the newly formulated refrigerants— whether pure HFOs, HFC/HFO blends such as R448A and R449A, or hydrocarbons like propane (R290), isobutane (R600a), and propylene (R1270)—while less detrimental to climate change, often exhibit highly flammable characteristics compared to their predecessors. Overall, this paradigm shift is introducing significant safety challenges to be overcome [81,82] into the refrigeration industry of today, potentially elevating the cost of associated equipment and demanding a new level of awareness and preparedness.

Consequently, the quest for finding a “perfect” sustainable refrigerant, while maybe utopic, remains a challenge of upmost importance because of the current world cooling needs. This search seems to be a balance of many properties, indicating the necessity for blend screening and the development of an adequate consistent methodology to find the right equilibrium, considering technical, safety, environmental and economic concerns.

1.2. Objectives of this thesis

The fundamental aim of this PhD thesis is to **develop robust and accurate multiscale modeling tools to rationally design 4th generation drop-in refrigerants for use in cooling and air-conditioning applications**. Additionally, it is desired to improve, via a proper choice, the carbon utilization of current fluorinated-GHGs in line with European Commission guidelines. To achieve these goals, the thesis will focus on the following specific objectives:

1. Employ a molecular-based equation of state for the comprehensive thermodynamic characterization of refrigerants and their blends.
2. Characterize the thermodynamic behavior of lubricant oils in contact with refrigerant agents and assess their impact on the overall cycle performance.
3. Optimize the performance of current refrigeration and air conditioning (RAC) systems through statistical analysis and molecular modeling.
4. Develop a preliminary modeling framework to assess the viability of replacing 3rd generation HFC refrigerants with low-GWP 4th generation alternatives.
5. Assess the compatibility of 3rd generation refrigerants with potential 4th generation replacements through a drop-in process simulation analysis aimed at minimizing retrofitting costs in existing systems.
6. Conduct a comprehensive evaluation of low-GWP drop-in alternatives against existing commercial refrigerants, assessing their performance across multiple criteria.
7. Evaluate the impact of advanced cooling technologies and configurations on the design of low-GWP refrigerants using a 4E (energy, exergy, environmental, and economics) analysis.
8. Perform an integrated Life Cycle Analysis (LCA) to estimate the carbon footprint of potential drop-ins, covering all stages from raw material extraction to end-of-life disposal.

9. Develop integrated machine learning frameworks to enhance the characterization of new cooling agents aligning with market needs, environmental concerns, and safety requirements. Demonstrate its reliability and predictive capability.

1.3. Thesis outline

Following this opening chapter, **Chapter 2** delves into the latest advancements in refrigeration technologies, offering a comprehensive review of current developments and innovations in the field as well as remaining challenges. This chapter sets the stage by outlining the current state of knowledge in key areas of refrigeration, setting up the reader for the in-depth analysis and discussions that will follow in the subsequent chapters.

Chapter 3 dives into the methodology employed in this thesis. It begins with an in-depth explanation of the polar soft-SAFT equation of state and its application for thermodynamic characterization. A molecular modeling subsection details the coarse-grain models used to characterize a long list of refrigerants examined in this thesis. Various process configurations are described next. These include the basic vapor compression refrigeration cycle, along with its advanced variations, such as the liquid-to-suction line heat exchanger, multi-compressor systems, and the cascade cycle designed for ultra-low temperature applications. Additionally, this chapter covers the four key performance indicators (KPIs)—energy, exergy, environmental, and economics—along with a holistic LCA. Statistical tools for the optimization of cooling cycles are also discussed in addition to artificial neural networks. The process involves four stages: the initial stage focuses on dataset generation using COSMO-RS, followed by fine-tuning the ANN's structure, evaluating the model's performance through regression and statistical assessments, and finally screening the properties of interest after thorough validation.

Chapters 4-8 contain the main results from this PhD thesis work, with a detailed discussion and main conclusions. **Chapter 4** presents a detailed thermodynamic characterization of the refrigerants listed in the coarse-grain characterization process. This chapter analyzes the physical significance of the polar soft-SAFT parameters and computes the contributions of terms related to Helmholtz energy. The validation process includes calculating a broad spectrum of thermophysical properties and predicting saturation characteristics for refrigerant mixtures with alkanes, carbon dioxide, and

fluorinated compounds, ensuring the accuracy of the coarse-grained models. The initial analysis chapter concludes by applying machine learning techniques to predict vapor-liquid equilibrium (VLE) data, including key saturation properties such as dew and bubble points.

Chapter 5 focuses on evaluating the compatibility of various lubricants, including PECs and PEGDMEs, with R513A, and examines their performance considering a balance between solubility, miscibility and viscosity. It concludes with a comprehensive energetic analysis quantifying the impact of the presence of the lubricant on the coefficient of performance of a residential cycle. The procedure implemented in this section allows tuning the performance of the refrigerant/lubricant pair, in a step forward on the search for low GWP refrigerants in air conditioning systems.

Chapter 6 builds on the theoretical frameworks introduced in **Chapter 4** by applying the soft-SAFT model to single-stage vapor compression refrigeration cycles. This chapter serves as the technical basis for analyzing and screening emerging eco-friendly refrigerants as potential replacements for existing third-generation compounds. It includes a compatibility analysis of 4th generation potential drop-ins to widely used HFCs, such as R134a and R410A, based on the 4E criteria—energy, exergy, environmental impact, and economics. To conclude, the chapter presents a prospective assessment of legislative scenarios designed to promote and speed up the upcoming adoption of drop-in alternatives.

Chapter 7 extends the preceding chapter research by focusing on advanced refrigeration cycle configurations, aiming to assess the transition from conventional to advanced refrigeration cycles using statistical methods. The use of ANN, 4E, and LCA methodologies is key to selecting optimal refrigerant mixtures that meet both technical, environmental, and safety requirements. Consequently, **Chapter 8** focuses into the formulation of CO_2-based refrigerant mixtures for ultra-low temperature applications in addition to drop-in alternatives for advanced cooling cycles.

The conclusive **Chapter 9** synthesize the key findings from this thesis research work and examines potential avenues for future research. Finally, this PhD thesis provides a summary of the publis**hed papers in indexed journals and contributions to scientific meetings** in addition to the **Annex**.

Chapter 2. State of the Art

The purpose of this chapter is to review recent advancements in the design of sustainable refrigerants, focusing on both natural refrigerants and binary blends of fluorinated compounds. Particular emphasis is placed on the importance of accurate modeling techniques, including polar soft-SAFT, molecular simulations, and modeling correlations. Additionally, the chapter assesses refrigerant modeling based on existing literature, covering experimental design methodologies and machine learning techniques, such as artificial neural networks.

2.1. Screening of new refrigerants

In response to the need to address the climate emergency derived from HFCs emissions, the National Institute of Standards and Technology (NIST) delivered a systematic overview of alternative refrigerants that possess null ODP, low GWP, moderate flammability and suitable thermodynamic properties to act as an efficient HFC replacement in cooling systems and chiller applications [47]. Special emphasis has been placed on the examination of unsaturated organic HFOs [83], compounds capable of accomplishing reduced critical temperatures although preserving satisfactory GWP, null ODP and low atmospheric lifetimes consistent with the double bond reactivity towards atmospheric hydroxyls [47]. Several studies [84,85] have yet confirmed HFOs effective attractiveness in nowadays functional air conditioning kits. Hence, with nominal modifications affecting both condenser and evaporator's circuitries exchanging areas, the automobile industry has recently been operating R1234yf as a profitable replacement of R134a in AC internal units. However, in part due to their flammability levels [51], its practical function in other cooling systems should be revised, leading to the consideration of blends as viable next-generation refrigerants. Particular emphasis must be paid to the design of these blends, requiring a property balance optimization procedure amid efficient performance ratios, practical operational cost, suitable environmental properties and acceptable corrosive, safety and sustainability standards in terms of flash point and non-hazardous toxicity.

Another option explored in the search for greener alternative refrigerants by McLinden *et al*. [48] involved screening a large array of possible substances from available databases and experimental datasets, resulting in a pool of 138 pure candidate refrigerants meeting required environmental and safety limits. The additional technical performance assisted in the identification of 27 possible low GWP single-component refrigerants finely balancing the trade-offs between the aforementioned two selection criteria. This includes natural refrigerants like hydrocarbons such as R170, R1270, and R290; carbon dioxide; and new HFOs like R1141, R1123, R1132(E), and R1225ye(Z). Such an effort was facilitated by the availability of extensive databases on relevant properties of known substances studied over the past 20 years. However, this becomes increasingly difficult in the case of newly developed green refrigerants, as the standard

experimental route of obtaining property measurements has long ceased to be capable of meeting the exponentially growing number of newly developed refrigerants and blends, with very recent publications on this behalf [52]. This has accelerated the rising need for predictive computational modeling tools for evaluating the thermodynamic behavior of these refrigerants and obtaining their relevant properties required for technical evaluation [47,86,87].

2.1.1. Binary mixtures

The hunt of low-GWP replacements is an already complex task for single-component refrigerants considering the trade-offs between the multiple desirable properties, becoming more exasperated for blends as their appropriate individual constituents and proportions must be determined. An additional selection criterion for refrigerant blends is their degree of azeotropy, with preference for azeotropic or near-azeotropic blends that behave as pure fluids in the RAC system [88,89]. Although zeotropic blends can be used, such as the ternary mixtures R407C (blend of R32 + R125 + R134a) and R404A (blend of R125 + R134 + (1,1,1-trifluoroethane) R143a), several operational challenges arise, including glitches through refrigerant charging, flooded evaporators, blend composition shifts during leakages, lower heat transfer efficiency, and lower overall efficiency [69,90,91]. Fully azeotropic blends are very limited, with only 17 mixtures registered and classified in the R500 series, part of which have either high-ODP or high-GWP [92]. Consequently, developing alternative near-azeotropic blends is more flexible [93], with a summary of promising replacements listed in **Table 2.1**. Certainly, 4th generation HFOs-based mixtures have appealed scientific attention and its exploration is up to date empowered, considering interactions across carbon dioxide [94], hydrocarbons [95], HFCs [96] and even hydrofluoroethers (HFEs) [97] specimens in rare occasions.

Table 2.1. *Comprehensive overview of current commercial low/medium-GWP refrigerant blends in the market, including GWP, ASHRAE safety classifications, and mass composition percentages.*

	GWP	ASHRAE	R32	R1234yf	R290	R152a	R1234ze(E)	R600a	R134a	R1270	RE170	R227ea	R600	R125	CO_2	R170	R1132a	R1336mzz(E)	R1336mzz(Z)	R1311	R1130t
R436C	1	A3			95			5													
R510A	1	A3						12			88										
R432A	2	A3								80	20										
R514A	2	B1																	75		25
R443A	3	A3			40			5		55											
R433A	3	A3			70					30											
R433C	3	A3			75					25											
R433B	3	A3			95					5											
R436A	3	A3			56			44													
R436B	3	A3			52			48													
R511A	3	A3			95						5										
R441A	3	A3			55			6					36			3					
R429A	14	A3				10		30			60										
R435A	26	A3				20					80										
R431A	38	A3			71	29															
R444A	93	A2L	12			5	83														
R430A	95	A3				76		24													
R516A	131	A2L		77		14			9												
R451A	133	A2L		90					10												
R445A	135	A2L					85		9						6						
R457A	139	A2L	18	70		12															
R440A	140	A2			1	97			2												
R466A	143	A2	49											11						40	
R465A	143	A2	21	71	8																
R459B	143	A2L	21	69			10														
R455A	145	A2L	22	75											3						
R454C	148	A2L	21	79																	
R471A	148	A1					79					4						17			
R468A	148	A2L	22	75													3				
R451B	160	A2L		89					11												
R512A	189	A2				95			5												
R454A	238	A2L	35	65																	
R449A	238	A2L	24				25		26					25							
R457B	251	A2L	35	55		10															
R444B	295	A2L	42			10	48														
R515B	299	A1					91					9									
R515A	387	A1					88					12									
R459A	460	A2L	68	26			6														
R454B	466	A2L	69	31																	
R446A	470	A2L	29				68						3								

In addition, it is notable that most commercial blends [98,99] with a GWP under 150 are characterized by superior flammability (2/3), toxicity (B), or glide (T_G >10 K), with notable exceptions like R516A (A2L), R451A (A2L), or R471A (A1), which are emerging as potential replacements to the industry benchmark R134a. Heredia-Aricapa et al. [74] review the latest refrigerant mixtures—HFC, HFO, HC, and CO_2—as substitutes for R134a, R410A, and R404A, emphasizing on low-GWP options (see **Table 2.1**). The evaluation considers performance metrics such as *COP*, *VCC*, and thermodynamic properties, including pressure-enthalpy diagrams, while setting aside concerns about glide and flammability. Particular attention should be paid to R513A

(R1234yf 56%w, R134a 44%w) in an attempt to replace 3rd generation refrigerant R134a, used in these days air conditioning applications, though its GWP > 500. Though out of the range displayed in **Table 2.1** (up to GWP = 500 per EU regulations [37]), a GWP reduction of around 56% is accomplished, succeeding in a significant step in the search for low GWP refrigerants. In addition, recent studies demonstrate that R513A presents higher mass flow rate and cooling capacity (higher efficiencies) than R134a when using evaporation temperatures between −15°C and 12.5°C, although at the price of a higher power consumption [100]. Even so, R513A is not the only 4th generation refrigerant that has been lately checked up in order to replace R134a, as new equipment also function with R450A, R1234yf, R744 or R717. Notwithstanding, although its reduced GWP, R744, R717 and R1234yf afford serious drawbacks to be considered as practical replacements of refrigerant R134a on account of R744 and R717 absolutely discordant critical and thermodynamic properties and R1234yf's mild flammability (A2L) [84]. Merely R513A and R450A meet the requirements for being regarded as suitable drop-in replacements to R134a, in view of the fact that all three compounds share extremely close critical and thermodynamic properties with the same safety group classification (A1). Consequently, existent AC equipment employing R134a can indeed operate with either R513A or R450A. R513A and R450A have a well-studied azeotropic behaviour [101] that combined with its low GWP, ensure adequate and competitive efficiencies, compared with those performed by R134a.

2.1.2. The effect of lubricants

However, in addition to having the right thermophysical properties and low GWP, further studies are needed before the alternative refrigerants can be put into final use. In this respect, one of the needs of assessing the validity of the new refrigerants for specific cooling applications is their interaction with lubricants. Lubrication oils are regularly used in refrigeration circuits, more precisely in the compressor, to minimize friction, cooling moving parts to remove excessive heat, sealing possible vapour leakages, diminishing noise and even acting as corrosion inhibitors [102,103]. Miscibility, lubricity, and chemical stability are essential properties to take in mind in the pursuit of commercial refrigerator oils. Although miscibility is established solely based on its molecular structure, lubricity and chemical stability with well-balanced physical properties are

greatly dependent on external agents [104]. Additives, for instance sulfonate dispersants, epoxy, or phosphite derivatives, are carefully dosed to the lubricant to form protective tribofilms at tribological conditions [105]. More information regarding the molecular science of lubricant additives and its impact on tribological characteristics can be found in the scientific contribution of Minami [106].

In a typical vapour compression cycle, the lubrication oil frequently escapes the compressor entering in contact with the refrigerant [107]. Once this happens, the oil mist is carried by the hot discharge gas to the condenser where it mixes with the liquid refrigerant and passes through the liquid line to the evaporator. As heat is being removed from the media to be cooled, the liquid refrigerant vaporizes while an oil film remains in the evaporator. In case of operating an azeotropic blend, the more volatile component may well escape the lubricant-refrigerants mixture at a greater speed rate as the oil gets enriched by the least volatile specimen. This process has two main consequences: it affects the level of lubrication needed for compression, and it increases the resistance for heat transfer in the heat exchangers. Jia *et al.* [108] quantified this effect in their study on the enthalpy change ratio and non-evaporated quantity at different oil circulation mass fractions and superheats. Certainly, most mechanical damages to reciprocating refrigeration compressors are attributable to inappropriate greasing of the sliding nodes, as properly acknowledged in the literature [109]. This development is explained by means of the accumulation of oil into the heat transfer devices or through the partial absorption of the same by refrigerants (via natural convection and molecular diffusion mechanism), as extensively assessed with 4th-generation refrigerants and blends like R1234yf, R1234ze(E), and R407C in multiple studies [110–112].

As a result, lubricity of the resulting oil-refrigerant mixture, the so-called “working fluid”, is diminished under regular process conditions. Nonetheless, if the working fluid has an appropriate solvability degree in the air conditioning operational range, the return of oil to the compressor is favoured and the material deterioration progressively gets undermined. Consequently, gas–oil miscibility and solubility are important criteria in selecting the proper lubricant for a cooling specified process, as both have a direct impact on the efficiency or Coefficient of Performance (*COP*), a primary focus in current studies [113]. Besides the working fluid intrinsic properties, the durability of AC equipment is also dependent on the presence or absence of oil synthetic additives,

although this effect is out of the scope of this work. Pentaerythritol esters (PECs), which are linear, branched and cyclic-chained esters are the main precursors and components of polyol esters (POEs) lubricants. They have captured researchers' attention in the context of searching for compatible low GWP refrigerants-lubricant pairs, with a large amount of experimental studies regarding PECs with R1234yf and R134a, as well as other fluorinated refrigerants including R1234ze(E), R32, R152a, R143a and R125 recently published [114–118]. PECs are excellent solvents and their use is also beneficial to dissolve most of residual impurities, for instance moisture, compressor wax and mineral oils in converted heat pump plants [119], preventing the fluid line from clogging in the most sensitive parts of the system (filters, vanes and valves). A throughout evaluation of POEs interactions with R450A was performed by Chen and collaborators [120], concluding that the implementation of this family of lubricants provides encouraging solubility and viscosity benefits from a thermodynamic point of view. This conclusion was later reinforced in further contributions, where POEs were used in the design of R450A industrial refrigeration circuits [121–123]. However, an equivalent modelling or experimental systematic study for R513A is still missing. In addition to PECs, the Polyethylene Glycol Dimethyl Ethers (PEGDMEs) family has also been explored as alternative lubricants. A high degree of interaction between refrigerant R134a and synthetic polyalkylene glycol-type fluids was proven in previous engineering efforts [124], successfully corroborating their use as compressor lubricants in R134a AC circuits. Effectively, there is numerous VLE data available for mixtures of PEGDMEs with R134a [124–130], while data for R1234yf, is very scarce [131].

2.1.3. The return of natural refrigerants

Predominantly, hydrofluorocarbon R32 is emerging as the most popular choice for mid-GWP refrigerant designs [38], closely followed by HFO R1234yf, and saturated hydrocarbon R290 [82,132], as can be clearly identified in **Table 2.1**. Refrigerants including R152a, R1234ze(E), and R600a also find usage [133–135], albeit to a lesser extent, while the broadly used agents R134a and R227ea, are currently experiencing a downturn in adoption, a trend largely driven by their higher GWP [136]. Newly introduced refrigerants [137], aligning with the latest EU regulations [37], such as dimethylether (RE170), 1,1-difluoroethylene (R1132a), trans/cis-1,1,1,4,4,4-hexafluoro-

2-butene R1336mzz(E/Z), trifluoroiodomethane (R13I1), and notably CO_2, are beginning to surface as viable low-GWP options, although their presence remains limited in the market. Particularly, CO_2 is distinguished by its potential [57–59], owed to its non-flammability and environmental friendliness in terms of GWP, despite facing technical challenges arising from its high critical pressure and low critical temperature, limiting its range of applications compared to standard F-gases. This limitation, capping CO_2 at 3-6% in commercial blends like R445A and R455A, is being reconsidered [138,139] by industry professionals who are increasingly balancing environmental benefits over safety standards, in response to evolving directives set by governmental authorities. Hence, the presence of CO_2 in refrigerant mixtures has been quite limited during the last 40 years. However, as abovementioned, this paradigm has changed due to the need for lower GWP alternatives, where the addition of CO_2 can help to reach this target. Therefore, there is a clear opportunity to delve deeper into CO_2-based mixtures with a wider array of components, such as HFCs, HFOs, HCFOs, and HCs, targeting improved properties. This scenario reveals a substantial scope for innovative development in refrigerant technology, particularly emphasizing the role of carbon dioxide, which could be a game-changer in the pursuit of environmentally sustainable cooling solutions. Hence, HFOs, HFCs and CO_2 mixtures are of great importance for the practical appeal to reduce the ignition temperature of the first, decrease the GWP of the second and simultaneously, improve the efficiency of the last afterwards declining the equipment's designing pressure and hence, operational cost. Recent contributions [140] have addressed this need by assessing various important properties when retrofitting 3rd refrigerants, including *COP*, pressure, irreversibility rate, exergy efficiency, and volumetric cooling capacity, leading to the identification of CO_2 zeotropic mixtures as promising alternatives.

Interestingly, CO_2-based mixtures with refrigerants have undergone extensive study, with their saturation properties for common HFCs like R32, R125, R134a, R152a, R227ea, R23, and R41 well-documented in the NIST database [141]. The database's scope was later extended to cover saturated hydrocarbons and hydroolefins including R170, R290, the R600-R601a sequence, R1150, R1270, along with dimethylether, R1234yf, R1234ze(E), and the novel R13I1 [142]. Advancements in this field have led to the generation of new saturation data for CO_2 mixtures with novel cooling agents, including R1123 [143], R1243zf [144], R7200 [145], R1234ze(Z) [146], R1336mzz(E)

[146], and R1233zd(E) [147] from 2019 to 2023. Key properties like density [142], viscosity [148], and thermal conductivity [149] have also been assessed for mixtures with selected alkanes, alkenes, R1234yf, R32, R134a, and R125. Data on density is also available for CO_2 blends with refrigerants like R1234ze(E), R152a, and R41, enhancing the understanding of their intrinsic behavior in a range of applications [142].

Also, a study [150] was conducted to find the best conditions for a CO_2 refrigeration system using mechanical sub-cooling, achieving peak performance at ambient temperatures of 25.0°C, 30.4°C, and 35.1°C, and evaporation temperatures between -15.6°C and -4.1°C. In recent years, CO_2 has gained significant attention for use in large-scale cascade cycles due to its safety, availability, and low cost, as highlighted in some reviews on natural refrigerants [151,152]. CO_2 is becoming a preferred choice for supermarket refrigeration in Europe, with around 16000 systems installed by late 2018, covering 14% of the market. Projections suggest 4000 to 6000 new installations annually from 2020 to 2030, potentially totaling 65000 to 85,000 by 2030. In the U.S., stricter regulations by the EPA and safety concerns about ammonia, particularly for systems over 1000 lbs, are also driving the shift towards CO_2 [59].

To conclude with viable, efficient natural refrigerants, hydrocarbons are considered excellent, environmentally friendly alternatives to HFCs, but their high flammability poses risks. Consequently, it is recommended to limit the amount of hydrocarbon refrigerant in domestic systems to 200 grams, as advised by James *et al*. [153]. Koh. *et al*. [21] recommend an even stricter limit of 150 grams for small, sealed systems, which remains practical due to hydrocarbons' lower charge requirements compared to synthetic refrigerants. In commercial settings, refrigerants are used in heat pumps and chillers from 0.3 to 150 kW [154]. R290 and R600a are common in domestic refrigerators, while R290 and R170 are used in commercial medium-temperature and low-temperature systems, reaching -80°C. Multiple manufacturers [22] have reported that mobile air-conditioner (MAC) systems operating with R290 are, on average, 10% more energy-efficient over comparable units employing R404A, with added benefits of lower costs and enhanced cooling performance. Superior performance is also noted as a drop in for R12 [155]. R600a and its blends are prevalent in domestic refrigeration across the European Union [27], and, along with R290, is also operated into nowadays air conditioners [53]. Furthermore, research by Saleh and Wendland [156] and Chang [157]

et al. further confirmed propylene as a viable replacement for HFC R22, offering improved *VCC* and efficiency. Additionally, certain hydrocarbon blends (e.g., a 50/50% mixture of ethane and isopropane) have proven more efficient than R134a, resulting in a 4% reduction in energy use while requiring an optimal charge load [158]. Abraham and Mohanraj [159] further demonstrated that the HFC/HC mixture R430A significantly enhanced the coefficient of performance, achieving an increase of 9% to 20%, while simultaneously decreasing energy consumption by 6% to 11% in MAC systems compared to R134a. In a separate study, Rasti et al. [160] evaluated the application of R436A and R600a in domestic refrigeration units, revealing that these refrigerants reduced energy consumption by 14.6% and 18.7%, respectively, relative to R134a. Furthermore, the total equivalent warming impact was reduced by 16% for R436A and 21% for R600a.

Water is primarily employed in absorption chillers due to its high latent heat, but its low vapor pressure restricts its use in standard vapor compression systems [161]. Ammonia, with its high specific heat capacity and minimal global warming, provides excellent heat transfer for condensation and evaporation in heat pumps up to around 90 °C. Nevertheless, its toxic and corrosive nature demand rigorous safety measures, significantly increasing the equipment's safety expenditures [162]. Air is used in specialized air-cycle refrigeration systems, such as those in aircraft, but its lower heat transfer efficiency limits its use in larger, conventional systems [163]. In light of global HFC phase-down regulations and the limitations of using natural refrigerants like water, ammonia, or air, the industry is moving towards HFOs, blends with HFC, CO_2, and/or HCs, as outlined in **Figure 2.1**. As observed, future refrigeration technologies are designed to achieve low GWP while simultaneously improving energy efficiency, optimizing thermodynamic performance, and reducing flammability and toxicity.

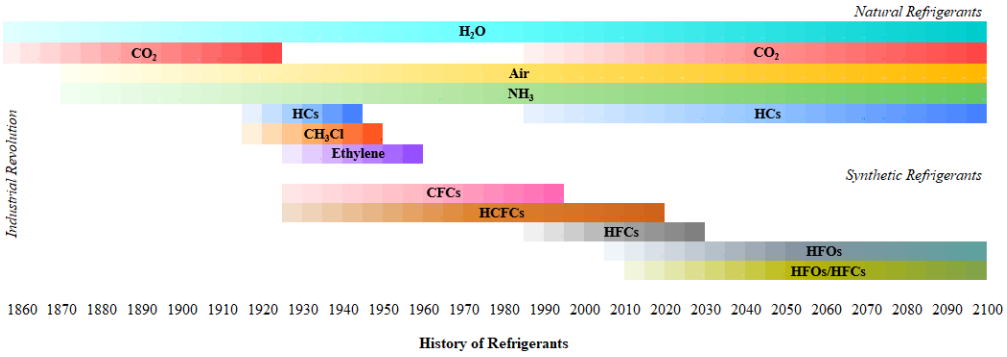

Figure 2.1. *Evolution of refrigerants by family from the industrial revolution to the present, with projections into the 22nd century.*

2.2. Modeling of refrigerants

Ascertaining the potentiality of these alternative refrigerants on technical facets is relevant but given a secondary priority as opposed to the more urgent environmental facets, hence their limited availability in the literature [48,84,85,164–168]. As already mentioned, eplacing the current commercially used 3rd generation refrigerants with a low GWP alternative is not straightforward, and might lead to retrofitting the existing system, resulting in a trade-off, often overlooked, between meeting environmental constraints and incurring additional costs or compromising system performance [26,77,169]. To blame for this is the lack of experimental data on the physicochemical properties of alternative refrigerants, essential for their accurate technical evaluation and projection on industrial scale [170]. This is expected as experimentally obtaining all relevant properties is quite taxing in temporal and monetary terms, given the number of different properties, varying operating conditions, and possible working fluids. As such, pragmatic and robust computational tools provide a possible remedy to overcome this hurdle, with the capability of rapidly determining potential HFCs-replacements, satisfying environmental and technical requirements. These tools allow for the evaluation of numerous compounds with minimal experimental dependence through the usage of transferable molecular parameters.

Notwithstanding, it remains difficult to assert the adequacy of one thermodynamic model over another for property predictions, as all these models suffer from some limitations, with no singular universal model. For example, molecular simulations, although accurate and with predictive power, are computationally expensive for force-field parametrization and data generation over a wide range of operating conditions of interest, as required for the detailed characterization of these compounds. Conversely, the accuracy of purely predictive COSMO-based models is qualitative rather than quantitative, which can be enhanced through adjusting some of the model's parameters on the expense of losing its fully predictive nature [171]. Lastly, molecular-based EoS such as SAFT require the availability of experimental data [172], even if somewhat limited in terms of type and range [173], to regress the parameters descriptive of the pure refrigerant. Granted these parameters can be transferable across molecular families with

specific analogues molecular characteristics [174], yet this approach is not fully foolproof alonw when applied to new compounds with unavailable data.

Conversely, the combination of different modeling approaches exploiting the synergetic benefits of several modeling tools have proved to be a beneficial endeavor for accelerating the development of molecular modeling tools for assessing emerging low GWP refrigerants, even in the absence of data. Amid numerous research efforts, Raabe and collaborators [175] coupled molecular simulations and PC-SAFT to study the phase equilibria of some 4th generation refrigerants with 3rd generation refrigerants and CO_2. These contributions relied on molecular simulations for data generation in the absence of experimental data. The simulation data was then used to parametrize the more rapid molecular-based EoSs, enabling extrapolation of property measurements at industrially relevant conditions without incurring high computational costs.

2.2.1. Advanced molecular-based models

With the rise of thermodynamic modeling approaches and computational power, such paradigms have been successfully developed for varying applications such as screening of materials for CO_2 capture [176–180], and solvents for other separation processes [181–184]. However, the main focus of this thesis lies on how computational modeling tools can be pragmatically employed for the rational design of refrigerant blends, taking into account imposed environmental and technical constraints [66,91,185,186]. With these tools, a multitude of possible blends can be rapidly, efficiently, and reliably screened with minimal need for experimental data, while being sufficiently flexible to examine diverse ranges of applications and amendments in environmental legislations. Yang *et al.* [187] applied entropy scaling with the REFPROP [188] reference EoS to model the thermal conductivity of several pure and mixed refrigerants. A review by Bell *et al*. [142] noted the adequacy of NIST's REFPROP semi-empirical model [188] for engineering applications, however, raising concerns on its predictive accuracy, parameters transferability, and extensive need for experimental data for new blends.

2.2.1.1. SAFT

Molecular-based equations of state such as those routed on the Statistical Associating Fluid Theory (SAFT) [189] have become indispensable tools in modeling the thermodynamic behavior of complex fluids. These have rigorous physical basis from statistical mechanics, enabling them to accurately capture the effect of intermolecular interactions (*i.e.,* dispersive, associating, polar) on macro-level phenomena. This is an added edge over conventional EoSs, that are incapable of explicitly modeling polar interactions governing the behavior of 3rd and 4th generation refrigerants and other green substances of polar nature [190]. As announced in the work of Goetzler *et al.* [164], the pressing demand for developing low GWP refrigerant mixtures makes essential to reproduce accurate phase behaviors and precisely forecast its thermophysical properties to ascertain the optimal composition ratio that establishes most favorable cooling capacities and azeotropic performances. In line with this effort, SAFT-type molecular-based EoSs have demonstrated success in accurately predicting multiple thermodynamic properties of F-based refrigerants, providing an attractive tool for the rational design of refrigerant blends [96,191,200,192–199]. Furthermore, the adoption of SAFT EoSs as a central pillar for screening tools has been steadily growing [201–205], holding the promise of similar success when applied to screening alternative eco-friendly refrigerants as drop-in replacements under the same operating conditions and technical criteria [206].

Vega and coworkers [49,83,96,103,207,208] employed different versions of the statistical associating fluid theory (SAFT) equation of state, mainly polar soft-SAFT [209], and also polar perturbed chain version (PC-SAFT) [210], to study a wide range of thermodynamic, interfacial, and transport properties of pure HFCs, HFOs, and HCFOs, demonstrating the efficacy of molecular modeling in the search for alternative eco-friendly materials [211]. More explicitly, the soft-SAFT EoS has been successfully applied to several highly non-ideal pure components and mixtures, including perfluoroalkanes [212], HFCs [196,206,213], water and aqueous mixtures [201,214–216], and 4th generation refrigerant mixtures [96,207]. Polishuk *et al.* [217] implemented PC-SAFT and the variable attractive range SAFT version (SAFT-VR) [218] to study the thermodynamic properties of 3rd generation HFCs and their mixtures. Mickoleit *et al.* [219] examined the effect of the thermodynamic model on the accuracy of screening and

designing refrigeration systems, examining models including classical cubic equations of state, COSMO-based models, and PCP-SAFT. Vinš *et al.* [220] developed a property model using PC-SAFT for the density and surface tension of 4th generation HFEs, while Wang *et al.* [221] integrated a polar version of PC-SAFT with process modeling and optimization to determine optimal refrigerants based on technical evaluation. In this thesis, following the approach of Alkhatib *et al.* [222] for highly polar fluids, the dipolar and quadrupolar nature of refrigerants is explicitly taken into account through a polar term in soft-SAFT, recently developed by Alkhatib *et al.* [209]. Although the original publication of polar soft-SAFT dates from 2020, it has been already applied to accurately predict the properties of various organic [222], hybrid solvents for acid gas removal [223], in addition to impurities [224], hydrogen [225], ketones, and benzene derivatives [209], ionic liquids-based solvents [226] and CO_2 chemisorption in diverse aqueous, anhydrous, and water-lean solvent systems [227], as well as sustainable refrigerants (one of the main contributions of this PhD thesis work) [49,103,228,229]. An additional study by Jovell *et al.* applies polar soft-SAFT coarse-grain models to assess low-GWP hydrofluoroethers as alternative working fluids in Organic Rankine Cycle (ORC) systems [230].

2.2.1.2. Molecular simulations

Of particular prominence are molecular modeling techniques, bridging microscopic characteristics of a fluid with its observable macroscopic properties, becoming indispensable for accurately predicting thermodynamic properties, and enhancing the fundamental understanding of complex systems [87,231–234]. Coarse-grained simulations are fundamental for enhancing research, enabling precise extrapolations from equations of state while efficiently supplying new data, thus reducing dependence on extensive fieldwork [235]. Outstanding contributions have been performed in this field. For instance, molecular simulation characterizations regarding HFCs have been expanded throughout the time by reason of a prolonged publication record [236–239]. Over time, the scope expanded to encompass additional properties such as shear viscosity and thermal conductivity [240], along with Joule-Thomson coefficients, Joule-Thomson inversion curves, and dew and bubble points [241,242]. Similarly, Fouad and Alasiri [243] employed molecular dynamics simulation to generate data for the viscosity and self-diffusion coefficient required for regressing parameters of polar PC-

SAFT of selected low GWP refrigerants. In parallel, a recent research by Khan *et al.* [244] has focused on molecular dynamics to study the homogeneous condensation and thermophysical properties of R134a drop-in blends, including R450A, R513A, and R515A. Moreover, a series of studies [245,246] have predicted surface tension data, a key thermodynamic property, for low-GWP refrigerants such as R1132(E) and R1132a, as well as for blends of R32/R13I1 and R1123/R13I1. Ultimately, Li *et al.* [191] established the aneotropic and azeotropic compositions of binary mixtures of HFOs (R1234yf/R1234ze(E)) and R600a using Molecular Dynamics (MD) simulations performed with the Large-Scale Atomic/Molecular Massively Parallel Simulator (LAMMPS) software. In this contribution, MD simulations were integrated with polar PC-SAFT characterizations to accurately assess the interfacial anomalies of selected refrigerant blends between HFOs and n-alkanes.

Recent advancements in molecular simulation force fields for hydrofluoroolefins and hydrochlorofluoroolefins have notably intensified, particularly for refrigerants such as R1234yf [247,248], R1234ze(E), R1123 [143], R1243zf, R1225ye(Z), R1233zd(E) [249], R1336mzz(E/Z), R1233zd(E/Z) [250], and other 4th generation refrigerants, as highlighted in the works of Raabe and coworkers [251–253]. To address the lack of experimental data, this approach [253] was further extended to novel refrigerants R1345fz, R1336yf, and R1224yd(E), not yet covered by NIST. Skvorova and Smith [254] subsequently applied these techniques to optimize refrigerant cycle designs, finding an in-depth analysis of current refrigerant force field models in the review by Raabe [25], providing insights into the future applications of molecular simulations. Following similar patterns, García *et al*. [255] performed a computational screening of forty experimentally available metal–organic frameworks (MOFs) exploring their application in adsorption air-conditioning cycles with selected low GWP refrigerants, searching for the optimal MOF-refrigerant pair through Grand Canonical Monte Carlo simulations. The computational study provides useful guidance on the MOF topology, composition and pore sizes needed to achieve the best performance with the selected low GWP refrigerants for this application. Lastly, Mambo-Lomba and Pricaud [256] developed a thermodynamic model for multiple pure refrigerants and their binary mixtures, based on different versions of the conductor-like screening model for real solvents (COSMO-RS) [257,258].

2.2.2. Correlations for accurate representation of flammability metrics

Flammability is an essential and complex characteristic of refrigerants, encompassing an array of properties and subject to various standards. According to the ANSI/ASHRAE Standard 34 [259] and ISO Standard 817 [260], flammability is classified based on a combination of factors, including heat of combustion, lower flammability limit (LFL), and laminar burning velocity. Within these standards, refrigerants are assigned to one of three classes, from Class 1, signifying no flame propagation under conditions of 60 °C and 101.3 kPa, to Class 3, signifying higher flammability with criteria such as a heat of combustion greater than 19 MJ/kg or an LFL less than 0.10 kg/m^3. A subclass "2L" adds further nuance to Class 2, imposing additional restrictions on burning velocity [261]. However, these distinctions do not always lead to a clear demarcation between flammable and nonflammable substances [262]. In fact, flammability exists on a continuum [263], where substances like propane display notable flammability, others like carbon dioxide are entirely non-flammable, and many substances fall along a spectrum of varying flammability levels in between. Certainly, the multifaceted nature of flammability does not end with classification; predicting flammability is further complicated by various factors [264,265], including flame propagation, thermal heat dissipation, and buoyancy, all of which require a deeper understanding. The work by researchers such as Egolfopoulos and Movaghar [266,267], and Linteris and Babushok [268–270] highlights the current state of understanding and the areas where more research is needed. This intricate interplay between different properties and influencing factors emphasizes the challenging yet vital nature of grasping flammability in the context of refrigerant science, a pursuit that continuously evolves with ongoing advancements in the field. The quest for an accurate representation of flammability has led to the adoption of various methodologies and metrics [261], among which the Normalized Flammability Index (NFI) has emerged as a significant tool.

In the context of this thesis, the NFI has been used to estimate flammability, and this choice is justified by several key attributes of the index. Unlike some conventional metrics, NFI takes into account a comprehensive range of factors, incorporating the heat of combustion, lower flammability limit, and laminar burning velocity [271], while also

allowing for normalization based on a reference substance. This enables a better understanding of flammability, offering insights that reflect the real-world complexity of the phenomenon, depending both on the substance's properties and the conditions of evaluation, including temperature, pressure, and mixture composition. By integrating these factors into a single index, the NFI succeeds in providing a more cohesive and holistic assessment of flammability, complementing other well-established methods such as the flame spread, flash point index, heat release rate, material calorific value, fire propagation, and limiting oxygen index. Historically, the development and utilization of the NFI trace back to 2019, as Linteris *et al*. [262] sought more accurate and comprehensive ways to understand and manage the risks associated with flammable substances. In the present-day context, the use of the NFI has expanded far beyond its original purpose, covering various fields within refrigeration, including the design of binary [272], ternary [60,273], and quartenary [274] 4th generation drop-ins along with comprehensive testing of different types of circuit configurations [275]. Further assessment of binary mixtures involving hydrocarbons and A2 or A2L components is presented in the work of Calleja-Anta *et al.* [276]. A more in-depth screening is needed to ensure the safety of new drop-ins, similar to the approach used by *Danfoss* (see **Figure 2.2**) for current refrigerants. This would address the flammability prediction gap for both novel and forthcoming 4th generation compounds.

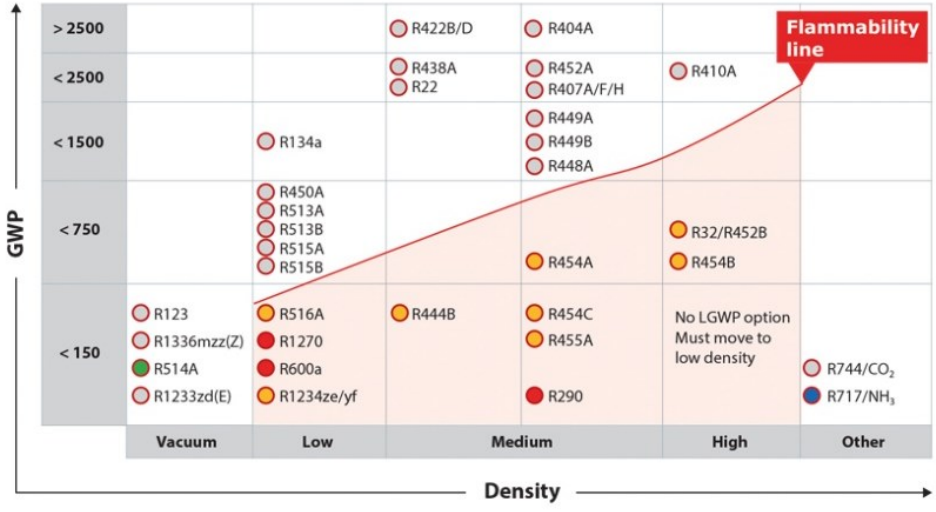

Figure 2.2. *GWP versus density for carbon-chain refrigerants (HCs, HFCs, HFOs, HCFCs), with safety classifications in different colors: grey for A1, yellow for A2L, red for A3, green for B1, and blue for B2L. Contours highlight the market availability of each mixture, with grey denoting those not available as of 2024. Adapted from reference [277].*

2.2.3. Design of experiments

Recently, several studies aimed to design refrigeration systems with low energy consumption and high efficiency by optimizing multiple sets of operating conditions, employing statistical analysis methods such as Taguchi and analysis of variance, to minimize the number of required experimental/modeling runs, as summarized in **Table 2.2**. Earlier works focused on capturing the trade-offs in selecting refrigerants for vapor compression refrigeration cycles operated with CFCs and HFCs, highlighting the role of fluid's critical temperature in enhancing the performance of the cycle on the expense of reduced cooling capacities [278,279]. Similar outcomes were pointed out from several works using a variety of statistical analysis tools such as Box-Behnken Designs (BBD) [280], Response Surface Methodologies (RSM) [281], and Complete Factorial Designs (CFD) [282] applied on hydrocarbon - or HFC-operated vapor compression refrigeration cycles (VCRCs). For novel cooling cycle configurations, the role of evaporator and condenser temperatures of the lower cycle, and the isentropic compressor efficiency on the coefficient of performance and exergy of a vapor compression cascade cycle operated with HFC-based refrigerants were highlighted [283]. The study by Ustaoglu *et al.* features pure CO_2, as well as NH_3, and the 4^{th} generation HC/RE170 blend R510A, as listed in **Table 2.1**, by means of an $L_{27}(3^{10})$ Taguchi array for experimental optimization. Similar analysis focused on minimizing exergy destruction and tuning control factors for R600a-operated vapor compression-based refrigeration [284,285], and optimum design of adiabatic capillary tubes in VCRCs using HCs refrigerants and their blends [286]. Further experimental studies on R600a-based air conditioning designs have measured the *COP*, as well as technical properties such as cooling capacity, discharge line temperature, and pressure ratio using an ANOVA design [287]. The application of statistical tools for system optimization even extended into heat pumps and organic Rankine cycles [288–293], and other novel technologies such as absorption refrigeration [294–297]. Additional insights into carbon dioxide and water as refrigerants are provided in [293], where Taguchi's orthogonal arrays are assessed to enhance the thermal efficiency of an ORC intercooler cycle.

Table 2.2 highlights the limited application of system optimization based on statistical analysis for cooling cycles operated with 4th generation refrigerants, considering the deployment of new units would be solely operated with low GWP refrigerants, in line with imposed environmental and governmental regulations. This would depend on determining optimal low GWP refrigerants satisfying environmental, safety, and technical requirements for new cooling cycles, followed by determination of optimal operating conditions and cycle configurations for these promising refrigerants that would invariably maximize technical efficiency and minimize cost and environmental footprint. Additionally, the majority of the body of literature is merely focused on optimal energetic and exergetic performance, disregarding their possible effects on economic and environmental performance.

Table 2.2. *Summary of systems, refrigerants, and statistical methodologies applied in the literature, including the type of DoE and outcomes/responses of the studies*.

System	Fluids	Research	Type of DoE	Responses	Ref.
CRS	R744, R404A, R410A, R717, R134a, R510A	Experimental	$L_{27}(3^{10})$ and ANOVA	*COP*, η_{UI}	[283]
VCRC	R600a	EES and Experimental	$L_9(3^4)$ and ANOVA	*COP*, $\dot{m}$, *H*, *S*	[284]
VCRC-HX	R600a and R134a	Experimental	$L_8(2^2 \cdot 4^1 \cdot 2^2)$ and ANOVA	*Exergy Analysis*	[285]
VCRC	R290 and R600 Mixture	Experimental	$L_{16}(4^5)$	$\dot{m}$	[286]
VCRC	13 CFCs	CSD EoS	FFD	*COP*, *CC*	[278]
VCRC	R410A	ASHRAE and Experimental	CFD	*Coil capacity*	[279]
VCRC	R134a	Experimental	BBD and ANOVA	*COP*, E_a	[280]
VCRC	R450A	Experimental	RSM and ANOVA	*COP*, *CC*, P_{comp}, *DLT*, $\dot{m}$	[281]
VCRC	R600a	Experimental	CFD	$\dot{m}$	[282]
VCRC	R600a and LPG	Experimental	ANOVA	*COP*, *CC*, ω_c, *DLT*, P_R	[287]
VCHP	R11, R12, R22, and BM	Experimental	$L_{16}(4^5)$ and ANOVA	*COP*, η_{UI}	[288]
VCHP	R22, R407C, and BM	Experimental	$L_{25}(5^6)$ and ANOVA	*COP*, η_{UI}	[289]
VCHP	R22, R404A, and BM	Experimental	$L_{25}(5^6)$ and ANOVA	*COP*, η_{UI}	[290]
MHP	R134a	Experimental	$L_{27}(3^9)$, RSM and ANOVA	*COP*	[298]
ORC-HX	R123, R245fa, R600	Self-designed model	$L_{27}(3^9)$ and ANOVA	*Thermal efficiency*	[291]
ORC-HX	R123, R245fa, R600	Self-designed model	$L_{27}(3^9)$, GRA and ANOVA	*1st and 2nd law efficiency*	[292]
ORC-HX	R134a, R717, R718, R236fa, R245fa, R600a	NA	$L_{18}(6^1 \cdot 3^2)$ and ANOVA	*Thermal efficiency*	[293]
ARS	NH_3-H_2O	Self-designed	$L_{27}(3^8)$, GRA and ANOVA	*COP*, *eCOP*	[294]
ARS	NH_3-H_2O	EES	$L_{16}(4^5)$ and Linear Regression	*COP*, η_{UI}	[295]
ARS	LiBr-H_2O	EES	BBD and ANOVA	*COP*	[296]

ARS	LiBr-H_2O	NA	$L_9(3^4)$ and ANOVA	*COP*	[297]
GCHP	R22	Experimental	$L_{27}(3^9)$ and ANOVA	*COP*	[299]
GSHP	R22	Experimental	$L_9(3^4)$ and ANOVA	*COP*	[300]
GSHP	R22	Experimental	$L_{18}(2^1 \cdot 3^7)$ and ANOVA	*COP*, $S_{Collector}$, L_{GHX}	[301]
SAR	AcC-Methanol, Zeolite-H_2O, AcC-H_2O	Statistical based on Experimental	FFD and ANOVA	*COP*	[302]
SAR	AcC- Methanol	Experimental	CFD and ANOVA	T_{Beds} , T_{Refrig}, *COP*	[303]
LPGRS	LPG	Experimental	$L_{27}(3^9)$ and ANOVA	T_{evap}	[304]
TAR	Air/He (any inert gas)	Experimental	$L_9(3^4)$ and Regression	ΔT	[305]

CRS – Cascade Refrigeration System; VCRC – Vapor Compression Refrigeration Cycle; HX – internal heat exchanger; VCHP – Vapor Compressor Heat-Pump; MHP – Mechanical Heat-Pump; ORC – Organic Rankine Cycle; ARS – Absorption Refrigeration System; GCHP – Ground Coupled Heat-Pump; GSHP – Ground Source Heat-Pump; SAR – Solar Adsorption Refrigeration; LPGRS – Liquefied Petroleum Gas Refrigeration System; TAE – Thermo Acoustic Refrigeration.

2.2.4. Machine learning hybrid models

The recent rise of the 4th industrial revolution paved the path for integrating artificial intelligence (AI) and machine learning (ML) with molecular modeling approaches for a number of applications including rational design of new green materials, predicting thermodynamic behavior of complex systems, and accelerating development of force-fields for molecular simulations [306]. Consequently, ML techniques have become popular for their versatile capability to forecast a multitude of properties, including solubility, thermal and electrical conductivity, surface tension, vapor pressure, pH, density, viscosity, and heat capacity, among others. Notably, recent studies had employed a range of inputs including critical coordinates, acentric factor, vapor pressure, molar mass, number of fluorine atoms, and Lennard-Jones interaction parameters, to accurately describe the solubility [307,308] and liquid density [309] of F-gases. Building on this potential, **Table 2.3** offers a comprehensive overview of ML models in the literature using σ-profiles from COSMO-RS [310] as inputs, encompassing various families of compounds, thus showcasing the versatility of such predictive approaches.

Table 2.3. *ML models developed in the literature using molecular descriptors sorted by year of publication.*

Compounds Family	Property Assessed	ML Method	Ref.
IL	Density, Molar Liquid Volume	MLR	[311]
Solvents	Polarizability	RBNN	[312]
IL	Density	NN	[313]
IL	Toxicological Effect	MLP	[314]
Organic Solvents + IL	Solvatochromic Parameter	RBNN	[315]
IL	Activity, Enantio-Selectivity	ANN + MLR	[316]
IL	Viscosity	MLR + SVM	[317]
IL	Heat Capacity	MLR + ELM	[318]
IL	H_2S Solubility	QSPR + ELM	[319]
IL	Ecotoxicity	MLR + MLP	[320]
IL	Refractive Index	ELM + MLR	[321]
IL	Henry's Law Constant	MLR + SVM + ELM	[322]
IL	Viscosity	ANN	[323]
DES	Viscosity	MLR + ANN	[324]
Cosmetic Oils	Viscosity	MLP	[325]
DES	Viscosity, Density	MLR	[326]
Ester-alkane	Mixing Energy	ANN	[327]
DES	Electrical Conductivity	MLR	[328]
ES	Density, Viscosity	MLR	[329]
IL	Viscosity, Conductivity, Density	SVR	[330]
ES	pH	MLR + ANN	[331]
DES	CO_2 Solubility	RF	[332]
Chemicals	Abraham Parameters, Solvation Free Energy, Solvation Enthalpy	DNN	[333]
Chemicals	Molar Mass, Boiling Temperature, Vapor Pressure, Density, Refractive Index, Aqueous Solubility	DNN	[334]
F-Refrigerants	Vapor Pressure	ANN	[335]
DES	pH	MLR + PLR + ANN	[336]
DES	Surface Tension	ANN	[337]
DES	Electrical Conductivity	ANN	[338]
IL + DES	Infinite Dilution Activity Coefficients	FM + DNN	[339]
Polymers	Glass Transition, Melting Temperature	ANN	[340]
DES	Eutectic Composition, Melting Temperature	DT + MLR	[341]
IL	Henry's Law Constants	SVM + RF + MLP	[342]
IL + DES	Thermal Conductivity	ANN	[343]
IL	Surface Tension, Speed of Sound	MLR + GBT	[344]
DES	CO_2 Solubility	ANN	[345]
DES	Heat Capacity	MNLR + ANN	[346]

Ionic Liquids (IL), Deep Eutectic Solvents (DES), Multiple Linear Regression (MLR), Radial Basis Neural Network (RBNN), Neural Network (NN), Multi-Layer Perceptron (MLP), Artificial Neural Network (ANN), Support Vector Machine (SVM), Extreme Learning Machine (ELM), Quantitative Structure-Property Relationship (QSPR), Random Forest (RF), Deep Neural Network (DNN), Piecewise Linear Regression (PLR), Factorization Machine (FM), Decision Trees (DT), Gradient Boosting Tree (GBT), and Multiple Non-Linear Regression (MNLR).

This integration of ML with molecular modeling approaches such as COSMO-RS has found success in predicting the thermodynamic behavior of several classes of green materials [313,328,329,331,347–352]. A wide-range of properties ranging from viscosity and pH to vapor pressure, surface tension, and conductivity have already been estimated through the use of quantum chemistry descriptors applied to ILs [316,323,343], DESs

[336–338,343,345,346], ESs [331], ester-alkanes [327], fluorinated refrigerants [335], and polymers [340]. However, these models remain purely empirical and limited in terms of functionality, with one model descriptive of a single thermodynamic property, thus requiring multiple models and expansive databases to cover a wide range of properties and fluids. In this manner, a significant gap remains in the adoption of machine learning techniques within refrigeration framework, particularly for advanced equations of state such as the polar soft-SAFT. Therefore, it can be expected that such an integration with molecular-based EoSs will exploit their rapid, accurate, and holistic modeling features for obtaining thermodynamic properties of emerging green refrigerants, combining large data processing with physics-oriented modeling. However, only two publications [335,353] stands as the sole documented instance in the literature to pioneer the use of ML, specifically through ANN, for evaluating F-based refrigerants through conductor-like screening model (COSMO) descriptors, underscoring its unique importance in this domain.

Even though accurate SAFT-based EoS have demonstrated a highly predictive ability [228], the use of binary parameters to describe mixture behavior remains imperative, decreasing the capacity of extrapolation to other systems and conditions. In this regard, current scientific efforts aim to cover these gaps by AI methods with molecular equations. In particular, the integration of the polar soft-SAFT EoS with AI-based approaches mark a significant advancement in the urgent demand for environmentally friendly and efficient cooling agents, aligning with global initiatives to combat climate change. This holistic approach is dependent on COSMO molecular descriptors as input parameters, enabling rapid and cost-effective first-screening predictions without the need of experimental efforts.

Chapter 3. Methodology

For the research work developed in this PhD thesis, five methodologies were employed. These include the use of the polar soft-SAFT to thermodynamically characterize refrigerants, and the definition of process configurations to simulate various cooling cycles, such as the single stage (SS), liquid-to-suction line heat exchanger (LL/SL-HX), two stage (TS) - VCRCs, in addition to cascade cycles. Additionally, a comprehensive 4E analysis, integrating a life cycle and a techno-economic assessment, is described. This chapter also outlines the core principles of the statistical methods used in the thesis, along with hybrid machine learning techniques, including artificial neural networks with COSMO σ-profiles as inputs.

3.1. Polar soft-SAFT

The term SAFT stands for Statistical Associating Fluid Theory and comprises a set of molecular based equations of state (EoS) based on Wertheim's first-order thermodynamic perturbation theory [354–357] for associating fluids. There are several versions of SAFT available, most of them differing on the description of the interactions of the reference fluid. SAFT-type equations are expressed in terms of the Helmholtz energy of a fluid (A) from which all other thermodynamic properties can be obtained by the corresponding derivatives. In SAFT, A (see **Eq. (3.1)**) is obtained as the sum of independent microscopic contributions, explicitly accounting for van der Waals interactions and strong short-range directional (associative) forces of a fluid or mixture of n components.

$$A = A^{ideal} + A^{ref} + A^{chain} + A^{assoc} + A^{polar} \tag{3.1}$$

where A^{ideal} corresponds to the ideal contribution to the Helmholtz energy, A^{ref} accounts for the influence of the reference monomeric fluid, A^{chain} includes the energy for the chain formation between monomers, A^{assoc} comprises associative forces, for instance hydrogen bonds that molecules may be affected by, and A^{polar} accounts for the dipole and quadrupole moments of the molecule in addition to the molecular charge distribution. A graphical representation of these effects is provided in **Figure 3.1**.

On the basis of the reference term, soft-SAFT [358], contains a Lennard-Jones (LJ) intermolecular potential, being calculated by using the expression provided by Johnson et al. [359], to concurrently consider repulsive and dispersive forces into the same term.

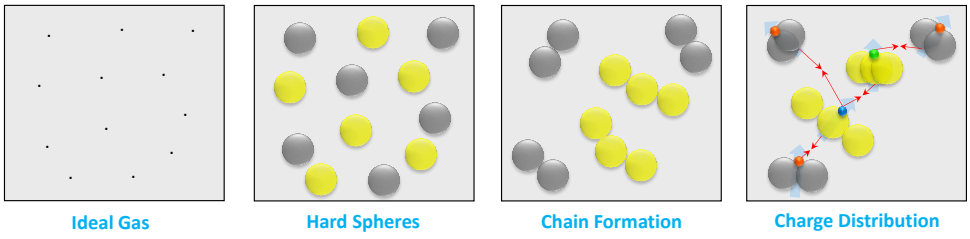

Figure 3.1. *soft-SAFT contributions to ideal, reference, chain, and polar terms, and its coarse-grain model for common dipolar refrigerants.*

The chain and association term in **Eq. (3.1)**, both obtained from Wertheim's TPT1, are readily applicable to mixtures, while the van der Waals one-fluid theory (vdw-1f)

[358] is used to extend the reference term, taking into account the differences the molecular volume and energy of the distinct compounds integrating the mixtures as an average value from those of the pure components. In this manner, the size and energy parameters for the resulting conformal pseudo-binary fluid can be expressed as follows:

$$m = \sum_{i=1}^{n} x_i m_i \tag{3.2}$$

$$\sigma^3 = \frac{\sum_i \sum_j x_i x_j m_i m_j \sigma_{ij}^3}{(\sum_i x_i m_i)^2} \tag{3.3}$$

$$\varepsilon\sigma^3 = \frac{\sum_i \sum_j x_i x_j m_i m_j \varepsilon_{ij} \sigma_{ij}^3}{(\sum_i x_i m_i)^2} \tag{3.4}$$

Hence, the van der Waals one-fluid theory permits to evaluate the crossed size and energy parameters by applying the modified Lorentz-Berthelot rules stipulated in **Eqs. (3.5)** and **(3.6)**.

$$\sigma_{ij} = \eta_{ij}\left(\frac{\sigma_{ii} + \sigma_{jj}}{2}\right) \tag{3.5}$$

$$\varepsilon_{ij} = \xi_{ij}\left(\varepsilon_{ii}\varepsilon_{jj}\right)^{1/2} \tag{3.6}$$

being η_{ij} and ξ_{ij} the size and energy binary parameters correcting deviations as a consequence of the presence of asymmetrical compounds with different size and energetic interactions (equivalent to 1-l_{ij} and 1-k_{ij} in classical cubic EoS). These parameters are fitted to phase equilibrium binary data, when needed, being soft-SAFT used in a predictive manner when both values are set to unity for mixture calculations.

From the Wertheim theory [356], the chain (**Eq. (3.7)** and associative (**Eqs. (3.8)-(3.10)**) contributions can be fully expressed, including the energy of the system due to the formation of monomer chains and the accurate description of the behavior of multi-component mixtures with hydrogen bonds and other associative interactions [360].

$$A^{chain} = RT \sum_i x_i (1 - m_i) \ln g_{ij}^{LJ} \tag{3.7}$$

$$A^{assoc} = RT \sum_i x_i \sum_\alpha \left(\ln X_{\alpha,i} - \frac{X_{\alpha,i}}{2}\right) + \frac{M_i}{2} \tag{3.8}$$

$$x_i{}^a = \frac{1}{1 + \rho \sum_{j=1}^{n} x_j \sum_{B=1}^{M_j} x_j{}^B \Delta^{A_i B_j}} \tag{3.9}$$

$$\Delta^{A_iB_j} = d_{ij}{}^3 g_{ij} \kappa^{A_iB_j} \left(e^{\frac{\varepsilon^{A_iB_j}}{k_B T}} - 1 \right) \quad \textbf{(3.10)}$$

where R is the universal ideal gas constant equivalent to the product amid Avogadro's number N_A and the Boltzmann constant k_B, T is the absolute temperature, g_{ij}^{LJ} the contact radial distribution function of a LJ chain and m_i the chain length parameter of molecule i. The chain term may be assimilated by a non-integer number, since when working with real compounds, spheres may possibly not be perfectly aligned and thus, the Lennard-Jones potential has no choice but to allow a certain degree of overlapping

In contrast, association depends on X_α which relates the fraction of molecules not bonded to site α and M_i, reminiscent of the overall number of association sites attributable to each component. This fraction can be solved through a mass action balance that depends on two additional parameters that define a site of association: the site-site bonding-volume of association $K_{\alpha\beta,ii}^{HB}$ and the site-site association energy $\varepsilon_{\alpha\beta,ii}^{HB}$.

The soft-SAFT variant has been corroborated for a wide-range variety of compounds with reference to amines, glycols, glymes [361], H_2O [215], H_2S [201], nitriles [362], DES [363], ILs [207], HFCs, HFOs [96] and even biodiesels and alcohols [364]. More details of the soft-SAFT association and chain terms can be found in the literature [214,358,365–371].

Soft-SAFT has become an accurate screening tool for the thermodynamic characterization of fluids, by coupling it with other theories, including specific treatments that allow quantitative estimations of the critical region [372], calculation of interfacial properties [373], estimation of transport properties [213] and, recently, by explicitly incorporating the polar interactions [209]. A brief explanation on the polar version of the soft-SAFT EoS is presented next.

In polar soft-SAFT, the dipole or quadrupole moments are explicitly considered by adding a polar term, A^{polar}, into **Eq. (3.1)**. The perturbation term was first introduced by Twu and Gubbins [374,375] and then extended to chain fluids [376]. For the case of dipolar and quadrupolar fluids, the change in free energy due to polar interactions is defined in **Eq. (3.11)** for a mixture of polar and non-polar spherical segments. Accordingly, A_2 and A_3 refer to the second and third order terms in the perturbation

expansion theory and are directly related to the dipolar/quadrupolar moment (μ_i / Q_i) of the molecule (see $A_{2/3}^{D/Q}$ and $A_{3A/B}^{Q}$ in **Eqs. (3.13)-(3.14)** in addition to **Eqs. (3.18)-(3.20)**). Higher order terms may be estimated using the Padé approximate [377].

$$A^{polar} = \frac{A_2}{1 - \frac{A_3}{A_2}} \tag{3.11}$$

$$A_2 = A_2^D + 2A_2^{cross} + A_2^Q \tag{3.12}$$

$$A_2^D = -\frac{2\pi N \rho_N}{3k_B T} \sum_{ij} x_i x_j \frac{\mu_i^2 \mu_j^2}{\sigma_{ij}^3} J_{ij}^{(6)} \tag{3.13}$$

$$A_2^Q = -\frac{14\pi N \rho_N}{5k_B T} \sum_{ij} x_i x_j \frac{Q_i^2 Q_j^2}{\sigma_{ij}^7} J_{ij}^{(10)} \tag{3.14}$$

$$A_3 = A_{3A} + A_{3B} \tag{3.15}$$

$$A_{3A} = 3A_{3A}^{cross1} + 6A_{3A}^{cross2} + 6A_{3A}^{cross3} + 3A_{3A}^{Q} \tag{3.16}$$

$$A_{3B} = A_{3B}^{D} + 3A_{3B}^{cross2} + 3A_{3B}^{cross3} + A_{3B}^{Q} \tag{3.17}$$

$$A_3^D = \sqrt{\frac{14\pi}{5}} \frac{32\pi^3}{135} \frac{{N\rho_N}^2}{(k_B T)^2} \sum_{ijk} x_i x_j x_k \frac{\mu_i^2 \mu_j^2 \mu_k^2}{\sigma_{ij}\sigma_{ik}\sigma_{jk}} K_{ijk}^{(222,333)} \tag{3.18}$$

$$A_{3A}^Q = \frac{144\pi N \rho_N}{245(k_B T)^2} \sum_{ij} x_i x_j \frac{Q_i^3 Q_j^3}{\sigma_{ij}^{12}} J_{ij}^{(15)} \tag{3.19}$$

$$A_{3B}^Q = \sqrt{2002\pi} \frac{32\pi^3}{2025} \frac{{N\rho_N}^2}{(k_B T)^2} \sum_{ijk} x_i x_j x_k \frac{Q_i^2 Q_j^2 Q_k^2}{\sigma_{ij}^3 \sigma_{ik}^3 \sigma_{jk}^3} K_{ijk}^{(444,555)} \tag{3.20}$$

$A_{2/3}^D$ and $A_{2/3A/3B}^Q$ represent the second- and third-order perturbation terms for dipole-dipole and quadrupole-quadrupole interactions, respectively, N is the number of molecules, ρ_N is the number density, k_B the Boltzmann constant, σ_i the diameter of an equivalent sphere with the same volume as the reference molecule, while J and K are the angular pair and triplet correlation functions for the LJ fluid referred in [378], with superscripts representing the relative positions and the interparticle distances. The integrals were calculated numerically based on molecular simulation data and then approximated with functions of reduced density and pressure, covering a broad range of states. This accounts for multipolar interactions by placing localized polar moments on specific segments of the chain molecules, oriented perpendicular to the molecular axis.

In this thesis, the focus will be on the polar soft-SAFT equation of state, *intentionally omitting the associative term to limit the number of parameters and minimize the potential for overfitting*. This is, of course, done due to the specific nature of the molecules studied. Most F-gases (HFCs and HFOs) exhibit polarity, but do not have a strong hydrogen bonding, so it is assumed that the polar term can reproduce this effect without the addition of an association model. As a result, a dipolar non-associating fluid requires a total of five molecular parameters: the segment diameter σ, the LJ dispersive energy between segments ε, the chain length m, the dipole/quadrupole moment μ/Q and the molecular fraction being affected by the dipole x_p.

In order to diminish the number of adjustable parameters, the polar parameters μ and x_p are fixed a priori in accordance with the experimental vacuum dipole moment and the molecular charge distribution to determine the direction of the dipole moment, following the procedure of Alkhatib et al. [209,379]. Thus, only the remaining three molecular parameters need to be fitted, usually standard physical arguments. Usually, these parameters are obtained by fitting to vapor-liquid equilibrium data by minimization of **Eq. (3.21)**.

$$min(F_{obj}) = \frac{\omega_1}{N_p}\sum_{i=1}^{N_p}\left(\frac{\left|\rho_{act} - \rho_{exp}\right|}{\rho_{exp}}\right) + \frac{(1-\omega_1)}{N_p}\sum_{i=1}^{N_p}\left(\frac{\left|P_{act} - P_{exp}\right|}{P_{exp}}\right) \quad \textbf{(3.21)}$$

being N_p, the total number of experiments accomplished and ω_1, a factor that gives more weight to vapor pressure or saturated liquid density factor (in all calculations, $\omega_1 = 0.8$). In the case of lubricant species, which have extremely low vapor pressure, equilibrium data cannot be used, and optimization is done by minimizing density data as a function of temperature in one phase.

It must be noted that the previous optimization may provide several sets of parameters compatible with the experimental data, particularly for the case of lubricants (fitted to a single property). Consequently, a careful check is always needed to ensure the consistency of these parameters. This is done in two ways: 1) revising the physical meaning of the parameters to ensure transferability among members of the same family, and 2) predicting the thermophysical properties and phase behavior of additional properties not included in the fitting (such as derivative properties) and mixtures.

3.1.1. Polar soft-SAFT molecular models

In order to apply soft-SAFT to experimental systems, a coarse grain model of the molecules is first needed. These molecules involve hydrofluorocarbons (HFCs), hydrofluoroolefins (HFOs), hydrochlorofluoroolefins (HCFOs), light hydrocarbons (HCs), carbon dioxide (CO_2) and two families of lubricants: pentaerythritol esters (PECs) and polyethylene glycol ethers (PEGMEs).

As mentioned, polar interactions in dipolar (HFCs, HFOs, HCFOs) and quadrupolar (CO_2) refrigerants are addressed through the explicit polar term in **Eqs. (3.11)-(3.14)**, similar to the methodology used for determining thermodynamic properties of refrigerants with other SAFT-type equations, such as PC-SAFT [83,102,208]. The coarse-grain benchmark model is composed as chains of homonuclear polar segments. The chain length, m, monomer diameter, σ, and van der Waals energy between monomers, ε, represent molecules of $m\sigma^3$ volume and $m\varepsilon$ dispersive energy. Then, the highly directional short-range polar forces are counted by means of the vacuum experimental dipole moment, μ, placed on one of the chain spheres of the soft-SAFT representation, and the molecular charge distribution to account for the fraction of segments containing the polar term, x_p. CO_2 is characterized through the usage of compatible molecular parameters alongside the vacuum experimental quadrupolar moment, Q, and a constant x_p value of one-third, based on the assumption that the oxygen atom is the sole contributor to the molecular quadrupole moment.

The number of homonuclear LJ segments is taken based on the equivalent *n*-hydrofluoroalkane and the way the negative charge is localized within the molecular structure, as perceived in **Table 3.1** for all refrigerant specimens evaluated in the current PhD thesis. Note that colors on a molecule's van der Waals surface depict the electrostatic potential gradient. Consequently, red represents electron-rich regions with negative potential, blue indicates electron-poor regions with positive potential, green denotes neutral potential, and yellow/orange reflects intermediate values.

Table 3.1. *SMILES, and dipole moment representation for all compounds assessed in this thesis. Atoms are assigned as follows: C as gray, H as white, O as red, F as reddish, Cl as green, and I as purple*

Compound	SMILES	Dipole Representation	Compound	SMILES	Dipole Representation
R41	CF	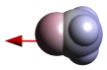	R1345fz	C=C(C(F)(F)F)C(F)(F)F	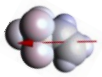
R32	C(F)F	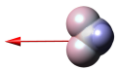	R1336mzz(E)	C(=CC(F)(F)F)C(F)(F)F	
R23	C(F)(F)F		R1336yf	C=C(C(F)(F)F)C(F)(F)F	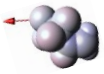
R161	CCF		R1233zd(E)	C(=CCl)C(F)(F)F	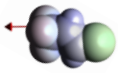
R152a	CC(F)F	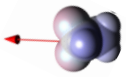	R1224yd(Z)	C(\C(F)(F)F)=C(\Cl)F	
R134a	C(C(F)(F)F)F	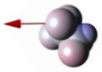	R1224yd(E)	C(\C(F)(F)F)=C(/F)\Cl	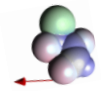
R125	C(C(F)(F)F)(F)F		R170	CC	
R245fa	C(C(F)F)C(F)(F)F	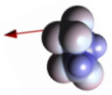	R290	CCC	
R236fa	C(C(F)(F)F)C(F)(F)F	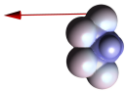	R600	CCCC	
R227ea	C(C(F)(F)F)(C(F)(F)F)F		R600a	CC(C)C	
R1123	CF=C(F)F	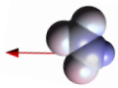	R601	CCCCC	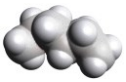
R1243zf	C=CC(F)(F)F	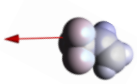	R601a	CC(C)CC	
R1234yf	C=C(C(F)(F)F)F	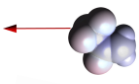	R1150	C=C	
R1234ze(E)	C(=CF)C(F)(F)F	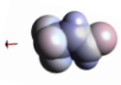	R1270	C=CC	

R1225ye(Z)	C(=C(C(F)(F)F)F)F		1-butene	C=CCC	
R1336mzz(Z)	C(=CC(F)(F)F)C(F)(F)F	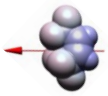	R13I1	C(F)(F)(F)I	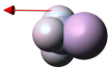
R1132a	C=C(F)F	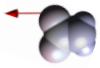	RE170	COC	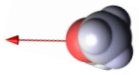
R1132(E)	C(=CF)F		CO_2	C(=O)=O	
R1234ze(Z)	C(=CF)C(F)(F)F	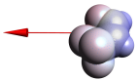	R7200	CCOC(C(C(C(F)(F)F)(F)F)(F)F)(F)F	

With reference to the lubricant characterization, PECs are represented as chains of homonuclear non-polar segments [380] given its extremely bulky properties, causing a decrease of the dipole's interaction Helmholtz free energy due to steric effects [102]. Likewise, PEGDMEs are also considered as non-associating homonuclear chainlike molecules as a result of the absence of any associative end group that would cause dipolar forces [379]. The interactions between lubricants (oxygen atom) and refrigerants (hydrogen groups) are taken into account through the dispersion term and the energetic binary parameter ξ_{ij} in **Eq. (3.6)** to correct the non-ideality of the considered mixtures.

3.2. Process configuration for simulated cooling cycles

The thermodynamic characterization done with soft-SAFT will serve to estimate the thermophysical behavior of fluids, with the aim to evaluate their performance in a refrigeration circuit. A simple single-stage VCRC (SS-VCRC) is depicted in **Figure 3.2a**.

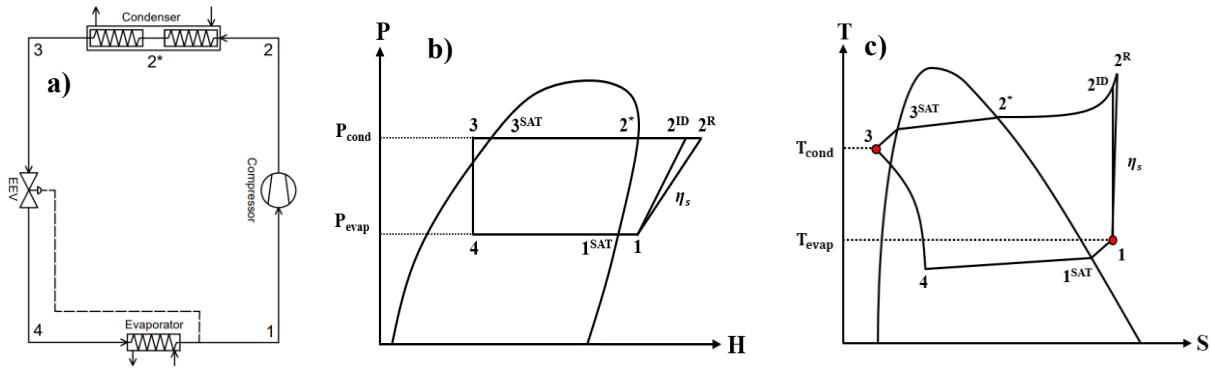

Figure 3.2. ***a)*** *Schematics for the basic SS-VCRC refrigeration cycle simulated in this thesis with its corresponding* ***b)*** *PH and* ***c)*** *TS diagrams. See text for details.*

The developed SS-VCRC operates with the non-isentropic compression of superheated vapor in the single-stage reciprocating air compressor (1 – 2), followed by the isobaric de-superheating of the working fluid in a series of shell-and-tube air-to-refrigerant heat exchangers (2 – 2^*). Condensation occurs afterward, releasing both its latent (2^* – 3^{SAT}) and specific (3^{SAT} – 3) heats to deliver a subcooled liquid phase working fluid. This is followed by temperature and pressure reductions in the electronic expansion valve (EEV) (3 – 4), with the multiphase mixture cooling the high-temperature heat sink in the evaporator coil by releasing its latent and sensible heats, reaching a single-phase superheated vapor (4 – 1).

The previous thermodynamic features can be easily interpreted in pressure-enthalpy (*PH*) and temperature-entropy (*TS*) projections, as shown in **Figure 3.2b-c**. As reflected in these Figures, a superheating and subcooling are usually applied to lengthen the lifespan of the compressor and EEV. Also, it is interesting to note that the *TS* diagrams for near-azeotropic blends (see **Figure 3.2c**) account for their phase change (*i.e.,* evaporation and condensation) along their T_G, rather than at constant temperature, as with pure refrigerants and azeotropic blends.

The assumptions for simulating SS-VCRC cycle include outlet evaporator temperature ($T_{evap} = T_1$), discharge condenser temperature ($T_{cond} = T_3$), compression yield, and superheating, or subcooling temperature drops in both heat exchangers, depending on the studied application on subsequent sections. All the *PH* and *TS* diagrams, used for evaluation of the fluid's performance, are predicted from the soft-SAFT molecular model at the chosen conditions with ideal gas enthalpy (H^{IG}) and entropy (S^{IG}) correlations from NIST REFPROP database for each refrigerant [188], with the iteration subroutines developed using polar soft-SAFT and represented in **Figure 3.3**.

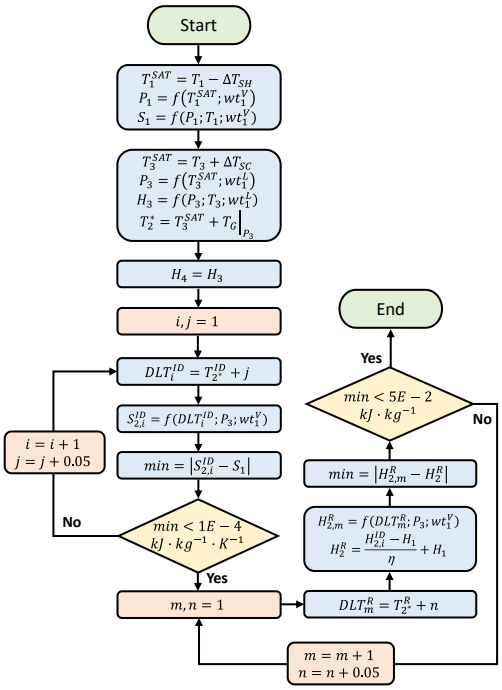

Figure 3.3. *Flowchart representation for the iteration algorithms for the SS-VCRC cycle examined in this thesis using polar soft-SAFT.*

In this thesis, additional advanced configurations have also been studied. One of them is the LL/SL-HX, whose configuration is shown in **Figure 3.4 top**. This one is similar to SS-VCRC, but with the addition of an internal heat exchanger (HX) between the evaporator's suction and liquid lines. This functions to further cool down the working fluid from the condenser outlet (3 – 3') by rejecting its heat to the working fluid exiting the evaporator (1 – 1'). This results in increased temperatures in the compressor's suction and discharge lines, while decreasing the condenser's outlet temperature, leading to enhanced cooling effect and prolonged compressor's lifetime [381].

In the specific case for optimizing the LL/SL-HX configuration, an additional target function is included, namely, the pinch point temperature (T_{PP}, as defined in **Eq. (3.30)**), which is a governing factor on the performance of waste heat recovery systems due to the inherent trade-offs between the heat exchanger area and the absorbed heat. This factor is determined by rearranging **Eq. (3.29)** to precisely locate the pinch point between the composite curves, thereby minimizing energy consumption, optimizing heat recovery, and enhancing the overall efficiency of the heat exchanger network design. To ensure an adequate pinch point temperature difference between the hot (3) and cold (1') streams in the internal HX, an intercooler effectiveness (ε^{HX}) between 50% and 80% is expected

[382,383]. This leads to increased absorbed heat and thereby produced cooling, yet on the expense of increasing the heat transfer area and cost of the heat exchanger [383].

Overall, this variation promises improved energy efficiency and reduced refrigerant mass flow rate [64]. The *UA* coefficient, as defined in **Eq. (3.32)**, is derived from **Eq. (3.31)** and characterizes both the dimensions and performance of the internal heat exchanger. This parameter effectively combines different heat transfer phenomenon into a single design factor: the heat transfer coefficient and the heat exchange area. The numerator relates to the heat flow rate, while the denominator exhibits the logarithmic mean temperature difference (*LMTD* in **Eq. (3.31))**, as the driving force for the heat transfer process. Specifically, ΔT_1 and ΔT_2 denote the temperature gradient between the cold and hot streams at the respective ends of the double-pipe internal heat exchanger. **Figure 3.5a** clarifies the routine used to simulate this cycle with the polar soft-SAFT EoS.

For the TS-VCRC (**Figure 3.4 bottom**), a more complex configuration is developed (see **Figure 3.5b**), with the addition of a two-stage compressor system in series. This promises enhanced overall system efficiency due to the reduced pressure ratio in the compression stages [384]. In this configuration, the flashed saturated vapor ($x_{4'}$) exiting the upper-side EEV (3 – 4') is bypassed (5) and fed into the second compression stage (1' – 2) prior to condensation to minimize the compression work. In contrast, the saturated liquid stream (1 – $x_{4'}$) contributing to the cooling capacity (4 – 1) is flashed at a temperature corresponding to the inter-stage pressure of the cycle (P_{flash}) [48].

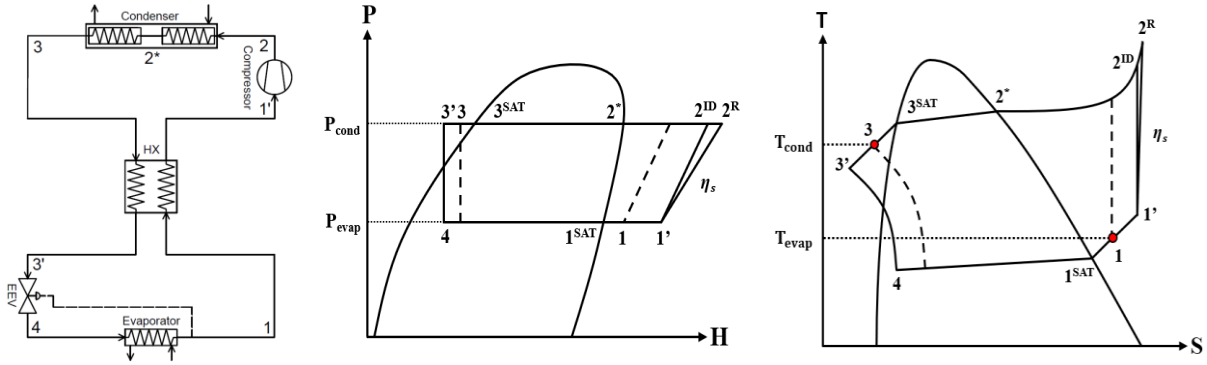

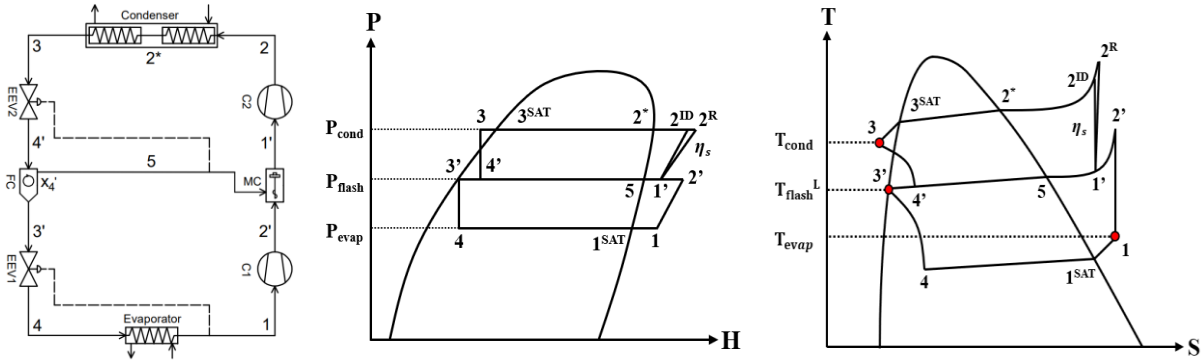

Figure 3.4. *Schematics for the different cooling cycles configurations simulated in this work for LL/SL-HX, and TS-VCRC, with their corresponding PH and TS-diagrams. Note the red dots on the TS-diagrams represent the cycles' pre-defined operating conditions.*

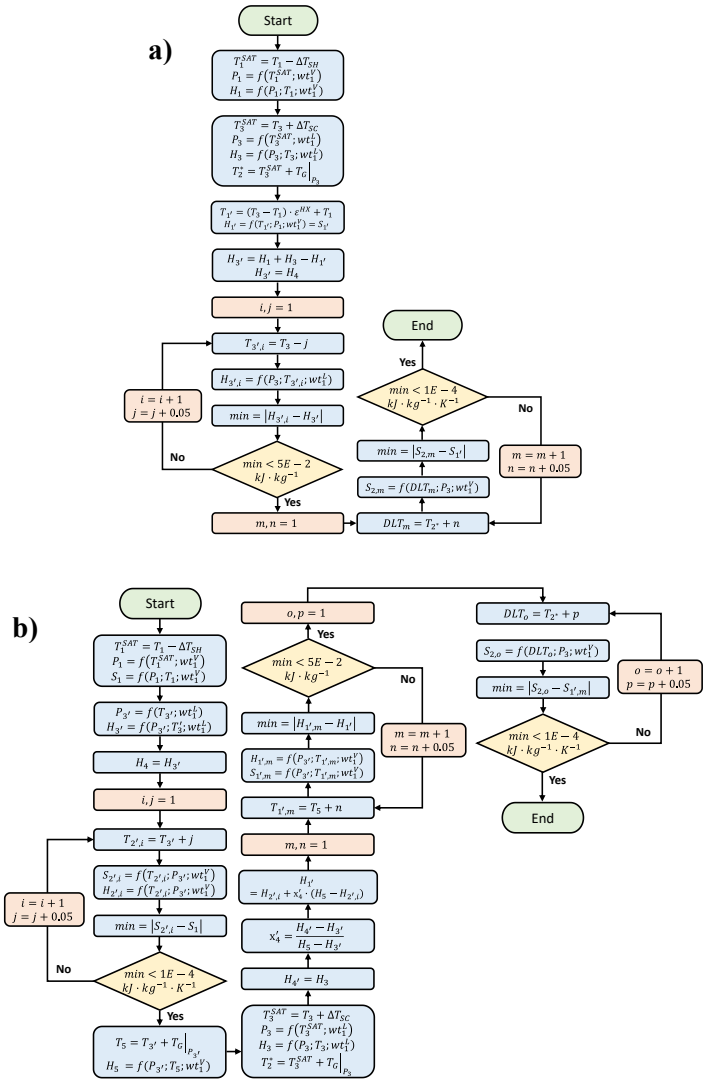

Figure 3.5 *Subroutine for simulating* ***a)*** *LL/SL-HX, and* ***b)*** *TS-VCRC using soft-SAFT for zeotropic blends.*

Details for the thermodynamic characterization for the processing units in the studied cooling cycles of this thesis are included in **Table 3.2**.

Table 3.2. *Thermodynamic characterization of studied cooling cycles.*

Compressor	
$\omega_c\|_{SS} = H_{2^*} - H_1 \quad \omega_c\|_{LL/SL-HX} = H_2 - H_{1'}$ $\omega_c\|_{TS} = [(H_2 - H_{1,}) + (H_{2,} - H_1) \cdot (1 - x_{4'})]$	**(3.22)**
$\dot{W} = \omega_c \cdot \dot{m}$	**(3.23)**
$H_{2^*}^R\|_{SS} = \frac{H_2{}^{ID} - H_1}{\eta_s} + H_1 \quad H_2^R\|_{LL/SL-HX,TS} = \frac{H_2{}^{ID} - H_{1'}}{\eta_s} + H_{1'}$	**(3.24)**
Evaporator	
$RE\|_{SS} = H_1 - H_3 \quad RE\|_{LL/SL-HX,TS} = H_1 - H_{3'}$	**(3.25)**
$CC = RE \cdot \dot{m}$	**(3.26)**
Condenser	
$Q_{cond} = H_3 - H_2$	**(3.27)**
$\dot{Q_{cond}} = Q_{cond} \cdot \dot{m}$	**(3.28)**
Internal Heat Exchanger	
$\varepsilon^{HX} = \frac{T_{1'} - T_1}{T_3 - T_1}$	**(3.29)**
$T_{PP} = \Delta T_1 = T_3 - T_{1'} = T_3 - (\varepsilon^{HX} \cdot [T_3 - T_1] + T_1)$	**(3.30)**
$\dot{Q}\big\|_{LL/SL-HX} = \dot{m} \cdot (H_3 - H_4) = \dot{m} \cdot (H_3 - H_{3'}) = \dot{m} \cdot (H_{1,} - H_1) = UA \cdot LMTD$	**(3.31)**
$UA = \frac{\dot{m} \cdot (H_3 - H_{3'})}{\frac{\Delta T_2 - \Delta T_1}{\ln\left(\frac{\Delta T_2}{\Delta T_1}\right)}} = \frac{\frac{CC}{RE} \cdot (H_3 - H_{3'})}{\frac{(T_{3'} - T_1) - (T_3 - T_{1'})}{\ln\left(\frac{T_{3'} - T_1}{T_3 - T_{1'}}\right)}} = \frac{\frac{CC}{RE} \cdot (H_{1'} - H_1)}{\frac{(T_{3'} - T_1) - (T_3 - T_{1'})}{\ln\left(\frac{T_{3'} - T_1}{T_3 - T_{1'}}\right)}}$	**(3.32)**

The final configuration explored in this thesis is a cascade refrigeration technology (see **Figure 3.6**), crucial for attaining ultra-low temperatures required in industries like food processing and pharmaceuticals.

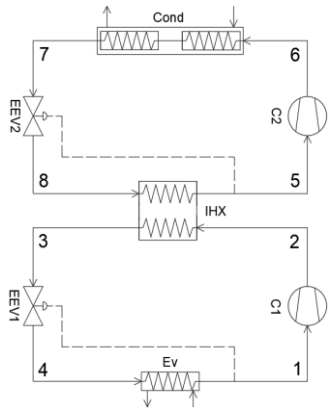

Figure 3.6. *Schematics for the basic cascade refrigeration cycle simulated in this thesis.*

In this ensemble, the process begins with the compression of the low-temperature refrigerant by compressor C1, which raises its pressure and temperature from state 1 to state 2. The refrigerant then passes through the HX (refer to **Eq. (3.33)**), where it exchanges heat with the higher-temperature refrigerant cycle, cooling it from state 2 to state 3. Following this, the refrigerant undergoes thermal expansion, reaching state 4, and absorbs heat in the evaporator. Simultaneously, the higher-temperature refrigerant undergoes its own cycle: compression by compressor C2, condensation, expansion through EEV2, and re-entry into the evaporator of the HX. The mean temperatures of the evaporator and condenser, as derived from **Eqs. (3.34)** and **(3.35)**, are fundamental for pinch analysis and the comprehensive exergy evaluation of auxiliary fluids in the main circuit.

$$(H_2 - H_3) \cdot \dot{m}_L = (H_5 - H_8) \cdot \dot{m}_H \quad \textbf{(3.33)}$$

$$\overline{T_{cond}} = \frac{1}{2} \cdot T_b + \frac{1}{2} \cdot T_d \quad \textbf{(3.34)}$$

$$\overline{T_{evap}} = \frac{1}{3} \cdot T_b + \frac{2}{3} \cdot T_d \quad \textbf{(3.35)}$$

This cascade configuration provides several advantages, including enhanced efficiency at ultra-low temperatures and significant energy savings. By dividing the temperature lift across multiple stages, each cycle operates within its optimal range, reducing the workload and improving the system's overall performance. Despite this, managing and maintaining such systems can be complex. The use of CO_2-based blends in subcritical conditions introduces challenges such as potential operational instability and safety concerns. These issues require careful consideration and management to ensure reliable and safe operation. Consequently, the effective application of subcritical cycles, as outlined in this thesis, is pivotal for obtaining precise results at ultra-low temperatures, particularly when making use of the polar soft-SAFT EoS for simulations, as outlined in the subroutine in **Figure 3.7**.

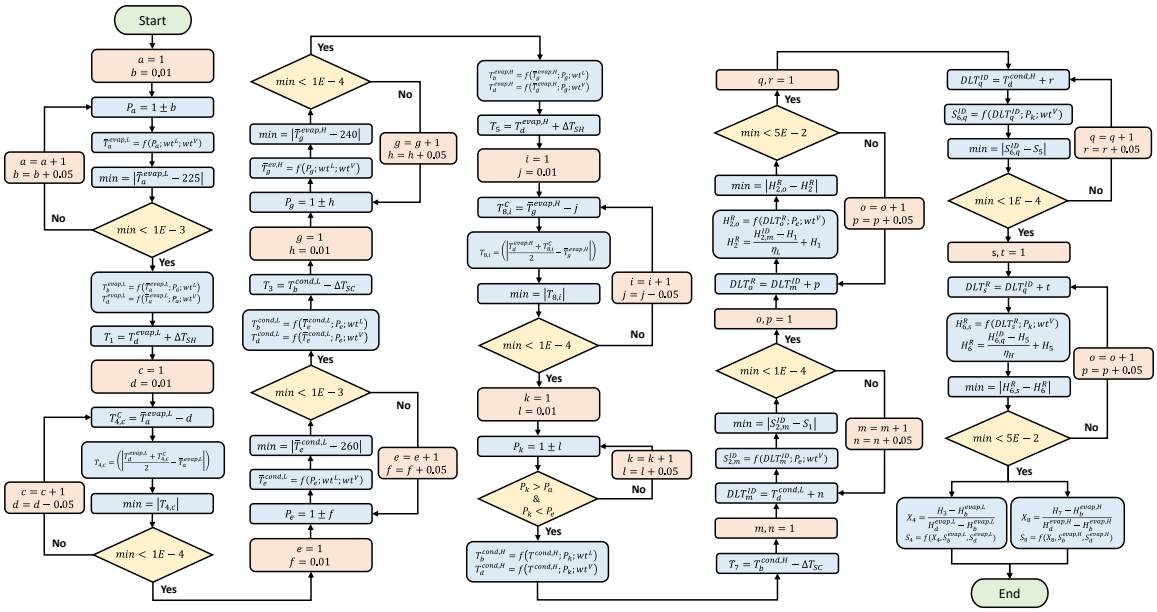

Figure 3.7. *Flowchart representation for the iteration algorithms for the cascade cycle examined in this PhD thesis using polar soft-SAFT.*

3.3. 4E key performance indicators

The procedure for the identification of low-GWP drop-ins for common HFCs followed in this thesis employs a two-stage methodology: (I) mixture selection and (II) drop-in analysis using the 4E framework. While the approach established contains the structural elements, multiple cycle configurations and a prospective life cycle assessment are additionally considered to ensure a comprehensive interpretation. A graphical outlook of the methodology is provided in **Figure 3.8**.

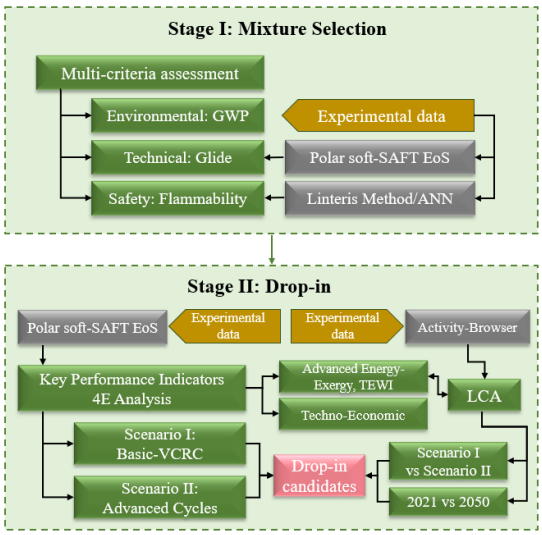

Figure 3.8. *Use of the 4E methodology to evaluate 4th generation drop-in refrigerants.*

3.3.1. Energy and exergy analysis

The non-monetized key performance indicators used for the subsequent assessments within **Chapters 6-8** are enlisted in **Table 3.3**. As appreciated, thermodynamic properties and performance criteria were included to assess the degree of compatibility including volumetric cooling capacity (*VCC*), discharge line temperature (*DLT*), condensing pressure (P_{cond}), isobaric heat capacity (C_P), speed of sound (ω), normal boiling point (*NBP*), pressure ratio (P_R), suction density (ρ_v), refrigeration effect (*RE*), power per ton of refrigeration (*PPTR*) and coefficient of performance (*COP*). Promising compounds are those minimizing *DLT*, P_{cond}, C_P, *NBP*, P_R and *PPTR*, while maximizing *VCC*, ω, *RE*, ρ_v and *COP*. *VCC* and *COP* are primary parameters indicative of energy efficiency (reflective of operating costs), and equipment size (reflective of capital costs) [385]. The *VCC* in **Eq. (3.36)** refers to the amount of cooling per unit volume of the refrigerant at the evaporator outlet impacting the efficiency of the cycle and the size of the compressor, with preference for high *VCC* values to ensure high *RE* while minimizing compression requirements [74]. Additionally, the exergetic efficiency (η_{II}) was also estimated to gain additional insight on the effectiveness of the designed blends [121,386–389], computed with the mathematical formulation in **Eq. (3.49)**.

Table 3.3. *KPIs for technical evaluation of drop-in replacement refrigerant blends for R134a and R410A.*

Drop-in KPIs			
Volumetric Cooling Capacity (*VCC*)	$VCC = RE \cdot \rho_V$		**(3.36)**
Discharge Line Temperature (*DLT*)	$DLT = T_{2^R}$	$=^*$	**(3.37)**
Condenser Pressure (P_{cond})	$P_{cond} = P_2 = P_{2^*} = P_3$		**(3.38)**
Other thermodynamic properties and performance metrics			
Isobaric Heat Capacity (C_p) [225]	$C_P = C_V + \frac{T\delta^2}{k_T\rho}$	min^*	**(3.39)**
Speed of Sound (ω)	$\omega = \sqrt{\frac{C_P}{C_V}\left(\frac{\partial P}{\partial \rho}\right)_T}$	max^*	**(3.40)**
Normal Boiling Point (*NBP*)	$NBP = T_{atm}^{SAT}$		**(3.41)**
Pressure Ratio (P_R)	$P_R = P_{cond} \cdot P_{evap}^{-1}$	min^*	**(3.42)**
Power Per Ton of Refrigeration (*PPTR*)	$PPTR = 3.5167 \cdot COP^{-1}$		**(3.43)**

Glide Temperature (T_G)	$T_{G,P} = \lvert T_d - T_b \rvert_P$	**(3.44)**
Suction Density (ρ_V)	$\rho_V\rvert_{SS,TS,cascade} = \rho_1$ $\rho_V\rvert_{LL/SL-HX} = \rho_{1'}$	**(3.45)**
Refrigeration Effect (RE)	Refer to **Eq. (3.25)**	
Coefficient of Performance (COP)	$COP = \frac{CC}{\dot{W}} = \frac{RE}{\omega_c} \leftrightarrow SS, LL/SL-HX$	**(3.46)**
	$COP\rvert_{TS} = \frac{(1-x_{4'})\cdot(H_1 - H_{3'})}{[(1-x_{4'})\cdot(H_{2'} - H_1)] + (H_2 - H_{1'})}$ *max**	**(3.47)**
	$COP\rvert_{cascade} = \frac{\dot{m}_L \cdot (H_1 - H_4)}{\dot{m}_L \cdot (H_2 - H_1) + \dot{m}_H \cdot (H_6 - H_5)}$	**(3.48)**
Exergetic Efficiency (η_{II})	$\eta_{II} = 1 - \left(\frac{\sum \dot{\chi}_d}{\sum \dot{\chi}_{in}}\right) = \frac{COP}{COP_{Carnot}}$	**(3.49)**

* *Variation to HFCs*

An exergy analysis is carried out to determine the irreversibility rates of the cooling cycles on the exergetic efficiency [121,386–389], computed considering the exergy destruction for each equipment, as:

Table 3.4. *Exergy destruction analysis for each configuration.*

General Overview	
$(\psi_i - \psi_j) = (H_i - H_j) - T_0 \cdot (S_i - S_j)$	**(3.50)**
$\sum \dot{\chi}_d\Big\rvert_{SS/TS} = \dot{\chi}_{d,comp,SS/TS} + \dot{\chi}_{d,comp,SS/TS} + \dot{\chi}_{d,cond,SS/TS} + \dot{\chi}_{d,evap,SS/TS}$ $\sum \dot{\chi}_d\Big\rvert_{LL/SL-HX} = \dot{\chi}_{d,comp,LL/SL-HX} + \dot{\chi}_{d,EEV,LL/SL-HX} + \dot{\chi}_{d,cond,LL/SL-HX} + \dot{\chi}_{d,evap,LL/SL-HX} + \dot{\chi}_{d,HX}$	**(3.51)**
Compressor	
$\dot{\chi}_{d,comp,SS} = \dot{W} + \dot{m}\cdot(\psi_1 - \psi_2)$ $\dot{\chi}_{d,comp,LL/SL-HX} = \dot{W} + \dot{m}\cdot(\psi_{1'} - \psi_2)$ $\dot{\chi}_{d,comp,TS} = \sum \dot{W} + \dot{m}_H \cdot [(1-x_{4'})\cdot(\psi_1 - \psi_{2'}) + (\psi_{1'} - \psi_2)]$	**(3.52)**
Evaporator	
$\dot{\chi}_{d,evap,SS,LL/SL-HX} = CC \cdot \left(\frac{\bar{T}_C - T_0}{\bar{T}_C}\right) + \dot{m}\cdot(\psi_4 - \psi_1)$ $\bar{T}_C = \frac{T_{h,in} - T_{h,out}}{\ln\left(\frac{T_{h,in}}{T_{h,out}}\right)}$ $\dot{\chi}_{d,evap,TS} = CC \cdot \left(\frac{\bar{T}_C - T_0}{\bar{T}_C}\right) + \dot{m}_L \cdot (\psi_4 - \psi_1)$	**(3.53)**
Condenser	
$\dot{\chi}_{d,cond,SS,LL/SL-HX} = -\dot{Q}_{cond} \cdot \left(\frac{\bar{T}_H - T_0}{\bar{T}_H}\right) + \dot{m}\cdot(\psi_2 - \psi_3)$ $\bar{T}_H = \frac{T_{c,out} - T_{c,in}}{\ln\left(\frac{T_{c,out}}{T_{c,in}}\right)}$ $\dot{\chi}_{d,cond,TS} = -\dot{Q}_{cond} \cdot \left(\frac{\bar{T}_H - T_0}{\bar{T}_H}\right) + \dot{m}_H \cdot (\psi_2 - \psi_3)$	**(3.54)**

EEV	
$\dot{\chi}_{d,EEV,SS} = \dot{m} \cdot T_0 \cdot (S_4 - S_3)$; $\dot{\chi}_{d,EEV,LL/SL-HX} = \dot{m} \cdot T_0 \cdot (S_4 - S_{3'})$ $\dot{\chi}_{d,EEV,TS} = \dot{m}_H \cdot T_0 \cdot [(1 - x_{4'}) \cdot (S_4 - S_{3'}) + (S_{4'} - S_3)]$	**(3.55)**
HX	
$\dot{\chi}_{d,HX} = \dot{m} \cdot (\psi_1 - \psi_{1'}) - \dot{m} \cdot (\psi_{3'} - \psi_3)$	**(3.56)**
Advanced Exergy Analysis	
$\dot{\chi}_{d,k}^{UN} = \left(\frac{\dot{\chi}_{d,k}}{\dot{\chi}_{p,k}}\right)^{UN} \cdot \dot{\chi}_{p,k}$	**(3.57)**
$\dot{\chi}_{d,k}^{AV} = \dot{\chi}_{d,k} - \dot{\chi}_{d,k}^{UN}$	**(3.58)**

where $\sum \dot{\chi}_d$ designates the total exergy destruction rate, $\sum \dot{\chi}_{in}$ is the rate of exergy input, ψ_i is the availability or specific exergy of stream *i,* and T_0, $\bar{T}_H$ and $\bar{T}_C$ are the dead-state, and entropy-averaged temperatures of the auxiliary fluid around the condenser and evaporator, respectively. Also, $\dot{\chi}_{d,k}^{UN}$ and $\dot{\chi}_{d,k}^{AV}$ are the unavoidable and avoidable irreversibility.

3.3.2. Environmental analysis

A first approach to evaluate the environmental impact associated with the refrigerants utilization and emissions is through the use of the total equivalent warming impact (TEWI in **Eq. (3.59)**) metric [390]. TEWI is a measure of the global warming impact derived from the direct (*i.e.,* refrigerant leakage and end-of-life disposal) and indirect (*i.e.,* compressor energy consumption) GHGs emissions related to the utilization of the refrigerant in the intended application, in terms of yearly tons of equivalent CO_2 emissions, as:

$$TEWI = \left\{GWP \cdot \left((L \cdot m \cdot n) + \left(m \cdot (1 - \alpha)\right)\right)\right\}_{Direct} + \{E_a \cdot \beta \cdot n\}_{Indirect} \quad \textbf{(3.59)}$$

$$E_a = \omega_c \cdot \dot{m} \cdot AOT = \omega_c \cdot \left(\frac{CC}{RE}\right) \cdot AOT = \left(\frac{CC}{COP}\right) \cdot AOT \quad \textbf{(3.60)}$$

Notice that, with this metric, the environmental assessment not only accounts for the GWP, but also includes the indirect impact associated with the energy consumption of the VCRC cycle (E_a in **Eq. (3.60)**). This is dependent on the type and efficiency of the cooling system, the properties of the refrigerant, and the level of decarbonization in the energy mix (*i.e.,* fuel type) within a specific country by considering the country-dependent indirect emission factor (β).

3.3.2.1. Life cycle assessment

The life cycle assessment (LCA) presented in this thesis is conducted according to the guidelines established by the ISO 14040:2006 standard, which includes three key stages: (I) defining the goal and scope, (II) performing a life cycle inventory (LCI), and (III) conducting a life cycle assessment (LCA) [391]. Therefore, the main goal in section (I) is to develop a comprehensive LCA framework for assessing the environmental impacts across multiple vapor compression refrigeration technologies. The second stage involves designing a life cycle inventory for 36 scenarios, combining combinations of six refrigerants, three VCRC configurations, and two cooling load levels. The resulting LCI compiles a detailed record of all inputs and outputs (e.g. cooling capacity in addition to emissions to air) associated with the refrigerant lifecycle, including production, utilization, emission and end-of-life management. Specifically, it accounts for the energy consumed by auxiliary systems, the electricity required for compressing refrigerants, the energy needs of condenser and evaporator units, or the refrigerant production derived from leakage losses, among other specified in **Table 3.5**.

Table 3.5. *Specifications for the LCI of Material Production (MP), Electricity (E), Refrigerant Production (ReP), Refrigerant Emissions (ReE), and Cooling Water (CW) inputs.*

Unit	Specifications	Value	LCI	Location	ecoinvent
Compressor	market for air compressor, 4kW screw-type	2.114E-7u	MP	GLO	Yes
HE	market for steel, low-alloyed	kg	MP	GLO	Yes
HE	market for aluminium, wrought alloy	kg	MP	GLO	Yes
Pump	market for pump, 40W	2.114E-7u	MP	GLO	Yes
-	(x2) market group for electricity, high voltage	kWh	E	GLO	Yes
Pump	market group for electricity, high voltage	0.0028kWh	E	GLO	Yes
-	(x2) market for refrigerant	kg	ReP	RoW	No*
-	(x2) refrigerant emission to air	kg	ReE	GLO	No^{+}
	CW Activity (MJ of Heat Duty)				
-	market for tap water	kg	-	GLO	Yes
-	emissions to air	m^3	ReE	GLO	Yes
-	emissions to water	m^3	ReE	GLO	Yes
Fan	market group for electricity, high voltage	0.0028kWh	E	GLO	Yes

* Only available for R134a, and R152a.

$^{+}$ Conversion factors for R1123, R1243zf, R1234yf and R1234ze(E) are extracted from *SimaPro* software. For ReP and ReE, a blend is considered based on the weight of its individual components.

The compression energy flow is computing using **Eq. (3.23)**, while **Eq. (3.28)** is used to determine the heat duty of the condenser. To pump auxiliary cooling water (by **Eq. (3.61)**) and compress air (by **Eq. (3.62)**) in both condenser and evaporator units, the process involves setting a pressure gradient while iterating the inlet temperature until entropy values converge. Energy requirements for refrigerant production (addressed in **Eqs. (3.63) – (3.64)**) were scaled from theoretical calculations to industrial levels using specific conversion factors [392]. For endothermic reactions, the theoretical heat demand was multiplied by 4.2, assuming natural gas as the heat source, while for exothermic processes, a conversion factor of 3.2 was used, assuming cooling energy from the European electricity mix. To determine the reaction energy and account for the electricity consumption in refrigerant production, the enthalpy of formation balance in **Eq. (3.65)** is applied according to the stoichiometry of the corresponding synthetic route. Furthermore, the inventory includes the total mass of materials (e.g. stainless steel, aluminum) used throughout the cycle in addition to the emissions resulting from refrigerant leakage and end-of-life disposal. The simulated shell-and-tube heat exchanger consists of 80% stainless steel for durability and corrosion resistance and 20% aluminum for enhanced thermal conductivity, providing an optimal balance of performance, durability, and cost. Additional data for material production, and refrigerant emissions was sourced from existing *ecoinvent* evidence or derived from process simulations, complemented with mathematical expressions in **Eqs. (3.66) – (3.69)** in order to complete the LCI. Note that the heat exchange area A is derived from **Eq. (3.31)**, and the material production for unitary units such as compressors, pumps, fans, and blowers is based on data from the *ecoinvent* database.

Table 3.6. *Mathematical expressions to complete the LCI at a given functional unit.*

$\dot{Q_{CW}} = P_{id} \cdot \eta = \dot{m}_{CW} \cdot \Delta_{CW}H \cdot \eta$	**(3.61)**	$\dot{Q_{Air}} = \dot{m_{air}} \cdot \left(\frac{H_{out}^{ID} - H_{in} + H_{in} \cdot \eta}{\eta} - H_{in}\right)$	**(3.62)**
$RP_{leak} = \frac{m \cdot L}{AOT}$	**(3.63)**	$RP_{closed-cycle} = \frac{m}{n \cdot AOT}$	**(3.64)**
$\Delta_f H = \tau_p \sum_P \Delta_f H - \tau_R \sum_R \Delta_f H$			**(3.65)**
$MP_{SS} = 0.8 \cdot A \cdot Th_{SS} \cdot \rho_{SS}$	**(3.66)**	$MP_{Al} = 0.2 \cdot A \cdot Th_{Al} \cdot \rho_{Al}$	**(3.67)**
$REm_{leak} = RP_{leak}$	**(3.68)**	$REm_{EoL} = \frac{m \cdot (1-\propto)}{n \cdot AOT}$	**(3.69)**

A comparative LCA is subsequently performed using the Activity-Browser (AB) software, based on the IPCC's Global Warming Potential metric over a 100-year time horizon [393]. This approach quantifies the long-term environmental impact of fluorinated greenhouse gases by measuring their contributions to global warming in terms of CO_2 equivalents per kilogram of refrigerant emissions. To conclude, a forward-looking LCA for the year 2050 is conducted, playing a critical role in the context of the Paris Agreement's targets to limit global temperature rise to well below 2°C, with an aspirational goal of 1.5°C. This prospective LCA examines the future environmental impacts of emerging technologies and processes, with a focus on their potential to align with and support the achievement of these climate objectives.

3.3.3. Techno-economic analysis

The total annualized cost (TAC, $\dot{C}$) for deploying the promising refrigerants in the VCRC cycle includes the capital (CAPEX, $\sum \dot{C_k}$), operating and maintenance (OPEX, $\dot{C_{op}}$), environmental (Enviro, $\dot{C_{env}}$), and set-up (C_{set-up}) costs, calculated according to **Eqs. (3.70) – (3.75)** as:

TAC ($·y^{-1})
$$\dot{C} = \sum \dot{C_k} + \dot{C_{op}} + \dot{C_{env}} + C_{set-up} \tag{3.70}$$

CAPEX ($·y^{-1})
$$\sum \dot{C_k} = \frac{C_k \cdot \phi}{3600 \cdot AOT} \cdot CRF = \frac{C_k \cdot \phi}{3600 \cdot AOT} \cdot \left(\frac{i \cdot (1+i)^n}{(1+i)^n - 1} \right) \tag{3.71}$$

OPEX ($·y^{-1})
$$\dot{C_{op}} = \sum \dot{W} \cdot AOT \cdot \alpha_{el} \tag{3.72}$$

Enviro ($·y^{-1})
$$\dot{C_{env}} = m_{CO_2,e} \cdot c_{CO_2} = (\beta \cdot E_a) \cdot c_{CO_2} \tag{3.73}$$

Set-up ($)
$$C_{set-up} = m' \cdot (RP + Tax_{HFC}) + Tax_{CO_2} \cdot (GWP \cdot [m \cdot L \cdot n + m \cdot (1-\alpha)]) \tag{3.74}$$

Lifetime load (kg)
$$m' = m + m \cdot L \cdot n \tag{3.75}$$

In estimating the capital cost, the main equipment shown in **Figure 3.2a** were considered, employing the unit cost functions provided in **Table 3.7** [394–396]. The expression for the CAPEX accounts for the capital recovery factor with a 14% annual interest rate (i) over the life time of the system (n) of 15 years with an annual operating time (AOT) of 8760 hours, in addition to an allowance for system maintenance with a maintenance factor (ϕ) of 1.06 [395–398]. The operating cost accounts for the electricity consumption required for running work-consuming devices such as pumps and

compressors, with an additional allowance for the variation in electricity unit cost (α_{el}) [395,397,398], for different regions. An additional monetized metric was included to account for the CO_2 penalty cost rate based on the annual GHGs emissions ($m_{CO_2,e}$) resulting from the energy consumption required for the VCRC cycle startup and operation, dependent on parameters affecting the indirect emissions in the TEWI assessment (*i.e.,* E_a and β) [395,397].

Table 3.7. *Cost functions of all units involved in the simulated cycles.*

Unit	C_k	Ref.
Evaporator/Condenser	$1397 \cdot A_{evap,cond}^{0.89}$	[395,397]
Compressor	$10167.5 \cdot \dot{W}^{0.46}$	[395,397,398]
HP Compressor	$9624.2 \cdot \dot{W}^{0.46}$	[395]
EEV	$114.5 \cdot \dot{m}$	[395,397]
HX	$2382.9 \cdot A_{HX}^{0.68}$	[398]
Flash Tank	$280.3 \cdot \dot{m}_H^{0.67}$	[395]

Additionally, the environmental cost accounts for the country-dependent average costs of CO_2 emissions avoidance (c_{CO_2}) from the integration of natural gas combined cycle power plants with carbon capture plants. The last considered monetized metric was the set-up cost of the cooling unit inclusive of the cost of initial refrigerant load charged in the startup of the cooling cycle, cost for additional 12.5% per annum recharge load accounting for refrigerant leakage rate over the unit's lifecycle, taxes on utilization of HFC-based refrigerants, and taxes on direct CO_2-equivalent emissions associated with the refrigerant annual leakage over the system's life cycle and the end-of-life disposal of the remaining refrigerant load. The HFC utilization tax is implemented to measure the required taxation level that can support a decline in the import of bulk HFCs, while incentivizing the development and consumption of next-generation refrigerants. The CO_2-eq tax might seem analogous to HFC utilization tax, however, the latter merely accounts for the tariff imposed on importing high-GWP cooling agents, while the former accounts for the associated negative environmental impacts from their emissions *via* leakage or end-of-life disposal (partial recycling), a factor typically overlooked in economic analysis of next generation refrigerants. This is added as a monetized KPI to allow examining the role of governmental policies on the development of consistent regulation to discourage the utilization of HFCs primarily focused on their environmental impact.

3.4. Statistical tools for cooling cycle performance optimization

To address the optimization problem to determine optimal operating conditions and cycle configurations, several statistical analysis tools were employed in this work. This was done to reduce the required computational time, while ensuring consistent and holistic mapping of the design search space, with minimal number of simulations runs. These include fractional factorial design (FFD) and Taguchi orthogonal array (OA) method to obtain the ranking of importance for the most influential design factors, with the addition of ANOVA and polynomial surface regression (PSR) model as validation tools for the ranking of importance, and lastly grey relational analysis (GRA) to build a consistent multi-objective optimization in a single expression.

3.4.1. Taguchi method and fractional factorial design

The Taguchi orthogonal array (OA) is a reliable statistical method utilized in design of experiments (DoE) and determination of impact of system parameters on performance for optimization problems. With this method, the most likely interactions are selected *a priori*, unlike the selection with FFD. The application of Taguchi and FFD depends on the selection of factors (design/operating conditions) and their levels (variation ranges), and accordingly the construction of the DoE structure that can best map the effect of individual factors on selected target functions (output responses) with minimal number of runs, depending on degrees of freedom (DOF) based on the number of factors and levels. The output from these tools is measured in the form of importance order ranking and contribution ratios of main factors to the target function. Among the most commonly used orthogonal arrays are the $L_9(3^4)$ and $L_{16}(2^{15})$ OAs. The former array, which is a 3^{4-1} fractional factorial design, involves four factors at three levels each, and requires a total of nine experimental runs. While compact, it confounds main effects with second-order interactions, ensuring additional runs to settle potential ambiguities. The $L_{16}(2^{15})$ array, a 2^5 fractional factorial design, adapts up to five factors with either two or three levels, requiring sixteen simulations. While mitigating the confounding of main effects with second-order interactions compared to the $L_9(3^4)$ OA, maintaining orthogonality can become challenging when adding multiple three-level factors. To find a resolution to this, levels within the original orthogonal array must be reshaped and reallocated using methods such as the Taguchi idle column technique or the dummy

treatment method. Two stages are required, first, the merging columns or multi-level technique creates four-level factors to then convert these into three-level columns through the application of the dummy treatment method. However, towards accommodating a considerable number of three-level factors into a two-level OA, previous records [399] recommend the implementation of the direct idle column treatment. Grove and Davis [400] highlighted that the resulting designs should be considered nearly orthogonal rather than purely orthogonal. Consequently, care must be taken when collapsing OA columns to accommodate new three-level factors. Additional details on the principles of developing Taguchi OAs and FFDs can be found elsewhere [401].

3.4.2. Complementary validation tools

Other statistical tools were included in the form of ANOVA and PSR model to validate the importance of each factor, order, and contribution ratios obtained from the DoE. For the ANOVA method, the importance of each factor on the target function was determined, and accordingly the rank for each factor was calculated by finding the statistical significance of the independent variable (factor) on the dependent variable (target function), with high *F*-test and low *p*-test values for a 95% confidence level denoting statistical significance of the factor. In the case of the PSR model, a 3D graphical hierarchical representation for the developed DoE is required to select a limited number of subset of experiments that are fully orthogonal and can fully map the responses. The PSR model is formulated to correlate the main factors with the target responses in a manner where the number of coefficients is equal to the number of experiments based on the structure of DoE. Note that a positive value for the coefficient is indicative of a high order of importance in the coefficient-set, reaffirming the results obtained from ANOVA. Moreover, the resulting correlation model can also enable prediction of the target responses at conditions not included in the limited experimental set. Further information on graphical presentation of factorial designs can be found in *Barton et al.*'s analysis [402].

3.4.3. Multi-objective optimization using grey relational analysis

Considering that the developed DoEs were used to measure the effect of each factor on each target response separately, the GRA method was used to encompass multiple target functions into a single objective function, that can simultaneously optimize their performance [292,294]. To do so, the results of the responses were normalized between 0 and 1 using **Eq. (3.76)** and **Eq. (3.77)**, followed by evaluating the grey relational coefficient *(ξi)* (**Eqs. (3.78)** and **(3.79)**) which expresses the relationship between desired and actual normalized values.

$$O_i(k) = \frac{x_i^o(k) - \min x_i^o(k)}{\max x_i^o(k) - \min x_i^o(k)} \tag{3.76}$$

$$O_i(k) = \frac{\max x_i^o(k) - x_i^o(k)}{\max x_i^o(k) - \min x_i^o(k)} \tag{3.77}$$

$$\xi_i(k) = \frac{\Delta_{min} + \varphi\,\Delta_{max}}{\Delta_{oi}(k) + \varphi\,\Delta_{max}} = \frac{\left(\min\limits_{\forall j \in i} \min\limits_{\forall k}[O_0(k) - O_i(k)]\right) + \varphi\left(\max\limits_{\forall j \in i} \max\limits_{\forall k}[O_0(k) - O_i(k)]\right)}{(O_0(k) - O_i(k)) + \varphi\left(\max\limits_{\forall j \in i} \max\limits_{\forall k}[O_0(k) - O_i(k)]\right)} \tag{3.78}$$

$$\Delta_{oi} = O_o(k) - O_i(k) \tag{3.79}$$

where $O_i\,(k)$ is the GRA normalization value, $x_i\,(k)$ is the property value, $\xi_i\,(k)$ is the grey relational coefficient, Δ_{oi} is the deviation value between $O_o\,(k)$ and $O_i\,(k)$, φ is the identification coefficient set to 0.5, *and* Δ_{min} and Δ_{max} are the minimum and maximum value of the Δ_{oi}.

The single objective function or grey relational grade (γ) (see **Eq. (3.80)**) provides a direct correlation encompassing the multiple target responses inclusive of different weight factors (ω_i) for each target function. The weight factors were obtained statistically as the ratio of each parameters' delta value to the total delta value of all assessed factors (see **Eq. (3.81)**).

$$\gamma_i = \frac{1}{n}\sum_{k=1}^{n} \omega_i \xi_i(k) \tag{3.80}$$

$$\omega_i = \frac{\sum_{j=1}^{p} \Delta_{i,j}}{\sum_{i=1}^{m}\sum_{j=1}^{p} \Delta_{i,j}} \tag{3.81}$$

The results are evaluated from the signal-to-noise ratios (*S/N*) to assess the reliability and accuracy of the developed DoE [403], with noise representing the

variability of the characteristic, while signal accounts for the average value. In this thesis, both the larger-is-better (**Eq. (3.82)**) and smaller-is-better (**Eq. (3.83)**) signal-to-noise (S/N) ratios were used. The former approach aimed to enhance system efficiency with higher S/N values for energy and exergy efficiency, while the latter pursuing reduced annual costs and environmental impacts by targeting lower S/N values.

$$S/N = -10 \cdot log_{10}\left(\frac{1}{n}\sum_{i=1}^{n}\frac{1}{O_i^2}\right) \quad \textbf{(3.82)}$$

$$S/N = -10 \cdot log_{10}\left(\frac{1}{n}\sum_{i=1}^{n}O_i^2\right) \quad \textbf{(3.83)}$$

being n the experiment replication number and O_i the data measured for the i^{th} performance characteristics.

3.4.4. Technique for order of preference by similarity to ideal solution

The Technique for Order of Preference by Similarity to Ideal Solution, or TOPSIS methos is a multi-criteria decision-making approach used to rank and select different responses. The process involves:

- Step I: Normalize data according to **Eq. (3.84)**.

$$r_{ij} = \frac{y_{ij}}{\sqrt{\sum_{i=1}^{m} O_{ij}^2}} \quad \textbf{(3.84)}$$

  where O_{ij} represents the performance of the i-th alternative on the j-th criterion, and r_{ij} denotes the normalized value.

- Step II: Assign weights to criteria based on their contribution and construct the weighted normalized decision matrix (see **Eq. (3.85)**).

$$v_{ij} = \omega_j \cdot r_{ij} \quad \textbf{(3.85)}$$

  where v_{ij} is the weighted normalized value, and w_j the weight of the j-th criterion.

- Step III: Determine the best (ideal solution) and worst (anti-ideal solution) performance values for each criterion, as outlined in **Eqs. (3.86)** and **(3.87)**.

$$A_j^+ = \begin{cases} \max_i v_{ij} \ \ if\ j \in benefit\ criterion \\ \min_i v_{ij} \ \ if\ j \in cost\ criterion \end{cases} \quad \textbf{(3.86)}$$

$$A_j^- = \begin{cases} \min_i v_{ij} \ \ if\ j \in benefit\ criterion \\ \max_i v_{ij} \ \ if\ j \in cost\ criterion \end{cases} \quad \textbf{(3.87)}$$

- Step IV: Compute the distance of each design from the ideal (**Eq. (3.88)**) and anti-ideal (**Eq. (3.89)**) solutions.

$$D_i^+ = \sqrt{\sum_{j=1}^{n} \left(v_{ij} - A_j^+\right)^2} \quad \textbf{(3.88)}$$

$$D_i^- = \sqrt{\sum_{j=1}^{n} \left(v_{ij} - A_j^-\right)^2} \quad \textbf{(3.89)}$$

- Step V: Compute a relative closeness measure (C_i in **Eq. (3.90)**) for design to the ideal solution.

$$C_i = \frac{D_i^-}{D_i^+ + D_i^-} \quad \textbf{(3.90)}$$

- Step VI: Rank alternatives by their relative closeness to the ideal solution, with higher values representing enhanced overall performance.

3.5. Artificial neural networks

Figure 3.9 details the step-by-step process for characterizing the ANN-based machine learning technique used in this study. It consists of four stages, starting with the use of COSMO-RS for dataset generation and providing the essential output data for ANN training and fitting. This is followed by the second stage with the fine-tuning of the model's inner layout, adjusting layers, neurons, and hidden layer activation functions for optimal performance. This step establishes a correlation between COSMO-RS molecular descriptors (inputs) and the observed outputs. The third stage entails a rigorous evaluation of the ANN, combining regression and statistical assessments with external validation of runs not included in the training stage. Upon concluding the model's comprehensive testing and validation, including outlier detection, the screening of the property of interest in stage four proceeds.

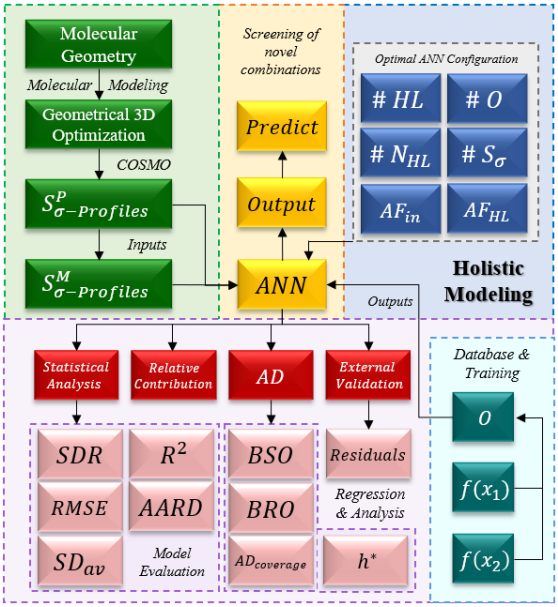

Figure 3.9. *Integrated QSPR modeling framework implemented in this PhD thesis.*

3.5.1. COSMO-RS

The COSMO-RS methodology applies a group contribution framework to estimate the activity coefficients of components in a mixture [404]. The total activity coefficient (τ_i) is decomposed into two main contributions: the combinatorial (τ_i^{comb}) and the residual term (τ_i^{res}), as appreciated in **Eqs. (3.91)-(3.92)**, and **(3.95)**. The combinatorial contribution is determined using the Staverman-Guggenheim equation, which accounts for molecular size and shape effects. The residual term, which addresses electrostatic interactions between solute and solvent molecules, is derived from the difference between the free energy required to restore the charge distribution around a solute molecule in solution (denoted as s) and in the pure liquid state (denoted as i).

The logarithms of the activity coefficients for individual surface segments, referred to as $\lambda_m^{i/s}$, are calculated through self-consistency **Eq. (3.98)**, which require numerical computation. The interaction energy between segments m and n (ΔW_{mn}) is assumed according to the formulation proposed by Lin and Sandler [258], modeling the interaction energy as a function of the charge density on segments m and n.

In subsequent equations (see **Eqs. (3.99)-(3.100)**), the model assessed probabilities $P_m^{i/s}$ based on either number or area probability, assuming all segments share the same effective surface area. Consequently, the mole fractions and surface area

fractions become equivalent. These probabilities are visually represented using σ-profiles, which are two-dimensional representations of the distribution of induced surface charges on a molecule's surface.

$$ln\,\tau_i = ln\,\tau_i^{comb} + ln\,\tau_i^{res} \tag{3.91}$$

$$ln\,\tau_i^{comb} = ln\frac{r_i x_i}{x_i \sum_j r_j x_j} + \frac{z}{2} q_i\, ln\frac{q_i x_i \sum_j r_j x_j}{r_i x_i \sum_j q_j x_j} + l_i - \frac{r_i x_i}{x_i \sum_j r_j x_j}\sum_j x_j l_j \tag{3.92}$$

$$r_i = \sum_k v_k^i R_k \tag{3.93}$$

$$q_i = \sum_k v_k^i Q_k \tag{3.94}$$

$$ln\,\tau_i^{res} = \sum_k v_k^i \left(ln\,\lambda_k - ln\,\lambda_k^i\right) = \sum_m n_m^i (ln\,\lambda_m^s - ln\,\lambda_m^i) \tag{3.95}$$

$$ln\,\lambda_k = Q_k\left[1 - ln\left(\sum_m \Theta_m T_{mk}\right) - \sum_m \frac{\Theta_m T_{mk}}{\sum_n \Theta_n T_{nk}}\right] \tag{3.96}$$

$$\Theta_m = \frac{\frac{\sum_j v_m^j x_j}{\sum_n \sum_j v_n^j x_j} Q_m}{\sum_n \frac{\sum_j v_n^j x_j}{\sum_o \sum_j v_o^j x_j} Q_n} \tag{3.97}$$

$$ln\,\lambda_m^{i/s} = -\,ln\left[\sum_n P_n^{i/s}\,\lambda_n^{i/s} e^{\frac{-\Delta W_{mn}}{RT}}\right] \tag{3.98}$$

$$P_m^i = \frac{\frac{A^i}{\alpha_{eff}{}_m}}{\frac{A^i}{\alpha_{eff}}} \tag{3.99}$$

$$P_m^s = \frac{\sum_i x_i n^i \alpha_{eff} P_m^i}{\sum_i x_i n^i \alpha_{eff}} \tag{3.100}$$

In this context, r and q represent the molecular volume and surface area of pure substances, which can be directly derived from the COSMO internal calculations. The coordination number z is fixed at 10, and l_j is defined as $\frac{z}{2}(r_j - q_j) - (r_j - 1)$. The term v_k^i represents the group number k in molecule i, while R_k and Q_k correspond to the volume and surface area parameters for group k. These parameters can be computed based on the van der Waals volume V_k and surface area A_k.

The residual activity coefficient of group k in the actual mixture is denoted as λ_k, and λ_k^i represents the residual activity coefficient when molecule i is present. The area fraction of group m, denoted as θ_m, is calculated based on the surface area A_i, with α_{eff} representing the standard segment surface area, which is uniform across all molecules.

The number of segments with charge density σ_m is denoted by n_m^i, and the total surface area of these segments is given by $N_m^i = \alpha_{eff}\, n_m^i$. The subscripts i/s indicate the fractions should be used when computing the segment activity coefficients.

3.5.1. Input σ-profiles molecular descriptors via COSMO-RS

Towards predicting the targeted property of interest, COSMO-RS is used to obtain molecular descriptors representative of the molecular structure and energy of the studied refrigerants, as ANN inputs. These descriptors are based on the σ-profile, which is the probability of specific charge density (σ) on a discrete surface segment, obtained from the density functional theory (DFT) level geometric optimization for molecules using COSMO-RS [257,258]. This underscores the significance of this work, as it establishes a direct correlation between molecular characteristics and any property of interest like flammability, or saturated temperatures, working with accessible inputs rather than depending on costly and resource-intensive experimental designs, which are often challenging for novel 4th generation systems. Given the thorough coverage of functional groups by COSMO-RS, additional descriptors based on group contribution methods [405,406] would increase the complexity of the ANN architecture without yielding significant enhancements in accuracy and predictive capability. The methodology for obtaining σ-profiles [407] starts with importing the SMILES notation for each pure compound into the Turbomole software (TmoleX v4.5.1) [408]. The 3D molecular structures were subsequently refined through a geometrical optimization at the DFT level using the def-TZVP basis set with the Becke–Perdew 86 (BP86) generalized gradient approximation, and a rigorous Self-Consistent Field (SCF) convergence criterion was set at 1×10^{-6} Hartree [335]. Post optimization, the molecular details are exported as COSMO [409] files and used as input data to generate intricate σ-profiles [407] in COSMOThermX software (version 19.0.5) through FastSigma coding, providing a comprehensive analysis of molecular characteristics and interactions in the ground-state level. Sigma profiles

($S^{P}_{\sigma-Profiles}$ in **Figure 3.9**), spanning a range of ±0.03 e/Å^2 and composed of 61 discretized data points [410], present a thorough insight into molecular surfaces, effectively delineating between polar and nonpolar areas of influence. Therefore, σ-profiles, mapping the electron density on a molecule's surface, are fundamental to gaining detailed insights into the interactions and ground-state geometric configurations of molecules in various environments [314,329]. To balance computational demands with analytical robustness, one alternative approach is to truncate the analysis to an eight-term descriptor set [331]. In this regard, each σ-profile was discretized into eight pre-defined electrostatic ranges representing the molecule's surface polarity, and the numerical integral of each segment was computed using the integral function within MATLAB R2023a, as expressed in **Eq. (3.101)**. This resulted in eight quantifiable descriptors that serve as reduced yet meaningful dimensional representations of the σ-profiles.

$$S_\sigma = \int_{\sigma_1}^{\sigma_2} spline\big(f(S_\sigma)\big)\, d\sigma = integral(@(\sigma)ppval\big(spline\big(\sigma, f(S_\sigma)\big), \sigma\big), \sigma_1, \sigma_2) \qquad \textbf{(3.101)}$$

where S_x serves as a truncated descriptor indexed from 1 to 8, each numerically capturing a specific electrostatic range within the σ-profile ($f(S_\sigma)$), and essentially quantifying the area under the polynomic curve for that specific segment of interpolation. In this context, S_1 focuses on σ/e·A^{-2} ranges from -0.030 to -0.0225, S_2 from -0.0225 to -0.015, S_3 from -0.015 to -0.0075, S_4 from -0.0075 to 0, S_5 from 0 to 0.0075, S_6 from 0.0075 to 0.015, S_7 from 0.015 to 0.0225, and S_8 from 0.0225 to 0.03. The advantage of using these molecular descriptors as inputs is that, aside from being obtained *a priori* without fitting, they also contain sufficient information indicative of the structural and energetic nature of the molecules, needed to predict their governing intermolecular interactions.

In the same manner, the molecular descriptors for mixtures were obtained in **Eq. (3.102)** relying on the additive nature of the blend constituents' σ-profiles [324]. This approach proves particularly effective in the simulation of complex, multi-component mixtures of molecular liquids and derivatives [328]. Hence, the σ-profile of a given blend is obtained as a linear combination of the constituent descriptors (S^{i}_{σ}), each weighted by their respective contributions, corresponding their mole fractions (x_i) in the blend, as:

$$S^{M}_{\sigma} = \sum_{i=1}^{N_c} (x_i \cdot S^{i}_{\sigma}) \qquad \textbf{(3.102)}$$

3.5.2. Model fine-tuning

Artificial Neural Networks (ANNs) [411], chosen for their ability in processing complex, nonlinear data, are particularly suited for analyzing detailed molecular fluid behaviors. ANNs draw their inspiration from biological neural networks and have undergone decades of evolution [412,413]. While initially a tool to mimic biological intelligence, the focus has shifted towards their utility in solving complex engineering challenges, particularly in the domains of product design and safety assurance. The Artificial Neural Network employed in this thesis correspond to a Feed-Forward network, employing the Levenberg-Marquardt (*trainlm*) algorithm (refer to **Eq. (3.103)**) for training [414–416], and the Mean Squared Error (MSE) as the loss function. This renders ANNs highly effective for pattern recognition and predictive modeling in medium-sized datasets, given the combination of both gradient descent (*traingd*) and Gauss-Newton (*traincg*) methods.

$$\Delta w = -\left(J_f^T J_f + \vartheta I_n\right)^{-1} J_f^T \cdot (O_{act} - O_{pred}) \tag{3.103}$$

where J_f represents the Jacobian matrix of the error function with respect to the weights, ϑ is the damping factor that balances the trade-off between both optimization methods, and I_n is the identity matrix. When $\vartheta I_n > J_f^T J_f$, the update behaves like gradient descent, while the Gauss-Newton method dominates when the inverse condition holds. The damping factor ϑ is dynamically fine-tuned during the training process based on the error after each epoch. Specifically, ϑ decreases as the error function decreases, allowing for faster convergence via second-order approximations. In contrast, smaller step sizes are applied when far from the minima, ensuring stability according to the *traingd* algorithm.

Compared to other algorithms like second-order Broyden–Fletcher–Goldfarb–Shanno (BFGS), the Levenberg-Marquardt offers faster convergence rates, robustness against local minima, and efficient memory utilization, making it a versatile and reliable choice for our study's specific needs. Alternatively, MSE is selected for its straightforward interpretability and sensitivity to large errors, with Mean Absolute Error (MAE) or Huber loss as alternatives for outlier-rich datasets. The basic architecture of a Feed-Forward ANN [417] comprises an input layer, one or multiple hidden layers, and an output layer.

Each layer contains a varying number of neurons or nodes, and each neuron in the network is associated with a weight, a bias term, and an activation function that transforms the neuron's output. Hidden layers perform transformations on input vectors through a series of linear and non-linear operations to facilitate the mapping from the input feature space to the output target space, thereby enabling the approximation of complex, multi-dimensional functions through adaptive learning. In this manner, the forward propagation of input data through the network is enabled *via* synaptic connections between neurons across successive layers. These connections, parameterized by weights and biases, serve as conduits for the computational flow, thereby facilitating the network's ability to learn and model complex relationships.

The input vectors are derived from σ-profile molecular descriptors [314], which in turn are obtained from quantum-level COSMO calculations, while the architecture of the Feed-Forward ANN is meticulously crafted using the advanced functionalities offered by MATLAB's Neural Network Toolbox. Several configurational parameters for ANN development were tested to determine optimal ANN structure including number of neurons in each hidden layer (1 up to 25 neurons) and hidden layers activation function such as hyperbolic tangent, logistic sigmoid, linear, radial basis, and rectified linear unit, selecting the final architecture of our ANN based on optimal statistical indicators. In this manner, **Table 3.8** presents the mathematical expressions for the activation functions used in hidden neurons across layers 1 and 2, along with their corresponding output functions. Note that d^* is the number of σ descriptors used, m and p the number of neurons in the first and second hidden layers, respectively, γ and C_k the spread and center vectors of the k-th hidden neuron for the radial basis function, while ω the weights, b the biases term, I the input descriptors, HL the hidden layer vectors, and O the outputs of the network.

Table 3.8. *Activation and corresponding output functions for both hidden and output layers.*

Hyperbolic Tangent (*tansig*)			
$HL_{1k} = \tanh\left(\sum_{i=1}^{d^*} \omega_{1ki} \cdot I_i + b_{1k}\right)$	$HL_{2k} = \tanh\left(\sum_{j=1}^{m} \omega_{2kj} \cdot HL_{1j} + b_{2k}\right)$	$O = \tanh\left(\sum_{k=1}^{p} \omega_{Ok} \cdot HL_{L2k} + b_O\right)$	**(3.104)**
Logistic Sigmoid (*logsig*)			
$HL_{1k} = \frac{1}{1+\exp\left(-\sum_{i=1}^{d^*} \omega_{1ki} \cdot I_i - b_{1k}\right)}$	$HL_{2k} = \frac{1}{1+\exp\left(-\sum_{j=1}^{m} \omega_{2kj} \cdot HL_{1j} - b_{2k}\right)}$	$O = \frac{1}{1+\exp\left(-\sum_{k=1}^{p} \omega_{Ok} \cdot HL_{2k} - b_O\right)}$	**(3.105)**
Linear (*purelin*)			
$HL_{1k} = \sum_{i=1}^{d^*} \omega_{1ki} \cdot I_i + b_{1k}$	$HL_{2k} = \sum_{j=1}^{m} \omega_{2kj} \cdot HL_{1j} + b_{2k}$	$O = \sum_{k=1}^{p} \omega_{Ok} \cdot HL_{2k} + b_O$	**(3.106)**
Radial Basis (*radbas*)			
$HL_{1k} = exp(-\omega_1 \cdot \lvert\lvert I - C_{k1} \rvert\rvert^2)$	$HL_{2k} = exp(-\omega_2 \cdot \lvert\lvert HL_{1k} - C_{k2} \rvert\rvert^2)$	$O = \sum_{k=1}^{p} \omega_{Ok} \cdot HL_{2k} + b_O$	**(3.107)**
Rectified Linear Unit (*ReLU*)			
$HL_{1k} = max\left(0, \sum_{i=1}^{d^*} \omega_{1ki} \cdot I_i + b_{1k}\right)$	$HL_{2k} = max\left(0, \sum_{j=1}^{m} \omega_{2kj} \cdot HL_{1j} + b_{2k}\right)$	$O = max\left(0, \sum_{k=1}^{p} \omega_{Ok} \cdot HL_{2k} + b_O\right)$	**(3.108)**

Training proceeded for up to 1000 iterations (also known as epochs), and targeting a MSE of 10^{-20}, including early stopping criteria to avert overfitting. Likewise, a rise in validation error for six consecutive epochs triggers MATLAB's default early stopping due to overfitting, halting the training and reverting the network to its lowest validation error state. The input/output dataset underwent partitioning into three principal subsets—training, validation, and testing—*via* the application of the *cvpartition* algorithm [418,419]. This division technique is designed to bolster the model's predictive performance and generalizability [420]. The allocation of data into these subsets occurs randomly yet in a stratified fashion, based on pre-defined user ratios (80% allocated to training, 20% to validation, and testing evenly split). By employing stratification [421], the algorithm maintains an analogous distribution of classes across the training and testing subsets, thereby ensuring that the testing subset accurately embodies the characteristics of the full dataset. While randomization introduces an element of variability, enabling different outcomes across multiple runs, the replicability of results is assured through the *genfunction* utility introduced in the MATLAB coding.

3.5.3. Model evaluation

The developed ANN model is subject to a rigorous evaluation *via* an assortment of statistical metrics in order to determine the accuracy of its training and testing processes [329,345,422]. Specifically, the Coefficient of Determination (R^2) was relied upon for assessing correlation adequacy, Root-Mean-Square Error (RMSE) for predictive accuracy, Average Absolute Relative Deviation (AARD) for precision, and Average Standard Deviation (SD_{av}) for data variability and dispersion, alongside Normalized Median Absolute Deviation (NMAD), pivotal for assessing multi-property scenarios, and providing a comprehensive insight into the model's fitting and predictive capabilities. This attribute complements the first quartet of metrics, all defined in **Eqs. (3.109) – (3.112)**, which distinctly assess the model's performance in both target responses. In contrast, NMAD, derived from the expression outlined in **Eq. (3.113)**, delivers a wide-ranging outline across the entirety of output runs, normalizing deviations in effect and diminishing its sensitivity to outliers in comparison with RMSE. In the inverse variance method, weights are assigned inversely to variances, favoring variables of lower variance due to their enhanced stability and reliability. Certainly, all considered KPIs yield an in-depth overview of the machine learning's fitting and predictive capabilities, shedding light on areas of potential improvement from general trends to specific deviations.

$$R^2 = 1 - \frac{\sum(O_{act} - O_{pred})^2}{\sum(O_{act} - \overline{O_{act}})^2} \tag{3.109}$$

$$RMSE = \sqrt{\sum \frac{1}{N} \cdot (O_{act} - O_{pred})^2} \tag{3.110}$$

$$AARD = \frac{1}{N} \cdot \sum \left| \frac{(O_{act} - O_{pred})}{O_{act}} \right| \tag{3.111}$$

$$SD_{av} = \frac{1}{N} \cdot \sum (O_{pred} - \overline{O_{pred}})^2 \tag{3.112}$$

$$NMAD = \sum \omega_i \cdot \left(\frac{1}{N} \cdot \sum |O_{act,i} - O_{pred,i}| \right);\ \omega_i = \frac{{var_{O_i}}^{-1}}{\sum_{k=1}^{2} var(O_k)^{-1}} \tag{3.113}$$

where N is the number of observations, while $\overline{O_{act}}$ and $\overline{O_{pred}}$ are the mean of the actual and predicted values.

3.5.4. Applicability domain

In order to determine the predictive power of the developed ANN model, particularly extrapolative capabilities, the applicability domain (AD) is used [423–426], working as an outlier detection mechanism, while also demarcating the space in which the model's predictions can be considered scientifically reliable, thereby establishing a domain for extrapolations. To build this multi-dimensional space, leverage values (h_i) and Standardized Residuals (SDR) are integrated and visualized *via* William's plots [427]. Leverage values are determined by **Eq. (3.114)**, where z_i corresponds to the descriptor row vector for molecule i, and Z to the descriptor matrix associated with the training set, essentially assessing a molecule's similarity to the dataset's central tendency. Concurrently, SDR evaluates the model's predictive capability using **Eq. (3.115)**, where σ^2 is the residual variance. Furthermore, it is essential to introduce a warning leverage threshold, h^*, which serves as an upper limit to flag predictions less trustworthy due to a higher degree of extrapolation. This is calculated using **Eq. (3.116)**, incorporating d^*, the count of descriptors, and p, the total number of samples in the training set. Operational boundaries in the William plot are set when accounting a SDR checkpoint of ± 3 units, instrumental for quantitatively assessing the AD's Coverage (see **Eq. (3.117)**), where p_{AD} represent the number of data points within the AD. Combined, these metrics and visual tools contribute to a holistic comprehension of the QSPR model's operational scope, aiding in both validation and subsequent application.

$$h_i = z_i (Z^T \cdot Z)^{-1} z_i^T \tag{3.114}$$

$$SDR = \frac{\left(O_{pred} - O_{act}\right)^2}{\sigma^2} = \frac{O_{pred} - O_{act}}{\sqrt{\frac{\sum\left(O_{pred} - O_{act}\right)^2}{N}}} \tag{3.115}$$

$$h^* = \frac{3(d^* + 1)}{p} \tag{3.116}$$

$$AD_{coverage} = \frac{p_{AD}}{N} \tag{3.117}$$

3.5.5. Input relative contribution assessment

In the pursuit of understanding the intricate relationship between input descriptors and their significance of predicting output response in the context of neural networks and regression analysis, an analytical approach known as the Partial Derivatives (PaD) method is employed [428–430]. At the heart of this approach is the concept of differentiation, which essentially measures the rate of change of a function's output relative to infinitesimal alterations or perturbations in its input variables [426]. This is achieved by computing the partial derivative of the output with respect to each individual input descriptor, offering insights into the significance or relative contribution of each descriptor to the system's response. In this thesis, the PaD method is computed *via* a limit approach, using a ΔS_σ value of 0.5% (0.0001%, $S_\sigma = 0$) for approximation, enabling a precise examination of infinitesimal variations and deepening insights into the system's intrinsic dynamics. Using **Eq. (3.118)**, the magnitudes of partial derivatives indicate the dynamic effect of each input on the assessed output, highlighting their relative contribution. A matrix space is structured, as in **Eq. (3.119)**, wherein the summation of columns denotes the relative influence of corresponding input on the assessed response.

$$\frac{\partial f}{\partial S_\sigma} = \lim_{\Delta S_\sigma \to 0} \frac{f(S_1, \dots S_\sigma + \Delta S_\sigma, \dots S_{d^*}) - f(S_1, \dots, S_\sigma, \dots S_{d^*})}{\Delta S_\sigma} \sim \frac{f(S_1, \dots S_\sigma + \Delta S_\sigma, \dots S_{d^*}) - f(S_1, \dots, S_\sigma, \dots S_{d^*})}{\Delta S_\sigma} \quad \textbf{(3.118)}$$

$$\left(\frac{\partial f}{\partial \sigma_1} \quad \dots \quad \frac{\partial f}{\partial \sigma_{d^*}}\right)_{\forall N,\, d^*} \quad \textbf{(3.119)}$$

Chapter 4. Thermophysical Characterization of Refrigerants by Molecular Modeling and Machine Learning Tools

In this chapter, a comprehensive thermodynamic characterization of the refrigerants listed in ***Table 3.1*** *is presented focused on the use and predictive capabilities of the polar soft-SAFT EoS [209]. The physical significance of the polar soft-SAFT parameters is analyzed, and the relative contributions of terms related to the residual Helmholtz energy are computed. The corresponding coarse-grained models are validated by determining a broad set of thermophysical properties, including the enthalpy of vaporization, isobaric heat capacities, single-phase densities, and speed of sound. Additionally, refrigerant mixtures, including combinations with alkanes, carbon dioxide, or fluorinated compounds, are compared with experimental data to rigorously assess their accuracy. The chapter concludes with the application of machine learning techniques to predict key properties, such as soft-SAFT molecular parameters and saturation properties, including dew and bubble points.*

The main outcomes presented in this chapter have been already published in peer-reviewed papers (cited as [49,335]) in the Q1 journals ACS Sustainable Chemistry & Engineering and Industrial & Engineering Chemistry Research. Additional insights on Artificial neural Networks (ANN) for predicting dew and bubble saturation temperatures of CO_2-based mixtures have been submitted for publication in the Journal of Chemical Information and Modeling under the title "Machine Learning Integration in Thermodynamics: Predicting CO_2 Mixture Saturation Properties for Sustainable Refrigeration Applications".

4.1. Single components

The polar soft-SAFT parameters for a diverse array of refrigerants—encompassing 10 HFCs, 12 HFOs, 3 HCFOs, 9 hydrocarbons, and 4 additional compounds containing either iodine or oxygen—have been optimized against experimental data or molecular simulation results in order to use the EoS to calculate the thermophysical properties of these systems. This parameterization highlights the impact of molecular intrinsic characteristics, such as polarity and molecular charge distribution, on the physicochemical properties of refrigerants and provides validation for the corresponding coarse-grained molecular models to be used in a predictive manner. The second part of this section presents results from employing an innovative parameterization strategy through the application of open-source artificial intelligence methods. Specifically, artificial neural networks act as precursors to predict a wide spectrum of thermodynamic properties, key for the design and further enhancement of next-generation refrigerants.

4.1.1. Polar soft-SAFT EoS

Towards assessing the compatibility of low GWP refrigerants as drop-in replacements, their thermodynamic behavior needs to be characterized. This characterization has been carried out using the polar soft-SAFT EoS. The coarse-grain molecular models of the examined refrigerants explicitly account for dipolar interactions governing their macroscopic behavior. The optimized polar soft-SAFT parameters for the examined pure refrigerants are provided in **Table 4.1**, using the parametrization approach highlighted in the methodology section (refer to **sub-section 3.1**). As appreciated, the database has been extended including a batch of new fluorine-based substances, refrigerants integrating non-standard elements into their carbon-based structures — such as R13I1, effectively incorporating iodine, and RE170, a short-chain ether, first reported in the literature post-2020. The addition of these compounds in the study opens up new frontiers for the exploration of saturation properties.

Table 4.1. *Polar soft-SAFT molecular parameters for HFCs, HFOs and HCFOs studied in this thesis.*

Compound	m	σ / Å	ε/k_B / K	$\mu\cdot10^{-30}$ / C·m[§]	x_p	AAD$_P$[†] / %	AAD$_\rho$[*] / %	T range / K	Ref
HFCs									
R41	1.371	3.400	180.3	6.17427	0.50	1.494	0.763	200-280	[49]
R32	1.376	3.506	164.5	6.59790	0.75	0.565	0.255	200-316	[49]
R23	1.397	3.610	147.9	5.50047	0.90	1.327	0.155	200-270	[49]
R161	1.577	3.693	232.3	6.47014	0.33	1.374	0.414	200-340	[49]
R152a	1.662	3.754	202.3	7.54522	0.50	0.993	0.792	200-356	[49]
R134a	1.813	3.770	169.5	6.86475	0.70	1.443	0.389	200-344	[49]
R125	1.887	3.790	165.1	5.21360	0.90	1.618	0.274	200-310	[49]
R245fa	2.479	3.675	197.1	5.16690	0.80	1.593	0.596	230-395	[49]
R236fa	2.056	4.012	172.4	6.61124	0.90	2.410	0.554	270-370	[49]
R227ea	2.131	4.033	190.7	4.85669	1.00	4.224	0.260	230-345	[49]
HFOs									
R1123	1.527	3.760	175.3	5.73730	0.80	2.963	0.199	230-300	[49]
R1243zf	1.904	3.880	170.0	8.16890	0.50	1.092	0.295	270-345	[49]
R1234yf	1.740	4.082	191.6	6.70790	0.70	1.150	0.314	250-331	[49]
R1234ze(E)	2.044	3.821	204.0	4.80330	0.75	3.016	0.555	250-351	[49]
R1225ye(Z)	2.077	3.845	172.4	6.03750	0.80	1.018	0.260	250-355	[49]
R1336mzz(Z)	1.806	4.430	195.6	10.6406	0.60	3.287	0.565	325-415	[49]
R1132a	1.750	3.530	160.93	4.5998	0.65	1.676	0.222	198-293	TT
R1132(E)	2.598	2.988	179.9	-	-	1.289	0.309	220-325	TT
R1234ze(Z)	1.541	4.271	180.66	9.6734	0.75	1.735	0.272	240-360	TT
R1345fz	2.031	4.150	143.56	9.4282	0.60	1.705	0.643	278-353	TT
R1336mzz(E)	3.633	3.386	184.6	-	-	1.847	0.605	286-375	TT
R1336yf	2.047	4.180	155.73	8.4175	0.70	2.112	0.546	278-353	TT
HCFOs									
R1233zd(E)	2.331	3.819	232.6	3.81190	0.80	2.936	0.506	250-400	[49]
R1224yd(Z)	2.278	3.899	202.4	5.63720	0.85	1.358	0.237	280-375	[49]
R1224yd(E)	2.171	3.957	190.47	6.8614	0.85	2.533	0.440	300-380	TT
HCs									
R170	1.413	3.756	204.93	-	-	2.136	0.822	150-280	TT
R290	1.801	3.811	222.38	-	-	1.470	0.396	150-340	TT
R600	2.134	3.871	237.7	-	-	-	-	-	[371]
R600a	1.942	4.036	240.3	-	-	-	-	200-400	[431]
R601	2.497	3.901	246.6	-	-	-	-	-	[371]
R601a	2.223	4.068	254.86	-	-	2.465	0.318	180-380	TT
R1150	1.711	3.372	170.54	-	-	1.889	0.446	180-270	TT
R1270	1.979	3.566	207.90	-	-	1.830	0.264	180-340	TT
1-butene	2.147	3.762	228.8	-	-	-	-	120-420	[370]
Others									
R13I1	2.004	3.830	223.00	3.4958	0.60	0.220	0.287	300-360	TT
RE170	2.009	3.447	225.04	4.3397	0.33	1.099	0.168	180-350	TT
CO_2^+	1.571	3.166	166.5	-	0.33	0.340	0.562	-	[224]
R7200	2.113	4.916	214.6	11.21	0.68	3.243	0.162	280-380	[230]

[§]Experimental dipole moments [25,141,208,250,253,432–435].

[†]Experimental vapor pressure from references [141,249,442–445,253,432,436–441].

[*]Experimental saturated densities from references [141,249,447–450,253,432,436,438,440,441,443,446].

[+] *Q = 14.68E-40 C·m²*.

TT ≡ This Thesis.

The adequacy of these regressed parameters can be established through comparing polar soft-SAFT calculations for coexisting densities and vapor pressure against experimental data used in the parameterization procedure, as provided in **Figure 4.1**, for selected 4th generation refrigerants (HFOs and HCFOs). These parameters accurately capture the experimental trends for these properties with an average deviation for saturated liquid density (AAD% ρ_L) below 1.0% in all cases, while for vapor pressure, the average absolute deviation (AAD% P) is below 3.0% in most cases, with some few exceptions that are within an acceptable 4.5%. It should be noted that in the vicinity of the critical region, polar soft-SAFT overestimates the critical properties of the pure fluids, due to the mean-field formulation of the theory. This limitation is shared by all SAFT-based EoSs, and can be solved through the addition of the crossover term [372], which is outside the scope of this thesis. Similar model performance was obtained for 3rd generation HFCs, with their polar soft-SAFT computed coexisting densities and vapor pressure included in **Figure A1** in the **Annex**.

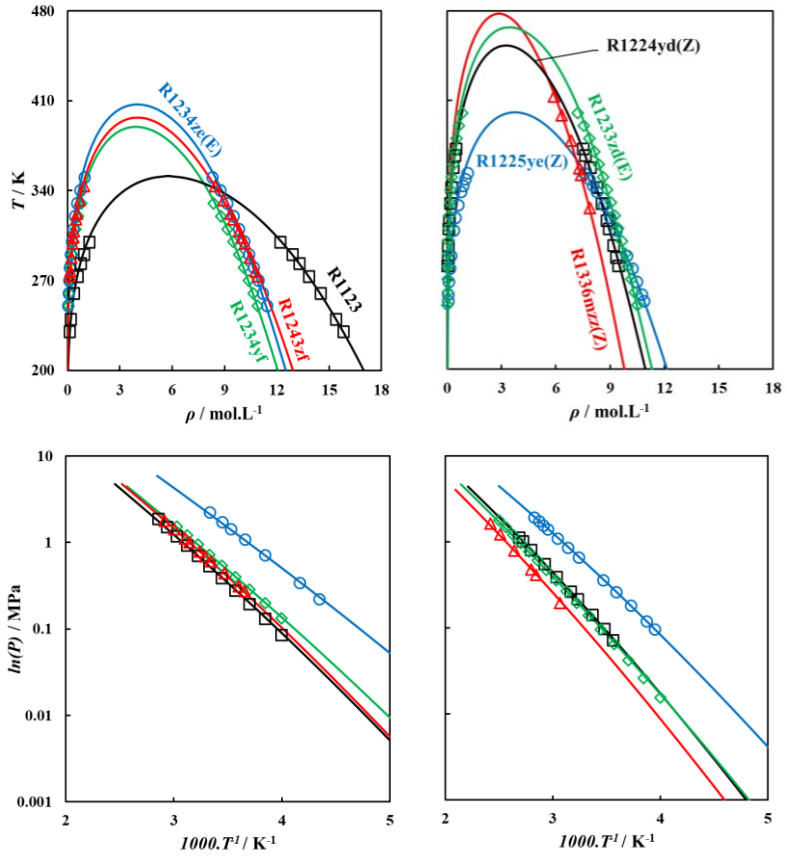

Figure 4.1. *Coexisting densities (**top**), and vapor pressure (**bottom**), of pure HFOs, and HCFOs studied in this work, with polar soft-SAFT calculations using parameters from **Table 4.1** (solid lines), compared to experimental data (symbols). References for the experimental data are provided in **Table 4.1**.*

4.1.1.1. Effect of molecular features on refrigerants physicochemical properties

The advantage of the previously optimized parameters is their physical meaning, related to the size and energy of the molecule, allowing extraction of molecular features, and understanding their effect on macro-level properties. This is of paramount importance as it helps in guiding experimental efforts in the design of alternative refrigerants with desirable physicochemical properties affecting the technical efficacy of the working fluids in their intended applications.

The change in the liquid density of a selection of refrigerants, predicted at $T = 250$ K, is closely related to the volume occupied by the molecule ($m\sigma^3$) as provided in **Figure 4.2**. The increase in molecular volume results in lower liquid molar densities, which also means higher vapor molar densities. This change is dependent on structural features such as the number of carbons in the chain, number and type of halogenated atoms, and the type of carbon-carbon bonds, with varying degrees of contributions. The most notable structural features with distinct impact on the size of the molecule are the carbon number and degree of halogenation, with their increase leading to a higher molecular volume. This fact is clearly observed in the single carbon series R41, R32, and R23, with increasing fluorine atoms, as well as for R32 and R152a (both with two fluorine atoms) when increasing the number of carbons.

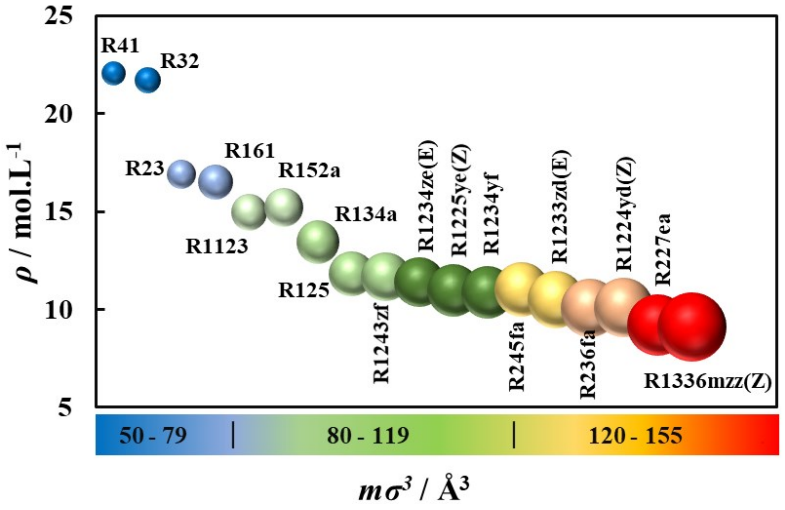

Figure 4.2. *Effect of molecular volume on predicted molar liquid density at T = 250 K for refrigerants using polar soft-SAFT. Notice that the size of the sphere reflects the molecular volume as shown in the color scale [49].*

Based on these trends, and in view of the objective of maximizing the suction density of the refrigerant (vapor phase), it can be expected that larger refrigerants, such as R227ea and R1336mzz(Z), would be adequate refrigerants judging solely by this criterion, reflective of smaller compressor sizing. It should be noted that for practical applications, the analysis can be done on the basis of liquid mass densities, with similar results albeit reversed trends, with refrigerants with lower molecular volumes having lower liquid mass densities, consistent with their lower molecular weights. Notice also that the effect of increasing carbon chain length from the two-carbon backbone HFCs to three-carbon backbone HFOs/HCFOs resulted in similar trends, consistent with increased molar mass of these refrigerants in as shown in **Figure 4.3**. Similarly, the replacement of chlorine in HCFOs with the fluorine in their counterpart HFOs (*i.e.,* R1233zd(E) *vs.* R1234ze(E), and R1224yd(Z) *vs.* R1225ye(Z)) has a larger impact on increasing the molecular volume of the refrigerant associated with chlorine's higher atomic weight. These trends are also supported by the increased contribution of the chain term (A^{chain}) to the residual Helmholtz energy of the molecules (A^{res}), obtained from **Eq. (3.1)** at $T = 250$ K, shown in **Figure 4.3**.

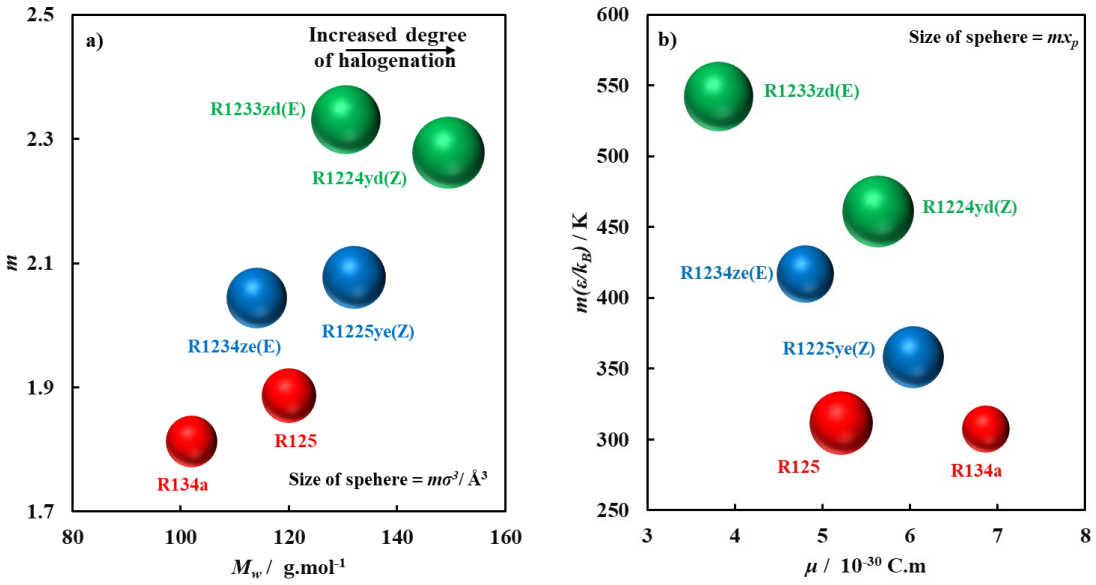

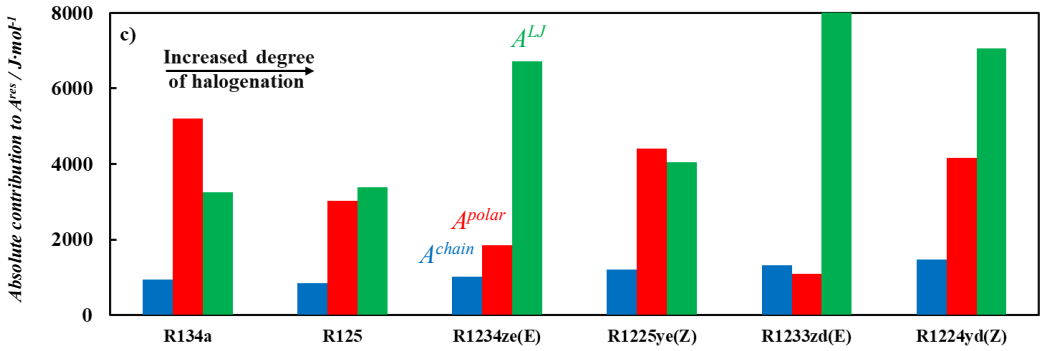

Figure 4.3. *Comparative analysis of polar soft-SAFT CG model parameters for the selected refrigerants in terms of* ***a)*** *effect of molecular weight on chain length and molecular volume of the refrigerants (represented by the size of sphere),* ***b)*** *dipole moment compared versus LJ molecular energy of the refrigerants and polar segments, mx_p (represented by the size of sphere), and* ***c)*** *polar soft-SAFT predicted absolute contributions of the different terms to residual Helmholtz energy at T = 250 K (**Eq. (3.1)** with $A^{assoc} = 0$). The values of the parameters are provided in **Table A2** in the **Annex**.*

Probing further into the molecular complexities, the chain length and segment diameter reveal an ordered progression consistent with the molecular size for tested hydrocarbons, given that R601 exhibits the longest chain, followed sequentially by R600, R600a, R290, and R170. In terms of segment diameter, a similar order is apparent with R601a displaying the largest value, moving down through R600a, R601, R600, R290, to R170.

Less noticeable effects are associated with the presence of double bonds *vs.* single bonds, the type of halogen atom, and their position in the molecule. The presence of double bonded carbons marginally reduces the molecular size as opposed to single bonded carbons, due to their lower bond length, as seen for the unsaturated R1225ye(Z) compared to the saturated R245fa. Expanding on the detailed analysis, it is discerned that within the di-carbon HFOs, R1123 is distinguished with the largest molecular volume and dipole effect, while R1132(E) exhibits greater chain length indicative of its linear conformation. Conversely, R1132a manifests a reduced dipole effect, a consequence of the alignment of fluorine atoms on the same carbon, which reduces the intensity of the molecular polarity in comparison to R1132(E). R1234ze(E) stands out among the tri-carbon HFO family members with its long chain length, a consequence of a more linear structural conformation, while R1234ze(Z) is notable for a bulkier size, evidenced by the larger segment diameter and molecular volume. R1234yf and R1243zf present an intermediate pattern, balancing molecular dimensions and reduced polarity due to a more localized effect of the dipole. On balance, increasing the degree of halogenation for HFOs,

and HCFOs, resulted in a reduction in the dispersive energy, accompanied with increased magnitude of dipole moment, and polar segments. This is also seen from the increased polar contribution and reduced reference term contribution (LJ interactions) to the residual Helmholtz energy shown in **Figure 4.3c**. Hence, this can be attributed to the presence of double-bonded carbons in these molecules, being polarizable, as opposed to saturated carbon bonds, and contributing to the charge asymmetry for these refrigerants. In similar notions, the presence of chlorine marginally increases the molecular size due to its larger atomic radius compared to fluorine atom, observed for the R1234ze(E) HFO, and its counterpart R1233zd(E) HCFO.

To better elucidate the importance of explicitly accounting for the polarity of the refrigerants investigated herein, the relative contribution of the different terms (*i.e.,* LJ reference, chain, and polar) to the residual Helmholtz free energy density (see **Eq. (3.1)**), were predicted from the thermodynamic model at T = 250 K, and P = 0.1 MPa, as provided in **Figure 4.4**.

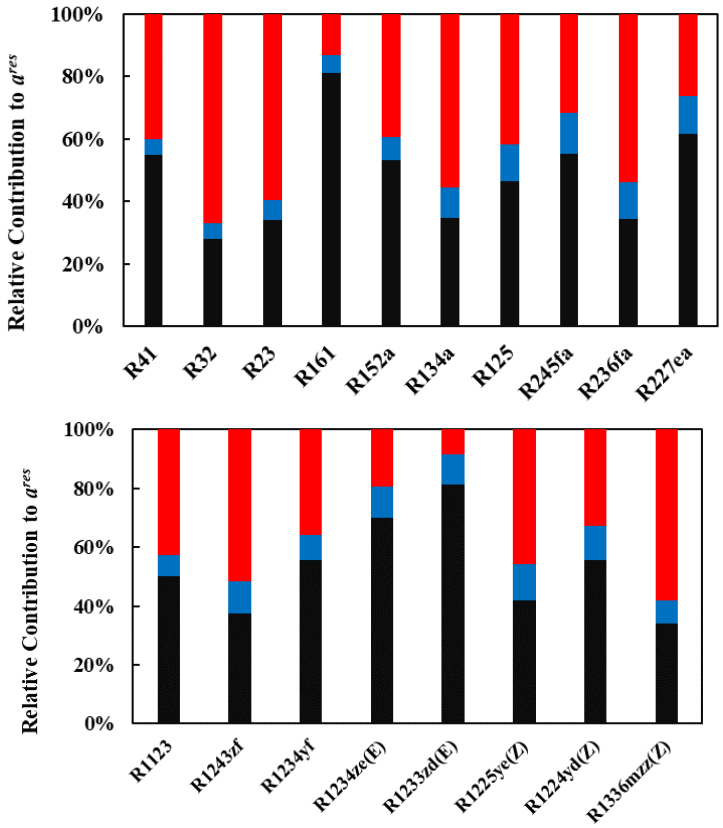

Figure 4.4. *Relative contribution of the various terms (LJ reference (■), chain (■), and polar (■)) to the residual Helmholtz energy (A^{res}) in the CG models for selected HFCs* ***(top)****, HFOs, and HCFOs* ***(bottom)*** *predicted from polar soft-SAFT at T = 250 K and P = 0.1 MPa.*

For the majority of the refrigerants, the polar contributions to the Helmholtz energy have a large impact in the range of 25 – 67%, with the exception for R1233zd(E), and R161, clearly demonstrating the importance of explicitly including the effect of dipolar interactions in their CG molecular models. These predictions can help in understanding the relative importance of the different intermolecular interactions on the physicochemical properties, similar to the aforementioned case with density. For saturated HFCs with similar carbon number such as R161, R152a, R134a, and R125 (all with two carbon atoms), a higher degree of fluorination is accompanied with increased contribution of dipolar interactions compared to dispersive, provided in **Figure 4.4 (top)**. This is distinctly seen moving from R161 (1 F), R152a (2 F) up to R134a (4 F), associated with the assumed increase in molecular segments influenced by the dipole moment (mx_p). Notice that the move from R134a (4 F) to R125 (5 F) resulted, however, in a reduction in the polar contribution attributed to the reduced dipole moment of the latter owing to the effect of the additional fluorine atom on making the charge distribution more symmetrical. The same trends were also observed for HFCs with one carbon atom (*i.e.,* R41, R32, and R23), and three carbon atoms (*i.e.,* R245fa, R236fa, and R227ea). Moving to HCFOs, R1233zd(E) has longer chain lengths, contrary to R1224yd(E), which exhibits a larger segment diameter, influenced by the spatial arrangement of the chlorine amidst the fluorine atoms.

Shifting the focus on the effect of the carbon number with similar degree of halogenation, such as R41 *vs.* R161 (1 fluorine atom), or R32 *vs.* R152a (two fluorine atoms), it is observed that the polar contribution decreases with increasing carbon chain length, as the increased size of the compound reduces the portion of the molecule influenced by the dipole moment, irrespective of its magnitude. This has also been previously observed for 2-ketones[209]. The effect of the degree of fluorination is quite different in the case of unsaturated HFOs, and HCFOs. For HFOs with similar carbon number (*i.e.,* three carbons), such as R1243zf, R1234yf, R1234ze(E), and R1233zd(E), the polar contribution is reduced with increasing the degree of fluorination. This can be associated with the higher polarizability of the double bonded carbons compared to single bonded carbons, leading to a more symmetrical charge distribution, dampening the effect of the dipole moment. The type of halogen atom also has an influence on the polar contribution, with HCFOs having lower polar contribution compared to their HFOs

counterparts (*i.e.,* R1233zd(E) *vs.* R1234ze(E)), consistent with the lower electronegativity of chlorine compared to fluorine. Regarding the dipolar contributions of RE170 and R13I1, particular attention is given to the electronegativity of constituent atoms, which plays a key role in determining the strength of the dipole effects. The hierarchy of electronegativity (fluorine > oxygen > chlorine) guides the impact of dipolar interactions, as iodine and hydrogen's minimal contributions have led to a dipole-affected fraction of 3/5 for R13I1, reflecting the iodine atom's dimensions within the molecular volume. For RE170, the relatively similar atomic weights of oxygen and carbon, unlike the heavier halogen atoms, justify a minimal ratio of 1/3. Further validation involved delving into alkanes and ethers, such as R290 and diethylene glycol dimethyl ether, respectively, establishing RE170's chain length at a midpoint. Also, it is important to notice the effect of the position of fluorine atoms seen in the case of R1234yf *vs.* R1234ze(E), with the increased polar contribution of R1234yf due to the proximity of the isolated fluorine to the fully fluorinated carbon, increasing the overlapping electrostatic potential and, consequently, the polarity of the molecule. As also appreciated, the dipole segment value for R1224yd(E) exceeds that of R1233zd(E), reflecting the complete bonding of its carbon structure to electronegative elements, either strongly polarizing fluorines or moderately electronegative chlorines.

These molecular tendencies will manifest on properties such as vapor pressure, and enthalpy of vaporization. For example, the low vapor pressure for R1336mzz(Z) is due to its high dipole moment, resulting in the highest polar contribution (see **Figure 4.4**). Still, it remains quite difficult to distinctly isolate the effect of polar interactions on these properties, as they are affected by the combined contribution of structural effects and intermolecular interactions. Note that the contributions reported in **Figure 4.4** are relative rather than absolute, normalized to each refrigerant’s residual energy.

4.1.1.2. Validation of the refrigerants coarse-grained molecular models

The strength of using molecular-based EoSs, even if some limited experimental data are needed for parametrization, is the fact that, once the CG molecular models are developed, they can be used in a fully predictive manner to obtain other thermodynamic properties not included in the parametrization. These predictions typically serve as another layer of reliability and accuracy testing, especially in the case of first- and second-order derivative properties, due to their heightened sensitivity to errors compared to modeling the vapor-liquid equilibria (VLE) of the pure fluid [96,431]. Additionally, explicit inclusion of dipole-dipole interactions in the model is paramount for accurate predictions of these derivative properties as demonstrated in the literature [190,209].

The additional predicted properties for the modeled refrigerants include enthalpy of vaporization (ΔH_{vap} *or* RE), single-phase density, isobaric heat capacity (C_P), and speed of sound (ω), as provided in **Figure 4.5**, for selected 4th generation refrigerants, while those for the remaining refrigerants can be found in **Figures A2 – A5** in the **Annex**. It should be noted that predictions for the isobaric heat capacity require the inclusion of the ideal gas isobaric heat capacities (C_p^{IG}), obtained from available literature data [432,451]. Quantitative agreement between model calculations and experimental data [432,452–454] is excellent (AAD < 3.0% in most cases) for the enthalpy of vaporization, single phase density, and speed of sound, while the deviations for predicted isobaric heat capacity are within an acceptable 5%, further attesting the accuracy and predictive capability of the equation in modeling refrigerants. The enthalpy of vaporization is another measure for the strength of the intermolecular interactions, with higher values reflective of stronger intermolecular interactions, as seen in the case of R1233zd(E), with its larger dipole moment and higher dipolar molecular segments compared to the others, requiring more energy to transition the molecule from the liquid to the vapor phase. In particular, R601a and R1224yd(E) stand out for their exceptional precision, with deviations below 1%, closely followed by R1234ze(Z) and R1336yf, with R1150 and R1270 proving slightly higher AARDs (4.84% and 3.18%, respectively). Additionally, the change in single-phase densities is consistent with their molecular volumes, with

R1233zd(E) having the lowest single-phase density, due to its larger molecular volume compared to the former two.

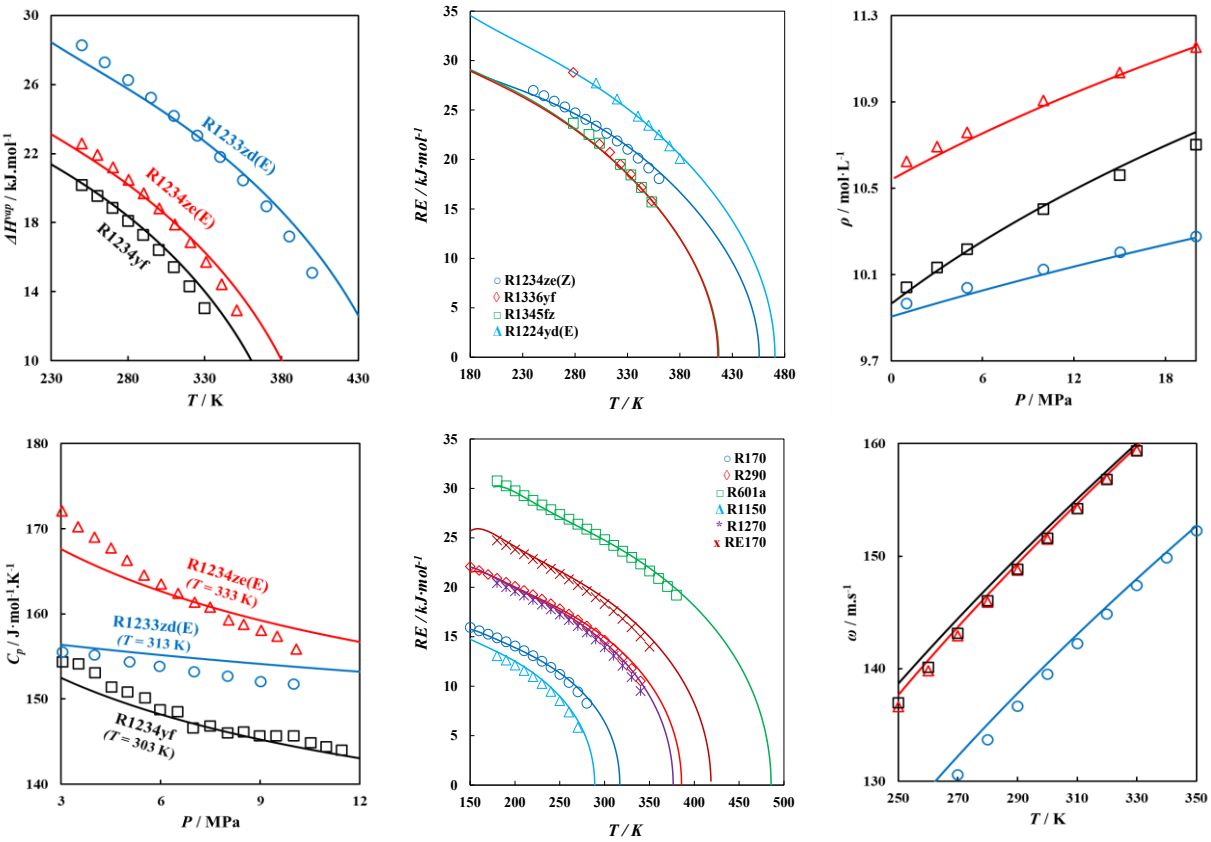

Figure 4.5. *Thermodynamic properties of low GWP refrigerants, including enthalpy of vaporization (see **Eq. (3.25)**), single phase density, isobaric heat capacity (see **Eq. (3.48)**), and speed of sound (see **Eq. (3.49)**), with polar soft-SAFT predictions (solid lines) compared to experimental data [141,253,452–454,432,441–445,449,450] (symbols).*

4.1.2. Artificial neural networks

Alternatively, another method for obtaining the saturation properties of refrigerants involves the use of machine learning techniques. Specifically, artificial neural networks can be employed to predict the molecular parameters that characterize their coarse-grained models.

4.1.2.1. σ-profile and molecular descriptors of selected refrigerants from COSMO-RS

Based on the aforementioned approach in the methodology section (refer to **sub-section 3.5.1**) and the geometrically optimized 3D structure for a selection of pure refrigerants, the discretized σ-profiles are provided in **Figure 4.6**. This approach has been applied to a subset of refrigerants in **Table 4.1**, as a preliminary test of the novel methodology under development, which could subsequently be extended to the remaining components of the list. The discretization of the σ-profiles into eight molecular descriptors with a σ step size of 0.00625 e/Å^2, provides insight on the atomistic nature of each molecule and their contribution to its governing intermolecular interactions based on the location, height, and width of the peaks [335]. For example, for HFCs with one carbon atom, such as R41, R32, and R23, seen in **Figure 4.6a**, the left-side skewness of their σ-profile increases with the number of fluorine atoms in the molecule, making their hydrogens more positively polarized (transition from S_4 to S_2 with decreasing peaks), while their fluorine less negatively polarized (transition from S_6 to S_5 with increasing peaks). The same is observed for HFCs with 2 or 3 carbon backbones, as shown in **Figure 4.6b**, and **c**, respectively. For HFOs in **Figure 4.6d**, and **e**, and HCFOs in **Figure 4.6f**, the small less distinct peaks seen in the slightly positive polarity region (S_4) can be attributed to the double-bonded carbons in their structure. For all examined refrigerants, no distinct peaks were observed in the strongly positive polarity (S_1), and strongly negative polarity (S_7 and S_8), as these regions are attributed to ions, as such, these descriptors were removed from the training dataset. In some cases, such as those for R23, R125, and R227ea, the small probability of strongly positive polarizable atoms shown from the small peaks in (S_2) was attributed to the effect of the halogens on polarizing the single hydrogen in their molecular structure. The ANN inputs dataset descriptors, *including the molecular weight and the five COSMO-RS discretized profiles,* are provided in **Table A1** in the **Annex**.

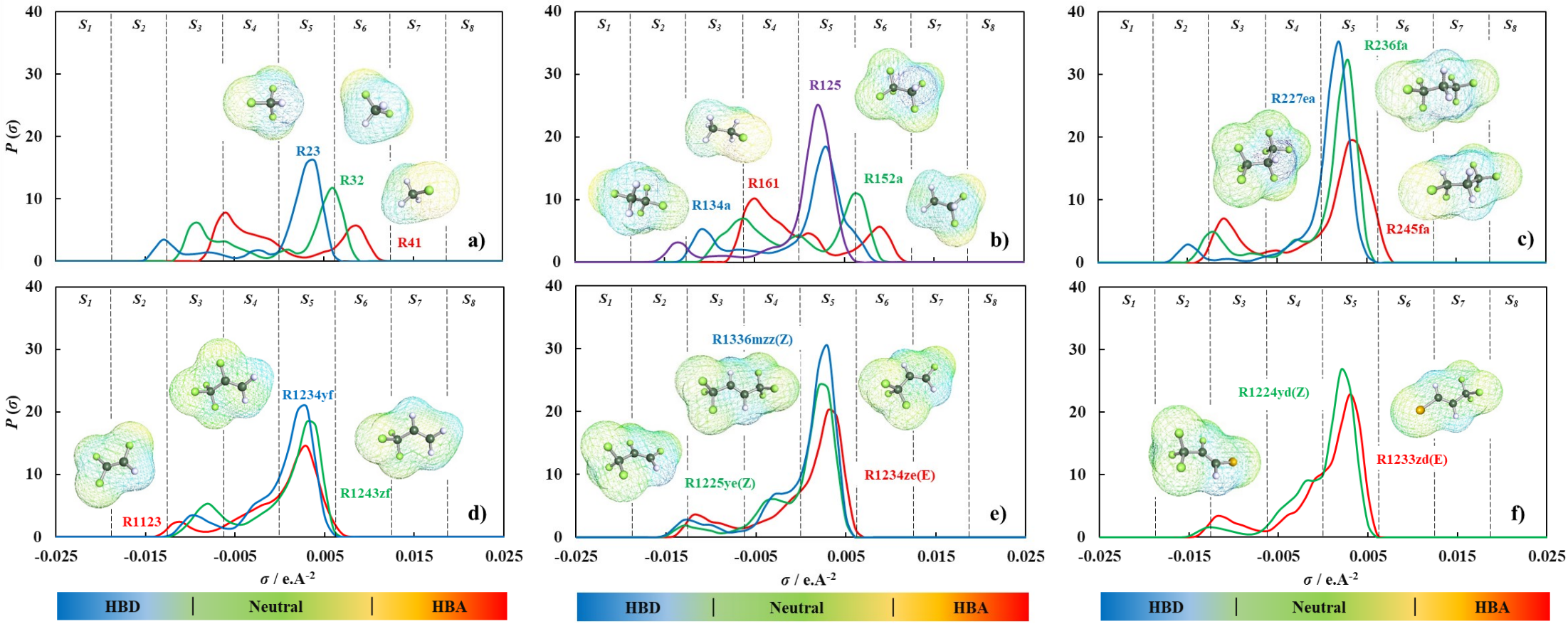

Figure 4.6. *COSMO-RS calculated σ-profiles for the 18 refrigerants with* ***a)*** *HFCs with 1 carbon,* ***b)*** *HFCs with 2 carbons,* ***c)*** *HFCs with 3 carbons,* ***d)*** *and* ***e)*** *HFOs, and* ***f)*** *HCFOs [335].*

4.1.2.2. Model performance and evaluation

With the datasets for the eighteen refrigerants obtained using the aforementioned molecular modeling approaches (COSMO-RS and polar soft-SAFT), the ANN model for predicting polar soft-SAFT molecular parameters was developed, with the network topography shown in **Figure 4.7**. The architect of the best performing network, out of the several options developed in earlier stages, required two hidden layers. The first hidden layer contained 12 neurons for directly computing the fraction of polar segments (x_p), and dipole moment (μ) of the molecule, with 3 and 9 neurons for each, respectively. The second hidden layer has a dimension of 4 neurons and receives inputs from the neurons of the first hidden layer. This second layer is used for calculating the remaining polar soft-SAFT parameters (*i.e.* chain length, volume, and LJ energy of the molecule). The network was trained with data for 15 refrigerants, while the remaining three (*i.e.,* R32, R134a, and R1243zf) were used for testing the trained ANN model. While the database may appear limited, it is important to acknowledge that this is a preliminary study, and the scope of data reflects the early stage of research. Overall, the developed network required 120 weights, and 16 biases, to correlate COSMO-RS molecular descriptors with the polar soft-SAFT molecular parameters of the studied refrigerants. The associated weights and biases for all links between neurons in each layer are provided in **Tables A3 – A5** in the **Annex**.

The architect of the developed network was chosen to segregate the molecular parameters applicable for all molecular families (*i.e.,* dispersive, associating, polar, *etc*.) from those specific for polar fluids (*i.e.,* μ, x_p), within the same integrated network. This framework has the possibility of flexible future application and extension to other molecular families with different chemical nature than the dipolar refrigerants included in this thesis. Additionally, during ANN model development, it was established that the number of hidden neurons in each processing layer was decisive in controlling the accuracy and complexity of the model. The number of neurons in each layer were incrementally changed up to the number of critical neurons in each layer without substantial improvement in modeling accuracy, while maintaining a relatively simple architecture.

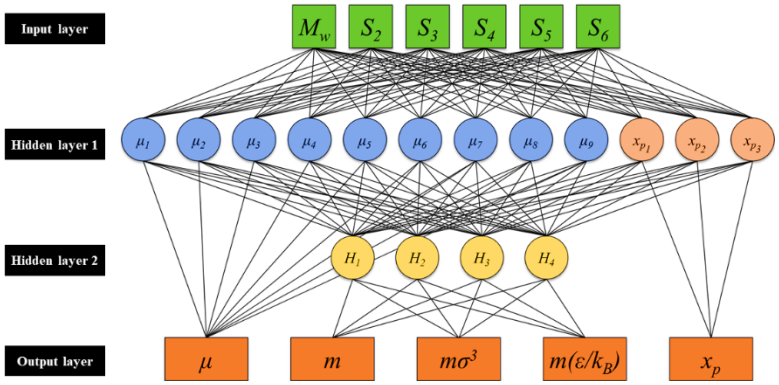

Figure 4.7. *The integrated 6-9-1, 6-3-1, and 6-12-4-3 ANN to predict polar soft-SAFT molecular parameters for the studied refrigerants.*

Provided in **Table 4.2** is a summary of the performance of the training and testing of the developed ANN model based on statistical indicators. The accurate training of the ANN model can be established from its high $R^2 > 0.99$, and narrow dispersion (*i.e.,* small RMSE), especially for μ, and x_p parameters, due to the high number of processing neurons, used in their correlation. Conversely, for the remaining parameters, the fitting provides a reasonable level of accuracy ($R^2 > 0.97$), and acceptable level of dispersion for some data points. This can also be visually supported from the parity plots shown in **Figure 4.8** comparing ANN predicted polar soft-SAFT parameters (y-axis), and those obtained using standard parametrization approach, fitting to experimental data (x-axis). It should be noted that the higher values of the statistical indicators for training and testing ANN for $m(\varepsilon/k_B)$ output parameter are associated with its larger magnitude. Notwithstanding, these results indicate an adequate training of the developed model and its ability to map the relation between the chosen inputs and outputs. The subsequent testing of the model's external predictive power using refrigerants R32, R134a, and R1243zf, also shown in **Table 4.2** and **Figure 4.8**, attests to its high predictive accuracy supported by the statistical indicators and acceptable agreement between predicted and fitted parameters for those refrigerants.

Table 4.2. *Statistical performance of ANN model training and testing for each network output.*

Indicator	***R^2***		***AARD%***		***RMSE***		***SD_{avg}***	
Parameter	**Training**	**Testing**	**Training**	**Testing**	**Training**	**Testing**	**Training**	**Testing**
$\mu \cdot 10^{-30}$ / C·m	0.9970	1.0000	1.32	0.49	0.0899	0.0355	0.05	0.02
x_p	0.9996	0.9998	0.31	0.24	0.0038	0.002	0.00	0.00
m	0.9786	0.9994	2.15	2.92	0.0510	0.050	0.03	0.03
$m\sigma^3$ / Å^3	0.9847	0.9452	2.72	5.97	3.561	5.229	1.97	3.64
$m(\varepsilon/k_B)$ / K	0.9841	0.7981	2.51	6.78	11.150	20.170	6.05	13.87

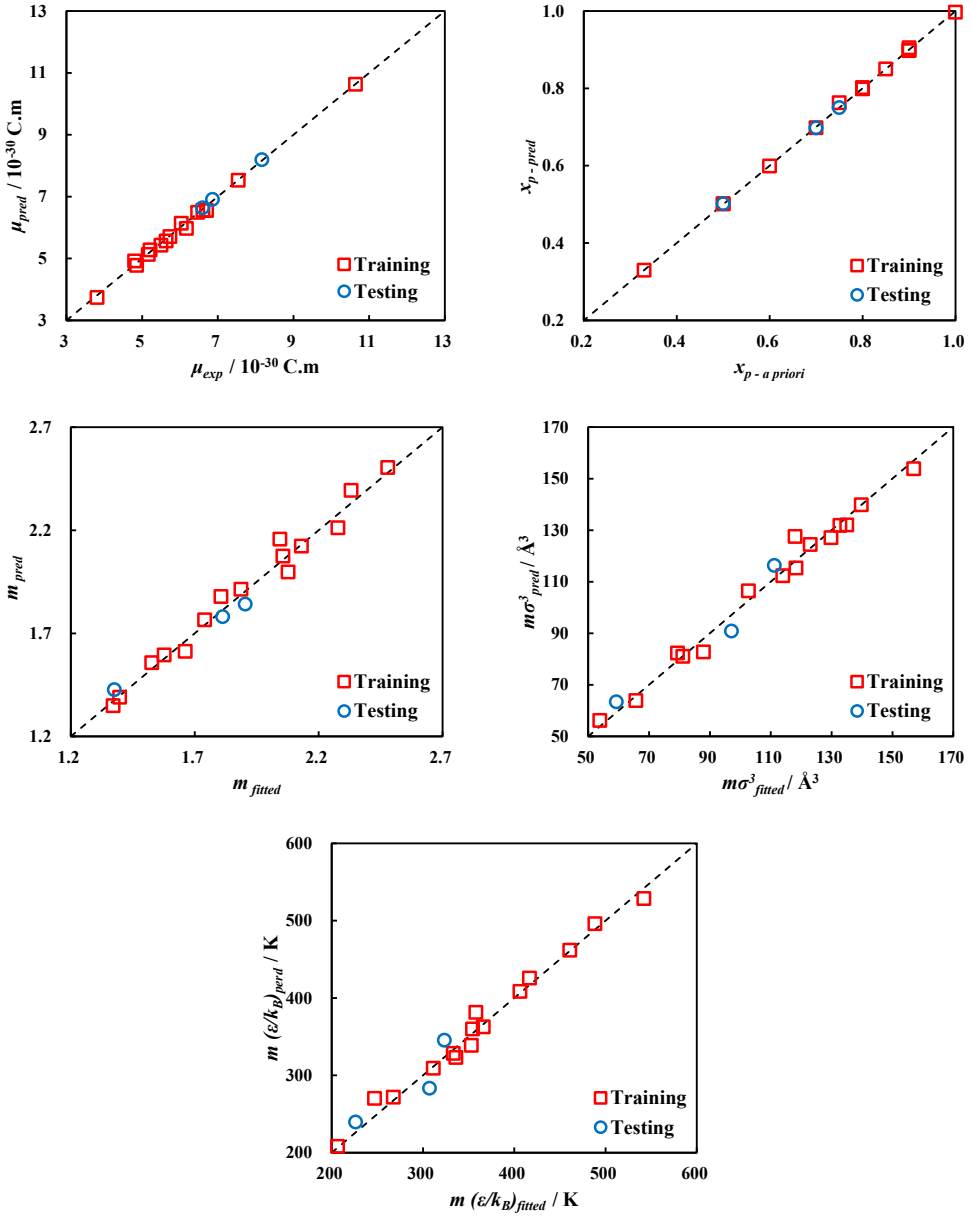

Figure 4.8. *Parity plots of fitted vs. ANN predicted polar soft-SAFT parameters for training and testing dataset.*

To better elucidate the impact of ANN accuracy on predicting molecular parameters for molecular theory, the ANN predicted parameters were utilized to predict the vapor pressure and saturated liquid density of the pure refrigerants using polar soft-SAFT compared to experimental property data [188,249,436–440,446–448] quantified in terms of absolute average deviation. As highlighted in **Table 4.3**, the standard parametrization has a higher accuracy in predicting the thermodynamic properties of pure refrigerants, with average *AAD* of 1.899%, and 0.405% for vapor pressure and saturated

liquid density, respectively. Although, the training of the ANN-model showed high accuracy (see **Table 4.2**), the application of the ANN predicted parameters into molecular theory was associated with higher deviations from experimental data than those seen earlier for parameters from standard procedure, with an average *AAD* of 4.753%, and 1.539% for vapor pressure and saturated liquid density, respectively. The higher deviation obtained for the vapor pressure is closely linked to the lower correlatability of COSMO-RS molecular descriptors with the dispersive energy of the molecules ($m\varepsilon/k_B$), in **Table 4.2**, as the *σ-profile* molecular descriptors are more descriptive of structural features rather than energetic ones, however, with sufficient details to obtain an acceptable mapping relationship between the inputs and outputs. It is expected than an increase of the database would probably enhance those results, decreasing the uncertainty in the vapor pressure calculation.

Table 4.3. *AAD for vapor pressure and saturated liquid density between polar soft-SAFT predictions and experimental data for the pure refrigerants. The deviations are computed using parameters obtained with standard parametrization produce and ANN-predicted.*

	Standard parametrization [49,103]		**ANN predicted**		***T* range / K**
Compound	AAD_{P^*} **/ %**[†]	AAD_{ρ} **/ %**[§]	AAD_{P^*} **/ %**[†]	AAD_{ρ} **/ %**[§]	
Training Set					
R41	1.494	0.763	7.110	1.068	200-280
R23	1.327	0.115	1.388	1.629	200-270
R161	1.374	0.414	2.678	2.403	200-340
R152a	0.993	0.792	5.259	2.607	200-356
R125	1.618	0.274	2.060	2.125	200-310
R245fa	1.593	0.596	6.880	0.780	230-395
R236fa	2.410	0.554	5.089	0.678	270-370
R227ea	4.224	0.260	4.985	0.312	230-345
R1123	2.963	0.199	8.659	1.002	230-300
R1234yf	1.150	0.314	4.402	0.526	250-331
R1234ze(E)	3.016	0.555	3.518	2.286	250-351
R1225ye(Z)	1.018	0.260	3.343	4.508	250-355
R1336mzz(Z)	3.287	0.265	1.226	0.353	325-415
R1233zd(E)	2.936	0.506	9.172	1.342	250-400
R1224yd(Z)	1.358	0.237	1.114	1.585	280-375
Testing Set					
R32	0.565	0.225	5.821	2.827	200-316
R134a	1.443	0.389	7.415	2.440	200-344
R1243zf	1.092	0.295	5.439	0.874	270-345
Average	1.899	0.405	4.753	1.539	-

[†]Experimental vapor pressure from references [188,249,436–440].
[§]Experimental saturated densities from references [188,249,436,438,440,446–448].

For the developed ANN, the relative importance of each input parameter descriptor and usefulness in predicting the polar soft-SAFT output parameters are provided in **Figure 4.9**. It can be seen that, for predicting the dipole moment, chain length, molecular volume, and molecular dispersive energy, the most important features are S_5 (denoting slightly negative regions) and the molecular weight. The connection between the molecular weight and the chain length and molecular volume has been previously highlighted in **Figure 4.3a**. The same can also be established for the importance of S_5 input feature, as it has the largest magnitude among all COSMO-RS inputs, related to the degree of fluorination, being the most influential factor on the intermolecular interactions of the refrigerants. In the case of the fraction of polar segments, the importance of S_2 feature is the largest, highlighting the direct relation between this parameter and the most positively polarized area of the compounds studied. Overall, both S_5 and molecular weight have the largest impact on correlating the polar soft-SAFT parameters, while the remaining input features have a similar level of importance ≈ 15%.

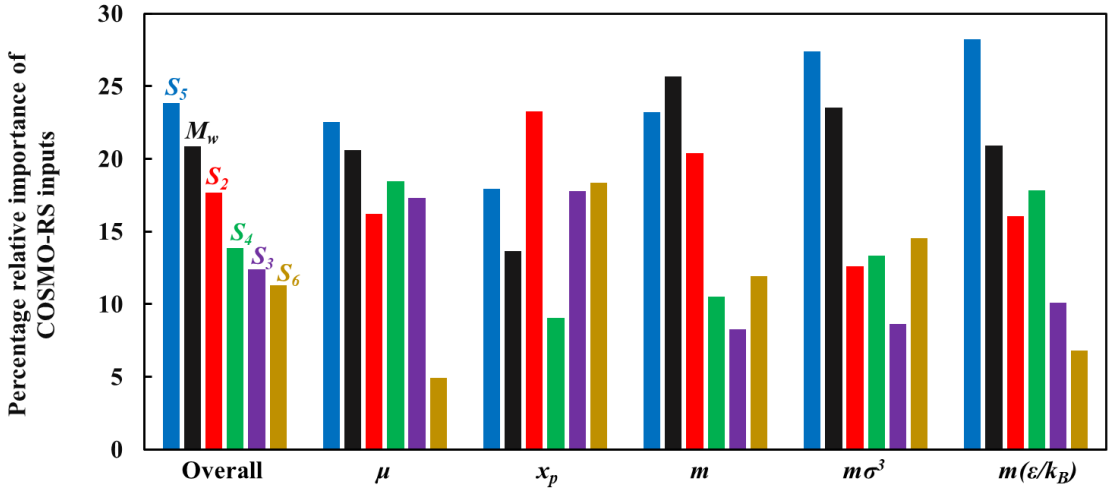

Figure 4.9. *Relative importance (%) of ANN inputs for predicting each polar soft-SAFT output parameters and in overall terms.*

4.1.2.3. Prediction of thermophysical properties of refrigerants using the developed model

An ultimate test for assessing the adequacy of the polar soft-SAFT molecular parameters predicted by the ANN was performed through using these parameters for the needed thermodynamic characterization of selected refrigerants, including co-existing densities, vapor pressure, single phase density, heat capacity, enthalpy of vaporization,

and speed of sound. This is a rigorous testing framework applicable for any thermodynamic model and methodology (as shown in **Figure 4.5** for classic fine-tune fitting to experimental data), and at the same time, showcases the versatility of polar soft-SAFT as a global thermodynamic model. Hence, the thermodynamic behavior using ANN predicted parameters was compared to those obtained using the standard parametrization, and available experimental data and results are presented in **Table 4.4**. The chosen refrigerants comprise R32, R134a, R1243zf, R236fa, and R1223zd(E), inclusive of different molecular features and refrigerants included in the training and testing sets.

Table 4.4. *Polar soft-SAFT molecular parameters for selected refrigerants using standard parametrization and the ANN model developed in this work.*

	Standard parametrization [49,103]					**ANN predicted**				
Compound	m	σ / Å	ε/k_B / K	$\mu\cdot10^{-30}$ / C·m	x_p	m	σ / Å	ε/k_B / K	$\mu\cdot10^{-30}$ / C·m	x_p
R32	1.376	3.506	164.5	6.598	0.75	1.427	3.541	167.9	6.635	0.75
R134a	1.813	3.770	169.5	6.865	0.70	1.780	3.709	159.1	6.908	0.70
R236fa	2.056	4.012	172.4	6.611	0.90	2.074	3.990	173.4	6.558	0.90
R1243zf	1.904	3.880	170.0	8.169	0.50	1.842	3.982	187.5	8.191	0.50
R1233zd(E)	2.331	3.819	232.6	3.812	0.80	2.393	3.759	220.9	3.740	0.80

Shown in **Figure 4.10**, is the performance of fitted and predicted polar soft-SAFT parameters in computing co-existing densities [188,438,446] and vapor pressures [188,437,438] for the selected refrigerants, as compared to available experimental data. Better agreement of the fitted parameters, as opposed to the predicted ones, is expected as these experimental data are included in the fitting procedure to obtain them. Nonetheless, the ANN predicted parameters capture the trend with a good agreement to experimental data with deviations for co-existing densities (*AAD* = 1.632%), and vapor pressure (*AAD* = 6.587%). These deviations are satisfactory considering that these parameters were predicted from the ANN without using any experimental data. The most consistent trends between fitted and predicted parameters were obtained for R236fa refrigerant, as the training set was more biased to refrigerants with similar molecular structures.

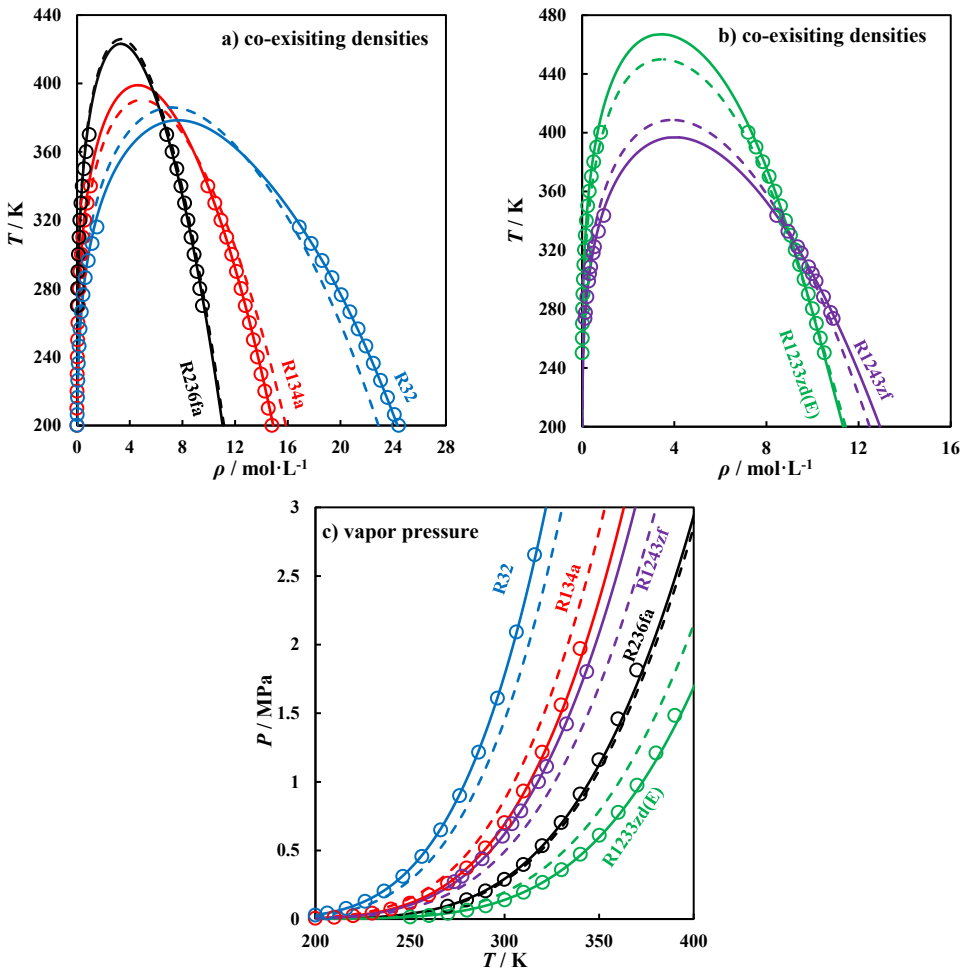

Figure 4.10. ***a)*** *and* ***b)*** *Co-existing densities, and* ***c)*** *vapor pressure for selected refrigerants obtained using polar soft-SAFT EoS, with fitted parameters (solid lines), ANN predicted parameters (dashed lines), and experimental data (symbols). See text for details.*

The ultimate stage of evaluating the adequacy of ANN predicted polar soft-SAFT parameters is through examining other thermodynamic properties not included in the standard parametrization approach. Obtaining these properties is considered a stringent criterion in evaluating any thermodynamic model, as first and second order derivative properties are very sensitive to small errors in modeling phase equilibria of pure fluids. As demonstrated from **Figure 4.11**, the trends using the fitted parameters and those calculated with the ANN predicted parameters are consistent with experimental data [188,453,455,456] for properties such as single phase density (AAD_{ANN} = 3.488%), and isobaric heat capacity (AAD_{ANN} = 1.311%). Unfortunately, the ANN predicted parameters presented higher deviations respect to the experimental data for the enthalpy of vaporization (AAD_{ANN} = 5.981%), owing to deviations in the predicted vapor pressures, and for the speed of sound (AAD_{ANN} = 10.525%), as this property encompasses other

derivative properties are (*i.e.,* isobaric and isochoric heat capacities, and inverse reduced bulk modulus) increasing its sensitivity to errors arising from those properties [172].

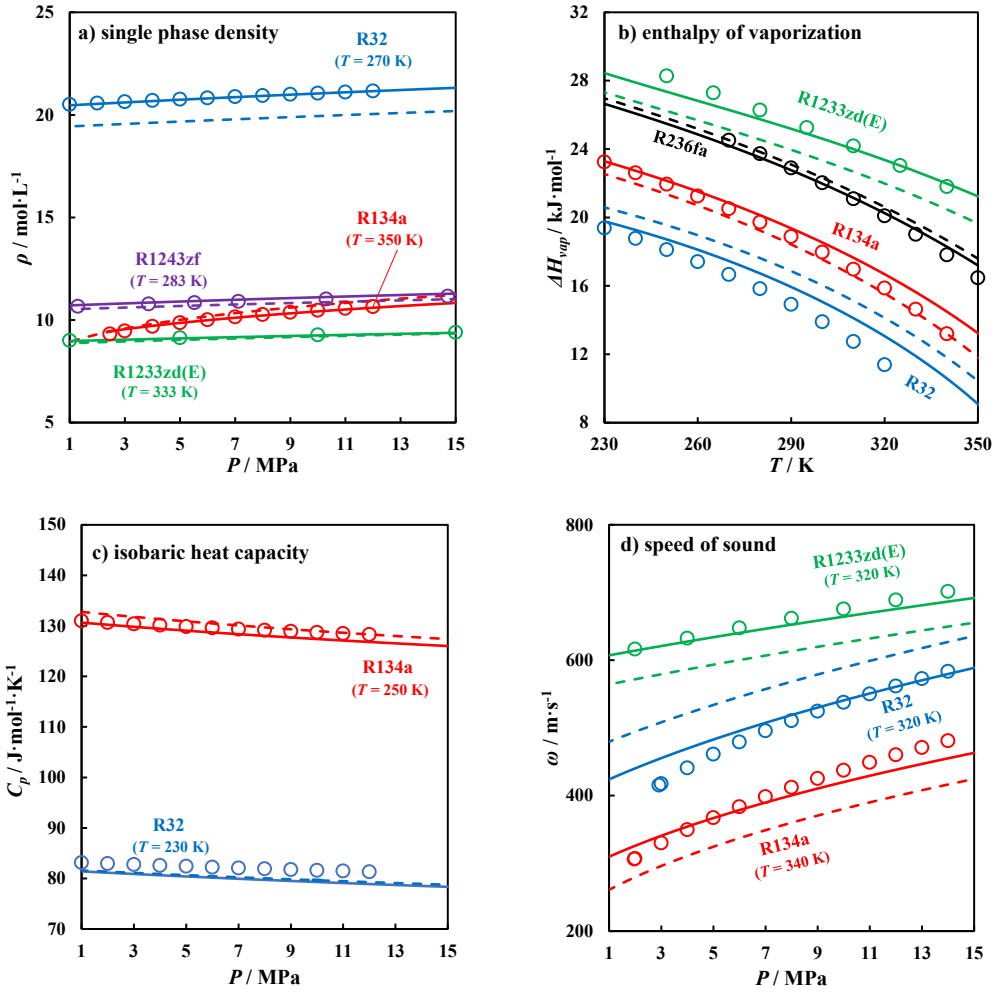

Figure 4.11. *Other predicted thermodynamic properties including* ***a)*** *single phase density,* ***b)*** *enthalpy of vaporization,* ***c)*** *isobaric heat capacity, and* ***d)*** *speed of sound for selected refrigerants predicted using polar soft-SAFT EoS, with fitted parameters (solid lines), ANN predicted parameters (dashed lines), and experimental data [188,453,455,456] (symbols).*

4.2. Binary mixtures

As shown in **Section 4.1**, reliable molecular models for the ten HFCs, twelve HFOs, three HCFO, nine HCs, and four other compounds included in this work, were previously developed (see **Table 4.1**) and validated through the description of a variety of thermophysical properties. The next step for a practical application of this approach is the accurate description of blends of compounds. For this purpose, the previous models are used here in a transferable manner, with minimal additional fine-tuning [49,103].

4.2.1. F-based binary mixtures

First, a thorough examination of the available VLE data for multi-polar binary blends has led to the compilation of **Table 4.5**, which presents data availability in the literature for nearly half a hundred systems.

Table 4.5. *Summary of the available VLE experimental data included in this thesis, involving 48 binary blends divided in three groups: HFCs + HFCs, HFCs+ HFOs, and HFOs + HCFOs, and binary energy parameter (ξ) fitted to experimental VLE data. η was, in all cases, fixed to unity; ξ_{ij}= 1.00 denotes full predictions from the model.*

Mixture	ξ_{ij}	Ref.	Mixture	ξ_{ij}	Ref.	Mixture	ξ_{ij}	Ref.
HFCs + HFCs			**HFCs + HFOs**			**HFOs + HFOs / HCFOs**		
R32 + R23	1.000	[457]	R41 + R1234yf	0.980	[458]	R1123 + R1234yf	1.000	[143]
R32 + R161	1.050	[459]	R32 + R1123	0.985	[143]	R1123 + R1234ze(E)	1.000	[143]
R32 + R152a	0.975	[460]	R32 + R1234yf	0.970	[461]	R1243zf + R1234ze(E)	1.010	[462]
R32 + R134a	0.980	[460]	R32+ R1234ze(E)	1.000	[463]	R1234yf + R1234ze(E)	1.000	[464]
R32 + R125	0.985	[460]	R23 + R1234yf	0.970	[465]	R1234yf + R1233zd(E)	0.990	[466]
R32 + R236fa	1.000	[467]	R161 + R1234yf	1.010	[461]			
R32 + R227ea	1.000	[468]	R161 + R1234ze(E)	1.010	[459]			
R23 + R152a	1.000	[469]	R152a + R1243zf	1.000	[470]			
R23 + R134a	1.000	[471]	R152a + R1234yf	0.980	[472]			
R23 + R125	0.975	[457]	R152a + R1234ze(E)	1.010	[473]			
R23 + R227ea	0.960	[474]	R134a + R1243zf	0.980	[475]			
R161 + R134a	1.045	[476]	R134a + R1234yf	0.983	[101]			
R161 + R125	1.030	[477]	R134a + R1234ze(E)	1.000	[463]			
R161 + R227ea	1.030	[478]	R125 + R1234yf	1.000	[101]			
R152a +R134a	1.000	[479]	R125 + R1234ze(E)	1.000	[480]			
R152a + R125	1.000	[481]	R245fa + R1234ze(E)	1.000	[482]			
R152a + R245fa	1.000	[483]	R227ea + R1234yf	1.000	[484]			
R152a + R227ea	1.000	[468]	R227ea + R1234ze(E)	1.000	[485]			
R134a + R125	0.993	[486]						
R134a + R245fa	1.000	[487]						
R134a + R236fa	1.000	[488]						
R134a + R227ea	0.990	[468]						
R125 + R245fa	0.985	[489]						
R125 + R236fa	0.980	[467]						
R125 + R227ea	0.990	[490]						

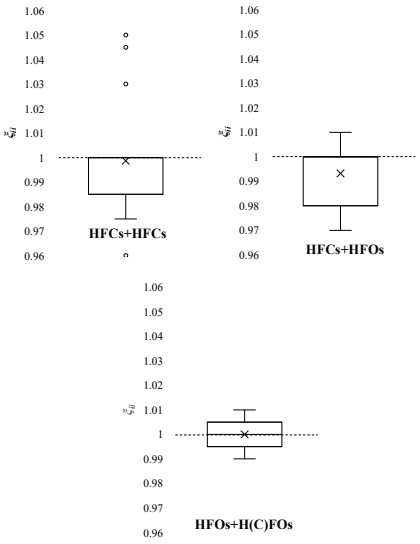

The reliability of polar soft-SAFT in modeling the thermodynamic behavior of refrigerant binary blends was validated by comparing the model performance to experimental data. This is required to ensure high fidelity in the model's predictions for all thermodynamic state variables used in the subsequent technical evaluation of identified promising refrigerant blends and for their performance evaluation. The phase equilibria of selected binary mixtures with R32, R134a, R1234yf, and R1234ze(E), depicted in **Figure 4.12**, demonstrate the predictive accuracy of the model from the highly precise correlations of experimental VLE data with minimal to no-calibration to the data, simply from the molecular parameters of the pure refrigerants. Additional plots for similar comparisons are included in **Figure A6** in the **Annex**. In the few cases where the model

required calibration, a temperature-independent binary energy parameter (ξ_{ij}) close to unity (see **Table 4.5)** was fine-tuned to experimental VLE data by minimizing the absolute average deviation. This was needed to correct the crossed dispersive interactions between the individual components of the blend, on account of approximating their dipolar interactions rather than their explicit parametrization. Notwithstanding, the ξ_{ij} energy binary parameter, when needed, proved highly transferable, as seen with blends of R1234ze(E) with R152a, R161, and R1243zf (see **Figure 4.12d**), modeled with the same binary parameter (ξ_{ij} = 1.010). These results ensure the reliability of the model as a platform for the rational design of refrigerant blends.

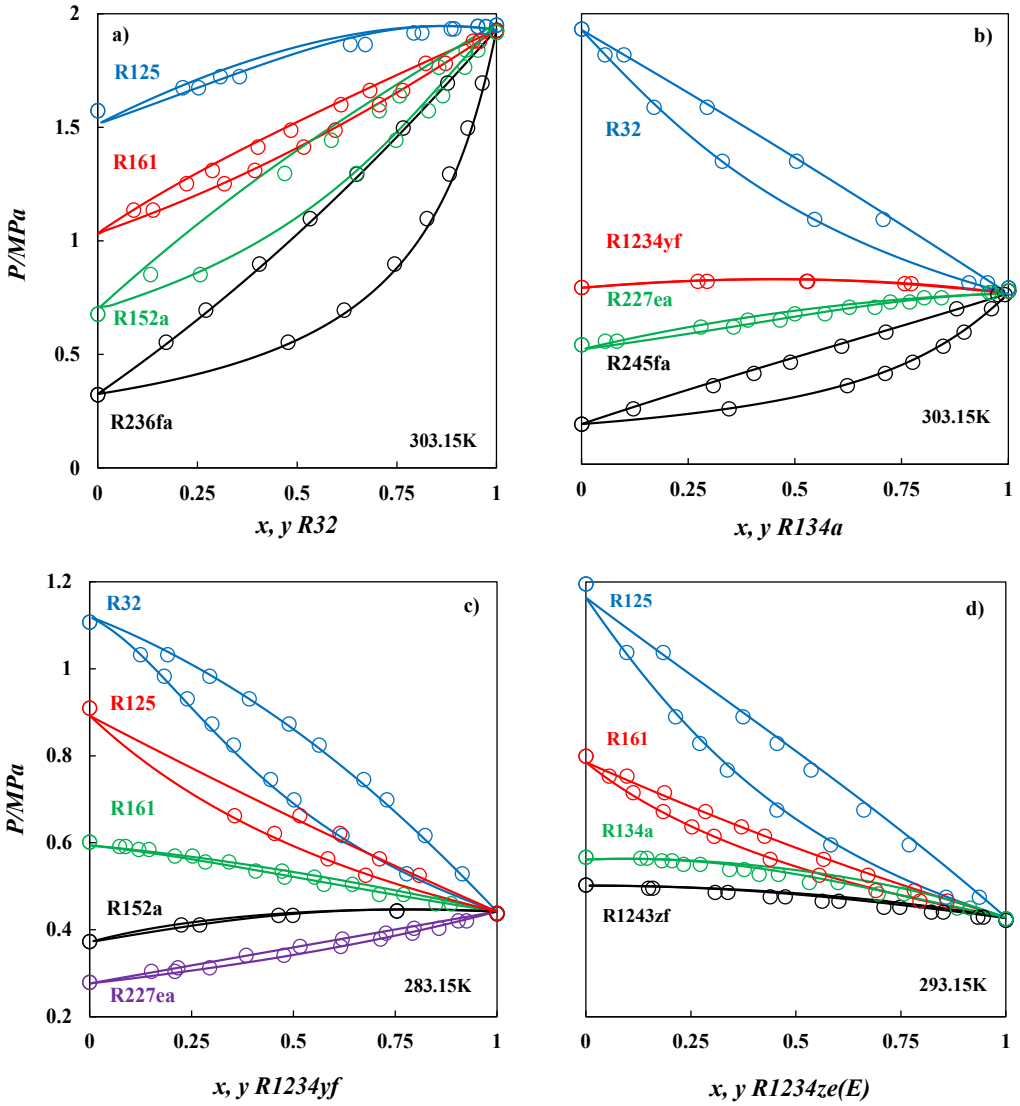

Figure 4.12. *VLE of selected refrigerants binary mixtures for those containing* ***a)*** *R32,* ***b)*** *R134a,* ***c)*** *R1234yf and* ***d)*** *R1234ze(E), using polar soft-SAFT (solid lines), compared to experimental data (symbols) from literature (see* ***Table 4.5*** *for references).*

4.2.2. Alkane-based binary mixtures

An additional demonstration of the accuracy of the model lies in capturing the effect of dipolar interactions. A more complex test is carried out through predicting the VLE for binary mixtures of dipolar + non-polar fluids. In this manner, the ability of the model to correctly approximate the contribution of dipole-dipole interactions can be isolated, as dipole interactions have a larger effect on the non-ideality of their VLEs with non-polar fluids [222,379]. For this end, binary mixtures of dipolar refrigerants with non-polar *n*-alkanes (modeled as a chainlike LJ fluid, using parameters included in **Table 4.1**) were predicted from the thermodynamic model for mixtures including ethane with R23 or R1234ze(E), and *n*-butane with R32, R152a, R134a, and R1234yf as dictated by available experimental data [491–496]. Indeed, the agreement between the experimental VLE data and model predictions is excellent with AAD_s = 1.0%, as seen in **Figure 4.13**, merely from the accurate representation of the behavior of the pure refrigerants.

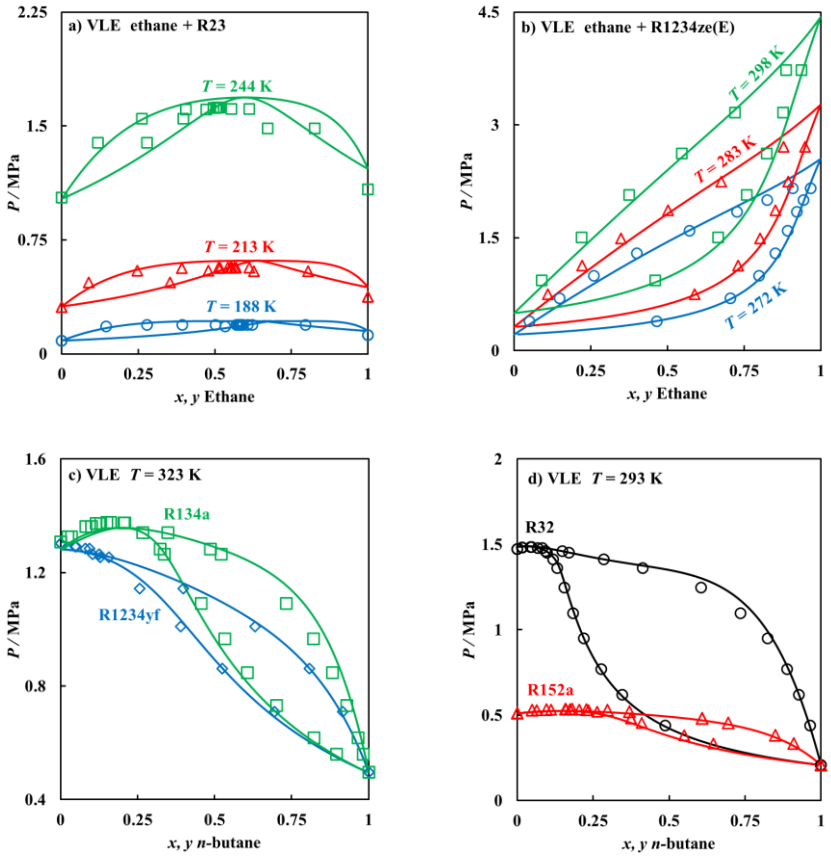

Figure 4.13. *Predicted VLE for binary mixtures of* ***a)*** *ethane + R23,* ***b)*** *ethane + R1234ze(E),* ***c)*** *n-butane + R134a or R1234yf at T = 323 K, and* ***d)*** *n-butane + R32 or R152a at T = 293 K. In all cases, polar soft-SAFT prediction (solid lines), compared to experimental data [491–496] (symbols).*

This behavior can also be better explained from the micro-level insights provided in **Figure 4.4**. For binary mixtures with ethane, the prominent polar contribution of R23 results in the formation of a distinct azeotropic mixture at nearly equimolar concentrations, while the lower polar contribution of R1234ze(E) due to its larger molecular volume results in near ideal VLE behavior for its mixture with ethane. Conversely, the formation of azeotropes at high refrigerant concentrations was seen for all binary mixtures with *n*-butane, with the degree of non-ideality associated with the magnitude of the polar contributions of the refrigerant. For saturated R134a, its high polarity compared to R1234yf results in a more distinct positive azeotrope, due to the increased asymmetrical energy scale between the stronger polarity of R134a with the non-polar *n*-butane. Notice that both refrigerants possess relatively similar dipole moments and fraction of polar segments; however, the larger molecular volume of R1234yf contributes to reducing its relative dipolar interactions. Similar observation is seen in the case of R32 and R152a, with a higher deviation from non-ideal behavior for mixture with R32 manifested in the form of a larger spread for the VLE. Even though the magnitude of the dipole moment of R152a is higher than R32, its larger size reduces the portion of the molecule influenced by the dipole moment.

4.2.3. CO_2-based binary mixtures

The study of binary systems is completed by a complete screening of CO_2-based mixtures. Of the 38 pure-components displayed in **Table 4.1**, 27 CO_2-based systems with existing experimental data in the literature are considered in the sequence of **Figure 4.14** and **A7**. These Figures display the VLE curves of CO_2 + refrigerant binary blends computed using polar soft-SAFT EoS. In a few cases, these binary mixtures are predicted directly from the model setting binary parameters to unity, while in other cases, a constant temperature-independent binary energy parameter (ξ_{ij}) is required regressed to a single isotherm for each studied mixture, as specified in **Table 4.6**. In all cases, good agreement between the polar soft-SAFT calculations and experimental data is noted, appropriately accounting for variations in the geometric average dispersive energy. Further examination of **Table 4.6** reveals that, while a third of combinations are predictively described (i.e. $\xi_{ij} = 1.00$), a majority of blends require minor adjustments from ideality ($0.98 < \xi_{ij} <$

1.02) for precise modeling. This suggests the model's robustness in fine-tuning the solubility of CO_2 in selected refrigerants of different nature.

Table 4.6. *Temperature-independent binary parameter, ξ_{ij} , employed for each CO_2-refrigerant pair. See **Eq. (3.6)** within the methodology for references.*

CO_2 +	ξ_{ij}	Ref.	CO_2 +	ξ_{ij}	Ref.	CO_2 +	ξ_{ij}	Ref.
R41	1.02	[141]	R1243zf	1.00	[144]	R600	0.96	[141]
R32	1.05	[141]	R1234yf	1.00	[497]	R600a	0.96	[141]
R23	1.03	[141]	R1234ze(E)	1.00	[498]	R601	0.98	[141]
R161	1.03	[141]	R1234ze(Z)	1.02	[146]	R601a	0.97	[141]
R152a	1.00	[141]	R1336mzz(E)	1.05	[146]	R1150	1.04	[141]
R134a	1.03	[141]	R1233zd(E)	1.00	[147]	R1270	1.01	[141]
R125	1.00	[141]	R7200	0.97	[145]	1-butene	1.00	[141]
R227ea	1.00	[141]	R170	0.97	[141]	R13I1	0.98	[499]
R1123	1.02	[143]	R290	0.97	[141]	RE170	1.05	[141]

The VLE results indicate azeotropic behavior when CO_2 is combined with R170 or R1150 (see **Figure 4.14**), corroborated by empirical evidence across various isotherms. A positive deviation from Raoult's law is particularly visible in the solubility behavior of CO_2 with HFCs, HFOs, HCFOs, HCs, and RE170, where strong attractive interactions may be taking effect. The analysis of P_{xy} solubility diagrams indicates stronger interactions of CO_2 with R32, R1336mzz(E), and RE170 (see **Figure A7**) than with other HFC and HFO refrigerants, a phenomenon linked to the increased asymmetry in its molecular structures. In contrast, for saturated hydrocarbons R13I1 and R7200, the trend inverts, indicating more repulsive forces than the simple geometric average within the mixture components, suggestive of van der Waals forces playing a predominant role in the phase behavior. This dichotomy illustrates the intricate interplay of molecular forces and the capability of the SAFT model in accounting for these dynamics.

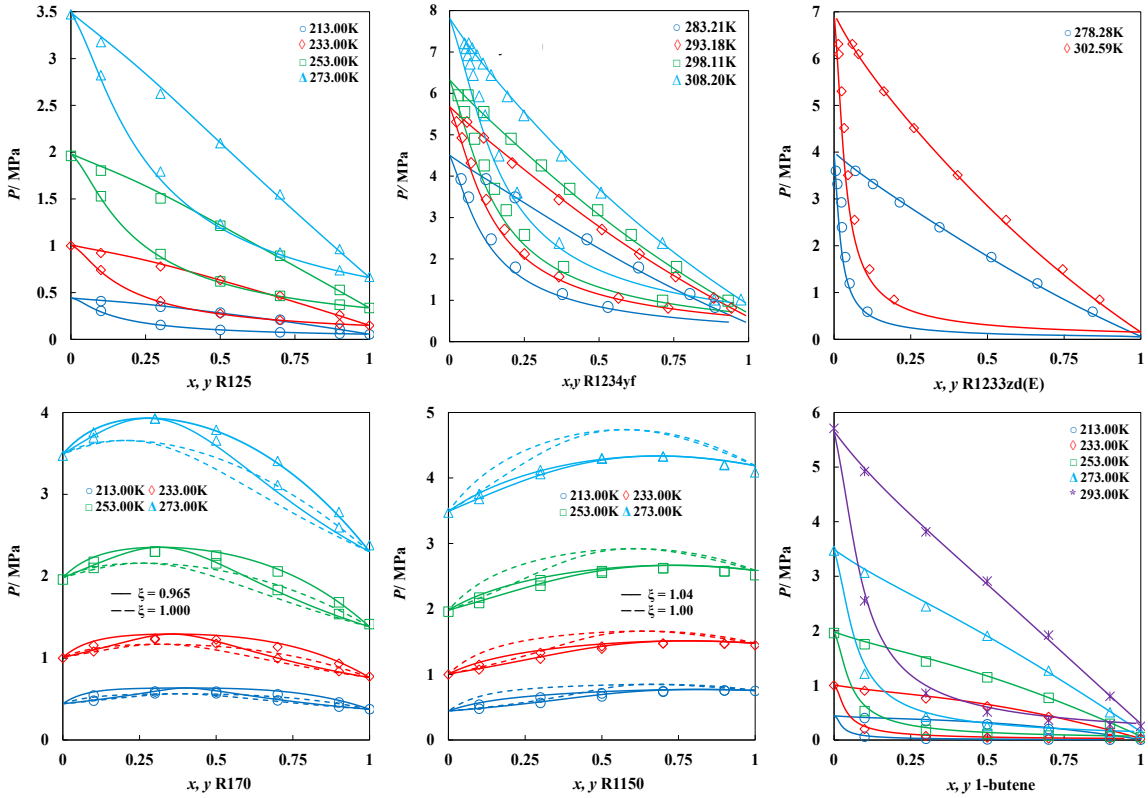

Figure 4.14. *Selected VLEs for CO_2-based binary mixtures. Symbols correspond to experimental data and solid lines to polar soft-SAFT characterizations.*

4.2.4. Binary mixtures data development through artificial neural networks

This subsection focuses on using ML techniques to directly obtain VLE data for CO_2-based mixtures with third- and fourth-generation refrigerants. Additionally, the same ANN approach is applied to determine the thermodynamic behavior of refrigerants and their blends with alkanes and other fluorinated components. Both assessments include validation against empirical data to ensure the model's reliability.

4.2.4.1. Fluorinated and alkane-based binary mixtures

The ANN being developed in **Chapter 4.1.2** is further validated by computing the VLE of BMs, such as n-alkane + HFC, HFC + HFC, and HFO + HFO, for several selected compounds within **Table 4.1** so as to ensure the accurate quantification of dipolar interactions in refrigerants [222,379]. The examined mixtures include R23 + ethane, R23 + R134a, and R1123 + R1234ze(E), with polar soft-SAFT employed in a predictive manner (binary interaction parameters kept at unity). The comparison of the VLE

description with the ANN predicted parameters, compared to the classical fitted parameters as opposed, revealed higher deviations in capturing the reported experimental/molecular simulation behavior of these binary mixtures [143,471,491] as shown in **Figure 4.15**. However, it seems clear that the errors with computing the VLE of these mixtures is caused by the errors in the pure refrigerant vapor pressure (see **Table 4.3**). Aside from that, the trends are rather consistent as seen from the correct prediction of azeotropic compositions in the case of ethane + R32 binary mixture. This limitation can be attributed to the narrow training set used in ANN development, with expected enhanced accuracy with a larger training dataset. Note that the error propagation decreases with reducing the temperature of the VLE, as the ANN predicted parameters are more accurate at low temperature regions. Notwithstanding, these errors are within an acceptable level of accuracy needed for the rapid screening of alternative eco-friendly refrigerants based on technical efficacy, guiding the experimental efforts.

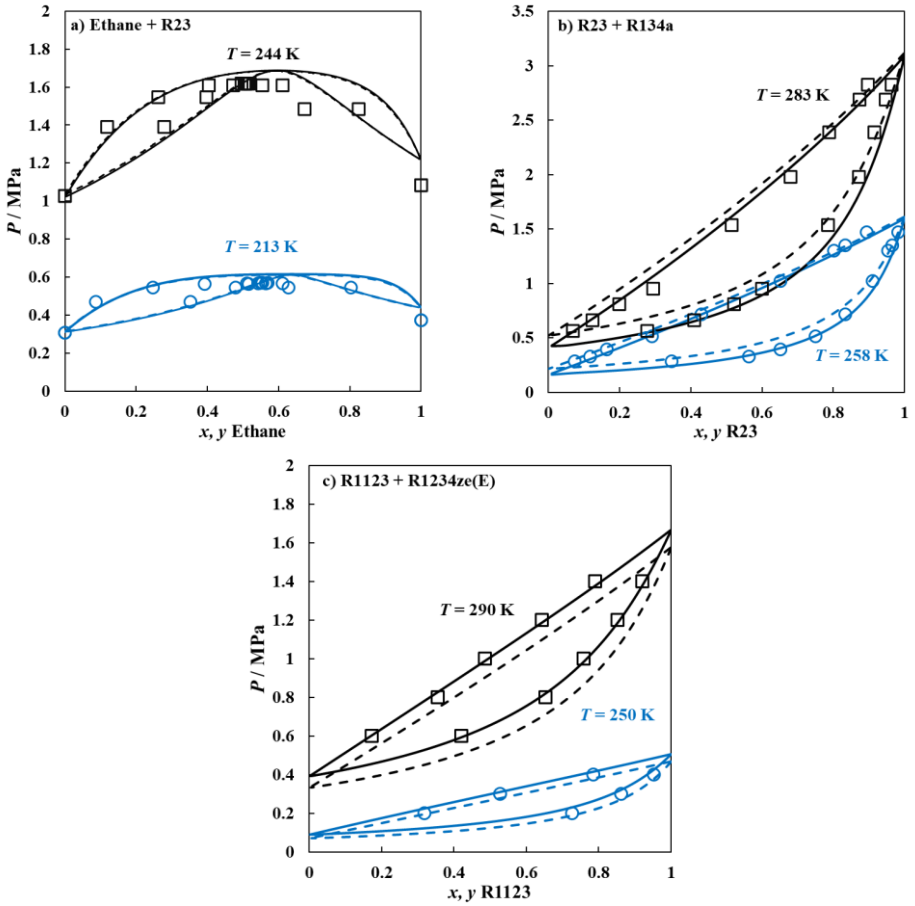

Figure 4.15. *Binary mixtures for* ***a)*** *Ethane + R23,* ***b)*** *R23 + R134a, and* ***c)*** *R1123 + R1234ze(E) predicted using polar soft-SAFT EoS, with fitted parameters (solid lines), ANN predicted parameters (dashed lines), and experimental data [143,471,491] (symbols).*

4.2.4.2. CO_2-based binary mixtures

This study aims to integrate the molecular-based EoS, namely, the polar soft-SAFT EoS , with AI-based technique, namely, artificial neural network to predict dew and bubble points of CO_2-based refrigerants, thus addressing a significant need in the field of refrigeration research. With the multitask ANN trained on soft-SAFT data and COSMO σ-profiles, both bubble and dew temperature sets can be determined next, verifying the model's reliability in the comprehensive characterization of CO_2-based blends encompassing both traditional and advanced 4th generation refrigerants.

Best-case configuration

Following the promising results obtained using ANNs for obtaining the molecular parameters of pure refrigerants, a new proposed AI algorithm is built to describe the VLE behavior of the CO_2 mixtures displayed in **Table 4.6**. In this context of data assembly and preprocessing, a wide-ranging array of data is compiled, serving as outputs to the AI-model, consisting of 531 data points for vapor-liquid equilibria of CO_2-based refrigerant blends. Specifically, this collection features 494 data points covering CO_2 compositions (both in liquid and vapor phases) ranging from 5% to 95% in mole fraction, combined with a total of 26 refrigerants of different nature. However, R7200 is excluded from consideration, due to extreme saturation pressure divergence from the comparative baseline established by commercial air conditioning standards. Additionally, the pronounced temperature glide with CO_2 [145]—irrespective of pressure and composition—renders this particular mixture less relevant, especially since it lies outside the targeted medium-low temperature range for air conditioning applications central to this thesis. The output database covers saturation targets for all 27-constituent pure-components (including pure CO_2), supplemented by 10 additional F-based single refrigerants. These include R245fa, R236fa, R1225ye(Z), R1336mzz(Z), R1132(E), R1132a, R1345fz, R1336yf, R1224yd(E), and R1224yd(Z).

The purpose of this study is to directly describe the vapor-liquid equilibrium behavior, focusing on bubble and dew temperatures as outputs, instead of addressing the molecular parameters of the pure compounds, as done in previous sections. In this approach, COSMO-RS is used to generate molecular descriptors, which are subsequently

employed as input parameters for the neural network model, as outlined in **Section 4.1.2.1**, but applied here to blends (see **Eq. (3.102)**). To prevent CO_2-based mixtures from solid state conversions, the working pressure is accordingly standardized at 1 MPa, aligning with CO_2's unique phase properties and ensuring its viability in refrigeration technologies. Hence, the effectiveness of ANNs was assessed with two hidden layers, each containing 1 to 25 neurons, treating the number of neurons in each hidden layer as an adjustable parameter. The analysis, based on the Root Mean Square Error (RMSE), is depicted in **Figure 4.16** and indicates that optimal network configurations were associated with higher neuron counts in both layers, lowering weighted RMSEs, especially for dew temperature predictions. In contrast, configurations with a lower degree of complexity consistently yielded RMSEs surpassing a threshold of 5 units when hyper-tuning the neuron counts in both hidden layers. Consequently, the optimal artificial neural network configurations for predicting bubble (24 HL1 – 20 HL2) and dew temperature (23 HL1 – 15 HL2) were identified through empirical analysis, with respective weighted RMSEs of 0.0388 and 0.2003. Such findings emphasize the necessity of a bigger architecture in the hidden layers for achieving precision in ANN-based predictions.

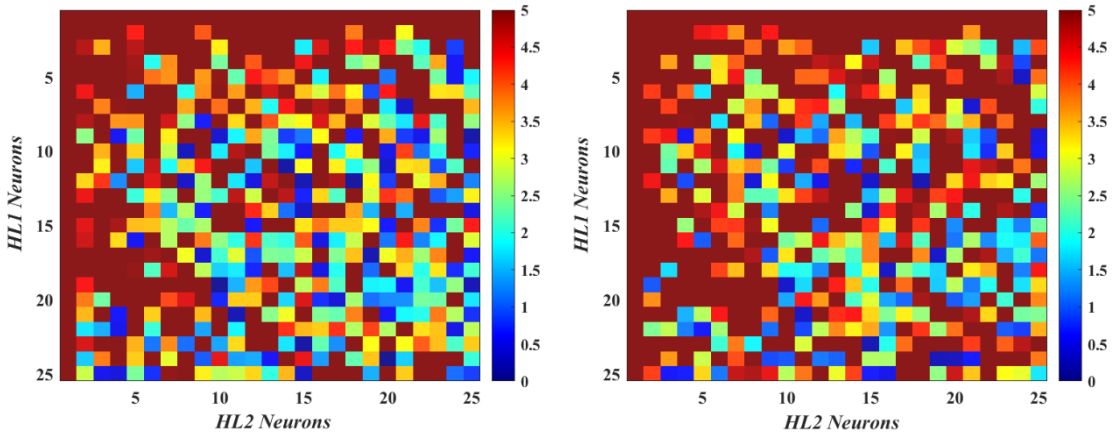

Figure 4.16. *RMSE colorbar from 0 (blue) to 5 (red) in relation to neuron counts in HL1 and 2.*

Figure 4.17 depicts the integrated multitask ANN architecture, optimized for predicting saturation temperatures at 1 This selected ANN layout, incorporating a multi-output framework, comprises a total of 3727 parameters and 84 biases, with 1964 and 1763 weights and 45 and 39 biases specifically allocated for bubble and dew temperatures layouts, respectively. The ensemble ANN setup is outlined in **Tables A6-7**, where

corresponding weights, biases, and output parameters streamline the fine-tuning of saturation properties for a range from pure to binary CO_2-based refrigerant blends. **Eq. (4.1)** depicts the bubble point output function, while the dew saturation temperature can be estimated through the use of **Eq. (4.2)**. It is important to ensure the importance of maintaining CO_2 within its triple (−56.60 °C, 5.26 MPa) and critical points (30.98 °C, 7.37 MPa) for effective refrigeration usage, ensuring ease of liquid-vapor transition. Hence, and in order to prevent CO_2-based mixtures from solid state conversions, the working pressure is standardized at 1 MPa, aligning with CO_2's unique phase properties and ensuring its viability in sub-critical cascade refrigeration technologies.

$$\begin{aligned} &1.0585(HH_1) - 0.2395(HH_2) - 1.3856(HH_3) - 0.5196(HH_4) + 0.5345(HH_5) \\ &+0.8107(HH_6) + 0.8575(HH_7) + 1.0926(HH_8) - 0.2386(HH_9) - 1.8389(HH_{10}) \\ &-0.4634(HH_{11}) - 0.7455(HH_{12}) + 0.5813(HH_{13}) + 0.5040(HH_{14}) + 0.6480(HH_{15}) \\ &+1.9120(HH_{16}) + 0.6951(HH_{17}) - 0.5351(HH_{18}) - 0.7133(HH_{19}) - 0.3663(HH_{20}) + 0.9781 \end{aligned} \quad \textbf{(4.1)}$$

$$\begin{aligned} &-1.6300(HH_1) - 0.9403(HH_2) + 0.4453(HH_3) - 0.5254(HH_4) + 1.8056(HH_5) \\ &+1.3672(HH_6) - 1.4100(HH_7) + 1.2360(HH_8) - 4.0551(HH_9) - 0.6360(HH_{10}) \\ &-1.3384(HH_{11}) - 3.1070(HH_{12}) - 1.2178(HH_{13}) - 0.5708(HH_{14}) + 1.5406(HH_{15}) + 0.0370 \end{aligned} \quad \textbf{(4.2)}$$

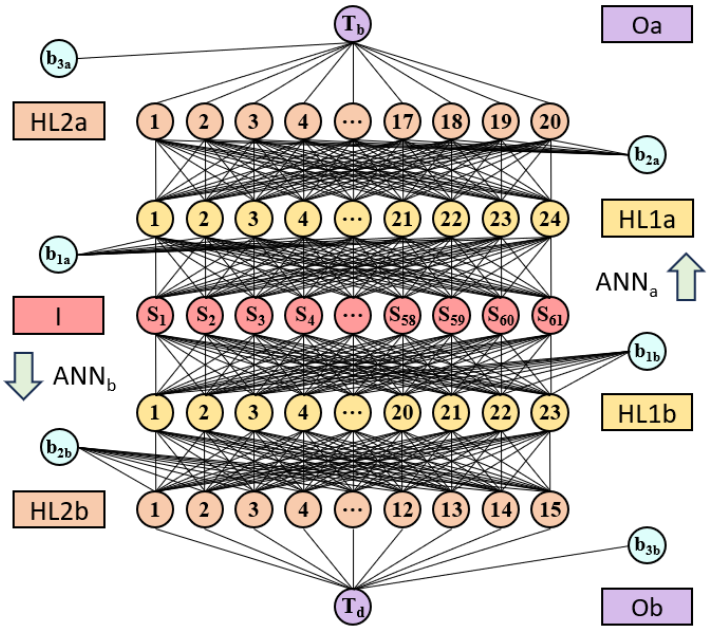

Figure 4.17. *Best-performing multitask model for predicting bubble and dew temperatures of CO_2-based mixtures, showcasing weights, and biases interconnections within the integrated ANN architecture.*

Optimal run evaluation

Based on the previous results for optimizing the performance of the ANN architect in **Figure 4.16**, the optimal ensemble ANN setup is rigorously evaluated using a blend of visual tools, such as parity plots and distribution patterns in **Figure 4.18a**, standardized residuals in **Figure 4.18b**, and statistical methods detailed in **Table 4.7**.

The parity plots present a a graphical representation of the model's performance, showcasing the relationship between the ANN-predicted saturation temperatures and the soft-SAFT data used as training outputs. For the liquid phase transition threshold, the majority of training data lies within a narrower temperature range of 200–300 K, accounting for over 90% of the validation and testing datasets. The model's high accuracy is a direct consequence of the distribution pattern within this range, as seen in the high degree of alignment along the $y = x$ diagonal. The developed ANN, however, exhibited a reduced accuracy for predictions above 350 K, as evidenced by the sole data point in this range showing significant deviation. In contrast, dew point predictions, trained on a more diverse temperature range including over 30% of data below 250 K and about 9.4% above 350 K, display higher overall residuals indicative of downgraded extrapolative capacity. This is particularly noticeable at temperatures above 300 K, where the model has been trained with a broader spectrum of data, a segment constituting 40.7% of the training data, as depicted in **Figure 4.18b**. Partly because of this basis, and further influenced by the substantially higher standard deviation of the vapor phase database at equilibrium (see **Figure 4.18b**), the overall residuals across all datasets show a marked increase relative to the bubble point. Enhancing the ANN's complexity or expanding the dataset, could further improve the model's projections on dew temperature outcomes, albeit challenged by the limited availability of CO_2-based blend data in literature.

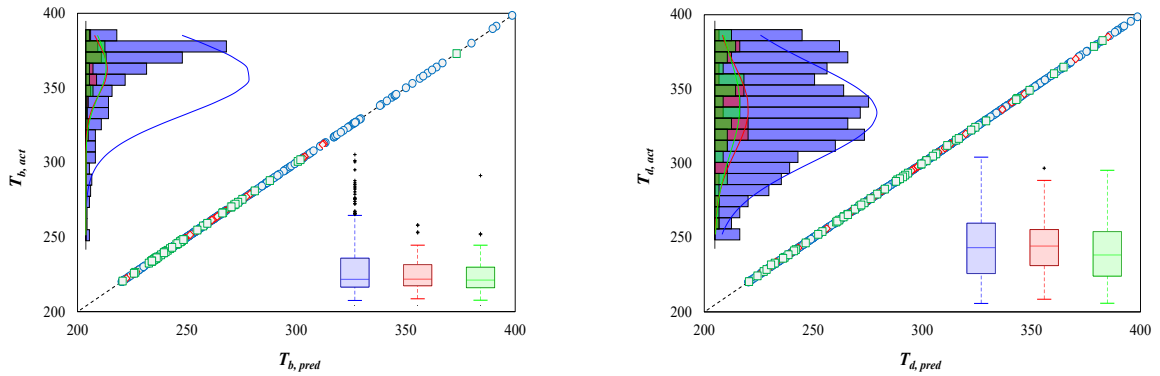

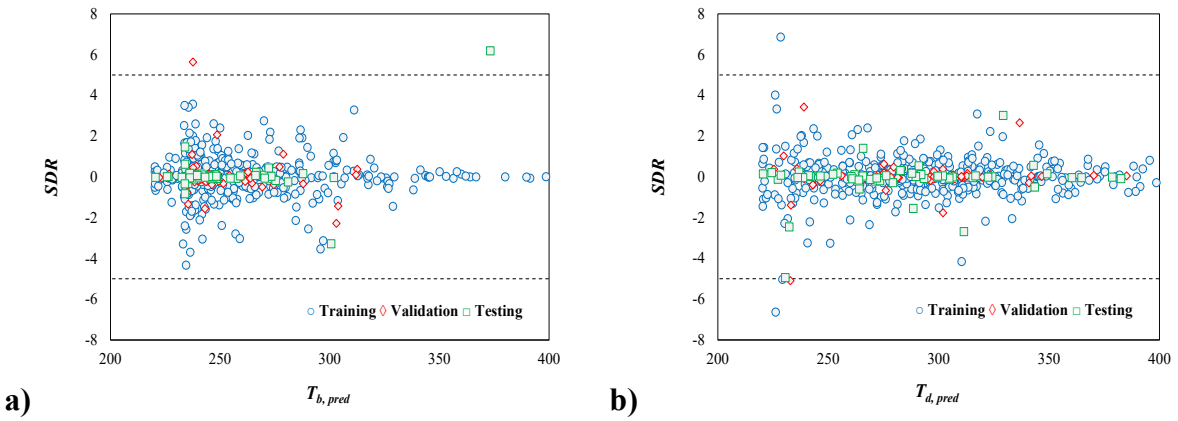

Figure 4.18. ***a)*** *Scatter, distribution patterns, box, and b) Standardized residual diagrams (SDR) for training (blue), validation (red), and testing (green) datasets and in correlation with both observed and predicted responses at 1MPa. The distribution plot displays the probability distribution of data in histograms, illustrating how values are spread across the datasets, while the box plot provides insights into central tendency and variability by depicting the median, quartiles, and outliers, ranging from minimum to maximum data points.*

Statistical analysis, shown in **Table 4.7**, provided a quantitative backbone to these observations. The KPIs such as R^2 values, exceeding 0.9999 for all cases, in addition to Normalized Median Absolute Deviations (refer to **Eq. (3.113)** in the methodology section), indicate the robustness of the developed neural network. However, a closer look at other KPIs reveals subtle differences in performance, especially in scenarios beyond the 300 K range. While bubble point predictions maintain high precision across datasets, the estimation of the dew phase exhibits slightly lower performance metrics, particularly when moving from training to validation and testing stages. These observations are directly related to data diversity and distribution in training ANN models. The model's accuracy in bubble points, trained on a 200 – 300 K range, contrasts with the broader range of temperatures in the vapor phase, demanding a more elaborated architecture to handle the increased complexity. In summary, our analysis highlights the efficacy of the ANN model in predicting saturation temperatures for dew and bubble points, with a notable distinction in performance due to data diversity.

Table 4.7. *Statistical KPIs for the developed ANN models in predicting dew and bubble points.*

Output	Metric	Training	Validation	Testing	Total
Bubble	R^2	1.0000	1.0000	1.0000	1.0000
Dew		1.0000	1.0000	1.0000	1.0000
Bubble	RMSE	0.0016	0.0135	0.0414	0.0172
Dew		0.0213	0.1691	0.2291	0.0959
Bubble	AARD/%	0.00043	0.00255	0.00446	0.00237
Dew		0.00494	0.02702	0.03563	0.02201
Bubble	SD_{av}	0.00077	0.00458	0.00921	0.00201
Dew		0.00953	0.04984	0.06804	0.01954
Both	NMAD	0.00018	0.00118	0.00176	0.00044
Both	Data Points	423	54	54	531

Determination of polar soft-SAFT binary parameters

The capability in accurately modeling the saturation properties of diverse CO_2 mixtures is finally checked in **Figure 4.19**, serving as a robust validation to the multitask artificial neural network. Using a fine-grained discretization approach with a 0.1% composition interval, each COSMO descriptor input corresponding to a specific mixture has been computed to the ANN to describe the vapor-liquid equilibria.

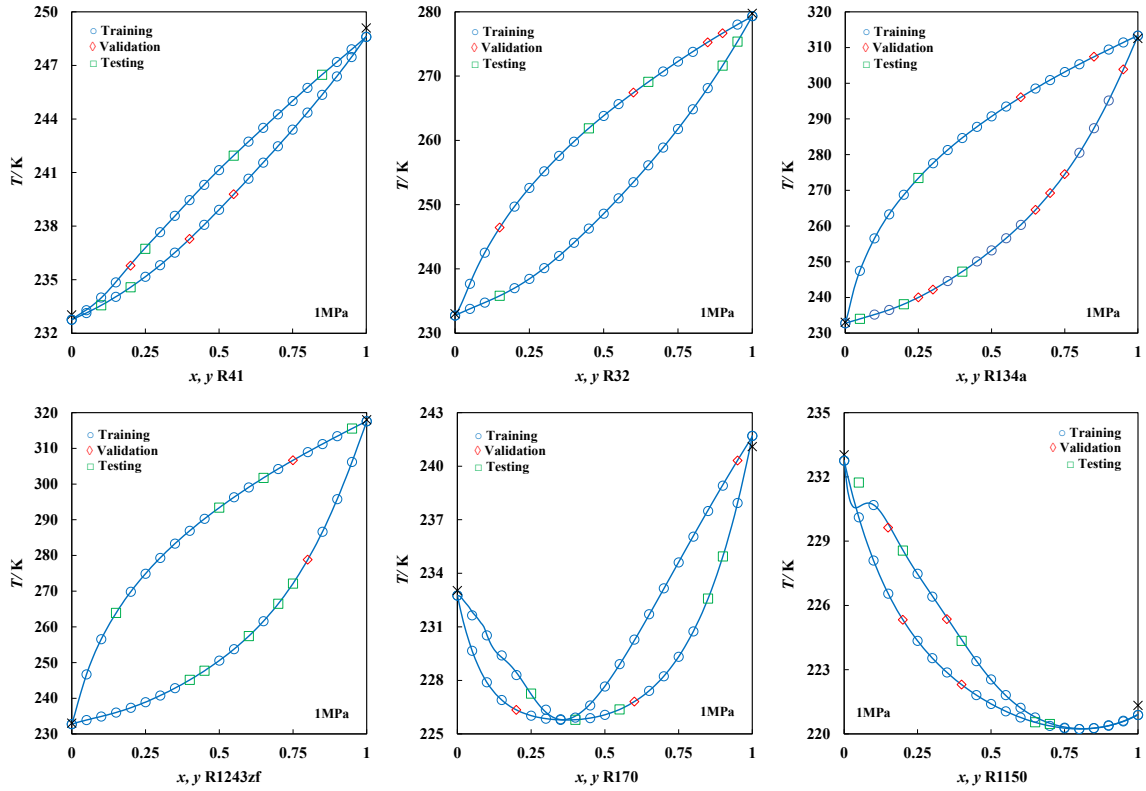

Figure 4.19. *Temperature-composition diagrams of selected CO_2-based blends at 1MPa. Symbols correspond to soft-SAFT data used for training (blue circle), validation (red diamond), or testing (green square), while x stands for experimental data, and lines for ANN calculations.*

The obtained results reveal an accurate description of azeotropic behaviors in CO_2 mixtures involving short-chained hydrocarbons (R170 and R1150), in contrast with the zeotropic nature observed in mixtures containing longer, bulkier compounds. Validation and testing data closely match polar soft-SAFT output data used in ANN development, with the exception in the dew phase of the CO_2 + R1150 mixture at low fractions of the light hydrocarbon, where unphysical behavior is obtained. This deviation – characterized as an underestimation – was anticipated from the residual plots in **Figure 4.18b**, where the testing point on the edge of the SDR limit of –5 falls outside the scope of the ANN's optimal range, indicating a limitation in its applicability. Special focus is needed on the dew phase, where three training points have SDRs exceeding ±5 and twelve points surpass an SDR of 3, underscoring the need for prudent interpretation around such extreme ranges. The discrepancy in the training point for the dew phase of the R170 and CO_2 mixture at 15% mole composition, with an SDR near 3, exemplifies the minor yet visible deviation observed. While outliers are present, the ANN's overall fitting closely matches SAFT outcomes across diverse mixtures, demonstrating its reliability through early deviation detection. Experimental saturation temperatures for pure substances from NIST, plotted with polar soft-SAFT estimates, are in excellent agreement with the ANN's outputs in all cases.

Based on the good descriptive nature of the presented ANN, the saturation properties of new CO_2-based blends, including HFOs and HCFOs without existing experimental or molecular simulation data, have been predicted. Indeed, the main advantage over classical fitting remains the possibility to estimate new mixtures fitting the soft-SAFT binary parameters to the dew and bubble points predicted from the ANN. These findings, presented in **Figure 4.20**, showcase the ANN's capability in forecasting saturation profiles for both liquid and vapor phases, leading to precise determination of binary parameters for selected F-based compounds, with R1336mzz(Z) and R1224yd(E) yielding ξ values of 1.02 and 1.03, respectively. Such domains align with established literature on CO_2 mixtures (see **Table 4.6**), consistently including HFCs, HFOs, and HCFOs. The characterization is validated through the NRTL model, and demonstrates the accuracy of the developed methodology, as evidenced by the AARD obtained for both mixtures.

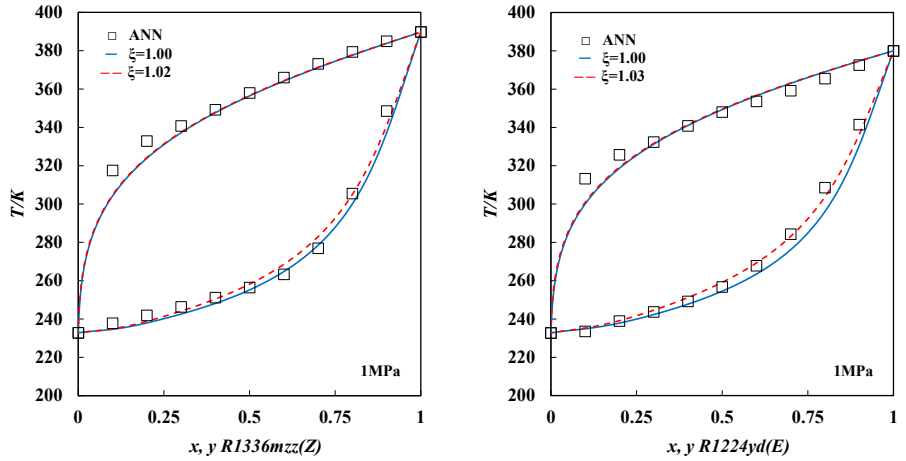

Figure 4.20. *Temperature-composition diagrams of selected CO_2-based blends excluded from ANN fitting or external validation at 1MPa. Symbols correspond to saturation data obtained from ANN calculations, while lines are soft-SAFT characterizations. Note that characterizations using an adjustable ξ_{ij} parameter is appreciated in discontinuous patterns, while pure predictions are depicted in solid lines.*

Specifically, the CO_2 mixture with R1336mzz(Z) is described with an overall AARD close to 3% for bubble temperatures and below one percent for dew points, indicating highly accurate predictions. Likewise, the mixture with R1224yd(E) shows deviations below 3.5% for both measures. In the liquid saturation phase, as detailed in **Table 4.8**, the ANN demonstrates enhanced predictive capability at mole concentrations close to pure CO_2, highlighting the need to expand our dataset to include a broader spectrum of 3rd and 4th generation refrigerant compounds and blends. Moreover, it is observed that bubble predictions deviate from actual data within the upper range of molar composition for the F-based compound. This discrepancy is attributed to insights from **Figure 4.18**, indicating the inadequacy of the ANN in capturing saturation temperatures within this specific temperature range, primarily due to limitations in the training dataset. Certainly, effective liquid phase characterization is essential for accurate SAFT descriptions ensuring reliable VLEs, particularly in highly zeotropic mixtures akin to **Figure 4.20**'s. This phenomenon, evident in CO_2-based mixtures from long-chain hydrocarbons (R600 to R601a) to F-based coolants like HFOs (R1336mzz(E), R1234ze(Z)), extending also to R13I1, results in a more subtle pressure gradient effect for the vapor phase when applying energy-based binary parameters.

Table 4.8. *Actual (NRTL) and predicted (ANN) bubble and dew temperatures in addition to the Average Absolute Relative Deviation (AARD) for the CO_2-based mixtures depicted in* ***Figure 4.20****.*

x_1, y_1	T_b^{NRTL} / K	T_d^{NRTL} / K	T_b^{ANN} / K	T_d^{NRTL} / K	ARD T_b	ARD T_d
(1) R1336mzz(Z) / CO_2						
0.9	312.63	383.95	348.53	384.92	11.48	0.25
0.8	285.94	378.80	305.41	379.39	6.81	0.15
0.7	270.90	373.17	276.90	373.10	2.21	0.02
0.6	260.86	366.92	263.26	365.99	0.92	0.25
0.5	253.50	359.86	256.36	357.98	1.13	0.52
0.4	247.76	351.63	251.15	349.19	1.37	0.69
0.3	243.11	341.66	246.33	340.68	1.33	0.29
0.2	239.22	328.77	241.87	332.85	1.11	1.24
0.1	235.90	309.41	237.81	317.46	0.81	2.60
(2) R1224yd(E) / CO_2						
0.9	308.47	372.61	341.54	372.61	10.72	1.65
0.8	284.42	365.53	308.61	365.53	8.50	1.15
0.7	270.20	359.21	284.39	359.21	5.25	0.97
0.6	260.49	353.70	267.89	353.70	2.84	1.22
0.5	253.29	348.12	256.81	348.12	1.39	1.70
0.4	247.64	340.89	249.23	340.89	0.64	2.05
0.3	243.04	332.38	243.73	332.38	0.28	2.54
0.2	239.19	325.79	238.98	325.79	0.08	4.62
0.1	235.88	313.30	233.62	313.30	0.96	7.07
				$AARD_1$ / %	3.02	0.67
				$AARD_2$ / %	3.41	2.55

4.3. Summary of key outcomes from Chapter 4

In this chapter, results concerning the thermodynamic characterization of refrigerants was extensively evaluated using the polar soft-SAFT model and artificial neural networks, with the additional use of COSMO-RS when needed. The study involved the thermodynamic optimization of molecular parameters for a diverse set of 38 refrigerants, encompassing HFCs, HFOs, HCFOs, hydrocarbons, and additional compounds such as CO_2, R170, R13I1, and R7200. The model achieved high accuracy, with deviations in saturated liquid density below 1.0% and vapor pressure under 3.0%, with some exceptions up to 4.5%. The analysis shows that larger molecular volumes result in lower liquid molar densities and higher vapor molar densities, which benefits applications requiring smaller compressors, as evidenced by refrigerants such as R227ea and R1336mzz(Z).

The model accurately predicted the enthalpy of vaporization, with deviations consistently under 3.0%, and matched single-phase densities with molecular volumes. Isobaric heat capacity predictions were within 5.0% of experimental values, with notable precision for R601a and R1224yd(E), where errors were under 1%. Predictions for R1234ze(Z) and R1336yf were also acceptable, while for more complex refrigerants such as R1150 and R1270, the model achieved AARDs of 4.8% and 3.2%, respectively.

In validating coarse-grain models with binary mixtures, the polar soft-SAFT model accurately predicted vapor-liquid equilibrium data, with AADs around 1.0% for blends of R32, R134a, and R1234yf, and CO_2-based blends requiring only minor adjustments. ANNs were used as a complement to predict SAFT-type molecular parameters in addition to vapor-liquid equilibrium behavior for CO_2-based mixtures. R^2 value greater than 0.99 was achieved in the parametrization of dipole moment and fraction of polar segments, but with higher deviations in vapor pressure and enthalpy of vaporization, with average absolute deviations of 4.8% and 5.9%, respectively. For predicting saturation properties of CO_2-based blends, the ANN methodology achieved average absolute relative deviations below 3.5% for both liquid and vapor phases, with high reliability and predictive capability for sub-critical systems below 300 K. The model handled 531 data combinations effectively, with outlier percentages of 2.6% for bubble phase and 2.4% for dew phase predictions.

Chapter 5. Analyzing the Lubricant Compatibility on Refrigerants: A Case Study

In terms of industrial application, one crucial aspect of a refrigerant is related to its compatibility with the lubricant that is present in the refrigeration equipment, given the fact that contamination by leakage is a common fact. In this sense, it is important to know how the thermophysical behaviours of the refrigerant are affected by small amounts of the lubricant, in order to prevent the impact that this will have in the performance of the system. The use of a molecular-based equation of state, such as soft-SAFT, can also be used to predict this behaviour and quantify the thermodynamics changes.

In this chapter, a case study related to the compatibility of the commercial alternative blend R513A with selected PEC/PEGDME lubricants (see molecular characterization ***Section 3.1.1*** *within the methodology) is carried out. The assessment highlights the key outcomes and trade-offs observed in cooling cycle applications involving lubricant oils, providing insights applicable to other F-based refrigerant blends derived from the compound list in* ***Table 4.1****.*

The main outcomes presented in this chapter are published in the International Journal of Refrigeration according to reference [103].

5.1. Lubricants characterization

The study departs from the thermodynamic characterization of two common families of lubricants: the PECs and the PEGDMEs. The molecular parameters of linear PEC5, PEC7 and PEC9 were fitted using saturated liquid density data correlated to the available experimental vapour pressures [380] by means of the Tammann-Tait correlation [500]. The soft-SAFT description presents vapour pressure absolute average deviations (AAD%) below 3.0% for PEC5, increasing up to almost 10.0% for PEC7 and PEC9. Even if the AAD% for the vapour pressure is high for the longer PECs, this relative error is utterly tolerated by virtue of the extremely low experimental vapour pressure values. Concerning the saturated density, the deviations are below 0.45% in all cases. The graphical representation of these equilibria properties for PEC5, PEC7 and PEC9 can be found in **Figure 5.1**.

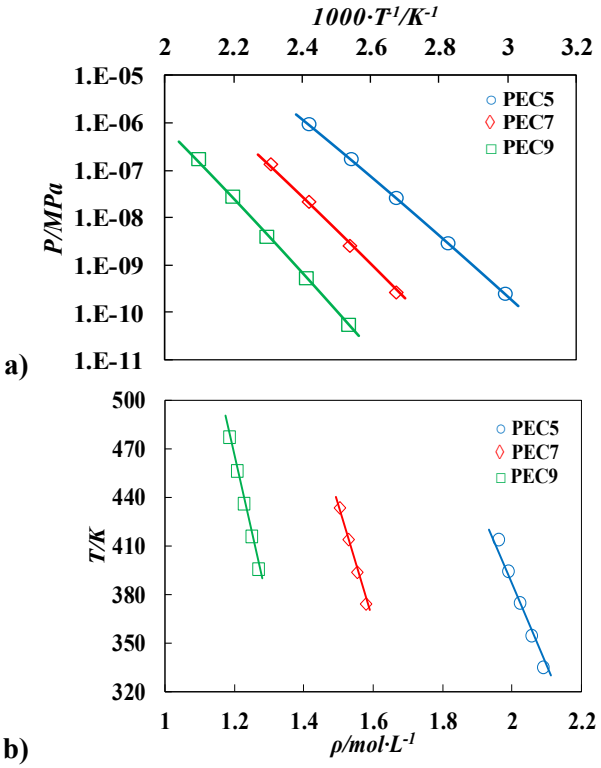

Figure 5.1. *Phase behavior of PEC5 (blue circles), PEC7 (red diamonds) and PEC9 (green squares).* ***a)*** *Vapor pressure in logarithmic scale vs. the reciprocal of temperature, and* ***b)*** *liquid density vs. temperature. Symbols are experimental data, while the lines correspond to the soft-SAFT modeling.*

In addition, and as observed with several regular chemical families [102,174,216,364,371,501], the molecular parameters of the PECs correlate well with the molecular weight of the compounds:

$$m = 0.0054 \cdot M_W + 7.0936 \quad \textbf{(5.1)}$$

$$m\sigma^3\ [\mathring{A}^3] = 1.8893 \cdot M_W - 226.04 \quad \textbf{(5.2)}$$

$$m\varepsilon/k_B[K] = 3.5649 \cdot M_W + 1169.9 \quad \textbf{(5.3)}$$

This shows the robustness and transferability power of SAFT models, as the parameters of other members of the family not included in the fitting procedure can be calculated using those correlations in a predictive manner. Indeed, this is the approach followed to establish the molecular soft-SAFT parameters for PEC4, PEC6 and PEC8, also studied in this work, for which no experimental data are available. The complete list of molecular parameters for all PECs is provided in **Table 5.1**.

Table 5.1. *Soft-SAFT molecular parameters for PEC and PEGDME families and Absolute Average Deviations (AAD%) for vapour pressure (P) and saturated liquid density (ρ).*

Compound	*m*	*σ* / Å	*ε*/k$_B$ / K	AAD$_P$ / %	AAD$_\rho$ / %	T range / K
PEC4	9.339	3.916	284.3	-	-	-
PEC5	9.640	4.108	296.1	2.913	0.430	334-414
PEC6	9.944	4.268	307.2	-	-	-
PEC7	10.250	4.405	317.6	9.680	0.201	373-434
PEC8	10.549	4.537	327.5	-	-	-
PEC9	10.850	4.652	336.8	9.949	0.028	394-477
MEGDME	2.434	3.898	296.0	5.092	0.320	300-400
DEGDME	3.124	4.027	314.0	7.307	0.078	280-435
TrEGDME	3.814	4.098	317.0	14.623	0.064	273-375
TEGDME	4.504	4.169	329.0	11.500	0.294	373-465

In a similar manner, the PEGDMEs family molecular parameters were calculated using the correlated data of the Tammann-Tait equation, based on experimental data taken from literature for monoethylene glycol dimethyl ether (MEGDME) [502,503], diethylene glycol dimethyl ether (DEGDME) [502,504], triethylene glycol dimethyl ether (TrEGDME) [505,506] and tetraethylene glycol dimethyl ether (TEGDME) [507]. The results of the optimization are also included in **Table 5.1** and plotted in **Figure 5.2**.

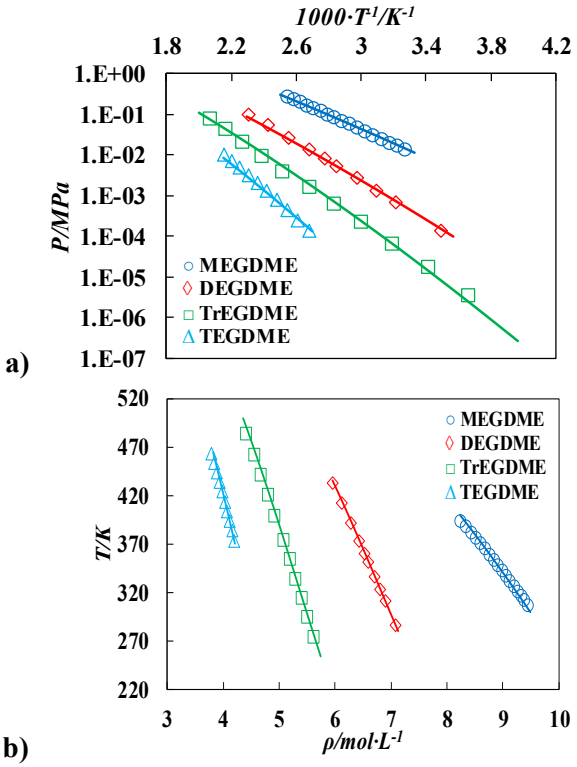

Figure 5.2. *Phase behavior of MEGDME (blue circles), TrEGDME (green squares) and TEGDME (light blue triangles).* ***a)*** *Vapor pressure in logarithmic scale vs. the reciprocal of temperature, and* ***b)*** *liquid density vs. temperature. Symbols are experimental data, while lines correspond to the soft-SAFT modeling.*

As observed for the PECs family, calculations for the vapour pressure of the PEGDMEs family exhibit modest to high deviations (7.0 to 14.6%), which are mainly caused by the low vapour pressure values, where minor differences and data uncertainty have a strong impact in the AAD%. Here, it is important to notice that vapor pressure data is not used in the fitting procedure on purpose, given the fact that these low values and high uncertainties could lead to misleading adjustments.

Concerning the molecular parameters, particular care was taken to keep them in a range that was proportional to their equivalent members of *n*-alkane [371] and polyethylene glycol [508] compounds, taking advantage of the transferability and physical basis of the soft-SAFT approach. Once again, it is important to remark that a key beneficial point on using a molecular-based model is to ensure the physical meaning of the parameters found in the fitting procedure, avoiding unphysical combinations that would fail to be representative of the molecule. Conversely, accurate molecular models are very reliable for calculating properties not included in the fitting procedure.

As for the PECs, linear correlations of m, $m\sigma^3$ and $m\varepsilon$ with the molecular weight were also obtained for the PEGDMEs family, provided in **Eqs. (5.4)-(5.6)**.

$$m = 0.0157 \cdot M_W + 1.0225 \quad \textbf{(5.4)}$$

$$m\sigma^3\ [\mathring{A}^3] = 1.3734 \cdot M_W + 19.721 \quad \textbf{(5.5)}$$

$$m\varepsilon/k_B\ [K] = 5.7024 \cdot M_W + 207.35 \quad \textbf{(5.6)}$$

5.2. Solubility of R1234yf and R134a in PECs and PEGDMEs

Once the molecular parameters of the refrigerants (notice that R1234yf and R134a molecular parameters are given in **Table 4.1**) and the different oils were determined, the solubility of R1234yf and R134a in commercial oils was independently evaluated before studying the solubility of the blend (R513A) in these lubricants.

The study of R1234yf binary mixtures with PEC4 [118], PEC5 [118], PEC6 [115], PEC7 [115], PEC8 [115] and PEC9 [114], was carried out fitting a ξ_{ij} temperature independent binary parameter for each PEC, in order to account for the differences in the dispersive energy between the two compounds, taking into account the highly asymmetry of compounds integrating the mixture. The results are summarized in **Table 5.2**.

Table 5.2. *Energy binary parameter, ξ_{ij}, used for each refrigerant-lubricant blend.*

R1234yf	ξ_{ij}	R134a	ξ_{ij}
PEC4	1.0450	PEC5	1.1000
PEC5	1.0330	PEC9	1.0230
PEC6	1.0225	MEGDME	1.1750
PEC7	1.0125	DEGDME	1.1410
PEC8	1.0000	TrEGDME	1.1500
PEC9	0.9900	TEGDME	1.1650
TrEGDME	1.0800	-	-

In a similar manner as done for the molecular parameters of the pure compounds, it is possible to linearly correlate the value of the ξ_{ij} energy binary parameter with the PECs molecular weight, allowing to predict the solubility of this refrigerant in other PECs, further reinforcing the robustness of the model for these types of systems:

$$\xi_{ij} = 0.0110 \cdot PEC + 1.0556\ ;\ R^2 > 0.999 \quad \textbf{(5.7)}$$

The previous correlation was built using the first four available PECs (from 4 to 7, see **Table 5.2**) and used to predict the corresponding values for PEC8 and PEC9.

Results for R1234yf in PEC4, PEC5, PEC6 and PEC7 are depicted in **Figure 5.3**, while predictions for the solubility of R1234yf in PEC8 and PEC9 are provided in **Figure B1**. As inferred from depicted characterizations, very good agreement is obtained between the polar soft-SAFT model and the experimental data in all cases, with the exception of some minor deviations at the highest two isotherms of PEC4 at high refrigerant fractions. The prediction of the solubility of heavier PECs using the correlated binary parameter from **Eq. (5.7)** does not deteriorate, demonstrating the transferability of the model.

However, while this original parameterization reveals an excellent description of the available data at all isotherms, it also predicts, for some PECs, an immiscible area at high concentrations of refrigerant and high temperatures. This evidence has not been confirmed experimentally, although the absence of data at the highest compositions and temperatures, particularly for the case of PEC9, is a possible indicator. In any case, the original liquid-liquid calculations obtained from soft-SAFT seems to overestimate this immiscibility gap, reaching some liquid-vapour equilibrium composition data points. In order to overcome this limitation, a second binary parameter, η_{ij} = 1.01, was added, representing small corrections from the original model (see **Eq. (3.5)**). The overall description of the system remains very good, with the exception of the highest concentration points, which are slightly underestimated at high temperatures (333.15 K and 343.15K). When implementing this modification, the immiscibility disappears for PEC5 and PEC6 in the range of temperatures studied, while a liquid phase split appears in the case of PEC9 (see **Figure B1**); further experimental measurements should be performed to assess the presence or not of the liquid-liquid equilibria (LLE) for this mixture.

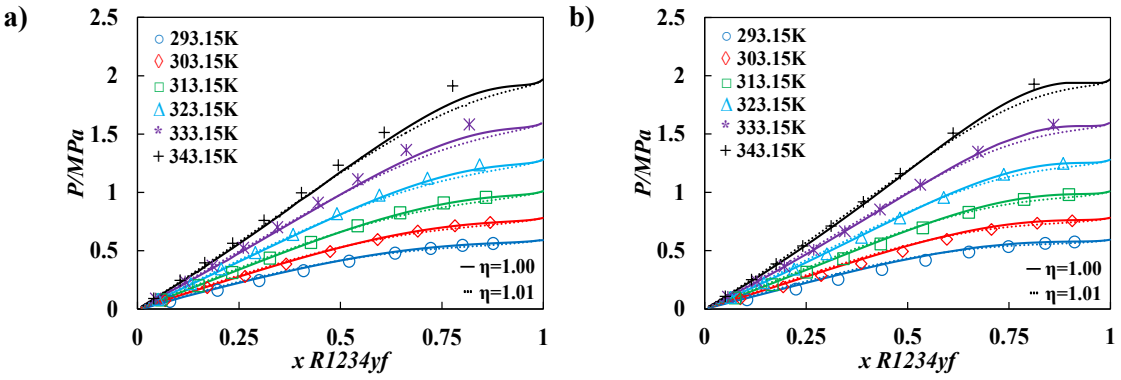

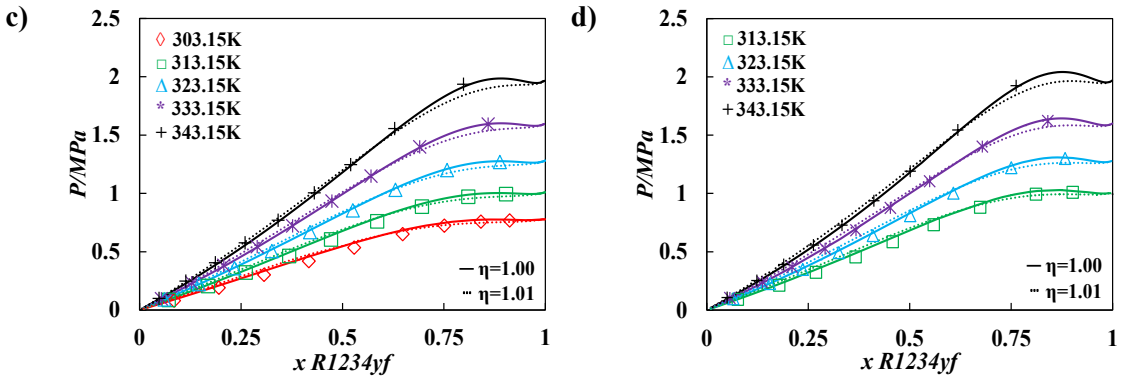

Figure 5.3. *Pressure-composition diagram at 293.15 K (blue circles), 303.15 K (red diamonds), 313.15 K (green squares), 323.15 K (light blue triangles), 333.15 K (magenta asterisks) and 343.15 K (black plusses) of the blends formed by a mixture of R1234yf and* ***a)*** *PEC4* ***b)*** *PEC5* ***c)*** *PEC6* ***d)*** *PEC7.*

Figure 5.4 depicts the *Pxy* solubility diagram of R134a in PEC5 [117] and PEC9 [116] at different temperatures. The polar soft-SAFT calculations, performed with temperature independent binary parameters (see **Table 5.2**), show very good agreement with available experimental data. In this case, no immiscible region was found for the studied temperatures range.

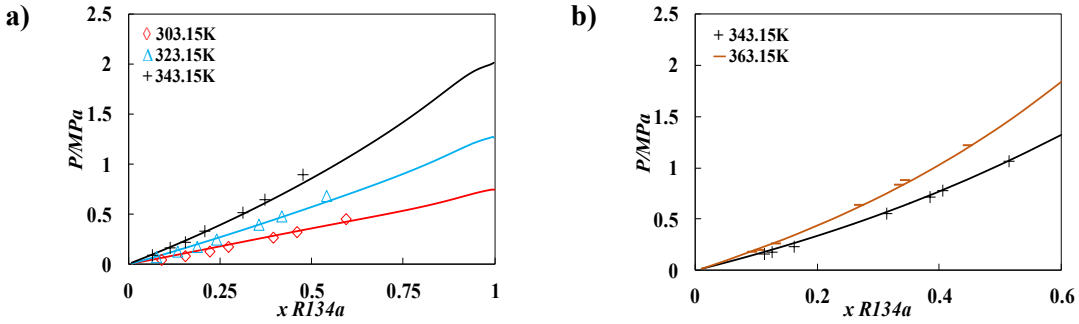

Figure 5.4. *Pressure-composition diagram at 303.15 K (red diamonds), 323.15 K (light blue triangles), 343.15 K (black plusses) and 363.15 K (brown horizontal lines) of the blends formed by a mixture of R134a and* ***a)*** *PEC5* ***b)*** *PEC9.*

In addition to PECs, the solubility of R1234yf and R134a in PEGDMEs has also been calculated for the systems R1234yf + TrEGDME [131], R134a + MEGDME [126], R134a + DEGDME [125], R134a + TrEGDME [128] and R134a + TEGDME [124]. These were accurately reproduced fitting a temperature independent binary parameter ξ_{ij} (see **Table 5.2**). Results are plotted in **Figure 5.5** for R1234yf and **Figure 5.6** for R134a. As also observed for PECs, ξ_{ij} is greater than unity, indicating more attractive interactions between the PEGDMEs and the refrigerants than the simple geometric average (see **Eq. (3.6)**), being stronger for R134a than for R1234yf. The theoretical description confirms

that both gases exhibit full miscibility across all temperatures covered and that refrigerants solubility decreases as the temperature increases.

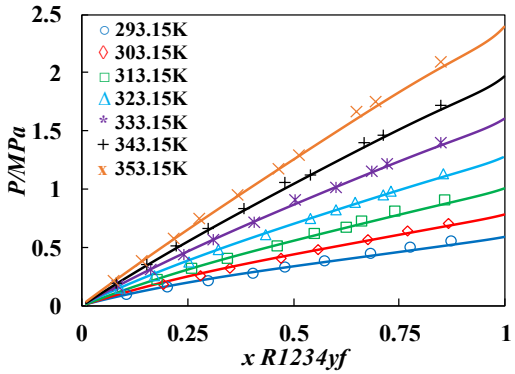

Figure 5.5. *Pressure-composition diagram of the mixture R1234yf and TrEGDME at 293.15 K (blue circles), 303.15 K (red diamonds), 313.15 K (green squares), 323.15 K (light blue triangles), 333.15 K (magenta asterisks), 343.15 K (black plusses) and 353.15 K (orange crosses).*

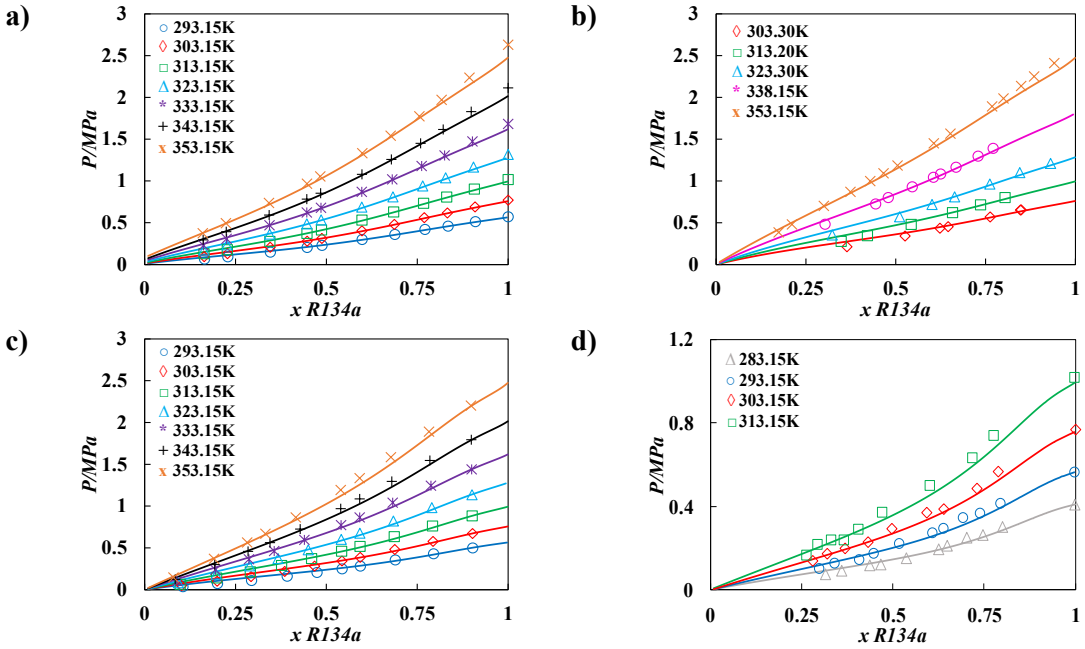

Figure 5.6. *Pressure-composition diagram at 283.15 K (grey triangles), 293.15 K (blue circles), 303.15 K and 303.30 K (red diamonds), 313.15 K and 313.20 K (green squares), 323.15 K and 323.30 K (light blue triangles), 333.15 K (magenta asterisks), 338.15 K (pink circles), 343.15 K (black plusses) and 353.15 K (orange crosses) of the mixtures of R134a and* ***a)*** *MEGDME* ***b)*** *DEGDME* ***c)*** *TrEGDME and* ***d)*** *TEGDME.*

5.3. Selection of optimal lubricant for R513A at process operating conditions

Once the solubility of the individual refrigerants on the two families of lubricants has been studied and the model validated, it is possible to address the solubility of R513A

on the different lubricants. However, the focus is given on those lubricants for which experimental data for both refrigerants composing the mixture were available. This reduces the study to PEC5, PEC9 and TrEGDME, whose results are shown in **Figure 5.3-Figure 5.6** and **B2**.

In addition to the visual inspection of these Figures, the solubility of R134a and R1234yf in these lubricants can be assessed through the evaluation of the Henry's constants, a thermodynamic parameter associated with the amount of gas dissolved in a solvent at a given temperature at infinite dilution. The results for the binary systems involving R134a or R1234yf with PEC5, PEC9 or TrEGDME as a function of temperature are plotted in **Figure B2**. A visual inspection reveals that the lowest Henry's constant (which means the highest solubility) corresponds to PEC9 for R1234yf (see **Figure B2a**) and PEC5 for R134a (see **Figure B2b**), while the values for TrEGDME are less promising. Among the two PECs, PEC9 has two clear disadvantages: first, there are evidences of immiscibility in a considerable range of composition, at least for the higher temperatures, according to the predictions achieved with soft-SAFT (see **Figure B1**). This is an undesirable situation as the formation of a second liquid phase would automatically decrease the efficiency of the system. Second, PEC9 has a high viscosity compared to PEC5, which is also a problem for the practical implementation in a cooling system. High-viscous oils are highly undesirable, as they affect the system efficiency due to excess work on the compressor [509]. PEC5 viscosity values are up to a 79% lower than PEC9 values in the temperature range between 303.15 K and 353.15 K and a constant pressure of 1 MPa, in accordance with the experimental viscosity available data [510,511]. Consequently, PEC5 is considered the best lubricant, among those investigated here, to be used with the low GWP R513A refrigerant.

Once the most compatible oil for the R513A components is chosen, the next step is to determine the mixtures' optimal working conditions. According to the available data and the soft-SAFT models described, PEC5 is fully miscible in R1234yf and R134a in the range of temperatures studied in this work. Consequently, safe operation is possible establishing an upper temperature limit of 343.15 K [512].

Finally, the performance of the ternary system formed by R513A (R1234yf 56% *wt*, R134a 44%*wt*) and PEC5 is explored in a fully predictive manner using the polar soft-

SAFT EoS. Soft-SAFT has proven to be predictive to multicomponent systems as far as the binary parameters of the mixtures are determined [370]. Hence, the bubble pressures have been predicted at different oil circulation fractions with R513A, in order to evaluate the impact of the lubricant in this property. The results are obtained using ξ_{ij} from the corresponding binary combinations: R1234yf + PEC5 (ξ_{ij} = 1.033), R134a + PEC5 (ξ_{ij} = 1.100) and R1234yf + R134a (ξ_{ij} = 0.983) and are shown in **Figure 5.7**.

As it can be seen, the impact of the addition of lubricant in the refrigerant blend is minor in the studied range of composition. Based on these conditions, the industrial performance of the mixture at lubricant leakages of 1, 3 and 5% (*wt*) (vertical lines) are simulated next. For comparative purposes, the same diagram for PAG (Polyalkylene Glycol) lubricant TrEGDME is provided in **Figure B3**. As expected, the solubility at isobaric conditions is lower compared to PEC5, and the impact of leakage becomes more significant.

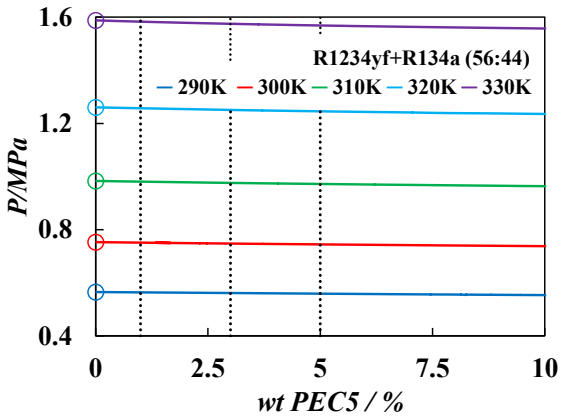

Figure 5.7. *Soft-SAFT liquid phase equilibria prediction of the ternary mixture R513A and lubricant PEC5 at 290 K (blue), 300 K (red), 310 K (green), 320 K (light blue) and 330 K (magenta). Circles represent polar soft-SAFT predictions of R513A at the corresponding isotherms.*

5.4. Energetic evaluation

A comprehensive and energetic evaluation of the performance of R513A when paired with the selected lubricant PEC5 is presented herein. The purpose is to determine the effect that PEC5 might cause on current refrigeration equipment employing R513A as refrigerant, in order to address the need of installing an oil separator on the discharge line of the compressor. The presence of the oil separator allows enough fluidity in the evaporator avoiding a viscosity increase in the liquid phase, as well ensuring an effective

lubrication in the compressor, where a viscosity decline may occur based on temperature effects [110]. The detailed process conditions are summarized in **Table B1**.

Oil circulation ratio (OCR) is defined as the proportion of oil's mass flow with respect to the total and is implemented in the thermodynamic assessment to fix a certain oil percentage within the ternary mixture. OCR% of 1, 3 and 5% in weight were computed to account for normal operating compressors (1%), compressors approaching their end of life (3%) and compressors beyond its service lifecycle or suffering a severe leakage (5%), correspondingly. As it can be seen in **Figure 5.8a**, the increase of the lubricant mass flow in the ternary mixture slightly diminishes the efficiency of the refrigeration cycle at a constant evaporator's temperature. Higher percentages lead to more severe efficiency drops (i.e. R513A *COP* decreases by 2.98% when the presence of PEC5 increases up to 5% at an evaporation temperature equal to 290 K). It is important to note that, at the same process requirements simulated, the polar soft-SAFT *COP* predictions are within a 5% difference respect to NRTL predictions, reinforcing the validity of the soft-SAFT model.

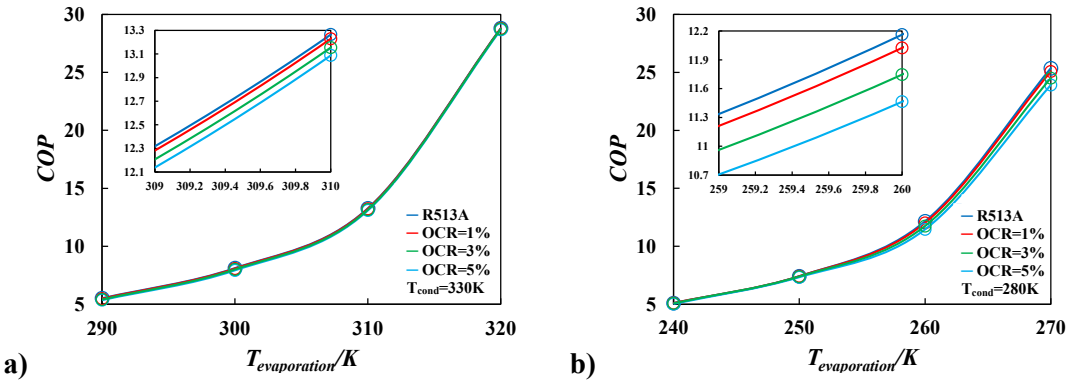

Figure 5.8. *Comparison of the COP of R513A (dark blue) with* ***a)*** *PEC5 and* ***b)*** *TrEGDME at a lubricant composition of 1% (wt) (red), 3% (wt) (green) and 5% (wt) (light blue) as a function of the evaporation temperature.*

In order to quantitatively check the effect of the lubricant's choice in diminishing the cycle's *COP*, additional calculations were performed at the same oil's mass compositions using TrEGDME (**Figure 5.8b**). Based on the preliminary results, the need of a separator module to purify the refrigerant mainstream from an excess of oil accumulated throughout the years is clear. To preserve a suitable outcome, the controller set-point should be designed to act when a lubricant leakage no greater than 5% is detected within the cooling system, as a result of a *COP* deficit of 6.05% (with respect to pure R513A, as seen in the inset of **Figure 5.8b**) under working evaporation temperatures

of 270 K and OCR equal to 5%. As expected, a better efficiency was obtained for lubricant PEC5, with a *COP* enhancement of near 13.50% at the lubricant's mass fraction of 5% and more extreme evaporation temperatures. This is a consequence of R513A higher solubility into PEC5, as shown in previous sub-sections.

Overall, this computational methodology allows the description of the impact of lubricants in the refrigerant, in case of leakage, facilitating the implementation of safety measures. For the particular case study, POE lubricants, such as PEC5, offer good trade-offs for the blend R513A, and can be extrapolated to alternative drop-in mixtures, due to comparable intrinsic characteristics relative to R513A. However, it is speculated that the use of PAG lubricants in the compressor, such as PEGDME, may be more suitable for CO_2-based fourth-generation blends, in contrast to the significant downgrade observed for R513A and other similar F-based refrigerant blends or mixtures with small HC weight fractions.

5.5. Summary of key outcomes from Chapter 5

This chapter addresses the impact of lubricant leaks on the performance of 4th generation refrigerant R513A, providing a case study applicable to similar F-based refrigerant blends. A complete thermodynamic analysis was carried out using the polar soft-SAFT EoS in a systematic manner. Various lubricants, including PECs and PEGDMEs of different chain lengths, were considered, and molecular parameters were optimized to reproduce the density of these compounds accurately. The models were then used to evaluate the solubility between the R1234yf and R134a refrigerants, integrating the R513A blend, and these lubricants, to assess the accuracy of the model and to search for trends in solubility. In all cases, excellent agreement with available experimental data was achieved using a temperature independent energy binary parameter, while a second size constant parameter was introduced to improve the description of long chain length PECs. PEC5 was selected as the most suitable lubricant based on gas-oil miscibility and viscosity. The thermodynamic behavior of R513A and PEC5 was then evaluated to predict the effect of lubricant leaks (1-5% by weight) on the coefficient of performance of a residential cooling cycle. **PEC5 emerged as the best lubricant for R513A, showing minimal impact on *COP*, with a reduction of up to 3%** compared to TrEGDME's 6.1%.

Chapter 6. Drop-in Assessment of Sustainable Refrigerants for Single-Stage Vapor Compression Refrigeration Cycles

In the previous chapters, two theoretical frameworks for characterizing single-component refrigerants and their binary blends were presented, in addition to assessing the suitability of lubricants for novel GWP refrigerants. In this chapter, the soft-SAFT model is used to integrate these results on to single-stage vapor compression refrigeration cycle (SS-VCRC), as illustrated in ***Figure 3.2****, and* ***Figure 3.3*** *of the methodology section. This forms the basis for all analyses in this chapter, establishing a technical modeling platform for the rapid screening of emerging eco-friendly refrigerants as potential drop-in replacements for current third-generation compounds. A compatibility analysis of widely used HFCs, such as R134a and R410A, is conducted to identify potential pure or binary drop-ins, with a detailed evaluation based on the 4E criteria—energy, exergy, environmental, and economics—alongside a prospective assessment of legislative scenarios to support their future adoption.*

The key outcomes discussed in this chapter are published in peer-reviewed Q1 journals Applied Thermal Engineering, ACS Sustainable Chemistry & Engineering, and Renewable and Sustainable Energy Reviews (refer to [49,228,229]).

6.1. Preliminary assessment on promising low-GWP refrigerants

The first step of this chapter consists of a technical screening for the evaluation of promising low-GWP refrigerants in a SS-VCRC. A set of selection criteria have been applied to narrow down the feasible search space of promising refrigerants for further evaluation and performance optimization. The study is limited to synthetic pure refrigerants, including 4th generation HFOs, and HCFOs, benchmarked to commonly used 3rd generation HFCs, R32 and R134a. The initial round of selection, based on environmental and safety criteria in accordance with EU legislation No 517/2014 [513], allowed the selection of refrigerants accounting for the following safety and environmental conditions:

1. GWP < 150.
2. Null ozone depletion potential (ODP) or ODP < 0.01.
3. Non-toxic (A).
4. Either non- or low-flammability (1, or 2L).

The list of refrigerants accounting for previous conditions is given in **Table C1** in the **Annex**. The technical performance of these compounds in a basic VCRC cycle was based on the technical KPIs defined in **Chapter 3.3** (**Section 3.3.1**). This includes thermodynamic properties and performance metrics like *NBP*, c_p, *RE*, η_{II}, ρ_V, P_{cond}, *COP*, and TEWI. Such evaluation was done at arbitrary operating conditions to facilitate the comparison of the refrigerants under the same conditions, which might not be optimal for each refrigerant, yet sufficient for the purpose of their preliminary screening. These conditions include (1) steady-state flow, (2) fixed evaporator and condenser temperatures (*i.e.,* T_{evap} = 270 K and T_{cond} = 300 K) ensuring a lift temperature of 30 K [48,514,515], (3) negligible superheating and subcooling, (4) zero pressure drop and isobaric conditions in both condenser and evaporator, and (5) ideal isentropic compressor efficiency, similar to a previous published work [103]. The main results are highlighted in **Figure 6.1** in a spider graphic.

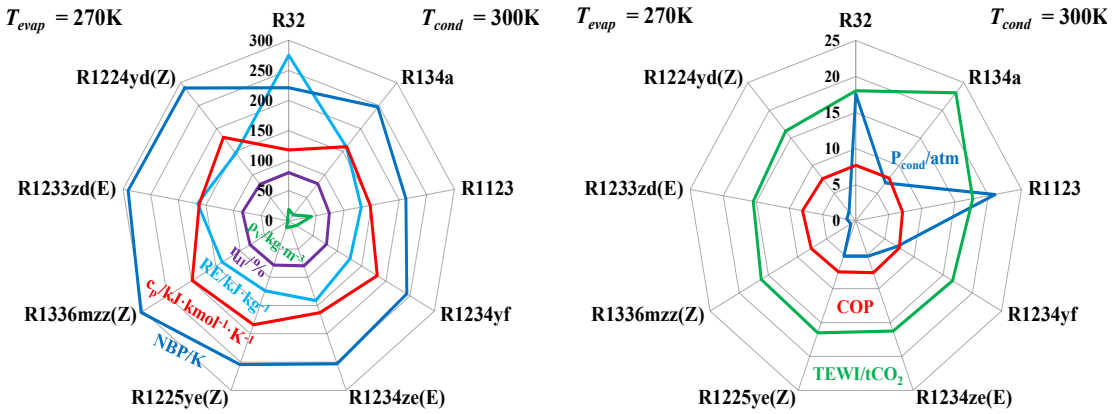

Figure 6.1. *Technical evaluation for promising environmentally friendly refrigerants, based on KPIs predicted using polar soft-SAFT. The normal boiling point (NBP), specific heat capacity (c_p), refrigeration effect (RE), exergy efficiency (η_{II}), and suction density (ρ_V) are listed on the* ***left****, while the condensing pressure (P_{cond}), coefficient of performance (COP), and total equivalent warming impact (TEWI) of selected refrigerants shown in* ***Table C1****, are depicted on the* ***right****. The calculated values for these KPIs are included in* ***Table C2****.*

The trade-offs between the different factors affecting the design and efficiency of the VCRC clearly increase the difficulty in discerning the suitability of a single refrigerant over others. Accordingly, the most suitable refrigerant would be the one that achieves an acceptable compromise between the different criteria as demonstrated from the comparative assessment in **Figure 6.2**. To this end, all technical KPIs were assessed with a scale from 1 – 9 denoting improved technical performance and suitability for intended the application.

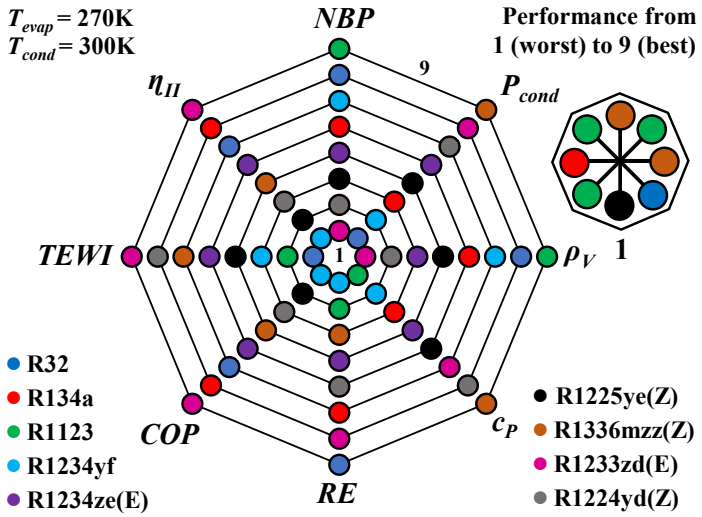

Figure 6.2. *Comparative assessment based on refrigerant characteristics for finding optimal refrigerant, with a scale of 1 – 9 (worst – best) denoting improved performance, based on results included in* ***Figure 6.1****, and* ***Table C2****. Refrigerants ranked as 1 are shown in the in-step in the right-hand side [229].*

As inferred from **Figure 6.2, t**he technical suitability of the benchmark 3rd generation refrigerants, R32 and R134a, is supported primarily by their low *NBP*, and high *RE*, *COP*, and η_{II}, while their low to moderate performance in environmental aspects is overshadowed by the alternative 4th generation refrigerants. In terms of environmental impact, commercial refrigerants such as R134a present the highest *TEWI* due to the substantial contribution of its direct emissions from its high GWP. A reduction in *TEWI* is seen for all alternative low GWP refrigerants, due to the diminished contribution from their direct emissions. Though presenting marginal variations in their indirect emissions levels, related to the effect of their properties on system efficiency and energy consumption (see **Table C2**), the impact of these marginal variations remains substantial considering the number of cooling cycles operated worldwide.

Among the alternatives, R1336mzz(Z), R1233zd(E), and R1224yd(Z) present the lowest condenser operating pressure (P_{cond} < 0.2 MPa). As such, limited reduction in the saturation temperature is expected, resulting in reduced compressor temperature lift and, consequently, compressor work. This will potentially reduce the operating costs and improve the systems' efficiency (*COP* and η_{II}), as seen with R1233zd(E). Notwithstanding, very low condenser operating pressures as with R1336mzz(Z) (P_{cond} < 0.1 MPa), though preferential for reducing compressor work, might still prove problematic during refrigerant loading/unloading process, in addition to higher propensity for air leakage into the system [516]. Nonetheless, a trade-off ensued with their high suction densities, requiring large compressors associated with increased capital investments. Additionally, the inverse correlation between the energetic properties of these refrigerants (*i.e.,* c_p and *RE*) revealed low specific energy requirements for subcooling (high c_p), yet with moderate cooling capacities (low-mid *RE*). Given its high *NBP* and reduced TEWI, these refrigerants might represent an attractive alternative for high temperature applications [515], even though their deployment in low-medium temperature applications is possible with the use of deep vacuum or multistage compressors, however, with significant capital and operating investments [517].

In terms of technical KPIs, R1123 is a potentially promising alternative refrigerant for low-medium temperature applications. Its low *NBP* value at atmospheric pressure is indicative of its ease of vaporization without the need for extremely low evaporator operating pressures, in addition to its high suction density and its impact on reducing

compressors sizing, being indicators of relatively reduced capital and operating investments. Moreover, R1123 energetic properties, including c_p and *RE*, are within acceptable levels, with moderate specific energy demand to sub-cool the condenser liquid outlet, and moderate cooling capacity output. However, these benefits are partially offset by its high condenser operating pressure (P_{cond} > 1.5 MPa) that can increase operating expenditure, while reducing the system energy and exergy efficiencies [518]. As a result, R1123 exhibits the lowest *COP* and $\eta_{II,}$ as seen in **Figure 6.2**.

Among the remaining fluids, R1234yf stands out due to its higher suction density at the evaporator outlet, which contributes to enhance its volumetric cooling capacity. However, this refrigerant offers a lower performance in other important KPIs, such as the *RE*, to *COP*, $\eta_{II,}$ c_p, and P_{cond}. In addition, R1234yf emits substantially higher indirect GHGs emissions throughout its lifespan compared to systems functioning with R1234ze(E) or R1225ye(Z), due to its lower efficiency in terms of refrigeration effect at constant cooling capacity requirements [519], resulting in higher mass flow rates and, consequently, increasing indirect GHGs emissions [520]. Another aspect to consider is the indirect effect caused by an increase in the net power output of compressed vapor, even at similar *RE* values, as seen for R1234yf compared to R1225ye(Z).

The final tier of possible alternatives, which has been finally pre-selected in this PhD thesis, include R1234ze(E) and R1225ye(Z) as potential refrigerants for the selected temperature range with an acceptable compromise in terms of technical KPIs. R1234ze(E) excels over 3rd generation refrigerants in terms of TEWI and key technical metrics such as c_p and P_{cond}, whereas R1225ye(Z) exhibits a mix of outcomes, balancing operating costs with performance efficiency. A slight concern to be considered, in terms of R1234ze(E), was related to its mid-flammability (A2L) based on ASHRAE standard safety class [521]. However, this system has been recently labelled as non-flammable (A1) by Honeywell and the U.S. Department of Transportation (DOT) [522], owing to the dependency of its flammability ratio on the experimental operating conditions [523].

6.2. Analysis of drop-in replacements for 3rd generation HFCs

Based on the information gathered from previous **Section 6.1**, some additional aspects have been evaluated to consider a drop-in replacement for the currently used 3rd generation refrigerants with the most compatible low GWP 4th generation refrigerants. The assessment is done relating the previous analysis with the technical criteria highlighted in the methodology for the examined VCRC cycle, involving the estimation of the Volume Cooling Capacity (*VCC*) and the Coefficient of Performance (*COP*). The *PH*- and *TS*-diagrams for all the pure refrigerants are predicted from polar soft-SAFT EoS, under the imposed operating conditions for the VCRC, and can be found in **Figures A8** and **A9** in **Annex A**.

The most convenient criterion for analyzing compatibility of drop-in replacements would be merely using *VCC* under the same VCRC operating conditions, as currently implemented in most works on searching for alternative refrigerants [74,439,524]. Similar *VCC* values between benchmark 3rd generation refrigerant, and low GWP 4th generation replacement signifies their compatibility without the need to retrofit units in existing refrigeration cycle, in particular the compressor [156].

Prior to implementing this criterion, it is worthy to test the validity of *VCC* predictions using polar soft-SAFT. This is done through linearly correlating predicted *VCC* values with the critical properties (*i.e.,* critical temperature and pressure) of the pure refrigerants [525], indicating the accuracy of the predicted *VCC* values. The critical properties for each refrigerant were obtained from the literature [432,437–439,444,526–528], while *VCC* values were directly predicted from polar soft-SAFT. As provided in **Figure 6.3**, the predicted *VCC* values and critical properties of the studied refrigerants indeed followed a linear correlation ($R^2 > 0.995$), with the exception of R23. This outlier was expected as the critical temperature of R23 (T_c = 299.29 K) is very close to the evaporator operating temperature for the VCRC (T_{evap} = 300 K). Notwithstanding, this simple test affirms the accuracy and predictive power of polar soft-SAFT in capturing the behavior of key technical criterion for evaluating the compatibility of drop-in replacements.

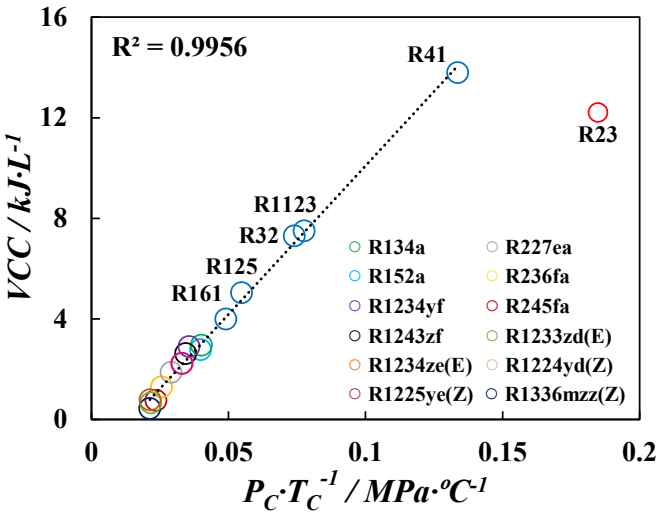

Figure 6.3. *Correlation between polar soft-SAFT predicted VCC values of refrigerants examined in this work, and their experimental critical properties from the literature [432,437–439,444,526–528].*

6.2.1. Replacement of R134a, R32, R152a, and R245fa with sustainable refrigerants

Highlighted in **Figure 6.4** are the most compatible 4th generation refrigerants with the ten 3rd generation refrigerants (HFCs) as benchmarks. The results show that 4th generation refrigerants R1123, R1234yf, and R1224yd(Z), have nearly compatibility for replacing R32, R152a, R134a, and R245fa, with their *VCC* values being within 5% of those for the benchmark refrigerants to be replaced. Conversely, although other refrigerants are available, such as replacing R41 or R23 with R1123, the low *VCC* value of R1123 indicates that the refrigeration cycle needs to be retrofitted. These dissimilar *VCC* values require an increase in the compressor size for equivalent volumes of compressor-displaced refrigerant. In this aspect, rational design of refrigerant blends might prove efficient for the replacement of those refrigerants without compatible low GWP single refrigerants.

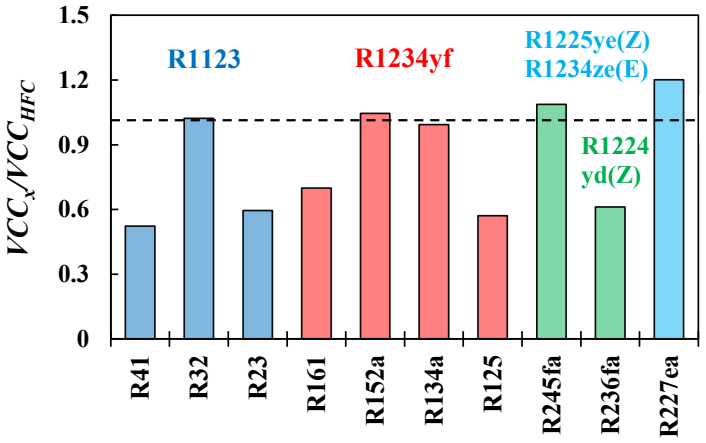

Figure 6.4. *Compatibility test for replacing 3rd generation refrigerants with 4th generation refrigerants based on polar soft-SAFT predicted VCC shown in* ***Figure 6.3****. The dashed line denotes similar VCC for 3rd generation benchmark and its 4th generation drop-in replacement.*

Building on the previous compatibility assessment, a drop-in initial evaluation has been addressed to explore potential pure replacements for R32, R152a, R134a, and R245fa. This is done through estimating the corresponding trade-off between *COP* versus *VCC*, as well as a thorough review of their main thermophysical properties (see **Section 6.1**). The initial focus for the detailed drop-in analysis was on R134a (see GWP in **Table C1** in **Annex C**), shown in **Figure 6.5**, due to its widespread commercial use and the urgent need to replace it [36,37]. Among the examined possible replacements, R1234yf and R1243zf, as well as R1234ze(E), and R1225ye(Z) to a lesser extent, emerge as attractive options with nearly similar *VCC* values, albeit more reduced *COP*. This shows that their usage has the possibility of not incurring additional capital cost associated with altering the design of the compressor, but on the expense of reduced system efficiency, which can be acceptable (performance drop inferior to 3% in all cases) considering their significantly lower GWP.

On another front, R1225ye(Z) might prove safer in operation due to its non-flammable nature, as opposed to the mildly flammable R1234yf, or the highly flammable R1243zf, which would be reflected on the cost needed for the installation of additional safety layers. Judging by additional technical criteria, R1234yf is indeed an attractive option with the limited need for adjusting the design of the compressor as supported by its *NBP*, its suction density being higher than that for R134a, and relatively similar condenser operating pressure and specific heat capacity (see **Section 6.1**). The incurred costs might be mainly operational due to the higher energy demand for compression, as

demonstrated from its lower *RE*. Recent publications [26,529] on searching for replacements for R134a [530] have indicated the promising use of the 3rd generation refrigerant R152a [530] for oil-free automotive air conditioning, guided by its lower GWP, low cost, and minimal equipment change. Nonetheless, its highly flammable nature is a concern. Hence, based on the outcome of the analysis in this work, R1234yf (GWP < 1 [530], and mild flammability 2L) is a more competent alternative to effectively replace R134a, compared to R152a.

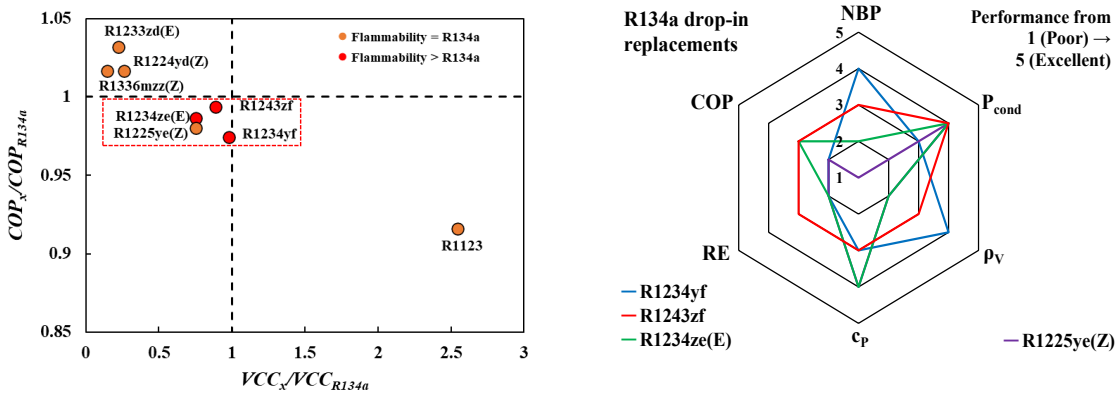

Figure 6.5. *Drop-in analysis for replacing R134a based on VCC and COP, benchmarked to R134a (**left**), and other technical criteria relative to R134a for promising replacements (**right**). See text and reference [49] for further details.*

In line with the previous analysis, the ability of the candidates to replace the other 3rd generation refrigerants, R32, R152a, and R245a, is included in **Figure 6.6**. In the current market, R32 (GWP = 677) [530] is used as a medium-GWP drop-in replacement to R410A (GWP = 2088) [530], which will also be phased-out soon. The most compatible drop-in replacement for R32 proved to be R1123, with relatively similar *VCC* value, albeit a 6.8% reduction in its *COP*. Though other 4th generation refrigerants have similar *COPs* to R32, their significantly lower *VCCs* indicated the need to fully retrofitting systems operating with R32. Notwithstanding, the prospect analysis of using R1123 as a drop-in replacement for R32 in terms of other KPIs showed that the only concerning factors would be the higher condenser pressure and lower *RE* of R1123, translated to increased operating costs.

In the case of drop-in replacement for R152a, several options are available including R1234yf, R1243zf, R1234ze(E) and R1225ye(Z), with comparable *VCCs* and nearly 5.0% reduction in *COPs*. Though R1234yf seemed like a good option judging

solely on its *VCC* and safety concerns, other technical criteria showed a reduced performance compared to R152a. On the other hand, a better compromise on *COP* and condenser pressure is achieved when employing R1234ze(E) and R1225ye(Z) as drop-in replacements.

Lastly, for replacing R245fa, high-*NBP* 4th generation refrigerants such as R1336mzz(Z), R1224yd(Z) and R1233zd(E) were found to be appropriate, along with demonstrated enhanced *COP*. The most compatible option would be R1224yd(Z) owing to its improved suction density and specific heat capacity, while maintaining relatively similar volumetric cooling capacities, condenser pressure and normal boiling point. It is important to notice that, in this case, the *NBP* performance is computed with reference to its maximization owing to its use in high temperature applications, as opposed to the low-medium temperature application of the aforementioned cases when finding replacements for R134a, R32 and R152a.

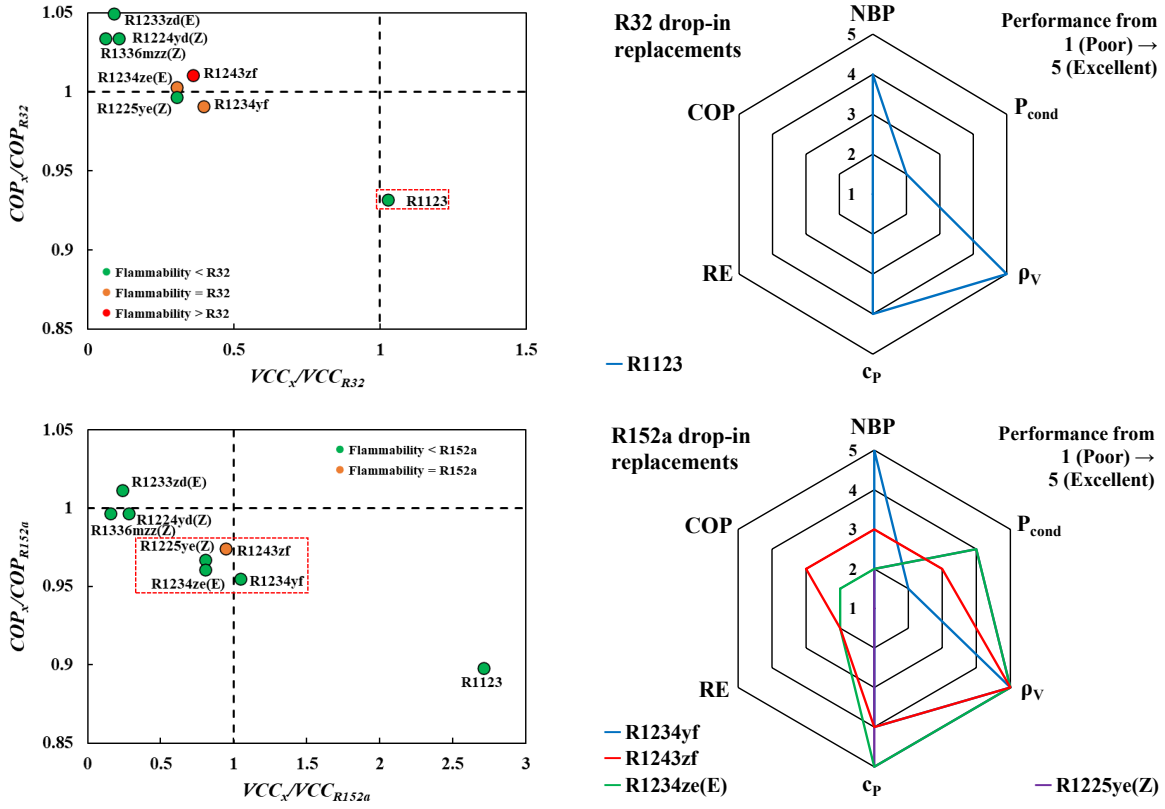

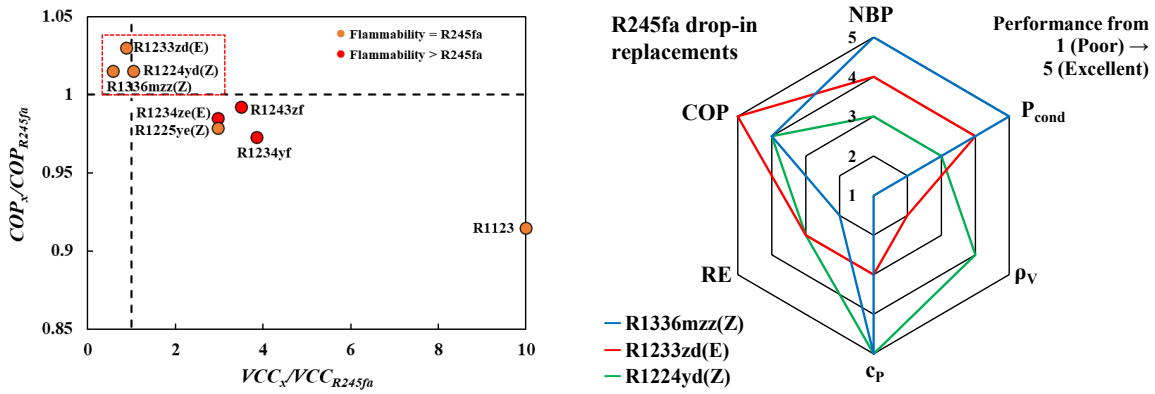

Figure 6.6. *Drop-in analysis for replacing R32, R152a, and R245a with 4th generation refrigerants, based on VCC, and COP benchmarked to each refrigerant (**left column**), and other technical criteria relative (**right column**). See text and reference [49] for further details.*

All these possible alternatives can be rationalized in view of their micro-level features. Notice that the replacements of a 3rd generation with a 4th generation refrigerant is possible for those with similar structural characteristics, such as carbon number and degree of fluorination (see **Chapter 4.1.1.1** for a deeper analysis). For example, compatibility of R134a and R152a with R1234yf is due to them being within the same molecular space in terms of carbon number and degree of fluorination, with a fine balance between structure and energy affecting the thermophysical properties. Their similar *VCC* values relative to R134a or R152a are due to the reduced vapor density of the replacements (owing to their slightly larger molecular volume), compensated with their increased enthalpy due to their higher polarity. Shifting farther from these structural features, such as seen in the case of the larger R1336mzz(Z), or less polar HCFOs, skewed the fine balance of molecular features on their properties compatible with R134a or R152a. Furthermore, they also proved to be compatible with R245fa due to similar structural characteristics.

6.2.2. Holistic 4E and drop-in assessment to replace R134a and R410A

In the previous section, replacements of refrigerants with pure fluids were explored, which, although practical, often lead to a reduced COP. To overcome this limitation, a more effective approach involves designing mixtures that strike a balance between key operational properties. Consequently, the application of polar soft-SAFT to rationally design low-GWP azeotropic/near-azeotropic refrigerant blends as drop-in

replacements has been extended to mixtures and applied to substitute the widely used commercial refrigerants R134a and R410A. The scope of this work is limited to binary blends with available phase equilibria experimental data to demonstrate the reliability of the model and proposed blend design framework in **Chapter 4.2.1**. Results were patented under U.S. Provisional Application No. 63/406,114 [531].

6.2.2.1. Short-listed refrigerant blends based on initial screening criteria

The selection of promising drop-in replacement blends is carried out based on the same criteria used for single-component candidates, wherein the alternative blend should:

(1) minimize GWP.
(2) minimize/eliminate flammability.
(3) be non-toxic and have null ozone depleting potential.
(4) maximize/maintain circuit efficiency.
(5) possess equivalent volumetric cooling capacity to ensure minimal retrofitting to key RAC system units, such as the compressor [274]. As seen in previous section, this is an already complex task for single-component refrigerants considering the trade-offs between the multiple desirable properties. While the use of mixtures expands the possibilities, the number of possible combinations makes this task harder.
(6) possess a high degree of azeotropy, with preference for azeotropic or near-azeotropic blends that behave as pure fluids in the RAC system.

The drop-in and subsequent 4E approach is focused on replacing R134a, and R410A, widely used into nowadays automotive and domestic air-conditioning, and in high pressure commercial and industrial refrigeration, respectively. The proportions of the blends listed in **Table 4.5** were examined in the composition range of 10 – 90 *wt.*%, discretized with 10 *wt.*%; resulting in 432 possible blends [228].

An initial screening was conducted to narrow down the number of blends based on their GWP, degree of azeotropy, toxicity, and flammability class, for further evaluation as potential drop-in replacements. For the environmental criterion, the blend GWP was computed as the sum of the weighted average of the GWP of its individual components [532]. The constraints on GWP were set to (1) GWP < 150, termed study A, based on

2022 EU legislation limits [37], and (2) 150 < GWP < 500, study B, emulating 2020 interim stage transitionary legislations [37]. For safety constraints, blends comprised of toxic components were eliminated, while those with flammable components (A2/A3) were still included, pending a flammability assessment dependent on their proportions, if satisfying remaining criteria. A graphical abstract for blend selection, based on the aforementioned environmental, technical, and safety criteria, is shown in **Figure C1**.

The technical criteria on the degree of azeotropy was evaluated based on the blend glide temperature (defined as the temperature variation between dew and bubble points at constant pressure and single-phase composition), obtained from VLE predictions for the binary blends using the molecular model. As highlighted earlier, blends with null (azeotropic) or small (near-azeotropic) T_G are preferred, behaving as pure fluids in RAC systems. In this study, a T_G threshold of 0.1 K was set, benchmarked to the T_G of the near-azeotropic blend R410A at atmospheric pressure [533]. This limit was applied to the entire pressure spectra to ensure applicability within common industrial operating pressures (*i.e.,*0.1 – 3 MPa), accounting for pressure fluctuations in system operations.

The flammability of the short-listed blends satisfying the previous criteria was subsequently evaluated using the empirical approach of Linteris *et al.* [262]. The flammability class for blends in-line with the ASHRAE classification are grouped based on their $\overline{\Pi}$ values (see **Eq. (6.1))**, with non-flammable class 1 ($\overline{\Pi} \leq 0$), mild-flammable class 2L ($0 < \overline{\Pi} < 50$), and flammable classes 2 and 3 ($\overline{\Pi} \geq 50$), with potential candidate blends exhibiting either 1 or 2L flammability classes. The temperature difference in the numerator in **Eq. (6.1)** is standardized by the upper limit adiabatic flame temperature of 2500 K. The $atan2$ function is employed to derive the four-quadrant arctangent angle within the domain [−π, π], accounting for coordinates in a two-dimensional Cartesian plane relative to the positive x-axis, prior to adjusting the perspective to span angles from -180° to 180°. The 1/2L boundary ($\pi_{1,2L}$) is set at 36, yielding a normalized flammability index ranging from zero, at this threshold, to an absolute value of 100, for highly flammable compounds. As a result of applying such approach, 12 candidates were identified, with 8 blends for study A, and 4 for study B, included in **Table 6.1**.

$$NFI \equiv \bar{\pi} = \frac{\left[\left(\frac{180}{\pi}\right) \cdot atan2\left\{\left(\frac{T_{ad} - 1600}{2500 - 1600}\right); \left(\frac{F}{F+H}\right)\right\}\right] - \pi_{1,2L}}{90 - \pi_{1,2L}} \cdot 100 \qquad \textbf{(6.1)}$$

Table 6.1. *Short-listed refrigerant blends and their compositions based on initial screening criteria: GWP, glide temperature and flammability.*

ID	Blend	*wt.*%[±]	GWP	T_G / K[*]	ASHRAE class
		Study A			
1	R1123 + R32	90.0	70	0.099	A1
2	R1234yf + R134a	90.0	130	0.010	A1
3	R1234yf + R152a	90.0	14	0.004	A2L
4	R1234yf + R152a	80.0	28	0.067	A2L
5	R1243zf + R1234ze(E)	60.0	< 1	0.041	A2L
6	R1243zf + R1234ze(E)	70.0	< 1	0.012	A2L
7	R1243zf + R1234ze(E)	80.0	< 1	0.002	A2L
8	R1243zf + R1234ze(E)	90.0	< 1	0.000	A2L
		Study B			
1'	R1234yf + R134a	70.0	390	0.019	A1
2'	R1234yf + R134a	80.0	260	0.000	
3'	R1234ze(E) + R227ea	90.0	336	0.013	A1
4'	R152a + R134a	80.0	370	0.084	A2L

[±]The mass fraction for the 1st component in the blend.
[*]Obtained at atmospheric pressure (0.1 MPa).

The environmental constraints set on the GWP of the investigated blends accounted for the largest exclusion rate (≈ 62%). Interestingly, acceptable combinations in view of EU guidelines [37] on GWP < 150 (study A) include HFCs + HFOs, and HFOs + HFOs blends, with the latter type being more capable of achieving diminished pollutants capacities (GWP < 1). Conversely, transitionary limits on GWP, study B, allowed for the inclusion of HFCs + HFCs blends like some commercially available. However, blends with R245fa were excluded on account of its toxicity.

The limits on GWP in study A are in line with those implemented in developed countries including USA, UK, and EU states, with the stringent guidelines on allowable GWP limits playing a major role by including HFOs in the pool of promising replacement refrigerants, the lowest GWP seen for blends 5 – 8 (see **Table 6.1**), fully composed of HFOs. Although blends 1 – 4 possess GWP below the required EU limits, their adoption in developed countries might be limited considering the imposed tariffs on HFCs utilization and import [31]. This will have an impact on the imports of HFCs from major producers such as China and India.

Conversely, the more relaxed limits in study B (GWP < 500), seen in developing countries such as China and India, might ensure the sustenance of HFCs manufacturers and their resistance to switch to HFOs production and manufacturing, considering that

the HFCs market still endures with the production of pure HFCs, or HFCs-based blends. However, blends 1'– 4' have nearly 50% lower GWP compared to the commercial R134a in circulation. These blends, if compatible as drop-in replacements, might present a compromise solution that permits HFC manufacturers to continue with their business-as-usual agendas, while circulating refrigerants with lower GWP.

In terms of degree of azeotropy, the formulation of near-azeotropic blends was more flexible than fully azeotropic blends, with only two blends recognized as fully-azeotropic (T_G = 0.000 K). Predictions from polar soft-SAFT established that dipolar refrigerants with relatively similar normal boiling points (ΔNBP < 5 K) and high structural similarity can easily result in near-azeotropic blends [534]. This can be seen in **Figure 6.7** from the reduced T_G magnitude for blends with R134a compared to R152a, denoting increased azeotropy for R1234yf + R134a due to similar molecular structures and polarity. The T_G predictions for the remaining blends in **Table 6.1** are provided in **Figure C2** in the **Annex C**.

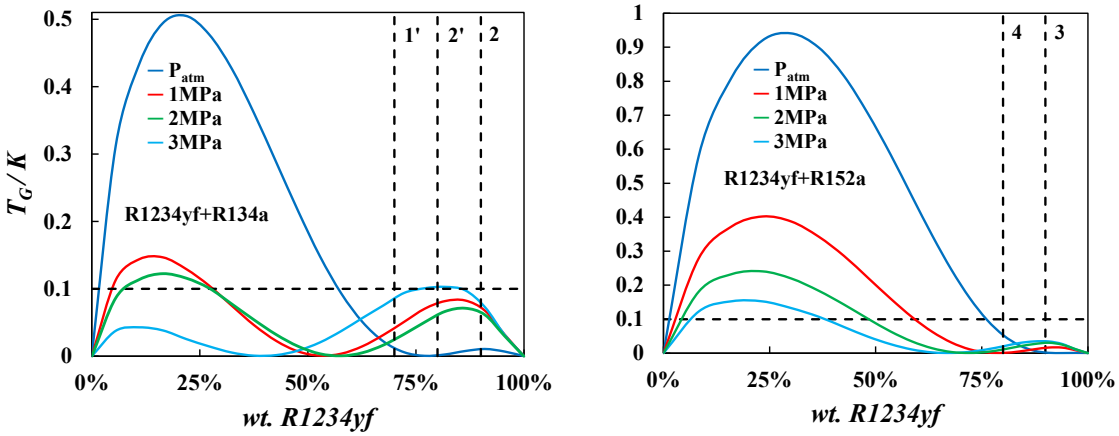

Figure 6.7. *Glide temperature versus weight percentage of the first component of the binary blend, at different pressures, for R1234yf + R134a blend (**left**), and R1234yf + R152a (**right**) as predicted from polar soft-SAFT. Dashed vertical lines denote blends from **Table 6.1**.*

The flammability assessment for blends satisfying GWP and T_G limits is provided in **Figure 6.8**. Plotting T_{ad} *vs.* $\frac{F}{F+H}$ conveniently allowed grouping the pure refrigerants and blends into different flammability regions corresponding to the ASHRAE classifications (A1, A2L, A2, and A3) [50]. The validity of the empirical approach can be seen from the consistent flammability rating of known pure refrigerants and commercial blends with ASHRAE Standards [535–538], with A1 class for R134a and commercial

blends (*i.e.,* R410A, R513A and R450A), and A2L classification for R32, R1234yf and R1234ze(E).

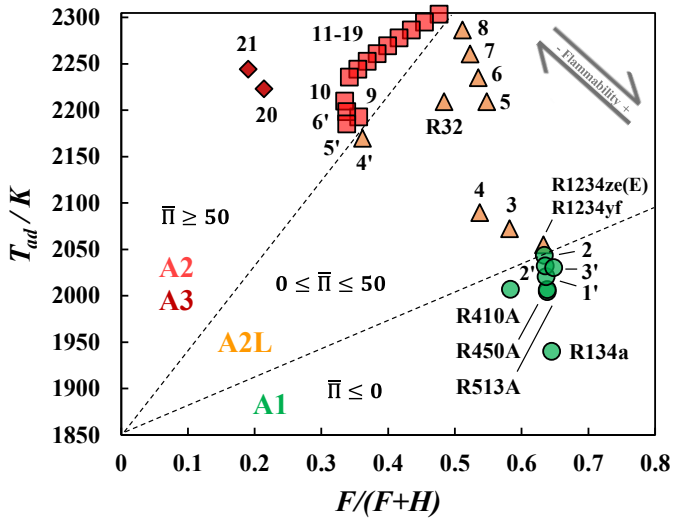

Figure 6.8. *Flammability assessment using T_{ad} and F/(F+H) for pure refrigerants and blends. The dashed lines represent the regions of different flammability. Colors and symbols correspond to the flammability of the refrigerants and blends: green circles for A1, yellow triangles for A2L, red squares for A2, and dark red diamonds for A3, while the numbers correspond to the blends presented in* ***Table 6.1*** *and* ***Table C3****.*

Based on **Figure 6.8**, non-flammable A1 blends with $\overline{\Pi} \leq 0$ include those composed of R1234yf + R134a at different compositions (blends 2, 1', and 2'), in-line with literature findings [535]. The increase in $\overline{\Pi}$ for these blends is due to the increased proportion for the A2L R1234yf. Another non-flammable blend is R1234ze(E) + R227ea (blend 3'), with a relatively similar formulation to the commercial A1 blends R515A (88 *wt.*% R1234ze(E)) and R515B (91 *wt.*% R1234ze(E)) [536,537]. Other potential blends are those in the mild-flammability region (A2L), including blends 3 and 4 with R1234yf + R152a, similar to R32. However, these blends are positioned in the lower mild-flammability area, promising lower rates of increasing pressures in the case of explosion than R32 [538]. Additionally, blends composed of R1243zf + R1234ze(E) (blends 5 – 8) are within the mild-flammability region, with increasing degree of mild-flammability with higher content of the A2 R1243zf. Interestingly, the presence of 10 *wt.*% of the A2L R1234ze(E) was sufficient to reduce the flammability of blend 8.

Several additional low-GWP blends with the required T_G (see **Table C3**) were at the boundary of flammable regions, including those composed of R152a + R1234ze(E) (blends 9 and 10), R152a + R1243zf (blends 11-19), R161 + R1234yf (blends 20 and 21),

and mixtures of R152a with R227ea or R134a (blends 5' and 6'). Their flammability is due to the high content of the A2 R152a, R1243zf, and A3 R161 (see **Figure C3**), hence their exclusion. Notice that the flammability of R32 + R1123 (blend 1) cannot be assessed with this method due to the lack of adiabatic flame temperature data for R1123. However, a recent study [51] has clarified that blends of R32 with more than 60 mol% R1123 can be safely operated at the spark ignition energy levels generated by an inverter-controlled air conditioning units. As such, blend 1 can be expected to be A1-2L owing to the small content of R32 (*i.e.,* 10 *wt.*%).

6.2.2.2. Drop-in assessment and technical compatibility of low-GWP blends

After the first screening concerning the required toxicity, safety, environmental (in terms of direct emissions, or simply GWP) and azeotropy conditions, the technical compatibility of the short-listed blends in **Table 6.1** was evaluated as drop-in replacements for R134a and R410A. Additionally, the single-component refrigerants (*i.e.,* R32, R1234yf, R1234ze(E), and R1225ye(Z)) [49], and commercial blends R450A, and R513A were included in the drop-in analysis for comparative purposes. The drop-in KPIs include equivalent *VCC*, *DLT*, and P_{cond}, to ensure minimal system retrofitting (see **Table 3.3** in the methodology).

The results for the drop-in assessment to replace R134a and R410A have been plotted in **Figure 6.9**. The dashed line indicates the property value corresponding to R134a or R410A, while the bars indicate the value of the alternative blend. When the bar matches the dashed line, it means that both mixtures are equivalent for that property.

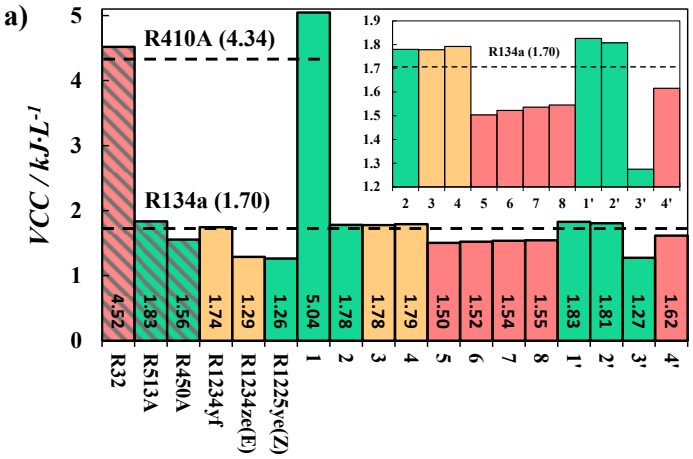

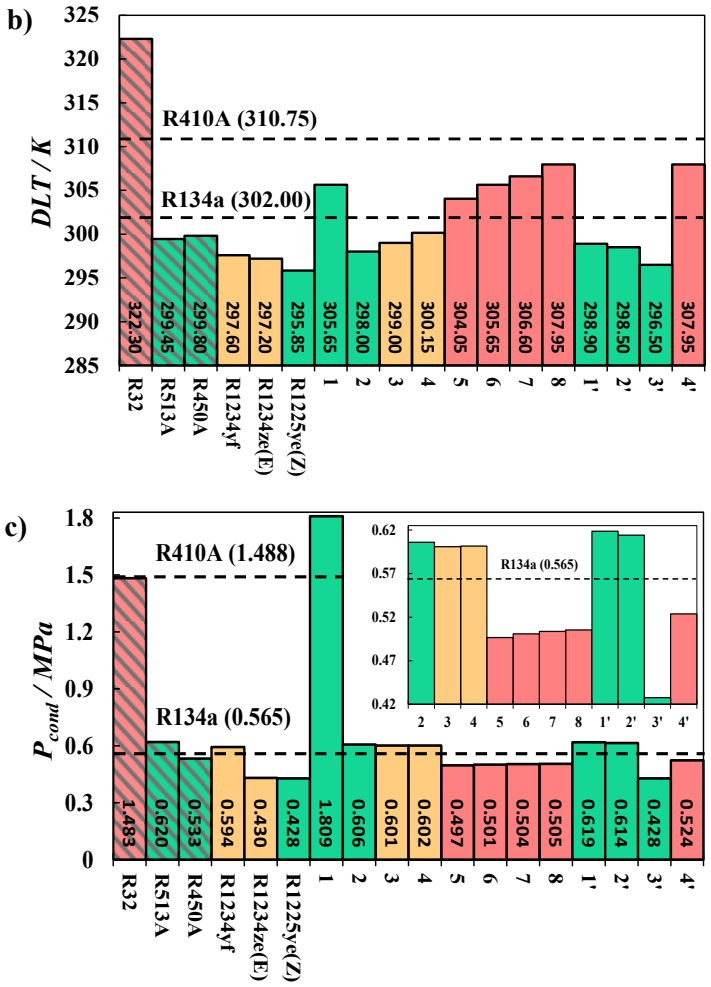

Figure 6.9. *Drop-in assessments [228] based on KPIs,* ***a)*** *VCC,* ***b)*** *DLT, and* ***c)*** P_{cond}*, for replacing commercial R134a and R410A. Note the bar color corresponds to the flammability class, with A1 (green), low A2L (yellow), and high A2L (red). The bars with* ▨ *denote refrigerants and blends with GWP > 500. The numbers on the lines and in the bars correspond to the values of each KPI.*

A quick look to this Figure reveals the high compatibility of several low-GWP designed blends, mostly HFCs + HFOs, with similar *VCC* and P_{cond} values to R134a albeit lower *DLT* values (see **Figure 6.9b**). These include blends of R1234yf with 10 – 20 *wt.*% of either R134a or R152a (blends 2 – 4). The compatibility of these blends was slightly better than the currently commercial alternative R513A for most drop-in KPIs, indicative of minimal compressor retrofitting. This can be attributed to the increased presence of R1234yf, which had previously demonstrated a high potential for replacing R134a, even as a pure fluid, in some applications [49]. Although pure R1234yf was slightly better than its blends in terms of *VCC* and P_{cond}, the presence of other refrigerants in these mixtures helped to increase the *DLT*. The advantage offered by these blends also includes their low-GWP (14 – 130) compared to the higher GWP of R513A (GWP = 608), facilitating

the full transition to low-GWP refrigerants. Concurrently, increasing the content of R134a (20 – 30 *wt.*%) in its blend with R1234yf (*e.g.,* blends 1' and 2') is also technically compatible for replacing pure R134a, with a lower GWP in-line with interim transition stages (*i.e.,* study B with 150 < GWP < 500). The compatibility of these blends was within 5% increased *VCC* and P_{cond}, but with lower *DLT* values, also resulting in minimal system retrofitting. Additionally, there is an improved lower flammability rating of HFC + R1234yf blends, moving from A2L (blends 3 and 4) to A1 (blends 2, 1' and 2') with increasing proportions of the A1 R134a, as opposed to the A2 R152a. A final remark concerns the fact that mixtures between HFOs (without the presence of HFCs) do not provide a good performance, with only 60 *wt.* % R1243zf + R1234ze(E) (blend 5) offering an acceptable compromise among KPIs was 60 *wt.* % R1243zf + R1234ze(E) (blend 5), however, with an A2L flammability similar to R32 (see **Figure 6.8)**.

Finding a replacement for R410A was a more challenging task, also shown in **Figure 6.9**. The single-component R32 was the most compatible drop-in replacement with its similar *VCC* and P_{cond}, however, with larger *DLT*, which would present an environmental advantage to R410A, but remains infeasible considering the upcoming GWP requirements. Among the designed blends, 90 *wt.*% R1123 + R32 (blend 1) had the only acceptable KPI magnitudes as R410A replacement, due to the presence of R32, yet being capable of meeting ultimate environmental and safety targets (GWP = 70 and A1). Unfortunately, there is a complete absence of suitable alternatives for the transitionary stage. This means that system retrofitting would be inevitable when replacing R410A with low-GWP alternatives. In recent studies, operational challenges for RAC systems employing R32 as a replacement for R410A were highlighted, such as hazardous compressor *DLT* and shortened compressor lifetime, calling for several retrofits to enhance the system operating lifetime [38,539]. Therefore, it seems quite reasonable to carry out such modifications with blend 1, or any other future suitable candidates.

6.2.2.3. Energy and exergy analysis

Based on the previous results, blends 2 – 5 (study A) and 1' – 2' (study B) were selected as possible candidates to replace R134a, while blend 1 was chosen as the best alternative for R410A. Next, the thermophysical and technical performance properties (*i.e., NBP*, P_R, ρ_v, *RE*, *PPTR*, η_{II}, and *COP*) for these promising blends are shown in

Figure 6.10, using a spider web graphic, based on a comparative ranking established in **Table C4**.

A closer examination of these properties revealed relative similarities with R134a for all promising blends (*i.e.,* blends 2 – 5, 1' and 2') with acceptable changes within 5% for *NBP*, P_R, *PPTR*, and *COP*. Larger changes were observed for ρ_V, and *RE*, indicative of lower system efficiency, and increased refrigerant mass flow rate directly affecting operational costs [540]. A similar outcome was seen for blend 1 for replacing R410A, with slightly better thermophysical properties than R32, but significantly lower *RE*, *PPTR*, η_{II}, and *COP* values.

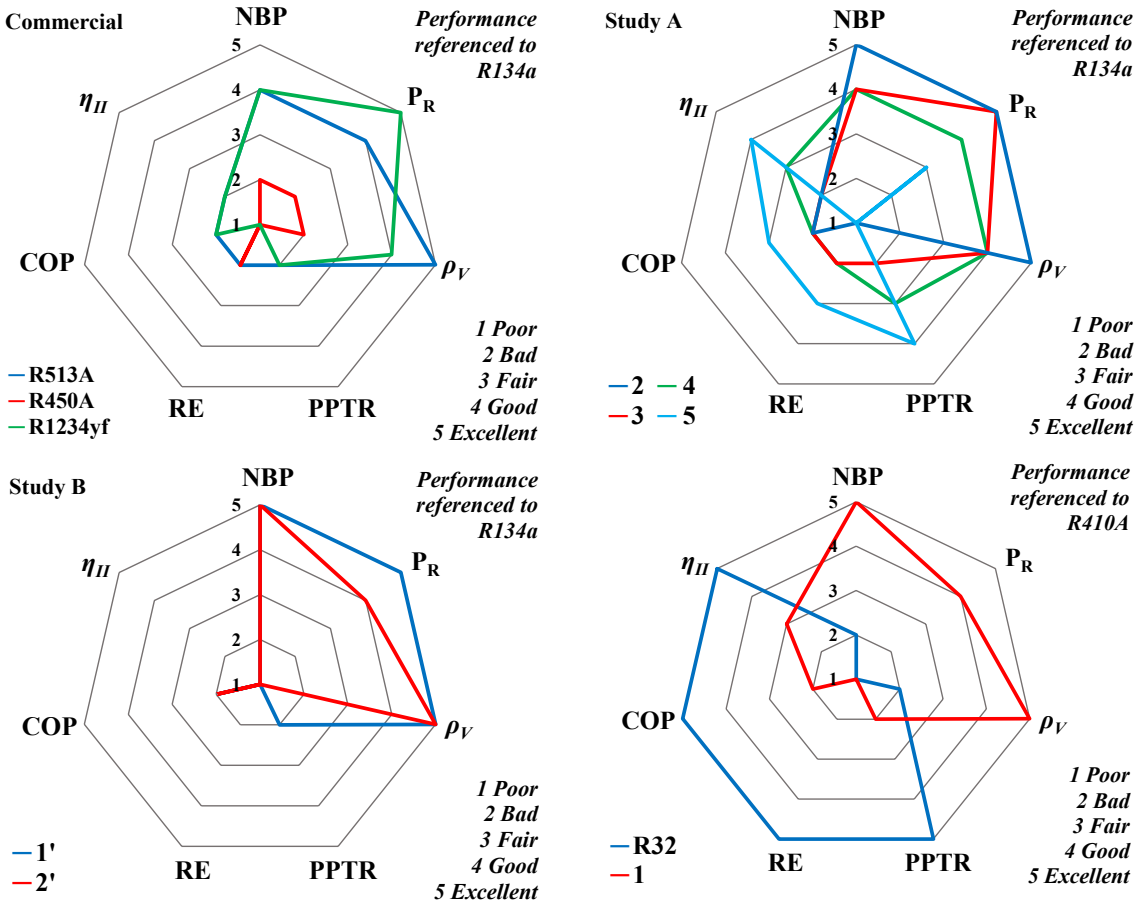

Figure 6.10. *Comparative analysis for thermophysical properties and technical performance criteria of promising drop-in blends compared to R134a and R410A.* ***Top left:*** *available commercial refrigerants performance referred to R134a;* ***top right:*** *selected refrigerants included in study A referred to R134a;* ***bottom left****: selected refrigerants included in study B referred to R134a;* ***bottom right****: refrigerant 1 and R32 performance referred to R410A. See text for details.*

Following the previous Figures and established rankings, a percentage of compatibility was calculated for the studied blends, and the results are included in **Table 6.2**. The most compatible blends (> 90%) for replacing R134a include blends 2 – 5, and blends 1' and 2', with the highest compatibility seen with blend 3, outperforming commercial blends R513A and R450A, and single-component refrigerants. In contrast, the only feasible blend for replacing R410A was blend 1, achieving a similar compatibility ratio (73%) to R32. The results of the ranking were consistent irrespective of the chosen operating conditions shown in **Figure C4** in **Annex C**.

Table 6.2. *Compatibility analysis of promising blends designed in this work for replacing R134a and R410A. Compatibility codes designate null (≥ 90%), partial, and complete (≤ 60%) – retrofitting required.*

		R32	**R513A**	**R450A**	**R1234yf**	**R1234ze(E)**	**R1225ye(Z)**	**1**	**2**	**3**	**4**	**5**	**6**	**7**	**8**	**1'**	**2'**	**3'**	**4'**
Performance 1: Poor 2: Bad 3: Fair 4: Good 5: Excellent	***NFI***	3	5	5	4	4	5	5	5	4	4	3	3	2	2	5	5	5	3
	NBP	4	2	2	2	5	1	5	2	2	2	1	2	2	2	2	2	1	2
	P_R	4	3	2	3	2	1	5	3	3	3	2	2	2	2	3	3	2	2
	ρ_V	5	3	2	3	2	1	5	3	3	3	2	2	2	2	3	3	1	2
	RE	4	1	1	1	1	1	1	1	1	1	2	2	2	2	1	1	1	3
	PPTR	3	3	2	3	4	3	1	3	3	4	5	5	5	5	3	3	4	5
	COP	3	3	2	3	4	3	1	3	3	4	4	4	4	5	3	3	4	5
	η_{II}	3	3	1	3	4	3	1	3	3	4	4	4	5	5	2	3	4	5
Drop-in KPIs R134a	***VCC***	1	4	4	5	2	2	1	5	5	4	4	4	4	4	4	4	2	4
	P_{cond}	1	5	5	5	4	4	1	5	5	5	5	5	5	5	5	5	4	5
	DLT	1	5	5	4	3	2	4	4	5	5	5	4	3	3	5	5	3	4
Drop-in KPIs R410A	***VCC***	5	1	1	1	1	1	4	1	1	1	1	1	1	1	1	1	1	1
	P_{cond}	5	3	2	3	2	2	4	3	3	3	2	2	2	2	3	3	2	2
	DLT	1	1	1	1	1	1	3	1	1	1	2	3	4	5	1	1	1	5

Compatibility / %	**R134a**	20	93	93	93	60	53	40	93	100	93	93	87	80	80	93	93	60	87
	R410A	73	33	27	33	27	27	73	33	33	33	33	40	47	53	33	33	27	53

6.2.2.4. Environmental analysis: estimation of direct and indirect emissions

Apart from the technical performance of the proposed blends already evaluated in the previous section, another key aspect of these refrigerants as alternatives is related to its overall environmental impact associated with their utilization and emissions in refrigeration cycles, which is highly relevant for assessing their contribution to global

warming phenomenon quantified in terms of the TEWI metric (see **Eq. (3.59)** in **Chapter 3**). Here, it is important to remark the difference between the pre-screening done in terms of GWP in **Section 6.2.2.1**, limited to this value, and the study carried out in this sub-section, where a deeper analysis considering direct and indirect emissions (accounting for molar flows, leakage rates, production of the compound, etc.) is done. Such analysis has been conducted considering the major global HFCs producers including the People's Republic of China (PRC), United States of America (USA), European Union (EU-27), Japan, and India [541], some of which have significantly contributed to current legislations on HFCs emissions and consumption (*i.e.,* USA, EU-27 and Japan) [542].

The parameters required for the TEWI evaluation are included in **Table C5**, with the technical cycle performance evaluated from polar soft-SAFT, and results are presented in **Figure 6.11**. The level of direct emissions related to the leakage rate and end-of-life cycle disposal of the refrigerants were similar across all examined geographical areas (see **Figure 6.11**, **top**), as the parameters concerning their estimations were fixed beforehand. This is simplistic for the sake of convenience; however, it suffices for a comparative analysis. Conversely, indirect emissions related to the energy consumption for system operation using the examined refrigerants varied across the different regions, attributed to the carbon footprint of the different energy resources, with the largest impact seen for India (dependent on fossil fuels), while the lowest was for EU-27 countries (mostly dependent on renewable energy resources).

Additional evaluation for the top-12 most densely populated EU-27 states, with more than 85% of the EU's overall population (see **Figure 6.11**, **bottom**), demonstrated the high level of direct emissions in Poland (POL) compared to the lowest levels in Sweden (SWE) and France (FRA), as the former largely depends on fossil fuels for energy consumption, while the latter two are more oriented towards renewable (particularly hydro and offshore wind power) and nuclear energy consumption, respectively. The dissimilar contributions of direct and indirect emissions demonstrate the relevant role of the degree of decarbonization of the energy mix, the effect of the refrigerant on cycle energy consumption and its efficiency in reducing the environmental footprint for deploying low GWP refrigerants. Surely, a higher benefit can be obtained through combining these low GWP refrigerants with renewable energy resources and high system efficiency to reduce both direct and indirect emissions levels.

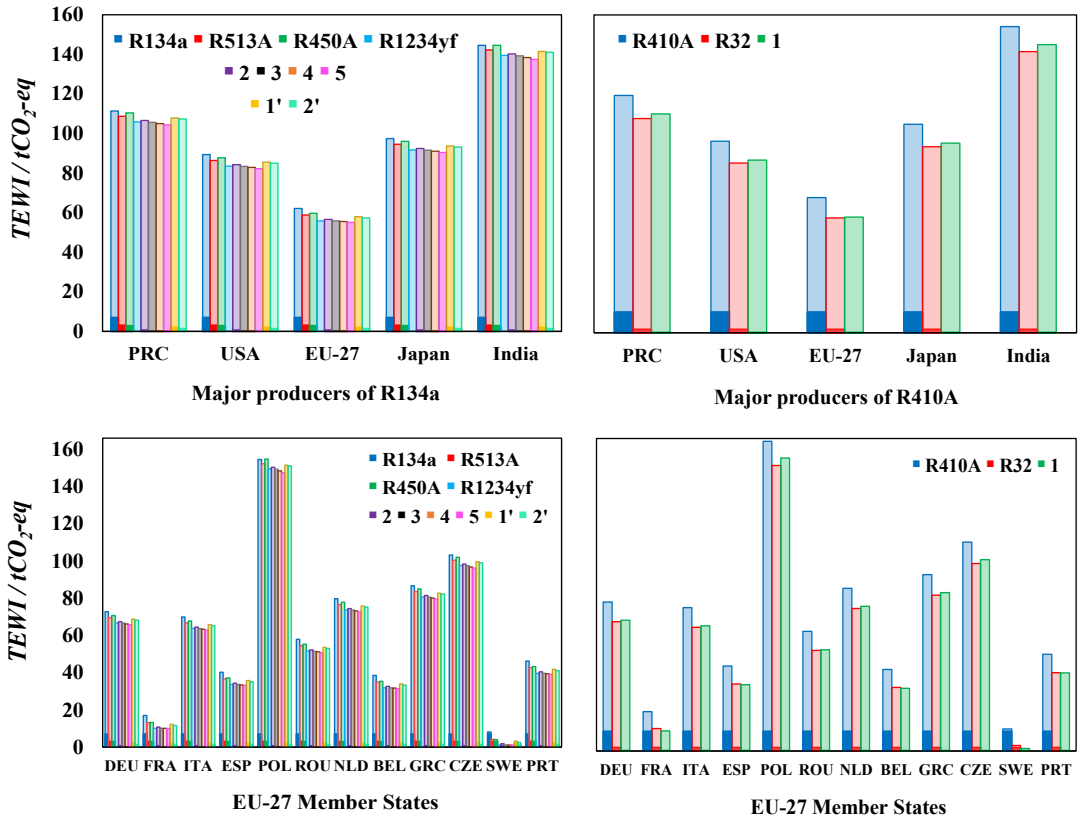

Figure 6.11. *TEWI (refer to **Eq. (3.59)** in the methodology) analysis for most promising alternatives for R134a (**left column**) and R410A (**right column**), with the bar colors corresponding to the studied benchmark refrigerants and designed blends, as per the legend inside the figures. **Top:** the different major HFCs producers, sorted by emission rates, and **bottom:** selected EU-27 countries, sorted by population from left to right. The strong color represents direct emissions, while the light-equivalent color stands for indirect emissions [228].*

In terms of refrigerants, both commercial R134a and R410A presented the highest direct emissions of 7.07 and 10.46 tCO_2-eq, respectively, closely related to their high GWP. Additionally, lower direct emissions were obtained with proposed commercial replacements R32 (1.77 tCO_2-eq), R450A (2.97 tCO_2-eq), and R513A (3.11 tCO_2-eq) within 50% lower than 3rd generation refrigerants. Clearly, the synthetic blends from this work present a major reduction in direct emissions, being almost 90% lower than R134a and R410A, with nearly negligible direct contributions for blends 1, 3, 4, and 5 due to the large proportion of low-GWP HFOs in these blends (*i.e.,* R1123, R1234yf, and R1243zf). Overall, the environmental burden associated with blends 2 – 5 are the lowest among all available options for replacing R134a with 8.9% – 11.4% reduced environmental footprint. These are attractive alternatives, given also their high technical compatibility (> 90%) with systems currently operated with R134a, indicative of lower capital cost requirements associated with retrofitting existing systems.

Conversely, larger indirect emissions contributions were obtained with nearly all refrigerants, closely related to the country-dependent energy mix, and refrigerant-dependent compressor work. All drop-in replacements, apart from blend 5, resulted in larger levels of indirect emissions compared to R134a. This is related to the variation in their thermodynamic properties and technical performance from R134a (**Figure 6.10**), even if highly compatible to minimize system retrofitting (**Table 6.2**). As highlighted earlier, these variations have larger impacts on the operational costs and energy consumption, hence, their larger indirect emissions. Similar tradeoffs were obtained for blend 1, as a substitute of R410A, considering the 0.89% (EU-27) larger electricity consumption required for this blend.

6.2.2.5. Techno-economic evaluation

Regardless of the producing country, the market availability and current relative prices for these refrigerants are an additional criterion to be included in this overall assessment. For instance, the estimated price for blends 2' and 2 – 4 can be approximately 5 times that of R134a ($12.9 per kg), based on the retail price of the individual constituents [515,529]. The cheapest R134a drop-in replacement corresponds to blend 5, with a relative cost of $45 per kg. However, the lower price of HFCs is minimized by their imposed utilization taxes [37], with an additional cost of $21.5 – 31.3 per kg for R134a or R410A [543].

Surely, the economics of scale will eventually play its role in reducing the prices of alternative refrigerants once their adoption becomes more widespread. This is connected to the last evaluation in this 4E, focused on the economic assessment of designed blends using monetized KPIs associated with capital, operating, environmental, and setup. Provided in **Figure 6.12** is the total annual cost, TAC, for deploying the designed blends and their benchmark commercial alternatives including cost variability in terms of country of deployment, computed on the basis of the SS-VCRC cycle for the major producers of R134a (**Figure 6.12a**) and R410A (**Figure 6.12b**). A similar assessment for each member of the EU-27 is shown in **Figure C5** in **Annex C**.

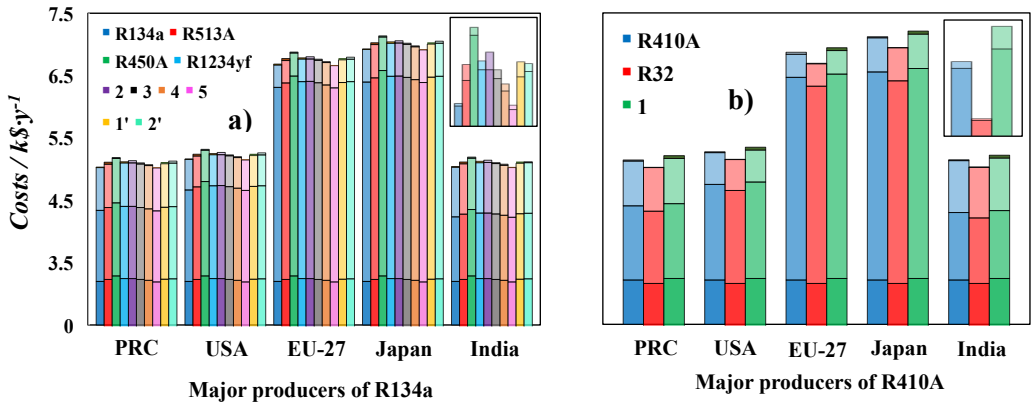

Figure 6.12. *Economic analysis [228] for most promising alternatives for* ***a)*** *R134a and* ***b)*** *R410A, for the different major HFCs producers based on total annual costs (TAC). The colors represent the different refrigerants and blends, as per the legend inside the figures. The different portions of the bars represent the split of the TAC, from bottom to top (darker to lighter colors): CAPEX, OPEX, Enviro, and set-up costs, calculated from* ***Eqs. (3.71)-(3.74)*** *utilized as monetized KPIs.*

The analysis of the results in **Figure 6.12** indicate that capital and maintenance costs had the largest contributions to TAC, consistent within the different countries, as they are dependent on the cost of manufacturing the operating units. The operating costs associated with the energy consumption for the operation of the cooling cycles are the second largest, affected largely by geographical location and its associated cost of electricity, and to a smaller degree by the type of refrigerant and its impact on the cycle's efficiency. In this regard, higher operating costs are associated with EU-27 and Japan, due to the higher cost of electricity, as opposed to lower OPEX in India due to the consumption of coal as a primary energy resource. The variation in OPEX due to refrigerants is less effective compared to cost of electricity, with most changes attributed to the impact of the refrigerant on the energy consumption. Similar OPEX levels to R134a are seen with blend 5 due to similar *COP*, and slightly higher OPEX for blend 1 replacing R410A is observed due to lower *COP* than R410A. Conversely, the lowest contributions are seen for the environmental and setup costs associated with the taxes on the CO_2 emissions from power consumption, the environmental impact of the refrigerant and its retail price, accounting for approximately 5.7% of the total costs. These cost factors are more indicative of the role of governmental and regulatory agencies in instilling barriers on adoption and deployment of technologies with high carbon footprint. Among the major HFC producers, the largest environmental costs are seen in India, owing to the environmental burdens from the utilization of the high-carbon emitting coal as a primary energy resource, though cheaper.

The economic viability of promising blends is highlighted in **Figure 6.13** as a country-dependent heatmap of additional TAC incurred from replacing current systems operated with R134a and R410A. Although blend 3 proved to be a highly compatible replacement for R134a, the additional economic assessment demonstrates an intermediate level of additional retrofitting costs in the range of 57.7 – 105.3 $\$\cdot y^{-1}$ compared to other alternative designed blends. Conversely, the addition of economics into the assessment framework shows that blend 5 is a far better alternative than blend 3, resulting in cost savings (-14.9 $\$\cdot y^{-1}$ for the EU-27 region) or marginal additional retrofitting costs, being a more economically viable replacement blend with relatively similar technical performance. Notice, that blend 5 can also be seen as more favorable based on environmental impact, with GWP < 1 owing to formulation based on HFOs, as opposed to blend 3 with GWP = 14, due to the presence of HFC even in small quantities.

In a similar fashion, replacing R410A with the only feasible blend identified in this work, blend 1, would result in retrofitting costs of similar levels to blend 3 when replacing R134a, in the range of 55.4 – 101.1 $\$\cdot y^{-1}$, depending on the country.

	5	4	3	1	1'	2'	2
DEU	-3.9	57.4	105.3	101.1	124.0	143.8	148.6
BEL	-3.7	52.0	93.9	92.6	111.7	129.7	135.2
DNK	-18.3	42.4	89.7	79.3	108.4	127.9	132.9
JPN	-3.7	50.3	90.3	89.9	107.9	125.3	131.0
ITA	-3.7	49.5	88.6	88.7	106.1	123.2	129.0
IRL	-18.2	40.1	84.8	75.6	103.0	121.8	127.0
AUT	-3.6	47.3	84.1	85.3	101.1	117.5	123.6
PRT	-3.6	47.1	83.7	85.0	100.8	117.1	123.2
CZE	-3.6	46.9	83.3	84.7	100.3	116.6	122.7
POL	-3.6	46.8	83.0	84.4	99.9	116.2	122.3
CYP	-18.2	37.0	78.3	70.7	96.0	113.8	119.4
GRC	-3.6	45.3	79.8	82.1	96.5	112.3	118.5
FRA	-3.5	44.7	78.6	81.2	95.3	110.8	117.1
ESP	-14.9	37.7	76.1	71.4	93.5	110.4	116.3
SWE	-3.5	43.9	77.0	80.0	93.5	108.8	115.2
EU-27	-10.4	39.3	74.8	73.5	91.7	107.7	113.9
ROU	-3.5	43.0	74.9	78.5	91.3	106.3	112.8
NLD	-3.5	41.7	72.2	76.4	88.4	102.9	109.6
EST	-18.1	33.7	71.5	65.6	88.7	105.4	111.3
USA	-3.4	39.8	68.3	73.5	84.1	98.0	104.9
BGR	-3.4	39.7	68.0	73.3	83.9	97.7	104.7
IND	-3.4	39.1	66.7	72.3	82.4	96.1	103.1
HUN	-3.4	38.0	64.5	70.7	80.0	93.4	100.5
PRC	-3.4	39.0	66.7	72.3	82.4	96.0	103.0
LVA	-18.0	30.5	64.6	60.5	81.2	96.8	103.1
LUX	-18.0	30.4	64.5	60.4	81.2	96.8	103.1
HRV	-3.4	39.1	66.7	72.3	82.4	96.1	103.1
FIN	-17.9	29.2	61.9	58.5	78.3	93.5	100.0
SVN	-17.9	29.1	61.7	58.4	78.2	93.3	99.8
SVK	-17.9	27.9	59.2	56.5	75.4	90.2	96.8
LTU	-17.9	27.5	58.3	55.8	74.4	89.0	95.7
MLT	-17.9	27.2	57.7	55.4	73.8	88.4	95.1
	Extra TAC vs HFC's / $y^{-1}						

Figure 6.13. *Heat map for the variation in TAC (calculated from **Eq. (3.70)**) of drop-in candidates benchmarked to R134a and R410A, respectively, ordered from highest to lowest [228]. The main producers of HFCs are highlighted in light blue in the left column.*

A closer inspection of the impact of the geographical location on the economic viability of replacing R134a with blend 5, and R410A with blend 1, with special emphasis on operating and environmental costs (CAPEX remains country independent), is provided in **Figure 6.14**.

A trade-off can be clearly observed between both monetized KPIs. The OPEX in India are among the lowest, while the environmental cost is the highest. This is attributed to the reliance on the cheaper coal for power generation, however, with high CO_2 emission factor. This was not found in the USA, given its reliance on the relatively cleaner natural gas, resulting in 38.8% reduced environmental costs. Conversely, within the EU-27, extremely low CO_2 emissions penalties are reported at the expense of elevated OPEX with the higher electricity prices, being a mixture of increased cost of imported energy resources for power generation and imposed environmental legislation on climate change. Within the EU member states, the lowest cost rates are found in Malta, Lithuania, and Slovakia with their cheaper electricity prices, as opposed to Germany, Belgium, and Ireland. A similar analysis for the remaining drop-in blends (2 – 4, and 1' – 2') can be found in **Figures C6 and C7** in **Annex C**.

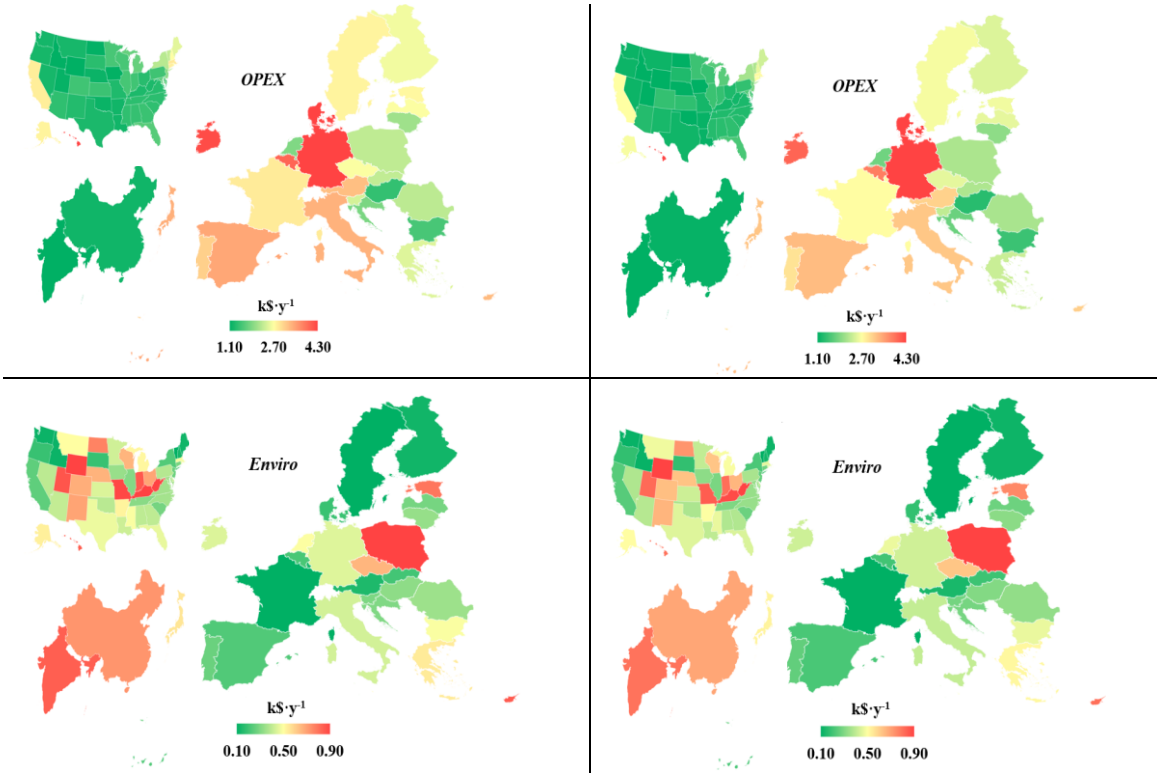

Figure 6.14. *Geographical variation in annualized operating (**top**) and environmental (**bottom**) costs for blend 1 (**left**), and blend 5 (**right**). See text and reference [228] for additional insights.*

Sensitivity analysis on role of policy to promote adoption of designed blends

The impact associated with governmental and legislative policies is the smallest among all the associated costs with 5.7% of total costs. Hence, the commercial barrier to the deployment of low GWP refrigerants is mainly due to the misalignment between HFC manufacturers financial interest and the effectiveness of governmental policies in reducing the economic attractiveness of HFCs-operated systems.[31,55] As such, a sensitivity analysis is presented herein based on legislative agendas that can be realistically implemented in upcoming years to boost the economic viability of next-generation refrigerants and effectively promote a transition to their manufacturing and deployment. These involves a tax-law analogues to CO_2 tax focused on direct HFC emissions through leakage and end-of life disposal, dubbed CO_2-eq tax, (Tax_{CO_2}), in addition to a multiplier on the current HFC utilization tax enacted in Spain to date (Tax_{HFC}), with the results provided in **Figure 6.15**.

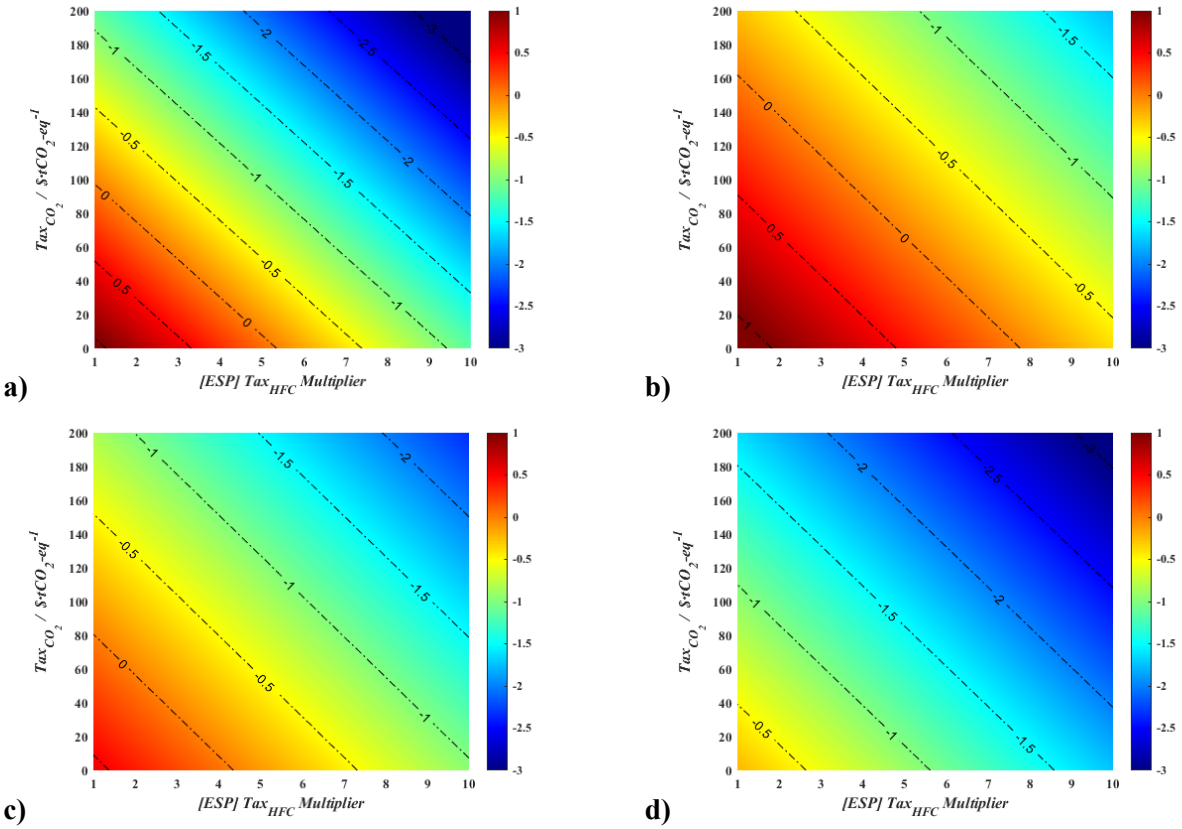

Figure 6.15. *Sensitivity analysis for change in TAC (in k$) of selected blends* ***a)*** *1,* ***b)*** *3,* ***c)*** *4, and* ***d)*** *5 based on HFC utilization tax multiplier on the Spanish framework (x-axis), and CO_2 equivalent tax for HFC emissions (y-axis). Negative values represent a retrofitting saving cost, while extra cost to the original configuration is estimated for dark red regions.*

Taking the EU-ETS's pan-European carbon tax as a benchmark (see **Table C5)**, **Figure 6.15** shows that there is a significant variation in the cycle cost rate as a function of the HFC tax multiplier, with blend 5 exhibiting the greatest enhancement. Similarly, the objective function is also reduced by the implementation of blends 4 and 1, only requiring a 2.3 and 3.2 multiplying factors to reach the annual costs of R134a and R410A, correspondingly. As an illustrative example, if the Swedish carbon tax on direct emissions is enacted (peak value within EU-ETS's market), neither blends 1, 4, or 5 would require additional costs without the need to apply further corrective factor to the original HFC tax standard. Additionally, the use of blend 3 leads to a multiplier effect between 1.9 and 5.7 when the carbon tax on direct GHG emissions increases by 63.73%, from \$49.7tCO_2-eq (EU-ETS) to \$137 tCO_2-eq (SWE). This measure exceeds the limits (multiplier factor > 5.0) when considering blends 2, 1', and 2', as accurately represented in **Figure C8** in **Annex C**.

In summary, only blend 5 exhibits beneficial retrofitting costs when applying the current EU-ETS carbon pricing proposal and the Spanish case law on HFC manufacturing. In essence, the high technical compatibility of blend 5 [(60/40) *wt.*% R1243zf + R1234ze(E)] with current cycles operated with R134a, even with a potentially higher blend cost compared to R134a, alongside the impact of its thermodynamic properties on enhanced cycle efficiency and energy consumption, are sufficient to ensure investment costs comparable to R134a. Alternatively, the drop-in blends 4 [(80/10) *wt.*% R1234yf + R152a] and 1 [(90/10) *wt.*% R1123 + R32] are also covered by such selection criterion, yet with a 2.2% increase HFC tax rate from those currently enacted by Spanish authorities. Accordingly, minor adjustments to current policies would be required to adjust the economics of scale to enhance the attractiveness of low GWP refrigerants.

6.3. Summary of key outcomes from Chapter 6

Chapter 6's analysis identifies promising low-GWP refrigerants as potential drop-in replacements for third-generation HFCs. R1234yf and R1234ze(E) showed Volumetric Cooling Capacity (*VCC*) values within 5% of R134a, but resulted in up to a 3% decrease in *COP*. R1225ye(Z) balanced performance and safety, being non-flammable. R1123 was found to be the most compatible replacement for R32, despite a 6.8% reduction in *COP*. For R152a, compatible alternatives included R1234yf, R1243zf,

R1234ze(E), and R1225ye(Z), all reaching *VCC* values within 5% of R152a but up to a 5% reduction in *COP*. For high-temperature applications, R1336mzz(Z), R1224yd(Z), and R1233zd(E) were promising, with R1224yd(Z) showing balanced performance and enhanced thermophysical properties.

Switching the attention to drop-in mixtures, 432 binary systems were evaluated, and 12 were identified as viable replacements for R134a and R410A. Blend 1 [(90/10) wt.% R1123 + R32] was 73% compatible with R410A, comparable to R32, with a volumetric cooling capacity at 90% of R410A, and a slightly higher discharge line temperature, highlighting the need for careful readjustments during retrofitting. Blend 2 [(90/10) wt.% R1234yf + R134a] demonstrated 85% compatibility with R134a, with similar efficiency but marginally reduced *VCC*. Notwithstanding, Blend 5 [(60/40) wt.% R1243zf + R1234ze(E)] stands out as the most promising alternative, offering 90% compatibility with R134a, a GWP of 30, and performance (energy and exergy-based) nearly identical to R134a. The environmental analysis showed that such drop-ins could reduce direct emissions by up to 90% compared to R134a and R410A, though indirect emissions varied with regional energy sources. The techno-economic evaluation indicated that, despite higher initial costs, selected drop-ins offer significant long-term environmental cost benefits. **Blend 5 was particularly effective, with superior energy and exergy efficiencies and reduced environmental impact, making it economically viable in regions with strict carbon pricing**. Sensitivity analyses suggested that increasing HFC and carbon taxes could enhance the appeal of low-GWP alternatives, with Blend 5 showing the greatest improvement in cost-effectiveness. On contrast, Blend 1 required only a 3.2-fold increase in HFC tax to match R410A's annual costs.

Chapter 7. Assessment of Novel Refrigerants in Advanced Cooling Systems

*Following the thermodynamic characterization of refrigerants in **Chapter 4** and their application to basic vapor compression refrigeration cycles (VCRC) in **Chapter 6**, this chapter focuses on advanced cycle configurations, such as the LL/SL-HX (**Figure 3.4 top**), TS-VCRC (**Figure 3.4 bottom**), and cascade cycles (**Figure 3.6**). It is expected to assess the transition from conventional VCRCs to advanced configurations using statistical methods, testing their suitability for drop-in applications. This involves the use of 4E and LCA methodologies to select optimal mixtures that fulfil both technical and environmental criteria.*

The main outcomes exposed in this chapter have been published in a peer-reviewed research paper (referenced as [229]) in the Q1 journal Applied Thermal Engineering. At the time of submitting this thesis, another contribution titled "The Delicate Balance between Energy, Exergy, Cost, and Environmental Impact in Sustainable Cooling Systems: Refrigerants and Cycles" is accepted by the same journal.

7.1. Parametric evaluation and optimization of cooling cycle designs

In **Chapter 6.1**, the demonstrated potentiality of R1234ze(E) and R1225ye(Z) as promising low GWP refrigerants for air conditioning applications was proved. However, that study was done at fixed specific VCRC conditions, in order to provide a fair screening among all selected refrigerants. Now, an additional assessment of the effect of the main cycle design features and operating conditions on energy and exergy savings is carried out. In other words, this sub-section aims to establish the optimal operating conditions for residential and industrial air conditioning cycles and determine the feasibility of transitioning from conventional vapor compression cycles (**Chapter 6**) to advanced configurations (**Chapter 7**) from a 4E perspective.

The strategy followed is done employing a DoE with the main cooling cycle parameters (factors) and their variation levels listed in **Table 7.1**.

Table 7.1. *Design factors and variation levels employed in the FFD analysis.*

Code	Factors	Level [-1]	Level [+1]
A	T_{evap}	263 K	268 K
B	T_{cond}	293 K	288 K
C	System	SS-VCRC	LL/SL-HX
D	η_s	80%	95%*
E	ΔT_{SC}	3 K	5 K
F	ΔT_{SH}	3 K	5 K
G	Refrigerant	R1225ye(Z)	R1234ze(E)

*Ideal compression is considered at 95% for real scenarios.

The selected operating conditions are representative of cooling cycles in North America, Europe, and Japan, designed to operate at cooling loads suitable for domestic air-conditioners [544]. The impact of these factors is assessed on three target functions, with *COP* and *VCC* for energy, and η_{II} for exergy. The subroutines for simulating SS-VCRC (C[-1]) and LL/SL-HX VCRC (C[+1]) with polar soft-SAFT are presented in **Figure 3.3** and **Figure 3.5a** in the methodology section. The basic-VCRC model addresses the compression discharge stage at level D, while the liquid to suction subroutine is inclusive of an additional iterative loop to consider pinch effects within the intercooler energy balance. The thermodynamic modeling of these cycles (*PH* and *TS* diagrams), previously detailed in **Figure 3.2** and **Figure 3.4** (**top**), is summarized in

Figure 7.1 for the reader's convenience, presenting the thermodynamic fundamentals of both cycles into a single illustration. The simulations are done at equivalent conditions to the basic VCRC, with the additional assumption of intercooler effectiveness (ε^{HX}= 60%) to ensure a minimum pinch point temperature (T_{PP}) of 4 K [383] between the hot and cold streams in the internal heat exchanger, modeled as a counter-current one.

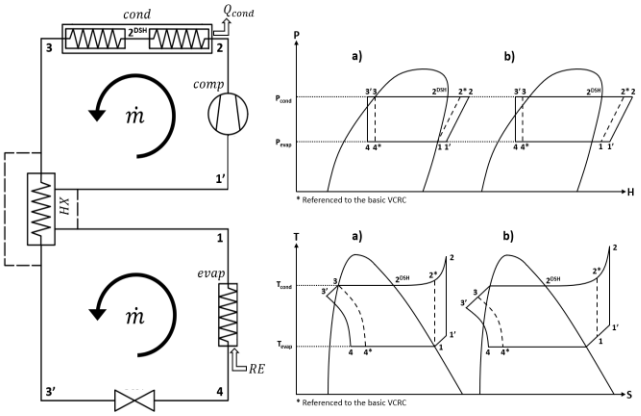

Figure 7.1. *Integrated view for the cooling cycles included in this **Section 7.1**: basics VCRC in dashed lines, and LL/SL-HX VCRC in solid lines, with superheating and subcooling effects in **a)** off, and **b)** on.*

The initial design of the DoE is done using a Taguchi $L_8(2^7)$ orthogonal array, equivalent to a 2^{7-4} FFD, as shown in **Figure D1** in the **Annex**, which can estimate the effect of individual factors, however, aliased (connected) with two-factor interactions. This implies that the main effects of the factors can be identified only if the two-way interactions are insignificant [545], possibly leading to inconclusive results. Accordingly, for the sake of reliability, though on the expense of more computationally taxing DoE, a resolution IV 2^{7-3} FFD has been adopted to separately consider the main effects of individual factors as well as two-factor interactions, with the DoE structure in **Figure D2a**. As such, the DoE requires 16 cases (see **Figure D2b**) to reliably estimate effects of all individual factors using only one-eighth of the number of runs for a complete factorial design, since higher-order interactions (*i.e.,* three-way, and higher) are considered insignificant. In this manner, the effect of individual factors are assembled in separate columns (1 – 7) from the two-factor interactions (8 – 15) to avoid any possible ambiguity in the alias pattern typically arising in resolution IV designs from aliasing two-factor interactions with each other [546]. Additional details on the principles of developing fractional factorial designs can be found elsewhere [401].

Provided in **Figure 7.2** and **Table D1** are the results of the FFD analysis on the effect of the cooling cycle factors on their energy and exergy performance.

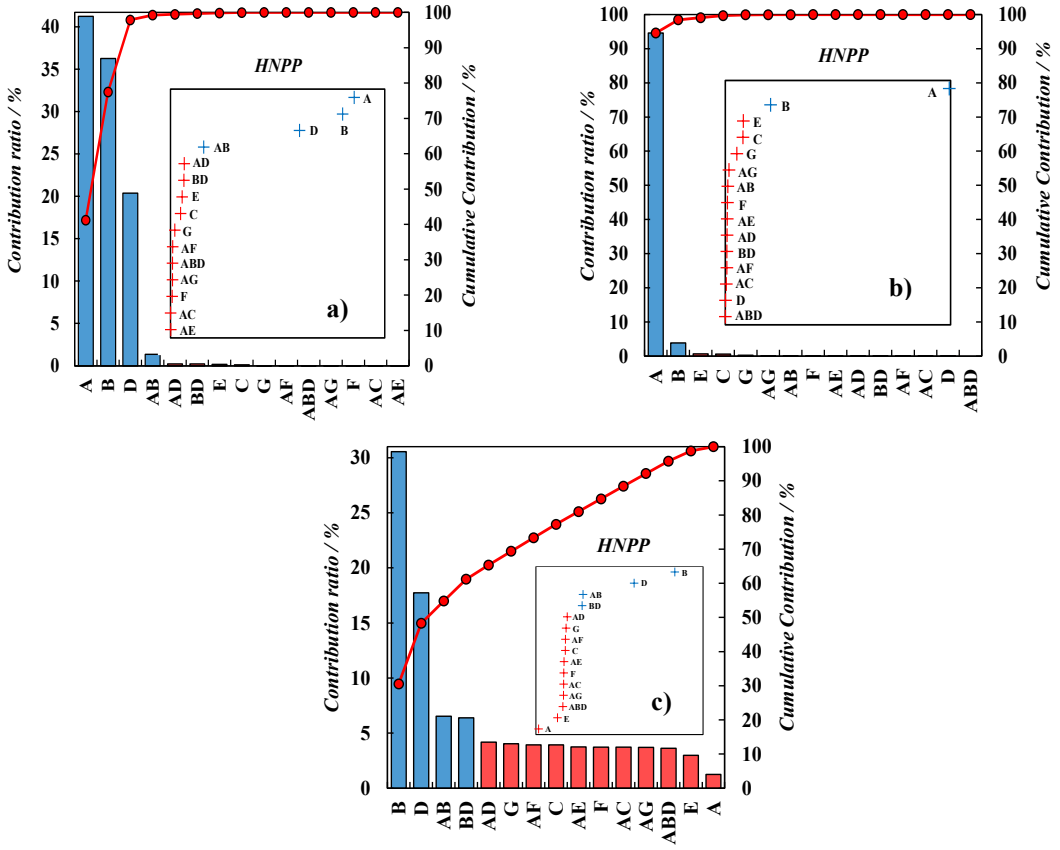

Figure 7.2. *Cumulative contribution and contribution ratio of design factors in* ***Table 7.1*** *on* ***a)*** *COP,* ***b)*** *VCC, and* ***c)*** η_{II}. *Note that bars denote the individual contribution of corresponding factors according to its Alias structure (see* ***Figure D2a)*** *while red dots indicate the cumulative contribution. The Half-Normal Probability Plot (HNPP), with a zoomed view, showcases the absolute values of the standardized effects of factors in correlation with the normal scores or labels presented on the y-axis.*

For a more energetically preferred performance (*i.e.,* enhanced *COP*, and *VCC*), the evaporator temperature was found to be the most influential; while superheating and refrigerant-type were insignificant factors. The evaporator temperature resulted in a Pareto principle (or 80/20 rule) for optimizing *VCC* (see **Figure 7.2b**), with 94.6% of the overall contribution ratio attributed solely to this design factor. In the case of optimizing *COP*, aside from evaporator temperature, the condenser temperature and compression yield were also found to be effective factors (see **Figure 7.2a**), with the three design factors accounting for 97.9% of the total cumulative contribution, consistent with similar analysis results [547]. Similar importance orders and contribution ratios were obtained using the ANOVA analysis (see **Table D2** in the **Annex)**.

Same design factors, though with differing orders, were obtained for improving the exergy efficiency (see **Figure 7.2c**) with larger impact seen with condenser temperature and compression yield, and lower contribution owed to evaporator temperature, similar to previous contributions [292], and confirmed with the ANOVA (see **Table D2**) and HNPP analysis (appreciate zoom regions within **Figure 7.2)**. Conversely, a diminished role was seen for superheating and fluid-type, also previously observed with the energy target functions, highlighted in the in-step probability plots in **Figure 7.2** for the three target functions.

The insignificance of refrigerant-type in this work, otherwise a crucial factor in performance of VCRC systems, is attributed to the similar molecular structure and functional groups for both refrigerants tested (*i.e.,* R1234ze(E) and R1225ye(Z)), with their relatively similar critical temperatures (within 2.5K) [278] resulting in equivalent performance. Based on the FFD and ANOVA results, the top two influential factors for each target response function are in the order of: $T_{evap} > T_{cond}$ for *COP* and *VCC,* and $T_{cond} > \eta_s$. for η_{II}. Although some other common factors are influential among the three target functions, their order of importance was rather diverging.

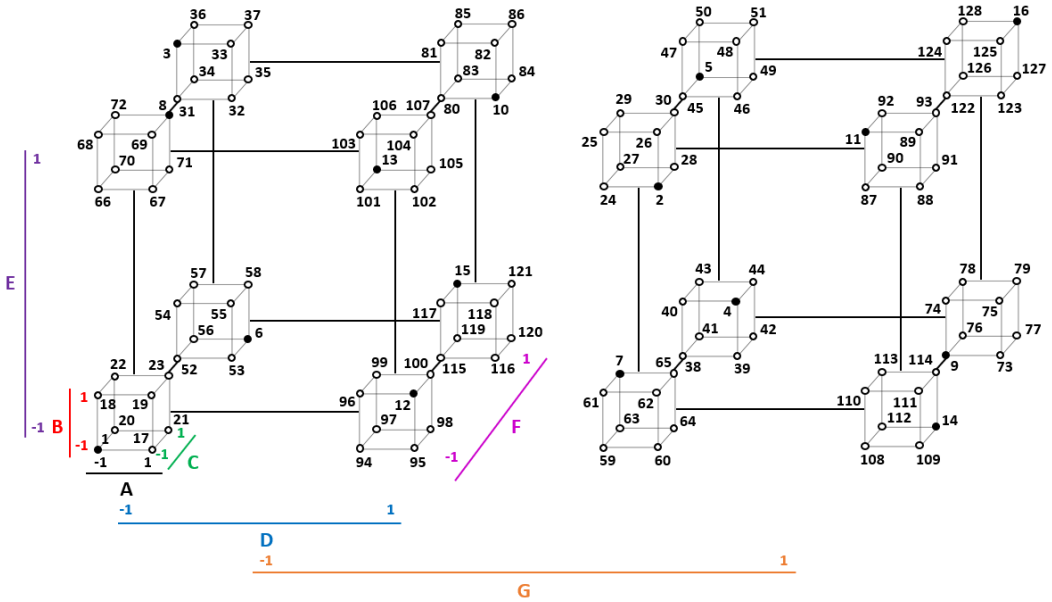

Figure 7.3. *Graphical framework or design-plot for the 2^{7-3} two-level fractional factorial design. Black run points denote the projections of the FFD within the one-hundred and twenty-eight markers of the complete DoE.*

An orthogonal 3D projection of the DoE was developed (see **Figure 7.3**) to generate a polynomial surface regression model (see **Eq. (7.1)**), as an additional validation test to the FFD and ANOVA results, as well as to enable quantifying the effect of the design factors on the target functions for the full-factorial experiments using only one-eighth of the total runs, shown in **Figure D3**. The order of the adopted hierarchy is described as: factors A and B constitute a two-dimensional medium, while the three-dimensional cube is built through the orthogonal projection of factor C. This first level or inner design representation is completed through the inclusion of multi-directional line segments for factors D, E, F and G. The location on the multi-directional line segment tells the levels of factors excluded from the hierarchy first level, holding these linking connections parallel to the coordinate axes. The estimated coefficients for the regression model are provided in **Table 7.2**.

Table 7.2. *Estimated regression coefficients fitted to the linear polynomial model.*

β_x	*COP*	*VCC* / kJ·L^{-1}	η_{II} / %	β_x	*COP*	*VCC* / kJ·L^{-1}	η_{II} / %
0	8.800	1.453	50.063	8	0.194	0.002	4.960
1	1.071	0.149	2.165	9	0.001	-0.001	-3.741
2	1.005	0.030	10.726	10	0.080	-0.001	-3.968
3	0.059	0.012	3.848	11	-0.002	-0.001	3.761
4	0.753	0.000	8.172	12	0.013	-0.001	3.853
5	0.068	0.012	-3.352	13	0.012	-0.002	-3.733
6	0.009	0.002	-3.747	14	0.078	-0.001	4.903
7	0.025	0.008	3.894	15	0.012	0.000	-3.692

The values of the regression coefficients set (*e.g.,* positive values indicative of synergetic effects) further validate the observations from the FFD and ANOVA results on the importance of T_{evap}, T_{cond}, and η_s with varying orders of importance for the three response functions. Additionally, the study of high-order interactions revealed they are insignificant effect, with the exception of AB, AD, and BD interactions (appreciate **Table 7.2**), finding significance for optimizing the three response targets.

$$y = \beta_0 + A \cdot \beta_1 + B \cdot \beta_2 + C \cdot \beta_3 + D \cdot \beta_4 + E \cdot \beta_5 + F \cdot \beta_6 + G \cdot \beta_7 + AB \cdot \beta_8 + AC \cdot \beta_9 + AD \cdot \beta_{10} + AE \cdot \beta_{11} + AF \cdot \beta_{12} + AG \cdot \beta_{13} + BD \cdot \beta_{14} + ABD \cdot \beta_{15} \quad \textbf{(7.1)}$$

where β_0 is the average theoretical value, β_1, β_2, β_3, β_4, β_5, β_6, β_7 are the factor effects, and β_8, β_9, β_{10}, β_{11}, β_{12}, β_{13}, β_{14}, β_{15} are the interaction effects corresponding to AB, AC, AD, AE, AF, AG, BD and ABD, as described in the Alias structure in **Figure D2a**.

Accordingly, the regression model was used to assess the effect of interactive interactions between these three main factors with statistically significant effects on each response function. The resulting 3D surface graphs are plotted in **Figure 7.4,** built on the basis of keeping the levels of remaining factors at the fixed values specified for the FFD in **Table 7.1**, while discretizing the top two factors for each target response.

Considerable improvement is observed with fixing the non-discretized factors to the upper bound with level +1 across all target functions, similar to that seen earlier with FFD and ANOVA. An enhanced performance for all target responses is seen with reducing the condenser temperature due to the increase in the compressor discharge pressure, at the expense of ensuring lower temperature lifts between heat-exchanging units. The opposite trend is seen with increasing the evaporator temperature, being more influential on energy rather than exergy performance, requiring higher thermal gradients to achieve comparable performance enhancement ratios. Lastly, the system's η_{II} is more sensitive to the degree of compressor yield as opposed to *COP* and *VCC*.

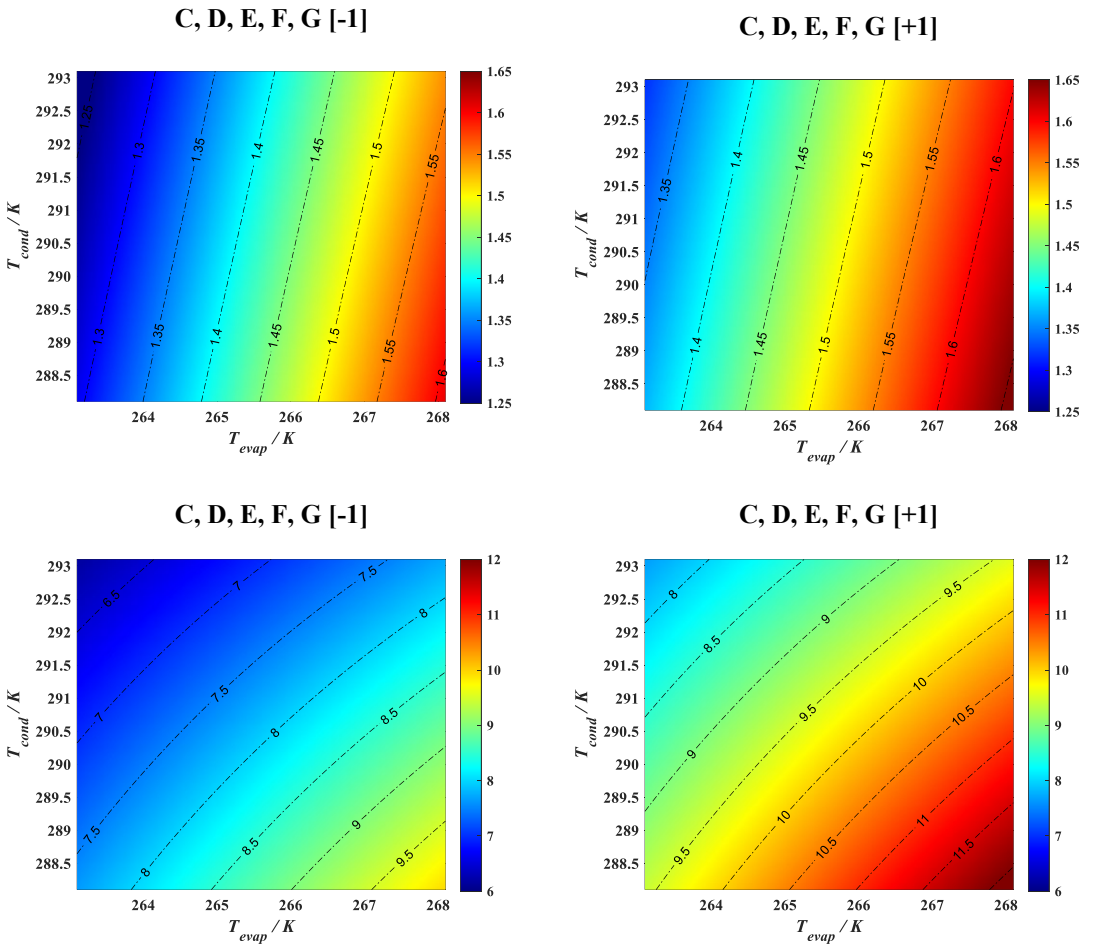

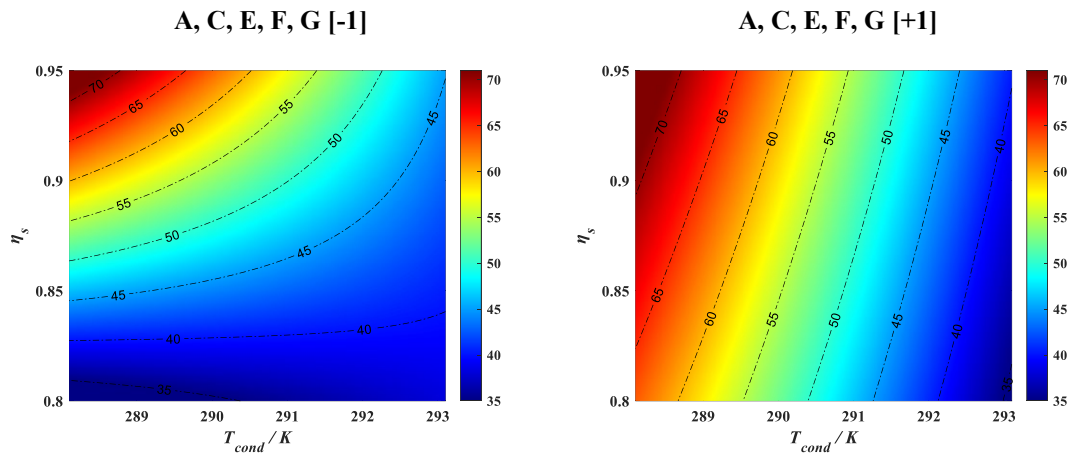

Figure 7.4. *Polynomial regression model for VCC (**top**), COP (**middle**), and η_{II} (**bottom**) as a function of the T_{evap} (A), T_{cond} (B), or η_s (D). Letters refer to the factors provided in **Table 7.1**.*

Notwithstanding, the three statistical analysis methods clearly establish the optimality of setting all design factors to the upper level (*i.e.,* level +1 in **Table 7.1**), attributed to the 16th case in the DoE, ensuring maximizing the three target functions, although with diverging order of importance for statistically significant design factors when investigating their impact on the target responses separately.

The GRA method (refer to **Eq. (3.76)-(3.81)**) is employed to link the three target functions into a single objective function, that can simultaneously attain the optimal performance of the three objectives. The Grey relational grade (γ) was developed with weight factors obtained statistically from each parameters' *S/N* ratio prior to estimating the total delta value of all assessed factors, as seen in **Eq. (7.2)**.

$$\gamma = 0.11 \cdot \gamma_{COP} + 0.05 \cdot \gamma_{VCC} + 0.85 \cdot \gamma_{\eta_{II}} \quad \textbf{(7.2)}$$

The computed γ is represented in **Figure 7.5a**, highlighting the optimality of the 16th case ($A_1B_1C_1D_1E_1F_1G_1$) as seen with FFD and ANOVA. Other cases with notably high performance are in the order of 12th > 11th > 15th case, obtained under $A_{+1}B_{+1}C_{-1}D_{+1}E_{-1}F_{-1}G_{-1}$, $A_{-1}B_{+1}C_{-1}D_{+1}E_{+1}F_{-1}G_{+1}$, and $A_{-1}B_{+1}C_{+1}D_{+1}E_{-1}F_{+1}G_{-1}$ factor levels, respectively. However, it should be stressed that the 12th case is potentially the most cost-effective owing to the implementation of a basic VCRC (C_{-1}), in addition to reduced degrees of subcooling (E_{-1}) and superheating (F_{-1}) for streams departing the condenser and evaporator.

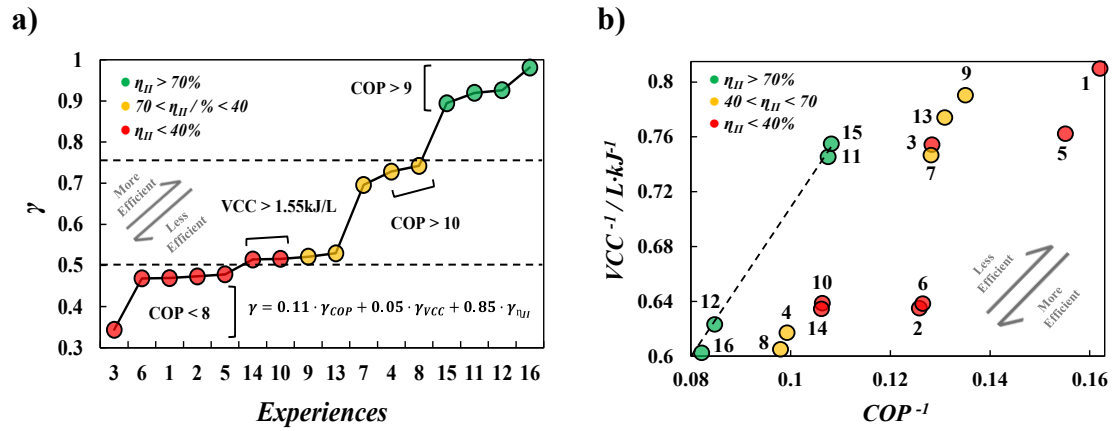

Figure 7.5. *Efficiency plot for maximum performance based on* ***a)*** *GRA, and* ***b)*** *FFD simulations.*

Additionally, the GRA method is a potent tool for determining a consistent importance order for the design factors among diverging targets, in the order of T_{cond} (B) >> η_s (D) >> T_{evap} (A) > refrigerant-type (G) > System-type (C) > T_{Super} (F) > T_{Sub} (E). The order of importance is relatively consistent with the collective results obtained from the previous statistical analysis methods. The top-three factors (*i.e.,* T_{evap}, T_{cond}, η_s) monopolize more than 93% of the cumulative contribution, while the remaining factors have almost identical impact on the response function with ~ 3% contribution ratios. The degree of superheating and refrigerant (*i.e.,* R1234ze(E) *vs.* R1225ye(Z)) were the least effective factors on optimizing performance characteristics, with contribution ratios << 1%, with additional tests benchmarked to the 16th case confirming the slight significance of refrigerant-type over superheating on inducing lager variation in target responses.

Provided in **Figure 7.5b**, is a comparative plot between the inverse of *COP* and *VCC* obtained earlier from FFD, with high-performance cases in the lower left quadrant similar to the approach of Domanski *et al*. [385], in order to analytically engineer optimal cooling processes. The fundamental trade-off between *COP* and *VCC* points to 4th, 8th, 10 – 12th, and 14 – 16th cases (see **Figure D2b**) as the optimum combination of factors to maximize both target functions based on energy savings. However, only the 11th, 12th, 15th, and 16th cases contribute to increasing the cycle's energy/exergy performance because of a significant throttling irreversibility drop. This consequently contributes to reducing the indirect CO_2-equivalent emissions associated with electricity emission factors. In particular, the transition from an underperforming system (3rd case) to the most efficient system (16th case) would result in 56.22% emissions reduction (from 47.86 tCO_2-

eq to 30.63 tCO_2-eq) computed in terms of the indirect TEWI when using R1234ze(E) (GWP = 1) in an LL/SL-HX VCRC cycle with nearly 95% compression yield and applying 5 K subcooling and superheating at evaporator and condenser temperatures of 268 K and 288 K, respectively.

7.2. Holistic optimization of LL/SL-HX design

Thus far, the most optimal performance from the preceding section is expected with R1234ze(E) using an LL/SL-HX advanced cooling cycle, instead of a classic VCRC. In this section, the aim is to fully transition to the use of the intercooler mode by fine-tuning specific operating conditions, which were previously fixed a priori, to achieve further enhancements in the cycle's performance.

Accordingly, a three-level DoE using Taguchi OA is applied considering factors that have direct implications on the heat transfer phenomena within the HX. This design excludes factors previously assessed, such as the evaporator and condenser temperature and compression yield. It can be argued that evaporator and condenser temperatures play a role in the heat transfer phenomenon, however, they were fixed to level +1 (see **Table 7.1**) responsible for optimal performance based on the previous DoE. The same level is applied to isentropic efficiency, with the addition to its minor role in optimizing heat transfer given its intrinsic connection to the compressor device. Alternatively, levels were applied to design factors including cooling load, intercooler efficiency, and degrees of superheating and subcooling, as provided in **Table 7.3**, considered as key performance factors in enhancing the heat transfer phenomena in HX-based systems. The cooling load (A') was varied in the range of 5 – 10 kW based on requirements for low-medium temperature cooling applications for cold-stores and freezers with dimensions between 20 – 40 m^2. Additionally, intercooler efficiency (B') was capped at 70% to avoid extremely reduced pinch point temperature differences in the intercooler under the specified evaporator and condenser temperatures, that can incur excessive capital costs.

The chosen target response functions for this DoE were focused on capital costs-related factors, including VCC and T_{pp}, and operating costs related including COP and η_{II} through the usage of the Taguchi and Pareto ANOVA approaches.

Table 7.3. *Design factors and variation levels employed in the Taguchi OA analysis.*

Code	Factors	Level [1]	Level [2]	Level [3]
A'	CC	5 kW	7.5 kW	10 kW
B'	ε^{HX}	0.5	0.6	0.7
C'	ΔT_{SC}	2.5 K	5.0 K	7.5 K
D'	ΔT_{SH}	2.5 K	5.0 K	7.5 K

For this three-level DoE, a variety of Taguchi OAs can be formulated, as shown in **Table D3**, with $L_{27}(3^{13})$ OA as the most technically beneficial choice. However, this is computationally expensive with an exhaustive number of cases required for a complete analysis. Alternatively, $L_{16}(2^{15})$ OA can effectively accommodate the required degree of freedom for the three-level factors, while reducing the number of total cases to 16, yet with a visible loss of orthogonality. This issue is resolved with an internal re-shaping and re-allocating process to successfully assign three-level factors (A' – D') to orthogonal arrays premeditatedly constructed to two-level factor settings [548], using the Taguchi's idle column array (ICA) technique [399], with the structure shown in **Figure D4**.

With this approach, the resulting DoE can be described as nearly orthogonal [400] (with OA loss of 4.4%), given special attention when collapsing the pairs of OA columns onto the levels of the new three-level factor [400]. Certainly, all factors are pre-allocated to avoid confusion between main-factors and second-order interactions, clustering interactive effects in alike columns. Details on the procedure for the ICA approach in the DoE can be found in the literature [549].

The S/N ratio from the DoE are converted into the Pareto-ANOVA plots in **Figure 7.6** to determine the importance order and effect of main factors on optimizing the selected target functions.

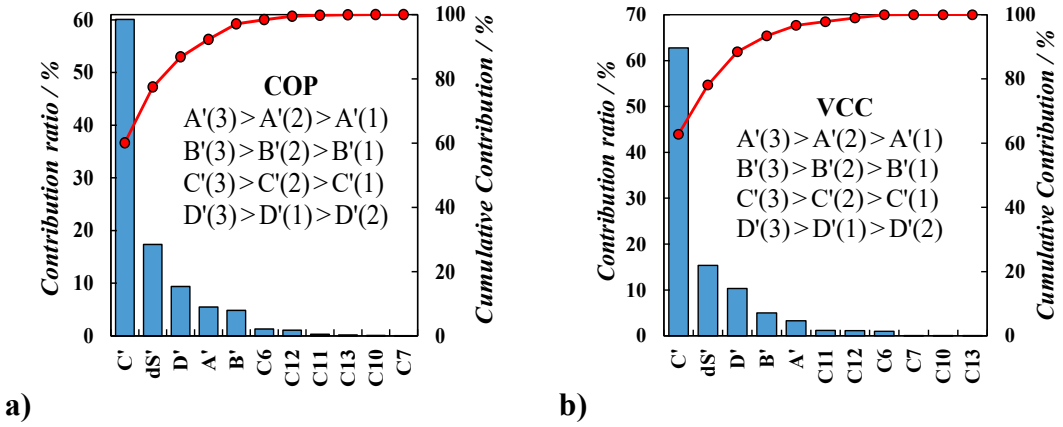

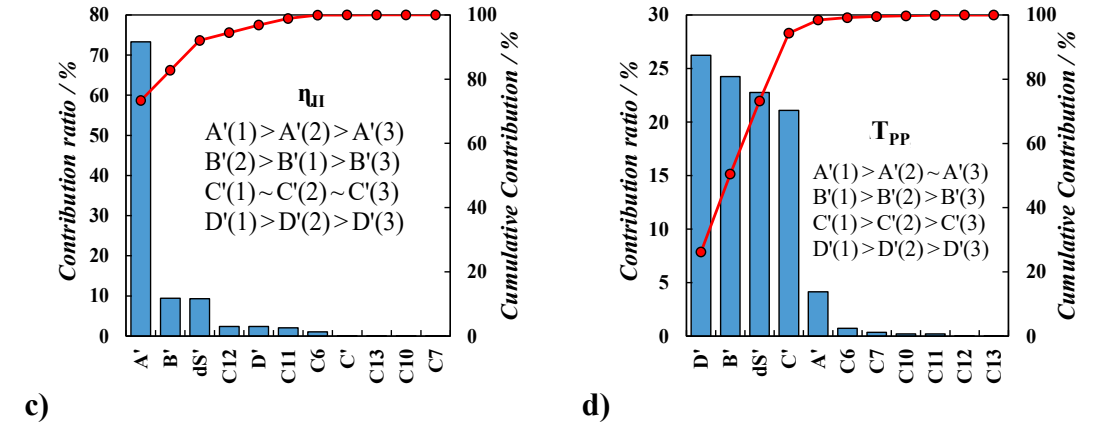

Figure 7.6. *Cumulative contribution and contribution ratio of design factors in **Table 7.3** on **a)** COP, **b)** VCC, **c)** η_{II}., and **d)** T_{PP}. Note that bars denote the individual contribution of corresponding factors, while red dots account for the cumulative contribution.*

An analysis of the results revealed that, for enhanced energy performance with high *COP* and *VCC* values (**Figure 7.6a** and **Figure 7.6b)**, the degree of subcooling was the most influential variable, with a cumulative ratio > 60%, followed to a lesser extent by the degree of superheating, and lastly, intercooler efficiency and cooling load. Interestingly, this ranking is reversed in the case of enhancing exergy performance (**Figure 7.6c)**, with the more dominant impact associated with cooling load (cumulative ratio > 70%) compared to other factors, following the ranking of $CC >> \varepsilon^{HX} > \Delta T_{SH} > \Delta T_{SC}$.

The outcomes are rather different for impacting T_{PP}, with larger contribution seen with the degree of superheating and intercooler efficiency compared to the other factors, otherwise influential for the energetic and exergy performance. It should be noted that the idle column (*dS'*), coming from the ICA procedure to enhance the orthogonality of the DoE, is present for all target functions, as its level served as the basis for the modification of the Taguchi OA, with those columns housing multi-factor interactions, yet with minimal contribution ratios ~ 2.4%.

The prior analysis demonstrated the divergent ranking of importance for the selected factors in the performance of the chosen target functions. This is also corroborated when considering the levels of the factors, with optimal performance for *COP* and *VCC* when settling the design factors at the highest values (level 3) (*COP*: $C_3' D_3' A_3' B_3'$, *VCC*: $C_3' D_3' B_3' A_3'$), while η_{II} is optimized at mixed values for levels 1 and 2 ($A_1' B_2' D_{1,2}' C_1'$), and T_{PP}, is optimized with factors at level 1 ($D_1' B_1' C_1' A_1'$). In summary, if

one chooses to enhance the energy performance of the cycle through increasing the set values for the design factors, the impact will be detrimental for the system's pinch temperature, while compromising its exergy efficiency.

Considering the trade-off between the impact of the design factors and their levels on the target functions for enhancing the performance of LL/SL-HX cycle configuration, the GRA method was again applied to encompass the multiple target responses in a single objective function, focused on the energy and exergy responses, while T_{PP} was settled as a constraint either equal to or higher than the value set for the 16th case from the two-level DoE (see **Chapter 7.1**), at 8 K. The resulting function is given in **Eq. (7.3)**.

$$\gamma = 0.17 \cdot \gamma_{COP} + 0.16 \cdot \gamma_{VCC} + 0.67 \cdot \gamma_{\eta_{II}} \tag{7.3}$$

Provided in **Figure 7.7** are the results of the multi-objective GRA optimization organized in ascending order per experience from low to high performance. The optimum operating conditions are also computed through the Technique for Order of Preference by Similarity to Ideal Solution (TOPSIS) procedure in **Table D4**, achieving similar outcomes regardless of the employed multi-criteria decision-making tool.

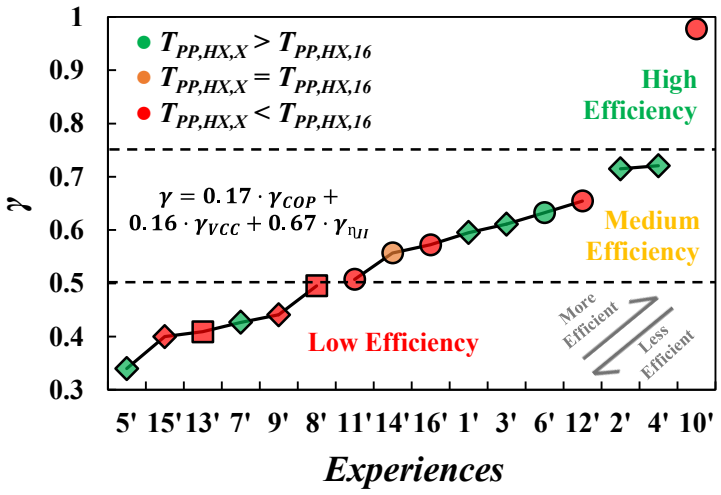

Figure 7.7. *Grey-relational grade for the maximum performance characteristic. Note that symbols correspond to the degree of enhancement regarding experience number sixteen: ● for enhancement in 100% of energy/exergy outcomes, ■ for enhancement in 66% of energy/exergy outcomes, and ♦ for enhancement in 0-33% of energy/exergy outcomes.*

An opposing behavior is obtained from the analysis, with high performance cases (run 10') being associated with reduced T_{PP}, while low performing cases (run 5') is associated with appropriate T_{PP} value. The only acceptable trade-off is seen with case 4' with factors set to $(A_1' B_2' C_2' D_1')$, while maintaining the set T_{PP} constraint. Otherwise, case 10' is expected to operate more efficiently, yet its low T_{PP} may prove to be inconvenient in cooling cycle operations.

For the best performing case (i.e., case 4'), the optimal design factors include: CC = 5.0 kW (A_1'), ε^{HX} = 60% (B_2'), and ΔT_{SC} and ΔT_{SH} of 5.0 K (C_2') and 2.5 K (D_1'), respectively. Under these conditions, the performance of the cycle is relatively similar in terms of energy efficiency to its baseline (case 16 in **Figure D2b**), but with 21% improved exergy efficiency and expanded pinch temperature, giving more room for waste-heat recovery and system optimization. In terms of extracting a definitive ranking for design factors on target responses, it can be discerned that intercooler efficiency needs to be operated at 60% due to its common impact on all target responses. For the other design factors, distinct trends are seen depending on the target response, with larger impact on T_{PP} associated with lowering the degree of superheating, enhanced energy performance with degree of subcooling, and linkage of cooling capacity to maximizing exergy.

To demonstrate the effect of enhanced exergy efficiency, the total cost (TC) and associated CO_2 emissions (TEWI) of the examined cases has been estimated and plotted in **Figure 7.8**, based on the data from **Tables C5** and **D5** in the **Annex**.

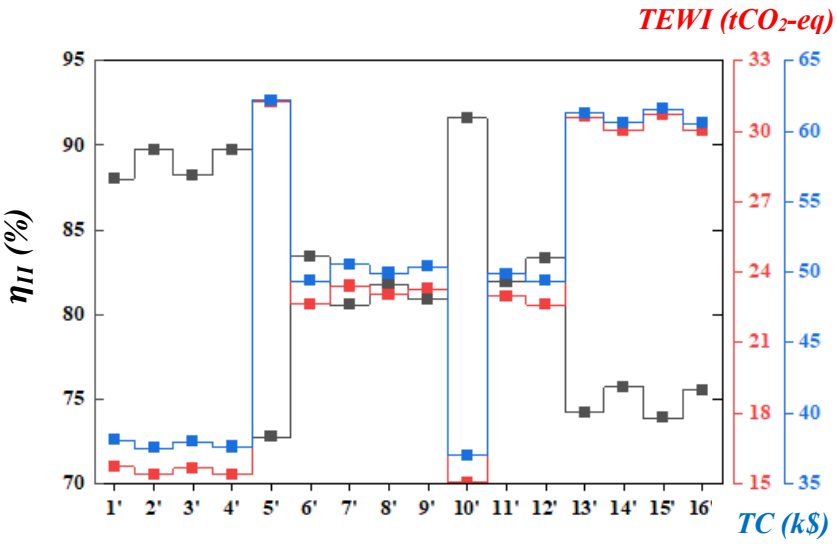

Figure 7.8. *Relation between exergy efficiency (grey) and its impact on total cost (TC) over 20 years (blue) and TEWI (red) for the DoE. See text for details.*

Interestingly, cases with the highest η_{II} (cases 1' – 4' and 10') resulted in the lowest TC and TEWI, denoting reduced cooling cycle cost and environmental impact. The opposite trend is seen with cases with the least η_{II} (case 5') resulting in the highest TC and TEWI.

A comparison between the optimal cycle design, (Case 4' with factors set to $(A'_1B'_2C'_2D'_1)$ associated with a total cost of \$ 37.58k (\$2.51k·yr^{-1}) and emissions of 15.38 tCO_2-eq (1.0256 tCO_2-eq·yr^{-1})) and the baseline (Case 16 $(A'_3B'_2C'_2D'_2)$ associated with total cost of \$ 61.40k (\$4.08k·yr^{-1}) and emissions of 30.63 tCO_2-eq (2.04 tCO_2-eq·yr^{-1})) results in a **net saving of \$ 23.82k (\$1.59k·yr^{-1}) and reduced carbon footprint of 15.25 tCO_2-eq (1.02 tCO_2-eq·yr^{-1})**. In this manner designing a cost-effective, efficient, and environmentally friendly cooling cycle operated with low GWP R1234ze(E) refrigerant in an LL/SL-HX configuration would be readily deployable to the market.

7.3. Drop-in and holistic 4E assessment to replace R134a and R410A

In the previous section, the significance of recent enhancements to the basic VCRC were highlighted. Building on this, the approach used in **Chapter 6.2.2** for the selection of an optimal blend is extended to target advanced cycles, such as LL/SL-HX and multi-compressor systems, in the search for fourth-generation drop-in replacements for R134a and R410A. Based on **Table 6.2** and the holistic approach outlined in **Chapter 6.2.2.3**, R513A and R32 were highlighted as potential mid-transition cooling agents for the future, with blends 1 and 5 as tangible alternatives to post-Kyoto third-generation HFCs.

7.3.1. Drop-in assessment

The drop-in compatibility is evaluated using the same drop-in KPIs used in the previous chapter (see **Table 3.3** in the methodology), *VCC*, P_{cond}, and *DLT*, for the three different cycle configurations. For consistency with previous results, such key properties are determined using polar soft-SAFT, based on the flowcharts provided in **Figure 3.3** and **Figure 3.5**. For all the simulated cooling cycle configurations, the same assumptions are implemented, including:

- Outlet evaporator temperature of 263.1 K.
- Discharge condenser temperature of 293.1 K.
- Isentropic compression (η_s = 85%) and zero pressure drop in all heat exchangers.
- 5 K superheating and subcooling.
- For the LL/SL-HX configuration, the intercooler effectiveness (ε^{HX} = 60%) was assumed to ensure an 8 K pinch point (T_{PP}) temperature difference between the hot and cold streams in the internal HX, as concluded in **Chapters 7.1** and **7.2**.
- For the TS-VCRC configuration, the saturated liquid stream was flashed at 278.1 K.

The results are provided in **Figure 7.9** for *DLT* and *VCC*, and in **Figure D5** for P_{cond}, with detailed numerical data in **Table D6**. It should be noted that the trends obtained in terms of working fluid are consistent irrespective of the chosen cooling cycle configuration, albeit slight differences in *VCC* and *DLT*.

For systems operating with R134a (**Figure 7.9a**), the circulation of commercial replacement R513A results in 7.5% increased *VCC*, achieving better cooling effect than R134a, with lower refrigerant vapor, and with minimal changes to the compressor. This is better than novel blend number 5 in **Table 6.1**, reducing *VCC* by 12% compared to R134a, proving the need for larger volume of fluid to achieve R134a's cooling effect.

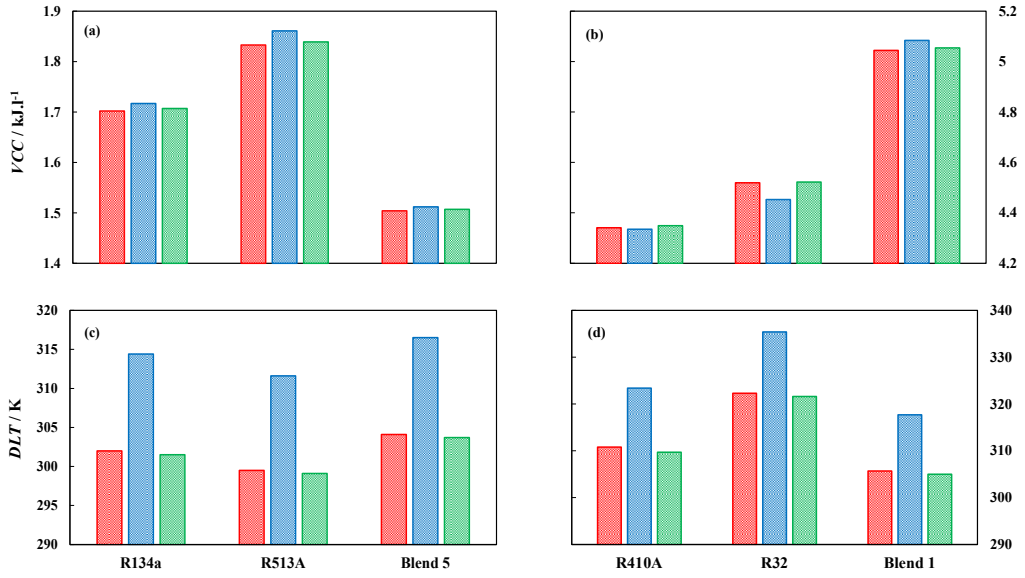

Figure 7.9. *Drop-in compatibility of refrigerants for replacing current working fluids R134a (**left**) and R410A (**right**), compared to commercial alternatives R513A and R32, and novel blends 5 and 1, based on **a, b)** VCC, and **c, d)** DLT, considering operation in SS-VCRC (red bars being replicated in **Figure 6.9**), LL/SL-HX VCRC (blue bars), and TS-VCRC (green bars).*

The narrative is different for systems operated with R410A in **Figure 7.9b**, with novel blend 1 (see **Table 6.1**) resulting in 16% increased *VCC*, compared to the 4% increased *VCC* with commercial option R32. As both working fluids offer an enhanced volumetric cooling effect than R410A, the difference will be checked on the energy consumption for the compressor. Among the different cycle configurations, the LL/SL-HX configuration offers slightly higher *VCC* within 0.8%, while TS-VCRC has an equivalent performance to the basic configuration [49]. This is true for all working fluids examined herein, except for R410A and R32, due to their molar heat capacities, resulting in lower *VCCs* with LL/SL-HX configuration.

Another important indicator is the *DLT*, which refers to the temperature of the superheated vapor discharged from the compressor. Though not a standalone measure, it is indicative of the compressor's work and cycle efficiency. Irrespective of the cycle configuration, R513A reduced the *DLT* by 0.5% from R134a, compared to blend 5 increased *DLT* by roughly 0.7% or 2.0 K, as seen in **Figure 7.9c**. These variations are within typical *DLT* variation ranges due to their small magnitude and are associated with the differences in working fluids thermodynamic properties. A similar result is obtained for replacing R410A with blend 1, reducing the *DLT* by roughly 5 K, compared to the 12 K increase when deploying commercial option R32 as shown in **Figure 7.9d**. This might prove problematic, leading to hazardous compressor *DLT* and shortened compressor lifetime, requiring several modifications to enhance the cycle operating lifetime [38,539]. Among the different configurations, switching from SS-VCRC to TS-VCRC drops *DLT* by fractional values 0.4 – 0.5 K for R134a-operated and 0.7 – 1.1 K for R410A-operated, and their respective replacements. Though in TS-VCRC the interstage cooling reduces the temperature after the first compression stage, the compression work in the second stage to the desired pressure can counteract the cooling effect, resulting in *DLTs* similar to a SS-VCRC operating at the same discharge pressure. Conversely, working fluids in the LL/SL-HX VCRC have a 12 K higher *DLT* compared to the basic configuration. This is related to the increased compression work, due to the higher temperature of the suction line on account of the subcooling in the internal HX of the liquid exiting the condenser.

Lastly, the trends obtained for P_{cond} (**Figure D5** in the **Annex**) are not affected by the cycle configuration, as this pressure has been fixed based on selected operating conditions. However, P_{cond} is rather affected by the working fluid choice based on

diverging saturation properties. Replacing R134a with R513A increased P_{cond} by 9%, compared to the 12% reduction with blend 5, in the three cycles, which is rather favorable as it reduces the upstream compressor's work and enhances the cooling capacity due to the lower saturation temperature at the condenser pressure. However, an unfavorable effect is seen for blend 1, increasing P_{cond} by 22% from its R410A benchmark.

Overall, the trade-off between *VCC* and P_{cond} for novel blends and commercial replacements can potentially equate their impact on cycles currently operated with R134a and R410A, with minimal retrofitting, noting relatively similar technical efficacy as drop-in replacements [228]. This also holds true for *DLT*, with the exception for R32, when fixing the cycle configuration. For varying the cycle configuration, similar *VCCs* and P_{cond} are obtained across the three configurations, except for higher *DLTs* with LL/SL-HX VCRC.

7.3.2. 4E assessment of promising, compatible blends

The analysis of the drop-in variables did not reveal substantial variations among cycles, with the exception of *DLT*s, and *VCCs* to a lesser extent.

7.3.2.1. Energy and exergy analysis

Next, the energy and exergy performance of studied working fluids and cycles was assessed using the KPIs outlined in **Chapter 6.2.2.3**, with energy and exergy efficiencies depicted in **Figure 7.10** and derived from the results in **Table D6**.

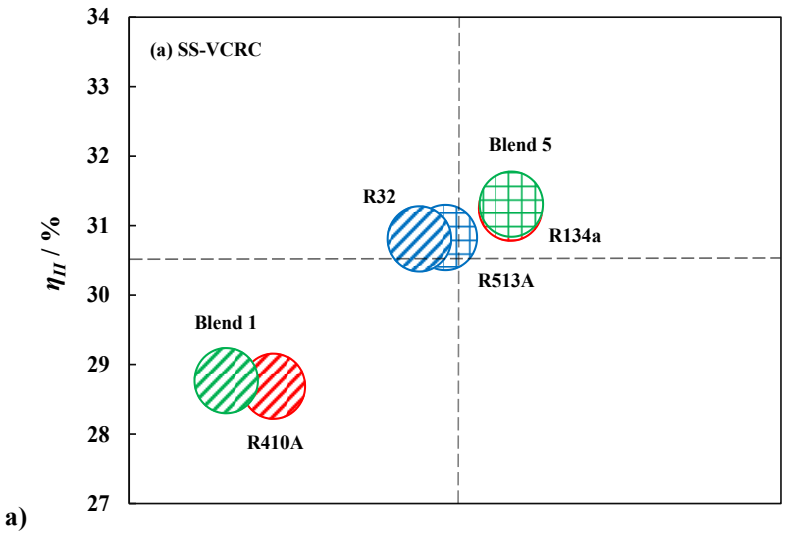

a)

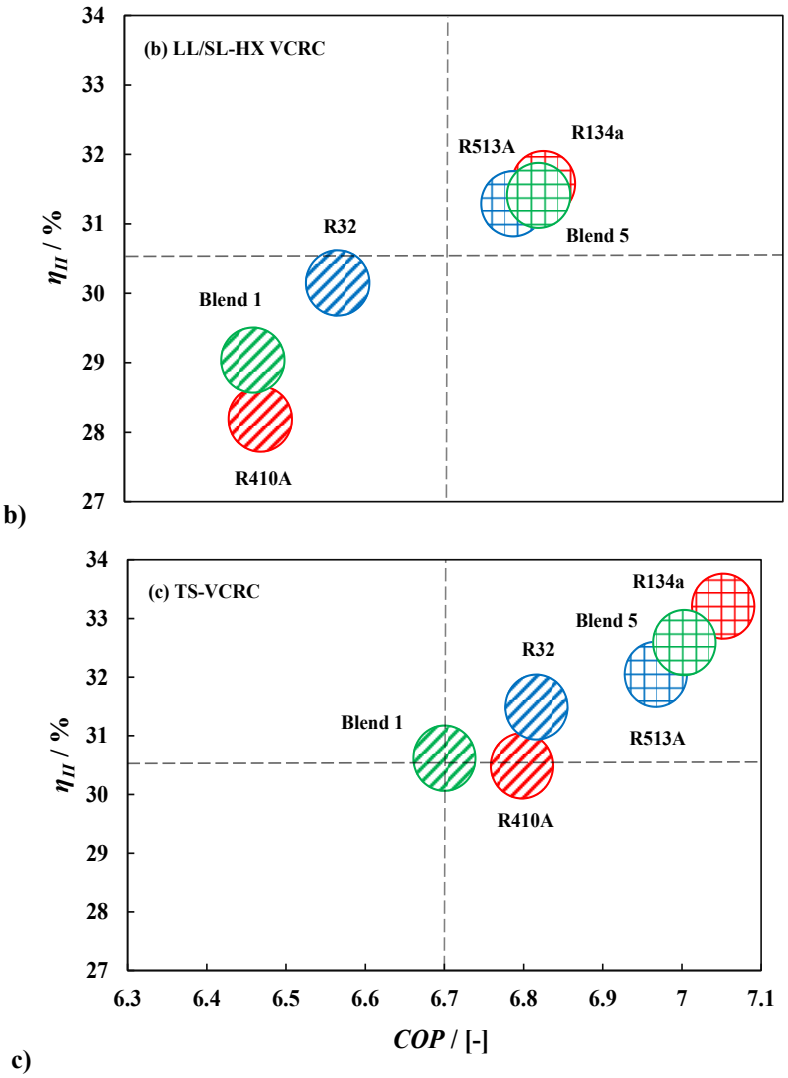

Figure 7.10. *Energy (COP) vs. exergy efficiencies (η_{II}) for replacing R134a and R410A with commercial alternatives and novel blends evaluated for* ***a)*** *SS-VCRC (main outcomes explained in* ***Chapter 6.2.2.3****),* ***b)*** *LL/SL-HX VCRC, and* ***c)*** *TS-VCRC cycles.*

The results indicated in **Figure 7.10a** correspond to the simple VCRC and have been commented in **Chapter 6.2.2.3**. With regard to LL/SL-HX, (see **Figure 7.10b**), marginal energy and exergy enhancements for R134a, R513A, blends 5 and 1 are obtained compared to the basic configuration. This is on account of the intercooler increasing the suction temperature and thereby reducing the suction density, consequently increasing the compressor discharge temperature [550–552]. Blend 5 and R513A present similar energy and exergy performance to R134a, with a slight edge for blend number 5. Conversely, both R410A and R32 suffer a worse performance, as opposed to novel blend 1. This is due to their lower molar heat capacities compared to the other working fluids [381].

Accordingly, the cycle performance is affected by the increased compression work rather than the enhanced cooling effect due to subcooling.

By contrast, larger enhancements are obtained with the TS-VCRC configuration in **Figure 7.10c** for all working fluids. For this cycle, blend 5 remains a good replacement for R134a, though at marginally lower efficiencies with 0.7% lower *COP* and 1.18% η_{II}. Moreover, for this configuration, the positive gap between R32 and R410A for SS- and LL/SL-HX cycles is narrowed down, with similar *COP*, yet slightly higher η_{II} for R32. Blend 1 trails at lower energy efficiency than R410A, though with similar η_{II}. Overall, regardless of the working fluid, utilization of advanced TS-VCRC configuration is energetically and exergetically promising, yet at the expense of additional investment costs. Novel blend number 5 is a good candidate for replacing R134a rather than R513A. By contrast, novel blend 1 is subpar to R32 as a replacement for R410A owing to its lower efficiency.

A detailed analysis of the exergy destruction mapping (see **Table D7 in the SI**), based on the equipment in the cycle for R134a and its replacements performed for the three cycle configurations, is highlighted in **Figure 7.11** (a similar analysis for R410A and its replacements can be found in **Figure D6**). For all working fluids, the transition from basic SS-VCRC to LL/SL-HX improves η_{II}, while larger improvements are obtained with the TS-VCRC. The improvement with TS-VCRC is due to the two-stage compression, reducing the overall pressure ratio across each stage, lowering the work required per stage, along with improved intercooling of working fluid. This is on account of by-passing the flashed vapor from the first EEV at intermediate pressure, reducing the degree of compression for the required cooling load [48].

For all configurations, the exergy destruction rate is in the order of evaporator > compressor > condenser. The largest contribution of the evaporator can be associated with the fixed heat transfer design parameters, increasing the inefficiencies of the cycles, which can be reduced through optimizing operating conditions [229]. The rate of avoidable exergy destruction is also similar across all configurations and working fluids, except for the evaporator in the LL/SL-HX VCRC. For this case, a larger percentage of avoidable exergy destruction are obtained for pure working fluids (*i.e.,* R134a, and R32) compared to blends. This denotes that cycle evaporators' inefficiencies can be slightly

reduced due to blends' slight T_G, allowing them to better match with the temperature of the heat source.

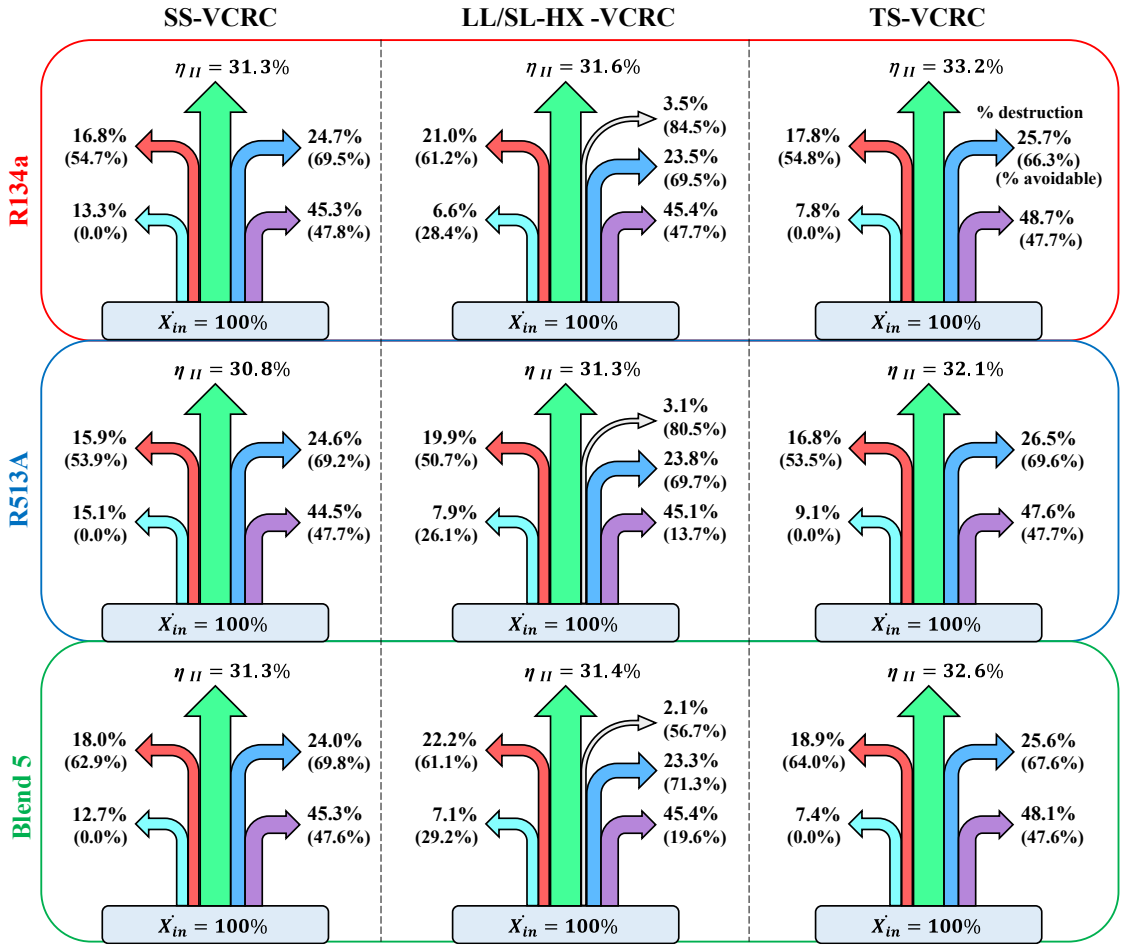

Figure 7.11. *Exergy destruction distribution for R134a and its replacements in the three cooling cycle configurations, with overall η_{II}% (light green), compressor $\sum \dot{\chi}_d$% (blue), evaporator $\sum \dot{\chi}_d$% (purple), condenser $\sum \dot{\chi}_d$% (red), EEV (teal), and HX (grey). Note the numbers in brackets are the percentage of avoidable exergy destruction within the total exergy destruction of the basic unit.*

Depicted in **Figure 7.12** is the exergy efficiency compared to percentage of avoidable exergy destruction ($\sum \dot{\chi}_d^{AV}$) for the examined cases. In terms of exergy efficiency, the configurations are in the order of SS-VCRC < LL/SL-HX << TS-VCRC, indicating a rise in the effectiveness of the cycles in converting the usable energy into usable work. However, it is important to note that in SS- and TS-VCRCs, high degrees of avoidable exergy are obtained, within 50%, for all working fluids, excepting for R134a. Though TS-VCRC is the most effective in utilizing available exergy, it has the highest percentage of avoidable exergy destruction, demonstrating the existence of inefficiencies that, once remedied, can increase the cycle's efficiency even further. One possible reason

for high avoidable exergy destruction may be the cooling between the compression stages due to the temperature difference between the flashed vapor and the working fluid exiting the first compression stage, while another reason is the fixed flash temperature, which, once optimized, can contribute to reducing the avoidable exergy destruction. By contrast, LL/SL-HX experience lower avoidable exergy destruction, due to the intercooler's contribution to a more efficient expansion process, minimizing exergy loss, although the cycle is, overall, at a lower exergy efficiency compared to TS-VCRC, and its margin for potential improvement is also lower than the other cycles.

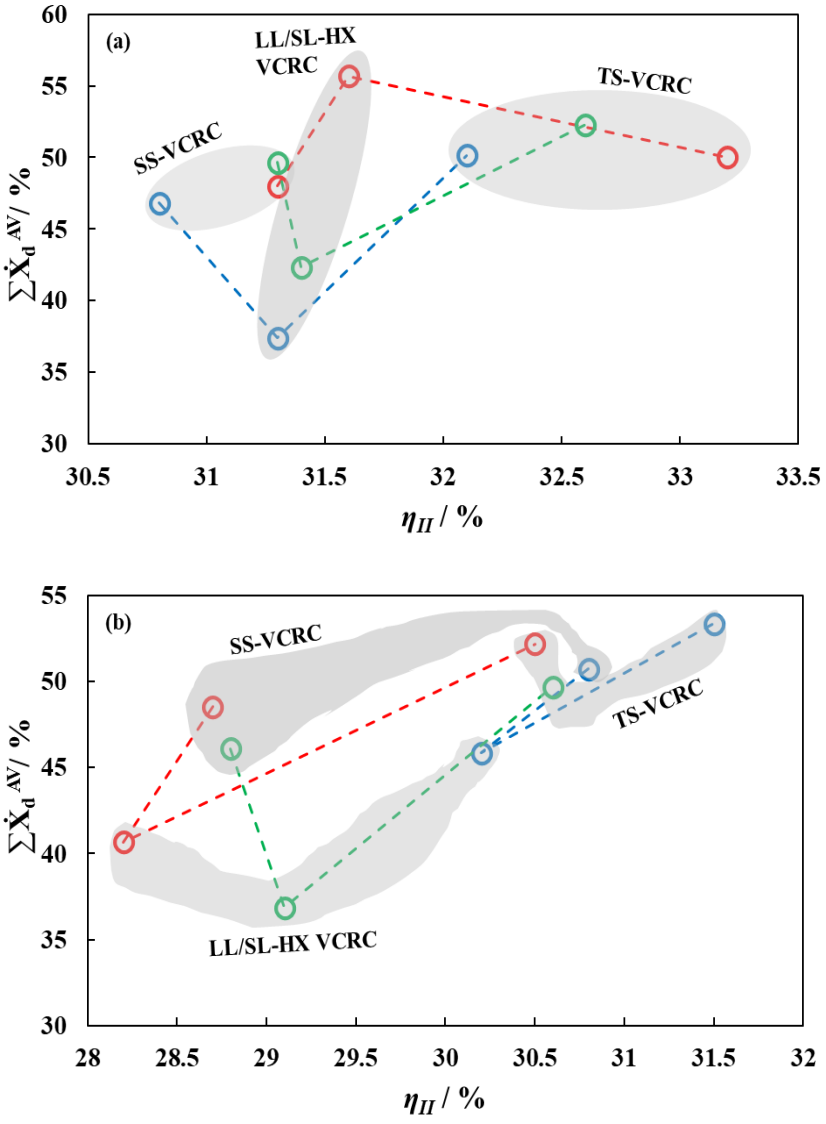

Figure 7.12. *η_{II} (%) and avoidable exergy ($\sum \dot{\chi}_d^{AV}$) (%) for **a)** R134a (red) and its replacements R513A (blue), and blend 5 (green), and **b)** R410A (red) and its replacement R32 (blue), and blend 1 (green). The grey regions denote the cycle configurations for SS-, LL/SL-HX, and TS-VCRC.*

7.3.2.2. Environmental analysis: estimation of direct and indirect emissions

Following the energy and exergy analysis, an environmental study, focused on emissions, is carried out through the calculation of the TEWI contributions for the examined working fluids.

The results corresponding to the direct TEWI emissions are plotted in **Figure 7.13**, and indicate that the cooling cycle configuration and geographical location have inconsequential impacts, making the direct TEWI values found for the basic cycle in **Figure 6.11** applicable regardless of tested configuration. This is expected considering that the direct TEWI accounts for the working fluid's leakage rate and end-of-life cycle disposal adjusted to its GWP, which has been fixed across all cooling cycle configurations.

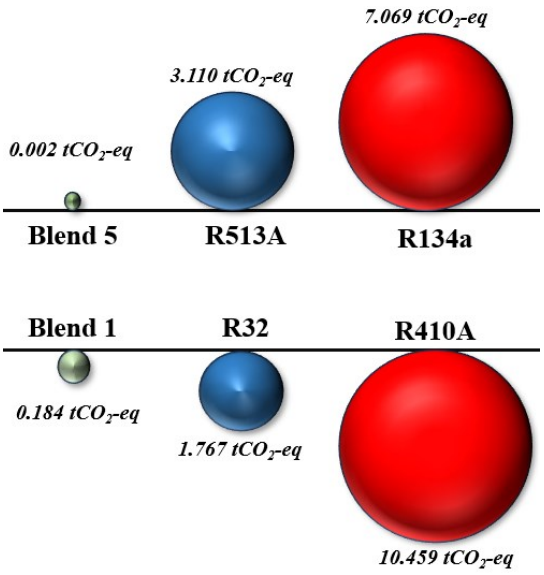

Figure 7.13. *Direct TEWI contribution in tCO_2-eq for the evaluated working fluids.*

Novel blend number 5 proved to be more effective than commercial R513A for replacing R134a, resulting in nearly 100% reduction in direct CO_2-eq emissions in contrast to the 56% reduction with R513A, on account of blend 5 near-null GWP (see **Table 6.1**), avoiding 7.0 tCO_2-eq emissions from a single cooling unit throughout its lifetime. Similarly, replacing R410A with blend 1 results in 98% reduced CO_2-eq emissions, and avoids at least 8.7 tCO_2-eq emissions per unit. This is due to blend 1's 90

wt.% R1123 with its almost null GWP, shifting its GWP to 10-times lower than commercial option R32 (*i.e.,* 70 *vs.* 677).

The indirect TEWI contribution as a function of working fluid, cooling cycle configuration, and country of deployment are shown in **Figure 7.14**, with **Table D8** providing further insights. Compared to the direct contribution, the indirect contribution is at least 7 – 15 folds larger in magnitude, and in some cases can reach 100-times for low-GWP working fluids, as with blends 5 and 1. This is because the indirect emissions are affected by the cycle's operating time and energy consumption, which depends on the country-specific energy mix, and its level of decarbonization. The dissimilarity in the magnitude of direct and indirect emissions highlights that, not only the use of low-GWP working fluids is required, but their effect on the cycle's energy efficiency and consumption coupled with low-carbon energy sources are equally important.

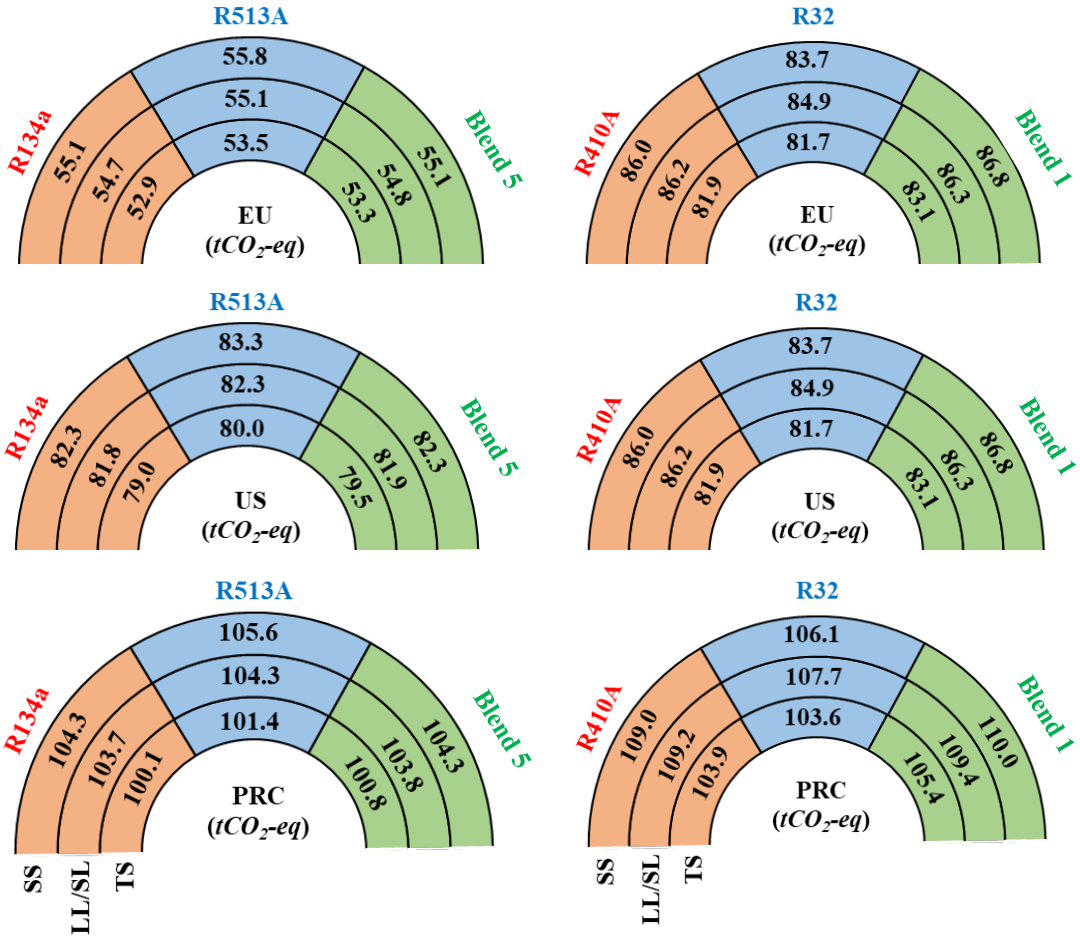

Figure 7.14. *Indirect TEWI in tCO_2-eq for* ***(left column)*** *R134a (orange) and its replacement R513A (blue) and blend 5 (green), and* ***(right column)*** *R410A (orange) and its replacements R32 (blue) and blend 1 (green), in SS-VCRC, LL/SL-HX VCRC, and TS-VCRC cycles, for European Union (EU), United States (US), and People's Republic of China (PRC).*

In terms of working fluids, their indirect impact is consistent across the different geographical locations, as previously illustrated for the basic architecture in **Figure 6.11**. Concerning cycle configuration, irrespective of the working fluid, the use of TS-VCRC promises the largest CO_2-eq emissions reductions, up to 4% reduction from SS-VCRC, compared to LL/SL-HX cycle's 0.5% reduction, on account of TS-VCRC higher energy efficiency and reduced energy consumption. Overall, changes in working fluids and cycle configurations result in small changes in environmental impact, surely important when looking at the number of deployed cooling cycles on a global scale.

However, larger reductions are more observable when examining geographical variations. Among the three studied regions, China (PRC) had the largest indirect CO_2-eq emissions, almost 2-fold and 1.5-fold than in the EU and the US, respectively. This is associated with the employed energy mix, highly dependent on coal as a primary energy resource in PRC, rather than the use of renewable resources and nuclear energy, or low-carbon natural gas in the US [553,554].

Overall, the lowest environmental impact, regardless of the region, are obtained when deploying blend 5, and either R32 or blend 1 in TS-VCRC cycles, reducing CO_2-eq emissions by roughly 7 – 14 tCO_2-eq per unit with respect to the CO_2-eq emissions using R134a or R410A in the SS-VCRC cycle. These reductions seem rather insignificant on the small scale; however, considering global utilization of AC units reaching 2 billion units worldwide [2,3], these changes can result in simple terms in 14 – 28 $GtCO_2$-eq emissions.

7.3.2.3. Techno-economic evaluation

The analysis is closed with the economic evaluation of these mixture in the selected configurations, in terms of Total Annual Cost (TAC). The results are summarized in **Table 7.4**, including the TAC range for the examined working fluids per cycle and country of deployment, based on results in **Table D9**. The benchmark scenario is based on the TAC gradient depicted in **Figure 6.13** of **Chapter 6.2.2.5**. Additionally, the average contributions of the TAC components are included, being relatively insensitive to changes in the working fluid.

Table 7.4. *TAC range and component contributions in PCR, US, and EU, averaged for all studied fluids.*

	PRC	US	EU
SS-VCRC			
TAC range / k$.y^{-1}	5.019 – 5.209	5.150-5.344	6.671 – 6.940
CAPEX / %	62.9	61.4	47.3
OPEX / %	22.9	28.7	47.0
Enviro / %	13.8	9.6	5.4
Set-up / %	0.4	0.4	0.4
LL/SL-HX VCRC			
TAC range / k$.y^{-1}	4.948 – 5.143	5.148-5.353	6.638-6.913
CAPEX / %	64.3	61.8	47.9
OPEX / %	23.1	28.6	47.0
Enviro / %	12.3	9.3	4.8
Set-up / %	0.4	0.4	0.4
TS-VCRC			
TAC range / k$.y^{-1}	5.706 – 5.895	5.899 – 6.098	7.338-7.600
CAPEX / %	70.0	67.7	54.4
OPEX / %	19.4	24.1	41.1
Enviro / %	10.3	7.9	4.2
Set-up / %	0.3	0.4	0.3

In terms of country of deployment, PRC is the cheapest based on the least TAC ranges, increasing by 29 – 35% in the EU depending on the cycle configuration. The economic feasibility in the US and PRC are rather similar with a 2.5 – 4.1% increase. The country of deployment is the largest factor impacting the economics of deploying cooling cycles, which can be gleaned from the relative contribution of the TAC components.

The CAPEX contribution seemingly decreases shifting from PRC to EU (in relative percentage). However, this should be treated with care, as the values of the CAPEX are the same regardless of the country of deployment, as they are dependent on the cost of manufacturing. The change in relative contribution is more reflective of the overall change in TAC components magnitudes. The reduction in CAPEX in EU is tied with its increasing OPEX, reflected from the rise in OPEX contribution shifting from PRC to EU. This is reasonable considering the higher cost of electricity in EU with its reliance on renewable energy resources compared to cheaper coal currently used in PRC. This of course comes with a minor cost penalty seen with increasing environmental costs between both regions, reflective of the higher carbon footprint highlighted from the indirect TEWI, shown earlier. Regardless, the setup cost is the least contributing irrespective of the region due to the minor working fluid leakage rate. Note that the values of the setup cost are slightly higher in the EU, for working fluids with GWP > 150, due

to the inclusion of HFC utilization tax [555], not implemented in the US and PRC. Relative to SS-VCRC, marginal TAC reductions of 0.16 – 1.5% are obtained with LL/SL-HX VCRC, compared to the 9.5 – 14.5% increase with TS-VCRC. This is due to the latter's larger CAPEX share, with its complex design and additional compression unit, although promising larger reductions in OPEX and Enviro due to its higher efficiency.

The economics in terms of replacement working fluid are depicted in **Figure 7.15** for the case of the EU, as it has the highest TAC among all examined regions. Similar results are also obtained for PRC and US. Coupling the change in working fluid with advanced cycle configurations revealed that, for most cases, the LL/SL-HX VCRC results in marginal TAC variations compared to benchmarks in the range of -1.30% – +0.42%, depending on the choice of working fluid.

Conversely, the TS-VCRC configuration consistently results in increased TAC by 8.0 – 10.0% due to its higher CAPEX. The economic analysis reveals that for drop-in replacements, blend 5 and R32 are the most economically favourable choices for SS-VCRC cycles operated with R134a and R410A, respectively. For deploying new cooling systems, ***blend 5 with LL/SL-HX is economically advantaged with annual cost savings of $39.0 per unit compared to R134a benchmark***. In contrast, ***R32 with the basic configuration is still the most economically preferred with its annual $153.0 cost savings per unit compared to its R410A benchmark***. Bearing in mind environmental legislations on GWP, deploying blend 1 with LL/SL-HX would be the second-best choice, yet bearing an additional $29.0 annually per unit.

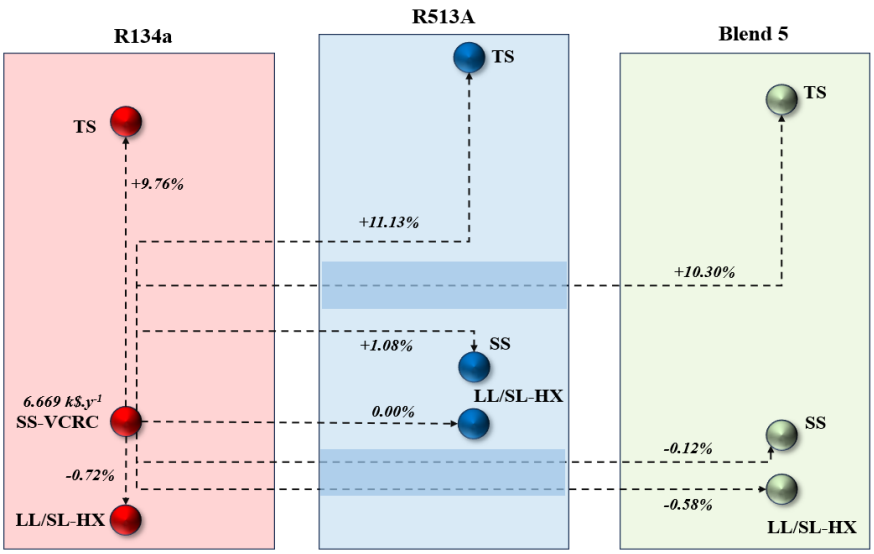

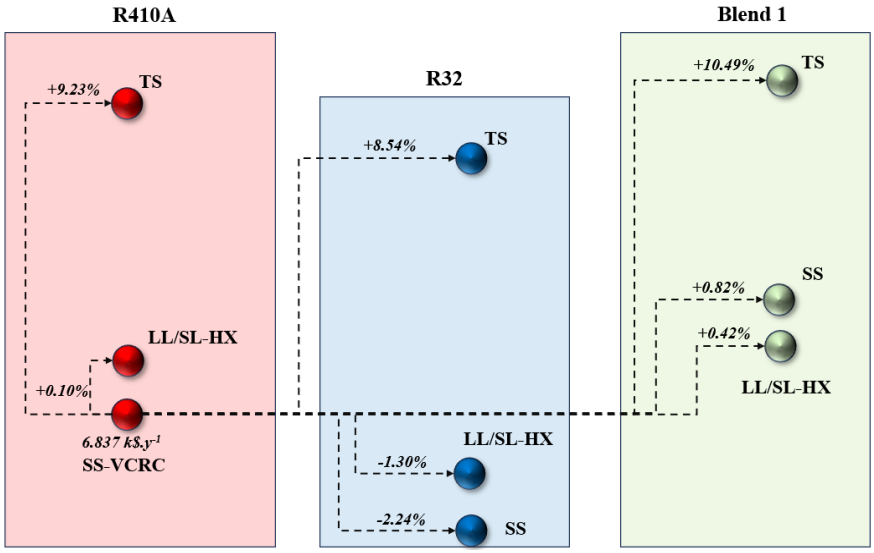

Figure 7.15. *Relative change in TAC for replacement working fluids and advanced cycles relative to R134a in SS-VCRC (**top**), and R410A in SS-VCRC (**bottom**) in the EU, based on data in **Table D9**.*

7.3.3. Preliminary life cycle analysis of designed drop-ins

Finally, the environmental assessment of the proposed blends in new cycle configurations is completed with additional inputs coming for a complete Life Cycle Analysis (LCA). This is done using the software Activity-Browser (AB), with all details of the methodology explained in **Chapter 3.3.2.1**.

The functional unit of the study is defined as 1 MJ of power refrigeration in the evaporator. The flow inventory is based on the conditions described in **Chapter 7.3.1** (in addition to specifications in **Table C5**), including in this section details for air compression and cooling water pumping key for a complete LCA. In this manner, power requirements are computed using a 100 kPa pressure gradient for cooling water and 0.5 kPa for air compression at the evaporator, both under atmospheric conditions typical of commercial air conditioning systems. A pinch analysis is subsequently applied, with a temperature difference between streams of 5 K. The refrigerant load is adjusted according to standard commercial requirements per ton of refrigeration (4.54 kg/ton).

Calculations for refrigerant production are based on synthetic routes and the electricity required to produce 1 kg of product at the reaction conditions of interest (refer to in **Eqs. D1a-f**), considering a mass flow rate of 0.01 kg/s and the enthalpies of formation detailed in **Table D10**. Cooling water accounts for cooling tower losses due to

evaporation and spray, along with associated emissions to air and water (see **Table 3.5** within the methodology section). The main LCA results are plotted in **Figure 7.16**.

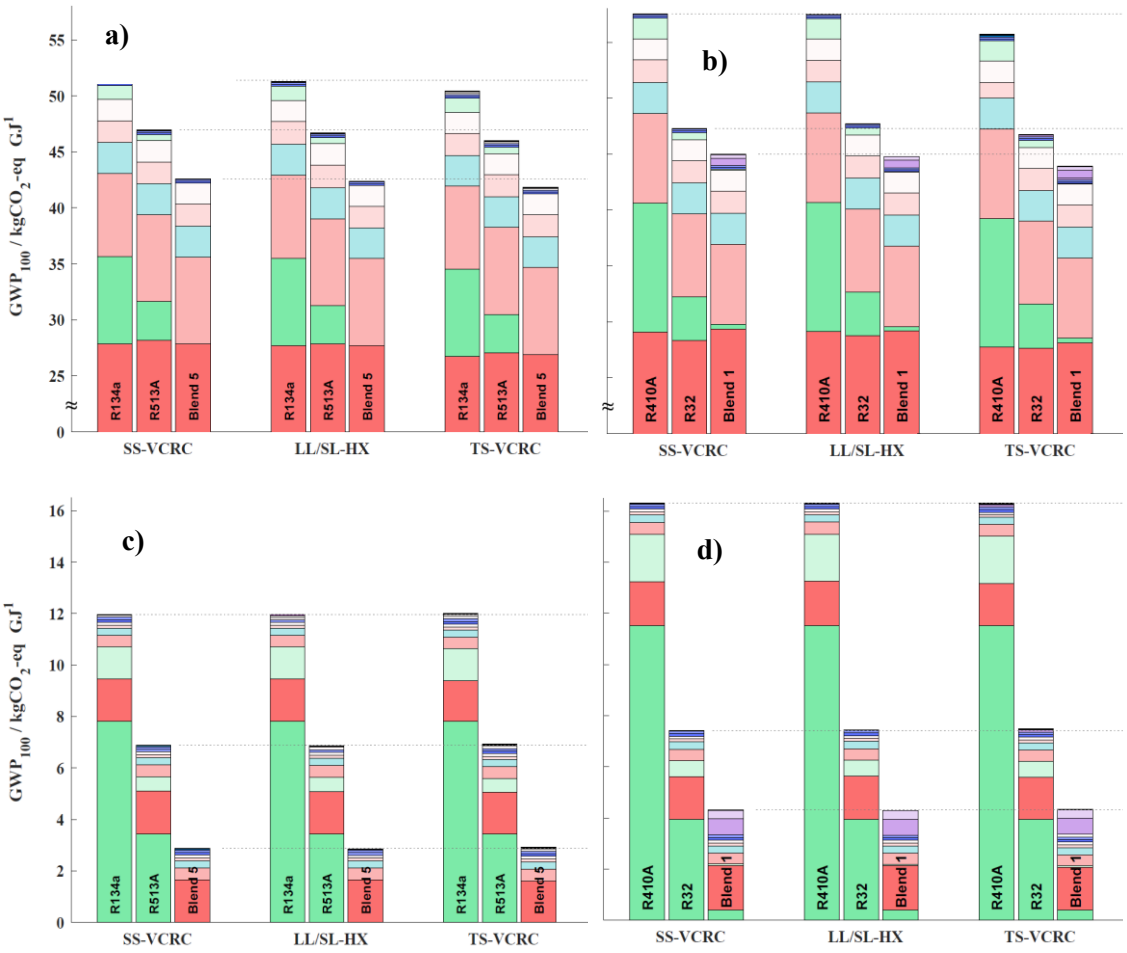

Figure 7.16. *IPCC 100-year GWP for replacing R134a in* ***a)*** *2021 and* ***c)*** *2050, and R410A in* ***b)*** *2021 and* ***d)*** *2050. Material production is shown with a gradient from intense to light blue, including main and auxiliary air compressors, stainless steel, aluminum, and auxiliary cooling water pump. Electricity consumption is depicted in a gradient from intense to light red, covering power use for the main and air compressors, cooling water pump, and air blower, refrigerant emissions in intense green for leakages and light green for end-of-life disposal while refrigerant production is depicted in intense purple due to leakages and light purple for the refrigerant running within the closed loop.*

Figure 7.16a-b (see **Table D11**, and **D12** for complete data) depicts the LCA results considering the impact of working fluid selection on GWP reduction, with an average reduction of 11.7% for R134a drop-ins. The role of the cycle configuration is secondary, resulting in a 0.83% decrease for R134a drop-ins and similar trends for R410A.

The greatest enhancement is achieved when replacing R410A in the basic cycle with Blend 1 in a multi-compressor cycle, resulting in a 23.7% decrease. This is due to Blend 1's lower direct TEWI contribution compared to R32 (see **Figure 6.11)**. A significant reduction is also observed —18.6%— when replacing R134a in the basic cycle with Blend 5 a TS-VCRC mode; in this case due to Blend 5's ultra-low GWP combined with enhanced energy and exergy efficiencies (refer to **Figure 6.10)**, both contributing to its reduced GWP.

The optimal IPP' GWP for fluid selection is ranked as follows: Blend 5 > Blend 1 >> R513A > R32 >> R134a >> R410A, with TS > LL/SL-HX > SS-VCRC hierarchy. The use of the intercooler cycle offers substantial benefits for refrigerants with low molar heat capacities, as highlighted in **Chapter 7.3.2**, leading to significant improvements compared to the basic cycle.

Figure 7.16c-d and **Tables D13-D14** repeat this analysis assuming a 2050 horizon time. In this hypothetical scenario, fluid selection remains the dominant factor in GWP reduction, while the impact of cycle optimization diminishes drastically. This is attributed to the projected decline in the role of electricity—e.g., kWh consumed by compressors, fans, blowers, and pumps—to the overall carbon footprint, as the impact of cycle efficiency diminishes. This effect is evident in 2021, with electricity impacts ranging from 70.0% (R419A in SS-VCRC) to 92.6% (Blend 5 in TS-VCRC) of the total contribution, while in 2050, those impacts are projected to an average of 16.9% for low-GWP, 43.3% for mid-GWP, and 67.6% for high-GWP agents. It must be noted, however, that in both timeframes low-GWP refrigerants exhibit substantial electricity contributions due to their minimal refrigerant emissions, with leakage and end-of-life emissions falling below 1%. In contrast, refrigerant emissions for R134a and R410A account for 20.6% of total contributions in 2021, rising sharply to 78.8% by 2050.

A similar trade-off is observed in refrigerant production, except for Blend 1 (refer to **Figure D7c-d**), where the synthetic route requires further environmental optimization. Material production, especially for main compressors, significantly impacts the overall GWP; however, overall contributions remain below 5% across all cycles and fluids in both 2021 and 2050, as appreciated in **Figure D7.** Blend 5 is the exception, though, due to its ultra-low GWP resulting from reductions in both electricity and emission KPIs.

Figure 7.17 presents an analysis of refrigerant emissions and production for various working fluids in both commercial (4.54 kg/ton of cooling capacity) and residential (2.5 kg for A1 or 1.25 kg for A2L) cooling applications.

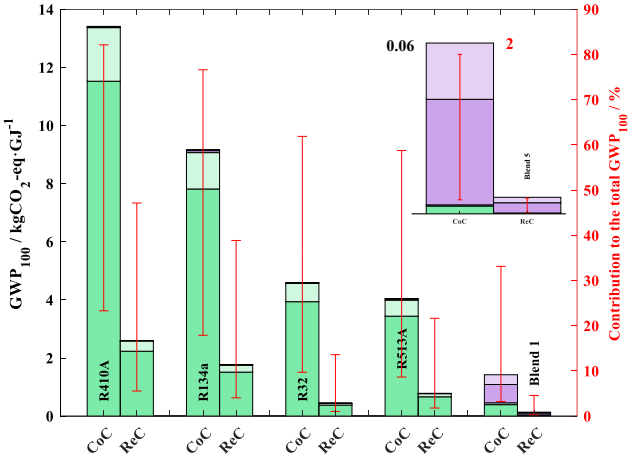

Figure 7.17. *IPCC 100-year GWP for refrigerant emissions and production due to leakages, end-of life disposal, and cooling load running within the closed loop for commercial (CoC) and residential (ReC) air conditioning applications. The Y2 axis is normalized to the GWP standards of the basic cycle, with the upper range reflecting the projected 2050 scenario and the lower range corresponding to the 2021 baseline set-up. The color pattern is consistent with the nomenclature detailed in* ***Figure 7.16****.*

This study focuses on the impact of these factors on the environmental impact of refrigerants, given that material production, cooling water, and electricity consumption remain constant across different mass flows or cycle configurations. Notably, the working fluids are ranked according to their environmental carbon footprint, demonstrating that residential applications achieve a two-thirds reduction in GWP compared to commercial applications. As previously noted, blends 1 and 5 contribute more significantly to refrigerant production due to leakage relative to their impact on refrigerant emissions. This discrepancy arises from non-optimal synthetic route in blend 1 and minimal direct emissions derived from blend 5.

This graphical representation also highlights the critical role of refrigerant production and emissions in future scenarios. Specifically, the contribution of refrigerant emissions and production to the overall GWP (refer to Y2 axis in **Figure 7.17**) is expected to exceed 40% for high-GWP refrigerants by 2050, compared to current standards around 5-20%. For mid-range and low-GWP agents, this effect is significantly mitigated, with projections proving that by 2050, contributions will be limited, with a maximum of 10% observed in 2021. An order of magnitude characterizes these classifications, with

residential applications showing contributions of around 22% for R513A in 2050, decreasing to 4% in 2021, while other mid-to-low GWP agents exhibit even lower contributions. In conclusion, the key findings from **Chapter 7.3.2.2** have been validated, demonstrating that the deployment of blend 5, in conjunction with either R32 (mid-GWP) or blend 1, within TS-VCRC cycles are the most environmentally advantageous options.

7.4. Summary of key outcomes from Chapter 7

In this chapter, a statistical analysis using polar soft-SAFT was adopted to assess the impact of design factors, such as cycle configuration, on the energy and exergy performance of AC cooling cycles. A grey-relational analysis ranked the importance of factors as follows: T_{cond} >> η_s >> T_{evap} > *refrigerant-type* > s*ystem-type* > ΔT_{SH} > ΔT_{SC}. Optimal performance was achieved with an LL/SL-HX cycle using R1234ze(E), featuring 95% isentropic compression, 5 K superheating and subcooling, and settled evaporator and condenser temperatures, resulting in a 56% reduction in CO_2-eq emissions. Further optimization with a three-level DOE improved heat transfer in the intercooler, leading to a 21% increase in exergy efficiency, yielding annual cost savings of $1.59k and a CO_2 emission reduction of 1.02 tons per year over a 15-year lifespan.

The 4E analysis revealed key insights into LL/SL-HX and TS-VCRC cooling cycle configurations. LL/SL-HX cycles offered substantial annual cost savings of $39.0 to $116.0 per unit and improved system, though achieving marginal reductions in environmental impact compared to the basic configuration in **Chapter 6**. TS-VCRC cycles, however, provided significant improvements in energy, exergy, and environmental efficiencies with the potential for further enhancements through optimization, albeit at the cost of higher total annual expenses, which increased by 8.0 to 10.0%, or $66.5 to $73.0 annually per unit. The holistic LCA analysis underscored the refrigerant choice as the main factor in reducing the carbon footprint. Specifically, replacing R410A with Blend 1 in a multi-compressor cycle led to a 23.7% decrease in GWP, while replacing R134a with Blend 5 from a basic to a TS-VCRC mode resulted in an 18.6% reduction. By 2050, high-GWP refrigerants are projected to account for over 40% of GWP through emissions and production costs but can be mitigated to a maximum of 10% for low- and mid-GWP agents. Therefore, refrigerant selection is deemed the most crucial factor for GWP reduction, with cycle optimization having a relatively minor impact.

Chapter 8. Design of CO_2-based Binary Mixtures in Cascade Cycles

This chapter will evaluate a novel configuration involving cascade cycles, as illustrated in ***Figure 3.6*** *of the methodology section. Preliminary assessments indicate that CO_2-based refrigerants are more suitable for this setup, addressing several criteria for further evaluation, including flammability predictions generated by an ANN approach due to the absence of empirical data. Promising blends will undergo a 4E assessment, and the optimal candidate will be identified using the TOPSIS method based on KPIs such as energy and exergy efficiency, environmental TEWI, total annual cost, discharge line temperature, volumetric cooling capacity, total irreversibility rate among others.*

The results presented in this section have been published in a peer-reviewed research paper (referenced as [353]) in ACS Sustainable Chemistry & Engineering.

8.1. Selection criteria

While the same KPIs for mixture selection discussed in **Chapter 6.2.2.1** are applied in this section of the thesis, there is a significant change in the glide temperature threshold, established here up to 15 K [556–558], due to the significant differences in polarity and thermophysical properties between CO_2 and its counterparts. Consequently, zeotropic mixtures are included, enabling the screening of 27 CO_2-based binary mixtures listed in **Table 4.6**, as well as mixtures with R1225ye(Z), R1132(E), and R1132a for which no experimental data are available. For such cases, binary parameter ξ_{ij} values are transferred from the closest mixtures in **Table 4.6**: R1234yf for R1225ye(Z), and R152a for the latter two. The initial screening criteria is plotted in **Figure 8.1**.

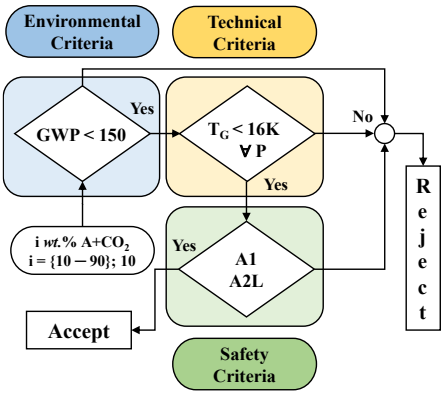

Figure 8.1. *Screening criteria for CO_2-based binary blends considering environmental, technical, and safety KPIs.*

This first screening included 270 binary mixtures, with 42 excluded due to excessive GWP (all HFCs/CO_2 blends), 164 excluded due to glide concerns, and the R1123/CO_2 mixture at a 90:10 weight ratio excluded because of a *NBP* exceeding 200 K, making it unsuitable for cascade applications despite meeting all criteria in. Overall, over three-quarters of CO_2-based blends with HFOs (67.5%) and saturated hydrocarbons (79.6%) were excluded due to a high zeotropic degree, predominantly impacting molecules with multiple heteroatoms and long chain lengths, such as R600-R601a series, R1233zd(E) and RE170.

The remaining 63 mixtures are listed in **Table 8.1**, an go through the next stage, related to a thorough flammability assessment to evaluate their safety suitability for the subsequent 4E analysis, as no direct correlation based on empirical data is available for this property, unlike GWP and glide.

Table 8.1. *Short-listed refrigerant blends and their compositions based on initial screening criteria.*

ID[+]	+ CO_2	*wt.*%[±]	GWP	T_G /K[*]	ID	+ CO_2	*wt.*%[±]	GWP	T_G /K[*]	ID	+ CO_2	*wt.*%[±]	GWP	T_G /K[*]
1	R41	10	12.5	0.667	**22**	R1243zf	10	<1.0	15.990	**43**	R170	40	3.0	0.155
2	R41	20	24.0	1.480	**23**	R1234yf	10	<1.0	10.037	**44**	R170	50	3.5	1.898
3	R41	30	35.5	1.763	**24**	R1234yf	20	<1.0	17.076	**45**	R170	60	4.0	3.487
4	R41	40	47.0	1.653	**25**	R1234ze(E)	10	1.0	15.778	**46**	R170	70	4.5	4.485
5	R41	50	58.5	1.413	**26**	R1225ye(Z)	10	1.2	16.463	**47**	R170	80	5.0	4.574
6	R41	60	70.0	1.183	**27**	R1132(E)	10	1.1	0.102	**48**	R170	90	5.5	3.290
7	R41	70	81.5	0.966	**28**	R1132(E)	20	1.2	5.364	**49**	R290	10	1.2	5.941
8	R41	80	93.0	0.728	**29**	R1132(E)	30	1.3	10.728	**50**	R290	20	1.4	15.721
9	R41	90	104.5	0.414	**30**	R1132(E)	40	1.4	15.131	**51**	R1150	10	1.3	9.293
10	R32	10	68.6	7.383	**31**	R1132a	10	<1.0	0.405	**52**	R1150	20	1.6	9.047
11	R32	20	136.2	11.525	**32**	R1132a	20	<1.0	0.236	**53**	R1150	30	1.9	7.281
12	R161	10	1.3	13.208	**33**	R1132a	30	<1.0	0.018	**54**	R1150	40	2.2	5.259
13	R134a	10	130.9	15.753	**34**	R1132a	40	<1.0	0.072	**55**	R1150	50	2.5	3.050
14	R1123	10	1.2	1.750	**35**	R1132a	50	<1.0	0.376	**56**	R1150	60	2.8	1.016
15	R1123	20	1.4	4.099	**36**	R1132a	60	<1.0	0.769	**57**	R1150	70	3.1	0.182
16	R1123	30	1.6	6.071	**37**	R1132a	70	<1.0	1.126	**58**	R1150	80	3.4	0.006
17	R1123	40	1.8	7.583	**38**	R1132a	80	<1.0	1.317	**59**	R1150	90	3.7	0.011
18	R1123	50	2.0	8.626	**39**	R1132a	90	<1.0	1.118	**60**	R1270	10	1.1	4.153
19	R1123	60	2.2	9.188	**40**	R170	10	1.5	9.860	**61**	R1270	20	1.2	12.186
20	R1123	70	2.4	9.249	**41**	R170	20	2.0	6.704	**62**	R13I1	10	1.0	7.768
21	R1123	80	2.6	8.569	**42**	R170	30	2.5	3.633	**63**	R13I1	20	1.0	15.356

[+] Pure CO_2 is identified as mixture #0.
[±] The mass fraction for the 1st component in the blend.
[*] Obtained at atmospheric pressure (0.1 MPa).

8.1.1. Flammability estimation

This sub-section completes the final step outlined in **Figure 8.1** (green stage) by using a machine learning technique to estimate the flammability class of the mixtures listed in **Table 8.1**, given the absence of empirical data or correlations in the literature. To address this task, an artificial neural network is designed and fine-tuned following a strategy similar to that detailed in **Chapters 4.1.2** and **4.2.4.2**.

The flammability is represented through the NFI [262], which is an empirical representation for the flammability of working fluids estimated using the refrigerant's adiabatic flame temperature, and degree of fluorination, expressed as the ratio of fluorine atoms to the total number of fluorine and hydrogen atoms. These parameters are inputs to calculate the NFI according to **Eq. (6.1)**, yielding a range to an absolute value of 100, for highly flammable compounds. Indeed, the flammability class for refrigerants in-line with the ASHRAE classification are grouped based on their NFI values, with non-flammable class 1 (NFI ≤ 0), mild-flammable class 2L (0 < NFI < 50), and flammable classes 2 and 3 (NFI ≥ 50).

8.1.2. σ-profiles of pure refrigerants from COSMO-RS as input descriptors

As explained in the methodology (**Section 3.5.1**), the *σ*-profiles of the different molecules are used as input descriptors in the ANN. Consequently, the *σ*-profiles of 23 refrigerants listed in **Table 8.1**, encompassing 20 pure-components (see methodology for extended details), as well as R1270, CO_2, and RE170 used in binary and ternary combinations, have been calculated. Detailed insight into their governing interactions and role on their flammability is accordingly highlighted in **Figure 4.6** and **Figure D1**. This concept relies on evidence that COSMO-RS descriptors effectively capture factors influencing flammability by considering surface charge density and molecular interactions, including the presence of specific functional groups, polarity, oxygen content, hydrogen bonding capacity, and the presence of heteroatoms like fluorine or chlorine. As an example, the *σ*-profiles of the CO_2 (R744) + propane (R290) binary mixture, and the ternary system with R134a, are depicted in **Figure 8.2**.

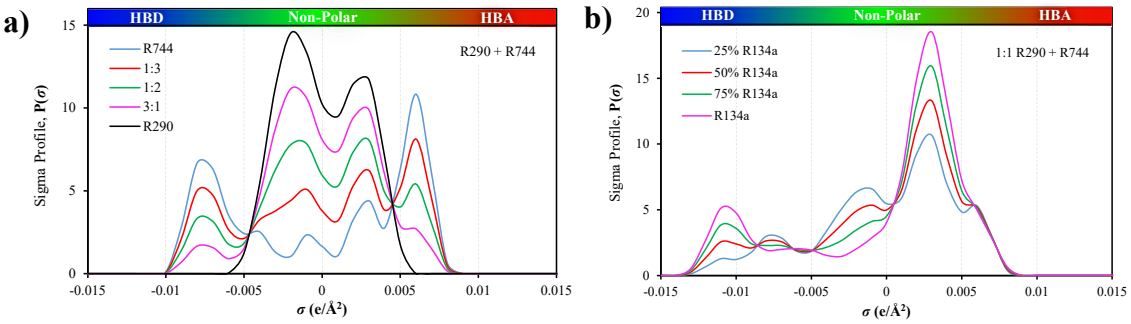

Figure 8.2. *σ-profiles of **a)** R744 (blue) + R290 (black) binary mixtures at 25 (red), 50 (green), and 75 (pink) mole% ratios of R290, and **b)** R744 + R290 at 1:1 ratio with the addition of 25 (blue), 50 (red), 75 (green), and 100% (pink) of R134a mole fractions.*

It can be observed that, in the binary system (see **Figure 8.2a**), a gradual shift towards R290's non-polar profile is observed, characterized by the diminishing HBD/HBA interactions of CO_2. This effect underlines a direct correlation between molecular interactions, as revealed by *σ*-profiles, and the mixture's overall flammability, emphasizing the significance of molecular composition in determining refrigerant behavior and safety. Further complexity arises in the ternary mixture of R290 and CO_2 with the inclusion of R134a at equimolar ratios, as depicted in **Figure 8.2b**. As the fraction of R134a in the ternary mixture increases, there is a decrease in flammability,

partially marked by a transitional enhancement in the non-polar peak around 0.0025e/Å^2 of the σ-profile, accompanied by a modest increase near the HBD region.

8.1.3. Selection of optimal configuration

The ANN for predicting the NFI for pure refrigerants and blends relying on their molecular descriptors from COSMO-RS has a two hidden layer general architecture. According to empirical evidences from various machine learning models [335,337,340,343,345], this particular setup constitutes a suitably deep network, optimally balancing learning capacity, computational efficiency, and generalization performance, thereby mitigating the risk of overfitting.

The number of neurons in each hidden layer, and activation functions were kept as variables to determine the best ANN configuration. Firstly, the number of neurons in each of the 2 hidden layers were changed from 1 to 25 neurons, running each network for eight randomized trials for each configuration, with their average RMSE as a function of number of neurons in each hidden layer shown in **Figure 8.3a**. The most effective configuration is found to be a [61 (*I*) × 14 (*HL1*) × 24 (*HL2*) × 1 (*O*)] configuration shown in **Figure 8.3b**, which has the lowest average RMSE of 0.430. This configuration ensured a RMSE < 1 in each of its randomized trials, signifying high precision and accuracy in all of its random tests.

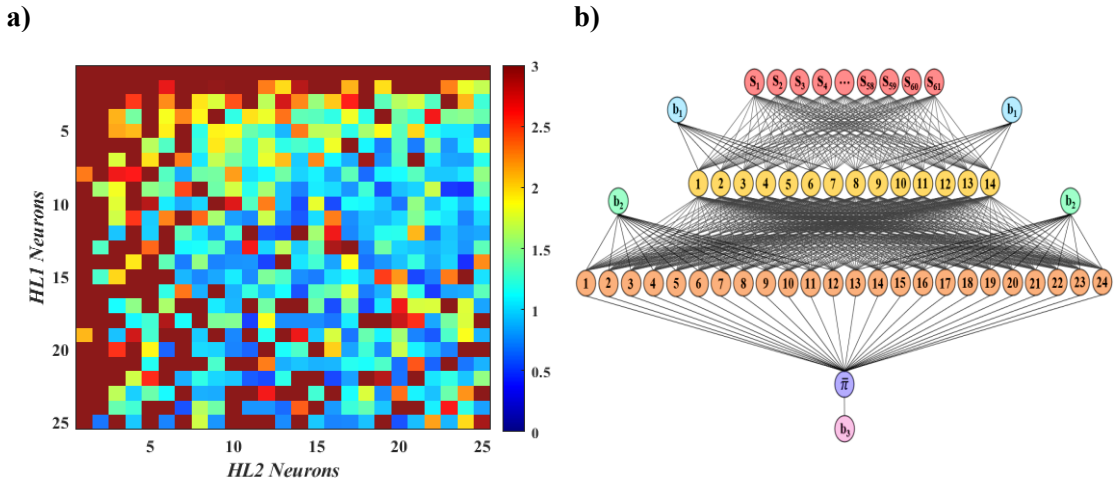

Figure 8.3. ***a)*** *Mapping the average RMSE variation in relation to the number of neurons in first (HL1) and second hidden layers (HL2) while using tansig activation function in both HL1 and HL2, and* ***b)*** *The configuration for the best performing ANN of [61 (I) × 14 (HL1) × 24 (HL2) × 1 (O)].*

The selected ANN configuration requires a total of 1190 weights and 39 biases to effectively correlate the molecular descriptors with the NFI of the refrigerants. Additionally, ANN configuration optimization reveals that arrangements with only a single neuron in any of the hidden layers often correspond to higher error rates, thereby highlighting the limitations of overly simplistic models. However, the process is not as straightforward as merely maximizing neuronal count: a configuration involving a high number of neurons in both hidden layers, such as [61 (*I*) × 25 (*HL1*) × 25 (*HL2*) × 1 (*O*)], can paradoxically lead to increased RMSE (*i.e.*, RMSE = 2.91). This underlines the delicate balance between model complexity and performance in the context of ANN architecture.

To further enhance the performance and check the sensitivity of the best ANN configuration depicted in **Figure 8.3b**, a series of additional tests were carried out, such as:

(1) introducing a third hidden layer.
(2) reducing the number of descriptors to 8 rather than the initial 61.
(3) changing the activation functions for the hidden layers.

On one hand, the introduction of an extra hidden layer can potentially increase the model accuracy (*i.e.,* reduce RMSE), but at the expense of increased computational time. On the other hand, reducing the descriptor count is expected to reduce the computational time, yet potentially at the cost of a reduced accuracy (*i.e.,* increased RMSE). Hence, the aim is to adjust these variables, finding the right balance between reducing the computational time and minimizing the RMSE.

As provided in **Figure 8.4a**, adding a third hidden layer to the pre-established optimal configuration (*i.e.,* [61 (*I*) × 14 (*HL1*) × 24 (*HL2*) × 1 (*O*)]) does not significantly lower the RMSE, regardless of the number of neurons in that layer (*i.e.,* 1 – 25 neurons), only observing a slight decrease in RMSE when using either 4 or 6 neurons. However, this comes at the expense of a threefold and eightfold increase (*i.e.*, ET/s = 18.9 for ANN configuration in **Figure 8.3b**) in the computational time (measured as the elapsed time per epoch), respectively, negating the minor enhancements in accuracy. As a consequence, the originally proposed two hidden layer configuration is preserved.

The reduction of molecular descriptors from 61 to 8 is analyzed in **Figure 8.4b**. As expected, computational time substantially decreases from 0.703 – 0.803 seconds to 0.155 – 0.181 seconds when using the 8 descriptors. Nevertheless, this substantial decrease in computational time produces a severe deterioration of the ANN performance, leading to a substantial increase in the RMSE. The least error, achieved *via* [8 (*I*) × 24 (*HL1*) × 19 (*HL2*) × 1 (*O*)]) configuration, exceeds an RMSE of 6.00, indicating a decrease in model accuracy. Comparatively (see **Figure 8.3a**), when using 61 descriptors, 86.4% of the total tested combinations culminate in a lower error value, typically with RMSE = 1. In summary, although the model performs calculations faster when using fewer descriptors, this speed comes with a cost in accuracy, compromising the practical application of the model. Accordingly, the number of inputs was kept at 61 descriptors.

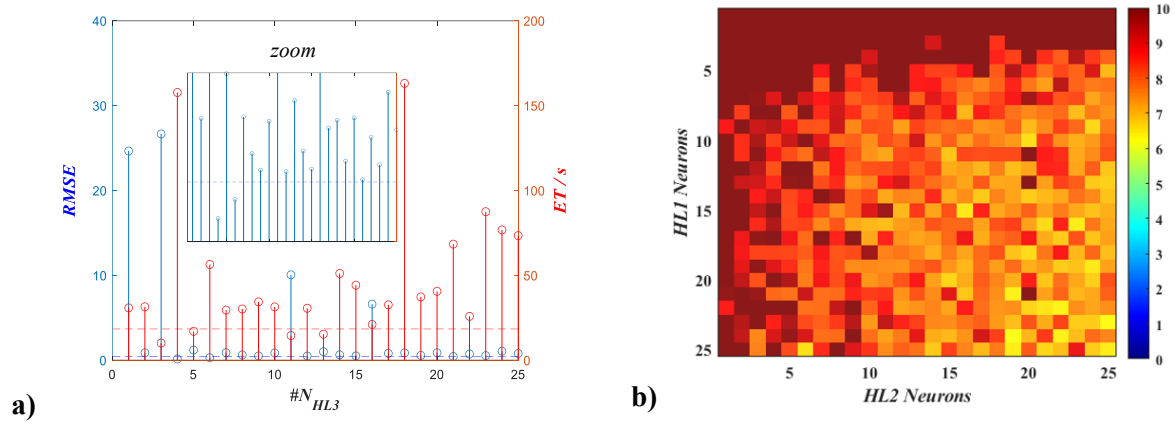

Figure 8.4. ***a)*** *RMSE and elapsed time per epoch for [61 (I) × 14 (HL1) × 24 (HL2) × X (HL3) × 1 (O)]) ANN architecture as a function of number of neurons in third hidden layer (HL3), and* ***b)*** *Mapping of the RMSE variation in relation to the number of neurons in HLs 1 and 2 when using 8 input descriptors.*

Having identified the [61 (*I*) × 14 (*HL1*) × 24 (*HL2*) × 1 (*O*)]) configuration as optimal, a systematic examination of various activation functions within the hidden layers has been conducted (see **Table 3.8**), including hyperbolic tangent (*tansig*), logistic sigmoid (*logsig*), linear (*purelin*), radial basis (*radbas*), and rectified linear unit (*ReLU*) functions, in order to fine-tune the performance for this specific configuration. The detailed results of this examination, averaged over ten random runs of the corresponding ANN configuration, are outlined in **Table 8.2**.

Table 8.2. *Analysis of the performance for activation functions in the hidden layers of the ANN model.*

AF	Equation	Range	Set	R^2	RMSE	AARD/%	SD_{av}
Hyperbolic Tangent (*tansig*)	$f(x) = \tanh(x)$	$[-1, 1]$	Train	0.9998	0.4299	3.9778	0.4268
			Validate	0.9991	1.0437	4.3304	1.0434
			Test	0.9994	0.8629	4.5404	0.8627
			Total	0.9997	0.5847	4.0694	0.5827
Logistic Sigmoid (*logsig*)	$f(x) = \frac{1}{1+e^{-x}}$	$[0, 1]$	Train	0.9998	0.4268	3.8884	0.4244
			Validate	0.9990	1.1260	3.8893	1.1250
			Test	0.9987	1.1822	6.1410	1.1800
			Total	0.9996	0.6651	4.1140	0.6639
Linear (*purelin*)	$f(x) = x$	$[-\infty, \infty]$	Train	0.9011	11.3709	92.1066	11.3732
			Validate	0.8988	11.5049	87.1327	11.4848
			Test	0.8785	12.6966	76.6944	12.7037
			Total	0.8984	11.5324	90.0660	11.5336
Radial Basis (*radbas*)	$f(x) = e^{-x^2}$	$[0, 1] \mid x \in [0, \infty)$	Train	0.9691	5.5479	47.5140	5.5477
			Validate	0.9425	7.8847	45.1713	7.8874
			Test	0.9496	7.1821	57.1790	7.1870
			Total	0.9643	6.0473	48.2469	6.0469
Rectified Linear Unit (*ReLU*)	$f(x) = max(0, x)$	$[0, \infty)$	Train	0.9982	1.4754	14.1345	1.4747
			Validate	0.9948	2.4795	14.8493	2.4790
			Test	0.9955	2.3021	17.6914	2.3022
			Total	0.9976	1.7079	14.5621	1.7073

From these observations, the *tansig* function is the best performing, achieving an R^2 of 0.9997 and RMSE of 0.5847 across all datasets (*i.e.,* training, testing, validation). The *logsig* function is another promising alternative on par with *tansig* function achieving an R^2 of 0.9996 and RMSE of 0.6651. Its consistent performance across validation and testing datasets (R^2 of 0.9990 and 0.9987, respectively) highlights its efficacy in predicting external datasets. The *ReLU* and *radbas* functions, although competent, exhibit lower R^2 values compared to *tansig* and *logsig* functions, hinting at a potential overfitting. However, the most notable discrepancy is observed with the use of the *purelin* function with an overall R^2 of 0.8984, denoting a considerable mismatch with the actual data.

In light of the previous analysis, it becomes clear that the optimal ANN for predicting NFI values for refrigerants using molecular descriptors from COSMO-RS is the [61 (*I*) × 14 (*HL1*) × 24 (*HL2*) × 1 (*O*)]) configuration using *tansig* activation functions in both hidden layers. This synthesis of insights paves the way to explore this specific configuration further, considering it as the best-case scenario for the targeted application.

8.1.4. Evaluation of optimal configuration

Figure 8.5a offers a visual comparison between actual and predicted NFI values for both training and external (validation and testing) sets, as a parity plot between ANN-predicted NFI (*y-axis*) and actual NFI data (*x-axis*) for the best performing ANN configuration from the previous section. The machine learning simulation achieved desired accuracy at epoch 134 in just over a minute (00:01:03), with a performance error of 0.00491. It reported a gradient of 2.83, and a μ of 0.001, striking a balance between training strategies.

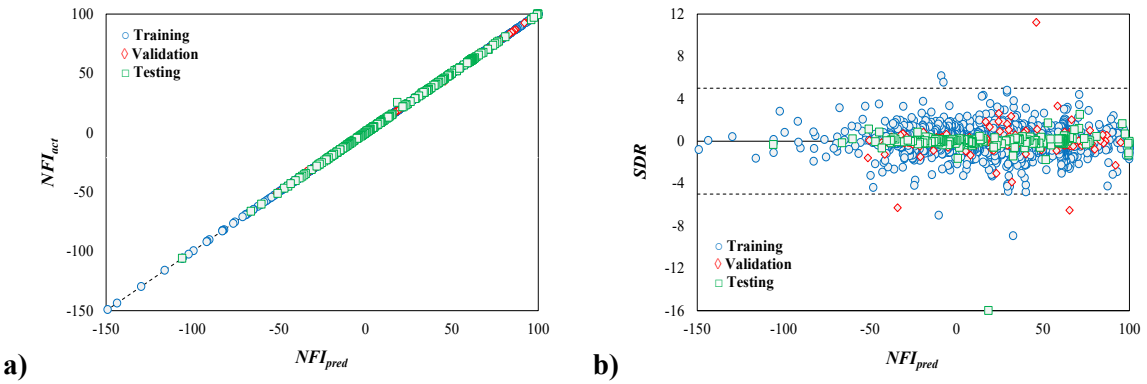

Figure 8.5. ***a)*** *Parity, and* ***b)*** *Standardized Residual plots between the actual and ANN-predicted NFI.*

These results confirm the successful training of the model, as most points fall along the $y = x$ diagonal. Consequently, the model is seen as a reliable tool for predicting flammability based on the given inputs, effectively avoiding overfitting, a common pitfall in machine learning. This accurate fitting underscores the model's precision and narrow dispersion in future predictions, as indicated by the excellent alignment with actual data in the external testing and validation datasets.

The residual plot, shown in **Figure 8.5b**, highlights the model's ability to predict the flammability index for binary and ternary mixture blends. As observed, most of the differences between predicted and actual values (residuals) are within a range of ±1, while almost all fall within a broader range of ±5 SDR, with only a few exceptions. Specifically, 0.72% of the training data, 0.96% of the validation data, and 0.32% of the testing data fall outside the SDR range of ±5, while a substantial 81.3% of the total dataset is found to be constrained within an SDR of ±1. The data analysis reveals that, in the worst-case scenario within an SDR of ±5, the NFI is marginally overestimated by 0.27, given that the NFI

spans a substantial range from -150 to +100. Consequently, this difference does not constitute a clear outlier.

Certainly, it is important to remark the accuracy along all safety flammability classifications. Notably, only two points (1.9% of the validation set) within the 2-3 flammability region, and a mere 0.44% of total validation data in the 1-2L discretized spectrum, display residual deviations over ±5, respectively, with no outliers detected during testing.

The detailed results of the statistical analysis, including specific key performance indicators are presented in **Table 8.3** to supplement the previous visual representation with statistical insights.

Table 8.3. *Statistical analysis of performance parameters for the developed ANN model.*

Metric	Training	Validation	Testing	Total
R^2	> 0.999	> 0.999	> 0.999	> 0.999
RMSE	0.0727	0.2546	0.4402	0.1735
AARD / %	0.7302	0.7957	1.1989	0.8091
SD_{av}	± 0.0357	± 0.0679	± 0.0812	± 0.0434
Data Points	2501	313	313	3127

As it can be seen, the R^2 value remained consistently high across all datasets, registering values greater than 0.999. Although demonstrating a robust linear relationship between predicted and actual NFI values, this consistency fails to delineate a clear trend; hence, further assessment through additional statistical descriptors becomes essential.

Unlike R^2, RMSE and AARD show a clear trend as the analysis moves from training to validation and testing stages, with values increasing progressively, thereby indicating the model's increasing deviation as it is exposed to new and unseen data. Indeed, while RMSE quantifies aggregate differences between predicted and actual values, AARD measures the average percentage deviation from the actual values, providing a complementary view of the model's performance across different stages of data analysis. This insight emphasizes the importance of careful evaluation in understanding how well the model may perform when applied to real-world scenarios.

Lastly, the SD_{av}, quantifying the residuals' dispersion or spread around the mean, reflects the inherent variability and complexity of each dataset, as the larger the deviation, the more the residuals spread out from the mean. This assessment reveals that the

predictions for the validation and testing stages are more spread out from the average error, highlighting the importance of both, the underlying data distribution in addition to the model's capacity to handle diverse complexities and inherent variations within different datasets.

An examination of **Figure 8.6** and **Table 8.4** provides insights into the applicability domain of the developed ANN model, contributing to the identification of potential outliers and anomalous data points lacking physical interpretation.

Table 8.4. *AD parameters, including borderline outliers in parenthesis, for the developed ANN model.*

	Training	**Validation**	**Testing**	**Total**
Structural Outliers (BSO)	15 (5)	0 (0)	5 (1)	20 (6)
Response Outliers (BRO)	47 (43)	6 (3)	2 (1)	55 (47)
$AD_{coverage}$ (+ BO) / %	97.60 (99.52)	98.08 (99.04)	97.76 (98.40)	97.67 (99.36)

h^* = 0.0744

Within this context, 20 structural outliers were identified, distributed in 15 and 5 from the training and testing stages, respectively. For assessing data points where h_i values range between h^* (0.0744) and 0.1, identified as borderline structural outliers, the number of instances falling outside the AD diminishes to 14, with 10 related to training and 4 to testing stages. In addition, the analysis reveals that response outliers, defined as data points with an SDR value outside ± 3, tally up to 55, comprising 47 for training, 6 for validation, and 2 for testing stages within the developed ANN. If the borderline response outliers (SDR between ± 5) are included within the AD, the outliers diminish to 8, distributed as 4 for training, 3 for validation, and 1 for testing. Most response outliers cluster near the SDR border of ± 4, defining a clear threshold between potential interpolation and extrapolation predictions.

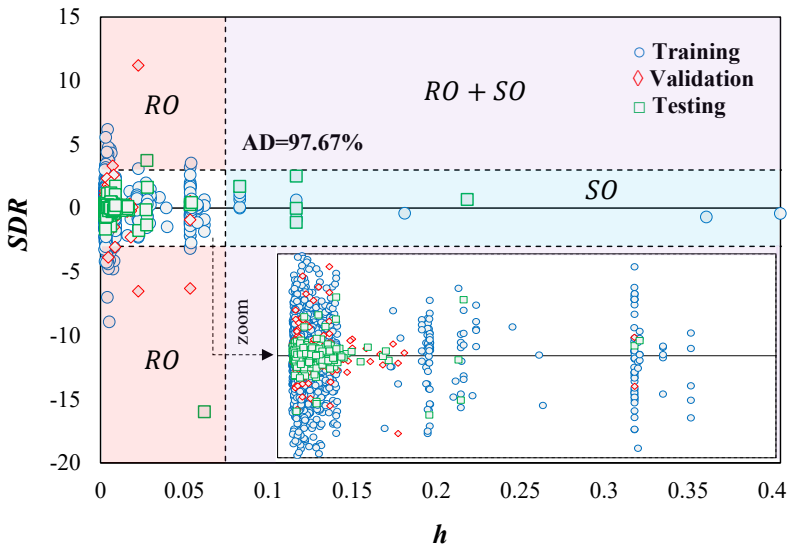

Figure 8.6. *William's plot delimitating the AD (white) boundaries for the total set of assessed compounds, with response outliers in red, structural outliers in turquoise, and areas with both in purple.*

Figure 8.6's zoomed view reveals an average AD coverage of 97.67% across the total 3D space, with 97.92% of the data points for external model evaluation falling within the AD. This percentage rises to 99.36% when including borderline outliers for both structural and response factors, reflecting the trend that most response outliers converge at the SDR border's limit. The cumulative evidence, as portrayed through the visual and statistical elements of **Figure 8.6** and **Table 8.4,** confirms the robust alignment of the ANN model, establishing that new predictions within this domain can be deemed consistently for comprehensive analyses and high-throughput screening applications.

Figure 8.7 illustrates the relative contribution of the 61 descriptors inputs to the NFI output, where the greater the absolute value of the contribution, the more pronounced the discrimination capability of the respective parameters. From the analysis, it becomes apparent that the primary contributor to the NFI is S_{50} ($\sum \frac{\partial f_x}{\partial s_\sigma}$, @ σ = 0.019 e/Å^2), accounting for 34.1% of the total contribution. This is followed by the notable influences of S_{23} (σ = -0.008 e/Å^2), S_{39} (σ = 0.008 e/Å^2), and S_{25} (σ = -0.006 e/Å^2), contributing 4.42%, 4.24%, and 4.14%, respectively. Further emphasizing the importance of certain regions, descriptors $S_{14\text{-}18}$, S_{20}, $S_{22\text{-}27}$, S_{31}, S_{32}, $S_{35\text{-}37}$, $S_{39\text{-}42}$, S_{44}, and S_{50} account for a remarkable 90.98% of the total contribution.

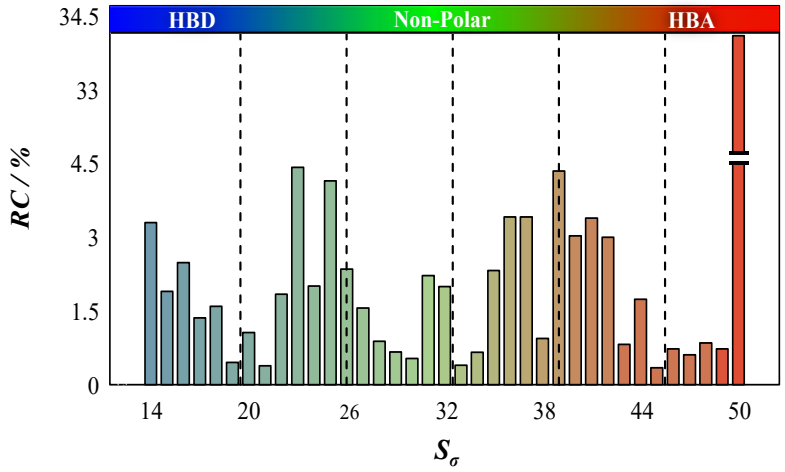

Figure 8.7. *Relative contribution of the input parameters used in the ANN model.*

Certainly, it is evident that polarized positive-charged segments (depicted in intense blue) and negative-charged segments (in intense red) significantly impact the NFI of the refrigerant mixtures, surpassing the weak hydrogen acceptor and donor regions, with the non-polar zone emerging as the least significant factor. This observed trend, evident from the data, aligns with the interplay of hydrogen bonding capabilities and electron-donating/accepting characteristics within the molecular structure. In this context, mildly strong acceptor or donor regions significantly influence the NFI through stable and potent interactions, while weak donors, acceptors, and non-polar regions yield lesser or minimal effects, due to their inherently weaker interactions that lack substantial influence on flammability dynamics.

In a further examination of the underlying dynamics, it is revealed that the molecular descriptors corresponding to $S_{1\text{-}13}$ and $S_{51\text{-}61}$, regions typically characterized by their role as predominantly HBD and HBA, respectively, manifest a complete absence of contributions. A plausible hypothesis for this observation might be rooted in the formation of stabilizing hydrogen bond networks within the molecular structure. These networks could act to stabilize the molecular system, reducing the available reactive sites and thereby diminishing the propensity for ignition. The intricate charge distribution and potential influence of surrounding molecular features might further mitigate the contributions of these charged regions to flammability.

8.1.5. Testing the predictive power of the model on flammability of quaternary mixtures

As illustrated in **Figure 8.7**, a substantial 90.98% of the total contribution to the NFI is ascribed to a specific set of 23 molecular descriptors. Hence, it is interesting to check the performance of the ANN if only those 23 descriptors were used. Consequently, the next step of the analysis involves a two-fold approach encompassing both, a comprehensive examination employing the full array of 61 molecular descriptors, and a targeted assessment utilizing the condensed subset of 23 specific descriptors. Both strategies employ consistent hidden layer layouts and activation functions, as detailed in the main outputs of **Figure 8.3-S35** and **Table 8.2**.

The ANN is exclusively trained and validated on pure substances and binary and ternary mixtures (see data assembly and preprocessing **Section 8.1.2**). Then, a total of 55 quaternary mixtures, not previously used for training or testing the model, are predicted as a stringent test of model integrity. These mixtures involve CO_2, HFOs (R1243zf, R1234yf, R1234ze(E)), and HFCs (R41, R134a, R227ea, R125, R32, R152a), representing a wide spectrum of compositions. For this purpose, the ANN configuration in **Figure 8.3b** operates using weights, biases, and output parameters from **Table E1** (HL1) and **Table 8.5** (HL2), in accordance with the mathematical expression presented in **Eq. (8.1)**. The resulting output function enables external predictions according to **Eq. (8.2)**.

Building on this configuration, the ensemble neural model is integrated into an **Excel Spreadsheet**, included as part of the Supplementary Material in *Albà et al.*'s work [353], enabling NFI calculations across pure to quaternary refrigerant mixtures. The Excel also includes the database for training, and testing, in addition to the quaternary compositions used for external validation, as outlined in the “DataBase“ and “External Validation DataBase“ subtabs.

$$NFI_{pred} = h_{purelin}\left\langle b_3 + \sum_{m=1}^{n}\left|\omega_m \cdot g_{tansig,HL2}\left\{b_2 + \sum_{k=1}^{l}\left[\omega_k \cdot f_{tansig,HL1}\left(b_1 + \sum_{i=1}^{j}\omega_{ik}\cdot S_i\right)\right]\right\}\right|\right\rangle \quad \textbf{(8.1)}$$

Table 8.5. *Developed ANN's (see **Figure 8.3b**) weights and biases for the second hidden layer (HH).*

	HH_1	HH_2	HH_3	HH_4	HH_5	HH_6	HH_7	HH_8	HH_9	HH_{10}	HH_{11}	HH_{12}
H_1	-0.9736	-0.9666	-0.2496	-1.0789	-1.7361	0.8504	0.1465	-0.0989	0.4060	0.6723	-0.0490	0.5446
H_2	-0.1403	-0.1408	-0.5551	-0.3780	0.5694	-0.1034	-0.2616	0.5531	1.2341	-0.1411	0.1482	1.0281
H_3	0.9141	-0.5179	0.5083	0.3097	1.1655	-0.1528	-1.0784	0.0616	-0.8161	-0.7366	1.1396	-0.4722
H_4	-0.0151	0.8341	0.1691	-0.1395	-0.6732	-1.1298	-0.0353	-0.4870	-0.0799	-0.7731	0.0268	-0.0450
H_5	-0.4041	-0.3617	-1.2703	-0.7659	-1.3013	-0.1552	0.0511	0.0172	1.1414	0.6586	-0.7818	1.6466
H_6	-1.5985	0.8163	0.0733	-0.9836	0.1540	-0.0187	0.3907	-1.3976	-0.8624	-0.8776	-0.6272	-0.4068
H_7	-0.3881	0.6095	0.0643	-0.3551	0.6241	0.4422	0.0965	0.0174	-0.4386	-0.3572	0.2783	0.0528
H_8	-0.4478	-1.3546	0.3756	-0.3951	-0.5737	-0.4195	0.1443	-0.2789	-0.5951	-0.3784	-0.9224	-0.9357
H_9	0.0216	-0.3010	-0.1021	-1.6722	-1.3522	0.2581	-0.5431	0.2483	0.4768	-0.3070	0.0820	0.5090
H_{10}	1.0890	-0.2895	0.4189	0.7706	-0.8508	0.1307	-0.1802	0.3936	0.2069	0.3856	0.5033	-0.0787
H_{11}	-0.3058	0.0690	0.2709	0.5627	-1.0444	-0.7898	-0.6406	-1.1523	0.0305	0.4805	0.3936	-1.7033
H_{12}	-0.0054	0.0633	-0.6880	1.9224	-0.1050	-1.0584	0.1281	-0.4816	0.6330	1.2022	-0.1686	1.1883
H_{13}	1.1005	-0.8841	-0.0160	0.5523	1.0234	0.5340	-0.7862	0.0010	0.9427	-0.1897	-0.8109	2.0533
H_{14}	0.4210	-0.7273	-0.5702	0.5410	0.9315	-0.6775	-0.0949	1.2565	-0.9530	-0.2399	-0.5506	-0.6708
b_2	1.4354	1.2921	1.3947	1.1705	1.4242	-0.1033	1.2042	-0.1800	1.3800	0.2428	0.6424	0.2635

	HH_{13}	HH_{14}	HH_{15}	HH_{16}	HH_{17}	HH_{18}	HH_{19}	HH_{20}	HH_{21}	HH_{22}	HH_{23}	HH_{24}
H_1	0.1277	0.3547	-0.5744	-0.1646	-0.6186	-0.2490	1.2647	-0.1917	-0.2853	-0.0538	0.5955	1.0445
H_2	0.9935	0.4954	-0.1891	0.3422	-1.5464	-1.4037	0.5618	0.4680	0.3774	-0.0625	0.6502	0.7284
H_3	-0.3273	0.4333	1.0209	-1.0051	-0.0063	0.5486	-1.0028	0.5176	1.5267	0.1244	1.0048	1.6874
H_4	-1.7088	-0.7940	0.1285	-0.0501	0.6612	-0.7574	0.0097	0.0305	0.5573	-0.1345	0.1096	-0.5886
H_5	-0.5840	0.1511	0.2030	-0.0389	-1.4057	0.2793	0.5602	0.3263	-0.3398	0.0903	-0.7871	1.0246
H_6	-0.4323	0.0185	-0.3368	0.3474	2.6329	1.9890	0.9805	0.3673	0.7953	0.9229	0.8087	-0.6728
H_7	0.1431	0.9938	0.4666	-0.2076	1.1721	0.1023	-0.6531	0.4515	0.2532	0.1245	0.1330	-0.8273
H_8	1.5987	-0.4215	-1.5950	0.0558	0.5198	0.1864	-1.6606	-0.3550	-0.4185	0.9727	0.0257	0.1225
H_9	-0.0561	0.8727	-0.5854	-0.7616	-0.1307	1.3431	1.0849	0.3158	0.3652	0.1168	-1.2679	-0.5087
H_{10}	-0.1359	-0.4421	1.9128	-0.2665	2.8886	0.9070	-0.0831	-0.6031	-0.2184	-1.5533	-0.3674	-0.1274
H_{11}	1.8617	-1.5216	-0.6076	-0.4293	-0.4676	-0.0239	0.6304	0.3375	-0.4912	-0.0163	0.1674	-0.9631
H_{12}	0.0334	0.0001	-0.4204	0.2932	0.7984	1.0063	0.4212	1.0249	0.7497	0.7885	0.2674	-0.8087
H_{13}	-0.1975	-1.1089	-0.0487	1.1674	-0.5084	0.0914	-1.5168	-0.0703	0.1331	0.6427	-0.7398	0.2498
H_{14}	-0.2919	1.3184	-1.1254	1.6070	1.0834	-0.9243	-1.2359	-0.0689	-0.2937	0.7242	0.6219	0.0282
b_2	0.4595	1.6282	-0.0898	-0.8157	0.0004	-1.7517	0.6497	-0.5375	-1.0831	-2.0170	1.4198	2.5383

$$\begin{aligned} &0.248097\,(HH_1) - 0.319464\,(HH_2) + 0.162838\,(HH_3) + 0.008849\,(HH_4) \\ &+1.808459\,(HH_5) + 0.085165\,(HH_6) + 0.205977\,(HH_7) + 0.264793\,(HH_8) \\ &-0.620327\,(HH_9) - 0.029470\,(HH_{10}) - 0.221097\,(HH_{11}) + 0.488371\,(HH_{12}) \\ &-0.178911\,(HH_{13}) - 0.272909\,(HH_{14}) + 0.123859\,(HH_{15}) - 0.151293\,(HH_{16}) \\ &+0.029668\,(HH_{17}) + 0.055991\,(HH_{18}) - 0.209633\,(HH_{19}) + 0.237560\,(HH_{20}) \\ &+0.126407\,(HH_{21}) + 0.166035\,(HH_{22}) + 0.111589\,(HH_{23}) - 0.611244\,(HH_{24}) \\ &-0.433878 \end{aligned} \quad \textbf{(8.2)}$$

As can be extracted from **Figure 8.8**, the 61-descriptor model achieves an RMSE of 0.0631, indicative of high accuracy, whereas the 23-descriptor model provides a less precise RMSE of 0.5158, but still offers the advantage of reduced computational time. As appreciated, the increase in RMSE represents a decrease in prediction accuracy, reflecting

the complexity of capturing intricate molecular interactions with a reduced descriptor set. **Figure 8.8a-b** present an in-depth and detailed graphical analysis of these trends.

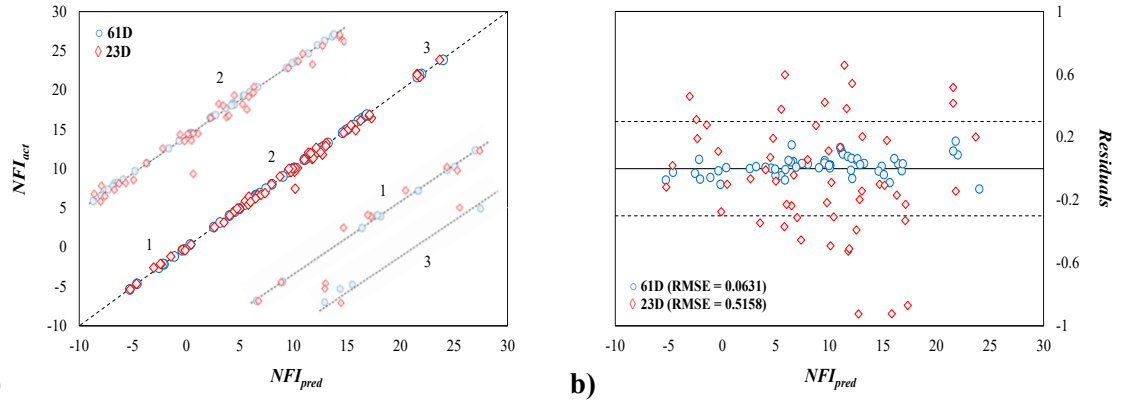

Figure 8.8. ***a)*** *Parity plot (letters denote the flammability region zooms), and* ***b)*** *residuals plot of actual [274] versus ANN-predicted NFI values for selected quaternary mixtures using the 61 (blue symbols) and 23 descriptor (red symbols) ANN models.*

Specifically, **Figure 8.8a** contrasts the actual and predicted NFI values using both the 61 and 23 descriptor sets, while **Figure 8.8b** showcases the distribution of residuals, revealing that 41.8% of the total data exhibit a residual of ± 3 when employing the simplified 23-descriptor model, an absent phenomenon in the data analysis concerning 61 descriptors. Interestingly, the AD method's application disclosed that only one mixture, composed of R1243zf, R1234ze(E), R1234yf, and CO_2 (52-32-12-4 mol%), falls outside the AD when using 23 descriptors, whereas a 100% AD is achieved with 61 descriptors.

In summary, the 61-descriptor approach emerges as highly predictive (average residual of 0.049) but computationally more demanding, while the more simplified model, although less precise with an average residual of 0.34, offers the benefit of reduced computational time and complexity. Given the broad NFI prediction range evaluated [-5 to 25], the ANN model's, particularly with 61 descriptors, stands as a very accurate and reliable tool for flammability screening.

8.1.6. Predicting the flammability of novel CO_2-based binary, ternary blends

After a robust phase of training and testing, including external validation with quaternary mixtures, the ANN model is deployed to predict the ignition propensity of a diverse set of binary and ternary mixtures of high interest for which no flammability data

are available. In this manner, crucial information on this safety feature becomes instrumental in facilitating the selection of refrigerant blends that strike an optimal balance between low GWP and moderate to low flammability without compromising safety-related characteristics.

Firstly, the list of binary mixtures summarized in **Table 8.1** in **Section 8.1**, including all mixtures who had passed the GWP and glide temperature criteria, are addressed. The results are ordered by increasing NFI in **Figure 8.9**, with each mixture related to the specific number indicated in **Table 8.1**.

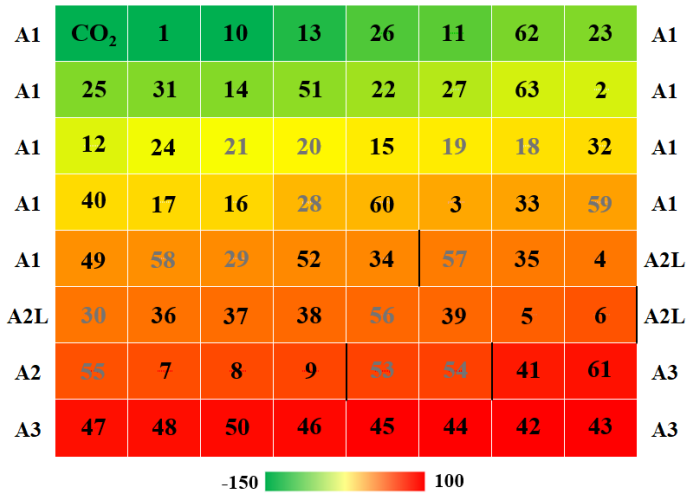

Figure 8.9. *NFI for the CO_2-based binary mixtures in **Chapter 8.1**. Grey nomenclature corresponds to mixtures with uncertainty leverage values higher to h^* (refer to **Figure 8.6**) while black separators delineate the flammability boundaries between A1/2L, 2L/2, 2/IND, and IND/A3 classifications. Refer to [276] for additional insights.*

Interestingly, most of them fulfill the mid to null flammability standards under review, serving as key criteria for the subsequent 4E study. Specifically, mixtures 4-6, 30, 35-39, and 56-57 exhibit a flammability standard corresponding to a 2L classification ($36 < \bar{\pi} < 60$), while 36 mixtures fall within the A1 region ($\bar{\pi} < 36$), having 26 of them a normalized flammability index below 0.

On the high flammability side, mixtures 53-54 (CO_2 + R1150), with an angle of 67.98 and 69.00, respectively, lie at the frontier between 2 and 3 regions ($60 < \bar{\pi} < 77$) [276]. These predictions are aligned with the estimates given by ASHRAE guidelines, shown in **Figure 8.10a**, which indicate that a mixture with 30 wt% R1150 becomes highly flammable. Unfortunately, the flammability of mixtures 55-59 seems to be slightly

underestimated, as a R1150 concentration above 30% should result in a high flammability classification, while the ANN' predictions provide intermediate values. The calculations were carried out based on expressions provided in **Eqs. E1** and supplemented with insights from both HOC [139,262,276] and LFL [559,560] KPIs.

Figure 8.10b further corroborates the ANN findings for blends 41-48, all assigned to A2/A3 safety classifications and consequently excluded from consideration. Notably, despite uncertainties in CO_2 blends with R1123 (18-21), R1132(E) (28-30), and R1150 (53-59), the predicted flammability indexes are consistent with empirical evidence from previous studies [48,561].

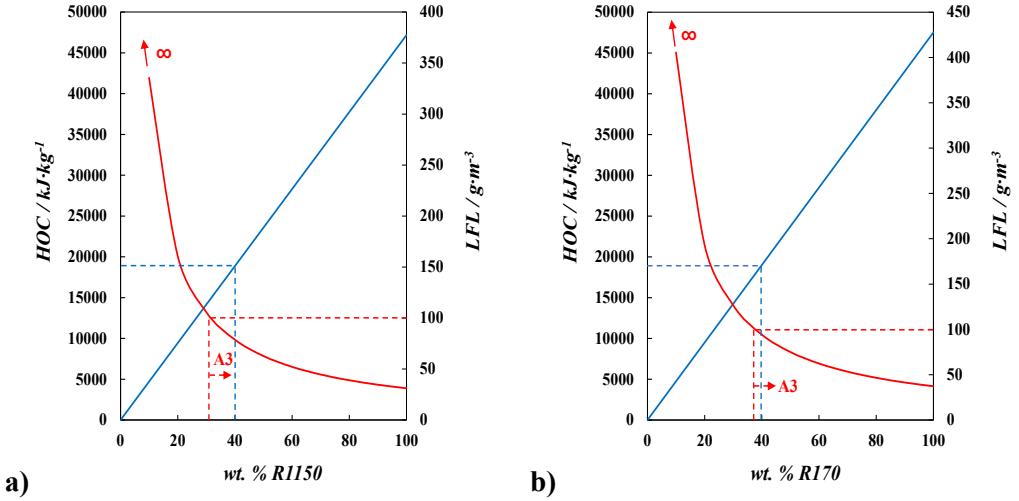

Figure 8.10. *Traditional ASHRAE methodology for delineating the boundary between flammability classes 2 and 3 for mixtures of CO_2 with **a)** R1150 and **b)** R170.*

On balance, since mixtures 56, 57, 58, and 59 are excluded due to proven uncertainty concerns, forty-three CO_2-based mixtures, along with pure CO_2, are selected, representing 69% of the total blends listed in **Table 8.1**, with only 15.9% of the blends originally screened being considered for further assessment

Beyond its main use on the hunt of binary CO_2-based mixtures with novel refrigerants (**Chapter 8.1**), the ANN model offers broad utility in exploring potential multicomponent alternatives to prevalent used R410A and R134a refrigerants [49,228]. As a further example of the capacity of the ANN, novel ternary blends comprised of CO_2, hydrocarbons, and F-based refrigerants are shown in **Figure 8.11**, elucidating the interplays among pure compounds at the vertices and binary mixtures along the edges. As

observed, all formulated mixtures incorporate CO_2 as a consistent component, complemented by commercialized carbon-based hydrocarbons R600a, R1270, or R290, and paired with F-based refrigerants covering all flammability ranges, as indicated in the Figure. Additional ternary diagrams in **Figures E2c, g-h, l-m** can be found in the **Annex**.

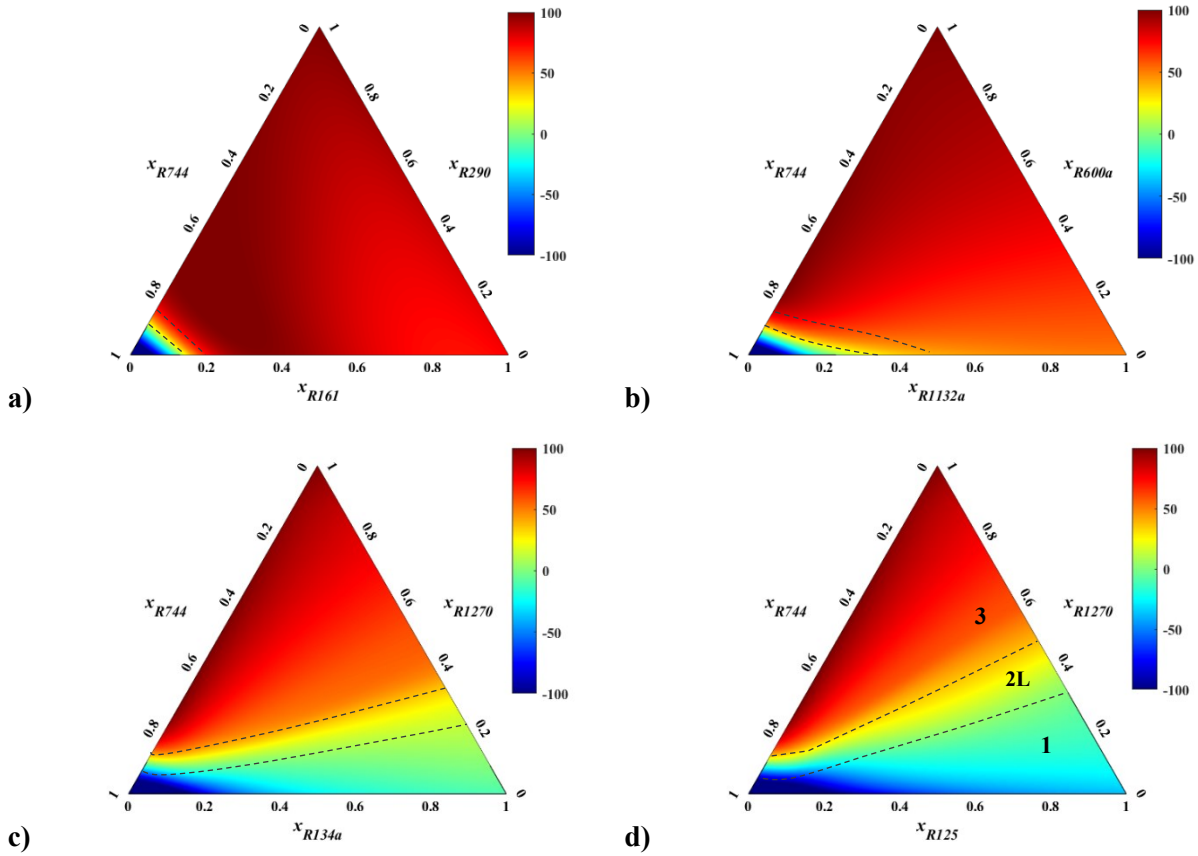

Figure 8.11. *Ternary contour plots by multitask ANN, showing predictions of NFI for CO_2 blends, including* ***a)*** *R290 + R161 (A3),* ***b)*** *R600a + R1132a (A2),* ***c)*** *R1270 + R134a (A1), and* ***d)*** *R1270 + R125 (A1).*

The analytical results reveal the influence of selected compounds' properties on the resulting mixtures [562]. CO_2, for instance, lowers both GWP and flammability, but increases the pressure and decreases the efficiency of the cycle. On the contrary, HCs, all with an A3 ASHRAE rating, lower GWP but increase flammability, while HFCs and HFOs exhibit a mixed set of attributes, underscoring the necessity for novel combinations.

From the results illustrated in **Figure 8.11**, it is observed that the choice of HC is not a primary factor in determining flammability, as all the considered carbon-based compounds are categorized under A3. Specifically, R1270 yields the lowest flammability, followed closely by R290 and R600a trailing behind. However, the choice and inherent

influence of F-based compounds, ranging from A1 to A3, has a more substantial impact on the resulting NFI of the assessed mixtures, with specific requirements on CO_2 composition to achieve desired flammability indices, along with constraints on GWP. Certainly, the mapping of the A1 flammability region, indicated in intense blue colormap, identifies a sequence of refrigerants by ignition propensity, ordered as R125 (A1) < R134a (A1) < R1234yf (A2L) ~ R1234ze(E) (A2L) < R1132a (A2) < R161 (A3).

In the case of A3 F-based refrigerants, a minimum mole composition of 90% CO_2 is required within the blend to achieve an A1 flammability index, irrespective of the hydrocarbon portion. This requirement for CO_2 could be reduced to 80% when A2-classified refrigerants (*e.g.,* R1132a) are mixed up with the same base constituents, leading to a refrigerant mixture with enhanced safety and maintenance features. However, utilizing A2L refrigerants like R1234yf or R1234ze(E) [563] grants even greater flexibility in designing A1 blends, allowing CO_2 compositions from a minimum of 75%. Concurrently, the percentage of hydrocarbon is restricted to a maximum of 15 mol%, a constraint that could be elevated to 20 – 25 mol% when using A1-classified F-based refrigerants (*e.g.,* R134a or R125). Indeed, within the formulation of refrigerant blends, it is consistently observed that the limiting factor governing the flammability of refrigerant blends invariably depends on the concentration of the carbon-based component. This constituent emerges as the maximum permissible concentration that can be added to the mixture, in accordance with the NFI contours in **Figure 8.11**, a threshold beyond which flammability becomes a paramount concern. Even though A3 refrigerants bear a degree of limitation akin to that of R1270, R600a, or R290. This highlights the critical role of hydrocarbons in the overall blend design in terms of safety.

Overall, the predicted results, although exploratory in nature, align with reasonable expectations, thus reinforcing the reliability of the model, while also providing a structured framework to guide the formulation of refrigerant blends that reconcile flammability, environmental, and safety requirements.

8.2. 4E Assessment of promising CO_2-based binary mixtures

Finally, the 43 mixtures from the upper quadrant of **Figure 8.9** meeting the required environmental, technical, and safety criteria (see **Figure 8.1**), are selected for further evaluation. Their performance in a sub-critical cascade cycle is evaluated

according to the specifications and working conditions depicted in **Figure 8.12**. In this assembly (see **Figure 3.6** and **Figure 3.7**), a refrigerant used in the high-temperature circuit serves both to supply medium-temperature services in addition to condense the fluid from the low-temperature service cycle, with the performance of drop-in mixture number 5 (as detailed in **Chapter 6.2.2**) being simulated for this regard. The objective is twofold: to substitute pure CO_2 with enhanced CO_2-based mixtures in the lower stage of the cascade cycle, in addition to introduce low-GWP drop-in refrigerants in the high-temperature circuit, thereby achieving a complete transition.

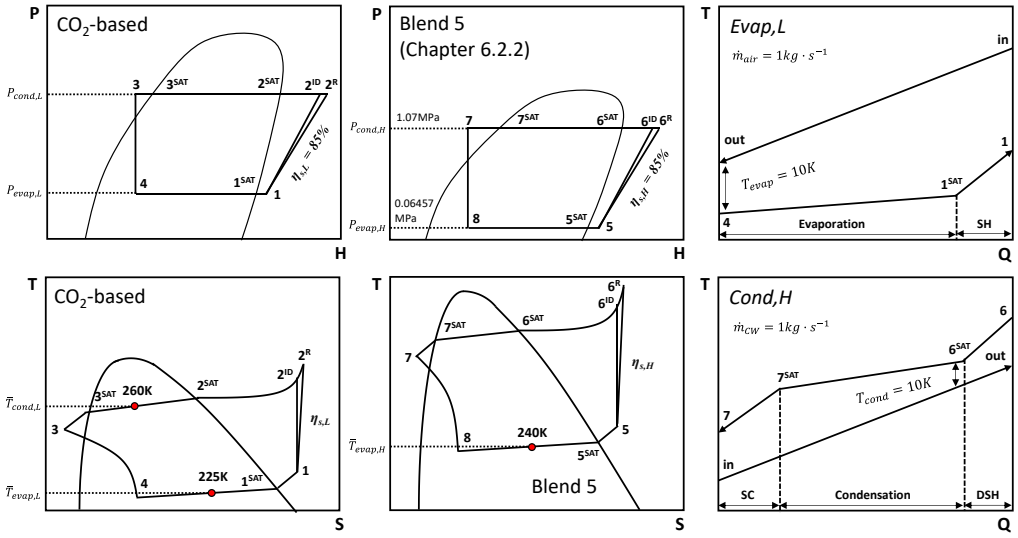

Figure 8.12. *Schematics of the cascade cycle simulated in this sub-section, including PH, TS, and pinch (TQ) diagrams for the CO_2-based/Blend 5 (**Table 6.1**) pair. Refer to **Figure 3.6** for nomenclature details.*

As depicted in **Figure 8.12**, the condenser and evaporator average temperatures are held constant (refer to **Eqs. (3.34)** and **(3.35)** in the methodology section). This is driven by the thermodynamic principles behind cascade cycles, where the pressure of the high-stage condenser (1.07 MPa) needs to exceed that of the low-stage evaporator (ranging from 0.2857 MPa for mixture 21 to 0.971 MPa for mixture 52) and be lower than that of the low-stage condenser (1.087 MPa to 2.92 MPa for mixtures 21 and 52, respectively), finding in the high-stage evaporator the lowest pressure at 0.0645 MPa. Temperature gradients are uniformly maintained across all evaluated blends, regardless of zeotropic behaviors or applied superheating (2.5 K) and subcooling (5.0 K) degrees. Additionally, all CO_2-based mixtures are operated within the temperature range of 216.8 to 304.2 K to prevent trans-critical scenarios, which would otherwise require the use of the crossover term in the polar soft-SAFT implementation for an accurate property

estimation. In the upper stage, simulations are performed with an average evaporator temperature of 321.26 K, peaking at 339.35 K at the compressor outlet stream, all falling within the temperature range for the near-azeotropic blend (refer to **Table 6.1**). The detailed iterative flowchart is presented in **Figure 3.7**, with formulas sourced from previous works of *Mota-Babiloni et al.* in **Eqs. (3.33)-(3.35)** [92,564,565].

The 4E analysis of CO_2 and its blends, is summarized in **Figure 8.13** and **Figure 8.14** in the form of an ordered heat map, identifying each mixture with a number, and providing valuable insights into their performance across key criteria.

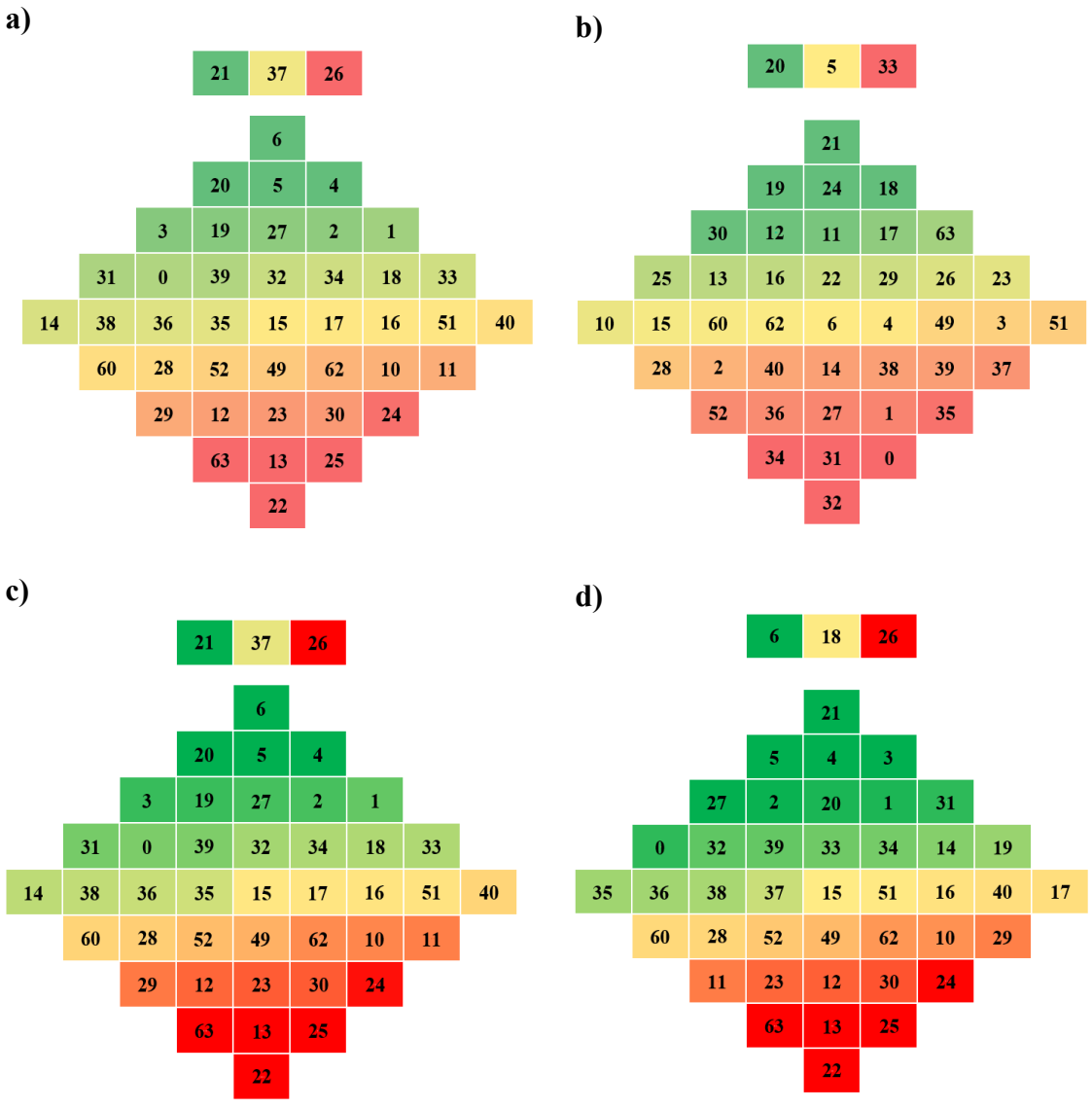

Figure 8.13. *4E on* ***a)*** *COP,* ***b)*** η_{II}, ***c)*** *TEWI, and* ***d)*** *TAC. The heatmap represents the 10th, 50th, and 90th percentile, with green for optimal blends and red the least favorable. The three mixtures at the top denote the optimal, middle (50th percentile), and least effective. Refer to* ***Figure 8.14*** *for the complete dataset.*

#	*DLT* *K*	P_{cond} *MPa*	P_R -	*VCC* $kJ \cdot L^{-1}$	*COP* -	$\sum x_d$ *kW*	η_{II} %	TEWI tCO_2	TAC $k\$ \cdot y^{-1}$
0	299.9	2.44	0.30	5.27	1.05	7.29	23.5	355.6	30.16
1	300.5	2.34	0.30	5.02	1.05	7.27	23.6	355.2	30.14
2	301.3	2.20	0.30	4.74	1.05	7.24	23.8	354.8	30.12
3	302.1	2.07	0.29	4.47	1.05	7.23	23.9	354.6	30.11
4	302.1	1.95	0.29	4.24	1.06	7.20	24.0	353.5	30.03
5	302.1	1.84	0.29	4.02	1.06	7.19	24.1	353.0	29.98
6	301.7	1.75	0.29	3.83	1.06	7.17	24.1	352.3	29.93
10	309.6	2.12	0.27	4.17	1.02	7.42	24.2	365.3	30.98
11	314.3	1.83	0.25	3.56	1.02	7.35	25.1	365.9	31.12
12	312.6	1.83	0.25	3.48	1.01	7.38	25.1	367.9	31.31
13	315.9	1.99	0.24	3.55	0.99	7.63	24.6	377.1	31.99
14	299.3	2.30	0.30	4.89	1.05	7.29	23.8	356.5	30.25
15	299.4	2.14	0.29	4.44	1.04	7.28	24.1	357.7	30.38
16	298.8	1.96	0.28	4.04	1.04	7.24	24.5	358.0	30.44
17	297.8	1.79	0.27	3.66	1.04	7.21	24.9	358.0	30.47
18	295.9	1.61	0.27	3.31	1.05	7.14	25.2	356.3	30.37
19	293.5	1.44	0.27	2.96	1.05	7.08	25.5	354.6	30.27
20	290.5	1.26	0.26	2.62	1.06	7.04	25.6	352.8	30.14
21	286.8	1.09	0.26	2.28	1.06	7.00	25.6	350.8	29.97
22	317.2	2.00	0.24	3.54	0.99	7.67	24.4	378.6	32.10
23	308.2	2.10	0.26	4.03	1.01	7.48	24.3	368.7	31.26
24	312.8	1.78	0.24	3.19	1.00	7.50	25.3	374.7	31.93
25	315.0	1.97	0.24	3.50	0.99	7.63	24.6	377.6	32.04
26	315.7	2.04	0.24	3.56	0.98	7.71	24.3	379.9	32.19
27	297.4	2.35	0.31	5.04	1.05	7.26	23.7	354.8	30.11
28	298.9	2.19	0.29	4.51	1.04	7.34	23.9	359.8	30.52
29	302.6	1.98	0.27	3.83	1.02	7.42	24.4	366.3	31.10
30	304.8	1.76	0.26	3.30	1.01	7.40	25.2	368.7	31.40
31	297.0	2.47	0.31	5.28	1.05	7.29	23.5	355.5	30.16
32	294.7	2.46	0.31	5.23	1.05	7.31	23.5	356.1	30.21
33	292.4	2.43	0.31	5.14	1.05	7.31	23.5	356.3	30.23
34	290.5	2.38	0.32	4.98	1.05	7.30	23.5	356.3	30.23
35	288.9	2.29	0.32	4.78	1.05	7.31	23.6	356.8	30.28
36	287.2	2.20	0.32	4.55	1.05	7.30	23.7	356.7	30.28
37	285.6	2.08	0.31	4.29	1.04	7.30	23.7	357.1	30.32
38	283.7	1.95	0.31	4.01	1.05	7.29	23.8	356.6	30.29
39	281.6	1.80	0.31	3.70	1.05	7.27	23.7	355.6	30.21
40	295.3	2.71	0.32	5.65	1.04	7.34	23.8	359.1	30.46
49	299.4	2.18	0.29	4.40	1.03	7.38	24.0	362.0	30.71
51	297.3	2.73	0.32	5.74	1.04	7.30	23.9	358.1	30.39
52	294.6	2.92	0.33	5.99	1.03	7.39	23.7	361.1	30.61
60	299.9	2.12	0.29	4.38	1.04	7.31	24.1	359.3	30.50
62	307.1	2.19	0.27	4.33	1.02	7.43	24.1	364.9	30.94
63	315.9	1.91	0.24	3.44	0.99	7.59	24.7	376.3	31.96

Figure 8.14. *Complete heatmap of technical and 4E KPIs for assessing novel CO_2-based mixtures. Refer to* ***Table 8.1*** *for nomenclature details.*

Notably, the heat map of technical KPIs (columns 1-4 in **Figure 8.14)** reveals that, while blends 31, 40, 51, and 52 enhance CO_2's *VCC* and *DLT* performance, they present drawbacks in terms of increased condensing pressure and pressure ratios. In contrast, blends 14-21 and 28 demonstrate a balanced improvement in *DLT* while reducing CO_2's excessive condensing pressure, with mixture 16 standing out for the optimal inverse trade-off between *VCC* and P_{cond}, highlighting its potential.

Under the 4E analysis, 12 mixtures outperform pure CO_2 (identified as number 1) in both energy and environmental performance (this means they are ranked better than mixture 1 in the heat map), 42 mixtures exhibit superior exergy efficiency, and 11 present improved economic prospects. Mixture 21 [(80/20) wt.% R1123 + CO_2] stands out as a leading candidate, achieving top rankings in *COP* and *TEWI*, and securing second place in both TAC and exergy efficiency.

In terms of exergy efficiency, mixture 25 [(10/90) wt.% R1234ze(E) + CO_2] secures a near top-ten position, despite ranking the third-worst performer across all 3E KPIs (*COP*, TEWI, and TAC). Similarly, mixtures 22 [(10/90) wt.% R1243zf + CO_2] and 26 [(10/90) wt.% R1225ye(Z) + CO_2], also among the lowest overall, achieve top quartile results for exergy efficiency. This discrepancy arises as exergy efficiency mainly focuses on the quality of energy utilization and minimizing irreversibilities to maximize useful work, whereas other metrics may be influenced by a broader range of system factors. However, and as explored in previous **Sections 6.2.2.3/4**, **7.2**, and **7.3.2**, improvements in energy and exergy metrics generally lead to reductions in indirect emissions and operational costs (OPEX), leading to a decrease in the annual costs of the air-conditioning system.

The total irreversibility rate (see column 6 in **Figure 8.14**) at a dead temperature of 303.15 K is 7.03 kW for the most efficient blend [(70/30) wt.% R1123 + CO_2], representing a 3.8% reduction relative to the rate of mixture 33 (the worst one). The distribution of irreversibility across individual components varies, with compressors accounting for 18.4–19.0%, condensers 21.0–21.8%, expansion valves 30.6–31.3%, evaporators 10.6–11.5%, and internal heat exchangers 17.7–18.0%. Notably, the greatest irreversibilities are associated with the expansion valve and the condenser in the upper circuit, with their combined contribution reaching a local minimum of 3.50 kW. This highlights the need for targeted optimization to enhance overall system efficiency. The correlation of these findings with energy, environmental, and economic KPIs is evident (as also appreciated in **Section 6.2.2.3/4/5**), revealing a clear trade-off among properties. For instance, mixtures 20 and 21 emerge as frontrunners, while mixture 6 excels in minimizing irreversibility while optimizing *COP*, TEWI, and TAC ratios. Conversely, blends 13, 22, 25-26, and 63 exhibit reduced performance in these metrics, with *COP* values consistently below 1.

To identify the best-performing mixture, the TOPSIS method is employed, assigning equal weights of 50% to both technical and 4E KPIs based on the noise-to-signal ratio of each response. Note that for *VCC*, *COP*, η_{II}, the response is maximized (see **Eq. (3.82)**), while a minimization of noise to signal ratio (see **Eq. (3.83)**) is targeted for remaining KPIs. The distances to the ideal and anti-ideal solutions, along with the relative closeness, are calculated using **Eqs. (3.88)-(3.90)** and the weights specified in

Table D2. The analysis in **Table 8.6** shows that pure CO_2 ranks 37th, placing it towards the lower end of the performance spectrum. In contrast, blends 21, 20, and 19 secure the top three positions on the podium, while blends 52, 40, and 51 are ranked at the lower end of the list. Certainly, over 30 mixtures have the potential to replace CO_2 in cascade refrigeration cycles, offering enhancements in pressure ratios and 4E KPIs, while maintaining comparable *VCC* values.

Table 8.6. *Distances to the TOPSIS ideal solution (D_i^+) and anti-ideal solution (D_i^-), along with the relative closeness (C_i) and ranking of the CO_2-based blends listed in* ***Table 8.1***.

#	D_i^+	D_i^-	C_i	Rank	#	D_i^+	D_i^-	C_i	Rank
0	0.002968	0.001969	0.3988	37	25	0.002286	0.002368	0.5088	17
1	0.002751	0.002033	0.4249	34	26	0.002403	0.002236	0.4820	22
2	0.002498	0.002161	0.4638	27	27	0.002793	0.001990	0.4161	35
3	0.002267	0.002323	0.5062	18	28	0.002524	0.002068	0.4504	30
4	0.002069	0.002499	0.5471	12	29	0.002231	0.002327	0.5106	16
5	0.001913	0.002670	0.5827	7	30	0.001995	0.002724	0.5773	8
6	0.001794	0.002833	0.6123	5	31	0.003035	0.001911	0.3863	38
10	0.002399	0.002204	0.4788	23	32	0.003053	0.001868	0.3796	40
11	0.001997	0.002725	0.5772	9	33	0.003019	0.001844	0.3791	41
12	0.002025	0.002674	0.5691	10	34	0.002933	0.001846	0.3863	39
13	0.002313	0.002342	0.5032	19	35	0.002806	0.001882	0.4014	36
14	0.002699	0.002027	0.4289	32	36	0.002653	0.001961	0.4250	33
15	0.002404	0.002185	0.4762	24	37	0.002481	0.002094	0.4576	28
16	0.002132	0.002433	0.5330	14	38	0.002307	0.002281	0.4972	21
17	0.001910	0.002731	0.5884	6	39	0.002141	0.002525	0.5412	13
18	0.001756	0.003060	0.6354	4	40	0.003596	0.001784	0.3315	43
19	0.001691	0.003407	0.6683	3	49	0.002539	0.002030	0.4443	31
20	0.001726	0.003763	0.6856	2	51	0.003622	0.001831	0.3358	42
21	0.001856	0.004129	0.6899	1	52	0.004117	0.001868	0.3121	44
22	0.002336	0.002313	0.4975	20	60	0.002400	0.002161	0.4738	26
23	0.002410	0.002171	0.4740	25	62	0.002523	0.002080	0.4519	29
24	0.002063	0.002721	0.5687	11	63	0.002198	0.002475	0.5297	15

8.3. Summary of key outcomes from Chapter 8

The results presented in this chapter highlight the value of the methodology proposed along the thesis to select an optimal refrigerant, being in this case extended to non-fluorinated substances, such as CO_2, in ultra-low temperature freezing applications and cascade refrigeration systems.

In the search for CO_2-based refrigerant mixtures to replace pure CO_2 a 4E analysis has been carried out, in a similar manner as done in previous chapters for F-gases blends. The lack of information to evaluate the flammability of these systems was overcome by developing an ANN model to predict the Normalized Flammability Index, achieving exceptional predictive accuracy with an R^2 of 0.999, an RMSE of 0.1735, and an AARD% of 0.8091. Further validation was achieved through the applicability domain analysis, demonstrating that 97.67% of the total 3D space was encompassed within the AD, a coverage that extends to 99.36% when considering borderline outliers.

In sub-critical cascade cycle tests, a total of 43 mixtures met the required environmental, technical, and safety criteria, with blends 31 [(10/90) wt.% R1132a + CO_2], 40 [(10/90) wt.% R170 + CO_2], 51 [(10/90) wt.% R1150 + CO_2], and 52 [(20/80) wt.% R1150 + CO_2] enhancing CO_2's *VCC* and *DLT*, but also leading to increased condensing pressures. Overall, twelve mixtures outperformed pure CO_2 in energy and environmental performance, 42 showed superior exergy efficiency, and 11 found improved economic prospects. Mixture 21 [(80/20) wt.% R1123 + CO_2] was notable for its high *COP* and TEWI rankings, while mixtures 22 [(10/90) wt.% R1243zf + CO_2] and 26 [(10/90) wt.% R1225ye(Z) + CO_2] excelled in exergy efficiency despite lower overall performance. The TOPSIS analysis confirmed Blend 21 stands out as the best option among all systems studied. In this manner, P_{cond} is improved by 55.3%, while exergy efficiency and TEWI enhance by 8.9% and 1.4%, respectively.

Chapter 9. Conclusions, Final Remarks and Future Work

This PhD thesis has been devoted to developing a comprehensive methodology, encompassing multiple simulation tools, to identify effective 4th generation drop-in refrigerants to replace high-GWP HFCs such as R32, R152a, R134a, R245fa, and R410A. This goal has been achieved by combining a variety of energy, exergy, environmental and economic (4E) analyses, as well as addressing issues related to the global warming potential and the flammability of blends. The proposed alternatives to current refrigerants have shown excellent compatibility and 4E performance in both simple vapor-compression systems and advanced air conditioning configurations. Promising retrofitting alternatives to CO_2 have also been tested, overcoming CO_2's safety limitations in sub-critical cascade cycles.

To tackle this challenge, the polar soft-SAFT molecular based equation of state was used for the thermodynamic characterization of refrigerants, fine-tuning the molecular parameters of 38 single-components including HFCs, HFOs, HCFOs, and hydrocarbons among others. A specific dipolar model was used to characterize all F-gas compounds. Such parametrization achieved high accuracy, with average deviations consistently below 1.0% in saturated liquid density and, in most cases, 3.0% in vapor pressure. The explicit inclusion of the dipolar interactions ensured a highly accurate and robust model, as demonstrated from predicted first and second order thermodynamic derivative properties. The enthalpy of vaporization closely matched experimental data with deviations under 3.0%, while single-phase densities aligned with molecular volumes, with R1233zd(E) exhibiting the lowest due to its size. Isobaric heat capacities were predicted within 5.0% of experimental values, with minimal errors within 1.0% observed for refrigerants like R601a and R1224yd(E). Alternatively, another method for obtaining the saturation properties of refrigerants involved the use of artificial neural networks, with deviations for co-existing densities and vapor pressure of 1.63% and 6.59%, respectively. Lastly, the polar soft-SAFT coarse-grain model demonstrated strong agreement with binary mixtures of polar + nonpolar azeotropic systems, and multi-polar compounds, achieving average absolute deviations of approximately 1.0%. For CO_2-based blends, the SAFT coarse-grain models accurately predicted solubility profiles across multiple isotherms, requiring only minor adjustments to the energy binary parameter.

Further thermodynamic studies, including a transferable parametrization of two families of common lubricants such as PECs and PEGDMEs, revealed that lubricant leaks (1-5% by weight) had a minimal impact on the energy efficiency of the cycle, with PEC5 resulting in a *COP* reduction of up to 3.0%, when paired with R513A. In contrast, TrEGDME, the most effective PEGDME, caused up to a 6.1% reduction in *COP*, being more suitable for other type of refrigerants.

The thermophysical behavior characterization served as a basis to perform a complete energy, exergy, environmental and economic 4E analysis to rapidly assess the suitability of 4th generation refrigerants over their 3rd generation counterparts, based on efficiency, flammability, emissions and economic KPIs.

The study was first applied to a basic compression refrigeration cycle (VCRC), doing a pre-screening looking for pure compound alternatives. The drop-in analysis for R134a indicated that R1234yf and R1234ze(E) provided adequate Volumetric Cooling Capacity (*VCC*) values within 5% of R134a, though leading to up to a 3% decrease in the Coefficient of Performance (*COP*). R1225ye(Z) showed a better balanced between performance and safety, with the added benefit of being non-flammable. Additionally, R1123 was identified as the most compatible replacement but for R32, even though experiencing a 6.8% reduction in *COP*. For R152a, compatible alternatives included R1234yf, R1243zf, R1234ze(E), and R1225ye(Z), all reaching *VCC* values within 5% of R152a but up to a 5% reduction in *COP*, while no competitive alternatives were found for R410A, apart from the 3rd generation R32 compound. Finally, when replacing high-temperature application R245fa, R1336mzz(Z), R1224yd(Z), and R1233zd(E) were selected as promising choices, with R1224yd(Z) offering balanced performance, improved suction density, and specific heat capacity.

In a second stage, the approach was extended to binary blends, with a focus on the two most common commercial refrigerants for drop-in, R134a and R410A. For the former, the mixture of HFOs R1243zf + R1234ze(E) (60/40) wt.% (identified as Blend 5 in this thesis) stood out as the most promising option, offering 90% compatibility, a GWP of 30, high efficiency, and energy and exergy performance nearly identical to R134a. Concerning R410A, the system R1123 + R32 (90/10) wt.% (identified as Blend 1), was found to be 73% compatible with R410A, comparable to R32, with a *VCC* at 90% of R410A, and a slightly higher discharge line temperature, highlighting the need for careful adjustments during retrofitting. The techno-economic analysis further demonstrated the need of raising taxes on HFC and carbon emissions to enhance the appeal of such low-GWP alternatives, with Blend 5 showing the most significant improvement in cost-effectiveness under higher tax rates. Similarly, Blend 1 required only a 3.2-fold increase in the HFC tax to align its annual costs with those of R410A.

A statistical analysis built on the use of soft-SAFT was adopted to evaluate the effect of design factors on the energy and exergy performance of air-conditioning cooling cycles. Using a two-level DoE with a fractional factorial design resolution, supported by ANOVA and polynomial response surface regression, the analysis ranked the design factors in descending order of importance as follows: $T_{cond} >> \eta_s >> T_{evap} >$ *refrigerant-*

type > s*ystem-type* > ΔT_{SH} > ΔT_{SC}. Further optimization using a three-level DoE enhanced heat transfer in the intercooler unit, resulting in a 21% increase in exergy efficiency, annual cost savings of $1,590 and a reduction in CO_2 emissions by 1.02 tons over a 15-year lifespan.

Furthermore, the impact of advanced cooling cycle configurations was evaluated using the same methodology. Results show that the use of LL/SL-HX cycles holds significant annual cost savings of $39 to $116 per unit, compared to the basic VCRC. In contrast, TS-VCRC offers considerable advantages in terms of energy and exergy efficiencies, with the potential for further enhancements through fine-tuning operating conditions. This results in improved energy and exergy efficiencies for all working fluids, along with a higher avoidable exergy rate. However, it comes with the trade-off of higher total annual costs, which increase by 8.0 to 10.0%, or $66.5 to $73.0 annually per unit, compared to the basic configuration. Despite the substantially higher CAPEX, the multi-compressor ensemble is more favourable in terms of energy, exergy, and environmental, especially when deployed as a new system.

The study in advanced cycles using the new proposed working fluids was completed by a detailed Life Cycle Analysis (LCA), focused on CO_2-eq emissions. The LCA revealed that the choice of refrigerant was the primary factor influencing GWP reduction, though. Specifically, replacing R410A with Blend 1 in a multi-compressor cycle led to a 23.7% decrease in GWP, while replacing R134a with Blend 5 from a basic to a TS-VCRC mode resulted in an 18.6% reduction. By 2050, the prospective LCA evaluation confirmed that high-GWP refrigerants will contribute more than 40% to GWP through direct and indirect emissions and production environmental costs, but can be mitigated to 10% or less with low- and mid-GWP agents.

The last part of this PhD thesis was focused on ultra-low refrigeration and, in particular, on finding suitable CO_2-based refrigerant mixtures for replacing pure carbon dioxide in sub-critical cascade applications. While the same approach done before was applied, the lack of flammability data was overcome by building an innovative ANN model, based on the σ-profiles from COSMO-RS as input descriptors, to predict the normalized flammability index. The ANN architecture demonstrated exceptional predictive performance, with metrics such as an R^2 of 0.999, RMSE of 0.1735, AARD%

of 0.8091, SD_{av} of ± 0.0434, and 81.3% of the dataset with SDR of ±1. Further validation was achieved through the applicability domain analysis, demonstrating that 97.67% of the total 3D space was encompassed within the AD, a coverage that extends to 99.36% when considering borderline outliers. Additionally, a second ANN-based model was also developed to predict the VLEs of CO_2-based mixtures with no experimental data, in order to have the required information for the energy/exergy calculations. The multitask model, based on the same type of descriptors, achieved high accuracy, with average absolute relative deviations under 3.5% for liquid and vapor phases, effectively handling 531 data combinations and showing minimal performance decline in dew phase predictions above 300 K. Outlier percentages for bubble and dew phase predictions were 2.63% and 2.44%, respectively, confirming the model's overall accuracy and effectiveness.

Following thorough validation, the flammability and thermophysical properties of CO_2-based mixtures was considered, resulting in the identification of 43 mixtures that met the required environmental, technical, and safety criteria. Twelve mixtures outperformed pure CO_2 in energy and environmental performance, 42 demonstrated superior exergy efficiency, and 11 showed improved economic prospects. Mixture 21 [(80/20) wt.% R1123 + CO_2] was particularly notable for its high *COP* and TEWI rankings, while mixtures [(10/90) wt.% R1243zf + CO_2] and 26 [(10/90) wt.% R1225ye(Z) + CO_2] excelled in exergy efficiency despite lower overall performance.

To sum up, the methodology developed and expanded in this thesis work is based first on the thermodynamic characterization of a series of fluids used in cooling systems using a variety of modeling tools, with the main focus in molecular-based equations of state and artificial neural networks. The study targeted two primary groups: commonly used refrigerant blends and additional promising agents in order to perform a systematic study of the required properties to be used as a sustainable refrigerant, aiming to meet low environmental impact criteria. Such framework supports the development of green and technically efficient refrigerant blends for retrofitting scenarios, assessing their performance in advanced refrigeration cycles—such as basic-VCRC, LL/SL-HX, multi-compression, and cascade systems for ultra-low temperature applications. To complete the process, the viability of the designed drop-in candidates is validated through a detailed techno-economic and life cycle assessment, supported by a machine learning-based approach to ensure appropriate safety characteristics.

The collective results presented herein not only demonstrate the ability of the proposed approach, built on molecular modeling, but also assists in rapidly examining the inherent trade-offs and potential challenges in selecting the next generation of sustainable refrigerants for climate change mitigation.

However, this thesis opens several interesting paths for future research, covering the following key areas, among others:

1. **Experimental Validation**: The next step involves testing the designed refrigerant blends as drop-in replacements for R134a, R410A, or CO_2. Additionally, the findings from this thesis should be validated by designing and implementing basic, advanced, and cascade-based VCRCs based on the specifications developed herein. It is also crucial to conduct flammability tests, adhering to ASHRAE standards, as detailed in **Chapter 8**.
2. **More in-depth Lubricant-Refrigerant Compatibility Evaluation**: Future work needs to be based on the compatibility of lubricants with the drop-in refrigerant blends developed in **Chapters 6** and **8**, focusing on enhanced solubility, miscibility, and viscosity. This should include commercial PECs commonly used in the AC market, such as PEC5, to ensure optimal performance and stability.
3. **Extend to Ternary Mixtures**: Future research should expand beyond single-component and binary mixtures to include ternary, quaternary, and superior complex blends as potential drop-in candidates.
4. **Advanced Molecular Modeling**: There is a need to apply molecular simulations to the design of new refrigerant molecules. Given the innovative nature of some refrigerants discussed in this thesis—many of which are not yet commercially available—molecular simulations could significantly impact the development of future refrigerants.
5. **Enhanced ANN-Based Approaches**: Implementing an artificial neural network approach to estimate the saturation properties of an extended database is crucial, as properly discussed in this thesis. Moving beyond the limited ANN model for CO_2-based mixtures, future work should include a

more diverse range of refrigerant blends. Developing deep-learning models that encompass a broad spectrum of compounds will enhance the extrapolative capabilities of the model, offering substantial benefits to the air conditioning industry. Exploring ANN-based methods like Graph Neural Networks or Recurrent Neural Networks could also provide valuable insights.

6. **Comprehensive Life Cycle Assessment**: A forward-looking life cycle assessment should consider a range of 2050 scenarios beyond those based solely on the Paris Agreement estimates. To address potential variations in global temperatures, it is essential to explore a spectrum of temperature scenarios and integrate these into a comprehensive LCA to ensure a more robust evaluation of refrigerants across diverse future conditions.

Outcomes from this PhD in terms of publications in indexed journals and contributions to scientific meetings

Papers published during the development of this thesis

1. Ismail II Alkhatib, Margarida L Ferreira, **Carlos G Albà**, Daniel Bahamon, Fèlix Llovell, Ana B Pereiro, João MM Araújo, Mohammad RM Abu-Zahra, Lourdes F Vega. (2020). Screening of Ionic Liquids and Deep Eutectic Solvents for Physical CO_2 Absorption by Soft-SAFT Using Key Performance Indicators. *Journal of Chemical & Engineering Data*, 65(12), 5844-5861. https://doi.org/10.1021/acs.jced.0c00750

2. Ismail *II* Alkhatib, **Carlos G Alba**, Daniel Bahamon, Fèlix Llovell, Lourdes F Vega. (2020). Assessing the Feasibility of Deep Eutectic Solvents for CO_2 Capture From Molecular And Process Modeling. https://doi.org/10.2118/202909-MS

3. Ismail II Alkhatib, Daniel Bahamon, **Carlos G Albà**, Fèlix Llovell, Lourdes F Vega. (2021). Thermodynamic and Process Modeling of Deep Eutectic Solvents for CO_2 Capture and Separation at Industrial Condition. http://dx.doi.org/10.2139/ssrn.3820933

4. **Carlos G Albà**, Fèlix Llovell, Lourdes F Vega. (2021). Searching for suitable lubricants for low global warming potential refrigerant R513A using molecular-based models: Solubility and performance in refrigeration cycles. *International Journal of Refrigeration*, 128, 252-263. https://doi.org/10.1016/j.ijrefrig.2021.04.010

5. **Carlos G Albà**, Ismail II Alkhatib, Fèlix Llovell, Lourdes F Vega. (2021). Assessment of low global warming potential refrigerants for drop-in replacement by connecting their molecular features to their performance. *ACS Sustainable Chemistry & Engineering*, 9(50), 17034-17048. https://doi.org/10.1021/acssuschemeng.1c05985

6. Ismail II Alkhatib, **Carlos G Albà**, Ahmad S Darwish, Fèlix Llovell, Lourdes F Vega. (2022). Searching for sustainable refrigerants by bridging molecular modeling with machine learning. *Industrial & Engineering Chemistry Research*, 61(21), 7414-7429. https://doi.org/10.1021/acs.iecr.2c00719
7. **Carlos G Albà**, Ismail II Alkhatib, Fèlix Llovell, Lourdes F Vega. (2023). *Hunting sustainable refrigerants fulfilling technical, environmental, safety and economic requirements. Renewable and Sustainable Energy Reviews*, 188, 113806. https://doi.org/10.1016/j.rser.2023.113806
8. **Carlos G Albà**, Ismail II Alkhatib, Fèlix Llovell, Lourdes F Vega. (2024). A novel approach for designing efficient and sustainable cooling cycles with low global warming potential refrigerants. *Applied Thermal Engineering*, 246, 122895. https://doi.org/10.1016/j.applthermaleng.2024.122895
9. **Carlos G Albà**, Ismail II Alkhatib, Lourdes F Vega, Fèlix Llovell. (2024). Mapping the Flammability Space of Sustainable Refrigerant Mixtures through an Artificial Neural Network Based on Molecular Descriptors. *ACS Sustainable Chemistry & Engineering*, 12(31), 11561–11577. https://doi.org/10.1021/acssuschemeng.4c01961
10. **Carlos G Albà**, Ismail II Alkhatib, Lourdes F Vega, Fèlix Llovell. (2024). US provisional Application No. 63/406,114 WO 2024/057105 A1 patent
11. Ismail II Alkhatib, **Carlos G Albà**, Fèlix Llovell, Lourdes F Vega. (2024). The Delicate Balance between Energy, Exergy, Cost and Environmental Impact to find Sustainable Cooling Systems: Refrigerants and Cycles. *Applied Thermal Engineering*. (*Accepted*)
12. **Carlos G Albà**, Ismail II Alkhatib, Lourdes F Vega, Fèlix Llovell. (TBD). Machine Learning Integration in Thermodynamics: Predicting CO_2 Mixture Saturation Properties for Sustainable Refrigeration Applications. *Journal of Chemical Information and Modeling*. (*Submitted*)
13. **Carlos G Albà**, Ismail II Alkhatib, Lourdes F Vega, Fèlix Llovell. (TBD). Modeling of 4th Generation CO_2-based Refrigerant Blends and their Performance

in Cascade Compression Refrigeration Cycles by means of the Polar soft-SAFT. *Energy*. (*In Preparation*)

14. **Carlos G Albà**, Ismail II Alkhatib, Lourdes F Vega, JD Medrano-García, G Guillen-Gosalbez, Fèlix Llovell. (TBD). Environmental Footprint of Cooling Systems: LCA of Drop-Ins in Advanced Cycles. *Green Chemistry*. (*In Preparation*)

Contributions to scientific meetings

1. **Carlos G Albà**, Fèlix Llovell, Lourdes F Vega. (2020, November 16-20). Solubility of low Global Warming Potential Refrigerant R513A in Lubricants and Analysis of their Performance in Refrigeration Cycles [*Virtual-Oral Presentation*]. 14th Mediterranean Congress of Chemical Engineering, Barcelona, Spain

2. **Carlos G Albà**, Ismail II Alkhatib, Lourdes F Vega, Fèlix Llovell. (2021, June 20-25). Assessment on low GWP Azeotropic Mixtures and Analysis of their Performance in Refrigeration Cycles by means of the Polar soft-SAFT EoS [*Virtual-Oral Presentation*]. 21st Symposium on Thermophysical Properties, Boulder (CO), United States of America

3. **Carlos G Albà**, Ismail II Alkhatib, Lourdes F Vega, Fèlix Llovell. (2021, July 5-9). Study of the Solubility of 4th Generation Refrigerant R513A with Compatible Lubricants and their Performance in Refrigeration Cycles using the Polar Soft-SAFT EoS [*Virtual-Oral Presentation*]. 31st European Symposium on Applied Thermodynamics 2021 (ESAT), Paris, France

4. **Carlos G Albà**. (2021, September 14-17). A multiscale modeling strategy for the selection of new low-GWP refrigerants in cooling systems [*Oral Presentation*]. 14th Mediterranean Congress of Chemical Engineering 2021, Barcelona, Spain

5. **Carlos G Albà**, Ismail II Alkhatib, Lourdes F Vega, Fèlix Llovell. (2022, July 17-20). Thermodynamic design of low-GWP drop-in replacements for R134a and

R410A by means of the polar soft-SAFT EoS [*Oral Presentation*]. 32nd European Symposium on Applied Thermodynamics 2022 (ESAT), Graz, Austria

6. **Carlos G Albà**, Ismail II Alkhatib, Yuting Li, Lourdes F Vega, Fèlix Llovell. (2022, September 7-9). Role of molecular theory in investigating phase and interfacial properties of azeotropic blends of fluorinated refrigerants [*Oral Presentation*]. 27th Thermodynamics Conference, Bath, United Kingdom

7. **Carlos G Albà**, Ismail II Alkhatib, Lourdes F Vega, Fèlix Llovell. (2022, November 13-18). Rational Design of Low Global Warming Potential Drop-in Replacements through a 3E Analysis [*Oral Presentation*]. 2022 AIChE Annual Meeting, Phoenix (AZ), United States of America

8. **Carlos G Albà**, Ismail II Alkhatib, Lourdes F Vega, Fèlix Llovell. (2023, May 18). Rational Design of Low Global Warming Potential Drop-in Replacements through a 4E (Energy, Exergy, Environmental and Economics) Analysis [*Poster Presentation*]. URV 2023 Doctoral Day, Tarragona, Spain

9. **Carlos G Albà**, Ismail II Alkhatib, Lourdes F Vega, Fèlix Llovell. (2023, May 21-25). Rational Design of Low Global Warming Potential Drop-in Replacements through a 4E (Energy, Exergy, Environmental and Economics) Analysis [*Poster Presentation*]. 2023 PPEPPD Congress, Tarragona, Spain

10. **Carlos G Albà**, Ismail II Alkhatib, Lourdes F Vega, Fèlix Llovell. (2023, May/June 30-2). On the hunt for sustainable refrigerants fulfilling technical, environmental, safety and economic requirement by using robust models [*Oral Presentation*]. 2023 Mediterranean Congress of Chemical Engineering, Barcelona, Spain

11. **Carlos G Albà**, Ismail II Alkhatib, Lourdes F Vega, Fèlix Llovell. (2023, September 10-13). On the hunt for sustainable refrigerants fulfilling technical, environmental, safety and economic requirement by using robust models [*Oral Presentation*]. ECTP 2023, Venice, Italy

12. **Carlos G Albà**, Ismail II Alkhatib, Lourdes F Vega, Fèlix Llovell. (2023, September 13-15). On the hunt for sustainable refrigerants fulfilling technical, environmental, safety and economic requirement by using robust models [*Oral Presentation*]. XXXVII Jornadas Nacionales de Ingeniería Química, Castelló de la Plana, Spain

13. **Carlos G Albà**, Ismail II Alkhatib, Fèlix Llovell, Lourdes F Vega. (2023, October-December). Towards Sustainable Cooling: The Role of 4E Analysis and Molecular Thermodynamics in the Design of low-GWP Refrigerant drop-in Alternatives [*Oral Presentation*]. RICH Internal Seminars, Abu Dhabi, United Arab Emirates

14. **Carlos G Albà**, Ismail II Alkhatib, Fèlix Llovell, Lourdes F Vega. (2023, November 25). Rational Design of Low-GWP Refrigerants as Drop-in Replacements through 4E Analysis using Robust Thermodynamic Models [*Oral Presentation*]. 1st UAE Thermo-Fluids Day, Abu Dhabi, United Arab Emirates

15. **Carlos G Albà**. (2023, December). [*Attendance*]. COP28-UAE, Dubai, United Arab Emirates

16. **Carlos G Albà**, Ismail II Alkhatib, Lourdes F Vega, Fèlix Llovell. (2024, May 16). Unveiling Sustainable Cooling Solutions: A 4E Analysis of Next-Generation Blends and Advanced AC Cycles [*Poster Presentation*]. URV 2024 Doctoral Day, Tarragona, Spain

17. **Carlos G Albà**, Ismail II Alkhatib, Lourdes F Vega, Fèlix Llovell. (2024, June 9-12). A Computational Approach to Assess the Flammability of Refrigerant Mixtures using Artificial Neural Networks Strategies [*Poster Presentation*]. 33rd European Symposium on Applied Thermodynamics 2024 (ESAT), Edinburgh, United Kingdom

18. **Carlos G Albà**, Ismail II Alkhatib, Lourdes F Vega, Fèlix Llovell. (2024, June 9-12). The Role of 4E Analysis and Thermodynamic Modeling in the Rational Design of Low-GWP Refrigerants as Drop-in Replacements [*Oral Presentation*].

33rd European Symposium on Applied Thermodynamics 2024 (ESAT), Edinburgh, United Kingdom

19. **Carlos G Albà**, Ismail II Alkhatib, Lourdes F Vega, Fèlix Llovell. (2024, June 23-28). Rational Design of Low-GWP Drop-in Replacements through a 4E Analysis using Robust Thermodynamic Models [*Poster Presentation*]. 22nd Symposium on Thermophysical Properties, Boulder (CO), United States of America

20. **Carlos G Albà**, Ismail II Alkhatib, Lourdes F Vega, Fèlix Llovell. (2024, June 23-28). Mapping the Flammability Space of Complex Refrigerant Mixtures Through Artificial Neural Networks based on Molecular Descriptors [*Oral Presentation*]. 22nd Symposium on Thermophysical Properties, Boulder (CO), United States of America
21. **Carlos G Albà**, Ismail II Alkhatib, Lourdes F Vega, Fèlix Llovell. (2024, September 9-12). A Comprehensive Framework for Designing Low-GWP Refrigerant drop-ins: A Thermodynamic and Environmental Analysis with Soft-SAFT and LCA [*Poster Presentation*]. XIII EQUIFASE, Évora, Portugal

22. **Carlos G Albà**, Ismail II Alkhatib, Lourdes F Vega, Fèlix Llovell. (2024, September 9-12). Innovative AI Applications in Thermodynamic Modeling of CO_2-based Mixtures [*Poster Presentation*]. XIII EQUIFASE, Évora, Portugal

References

[1] Assessing the Global Climate in February 2024 | News | National Centers for Environmental Information (NCEI), (2024).

[2] FacilityExecutive, The Future Of Cooling, (2022).

[3] IEA, The Future of Cooling – Analysis - IEA, (2022).

[4] Climate Central, Hotter Climate, Higher Cooling Demand | Climate Central, (2023).

[5] IEA, Cooling - Fuels & Technologies - IEA, 2022.

[6] M.O. McLinden, M.L. Huber, (R)Evolution of Refrigerants, J. Chem. Eng. Data. 65 (2020) 4176–4193. doi:10.1021/acs.jced.0c00338.

[7] J. González, F. Llovell, J.M. Garrido, H. Quinteros-Lama, A study of the optimal conditions for organic Rankine cycles coupled with vapour compression refrigeration using a rigorous approach based on the Helmholtz energy function, Energy. 285 (2023) 129554. doi:10.1016/j.energy.2023.129554.

[8] M. Ndamé Ngangué, N. Nguefack Lekané, J.P. Njock, O.T. Sosso, P. Stouffs, Working fluid selection for a high efficiency integrated power/cooling system combining an organic Rankine cycle and vapor compression-absorption cycles, Energy. 277 (2023). doi:10.1016/j.energy.2023.127709.

[9] L. Zhao, W. Cai, X. Ding, W. Chang, Model-based optimization for vapor compression refrigeration cycle, Energy. 55 (2013) 392–402. doi:10.1016/j.energy.2013.02.071.

[10] A. Ustaoglu, Parametric study of absorption refrigeration with vapor compression refrigeration cycle using wet, isentropic and azeotropic working fluids: Conventional and advanced exergy approach, Energy. 201 (2020) 117491. doi:10.1016/j.energy.2020.117491.

[11] X. Yin, X. Wang, S. Li, W. Cai, Energy-efficiency-oriented cascade control for vapor compression refrigeration cycle systems, Energy. 116 (2016) 1006–1019. doi:10.1016/j.energy.2016.10.059.

[12] X. Wang, J. Yu, M. Zhou, X. Lv, Comparative studies of ejector-expansion vapor compression refrigeration cycles for applications in domestic refrigerator-freezers, Energy. 70 (2014) 635–642. doi:10.1016/j.energy.2014.04.076.

[13] M. Elakhdar, B.M. Tashtoush, E. Nehdi, L. Kairouani, Thermodynamic analysis of a novel Ejector Enhanced Vapor Compression Refrigeration (EEVCR) cycle, Energy. 163 (2018) 1217–1230. doi:10.1016/j.energy.2018.09.050.

[14] R. Selbaş, Ö. Kizilkan, A. Şencan, Thermoeconomic optimization of subcooled and superheated vapor compression refrigeration cycle, Energy. 31 (2006) 2108–2128. doi:10.1016/j.energy.2005.10.015.

[15] H. Zhang, L. Tong, Z. Zhang, Y. Song, J. Yang, Y. Yue, Z. Wu, Y. Wang, Z. Yu,

J. Zhang, A integrated mechanical vapor compression enrichment system of radioactive wastewater: Experimental study, model optimization and performance prediction, Energy. 282 (2023). doi:10.1016/j.energy.2023.128868.

[16] M.Q. Zeng, Q.Y. Zheng, X.L. Zhang, F.Y. Mo, X.R. Zhang, Thermodynamic analysis of a novel multi-target temperature transcritical CO2 ejector-expansion refrigeration cycle with vapor-injection, Energy. 259 (2022) 125016. doi:10.1016/j.energy.2022.125016.

[17] J. Wang, Y. Dai, L. Gao, Parametric analysis and optimization for a combined power and refrigeration cycle, Appl. Energy. 85 (2008) 1071–1085. doi:10.1016/j.apenergy.2008.02.014.

[18] M. Khennich, N. Galanis, M. Sorin, Effects of design conditions and irreversibilities on the dimensions of ejectors in refrigeration systems, Appl. Energy. 179 (2016) 1020–1031. doi:10.1016/j.apenergy.2016.07.053.

[19] A. Grauberger, D. Young, T. Bandhauer, Off-design performance of an organic Rankine-vapor compression cooling cycle using R1234ze(E), Appl. Energy. 321 (2022) 119421. doi:10.1016/j.apenergy.2022.119421.

[20] A.K.S. Al-Sayyab, A. Mota-Babiloni, J. Navarro-Esbrí, Performance evaluation of modified compound organic Rankine-vapour compression cycle with two cooling levels, heating, and power generation, Appl. Energy. 334 (2023). doi:10.1016/j.apenergy.2023.120651.

[21] J.H. KOH, Z. ZAKARIA, Hydrocarbons as Refrigerants—A Review, ASEAN J. Sci. Technol. Dev. 34 (2017) 35. doi:10.29037/ajstd.73.

[22] R. Ciconkov, Refrigerants: There is still no vision for sustainable solutions, Int. J. Refrig. 86 (2018) 441–448. doi:10.1016/J.IJREFRIG.2017.12.006.

[23] IPCC, Summary for Policy Makers., in: V. Masson-Delmotte, P. Zhai, Y. Chen, L. Goldfarb, M.I. Gomis, J.B.R. Matthews, S. Berger, M. Huang, O. Yelekçi, R. Yu, B. Zhou, E. Lonnoy, T.K. Maycock, T. Waterfield, K. Leitzell, N. Caud (Eds.), Clim. Chang. 2021 Phys. Sci. Basis, Cambridge University Press, 2021.

[24] D. of Commerce, https://www.climate.gov/news-features/understanding-climate/climate-change-global-temperature Consulted [10/08/2024].

[25] G. Raabe, Molecular simulation studies on refrigerants past – present – future, Fluid Phase Equilib. 485 (2019) 190–198. doi:10.1016/j.fluid.2018.12.022.

[26] J.M. Calm, The next generation of refrigerants – Historical review, considerations, and outlook, Int. J. Refrig. 31 (2008) 1123–1133. doi:10.1016/j.ijrefrig.2008.01.013.

[27] N. Abas, A.R. Kalair, N. Khan, A. Haider, Z. Saleem, M.S. Saleem, Natural and synthetic refrigerants, global warming: A review, Renew. Sustain. Energy Rev. 90 (2018) 557–569. doi:10.1016/j.rser.2018.03.099.

[28] J.M. Calm, D.A. Didion, Trade-offs in refrigerant selections: past, present, and future, Int. J. Refrig. 21 (1998) 308–321. doi:10.1016/S0140-7007(97)00089-3.

[29] Z. Yang, B. Feng, H. Ma, L. Zhang, C. Duan, B. Liu, Y. Zhang, S. Chen, Z. Yang, Analysis of lower GWP and flammable alternative refrigerants, Int. J. Refrig. 126 (2021) 12–22. doi:10.1016/j.ijrefrig.2021.01.022.

[30] V. Nair, HFO refrigerants: A review of present status and future prospects., Int. J. Refrig. 122 (2021) 156–170. doi:10.1016/j.ijrefrig.2020.10.039.

[31] B.K. Sovacool, S. Griffiths, J. Kim, M. Bazilian, Climate change and industrial F-gases: A critical and systematic review of developments, sociotechnical systems and policy options for reducing synthetic greenhouse gas emissions, Renew. Sustain. Energy Rev. 141 (2021) 110759. doi:10.1016/j.rser.2021.110759.

[32] U. Nations, F. Convention, C. Change, U. States, M. Protocol, T.U. States, U. Parties, I. Panel, C. Change, N. Greenhouse, G. Inventories, Executive Summary, 4 (2015) 1–29.

[33] UN Environment Ozone Secretariat, Ratification of the Kigali Amendment, United Nations Environ. Program. (2017).

[34] G.J.M. Velders, J.S. Daniel, S.A. Montzka, I. Vimont, M. Rigby, P.B. Krummel, J. Muhle, S. O'Doherty, R.G. Prinn, R.F. Weiss, D. Young, Projections of hydrofluorocarbon (HFC) emissions and the resulting global warming based on recent trends in observed abundances and current policies, Atmos. Chem. Phys. 22 (2022) 6087–6101. doi:10.5194/acp-22-6087-2022.

[35] G.J.M. Velders, D.W. Fahey, J.S. Daniel, S.O. Andersen, M. McFarland, Future atmospheric abundances and climate forcings from scenarios of global and regional hydrofluorocarbon (HFC) emissions, Atmos. Environ. 123 (2015) 200–209. doi:10.1016/j.atmosenv.2015.10.071.

[36] EU, Directive, E. U. "40/EC of the European parliament and of the council of 17 May 2006 relating to emissions from air-conditioning systems in motor vehicles." Official J EU L 161 (2006): 12-18., (2016).

[37] M. Schulz, D. Kourkoulas, Regulation (EU) No 517/2014 of the European Parliament and of the Council of 16 April 2014 on fluorinated greenhouse gases and repealing Regulation (EC) No 842/2006, Off. J. Eur. Union. 2014 (2014) L150/195-230. doi:https://doi.org/10.4271/1999-01-0874.

[38] A. Mota-Babiloni, J. Navarro-Esbrí, P. Makhnatch, F. Molés, Refrigerant R32 as lower GWP working fluid in residential air conditioning systems in Europe and the USA, Renew. Sustain. Energy Rev. 80 (2017) 1031–1042. doi:10.1016/j.rser.2017.05.216.

[39] D. Wu, B. Hu, R.Z. Wang, Vapor compression heat pumps with pure Low-GWP refrigerants, Renew. Sustain. Energy Rev. 138 (2021). doi:10.1016/j.rser.2020.110571.

[40] Graaf, D. D., Elsner, C., Hoffmann, G., Martens, K., Thalheim, D., & Plehn, W. (2021). Hydrofluorocarbon emission reduction. A crucial contribution to climate protection. Proposals to enhance European climate ambition.

[41] US-EPA, US Environmental Protection Agency. "EPA and NHTSA set standards

to reduce greenhouse gases and improve fuel economy for model years 2017–2025 cars and light trucks.," (2012).

[42] US-EPA, Environmental Protection Agency. "Protection of stratospheric ozone: Change of listing status for certain substitutes under the significant new alternatives policy program; final rule." Federal Register, Rules and Regulations (2015): 80., (2015).

[43] AIM Act | US EPA.

[44] P. Purohit, L. Höglund-Isaksson, Global emissions of fluorinated greenhouse gases 2005–2050 with abatement potentials and costs, Atmos. Chem. Phys. 17 (2017) 2795–2816. doi:10.5194/acp-17-2795-2017.

[45] J. Lin, N. Khanna, X. Liu, W. Wang, J. Gordon, F. Dai, Opportunities to tackle short-lived climate pollutants and other greenhouse gases for China, Sci. Total Environ. 842 (2022) 156842. doi:10.1016/j.scitotenv.2022.156842.

[46] S.J. Darby, G.P. Hammond, J. Wu, Briefing: Stocktaking global warming: the outcomes of the 2023 Dubai Climate Summit (COP28), Proc. Inst. Civ. Eng. - Energy. (2024) 1–12. doi:10.1680/jener.24.00005.

[47] A. Kazakov, M.O. McLinden, M. Frenkel, Computational design of new refrigerant fluids based on environmental, safety, and thermodynamic characteristics, Ind. Eng. Chem. Res. 51 (2012) 12537–12548. doi:10.1021/ie3016126.

[48] M.O. McLinden, J.S. Brown, R. Brignoli, A.F. Kazakov, P.A. Domanski, Limited options for low-global-warming-potential refrigerants, Nat. Commun. 8 (2017) 14476. doi:10.1038/ncomms14476.

[49] C.G. Albà, I.I.I. Alkhatib, F. Llovell, L.F. Vega, Assessment of Low Global Warming Potential Refrigerants for Drop-In Replacement by Connecting their Molecular Features to Their Performance, ACS Sustain. Chem. Eng. 9 (2021) 17034–17048. doi:10.1021/acssuschemeng.1c05985.

[50] ASHRAE, ANSI/ASHRAE standard 34–2016 designation and safety classification of refrigerants., (2016).

[51] X. Wu, C. Dang, S. Xu, E. Hihara, State of the art on the flammability of hydrofluoroolefin (HFO) refrigerants, Int. J. Refrig. 108 (2019) 209–223. doi:10.1016/j.ijrefrig.2019.08.025.

[52] P. Giménez-Prades, J. Navarro-Esbrí, C. Arpagaus, A. Fernández-Moreno, A. Mota-Babiloni, Novel molecules as working fluids for refrigeration, heat pump and organic Rankine cycle systems, Renew. Sustain. Energy Rev. 167 (2022) 112549. doi:10.1016/j.rser.2022.112549.

[53] B.O. Bolaji, Z. Huan, Ozone depletion and global warming: Case for the use of natural refrigerant – a review, Renew. Sustain. Energy Rev. 18 (2013) 49–54. doi:10.1016/j.rser.2012.10.008.

[54] A.K. Vuppaladadiyam, E. Antunes, S.S.V. Vuppaladadiyam, Z.T. Baig, A. Subiantoro, G. Lei, S.Y. Leu, A.K. Sarmah, H. Duan, Progress in the development

and use of refrigerants and unintended environmental consequences, Sci. Total Environ. 823 (2022) 153670. doi:10.1016/j.scitotenv.2022.153670.

[55] K. Sanguri, K. Ganguly, A. Pandey, Modelling the barriers to low global warming potential refrigerants adoption in developing countries: A case of Indian refrigeration industry, J. Clean. Prod. 280 (2021) 124357. doi:10.1016/j.jclepro.2020.124357.

[56] K.M. Adamson, T.G. Walmsley, J.K. Carson, Q. Chen, F. Schlosser, L. Kong, D.J. Cleland, High-temperature and transcritical heat pump cycles and advancements: A review, Renew. Sustain. Energy Rev. 167 (2022) 112798. doi:10.1016/j.rser.2022.112798.

[57] P. Bansal, A review – Status of CO2 as a low temperature refrigerant: Fundamentals and R&D opportunities, Appl. Therm. Eng. 41 (2012) 18–29. doi:10.1016/j.applthermaleng.2011.12.006.

[58] F. Bruno, M. Belusko, E. Halawa, CO2 Refrigeration and Heat Pump Systems—A Comprehensive Review, Energies. 12 (2019) 2959. doi:10.3390/en12152959.

[59] K. Zolcer Skačanová, M. Battesti, Global market and policy trends for CO2 in refrigeration, Int. J. Refrig. 107 (2019) 98–104. doi:10.1016/j.ijrefrig.2019.08.010.

[60] T. Halon, B. Gil, B. Zajaczkowski, Comparative investigation of low-GWP binary and ternary blends as potential replacements of HFC refrigerants for air conditioning systems, Appl. Therm. Eng. 210 (2022) 118354. doi:10.1016/j.applthermaleng.2022.118354.

[61] G. Bamorovat Abadi, K.C. Kim, Investigation of organic Rankine cycles with zeotropic mixtures as a working fluid: Advantages and issues, Renew. Sustain. Energy Rev. 73 (2017) 1000–1013. doi:10.1016/j.rser.2017.02.020.

[62] R. Llopis, D. Sánchez, R. Cabello, J. Catalán-Gil, L. Nebot-Andrés, Experimental analysis of R-450A and R-513A as replacements of R- 134a and R-507A in a medium temperature commercial refrigeration system, Int. J. Refrig. 84 (2017) 52–66. doi:10.1016/j.ijrefrig.2017.08.022.

[63] P. Makhnatch, A. Mota-Babiloni, R. Khodabandeh, Experimental study of R450A drop-in performance in an r134a small capacity refrigeration unit, Int. J. Refrig. 84 (2017) 26–35. doi:10.1016/j.ijrefrig.2017.08.010.

[64] A. Mota-Babiloni, J. Navarro-Esbrí, A. Barragán-Cervera, F. Molés, B. Peris, Drop-in analysis of an internal heat exchanger in a vapour compression system using R1234ze(E) and R450A as alternatives for R134a, Energy. 90 (2015) 1636–1644. doi:10.1016/j.energy.2015.06.133.

[65] C. Aprea, A. Greco, A. Maiorino, Comparative performance analysis of HFO1234ze/ HFC134a binary mixtures working as a drop-in of HFC134a in a domestic refrigerator, Int. J. Refrig. 82 (2017) 71–82. doi:10.1016/j.ijrefrig.2017.07.001.

[66] C. Aprea, A. Greco, A. Maiorino, HFOs and their binary mixtures with HFC134a working as drop-in refrigerant in a household refrigerator: Energy analysis and

environmental impact assessment, Appl. Therm. Eng. 141 (2018) 226–233. doi:10.1016/j.applthermaleng.2018.02.072.

[67] K. Harby, Hydrocarbons and their mixtures as alternatives to environmental unfriendly halogenated refrigerants: An updated overview, Renew. Sustain. Energy Rev. 73 (2017) 1247–1264. doi:10.1016/j.rser.2017.02.039.

[68] V. Oruç, A.G. Devecioğlu, Experimental investigation on the low-GWP HFC/HFO blends R454A and R454C in a R404A refrigeration system, Int. J. Refrig. 128 (2021) 242–251. doi:10.1016/j.ijrefrig.2021.04.007.

[69] A. Mota-Babiloni, J. Haro-Ortuño, J. Navarro-Esbrí, Á. Barragán-Cervera, Experimental drop-in replacement of R404A for warm countries using the low GWP mixtures R454C and R455A, Int. J. Refrig. 91 (2018) 136–145. doi:10.1016/j.ijrefrig.2018.05.018.

[70] R. Llopis, D. Calleja-Anta, D. Sánchez, L. Nebot-Andrés, J. Catalán-Gil, R. Cabello, R-454C, R-459B, R-457A and R-455A as low-GWP replacements of R-404A: Experimental evaluation and optimization, Int. J. Refrig. 106 (2019) 133–143. doi:10.1016/j.ijrefrig.2019.06.013.

[71] K. Thu, K. Takezato, N. Takata, T. Miyazaki, Y. Higashi, Drop-in experiments and exergy assessment of HFC-32/HFO-1234yf/R744 mixture with GWP below 150 for domestic heat pumps, Int. J. Refrig. 121 (2021) 289–301. doi:10.1016/j.ijrefrig.2020.10.009.

[72] S. Karagoz, M. Yilmaz, O. Comakli, O. Ozyurt, R134a and various mixtures of R22/R134a as an alternative to R22 in vapour compression heat pumps, Energy Convers. Manag. 45 (2004) 181–196. doi:10.1016/S0196-8904(03)00144-4.

[73] J.L.C. Fannou, C. Rousseau, L. Lamarche, S. Kajl, A comparative performance study of a direct expansion geothermal evaporator using R410A and R407C as refrigerant alternatives to R22, Appl. Therm. Eng. 82 (2015) 306–317. doi:10.1016/j.applthermaleng.2015.02.079.

[74] Y. Heredia-Aricapa, J.M. Belman-Flores, A. Mota-Babiloni, J. Serrano-Arellano, J.J. García-Pabón, Overview of low GWP mixtures for the replacement of HFC refrigerants: R134a, R404A and R410A, Int. J. Refrig. 111 (2020) 113–123. doi:10.1016/j.ijrefrig.2019.11.012.

[75] A. Khalid Shaker Al-Sayyab, A. Mota-Babiloni, J. Navarro-Esbrí, Novel compound waste heat-solar driven ejector-compression heat pump for simultaneous cooling and heating using environmentally friendly refrigerants, Energy Convers. Manag. 228 (2021). doi:10.1016/j.enconman.2020.113703.

[76] A. Mota-Babiloni, J.M. Belman-Flores, P. Makhnatch, J. Navarro-Esbrí, J.M. Barroso-Maldonado, Experimental exergy analysis of R513A to replace R134a in a small capacity refrigeration system, Energy. 162 (2018) 99–110. doi:10.1016/j.energy.2018.08.028.

[77] Z. Roy, G. Halder, Replacement of halogenated refrigerants towards sustainable cooling system: A review, Chem. Eng. J. Adv. 3 (2020) 100027. doi:10.1016/j.ceja.2020.100027.

[78] H.K. Hsieh, T.P. Teng, Retrofit assessment of automobile air conditioners using hydrocarbon refrigerants, Appl. Therm. Eng. 214 (2022) 118781. doi:10.1016/J.APPLTHERMALENG.2022.118781.

[79] M. Ghanbarpour, A. Mota-Babiloni, B.E. Badran, R. Khodabandeh, Energy, Exergy, and Environmental (3E) Analysis of Hydrocarbons as Low GWP Alternatives to R134a in Vapor Compression Refrigeration Configurations, Appl. Sci. 11 (2021) 6226. doi:10.3390/app11136226.

[80] S. Gupta, S. Pendyala, Flammability issue of hydrocarbons in air conditioning industry, Mater. Today Proc. 28 (2020) 2247–2250. doi:10.1016/j.matpr.2020.04.555.

[81] M. Walid Faruque, M. Hafiz Nabil, M. Raihan Uddin, M. Monjurul Ehsan, S. Salehin, Thermodynamic assessment of a triple cascade refrigeration system utilizing hydrocarbon refrigerants for ultra-low temperature applications, Energy Convers. Manag. X. 14 (2022) 100207. doi:10.1016/j.ecmx.2022.100207.

[82] S. Kujak, K. Schultz, Insights into the next generation HVAC&R refrigerant future, Sci. Technol. Built Environ. 22 (2016) 1226–1237. doi:10.1080/23744731.2016.1203239.

[83] W.A. Fouad, L.F. Vega, Transport properties of HFC and HFO based refrigerants using an excess entropy scaling approach, J. Supercrit. Fluids. 131 (2018) 106–116. doi:10.1016/j.supflu.2017.09.006.

[84] C. Zilio, J.S. Brown, G. Schiochet, A. Cavallini, The refrigerant R1234yf in air conditioning systems, Energy. 36 (2011) 6110–6120. doi:10.1016/j.energy.2011.08.002.

[85] H. Cho, H. Lee, C. Park, Performance characteristics of an automobile air conditioning system with internal heat exchanger using refrigerant R1234yf, Appl. Therm. Eng. 61 (2013) 563–569. doi:10.1016/j.applthermaleng.2013.08.030.

[86] G.M. Kontogeorgis, R. Dohrn, I.G. Economou, J.C. De Hemptinne, A. Kate, S. Kuitunen, M. Mooijer, L.F. Zilnik, V. Vesovic, Industrial requirements for thermodynamic and transport properties: 2020, Ind. Eng. Chem. Res. 60 (2021) 4987–5013. doi:10.1021/acs.iecr.0c05356.

[87] R. Hardian, Z. Liang, X. Zhang, G. Szekely, Artificial intelligence: The silver bullet for sustainable materials development, Green Chem. 22 (2020) 7521–7528. doi:10.1039/d0gc02956d.

[88] K. Uddin, S. Arakaki, B.B. Saha, Thermodynamic analysis of low-GWP blends to replace R410A for residential building air conditioning applications, Environ. Sci. Pollut. Res. 28 (2021) 2934–2947. doi:10.1007/s11356-020-10656-9.

[89] J. Liu, F. Zhou, N. Lyu, H. Fan, X. Zhang, Analysis of low GWP ternary zeotropic mixtures applied in high-temperature heat pump for waste heat recovery, Energy Convers. Manag. 292 (2023) 117381. doi:10.1016/j.enconman.2023.117381.

[90] R. Mastrullo, A.W. Mauro, G. Napoli, F. Pelella, L. Viscito, Flow boiling of azeotropic and non-azeotropic mixtures. Effect of the glide temperature difference

on the nucleate boiling contribution: Assessment of methods, in: J. Phys. Conf. Ser., 2020: p. 012053. doi:10.1088/1742-6596/1599/1/012053.

[91] Y. Zhao, Z. Li, X. Zhang, X. Wang, X. Dong, B. Gao, M. Gong, J. Shen, Azeotropic refrigerants and its application in vapor compression refrigeration cycle, Int. J. Refrig. 108 (2019) 1–13. doi:10.1016/j.ijrefrig.2019.08.024.

[92] P. Makhnatch, A. Mota-Babiloni, R. Khodabandeh, The effect of temperature glide on the performance of refrigeration systems., in: 5th IIR Conf. Thermophys. Prop. Transf. Process. Refrig., 2017: p. 8. doi:10.18462/iir.tptpr.2017.0059.

[93] D.A. Didion, D.B. Bivens, Role of refrigerant mixtures as alternatives to CFCs, Int. J. Refrig. 13 (1990) 163–175. doi:10.1016/0140-7007(90)90071-4.

[94] K. Yamaya, A. Matsuguchi, N. Kagawa, S. Koyama, Isochoric Specific Heat Capacity of trans -1,3,3,3-Tetrafluoropropene (HFO-1234ze(E)) and the HFO-1234ze(E) + CO 2 Mixture in the Liquid Phase, J. Chem. Eng. Data. 56 (2011) 1535–1539. doi:10.1021/je101209e.

[95] Y. Maalem, A. Zarfa, Y. Tamene, S. Fedali, H. Madani, Prediction of thermodynamic properties of the ternary azeotropic mixtures, Fluid Phase Equilib. 517 (2020) 112613. doi:10.1016/j.fluid.2020.112613.

[96] C.G. Albà, L.F. Vega, F. Llovell, A consistent thermodynamic molecular model of n-hydrofluoroolefins and blends for refrigeration applications, Int. J. Refrig. 113 (2020) 145–155. doi:10.1016/j.ijrefrig.2020.01.008.

[97] С.В. Артеменко, Sustainable refrigerant selection in binary blends of the R1234YF – hydrofluoroethers, Eastern-European J. Enterp. Technol. 2 (2010) 42–47. doi:10.15587/1729-4061.2010.2701.

[98] B.O. Bolaji, Theoretical assessment of new low global warming potential refrigerant mixtures as eco-friendly alternatives in domestic refrigeration systems, Sci. African. 10 (2020) e00632. doi:10.1016/j.sciaf.2020.e00632.

[99] B. Yu, H. Ouyang, J. SHI, W. LIU, J. CHEN, Evaluation of low-GWP and mildly flammable mixtures as new alternatives for R410A in air-conditioning and heat pump system, Int. J. Refrig. 121 (2021) 95–104. doi:10.1016/j.ijrefrig.2020.09.018.

[100] A. Mota-Babiloni, P. Makhnatch, R. Khodabandeh, Recent investigations in HFCs substitution with lower GWP synthetic alternatives: Focus on energetic performance and environmental impact, Int. J. Refrig. (2017). doi:10.1016/j.ijrefrig.2017.06.026.

[101] T. Kamiaka, C. Dang, E. Hihara, Vapor-liquid equilibrium measurements for binary mixtures of R1234yf with R32, R125, and R134a, Int. J. Refrig. 36 (2013) 965–971. doi:10.1016/j.ijrefrig.2012.08.016.

[102] W.A. Fouad, L.F. Vega, Molecular modeling of the solubility of low global warming potential refrigerants in polyol ester lubricants, Int. J. Refrig. 103 (2019) 145–154. doi:10.1016/j.ijrefrig.2019.04.004.

[103] C.G. Albà, F. Llovell, L.F. Vega, Searching for suitable lubricants for low global

warming potential refrigerant R513A using molecular-based models: Solubility and performance in refrigeration cycles, Int. J. Refrig. 128 (2021) 252–263. doi:10.1016/j.ijrefrig.2021.04.010.

[104] S. Komatsuzaki, Y. Homma, Lubricants for HFC Refrigerant Compressors., J. Japan Pet. Inst. 37 (1994) 226–235. doi:10.1627/jpi1958.37.226.

[105] D. Philippon, M.-I. De Barros-Bouchet, T. Le Mogne, O. Lerasle, A. Bouffet, J.-M. Martin, Role of nascent metallic surfaces on the tribochemistry of phosphite lubricant additives, Tribol. Int. 44 (2011) 684–691. doi:10.1016/j.triboint.2009.12.014.

[106] I. Minami, Molecular Science of Lubricant Additives, Appl. Sci. 7 (2017) 445. doi:10.3390/app7050445.

[107] K.N. Marsh, M.E. Kandil, Review of thermodynamic properties of refrigerants + lubricant oils, Fluid Phase Equilib. 199 (2002) 319–334. doi:10.1016/S0378-3812(02)00025-0.

[108] X. Jia, J. Wang, X. Wang, Y. Hu, Y. Sun, Phase equilibrium of R1234yf and R1234ze(E) with POE lubricant and thermodynamic performance on the evaporator, Fluid Phase Equilib. 514 (2020) 112562. doi:10.1016/j.fluid.2020.112562.

[109] K. Górny, A. Stachowiak, P. Tyczewski, W. Zwierzycki, Lubricity evaluation of oil–refrigerant mixtures with R134a and R290, Int. J. Refrig. 69 (2016) 261–271. doi:10.1016/j.ijrefrig.2016.06.011.

[110] M. Youbi-Idrissi, J. Bonjour, C. Marvillet, F. Meunier, Impact of refrigerant–oil solubility on an evaporator performances working with R-407C, Int. J. Refrig. 26 (2003) 284–292. doi:10.1016/S0140-7007(02)00129-9.

[111] R. Zhai, Z. Yang, B. Feng, Miscibility performance of trans-1,3,3,3-tetrafluoroprop-1-ene and its binary blends with lubricating oil, Int. J. Refrig. 75 (2017) 95–103. doi:10.1016/j.ijrefrig.2016.12.016.

[112] M.A. Marcelino Neto, R.M. França, J.R. Barbosa, Convection-driven absorption of R-1234yf in lubricating oil, Int. J. Refrig. 44 (2014) 151–160. doi:10.1016/j.ijrefrig.2014.05.008.

[113] H. Tangri, N. Purohit, A. Sethi, R. Hulse, Solubility, miscibility and compatibility studies of low GWP non-flammable refrigerants and lubricants for refrigeration and air conditioning applications, Int. J. Refrig. 148 (2023) 45–63. doi:10.1016/j.ijrefrig.2022.12.022.

[114] Y. Sun, G. Di, J. Wang, X. Wang, M. He, Phase behavior of R1234yf and R600a in pentaerythritol tetranonanoate, Int. J. Refrig. 109 (2020) 135–142. doi:10.1016/j.ijrefrig.2019.10.005.

[115] Y. Sun, X. Wang, D. Wang, L. Jin, Measurement and correlation for phase equilibrium of HFO1234yf with three pentaerythritol esters from 293.15 K to 348.15 K, J. Chem. Thermodyn. 112 (2017) 122–128. doi:10.1016/j.jct.2017.04.020.

[116] Å. Wahlström, L. Vamling, Solubility of HFCs in Pentaerythritol Tetraalkyl Esters, J. Chem. Eng. Data. 45 (2000) 97–103. doi:10.1021/je990171n.

[117] Å. Wahlström, L. Vamling, Solubility of HFC32, HFC125, HFC134a, HFC143a, and HFC152a in a Pentaerythritol Tetrapentanoate Ester, J. Chem. Eng. Data. 44 (1999) 823–828. doi:10.1021/je980235e.

[118] X. Wang, Y. Sun, N. Gong, Experimental investigations for the phase equilibrium of R1234yf and R1234ze(E) with two linear chained pentaerythritol esters, J. Chem. Thermodyn. 92 (2016) 66–71. doi:10.1016/j.jct.2015.08.038.

[119] L. Herbe, P. Lundqvist, CFC and HCFC refrigerants retrofit — experiences and results, Int. J. Refrig. 20 (1997) 49–54. doi:10.1016/S0140-7007(96)00050-3.

[120] Y. Chen, J.-T. Hung, H.-H. Tang, J.-S. Tsaih, The Influence of Lubricant in HFC & HFO Blend Refrigeration system, 17th Int. Refrig. Air Cond. Conf. Purdue, 2341. (2018).

[121] J. Gill, J. Singh, O.S. Ohunakin, D.S. Adelekan, Exergy analysis of vapor compression refrigeration system using R450A as a replacement of R134a, J. Therm. Anal. Calorim. 136 (2019) 857–872. doi:10.1007/s10973-018-7675-z.

[122] J.M. Mendoza-Miranda, A. Mota-Babiloni, J. Navarro-Esbrí, Evaluation of R448A and R450A as low-GWP alternatives for R404A and R134a using a micro-fin tube evaporator model, Appl. Therm. Eng. 98 (2016) 330–339. doi:10.1016/j.applthermaleng.2015.12.064.

[123] A. Mota-Babiloni, J. Navarro-Esbrí, Á. Barragán-Cervera, F. Molés, B. Peris, Experimental study of an R1234ze(E)/R134a mixture (R450A) as R134a replacement, Int. J. Refrig. 51 (2015) 52–58. doi:10.1016/j.ijrefrig.2014.12.010.

[124] S.I. Tseregounis, M.J. Riley, Solubility of HFC-134a refrigerant in glycol-type compounds: Effects of glycol structure, AIChE J. 40 (1994) 726–737. doi:10.1002/aic.690400415.

[125] R. Zehioua, C. Coquelet, A.-H. Meniai, D. Richon, p − T − x Measurements for Some Working Fluids for an Absorption Heat Transformer: 1,1,1,2-Tetrafluoroethane (R134a) + Dimethylether Diethylene Glycol (DMEDEG) and Dimethylether Triethylene Glycol (DMETrEG), J. Chem. Eng. Data. 55 (2010) 2769–2775. doi:10.1021/je9009915.

[126] S.K. Chaudhari, D. Salavera, X. Esteve, A. Coronas, Vapour–liquid equilibria of the system 1,1,1,2-tetrafluoroethane+monoethylene-glycol dimethylether from 283.15 to 353.15K: New modified UNIFAC parameters, Fluid Phase Equilib. 271 (2008) 28–33. doi:10.1016/j.fluid.2008.07.003.

[127] E.R. López, A.M. Mainar, J. García, J.S. Urieta, J. Fernández, Experimental and Prediated Solubilities of HFC134a (1,1,1,2-Tetrafluoroethane) in Polyethers, Ind. Eng. Chem. Res. 43 (2004) 1523–1529. doi:10.1021/ie030623w.

[128] A. Coronas, A.M. Mainar, K.R. Patil, A. Conesa, S. Shen, S. Zhu, Solubility of 1,1,1,2-Tetrafluoroethane in Triethylene Glycol Dimethyl Ether, J. Chem. Eng. Data. 47 (2002) 56–58. doi:10.1021/je0101931.

[129] P. Marchi, G. Scalabrin, E.C. Ihmels, K. Fischer, J. Gmehling, P ρ Tx Measurements for (1,1,1,2-Tetrafluoroethane + Triethylene Glycol Dimethyl Ether) at High Haloalkane Content, J. Chem. Eng. Data. 51 (2006) 992–996. doi:10.1021/je050503q.

[130] E.R. López, A.M. Mainar, J.S. Urieta, J. Fernández, Solubility of HFC134a (1,1,1,2-Tetrafluoroethane) in Two Dialkyl Carbonates †, J. Chem. Eng. Data. 54 (2009) 2609–2615. doi:10.1021/je900138j.

[131] Y. Fang, W. Guan, K. Bao, Y. Wang, X. Han, G. Chen, Isothermal Vapor–Liquid Equilibria of the Absorption Working Pairs (R1234yf + NMP, R1234yf + DMETrEG) at Temperatures from 293.15 K to 353.15 K, J. Chem. Eng. Data. 63 (2018) 1212–1219. doi:10.1021/acs.jced.7b00821.

[132] S. Yadav, J. Liu, S.C. Kim, A comprehensive study on 21st-century refrigerants - R290 and R1234yf: A review, Int. J. Heat Mass Transf. 182 (2022) 121947. doi:10.1016/j.ijheatmasstransfer.2021.121947.

[133] A. Miyara, Developments of next generation refrigerants and heat transfer, MATEC Web Conf. 204 (2018) 00004. doi:10.1051/matecconf/201820400004.

[134] D. Sánchez, A. Andreu-Nácher, D. Calleja-Anta, R. Llopis, R. Cabello, Energy impact evaluation of different low-GWP alternatives to replace R134a in a beverage cooler. Experimental analysis and optimization for the pure refrigerants R152a, R1234yf, R290, R1270, R600a and R744, Energy Convers. Manag. 256 (2022) 115388. doi:10.1016/j.enconman.2022.115388.

[135] D. Sánchez, R. Cabello, R. Llopis, I. Arauzo, J. Catalán-Gil, E. Torrella, Energy performance evaluation of R1234yf, R1234ze(E), R600a, R290 and R152a as low-GWP R134a alternatives, Int. J. Refrig. 74 (2017) 269–282. doi:10.1016/j.ijrefrig.2016.09.020.

[136] N. Kumma, S.. H. Kruthiventi, Current status of refrigerants used in domestic applications: A review, Renew. Sustain. Energy Rev. 189 (2024) 114073. doi:10.1016/j.rser.2023.114073.

[137] L. Fedele, G. Lombardo, I. Greselin, D. Menegazzo, S. Bobbo, Thermophysical Properties of Low GWP Refrigerants: An Update, Int. J. Thermophys. 44 (2023) 80. doi:10.1007/s10765-023-03191-5.

[138] K. Braimakis, A. Mikelis, A. Charalampidis, S. Karellas, Exergetic performance of CO2 and ultra-low GWP refrigerant mixtures as working fluids in ORC for waste heat recovery, Energy. 203 (2020) 117801. doi:10.1016/j.energy.2020.117801.

[139] B. Dai, M. Li, Y. Ma, Thermodynamic analysis of carbon dioxide blends with low GWP (global warming potential) working fluids-based transcritical Rankine cycles for low-grade heat energy recovery, Energy. 64 (2014) 942–952. doi:10.1016/j.energy.2013.11.019.

[140] F. Zhou, T. Zhang, D. Wei, J. Liu, X. Zhang, Optimal refrigerant selection and parameter analysis of a wastewater heat pump using CO2 zeotropic mixtures, Appl. Therm. Eng. 253 (2024) 123789.

doi:10.1016/j.applthermaleng.2024.123789.

[141] E.W. Lemmon, M.L. Huber, M.O. McLinden, NIST standard reference database 23: reference fluid thermodynamic and transport properties (REFPROP), version 9.1, National Institute of Standards and Technology, Standard reference data program., (2010). http://www.nist.gov/srd/upload/REFPROP9.pdf.

[142] I.H. Bell, D. Riccardi, A. Bazyleva, M.O. McLinden, Survey of data and models for refrigerant mixtures containing halogenated olefins, J. Chem. Eng. Data. 66 (2021) 2335–2354. doi:10.1021/acs.jced.1c00192.

[143] G. Raabe, Molecular simulation data for the vapor-liquid phase equilibria of binary mixtures of HFO-1123 with R-32, R-1234yf, R-1234ze(E), R-134a and CO2 and their modelling by the PCP-SAFT equation of state, Data Br. 25 (2019) 104014. doi:10.1016/j.dib.2019.104014.

[144] M.S. Sadaghiani, A. Arami-Niya, B. Marsh, S.Z.S. Al Ghafri, E.F. May, Vapor–Liquid Equilibria for Carbon Dioxide + 3,3,3-Trifluoropropene Binary Mixtures at Temperatures between (288 and 348) K, J. Chem. Eng. Data. 66 (2021) 4044–4055. doi:10.1021/acs.jced.1c00297.

[145] H. Matsuda, T. Suga, T. Tsuji, K. Tochigi, K. Kurihara, A.K. Nelson, C. McCabe, Vapor-liquid equilibria for binary systems carbon dioxide + 1,1,1,2,3,3-hexafluoro-3-(2,2,2-trifluoroethoxy)propane or 1-ethoxy-1,1,2,2,3,3,4,4,4-nonafluorobutane at 303.15–323.15 K, Fluid Phase Equilib. 524 (2020) 112814. doi:10.1016/j.fluid.2020.112814.

[146] J. Luo, Z. Ye, Z. Zhao, K. Yang, S. Zhang, Q. Wang, Vapor-liquid equilibrium measurement and heating performance modeling on eco-friendly zeotropic blends of CO2/R1234ze(Z) and CO2/R1336mzz(E), Appl. Therm. Eng. 229 (2023) 120576. doi:10.1016/j.applthermaleng.2023.120576.

[147] J. El Abbadi, J. Brocus, A. Valtz, C. Coquelet, C. Houriez, Experimental Measurements and Modeling of Vapor–Liquid Equilibria for Eight Mixtures Containing trans -1-Chloro-3,3,3-trifluoropropene (R1233zd(E)) and 2-Chloro-3,3,3-trifluoropropene (R1233xf), J. Chem. Eng. Data. 68 (2023) 2316–2331. doi:10.1021/acs.jced.3c00296.

[148] X. Yang, A. Arami-Niya, X. Xiao, D. Kim, S.Z.S. Al Ghafri, T. Tsuji, Y. Tanaka, Y. Seiki, E.F. May, Viscosity Measurements of Binary and Multicomponent Refrigerant Mixtures Containing HFC-32, HFC-125, HFC-134a, HFO-1234yf, and CO 2, J. Chem. Eng. Data. 65 (2020) 4252–4262. doi:10.1021/acs.jced.0c00228.

[149] D. Kim, X. Yang, A. Arami-Niya, D. Rowland, X. Xiao, S.Z.S. Al Ghafri, T. Tsuji, Y. Tanaka, Y. Seiki, E.F. May, Thermal conductivity measurements of refrigerant mixtures containing hydrofluorocarbons (HFC-32, HFC-125, HFC-134a), hydrofluoroolefins (HFO-1234yf), and carbon dioxide (CO2), J. Chem. Thermodyn. 151 (2020) 106248. doi:10.1016/j.jct.2020.106248.

[150] L. Nebot-Andrés, J. Catalán-Gil, D. Sánchez, D. Calleja-Anta, R. Cabello, R. Llopis, Experimental determination of the optimum working conditions of a

transcritical CO2 refrigeration plant with integrated mechanical subcooling, Int. J. Refrig. 113 (2020) 266–275. doi:10.1016/j.ijrefrig.2020.02.012.

[151] P. Kasi, M. Cheralathan, Performance analysis of cascade refrigeration system with alternative refrigerants to reduce carbon emission, J. Therm. Anal. Calorim. 148 (2023) 4389–4399. doi:10.1007/s10973-023-11989-6.

[152] F. Alsouda, N.S. Bennett, S.C. Saha, F. Salehi, M.S. Islam, Vapor Compression Cycle: A State-of-the-Art Review on Cycle Improvements, Water and Other Natural Refrigerants, Clean Technol. 5 (2023) 584–608. doi:10.3390/cleantechnol5020030.

[153] R.. James, J.. Missenden, The use of propane in domestic refrigerators, Int. J. Refrig. 15 (1992) 95–100. doi:10.1016/0140-7007(92)90033-Q.

[154] B. Palm, Hydrocarbons as refrigerants in small heat pump and refrigeration systems – A review, Int. J. Refrig. 31 (2008) 552–563. doi:10.1016/j.ijrefrig.2007.11.016.

[155] E. Halimic, D. Ross, B. Agnew, A. Anderson, I. Potts, A comparison of the operating performance of alternative refrigerants, Appl. Therm. Eng. 23 (2003) 1441–1451. doi:10.1016/S1359-4311(03)00081-4.

[156] B. Saleh, M. Wendland, Screening of pure fluids as alternative refrigerants, Int. J. Refrig. 29 (2006) 260–269. doi:10.1016/j.ijrefrig.2005.05.009.

[157] Y.. Chang, M.. Kim, S.. Ro, Performance and heat transfer characteristics of hydrocarbon refrigerants in a heat pump system, Int. J. Refrig. 23 (2000) 232–242. doi:10.1016/S0140-7007(99)00042-0.

[158] C.-S. Jwo, C.-C. Ting, W.-R. Wang, Efficiency analysis of home refrigerators by replacing hydrocarbon refrigerants, Measurement. 42 (2009) 697–701. doi:10.1016/j.measurement.2008.11.006.

[159] J.D. Andrew Pon Abraham, M. Mohanraj, Thermodynamic performance of automobile air conditioners working with R430A as a drop-in substitute to R134a, J. Therm. Anal. Calorim. 136 (2019) 2071–2086. doi:10.1007/s10973-018-7843-1.

[160] M. Rasti, S. Aghamiri, M.-S. Hatamipour, Energy efficiency enhancement of a domestic refrigerator using R436A and R600a as alternative refrigerants to R134a, Int. J. Therm. Sci. 74 (2013) 86–94. doi:10.1016/j.ijthermalsci.2013.07.009.

[161] P.S. Arshi Banu, N.M. Sudharsan, Review of water based vapour absorption cooling systems using thermodynamic analysis, Renew. Sustain. Energy Rev. 82 (2018) 3750–3761. doi:10.1016/j.rser.2017.10.092.

[162] J. Reinvall, Refrigerants Used in Industrial Heat Pumps in the Future, (2024). https://www.theseus.fi/handle/10024/841623 (accessed August 26, 2024).

[163] M. Bentrcia, M. Alshitawi, H. Omar, Developmens of alternative systems for automotive air conditioning - A review, J. Mech. Sci. Technol. 32 (2018) 1857–1867. doi:10.1007/s12206-018-0342-2.

[164] B.J. Goetzler W, Sutherland T, Rassi M, Research & development roadmap for next-generation low global warming potential refrigerants, Build. Technol. Off. Off. Energy Effic. Renew. Energy, US Dep. Energy. (2014).

[165] S. Daviran, A. Kasaeian, S. Golzari, O. Mahian, S. Nasirivatan, S. Wongwises, A comparative study on the performance of HFO-1234yf and HFC-134a as an alternative in automotive air conditioning systems, Appl. Therm. Eng. 110 (2017) 1091–1100. doi:10.1016/j.applthermaleng.2016.09.034.

[166] B. Feng, Z. Yang, R. Zhai, Experimental study on the influence of the flame retardants on the flammability of R1234yf, Energy. 143 (2018) 212–218. doi:10.1016/j.energy.2017.10.078.

[167] P. Gullo, G. Cortella, Theoretical evaluation of supermarket refrigeration systems using R1234ze(E) as an alternative to high-global warming potential refrigerants, Sci. Technol. Built Environ. 22 (2016) 1145–1155. doi:10.1080/23744731.2016.1223996.

[168] A. Mota-Babiloni, J. Navarro-Esbrí, F. Molés, Á.B. Cervera, B. Peris, G. Verdú, A review of refrigerant R1234ze(E) recent investigations, Appl. Therm. Eng. 95 (2016) 211–222. doi:10.1016/j.applthermaleng.2015.09.055.

[169] H. Wang, L. Zhao, R. Cao, W. Zeng, Refrigerant alternative and optimization under the constraint of the greenhouse gas emissions reduction target, J. Clean. Prod. 296 (2021) 126580. doi:10.1016/j.jclepro.2021.126580.

[170] S. Bobbo, G. Di Nicola, C. Zilio, J.S. Brown, L. Fedele, Low GWP halocarbon refrigerants: A review of thermophysical properties, Int. J. Refrig. 90 (2018) 181–201. doi:10.1016/j.ijrefrig.2018.03.027.

[171] M. Klajmon, Purely Predicting the Pharmaceutical Solubility: What to Expect from PC-SAFT and COSMO-RS?, Mol. Pharm. 19 (2022) 4212–4232. doi:10.1021/acs.molpharmaceut.2c00573.

[172] F. Llovell, L.F. Vega, Prediction of thermodynamic derivative properties of pure fluids through the soft-SAFT equation of state, J. Phys. Chem. B. 110 (2006) 11427–11437. doi:10.1021/jp0608022.

[173] K. Albers, G. Sadowski, Minimal Experimental Data Set Required for Estimating PCP-SAFT Parameters, Ind. Eng. Chem. Res. 50 (2011) 11746–11754. doi:10.1021/ie2010803.

[174] M.L. Ferreira, J.M.M. Araújo, A.B. Pereiro, L.F. Vega, Insights into the influence of the molecular structures of fluorinated ionic liquids on their thermophysical properties. A soft-SAFT based approach, Phys. Chem. Chem. Phys. 21 (2019) 6362–6380. doi:10.1039/c8cp07522k.

[175] G. Raabe, Molecular Simulation Studies on the Vapor–Liquid Phase Equilibria of Binary Mixtures of R-1234yf and R-1234ze(E) with R-32 and CO 2, J. Chem. Eng. Data. 58 (2013) 1867–1873. doi:10.1021/je4002619.

[176] T. Yan, Y. Lan, M. Tong, C. Zhong, Screening and Design of Covalent Organic Framework Membranes for CO2/CH4 Separation, ACS Sustain. Chem. Eng. 7

(2019) 1220–1227. doi:10.1021/acssuschemeng.8b04858.

[177] F. Barzagli, C. Giorgi, F. Mani, M. Peruzzini, Screening Study of Different Amine-Based Solutions as Sorbents for Direct CO2 Capture from Air, ACS Sustain. Chem. Eng. 8 (2020) 14013–14021. doi:10.1021/acssuschemeng.0c03800.

[178] K.T. Leperi, Y.G. Chung, F. You, R.Q. Snurr, Development of a General Evaluation Metric for Rapid Screening of Adsorbent Materials for Postcombustion CO2 Capture, ACS Sustain. Chem. Eng. 7 (2019) 11529–11539. doi:10.1021/acssuschemeng.9b01418.

[179] G. Jing, Y. Qian, X. Zhou, B. Lv, Z. Zhou, Designing and Screening of Multi-Amino-Functionalized Ionic Liquid Solution for CO2 Capture by Quantum Chemical Simulation, ACS Sustain. Chem. Eng. 6 (2018) 1182–1191. doi:10.1021/acssuschemeng.7b03467.

[180] Z. Song, Z. Song, X. Hu, H. Wu, M. Mei, S. Linke, T. Zhou, T. Zhou, Z. Qi, K. Sundmacher, Systematic Screening of Deep Eutectic Solvents as Sustainable Separation Media Exemplified by the CO2 Capture Process, ACS Sustain. Chem. Eng. 8 (2020) 8741–8751. doi:10.1021/acssuschemeng.0c02490.

[181] D. Peng, A.J. Kleiweg, J.G.M. Winkelman, Z. Song, F. Picchioni, A Hierarchical Hybrid Method for Screening Ionic Liquid Solvents for Extractions Exemplified by the Extractive Desulfurization Process, ACS Sustain. Chem. Eng. 9 (2021) 2705–2716. doi:10.1021/acssuschemeng.0c07866.

[182] Z. Song, T. Zhou, Z. Qi, K. Sundmacher, Systematic Method for Screening Ionic Liquids as Extraction Solvents Exemplified by an Extractive Desulfurization Process, ACS Sustain. Chem. Eng. 5 (2017) 3382–3389. doi:10.1021/acssuschemeng.7b00024.

[183] Y. Wang, X. Yang, W. Bai, J. Zhang, X. Zhou, X. Guo, J. Peng, J. Qi, Z. Zhu, Screening of Imidazole Ionic Liquids for Separating the Acetone-n-Hexane Azeotrope by COSMO-SAC Simulations and Experimental Verification, ACS Sustain. Chem. Eng. 8 (2020) 4440–4450. doi:10.1021/acssuschemeng.9b07358.

[184] X. Liu, Y. Nie, Y. Liu, S. Zhang, A.L. Skov, Screening of Ionic Liquids for Keratin Dissolution by Means of COSMO-RS and Experimental Verification, ACS Sustain. Chem. Eng. 6 (2018) 17314–17322. doi:10.1021/acssuschemeng.8b04830.

[185] A. Fernández-Moreno, A. Mota-Babiloni, P. Giménez-Prades, J. Navarro-Esbrí, Optimal refrigerant mixture in single-stage high-temperature heat pumps based on a multiparameter evaluation, Sustain. Energy Technol. Assessments. 52 (2022) 101989. doi:10.1016/j.seta.2022.101989.

[186] A. Arami-Niya, X. Xiao, S.Z.S. Al Ghafri, F. Jiao, M. Khamphasith, E. Sadeghi Pouya, M.S. Sadaghiani, X. Yang, T. Tsuji, Y. Tanaka, Y. Seiki, E.F. May, Measurement and modelling of the thermodynamic properties of carbon dioxide mixtures with HFO-1234yf, HFC-125, HFC-134a, and HFC-32: vapour-liquid equilibrium, density, and heat capacity, Int. J. Refrig. 118 (2020) 514–528. doi:10.1016/j.ijrefrig.2020.05.009.

[187] X. Yang, D. Kim, E.F. May, I.H. Bell, Entropy Scaling of Thermal Conductivity: Application to Refrigerants and Their Mixtures, Ind. Eng. Chem. Res. 60 (2021) 13052–13070. doi:10.1021/ACS.IECR.1C02154/SUPPL_FILE/IE1C02154_SI_001.PDF.

[188] E.W. Lemmon, M.L. Huber, M.O. McLinden, NIST Reference Fluid Thermodynamic and Transport Properties — REFPROP, Version 9.0, National Institute of Standards and Technology, Gaithersburg, MD, 2013.

[189] W.G. Chapman, K.E. Gubbins, G. Jackson, M. Radosz, SAFT: Equation-of-State Solution Model for Associating Fluids, Fluid Phase Equilib. 52 (1989) 31–38. doi:10.1016/0378-3812(89)80308-5.

[190] C. Zhu, M. He, X. Liu, G.M. Kontogeorgis, X. Liang, Quantification of Dipolar Contribution and Modeling of Green Polar Fluids with the Polar Cubic-Plus-Association Equation of State, ACS Sustain. Chem. Eng. 9 (2021) 7602–7619. doi:https://doi.org/10.1021/acssuschemeng.1c01545.

[191] Y. Li, W.A. Fouad, L.F. Vega, Interfacial anomaly in low global warming potential refrigerant blends as predicted by molecular dynamics simulations, Phys. Chem. Chem. Phys. 21 (2019) 22092–22102. doi:10.1039/c9cp03231b.

[192] W.A. Fouad, L.F. Vega, The phase and interfacial properties of azeotropic refrigerants: The prediction of aneotropes from molecular theory, Phys. Chem. Chem. Phys. 19 (2017) 8977–8988. doi:10.1039/c6cp08031f.

[193] W.A. Fouad, Thermal Conductivity of Pure Fluids and Multicomponent Mixtures Using Residual Entropy Scaling with PC-SAFT - Application to Refrigerant Blends, J. Chem. Eng. Data. 65 (2020) 5688–5697. doi:10.1021/acs.jced.0c00682.

[194] I. Polishuk, E. Assor, N. Cohen, R. Potievsky, Implementation of PC-SAFT and SAFT + Cubic for modeling thermodynamic properties of haloalkanes. II. 7 Haloethanes and their mixtures, Int. J. Refrig. 36 (2013) 980–991. doi:10.1016/j.ijrefrig.2012.10.034.

[195] M. Lampe, M. Stavrou, J. Schilling, E. Sauer, J. Gross, A. Bardow, Computer-aided molecular design in the continuous-molecular targeting framework using group-contribution PC-SAFT, Comput. Chem. Eng. 81 (2015) 278–287. doi:10.1016/j.compchemeng.2015.04.008.

[196] O. Vilaseca, F. Llovell, J. Yustos, R.M. Marcos, L.F. Vega, Phase equilibria, surface tensions and heat capacities of hydrofluorocarbons and their mixtures including the critical region, J. Supercrit. Fluids. 55 (2010) 755–768. doi:10.1016/j.supflu.2010.10.015.

[197] A. Galindo, A. Gil-Villegas, P.J. Whitehead, G. Jackson, A.N. Burgess, Prediction of phase equilibria for refrigerant mixtures of difluoromethane (HFC-32), 1,1,1,2-tetrafluoroethane (HFC-134a), and pentafluoroethane (HFC-125a) using SAFT-VR, J. Phys. Chem. B. 102 (1998) 7632–7639. doi:10.1021/jp9809437.

[198] C. Avendaño, T. Lafitte, C.S. Adjiman, A. Galindo, E.A. Müller, G. Jackson, SAFT-γ force field for the simulation of molecular fluids: 2. Coarse-grained models of greenhouse gases, refrigerants, and long alkanes, J. Phys. Chem. B. 117

(2013) 2717–2733. doi:10.1021/jp306442b.

[199] S. Swaminathan, D.P. Visco, Thermodynamic modeling of refrigerants using the statistical associating fluid theory with variable range. 1. Pure components, Ind. Eng. Chem. Res. 44 (2005) 4798–4805. doi:10.1021/ie048863e.

[200] W.A. Fouad, L.F. Vega, On the anomalous composition dependence of viscosity and surface tension in refrigerant blends, J. Mol. Liq. 268 (2018) 190–200. doi:10.1016/j.molliq.2018.07.056.

[201] I.I.I. Alkhatib, L.M.C. Pereira, L.F. Vega, 110th Anniversary: Accurate Modeling of the Simultaneous Absorption of H 2 S and CO 2 in Aqueous Amine Solvents, Ind. Eng. Chem. Res. 58 (2019) 6870–6886. doi:10.1021/acs.iecr.9b00862.

[202] I.I.I. Alkhatib, L.M.C. Pereira, A. AlHajaj, L.F. Vega, Performance of non-aqueous amine hybrid solvents mixtures for CO2 capture: A study using a molecular-based model, J. CO2 Util. 35 (2020) 126–144. doi:10.1016/j.jcou.2019.09.010.

[203] D. Bahamon, I.I.I. Alkhatib, N. Alkhatib, S. Builes, M. Sinnokrot, L.F. Vega, A comparative assessment of emerging solvents and adsorbents for mitigating CO2 emissions from the industrial sector by using molecular modeling tools., Front. Energy Res. 8 (2020) 165. doi:https://doi.org/10.3389/fenrg.2020.00165.

[204] I.I.I. Alkhatib, M.L. Ferreira, C.G. Alba, D. Bahamon, F. Llovell, A.B. Pereiro, J.M.M. Araújo, M.R.M. Abu-Zahra, L.F. Vega, Screening of Ionic Liquids and Deep Eutectic Solvents for Physical CO 2 Absorption by Soft-SAFT Using Key Performance Indicators, J. Chem. Eng. Data. 65 (2020) 5844–5861. doi:10.1021/acs.jced.0c00750.

[205] L.M.C. Pereira, L.F. Vega, A systematic approach for the thermodynamic modelling of CO2-amine absorption process using molecular-based models, Appl. Energy. 232 (2018) 273–291. doi:10.1016/j.apenergy.2018.09.189.

[206] S. Asensio-Delgado, D. Jovell, G. Zarca, A. Urtiaga, F. Llovell, Thermodynamic and process modeling of the recovery of R410A compounds with ionic liquids, Int. J. Refrig. (2020) 10.1016/j.ijrefrig.2020.04.013. doi:10.1016/j.ijrefrig.2020.04.013.

[207] C.G. Albà, L.F. Vega, F. Llovell, Assessment on Separating Hydrofluoroolefins from Hydrofluorocarbons at the Azeotropic Mixture R513A by Using Fluorinated Ionic Liquids: A Soft-SAFT Study, Ind. Eng. Chem. Res. 59 (2020) 13315–13324. doi:10.1021/acs.iecr.0c02331.

[208] W.A. Fouad, L.F. Vega, Next generation of low global warming potential refrigerants: Thermodynamic properties molecular modeling, AIChE J. 64 (2018) 250–262. doi:10.1002/aic.15859.

[209] I.I.I. Alkhatib, L.M.C. Pereira, J. Torne, L.F. Vega, Polar soft-SAFT: theory and comparison with molecular simulations and experimental data of pure polar fluids, Phys. Chem. Chem. Phys. 22 (2020) 13171–13191. doi:10.1039/D0CP00846J.

[210] J. Gross, G. Sadowski, Perturbed-Chain SAFT: An Equation of State Based on a

Perturbation Theory for Chain Molecules, Ind. Eng. Chem. Res. 40 (2001) 1244–1260. doi:10.1021/ie0003887.

[211] L.F. Vega, D. Bahamon, I.I.I. Alkhatib, W.A. Fouad, F. Llovell, L.M.C. Pereira, O. Vilaseca, How Molecular Modelling Tools Can Help in Mitigating Climate Change, in: E.J. Maginn, J. Errington (Eds.), Found. Mol. Model. Simul., Springer Singapore, Singapore, 2021: pp. 181–220.

[212] A.M.A. Dias, F. Llovell, J.A.P. Coutinho, I.M. Marrucho, L.F. Vega, Thermodynamic characterization of pure perfluoroalkanes, including interfacial and second order derivative properties, using the crossover soft-SAFT EoS, Fluid Phase Equilib. 286 (2009) 134–143. doi:10.1016/j.fluid.2009.08.018.

[213] F. Llovell, R.M. Marcos, L.F. Vega, Transport properties of mixtures by the soft-SAFT + Free-volume theory: Application to mixtures of n-alkanes and hydrofluorocarbons, J. Phys. Chem. B. 117 (2013) 5195–5205. doi:10.1021/jp401754r.

[214] L.F. Vega, F. Llovell, Review and new insights into the application of molecular-based equations of state to water and aqueous solutions, Fluid Phase Equilib. 416 (2016) 150–173. doi:10.1016/j.fluid.2016.01.024.

[215] L.F. Vega, F. Llovell, F.J. Blas, Capturing the Solubility Minima of n -Alkanes in Water by Soft-SAFT, J. Phys. Chem. B. 113 (2009) 7621–7630. doi:10.1021/jp9018876.

[216] F. Llovell, O. Vilaseca, N. Jung, L.F. Vega, Water+1-alkanol systems: Modeling the phase, interface and viscosity properties, Fluid Phase Equilib. 360 (2013) 367–378. doi:10.1016/j.fluid.2013.10.002.

[217] I. Polishuk, A. Chiko, E. Cea-Klapp, J.M. Garrido, Implementation of CP-PC-SAFT and CS-SAFT-VR-Mie for Predicting Thermodynamic Properties of C1-C3Halocarbon Systems. I. Pure Compounds and Mixtures with Nonassociating Compounds, Ind. Eng. Chem. Res. 60 (2021) 9624–9636. doi:10.1021/acs.iecr.1c01700.

[218] C. McCabe, G. Jackson, SAFT-VR modelling of the phase equilibrium of long-chain n-alkanes, Phys. Chem. Chem. Phys. 1 (1999) 2057–2064. doi:10.1039/a808085b.

[219] E. Mickoleit, C. Breitkopf, A. Jäger, Influence of equations of state and mixture models on the design of a refrigeration process, Int. J. Refrig. 121 (2021) 193–205. doi:10.1016/j.ijrefrig.2020.10.017.

[220] V. Vinš, A. Aminian, D. Celný, M. Součková, J. Klomfar, M. Čenský, O. Prokopová, Surface tension and density of dielectric heat transfer fluids of HFE type-experimental data at 0.1 MPa and modeling with PC-SAFT equation of state and density gradient theory, Int. J. Refrig. 131 (2021) 956–969. doi:10.1016/j.ijrefrig.2021.06.029.

[221] J. Wang, D. Chen, L. Zhu, Integrated Working Fluids and Process Optimization for Refrigeration Systems Using Polar PC-SAFT, Ind. Eng. Chem. Res. 60 (2021) 17640–17649.

doi:10.1021/ACS.IECR.1C03624/SUPPL_FILE/IE1C03624_SI_001.PDF.

[222] I.I.I. Alkhatib, L.F. Vega, Quantifying the effect of polar interactions on the behavior of binary mixtures: Phase, interfacial, and excess properties, J. Chem. Phys. 154 (2021) 164503. doi:10.1063/5.0046034.

[223] I.I.I. Alkhatib, O. Khalifa, D. Bahamon, M.R.M. Abu-Zahra, L.F. Vega, Sustainability criteria as a game changer in the search for hybrid solvents for CO2 and H2S removal, Sep. Purif. Technol. 277 (2021) 119516. doi:10.1016/j.seppur.2021.119516.

[224] I.I.I. Alkhatib, F. Llovell, L.F. Vega, Assessing the effect of impurities on the thermophysical properties of methane-based energy systems using polar soft-SAFT, Fluid Phase Equilib. 527 (2021) 112841. doi:10.1016/j.fluid.2020.112841.

[225] I.I.I. Alkhatib, A. AlHajaj, A. Almansoori, L.F. Vega, Accurate Predictions of the Effect of Hydrogen Composition on the Thermodynamics and Transport Properties of Natural Gas, Ind. Eng. Chem. Res. 61 (2022) 6214–6234. doi:10.1021/acs.iecr.2c00363.

[226] I.I.I. Alkhatib, D. Bahamon, A. Al Hajaj, L.F. Vega, Molecular Thermodynamic Modeling of Hybrid Ionic Liquids for Biogas Upgrading, Ind. Eng. Chem. Res. 61 (2022) 12190–12207. doi:10.1021/acs.iecr.2c00710.

[227] I.I.I. Alkhatib, A. Galindo, L.F. Vega, Systematic study of the effect of the co-solvent on the performance of amine-based solvents for CO2 capture, Sep. Purif. Technol. 282 (2022) 120093. doi:10.1016/j.seppur.2021.120093.

[228] C.G. Albà, I.I.I. Alkhatib, F. Llovell, L.F. Vega, Hunting sustainable refrigerants fulfilling technical, environmental, safety and economic requirements, Renew. Sustain. Energy Rev. 188 (2023) 113806. doi:10.1016/j.rser.2023.113806.

[229] C.G. Albà, I.I.I. Alkhatib, F. Llovell, L.F. Vega, A novel approach for designing efficient and sustainable cooling cycles with low global warming potential refrigerants, Appl. Therm. Eng. 246 (2024) 122895. doi:10.1016/j.applthermaleng.2024.122895.

[230] D. Jovell, R. Gonzalez-Olmos, F. Llovell, A computational drop-in assessment of hydrofluoroethers in Organic Rankine Cycles, Energy. 254 (2022) 124319. doi:10.1016/j.energy.2022.124319.

[231] J. Wu, J.M. Prausnitz, 110th Anniversary: Molecular Thermodynamics: An Endless Frontier, Ind. Eng. Chem. Res. 58 (2019) 9707–9708. doi:10.1021/acs.iecr.9b01597.

[232] S. Abbott, J.J. Booth, S. Shimizu, Practical molecular thermodynamics for greener solution chemistry, Green Chem. 19 (2017) 68–75. doi:10.1039/c6gc03002e.

[233] L.F. Vega, O. Vilaseca, F. Llovell, J.S. Andreu, Modeling ionic liquids and the solubility of gases in them: Recent advances and perspectives, Fluid Phase Equilib. 294 (2010) 15–30. doi:10.1016/j.fluid.2010.02.006.

[234] I.I.I. Alkhatib, D. Bahamon, F. Llovell, M.R.M. Abu-Zahra, L.F. Vega, Perspectives and guidelines on thermodynamic modelling of deep eutectic

solvents, J. Mol. Liq. 298 (2020) 112183. doi:10.1016/j.molliq.2019.112183.

[235] A. Mejía, M. Cartes, H. Segura, E.A. Müller, Use of Equations of State and Coarse Grained Simulations to Complement Experiments: Describing the Interfacial Properties of Carbon Dioxide + Decane and Carbon Dioxide + Eicosane Mixtures, J. Chem. Eng. Data. 59 (2014) 2928–2941. doi:10.1021/je5000764.

[236] M. Lísal, R. Budinský, V. Vacek, K. Aim, Vapor-liquid equilibria of alternative refrigerants by molecular dynamics simulations, Int. J. Thermophys. 20 (1999) 163–174. doi:10.1023/A:1021490500152.

[237] G. Gao, W. Wang, X.C. Zeng, Vapor-liquid equilibria for pure HCFC/HFC substances by Gibbs ensemble simulation of Stockmayer potential molecules, Fluid Phase Equilib. 137 (1997) 87–98. doi:10.1016/s0378-3812(97)00087-3.

[238] S. Higashi, A. Takada, Molecular dynamics study of liquid CH2 F2 (HFC-32), Mol. Phys. 92 (1997) 641–650. doi:10.1080/002689797169925.

[239] M. Lísal, V. Vacek, Molecular dynamics simulations of fluorinated ethanes, Mol. Phys. 87 (1996) 167–187. doi:10.1080/00268979600100091.

[240] G.A. Fernández, J. Vrabec, H. Hasse, Shear viscosity and thermal conductivity of dipolar real fluids from equilibrium molecular dynamics simulation, Cryogenics (Guildf). 46 (2006) 711–717. doi:10.1016/j.cryogenics.2006.05.004.

[241] S. Figueroa-Gerstenmaier, M. Lísal, I. Nezbeda, W.R. Smith, V.M. Trejos, Prediction of isoenthalps, Joule–Thomson Coefficients and Joule–Thomson inversion curves of refrigerants by molecular simulation, Fluid Phase Equilib. 375 (2014) 143–151. doi:10.1016/j.fluid.2014.05.011.

[242] W.R. Smith, S. Figueroa-Gerstenmaier, M. Skvorova, Molecular simulation for thermodynamic properties and process modeling of refrigerants, J. Chem. Eng. Data. 59 (2014) 3258–3271. doi:10.1021/je500260d.

[243] W.A. Fouad, H. Alasiri, Molecular dynamic simulation and SAFT modeling of the viscosity and self-diffusion coefficient of low global warming potential refrigerants, J. Mol. Liq. 317 (2020) 113998. doi:10.1016/j.molliq.2020.113998.

[244] M. Khan, J. Wen, M.A. Shakoori, W. Tao, Homogeneous condensation and thermophysical properties of R450A, R513A and R515A using molecular dynamics simulations, J. Mol. Liq. 353 (2022) 118795. doi:10.1016/j.molliq.2022.118795.

[245] T. Imai, T. Kawahara, R. Nonaka, S. Tomassetti, T. Okumura, Y. Higashi, G. Di Nicola, C. Kondou, Surface tension measurement and molecular simulation for new low global warming potential refrigerants R1132(E) and R1132a, J. Mol. Liq. 407 (2024) 125262. doi:10.1016/j.molliq.2024.125262.

[246] T. KAWAHARA, T. IMAI, T. OKUMURA, C. KONDOU, Molecular simulation and experimental validation for surface tension of new Low-GWP refrigerant mixtures R32/CF3I and R1123/CF3I, J. Mol. Liq. 386 (2023) 122532. doi:10.1016/j.molliq.2023.122532.

[247] G. Raabe, E.J. Maginn, A force field for 3,3,3-fluoro-1-propenes, including HFO-

1234yf, J. Phys. Chem. B. 114 (2010) 10133–10142. doi:10.1021/jp102534z.

[248] G. Raabe, E.J. Maginn, Molecular modeling of the vapor-liquid equilibrium properties of the alternative refrigerant 2,3,3,3-tetrafluoro-1-propene (HFO-1234yf), J. Phys. Chem. Lett. 1 (2010) 93–96. doi:10.1021/jz900070h.

[249] G. Raabe, Molecular simulation studies in hydrofluoroolefine (HFO) working fluids and their blends, Sci. Technol. Built Environ. 22 (2016) 1077–1089. doi:10.1080/23744731.2016.1206796.

[250] G. Raabe, Molecular Simulation Studies on the Vapor-Liquid Equilibria of the cis- and trans-HCFO-1233zd and the cis-and trans-HFO-1336mzz, J. Chem. Eng. Data. 60 (2015) 2412–2419. doi:10.1021/acs.jced.5b00286.

[251] G. Raabe, Applications of Molecular Simulations to Studies on Working Fluids, in: Mol. Simul. Stud. Thermophys. Prop., Springer, 2017: pp. 257–289.

[252] G. Raabe, Parameterization Approach for a Systematic Extension of the Hydrofluoroolefin Force Field to Fluorinated Butenes and Hydrochlorofluoroolefin Compounds, J. Chem. Eng. Data. 65 (2020) 1234–1242. doi:10.1021/acs.jced.9b00588.

[253] G. Raabe, Purely Predictive Vapor–Liquid Equilibrium Properties of 3,3,4,4,4-Pentafluoro-1-butene (HFO-1345fz), 2,3,3,4,4,4-Hexafluoro-1-butene (HFO-1336yf), and trans -1-Chloro-2,3,3,3-tetrafluoropropene (HCFO-1224yd(E)) from Molecular Simulation, J. Chem. Eng. Data. 65 (2020) 4318–4325. doi:10.1021/acs.jced.0c00325.

[254] M. Skvorova, W.R. Smith, Molecular-level simulation of bubble and dew points of fluid mixtures and application to refrigerant cycle design, Int. J. Refrig. 42 (2014) 1–7. doi:10.1016/j.ijrefrig.2014.02.007.

[255] E.J. García, D. Bahamon, L.F. Vega, Systematic Search of Suitable Metal-Organic Frameworks for Thermal Energy-Storage Applications with Low Global Warming Potential Refrigerants, ACS Sustain. Chem. Eng. 9 (2021) 3157–3171. doi:10.1021/acssuschemeng.0c07797.

[256] D. Mambo-Lomba, P. Paricaud, Predictions of thermodynamic properties and phase equilibria of refrigerant systems with COSMO approaches, Int. J. Refrig. 124 (2021) 52–63. doi:10.1016/j.ijrefrig.2020.11.005.

[257] F. Eckert, A. Klamt, Fast Solvent Screening via Quantum Chemistry: COSMO-RS Approach, AIChE J. 48 (2002) 369–385. doi:10.1002/aic.690480220.

[258] S.T. Lin, S.I. Sandler, A priori phase equilibrium prediction from a segment contribution solvation model, Ind. Eng. Chem. Res. 41 (2002) 899–913. doi:10.1021/ie001047w.

[259] ASHRAE, ASHRAE. ANSI/ASHRAE Standard 34–2019 Designation and Safety Classification of Refrigerants 2019, (2019).

[260] ISO, “ISO 817:2014 Refrigerants—Designation and safety classification” (2014); www.iso.org/standard/52433.html.

[261] S.G. Davis, J.L. Pagliaro, T.F. Debold, M. van Wingerden, K. van Wingerden, Flammability and explosion characteristics of mildly flammable refrigerants, J. Loss Prev. Process Ind. 49 (2017) 662–674. doi:10.1016/j.jlp.2017.05.019.

[262] G.T. Linteris, I.H. Bell, M.O. McLinden, An empirical model for refrigerant flammability based on molecular structure and thermodynamics, Int. J. Refrig. 104 (2019) 144–150. doi:10.1016/j.ijrefrig.2019.05.006.

[263] Williams, Forman Arthur. A unified view of fire suppression. J. Fire and Flammability, 1974, 5: 54-63.

[264] F. Zhu, X. Huang, S. Wang, Flame Spread over Polyethylene Film: Effects of Gravity and Fuel Inclination, Microgravity Sci. Technol. 34 (2022) 1–14. doi:10.1007/S12217-022-09945-4/TABLES/1.

[265] K.R. Sacksteder, J.S. Tien, Buoyant downward diffusion flame spread and extinction in partial-gravity accelerations, Symp. Combust. 25 (1994) 1685–1692. doi:10.1016/S0082-0784(06)80816-7.

[266] F.N. Egolfopoulos, C.K. Law, Chain mechanisms in the overall reaction orders in laminar flame propagation, Combust. Flame. 80 (1990) 7–16. doi:10.1016/0010-2180(90)90049-W.

[267] A. Movaghar, R. Lawson, F.N. Egolfopoulos, Confined spherically expanding flame method for measuring laminar flame speeds: Revisiting the assumptions and application to C1C4 hydrocarbon flames, Combust. Flame. 212 (2020) 79–92. doi:10.1016/J.COMBUSTFLAME.2019.10.023.

[268] G. Linteris, V. Babushok, Laminar burning velocity predictions for C1 and C2 hydrofluorocarbon refrigerants with air, J. Fluor. Chem. 230 (2020) 109324. doi:10.1016/J.JFLUCHEM.2019.05.002.

[269] V.I. Babushok, G.T. Linteris, D.R. Burgess, P.T. Baker, Hydrocarbon flame inhibition by C3H2F3Br (2-BTP), Combust. Flame. 162 (2015) 1104–1112. doi:10.1016/J.COMBUSTFLAME.2014.10.002.

[270] J.L. Pagliaro, G.T. Linteris, V.I. Babushok, Premixed flame inhibition by C2HF3Cl2 and C2HF5, Combust. Flame. 163 (2016) 54–65. doi:10.1016/J.COMBUSTFLAME.2015.08.015.

[271] K. Takizawa, K. Tokuhashi, S. Kondo, Flammability assessment of CH2CFCF3: Comparison with fluoroalkenes and fluoroalkanes, J. Hazard. Mater. 172 (2009) 1329–1338. doi:10.1016/j.jhazmat.2009.08.001.

[272] H. Li, K. Tang, A comprehensive study of drop-in alternative mixtures for R134a in a mobile air-conditioning system, Appl. Therm. Eng. 203 (2022) 117914. doi:10.1016/j.applthermaleng.2021.117914.

[273] A. Mota-Babiloni, A. Fernández-Moreno, P. Giménez-Prades, C.-M. Udroiu, J. Navarro-Esbrí, Ternary refrigerant blends for ultra-low temperature refrigeration, Int. J. Refrig. 148 (2023) 108–116. doi:10.1016/j.ijrefrig.2023.01.006.

[274] I.H. Bell, P.A. Domanski, M.O. McLinden, G.T. Linteris, The hunt for nonflammable refrigerant blends to replace R-134a, Int. J. Refrig. 104 (2019) 484–

495. doi:10.1016/j.ijrefrig.2019.05.035.

[275] Z. Li, B. Shen, K.R. Gluesenkamp, Multi-objective optimization of low-GWP mixture composition and heat exchanger circuitry configuration for improved system performance and reduced refrigerant flammability, Int. J. Refrig. 126 (2021) 133–142. doi:10.1016/j.ijrefrig.2021.01.003.

[276] D. Calleja-Anta, L. Nebot-Andres, R. Cabello, D. Sánchez, R. Llopis, A3 and A2 refrigerants: Border determination and hunt for A2 low-GWP blends, Int. J. Refrig. 134 (2022) 86–94. doi:10.1016/j.ijrefrig.2021.11.012.

[277] Danfoss, https://www.danfoss.com/en-us/service-and-support/refrigerant-center/refrigerants-with-low-gwp. Consulted [15/08/2024].

[278] M.O. McLinden, Thermodynamic evaluation of refrigerants in the vapour compression cycle using reduced properties, Int. J. Refrig. 11 (1988) 134–143. doi:10.1016/0140-7007(88)90027-8.

[279] S. Saleem, O. Sarfraz, C.R. Bradshaw, C.K. Bach, Development of novel experimental infrastructure for collection of high-fidelity experimental data for refrigerant to air heat exchangers, Int. J. Refrig. 114 (2020) 189–200. doi:10.1016/j.ijrefrig.2020.02.024.

[280] S.A. Borikar, M.M. Gupta, M.A. Alazawi, P.D. Malwe, E.B. Moustafa, H. Panchal, A. Elsheikh, A case study on experimental and statistical analysis of energy consumption of domestic refrigerator, Case Stud. Therm. Eng. 28 (2021) 101636. doi:10.1016/j.csite.2021.101636.

[281] A. Zendehboudi, A. Mota-Babiloni, P. Makhnatch, R. Saidur, S.M. Sait, Modeling and multi-objective optimization of an R450A vapor compression refrigeration system, Int. J. Refrig. 100 (2019) 141–155. doi:10.1016/j.ijrefrig.2019.01.008.

[282] M. Schenk, L.R. Oellrich, Experimental investigation of the refrigerant flow of isobutane (R600a) through adiabatic capillary tubes, Int. J. Refrig. 38 (2014) 275–280. doi:10.1016/j.ijrefrig.2013.08.024.

[283] A. Ustaoglu, B. Kursuncu, M. Alptekin, M.S. Gok, Performance optimization and parametric evaluation of the cascade vapor compression refrigeration cycle using Taguchi and ANOVA methods, Appl. Therm. Eng. 180 (2020) 115816. doi:10.1016/j.applthermaleng.2020.115816.

[284] M.I. Alhamid, N. Nasruddin, Budihardjo, E. Susanto, T.F. Vickary, M. Arif Budiyanto, Refrigeration cycle exergy-based analysis of hydrocarbon (R600a) refrigerant for optimization of household refrigerator, Evergreen. 6 (2019) 71–77. doi:10.5109/2321015.

[285] M.M. Joybari, M.S. Hatamipour, A. Rahimi, F.G. Modarres, Exergy analysis and optimization of R600a as a replacement of R134a in a domestic refrigerator system, Int. J. Refrig. 36 (2013) 1233–1242. doi:10.1016/j.ijrefrig.2013.02.012.

[286] S. Sulaimon, H. Nasution, A.A. Aziz, A.H. Abdul-Rahman, A.N. Darus, Taguchi method for development of mass flow rate correlation using hydrocarbon refrigerant mixture in capillary tube, J. Eng. Technol. Sci. 46 B (2014) 141–151.

doi:10.5614/j.eng.technol.sci.2014.46.2.2.

[287] G. Jatinder, O.S. Ohunakin, D.S. Adelekan, O.E. Atiba, A.B. Daniel, J. Singh, A.A. Atayero, Performance of a domestic refrigerator using selected hydrocarbon working fluids and TiO2–MO nanolubricant, Appl. Therm. Eng. 160 (2019) 114004. doi:10.1016/j.applthermaleng.2019.114004.

[288] Ö. Çomakli, C. Çelik, S. Erdogan, Determination of optimum working conditions in heat-pumps using nonazeotropic refrigerant mixtures, Energy Convers. Manag. 40 (1999) 193–203. doi:10.1016/S0196-8904(98)00047-8.

[289] Ö. Comakli, K. Comakli, N. Ozdemir, M. Yilmaz, Analysis of heat pumps with zeotropic refrigerant mixtures by taguchi method, Isi Bilim. Ve Tek. Dergisi/ J. Therm. Sci. Technol. 30 (2010) 113–122.

[290] K. Comakli, F. Simsek, O. Comakli, B. Sahin, Determination of optimum working conditions R22 and R404A refrigerant mixtures in heat-pumps using Taguchi method, Appl. Energy. 86 (2009) 2451–2458. doi:10.1016/j.apenergy.2009.03.003.

[291] A.H. Bademlioglu, A.S. Canbolat, N. Yamankaradeniz, O. Kaynakli, Investigation of parameters affecting Organic Rankine Cycle efficiency by using Taguchi and ANOVA methods, Appl. Therm. Eng. 145 (2018) 221–228. doi:10.1016/j.applthermaleng.2018.09.032.

[292] A.H. Bademlioglu, A.S. Canbolat, O. Kaynakli, Multi-objective optimization of parameters affecting Organic Rankine Cycle performance characteristics with Taguchi-Grey Relational Analysis, Renew. Sustain. Energy Rev. 117 (2020) 109483. doi:10.1016/j.rser.2019.109483.

[293] A.H. BademliOğlu, A.S. Canbolat, N. Yamankaradeniz, Ö. Kaynakli, A parametric analysis of the performance of organic rankine cycle with heat recovery exchanger and its statistical evaluation, Isi Bilim. Ve Tek. Dergisi/ J. Therm. Sci. Technol. 39 (2019) 121–135.

[294] A.S. Canbolat, A.H. Bademlioglu, N. Arslanoglu, O. Kaynakli, Performance optimization of absorption refrigeration systems using Taguchi, ANOVA and Grey Relational Analysis methods, J. Clean. Prod. 229 (2019) 874–885. doi:10.1016/j.jclepro.2019.05.020.

[295] V.H. Oza, N.M. Bhatt, Optimization of Ammonia-Water Absorption Refrigeration System using Taguchi Method of Design of Experiment, 2018. http://www.ripublication.com/ijms.htm.

[296] M. Shashi, N. Gupta, Performance Optimization of Absorption Refrigeration Systems Using Box-Behnken Design, Int. J. Sci. Res. Eng. Trends. 7 (2021) 2508–2512.

[297] S. Manu, T.K. Chandrashekar, C. Girisha, Optimization Lithium Bromide (LiBr)–Water Absorption Refrigration using Taguchi for Low Capacity, Indian J. Sci. Technol. 9 (2016). doi:10.17485/ijst/2016/v9i45/104607.

[298] S. Coşkun, A.R. Motorcu, N. Yamankaradeniz, E. Pulat, Evaluation of control

parameters' effects on system performance with Taguchi method in waste heat recovery application using mechanical heat pump, Int. J. Refrig. 35 (2012) 795–809. doi:10.1016/j.ijrefrig.2011.12.008.

[299] H. Esen, E. Turgut, Optimization of operating parameters of a ground coupled heat pump system by Taguchi method, Energy Build. 107 (2015) 329–334. doi:10.1016/j.enbuild.2015.08.042.

[300] T. Sivasakthivel, K. Murugesan, H.R. Thomas, Optimization of operating parameters of ground source heat pump system for space heating and cooling by Taguchi method and utility concept, Appl. Energy. 116 (2014) 76–85. doi:10.1016/j.apenergy.2013.10.065.

[301] V. Verma, K. Murugesan, Optimization of solar assisted ground source heat pump system for space heating application by Taguchi method and utility concept, Energy Build. 82 (2014) 296–309. doi:10.1016/j.enbuild.2014.07.029.

[302] G.M. Tashtoush, A Statistical Approach to Optimize the Solar Adsorption Refrigeration System, Energy Sci. Technol. 3 (2012) 18–28. doi:10.3968/j.est.1923847920120302.216.

[303] G.M. Tashtoush, B.M. Tashtoush, M.M. Jaradat, Experimental Study of a Solar Adsorption Refrigeration Unit, Factorial Analysis, Smart Grid Renew. Energy. 03 (2012) 126–132. doi:10.4236/sgre.2012.32018.

[304] S. Boopathi, Experimental investigation and parameter analysis of LPG refrigeration system using Taguchi method, SN Appl. Sci. 1 (2019) 1–7. doi:10.1007/s42452-019-0925-2.

[305] K.A. Babu, P. Sherjin, Experimental investigations of the performance of a thermoacoustic refrigerator based on the Taguchi method, J. Mech. Sci. Technol. 32 (2018) 929–935. doi:10.1007/s12206-018-0143-x.

[306] J. Ding, N. Xu, M.T. Nguyen, Q. Qiao, Y. Shi, Y. He, Q. Shao, Machine learning for molecular thermodynamics, Chinese J. Chem. Eng. 31 (2021) 227–239. doi:10.1016/j.cjche.2020.10.044.

[307] C.A. Faúndez, R.A. Campusano, J.O. Valderrama, Misleading results on the use of artificial neural networks for correlating and predicting properties of fluids. A case on the solubility of refrigerant R-32 in ionic liquids, J. Mol. Liq. 298 (2020) 112009. doi:10.1016/j.molliq.2019.112009.

[308] S. Asensio-Delgado, F. Pardo, G. Zarca, A. Urtiaga, Machine learning for predicting the solubility of high-GWP fluorinated refrigerants in ionic liquids, J. Mol. Liq. 367 (2022) 120472. doi:10.1016/j.molliq.2022.120472.

[309] B.J. Befort, R.S. DeFever, E.J. Maginn, A.W. Dowling, Machine Learning-Enabled Optimization of Force Fields for Hydrofluorocarbons, in: Comput. Aided Chem. Eng., Elsevier, 2022: pp. 1249–1254. doi:10.1016/B978-0-323-85159-6.50208-6.

[310] A. Klamt, V. Jonas, T. Bürger, J.C.W. Lohrenz, Refinement and Parametrization of COSMO-RS, J. Phys. Chem. A. 102 (1998) 5074–5085. doi:10.1021/jp980017s.

[311] J. Palomar, V.R. Ferro, J.S. Torrecilla, F. Rodríguez, Density and molar volume predictions using COSMO-RS for ionic liquids. An approach to solvent design, Ind. Eng. Chem. Res. 46 (2007) 6041–6048. doi:10.1021/ie070445x.

[312] J. Palomar, J.S. Torrecilla, J. Lemus, V.R. Ferro, F. Rodríguez, Prediction of non-ideal behavior of polarity/polarizability scales of solvent mixtures by integration of a novel COSMO-RS molecular descriptor and neural networks, Phys. Chem. Chem. Phys. 10 (2008) 5967. doi:10.1039/b807617k.

[313] J. Palomar, J.S. Torrecilla, V.R. Ferro, F. Rodríguez, Development of an a Priori Ionic Liquid Design Tool. 2. Ionic Liquid Selection through the Prediction of COSMO-RS Molecular Descriptor by Inverse Neural Network, Ind. Eng. Chem. Res. 48 (2009) 2257–2265. doi:10.1021/ie8009507.

[314] J.S. Torrecilla, J. Palomar, J. Lemus, F. Rodríguez, A quantum-chemical-based guide to analyze/quantify the cytotoxicity of ionic liquids, Green Chem. 12 (2010) 123–134. doi:10.1039/B919806G.

[315] J. Palomar, J.S. Torrecilla, J. Lemus, V.R. Ferro, F. Rodríguez, A COSMO-RS based guide to analyze/quantify the polarity of ionic liquids and their mixtures with organic cosolvents, Phys. Chem. Chem. Phys. 12 (2010) 1991. doi:10.1039/b920651p.

[316] N.L. Mai, Y.-M. Koo, Quantitative prediction of lipase reaction in ionic liquids by QSAR using COSMO-RS molecular descriptors, Biochem. Eng. J. 87 (2014) 33–40. doi:10.1016/j.bej.2014.03.010.

[317] Y. Zhao, Y. Huang, X. Zhang, S. Zhang, A quantitative prediction of the viscosity of ionic liquids using Sσ-profile molecular descriptors, Phys. Chem. Chem. Phys. 17 (2015) 3761–3767. doi:10.1039/c4cp04712e.

[318] Y. Zhao, S. Zeng, Y. Huang, R.M. Afzal, X. Zhang, Estimation of Heat Capacity of Ionic Liquids Using S σ-profile Molecular Descriptors, Ind. Eng. Chem. Res. 54 (2015) 12987–12992. doi:10.1021/acs.iecr.5b03576.

[319] Y. Zhao, J. Gao, Y. Huang, R.M. Afzal, X. Zhang, S. Zhang, Predicting H 2 S solubility in ionic liquids by the quantitative structure–property relationship method using S σ-profile molecular descriptors, RSC Adv. 6 (2016) 70405–70413. doi:10.1039/C6RA15429H.

[320] O. Ben Ghanem, M.I.A. Mutalib, J.-M. Lévêque, M. El-Harbawi, Development of QSAR model to predict the ecotoxicity of Vibrio fischeri using COSMO-RS descriptors, Chemosphere. 170 (2017) 242–250. doi:10.1016/j.chemosphere.2016.12.003.

[321] X. Kang, Y. Zhao, J. Li, Predicting refractive index of ionic liquids based on the extreme learning machine (ELM) intelligence algorithm, J. Mol. Liq. 250 (2018) 44–49. doi:10.1016/j.molliq.2017.11.166.

[322] X. Kang, C. Liu, S. Zeng, Z. Zhao, J. Qian, Y. Zhao, Prediction of Henry's law constant of CO2 in ionic liquids based on SEP and Sσ-profile molecular descriptors, J. Mol. Liq. 262 (2018) 139–147. doi:10.1016/j.molliq.2018.04.026.

[323] I. Díaz, M. Rodríguez, M. González-Miquel, E.J. González, COSMO-derived descriptors applied in ionic liquids physical property modelling using machine learning algorithms, in: Comput. Aided Chem. Eng., 2018: pp. 121–126. doi:10.1016/B978-0-444-64235-6.50023-1.

[324] Y. Benguerba, I.M. Alnashef, A. Erto, M. Balsamo, B. Ernst, A quantitative prediction of the viscosity of amine based DESs using Sσ-profile molecular descriptors, J. Mol. Struct. 1184 (2019) 357–363. doi:10.1016/j.molstruc.2019.02.052.

[325] V. Goussard, F. Duprat, J. Ploix, G. Dreyfus, V. Nardello-Rataj, J. Aubry, A New Machine-Learning Tool for Fast Estimation of Liquid Viscosity. Application to Cosmetic Oils, J. Chem. Inf. Model. 60 (2020) 2012–2023. doi:10.1021/acs.jcim.0c00083.

[326] T. Lemaoui, N.E.H. Hammoudi, I.M. Alnashef, M. Balsamo, A. Erto, B. Ernst, Y. Benguerba, Quantitative structure properties relationship for deep eutectic solvents using Sσ-profile as molecular descriptors, J. Mol. Liq. 309 (2020) 113165. doi:10.1016/j.molliq.2020.113165.

[327] A. Sosa, J. Ortega, L. Fernández, J. Palomar, Development of a method to model the mixing energy of solutions using COSMO molecular descriptors linked with a semi-empirical model using a combined ANN-QSPR methodology, Chem. Eng. Sci. 224 (2020) 115764. doi:10.1016/j.ces.2020.115764.

[328] T. Lemaoui, A.S. Darwish, N.E.H. Hammoudi, F. Abu Hatab, A. Attoui, I.M. Alnashef, Y. Benguerba, Prediction of Electrical Conductivity of Deep Eutectic Solvents Using COSMO-RS Sigma Profiles as Molecular Descriptors: A Quantitative Structure–Property Relationship Study, Ind. Eng. Chem. Res. 59 (2020) 13343–13354. doi:10.1021/acs.iecr.0c02542.

[329] T. Lemaoui, A.S. Darwish, A. Attoui, F. Abu Hatab, N.E.H. Hammoudi, Y. Benguerba, L.F. Vega, I.M. Alnashef, Predicting the density and viscosity of hydrophobic eutectic solvents: Towards the development of sustainable solvents, Green Chem. 22 (2020) 8511–8530. doi:10.1039/d0gc03077e.

[330] O. Nordness, P. Kelkar, Y. Lyu, M. Baldea, M.A. Stadtherr, J.F. Brennecke, Predicting thermophysical properties of dialkylimidazolium ionic liquids from sigma profiles, J. Mol. Liq. 334 (2021) 116019. doi:10.1016/j.molliq.2021.116019.

[331] T. Lemaoui, F. Abu Hatab, A.S. Darwish, A. Attoui, N.E.H. Hammoudi, G. Almustafa, M. Benaicha, Y. Benguerba, I.M. Alnashef, Molecular-Based Guide to Predict the pH of Eutectic Solvents: Promoting an Efficient Design Approach for New Green Solvents, ACS Sustain. Chem. Eng. 9 (2021) 5783–5808. doi:10.1021/acssuschemeng.0c07367.

[332] J. Wang, Z. Song, L. Chen, T. Xu, L. Deng, Z. Qi, Prediction of CO2 solubility in deep eutectic solvents using random forest model based on COSMO-RS-derived descriptors, Green Chem. Eng. 2 (2021) 431–440. doi:10.1016/j.gce.2021.08.002.

[333] Y. Chung, F.H. Vermeire, H. Wu, P.J. Walker, M.H. Abraham, W.H. Green, Group

Contribution and Machine Learning Approaches to Predict Abraham Solute Parameters, Solvation Free Energy, and Solvation Enthalpy, J. Chem. Inf. Model. 62 (2022) 433–446. doi:10.1021/acs.jcim.1c01103.

[334] D.O. Abranches, Y. Zhang, E.J. Maginn, Y.J. Colón, Sigma profiles in deep learning: towards a universal molecular descriptor, Chem. Commun. 58 (2022) 5630–5633. doi:10.1039/D2CC01549H.

[335] I.I.I. Alkhatib, C.G. Albà, A.S. Darwish, F. Llovell, L.F. Vega, Searching for Sustainable Refrigerants by Bridging Molecular Modeling with Machine Learning, Ind. Eng. Chem. Res. 61 (2022) 7414–7429. doi:10.1021/acs.iecr.2c00719.

[336] M. Panić, M. Radović, M. Cvjetko Bubalo, K. Radošević, M. Rogošić, J.A.P. Coutinho, I. Radojčić Redovniković, A. Jurinjak Tušek, Prediction of pH Value of Aqueous Acidic and Basic Deep Eutectic Solvent Using COSMO-RS σ Profiles' Molecular Descriptors, Molecules. 27 (2022) 4489. doi:10.3390/molecules27144489.

[337] T. Lemaoui, A. Boublia, A.S. Darwish, M. Alam, S. Park, B. Jeon, F. Banat, Y. Benguerba, I.M. AlNashef, Predicting the Surface Tension of Deep Eutectic Solvents Using Artificial Neural Networks, ACS Omega. 7 (2022) 32194–32207. doi:10.1021/acsomega.2c03458.

[338] A. Boublia, T. Lemaoui, F. Abu Hatab, A.S. Darwish, F. Banat, Y. Benguerba, I.M. AlNashef, Molecular-based artificial neural network for predicting the electrical conductivity of deep eutectic solvents, J. Mol. Liq. 366 (2022) 120225. doi:10.1016/j.molliq.2022.120225.

[339] J. Li, J.L. Anderson, E.A. Smith, Determination of Infinite Dilution Activity Coefficients of Molecular Solutes in Ionic Liquids and Deep Eutectic Solvents by Factorization-Machine-Based Neural Networks, ACS Sustain. Chem. Eng. 10 (2022) 13927–13935. doi:10.1021/acssuschemeng.2c02600.

[340] A. Boublia, T. Lemaoui, J. AlYammahi, A.S. Darwish, A. Ahmad, M. Alam, F. Banat, Y. Benguerba, I.M. AlNashef, Multitask Neural Network for Mapping the Glass Transition and Melting Temperature Space of Homo- and Co-Polyhydroxyalkanoates Using σ Profiles Molecular Inputs, ACS Sustain. Chem. Eng. 11 (2023) 208–227. doi:10.1021/acssuschemeng.2c05225.

[341] A.S. Darwish, T. Lemaoui, J. AlYammahi, H. Taher, Y. Benguerba, F. Banat, I.M. AlNashef, Molecular insights into potential hydrophobic deep eutectic solvents for furfural extraction guided by COSMO-RS and machine learning, J. Mol. Liq. 379 (2023) 121631. doi:10.1016/j.molliq.2023.121631.

[342] W. Zhang, Y. Wang, S. Ren, Y. Hou, W. Wu, Novel Strategy of Machine Learning for Predicting Henry's Law Constants of CO 2 in Ionic Liquids, ACS Sustain. Chem. Eng. 11 (2023) 6090–6099. doi:10.1021/acssuschemeng.3c00874.

[343] T. Lemaoui, A.S. Darwish, G. Almustafa, A. Boublia, P.R. Sarika, N.A. Jabbar, T. Ibrahim, P. Nancarrow, K.K. Yadav, A.M. Fallatah, M. Abbas, J.S. Algethami, Y. Benguerba, B. Jeon, F. Banat, I.M. AlNashef, Machine learning approach to map the thermal conductivity of over 2,000 neoteric solvents for green energy storage

applications, Energy Storage Mater. 59 (2023) 102795. doi:10.1016/j.ensm.2023.102795.

[344] M. Mohan, M.D. Smith, O.N. Demerdash, B.A. Simmons, S. Singh, M.K. Kidder, J.C. Smith, Quantum Chemistry-Driven Machine Learning Approach for the Prediction of the Surface Tension and Speed of Sound in Ionic Liquids, ACS Sustain. Chem. Eng. 11 (2023) 7809–7821. doi:10.1021/acssuschemeng.3c00624.

[345] T. Lemaoui, A. Boublia, S. Lemaoui, A.S. Darwish, B. Ernst, M. Alam, Y. Benguerba, F. Banat, I.M. AlNashef, Predicting the CO 2 Capture Capability of Deep Eutectic Solvents and Screening over 1000 of their Combinations Using Machine Learning, ACS Sustain. Chem. Eng. 11 (2023) 9564–9580. doi:10.1021/acssuschemeng.3c00415.

[346] A.S. Darwish, R.A. Alwan, A. Boublia, T. Lemaoui, I.M. Alnashef, F. Banat, A. Dhabi, A.W. Technology, A. Dhabi, A.S. Darwish, F. Banat, Accurate Heat Capacity Predictions of Deep Eutectic Solvents Using Machine Learning, J. Meas. (2023). doi:doi.org/10.2139/ssrn.4458944.

[347] Z. Wang, Y. Su, S. Jin, W. Shen, J. Ren, X. Zhang, J.H. Clark, A novel unambiguous strategy of molecular feature extraction in machine learning assisted predictive models for environmental properties, Green Chem. 22 (2020) 3867–3876. doi:10.1039/d0gc01122c.

[348] X. Zhang, T. Zhou, L. Zhang, K.Y. Fung, K.M. Ng, Food Product Design: A Hybrid Machine Learning and Mechanistic Modeling Approach, Ind. Eng. Chem. Res. 58 (2019) 16743–16752. doi:10.1021/acs.iecr.9b02462.

[349] M. Gonzalez-Miquel, M. Talreja, A.L. Ethier, K. Flack, J.R. Switzer, E.J. Biddinger, P. Pollet, J. Palomar, F. Rodriguez, C.A. Eckert, C.L. Liotta, COSMO-RS Studies: Structure-property relationships for CO2 capture by reversible ionic liquids, Ind. Eng. Chem. Res. 51 (2012) 16066–16073. doi:10.1021/ie302449c.

[350] S. Yuan, Z. Jiao, N. Quddus, J.S.I. Kwon, C. V. Mashuga, Developing Quantitative Structure-Property Relationship Models to Predict the Upper Flammability Limit Using Machine Learning, Ind. Eng. Chem. Res. 58 (2019) 3531–3537. doi:10.1021/acs.iecr.8b05938.

[351] S. Chinta, R. Rengaswamy, Machine Learning Derived Quantitative Structure Property Relationship (QSPR) to Predict Drug Solubility in Binary Solvent Systems, Ind. Eng. Chem. Res. 58 (2019) 3082–3092. doi:10.1021/acs.iecr.8b04584.

[352] A. Nandy, C. Duan, J.P. Janet, S. Gugler, H.J. Kulik, Strategies and Software for Machine Learning Accelerated Discovery in Transition Metal Chemistry, Ind. Eng. Chem. Res. 57 (2018) 13973–13986. doi:10.1021/acs.iecr.8b04015.

[353] C.G. Albà, I.I.I. Alkhatib, L.F. Vega, F. Llovell, Mapping the Flammability Space of Sustainable Refrigerant Mixtures through an Artificial Neural Network Based on Molecular Descriptors, ACS Sustain. Chem. Eng. 12 (2024) 11561–11577. doi:10.1021/acssuschemeng.4c01961.

[354] M.S. Wertheim, Fluids with highly directional attractive forces. I. Statistical

thermodynamics, J. Stat. Phys. 35 (1984) 19–34. doi:10.1007/BF01017362.

[355] M.S. Wertheim, Fluids with highly directional attractive forces. II. Thermodynamic perturbation theory and integral equations, J. Stat. Phys. 35 (1984) 35–47. doi:10.1007/BF01017363.

[356] M.S. Wertheim, Fluids with Highly Directional Attractive Forces. III. Multiple Attraction Sites, J. Stat. Phys. 42 (1986) 459–476. doi:https://doi.org/10.1007/BF01127721.

[357] M.S. Wertheim, Fluids with highly directional attractive forces. IV. Equilibrium polymerization, J. Stat. Phys. 42 (1986) 477–492. doi:10.1007/BF01127722.

[358] F.J. Blas, L.F. Vega, Thermodynamic behaviour of homonuclear and heteronuclear Lennard-Jones chains with association sites from simulation and theory, Mol. Phys. 92 (1997) 135–150. doi:10.1080/002689797170707.

[359] J.K. Johnson, E.A. Mueller, K.E. Gubbins, Equation of State for Lennard-Jones Chains, J. Phys. Chem. 98 (1994) 6413–6419. doi:10.1021/j100076a028.

[360] R.M. Ojeda, F. Llovell, Soft-SAFT Transferable Molecular Models for the Description of Gas Solubility in Eutectic Ammonium Salt-Based Solvents, J. Chem. Eng. Data. (2018) acs.jced.7b01103. doi:10.1021/acs.jced.7b01103.

[361] I.I.I. Alkhatib, L.M.C. Pereira, A. AlHajaj, L.F. Vega, Performance of non-aqueous amine hybrid solvents mixtures for CO2 capture: A study using a molecular-based model, J. CO2 Util. 35 (2020) 126–144. doi:10.1016/j.jcou.2019.09.010.

[362] A. Belkadi, M.K. Hadj-Kali, F. Llovell, V. Gerbaud, L.F. Vega, Soft-SAFT modeling of vapor-liquid equilibria of nitriles and their mixtures, Fluid Phase Equilib. 289 (2010) 191–200. doi:10.1016/j.fluid.2009.12.012.

[363] J.O. Lloret, L.F. Vega, F. Llovell, Accurate description of thermophysical properties of Tetraalkylammonium Chloride Deep Eutectic Solvents with the soft-SAFT equation of state, Fluid Phase Equilib. 448 (2017) 81–93. doi:10.1016/j.fluid.2017.04.013.

[364] M.B. Oliveira, S.V.D. Freitas, F. Llovell, L.F. Vega, J.A.P. Coutinho, Development of simple and transferable molecular models for biodiesel production with the soft-SAFT equation of state, Chem. Eng. Res. Des. 92 (2014). doi:10.1016/j.cherd.2014.02.025.

[365] F. Llovell, R.M. Marcos, L.F. Vega, Free-volume theory coupled with soft-SAFT for viscosity calculations: Comparison with molecular simulation and experimental data, J. Phys. Chem. B. 117 (2013). doi:10.1021/jp401307t.

[366] F. Llovell, O. Vilaseca, L.F. Vega, Thermodynamic Modeling of Imidazolium-Based Ionic Liquids with the [PF 6] − Anion for Separation Purposes, Sep. Sci. Technol. 47 (2012) 399–410. doi:10.1080/01496395.2011.635625.

[367] F. Llovell, L.F. Vega, Accurate modeling of supercritical CO2 for sustainable processes: Water+CO2 and CO2+fatty acid esters mixtures, J. Supercrit. Fluids. 96 (2015) 86–95. doi:10.1016/j.supflu.2014.09.040.

[368] M.B. Oliveira, F. Llovell, J.A.P. Coutinho, L.F. Vega, Modeling the [NTf 2] Pyridinium Ionic Liquids Family and Their Mixtures with the Soft Statistical Associating Fluid Theory Equation of State, J. Phys. Chem. B. 116 (2012) 9089–9100. doi:10.1021/jp303166f.

[369] F.J. Blas, L.F. Vega, Associating Fluid Theory (SAFT) Equation of State, Ind. Eng. Chem. Res. 5885 (1998) 660–674.

[370] F.J. Blas, L.F. Vega, Prediction of Binary and Ternary Diagrams Using the Statistical Associating Fluid Theory (SAFT) Equation of State, Ind. Eng. Chem. Res. 5885 (1998) 660–674. doi:10.1021/ie970449+.

[371] J.C. Pàmies, L.F. Vega, Vapor−Liquid Equilibria and Critical Behavior of Heavy n -Alkanes Using Transferable Parameters from the Soft-SAFT Equation of State, Ind. Eng. Chem. Res. 40 (2001) 2532–2543. doi:10.1021/ie000944x.

[372] F. Llovell, J.C. Pàmies, L.F. Vega, Thermodynamic properties of Lennard-Jones chain molecules: Renormalization-group corrections to a modified statistical associating fluid theory, J. Chem. Phys. 121 (2004) 10715–10724. doi:10.1063/1.1809112.

[373] D. Duque, J.C. Pàmies, L.F. Vega, Interfacial properties of Lennard-Jones chains by direct simulation and density gradient theory, J. Chem. Phys. 121 (2004) 11395. doi:10.1063/1.1818679.

[374] C.H. Twu, K.E. Gubbins, Thermodynamics of polyatomic fluid mixtures—II, Chem. Eng. Sci. 33 (1978) 879–887. doi:10.1016/0009-2509(78)85177-X.

[375] K.E. Gubbins, C.H. Twu, Thermodynamics of polyatomic fluid mixtures—I theory, Chem. Eng. Sci. 33 (1978) 863–878. doi:10.1016/0009-2509(78)85176-8.

[376] P.K. Jog, S.G. Sauer, J. Blaesing, W.G. Chapman, Application of Dipolar Chain Theory to the Phase Behavior of Polar Fluids and Mixtures, Ind. Eng. Chem. Res. 40 (2001) 4641–4648. doi:10.1021/ie010264+.

[377] G.S. Rushbrooke, G. Stell, J.S. Høye, Theory of polar liquids, Mol. Phys. 26 (1973) 1199–1215. doi:10.1080/00268977300102411.

[378] M. Luckas, K. Lucas, U. Deiters, K.E. Gubbins, Integrals over pair- and triplet-correlation functions for the lennard-jones (12-6)-fluid, Mol. Phys. 57 (1986) 241–253. doi:10.1080/00268978600100191.

[379] I.I.I. Alkhatib, L.F. Vega, Quantifying the Effect of Polarity on the Behavior of Mixtures of n-Alkanes with Dipolar Solvents using Polar soft-SAFT, AIChE J. 67 (2020) e16649. doi:10.1002/aic.16649.

[380] A. Razzouk, I. Mokbel, J. García, J. Fernandez, N. Msakni, J. Jose, Vapor pressure measurements in the range 10−5Pa to 1Pa of four pentaerythritol esters, Fluid Phase Equilib. 260 (2007) 248–261. doi:10.1016/j.fluid.2007.07.029.

[381] P.. Domanski, D.. Didion, J.. Doyle, Evaluation of suction-line/liquid-line heat exchange in the refrigeration cycle, Int. J. Refrig. 17 (1994) 487–493. doi:10.1016/0140-7007(94)90010-8.

[382] Z. Ye, Y. Wang, Y. Song, X. Yin, F. Cao, Optimal discharge pressure in transcritical CO2 heat pump water heater with internal heat exchanger based on pinch point analysis, Int. J. Refrig. 118 (2020) 12–20. doi:10.1016/j.ijrefrig.2020.06.003.

[383] S.Y. Wu, S.M. Zhou, L. Xiao, Y.R. Li, C. Liu, J.L. Xu, Determining the optimal pinch point temperature difference of evaporator for waste heat recovery, J. Energy Inst. 87 (2014) 140–151. doi:10.1016/j.joei.2014.03.010.

[384] C. Mateu-Royo, J. Navarro-Esbrí, A. Mota-Babiloni, M. Amat-Albuixech, F. Molés, Theoretical evaluation of different high-temperature heat pump configurations for low-grade waste heat recovery, Int. J. Refrig. 90 (2018) 229–237. doi:10.1016/j.ijrefrig.2018.04.017.

[385] P.A. Domanski, J. Steven Brown, J. Heo, J. Wojtusiak, M.O. McLinden, A thermodynamic analysis of refrigerants: Performance limits of the vapor compression cycle, Int. J. Refrig. 38 (2014) 71–79. doi:10.1016/j.ijrefrig.2013.09.036.

[386] J. Ahamed, R. Saidur, H.H. Masjuki, A review on exergy analysis of vapor compression refrigeration system, Renew. Sustain. Energy Rev. 15 (2011) 1593–1600. doi:10.1016/j.rser.2010.11.039.

[387] H.C. Bayrakçi, A.E. Özgür, Energy and exergy analysis of vapor compression refrigeration system using pure hydrocarbon refrigerants, Int. J. Energy Res. 33 (2009) 1070–1075. doi:10.1002/er.1538.

[388] E. Gholamian, P. Hanafizadeh, P. Ahmadi, Advanced exergy analysis of a carbon dioxide ammonia cascade refrigeration system, Appl. Therm. Eng. 137 (2018) 689–699. doi:10.1016/j.applthermaleng.2018.03.055.

[389] A.K.S. Al-Sayyab, J. Navarro-Esbrí, A. Mota-Babiloni, Energy, exergy, and environmental (3E) analysis of a compound ejector-heat pump with low GWP refrigerants for simultaneous data center cooling and district heating, Int. J. Refrig. 133 (2022) 61–72. doi:10.1016/J.IJREFRIG.2021.09.036.

[390] T.Q. Jonathan Fryer, Kevin Lee, Methods of calculating Total Equivalent Warming Impact (TEWI), Aust. Inst. Refrig. Air Cond. Heat. (2012) 21.

[391] R. Gonzalez-Olmos, F. Llovell, Life cycle assessment of fluorinated gas recovery from waste refrigerants through vacuum swing adsorption, Sustain. Mater. Technol. 39 (2024) e00811. doi:10.1016/j.susmat.2023.e00811.

[392] D. Jovell, J.O. Pou, F. Llovell, R. Gonzalez-Olmos, Life Cycle Assessment of the Separation and Recycling of Fluorinated Gases Using Ionic Liquids in a Circular Economy Framework, ACS Sustain. Chem. Eng. 10 (2022) 71–80. doi:10.1021/acssuschemeng.1c04723.

[393] K. Chelvam, M.M. Hanafiah, K. Al Ali, A. Al Blooshi, Gate-to-gate life cycle analysis of a pilot-scale solar driven two-step thermochemical hydrogen sulfide decomposition for hydrogen production, J. Clean. Prod. 428 (2023) 139369. doi:10.1016/j.jclepro.2023.139369.

[394] T. Parikhani, A. Bahman, D. Ziviani, A.M. Bahman, Techno-Economic Analysis for Two-Stage Vapor Injected System Techno-Economic Analysis for Two-Stage Vapor Injected System for Heating Applications for Heating Applications Techno-Economic Analysis for Two-Stage Vapor Injected System for Heating Applicatio, Int. Refrig. Air Cond. Conf. (2021). https://docs.lib.purdue.edu/iracc (accessed April 8, 2022).

[395] A.H. Mosaffa, L.G. Farshi, C.A. Infante Ferreira, M.A. Rosen, Exergoeconomic and environmental analyses of CO2/NH3 cascade refrigeration systems equipped with different types of flash tank intercoolers, Energy Convers. Manag. 117 (2016) 442–453. doi:10.1016/j.enconman.2016.03.053.

[396] M. Navidbakhsh, A. Shirazi, S. Sanaye, Four E analysis and multi-objective optimization of an ice storage system incorporating PCM as the partial cold storage for air-conditioning applications, Appl. Therm. Eng. 58 (2013) 30–41. doi:10.1016/j.applthermaleng.2013.04.002.

[397] R. Roy, B.K. Mandal, Thermo-economic Assessment and Multi-Objective Optimization of Vapour Compression Refrigeration System using Low GWP Refrigerants, in: 2019 8th Int. Conf. Model. Simul. Appl. Optim., IEEE, 2019: pp. 1–5. doi:10.1109/ICMSAO.2019.8880390.

[398] M.S. Turgut, O.E. Turgut, Comparative investigation and multi objective design optimization of R744/R717, R744/R134a and R744/R1234yf cascade rerfigeration systems, Heat Mass Transf. Und Stoffuebertragung. 55 (2019) 445–465. doi:10.1007/S00231-018-2435-Y/FIGURES/14.

[399] K.N. Anand, Development of process technology in wire-cut operation for improving machining quality, Total Qual. Manag. 7 (1996) 11–28. doi:10.1080/09544129650035016.

[400] D.M. Grove, T.P. Davis, Shorter communication: Taguchi's idle column method, Technometrics. 33 (1991) 349–353. doi:10.1080/00401706.1991.10484840.

[401] R.F. Gunst, R.L. Mason, Fractional factorial design, Wiley Interdiscip. Rev. Comput. Stat. 1 (2009) 234–244. doi:10.1002/wics.27.

[402] R.R. Barton, Design-Plots for Factorial and Fractional-Factorial Designs, in: Graph. Methods Des. Exp., 1999: pp. 55–92. doi:10.1007/978-1-4612-1398-7_3.

[403] Y.C. Lee, T.M. Yen, C.H. Tsai, Modify IPA for quality improvement: Taguchi's signal-to-noise ratio approach, TQM J. 20 (2008) 488–501. doi:10.1108/17542730810898458.

[404] W. Yan, A robust and efficient solution for COSMO-based activity coefficient models, Chem. Eng. Sci. 300 (2024). doi:10.1016/j.ces.2024.120652.

[405] Z. Wu, Z. Xian, W. Ma, Q. Liu, X. Huang, B. Xiong, S. He, W. Zhang, Artificial neural network approach for predicting blood brain barrier permeability based on a group contribution method, Comput. Methods Programs Biomed. 200 (2021) 105943. doi:10.1016/j.cmpb.2021.105943.

[406] W.L. Kubic, R.W. Jenkins, C.M. Moore, T.A. Semelsberger, A.D. Sutton,

Artificial Neural Network Based Group Contribution Method for Estimating Cetane and Octane Numbers of Hydrocarbons and Oxygenated Organic Compounds, Ind. Eng. Chem. Res. 56 (2017) 12236–12245. doi:10.1021/acs.iecr.7b02753.

[407] E. Mullins, R. Oldland, Y.A. Liu, S. Wang, S.I. Sandler, C.-C. Chen, M. Zwolak, K.C. Seavey, Sigma-Profile Database for Using COSMO-Based Thermodynamic Methods, Ind. Eng. Chem. Res. 45 (2006) 4389–4415. doi:10.1021/ie060370h.

[408] TURBOMOLE, Quantum Chemistry, BIOVIA - Dassault Systèmes®.

[409] A. Klamt, G. Schüürmann, COSMO: A new approach to dielectric screening in solvents with explicit expressions for the screening energy and its gradient, J. Chem. Soc. Perkin Trans. 2. (1993) 799–805. doi:10.1039/P29930000799.

[410] L. Moity, M. Durand, A. Benazzouz, C. Pierlot, V. Molinier, J.-M. Aubry, Panorama of sustainable solvents using the COSMO-RS approach, Green Chem. 14 (2012) 1132. doi:10.1039/c2gc16515e.

[411] Haykin, S. (2009). Neural networks and learning machines, 3/E. Pearson Education India.

[412] M. Mohammadhassani, H. Nezamabadi-pour, M.Z. Jumaat, M. Jameel, A.M.S. Arumugam, Application of artificial neural networks (ANNs) and linear regressions (LR) to predict the deflection of concrete deep beams, Comput. Concr. 11 (2013) 237–252. doi:10.12989/cac.2013.11.3.237.

[413] F. Marini, R. Bucci, A.L. Magrì, A.D. Magrì, Artificial neural networks in chemometrics: History, examples and perspectives, Microchem. J. 88 (2008) 178–185. doi:10.1016/j.microc.2007.11.008.

[414] R. Kocjančič, J. Zupan, Application of a Feed-Forward Artificial Neural Network as a Mapping Device, J. Chem. Inf. Comput. Sci. 37 (1997) 985–989. doi:10.1021/ci970223h.

[415] K. Paduszyński, U. Domańska, Viscosity of Ionic Liquids: An Extensive Database and a New Group Contribution Model Based on a Feed-Forward Artificial Neural Network, J. Chem. Inf. Model. 54 (2014) 1311–1324. doi:10.1021/ci500206u.

[416] M. Karelson, D.A. Dobchev, O. V. Kulshyn, A.R. Katritzky, Neural Networks Convergence Using Physicochemical Data, J. Chem. Inf. Model. 46 (2006) 1891–1897. doi:10.1021/ci0600206.

[417] K. Saeed, W. Homenda, Computer Information Systems and Industrial Management, Springer International Publishing, Cham, 2016. doi:10.1007/978-3-319-45378-1.

[418] P. Cabrera, J.A. Carta, J. González, G. Melián, Artificial neural networks applied to manage the variable operation of a simple seawater reverse osmosis plant, Desalination. 416 (2017) 140–156. doi:10.1016/j.desal.2017.04.032.

[419] B. Paul, B. Karn, Heart disease prediction using scaled conjugate gradient backpropagation of artificial neural network, Soft Comput. 27 (2023) 6687–6702. doi:10.1007/s00500-022-07649-w.

[420] P. Jain, Meenu, Recognition of Mechanical Tools Using Artificial Neural Network, in: 2021: pp. 637–644. doi:10.1007/978-981-15-8704-7_78.

[421] R.J. May, H.R. Maier, G.C. Dandy, Data splitting for artificial neural networks using SOM-based stratified sampling, Neural Networks. 23 (2010) 283–294. doi:10.1016/j.neunet.2009.11.009.

[422] C. Ji, S. Yuan, Z. Jiao, M. Huffman, M.M. El-Halwagi, Q. Wang, Predicting flammability-leading properties for liquid aerosol safety via machine learning, Process Saf. Environ. Prot. 148 (2021) 1357–1366. doi:10.1016/j.psep.2021.03.012.

[423] A. Tropsha, P. Gramatica, V. Gombar, The Importance of Being Earnest: Validation is the Absolute Essential for Successful Application and Interpretation of QSPR Models, QSAR Comb. Sci. 22 (2003) 69–77. doi:10.1002/qsar.200390007.

[424] A. Tropsha, Best Practices for QSAR Model Development, Validation, and Exploitation, Mol. Inform. 29 (2010) 476–488. doi:10.1002/minf.201000061.

[425] L. Eriksson, J. Jaworska, A.P. Worth, M.T.D. Cronin, R.M. McDowell, P. Gramatica, Methods for reliability and uncertainty assessment and for applicability evaluations of classification- and regression-based QSARs., Environ. Health Perspect. 111 (2003) 1361–1375. doi:10.1289/ehp.5758.

[426] P. Gramatica, Principles of QSAR models validation: internal and external, QSAR Comb. Sci. 26 (2007) 694–701. doi:10.1002/qsar.200610151.

[427] N. Minovski, Š. Župerl, V. Drgan, M. Novič, Assessment of applicability domain for multivariate counter-propagation artificial neural network predictive models by minimum Euclidean distance space analysis: A case study, Anal. Chim. Acta. 759 (2013) 28–42. doi:10.1016/j.aca.2012.11.002.

[428] Y. Dimopoulos, P. Bourret, S. Lek, Use of some sensitivity criteria for choosing networks with good generalization ability, Neural Process. Lett. 2 (1995) 1–4. doi:10.1007/BF02309007.

[429] I. Dimopoulos, J. Chronopoulos, A. Chronopoulou-Sereli, S. Lek, Neural network models to study relationships between lead concentration in grasses and permanent urban descriptors in Athens city (Greece), Ecol. Modell. 120 (1999) 157–165. doi:10.1016/S0304-3800(99)00099-X.

[430] M. Gevrey, I. Dimopoulos, S. Lek, Review and comparison of methods to study the contribution of variables in artificial neural network models, Ecol. Modell. 160 (2003) 249–264. doi:10.1016/S0304-3800(02)00257-0.

[431] F. Llovell, C.J. Peters, L.F. Vega, Second-order thermodynamic derivative properties of selected mixtures by the soft-SAFT equation of state, Fluid Phase Equilib. 248 (2006) 115–122. doi:10.1016/j.fluid.2006.07.018.

[432] E.W. Lemmon, M.L. Huber, M.O. McLinden, NIST standard reference database 23: reference fluid thermodynamic and transport properties-REFPROP. Gaithersburg, USA: National Institute of Standards and Technology, Standard

Reference Data Program; 2013. Version 9.1., (2013).

[433] G. Di Nicola, G. Coccia, M. Pierantozzi, S. Tomassetti, Equations for the surface tension of low GWP halogenated alkene refrigerants and their blends, Int. J. Refrig. 86 (2018) 410–421. doi:10.1016/j.ijrefrig.2017.11.023.

[434] M.D. Hanwell, D.E. Curtis, D.C. Lonie, T. Vandermeersch, E. Zurek, G.R. Hutchison, Avogadro: an advanced semantic chemical editor, visualization, and analysis platform, J. Cheminform. 4 (2012) 17. doi:10.1186/1758-2946-4-17.

[435] M.T. Bowers, J.B. Laudenslager, Mechanism of Charge Transfer Reactions: Reactions of Rare Gas Ions with the trans-, cis- , and 1,1-Difluoroethylene Geometric Isomers, J. Chem. Phys. 56 (1972) 4711–4712. doi:10.1063/1.1677922.

[436] I.H. Bell, J. Wronski, S. Quoilin, V. Lemort, Pure and Pseudo-pure Fluid Thermophysical Property Evaluation and the Open-Source Thermophysical Property Library CoolProp, Ind. Eng. Chem. Res. 53 (2014) 2498–2508. doi:doi.org/10.1021/ie4033999.

[437] J.S. Brown, G. Di Nicola, L. Fedele, S. Bobbo, C. Zilio, Saturated pressure measurements of 3,3,3-trifluoroprop-1-ene (R1243zf) for reduced temperatures ranging from 0.62 to 0.98, Fluid Phase Equilib. 351 (2013) 48–52. doi:10.1016/j.fluid.2012.09.036.

[438] HoneyWell's Genetron Properties software, HoneyWell's Genetron Properties software (version 1.4), 2010.

[439] L. Fedele, G. Di Nicola, J.S. Brown, L. Colla, S. Bobbo, Saturated pressure measurements of cis-pentafluoroprop-1-ene (R1225ye(Z)), Int. J. Refrig. 69 (2016) 243–250. doi:10.1016/j.ijrefrig.2015.10.012.

[440] K. Tanaka, R. Akasaka, E. Sakaue, J. Ishikawa, K.K. Kontomaris, Thermodynamic properties of cis-1,1,1,4,4,4-hexafluoro-2-butene (HFO-1336mzz(Z)): Measurements of the pρT property and determinations of vapor pressures, saturated liquid and vapor densities, and critical parameters, J. Chem. Eng. Data. 61 (2016) 2467–2473. doi:10.1021/acs.jced.6b00169.

[441] R. Low, Evaluation of potential use of R1132A as a refrigerant blend component, in: Proc. 1st IIR Int. Conf. Appl. HFO Refrig., 2018: p. Paper 1183. doi:10.18462/iir.hfo.2018.1183.

[442] U.A. Perera, N. Sakoda, T. Miyazaki, K. Thu, Y. Higashi, Measurements of saturation pressures for the novel refrigerant R1132(E), Int. J. Refrig. 135 (2022) 148–153. doi:10.1016/j.ijrefrig.2021.12.014.

[443] C. Kondou, Okumura, Miura, Liu, Molecular simulation for liquid vapour equilibria of ethylene,R1132a, R1132(E) and R1123, in: 30028776, 2021: p. 1006. doi:http://dx.doi.org/10.18462/iir.HFO.2021.1006.

[444] N. Sakoda, Y. Higashi, R. Akasaka, Measurements of PvT Properties, Vapor Pressures, Saturated Densities, and Critical Parameters for trans -1,1,1,4,4,4-Hexafluoro-2-butene (R1336mzz(E)), J. Chem. Eng. Data. 66 (2021) 734–739. doi:10.1021/acs.jced.0c00848.

[445] Y.-Y. Duan, M.-S. Zhu, L.-Z. Han, Experimental vapor pressure data and a vapor pressure equation for trifluoroiodomethane (CF3I), Fluid Phase Equilib. 121 (1996) 227–234. doi:10.1016/0378-3812(96)03005-1.

[446] C. Kondou, R. Nagata, N. Nii, S. Koyama, Y. Higashi, Surface tension of low GWP refrigerants R1243zf, R1234ze(Z), and R1233zd(E), Int. J. Refrig. 53 (2015) 80–89. doi:10.1016/j.ijrefrig.2015.01.005.

[447] J.S. Brown, L. Fedele, G. Di Nicola, S. Bobbo, G. Coccia, Compressed Liquid Density and Vapor Phase PvT Measurements of cis -1,2,3,3,3-Pentafluoroprop-1-ene (R1225ye(Z)), J. Chem. Eng. Data. 60 (2015) 3333–3340. doi:10.1021/acs.jced.5b00562.

[448] C. Kondou, Y. Higashi, S. Iwasaki, Surface Tension and Parachor Measurement of Low-Global Warming Potential Working Fluid cis-1-Chloro-2,3,3,3-tetrafluoropropene (R1224yd(Z)), J. Chem. Eng. Data. 64 (2019) 5462–5468. doi:10.1021/acs.jced.9b00613.

[449] X. Zhang, G. Zhao, J. Yin, S. Ma, Experimental investigation of saturated liquid kinematic viscosity and surface tension of two isomeric refrigerants trans-1,1,1,4,4,4-hexafluoro-butene (R1336mzz(E)) and cis-1,1,1,4,4,4-hexafluoro-butene (R1336mzz(Z)) by surface light scattering, Fluid Phase Equilib. 559 (2022) 113468. doi:10.1016/j.fluid.2022.113468.

[450] Y.-Y. Duan, L. Shi, M.-S. Zhu, L.-Z. Han, Critical Parameters and Saturated Density of Trifluoroiodomethane (CF 3 I), J. Chem. Eng. Data. 44 (1999) 501–504. doi:10.1021/je980251b.

[451] A. Yokozeki, H. Sato, K. Watanabe, Ideal-Gas Heat Capacities and Virial Coefficients of HFC Refrigerants, Int. J. Thermophys. 19 (1998) 89–127. doi:10.1023/A:1021499018749.

[452] Y. Liu, X. Zhao, H. He, R. Wang, Heat Capacity of R1234ze(E) at Temperatures from 313 to 393 K and Pressures up to 10 MPa, J. Chem. Eng. Data. 63 (2018) 113–118. doi:10.1021/acs.jced.7b00713.

[453] Y. Liu, X. Zhao, Measurement of the heat capacity of R1233zd(E), Int. J. Refrig. 86 (2018) 127–132. doi:10.1016/j.ijrefrig.2017.11.015.

[454] Y. Liu, X. Zhao, S. Lv, H. He, Isobaric Heat Capacity Measurements for R1234yf from 303 to 373 K and Pressures up to 12 MPa, J. Chem. Eng. Data. 62 (2017) 1119–1124. doi:10.1021/acs.jced.6b00959.

[455] R. Romeo, P.A. Giuliano Albo, S. Lago, J.S. Brown, Experimental liquid densities of cis -1,3,3,3-tetrafluoroprop-1-ene (R1234ze(Z)) and trans -1-chloro-3,3,3-trifluoropropene (R1233zd(E)), Int. J. Refrig. 79 (2017) 176–182. doi:10.1016/j.ijrefrig.2017.04.003.

[456] G. Di Nicola, J. Steven Brown, L. Fedele, M. Securo, S. Bobbo, C. Zilio, Subcooled liquid density measurements and PvT measurements in the vapor phase for 3,3,3-trifluoroprop-1-ene (R1243zf), Int. J. Refrig. 36 (2013) 2209–2215. doi:10.1016/j.ijrefrig.2013.08.004.

[457] J.S. Lim, J.Y. Park, B.G. Lee, Vapor-liquid equilibria of CFC alternative refrigerant mixtures: Trifluoromethane (HFC-23) + difluoromethane (HFC-32), trifluoromethane (HFC-23) + pentafluoroethane (HFC-125), and pentafluoroethane (HFC-125) + 1,1-difluoroethane (HFC-152a), Int. J. Thermophys. 21 (2000) 1339–1349. doi:10.1023/A:1006653309953.

[458] Y. Qin, N. Li, H. Zhang, B. Liu, Energy and exergy analysis of a Linde-Hampson refrigeration system using R170, R41 and R1132a as low-GWP refrigerant blend components to replace R23, Energy. 229 (2021) 120645. doi:10.1016/j.energy.2021.120645.

[459] X. Meng, X. Hu, T. Yang, J. Wu, Vapor liquid equilibria for binary mixtures of difluoromethane (R32) + fluoroethane (R161) and fluoroethane (R161) + trans-1,3,3,3-tetrafluoropropene (R1234ze(E)), J. Chem. Thermodyn. 118 (2018) 43–50. doi:10.1016/j.jct.2017.10.015.

[460] B.G. Lee, J.Y. Park, J.S. Lim, S.Y. Cho, K.Y. Park, Phase equilibria of chlorofluorocarbon alternative refrigerant mixtures, J. Chem. Eng. Data. 44 (1999) 190–192. doi:10.1021/je980180g.

[461] X. Hu, T. Yang, X. Meng, S. Bi, J. Wu, Vapor liquid equilibrium measurements for difluoromethane (R32) + 2,3,3,3-tetrafluoroprop-1-ene (R1234yf) and fluoroethane (R161) + 2,3,3,3-tetrafluoroprop-1-ene (R1234yf), Fluid Phase Equilib. 438 (2017) 10–17. doi:10.1016/j.fluid.2017.01.024.

[462] Z. Yang, A. Valtz, C. Coquelet, J. Wu, J. Lu, Experimental measurement and modelling of vapor-liquid equilibrium for 3,3,3- Trifluoropropene (R1243zf) and trans-1,3,3,3-Tetrafluoropropene (R1234ze(E)) binary system, Int. J. Refrig. 120 (2020) 137–149. doi:10.1016/j.ijrefrig.2020.08.016.

[463] L. Kou, Z. Yang, X. Tang, W. Zhang, J. Lu, Experimental measurements and correlation of isothermal vapor-liquid equilibria for HFC-32 + HFO-1234ze (E) and HFC-134a + HFO-1234ze (E) binary systems, J. Chem. Thermodyn. 139 (2019) 105798. doi:10.1016/j.jct.2019.04.020.

[464] X. Han, G. Ye, Y. Fang, Z. Guo, H. Ni, Y. Zhuang, G. Chen, Experimental investigation of vapor-liquid equilibrium for 2,3,3,3-tetrafluoropropene (HFO-1234yf) + trans-1,3,3,3-tetrafluoropropene (HFO-1234ze(E)) at Temperatures from 284 to 334 K, J. Chem. Eng. Data. 66 (2021) 1741–1753. doi:10.1021/acs.jced.0c01033.

[465] H. Madani, A. Valtz, F. Zhang, J. El Abbadi, C. Houriez, P. Paricaud, C. Coquelet, Isothermal vapor-liquid equilibrium data for the trifluoromethane (R23) + 2,3,3,3-tetrafluoroprop-1-ene (R1234yf) system at temperatures from 254 to 348 K, Fluid Phase Equilib. 415 (2016) 158–165. doi:10.1016/j.fluid.2016.02.005.

[466] J. El Abbadi, C. Coquelet, A. Valtz, C. Houriez, Experimental measurements and modelling of vapour−liquid equilibria for four mixtures of 2,3,3,3−tetrafluoropropene (R1234yf) with 1,1,1,2−tetrafluoroethane (R134a) or 1,1−difluoroethane (R152a) or trans−1−chloro−3,3,3−trifluoropropene (R1233zd(E)) or 2−c, Int. J. Refrig. 140 (2022) 172–185. doi:10.1016/j.ijrefrig.2022.05.006.

[467] S. Bobbo, R. Camporese, R. Stryjek, Vapor-liquid equilibria for difluoromethane (R32) + and pentafluoroethane (R125) + 1,1,1,3,3,3-hexafluoropropane (R236fa) at 303.2 and 323.3 K, J. Chem. Eng. Data. 44 (1999) 349–352. doi:10.1021/je980195e.

[468] J.Y.Park, J.S.Lim, B.G.Lee, Y.W.Lee, Phase Equilibria of CFC Alternative Refrigerant Mixtures: 1, 1, 1, 2, 3, 3, 3-Heptafluoropropane (HFC-227ea)+ Difluoromethane (HFC-32),+ 1, 1, 1, 2-Tetrafluoroethane, Int. J. Thermophys. 22 (2001) 901–917. doi:10.1023/A:1010735318011.

[469] J.S. Lim, K.H. Park, B.G. Lee, Phase equilibria of HFC mixtures: Binary mixtures of trifluoromethane + 1,1-difluoroethane and trifluoromethane + 1,1,1-trifluoroethane at 283.15 and 293.15 K, J. Chem. Eng. Data. 47 (2002) 582–586. doi:10.1021/je0102311.

[470] S. Peng, E. Wang, Z. Yang, Y. Duan, Vapor-liquid equilibrium measurements for the binary mixtures of 1,1-difluoroethane (R152a) with trans-1,3,3,3-tetrafluoropropene (R1234ze(E)) and 3,3,3-trifluoropropene (R1243zf), Fluid Phase Equilib. 558 (2022). doi:10.1016/j.fluid.2022.113470.

[471] X.L. Cui, G.M. Chen, X.H. Han, C.S. Li, Vapor−Liquid Equilibria for the Trifluoromethane + 1,1,1,2-Tetrafluoroethane System, J. Chem. Eng. Data. 51 (2006) 1927–1930. doi:10.1021/je0602622.

[472] T. Yang, X. Hu, X. Meng, J. Wu, Vapor-Liquid Equilibria for the Binary and Ternary Systems of Difluoromethane (R32), 1,1-Difluoroethane (R152a), and 2,3,3,3-Tetrafluoroprop-1-ene (R1234yf), J. Chem. Eng. Data. 63 (2018) 771–780. doi:10.1021/acs.jced.7b00950.

[473] Z. Yang, M. Gong, H. Guo, X. Dong, J. Wu, Phase equilibrium for the binary mixture of {1,1-difluoroethane (R152a)+trans-1,3,3,3-tetrafluoropropene (R1234ze (E))} at various temperatures from 258.150 to 288.150K, Fluid Phase Equilib. 355 (2013) 99–103. doi:10.1016/j.fluid.2013.06.017.

[474] J.S. Lim, K.H. Park, B.G. Lee, J.D. Kim, Phase equilibria of CFC alternative refrigerant mixtures. Binary systems of trifluoromethane (HFC-23) + 1,1,1,2-tetrafluoroethane (HFC-134a) and trifluoromethane (HFC-23) + 1,1,1,2,3,3,3-heptafluoropropane (HFC-227ea) at 283.15 and 293.15 K, J. Chem. Eng. Data. 46 (2001) 1580–1583. doi:10.1021/je010103c.

[475] X. Yao, L. Ding, X. Dong, Y. Zhao, X. Wang, J. Shen, M. Gong, Experimental measurement of vapor-liquid equilibrium for 3,3,3-trifluoropropene(R1243zf) + 1,1,1,2-tetrafluoroethane(R134a) at temperatures from 243.150 to 293.150 K, Int. J. Refrig. 120 (2020) 97–103. doi:10.1016/j.ijrefrig.2020.09.008.

[476] X. Dong, M. Gong, Y. Zhang, J. Wu, Vapor-liquid equilibria of the fluoroethane (R161) + 1,1,1,2- tetrafluoroethane (R134a) system at various temperatures from (253.15 to 292.92) K, J. Chem. Eng. Data. 53 (2008) 2193–2196. doi:10.1021/je800505y.

[477] X.H. Han, G.M. Chen, C.S. Li, X.G. Qiao, X.L. Cui, Q. Wang, Isothermal vapor - Liquid equilibrium of (pentafluoroethane + fluoroethane) at temperatures between

(265.15 and 303.15) K obtained with a recirculating still, J. Chem. Eng. Data. 51 (2006) 1232–1235. doi:10.1021/je050539i.

[478] Q. Wang, Y.J. Xu, Z.J. Gao, Y. Qiu, X.W. Min, X.H. Han, G.M. Chen, Isothermal vapor-liquid equilibrium data for the binary mixture ethyl fluoride (HFC-161)+1,1,1,2,3,3,3-heptafluoroproane (HFC-227ea) over a temperature range from 253.15K to 313.15K, Fluid Phase Equilib. 297 (2010) 67–71. doi:10.1016/j.fluid.2010.06.006.

[479] M. Kleiber, Vapor-liquid equilibria of binary refrigerant mixtures containing propylene or R134a, Fluid Phase Equilib. 92 (1994) 149–194. doi:10.1016/0378-3812(94)80046-4.

[480] T. Yang, X. Hu, X. Meng, J. Wu, Vapour-liquid equilibria for the binary systems of pentafluoroethane {(R125) + 2,3,3,3-tetrafluoroprop-1-ene (R1234yf)} and {trans-1,3,3,3-tetrafluoropropene R1234ze(E)}, J. Chem. Thermodyn. 150 (2020) 106222. doi:10.1016/j.jct.2020.106222.

[481] H. Nishiumi, H. Akita, S. Akiyama, High pressure vapor-liquid equilibria for the HFC125-HFC152a system, Korean J. Chem. Eng. 14 (1997) 359–364. doi:10.1007/BF02707052.

[482] X. Li, Q. Pang, J. Liu, Q. Ning, G. He, Isothermal vapour-liquid equilibrium data for environmentally friendly binary system {R1234ze(E) + R245fa}, J. Chem. Thermodyn. 175 (2022). doi:10.1016/j.jct.2022.106894.

[483] L. Yang, M. Gong, H. Guo, X. Dong, J. Wu, (Vapour + liquid) equilibrium data for the {1,1-difluoroethane (R152a) + 1,1,1,3,3-pentafluoropropane (R245fa)} system at temperatures from (323.150 to 353.150) K, J. Chem. Thermodyn. 91 (2015) 414–419. doi:10.1016/j.jct.2015.08.024.

[484] P. Hu, L.X. Chen, W.B. Zhu, L. Jia, Z.S. Chen, Vapor-liquid equilibria for the binary system of 2,3,3,3-tetrafluoroprop-1-ene (HFO-1234yf)+1,1,1,2,3,3,3-heptafluoropropane (HFC-227ea), Fluid Phase Equilib. 379 (2014) 59–61. doi:10.1016/j.fluid.2014.07.014.

[485] Honeywell, SOLSTICE N15 (R-515B) Technical Data Sheet, (2021). https://sustainability.honeywell.com/content/dam/sustainability/en/documents/document-lists/technical/refrigerants-solstice-n15-datasheet.pdf.

[486] R. Kato, H. Nishiumi, Vapor-liquid equilibria and critical loci of binary and ternary systems composed of CH2F2, C2HF5 and C2H2F4, Fluid Phase Equilib. 249 (2006) 140–146. doi:10.1016/j.fluid.2006.07.017.

[487] S. Bobbo, L. Fedele, M. Scattolini, R. Camporese, Isothermal VLE measurements for the binary mixtures HFC-134a + HFC-245fa and HC-600a + HFC-245fa, Fluid Phase Equilib. 185 (2001) 255–264. doi:10.1016/S0378-3812(01)00475-7.

[488] S. Bobbo, R. Stryjek, N. Elvassore, A. Bertucco, A recirculation apparatus for vapor-liquid equilibrium measurements of refrigerants. Binary mixtures of R600a, R134a and R236fa, Fluid Phase Equilib. 150 (1998) 343–352. doi:10.1016/s0378-3812(98)00334-3.

[489] S. Bobbo, R. Camporese, G. Scalabrin, Isothermal vapour-liquid equilibrium measurements for the binary mixtures HFC-125 + HFC-245fa and HC-290 + HFC-245fa, High Temp. - High Press. 32 (2000) 441–447. doi:10.1068/htwu123.

[490] S.X. Hou, Y.Y. Duan, Isothermal vapor-liquid equilibria for the pentafluoroethane + propane and pentafluoroethane + 1,1,1,2,3,3,3-heptafluoropropane systems, Fluid Phase Equilib. 290 (2010) 121–126. doi:10.1016/j.fluid.2009.09.008.

[491] Y. Zhang, M. Gong, H. Zhu, J. Wu, Vapor−Liquid Equilibrium Data for the Ethane + Trifluoromethane System at Temperatures from (188.31 to 243.76) K, J. Chem. Eng. Data. 51 (2006) 1411–1414. doi:10.1021/je0601107.

[492] Y. Liu, A. Valtz, J. El Abbadi, G. He, C. Coquelet, Isothermal Vapor–Liquid Equilibrium Measurements for the (R1234ze(E) + Ethane) System at Temperatures from 272.27 to 347.52 K, J. Chem. Eng. Data. 63 (2018) 4185–4192. doi:10.1021/acs.jced.8b00653.

[493] J.S. Lim, G. Seong, H.S. Byun, Vapor-liquid equilibria for the binary system of 1,1-difluoroethane (HFC-152a) + n-butane (R-600) at various temperatures, Fluid Phase Equilib. 259 (2007) 165–172. doi:10.1016/j.fluid.2007.07.010.

[494] J. Im, M. Kim, B.G. Lee, H. Kim, Vapor-liquid equilibria of the binary n-butane (HC-600) + Difluoromethane (HFC-32), + Pentafluoroethane (HFC-125), + 1,1,1,2-tetrafluoroethane (HFC-134a) systems, J. Chem. Eng. Data. 50 (2005) 359–363. doi:10.1021/je049817o.

[495] L. Fedele, S. Bobbo, M. Scattolini, R. Camporese, R. Stryjek, Vapor−Liquid Equilibrium for the Difluoromethane (R32) + n -Butane (R600) System, J. Chem. Eng. Data. 50 (2005) 44–48. doi:10.1021/je049874h.

[496] P. Hu, N. Zhang, L.-X. Chen, X.-D. Cai, Vapor–Liquid Equilibrium Measurements for 2,3,3,3-Tetrafluoroprop-1-ene + Butane at Temperatures from 283.15 to 323.15 K, J. Chem. Eng. Data. 63 (2018) 1507–1512. doi:10.1021/acs.jced.7b01073.

[497] N. Juntarachat, A. Valtz, C. Coquelet, R. Privat, J.-N. Jaubert, Experimental measurements and correlation of vapor–liquid equilibrium and critical data for the CO 2 + R1234yf and CO 2 + R1234ze(E) binary mixtures, Int. J. Refrig. 47 (2014) 141–152. doi:10.1016/j.ijrefrig.2014.09.001.

[498] S. Wang, R. Fauve, C. Coquelet, A. Valtz, C. Houriez, P.-A. Artola, E. El Ahmar, B. Rousseau, H. Hu, Vapor–liquid equilibrium and molecular simulation data for carbon dioxide (CO2) + trans-1,3,3,3-tetrafluoroprop-1-ene (R-1234ze(E)) mixture at temperatures from 283.32 to 353.02 K and pressures up to 7.6 MPa, Int. J. Refrig. 98 (2019) 362–371. doi:10.1016/j.ijrefrig.2018.10.032.

[499] Z. Yuan, Y. Tu, C. Wang, Y. Zhao, X. Dong, Experimental research on (vapor + liquid) equilibria for the {trifluoroiodomethane (CF3I) + carbon dioxide (CO2)} system from 243.150 to 273.150 K, J. Chem. Thermodyn. 101 (2016) 49–53. doi:10.1016/j.jct.2016.05.012.

[500] S.M. Hosseini, M.M. Alavianmehr, New version of Tammann-Tait equation: Application to nanofluids, J. Mol. Liq. 220 (2016) 404–408. doi:10.1016/j.molliq.2016.04.088.

[501] M.L. Ferreira, F. Llovell, L.F. Vega, A.B. Pereiro, J.M.M. Araújo, Systematic study of the influence of the molecular structure of fluorinated ionic liquids on the solubilization of atmospheric gases using a soft-SAFT based approach, J. Mol. Liq. 294 (2019) 111645. doi:10.1016/j.molliq.2019.111645.

[502] M.J.P. Comuñas, A. Baylaucq, C. Boned, J. Fernández, Volumetric Properties of Monoethylene Glycol Dimethyl Ether and Diethylene Glycol Dimethyl Ether up to 60 MPa, J. Chem. Eng. Data. 48 (2003) 1044–1049. doi:10.1021/je0340304.

[503] W. V. Steele, R.D. Chirico, S.E. Knipmeyer, A. Nguyen, N.K. Smith, Thermodynamic Properties and Ideal-Gas Enthalpies of Formation for Butyl Vinyl Ether, 1,2-Dimethoxyethane, Methyl Glycolate, Bicyclo[2.2.1]hept-2-ene, 5-Vinylbicyclo[2.2.1]hept-2-ene, trans -Azobenzene, Butyl Acrylate, Di- tert -butyl Ether, and Hexane-1, J. Chem. Eng. Data. 41 (1996) 1285–1302. doi:10.1021/je960117w.

[504] D.R. Stull, Vapor Pressure of Pure Substances. Organic and Inorganic Compounds, Ind. Eng. Chem. 39 (1947) 517–540. doi:10.1021/ie50448a022.

[505] M.J.P. Comuñas, E.R. López, P. Pires, J. García, J. Fernández, Pressure Density Temperature Measurements of Polyethylene Glycol Dimethylethers Between 278.15 and 328.15 K at Pressures to 12 MPa, Int. J. Thermophys. 21 (2000). doi:10.1023/A:1006606122944.

[506] Clariant, Triethylene glycol dimethyl ether, Tech. Data Sheet. (2019).

[507] P. Navarro, E.A. Crespo, J.M.L. Costa, F. Llovell, J. García, F. Rodríguez, P.J. Carvalho, L.F. Vega, J.A.P. Coutinho, New Experimental Data and Modeling of Glymes: Toward the Development of a Predictive Model for Polyethers, Ind. Eng. Chem. Res. 56 (2017) 7830–7844. doi:10.1021/acs.iecr.7b01532.

[508] N. Pedrosa, J.C. Pàmies, J.A.P. Coutinho, I.M. Marrucho, L.F. Vega, Phase Equilibria of Ethylene Glycol Oligomers and Their Mixtures, Ind. Eng. Chem. Res. 44 (2005) 7027–7037. doi:10.1021/ie050361t.

[509] C. Ciantar, M. Hadfield, A.. Smith, A. Swallow, The influence of lubricant viscosity on the wear of hermetic compressor components in HFC-134a environments, Wear. 236 (1999) 1–8. doi:10.1016/S0043-1648(99)00267-7.

[510] A.S. Pensado, M.J.P. Comuñas, J. Fernández, Relationship between viscosity coefficients and volumetric properties: Measurements and modeling for pentaerythritol esters, Ind. Eng. Chem. Res. 45 (2006) 9171–9183. doi:10.1021/ie0606035.

[511] A.S. Pensado, M.J.P. Comuñas, L. Lugo, J. Fernández, High-pressure characterization of dynamic viscosity and derived properties for squalane and two pentaerythritol ester lubricants: Pentaerythritol tetra-2-ethylhexanoate and pentaerythritol tetranonanoate, Ind. Eng. Chem. Res. 45 (2006) 2394–2404. doi:10.1021/ie051275w.

[512] S. Bobbo, C. Zilio, M. Scattolini, L. Fedele, R1234yf as a substitute of R134a in automotive air conditioning. Solubility measurements in two commercial PAG oils, Int. J. Refrig. 40 (2014) 302–308. doi:10.1016/j.ijrefrig.2013.08.002.

[513] M. Ghodbane, An investigation of R152a and hydrocarbon refrigerants in mobile air conditioning, in: SAE Tech. Pap., 1999: p. L150/195-230. doi:10.4271/1999-01-0874.

[514] A. Kilicarslan, N. Müller, A comparative study of water as a refrigerant with some current refrigerants, Int. J. Energy Res. 29 (2005) 947–959. doi:10.1002/er.1084.

[515] C. Arpagaus, F. Bless, M. Uhlmann, J. Schiffmann, S.S. Bertsch, High temperature heat pumps: Market overview, state of the art, research status, refrigerants, and application potentials, Energy. 152 (2018) 985–1010. doi:10.1016/j.energy.2018.03.166.

[516] F. Dawo, J. Fleischmann, F. Kaufmann, C. Schifflechner, S. Eyerer, C. Wieland, H. Spliethoff, R1224yd(Z), R1233zd(E) and R1336mzz(Z) as replacements for R245fa: Experimental performance, interaction with lubricants and environmental impact, Appl. Energy. 288 (2021) 116661. doi:10.1016/j.apenergy.2021.116661.

[517] D. Van Orshoven, S.A. Klein, W.A. Beckman, An investigation of water as a refrigerant, J. Energy Resour. Technol. Trans. ASME. 115 (1993) 257–263. doi:10.1115/1.2906430.

[518] P.A. Domanski, R. Brignoli, J.S. Brown, A.F. Kazakov, M.O. McLinden, Frigorigènes à faible GWP pour les applications à moyenne et haute pression, Int. J. Refrig. 84 (2017) 198–209. doi:10.1016/j.ijrefrig.2017.08.019.

[519] Q. Chen, R.C. Prasad, Simulation of a vapour-compression refrigeration cycles using HFC134A and CFC12, Int. Commun. Heat Mass Transf. 26 (1999) 513–521. doi:10.1016/S0735-1933(99)00037-8.

[520] A. Setyawan, T. Sutandi, Faldian, A.S. Margana, Simulation of the effect of the condensing temperature on the performance of a split AC with R-410a under constant cooling capacity, in: AIP Conf. Proc., 2018: p. 020005. doi:10.1063/1.5049965.

[521] ASHRAE, ANSI. “Standard 34-2019 Designation and Safety Classification of Refrigerants.” American Society of Heating, Refrigerating, and Air-Conditioning Engineers, Inc (2019).

[522] Z. Yang, X. Wu, T. Tian, Flammability of Trans-1, 3, 3, 3-tetrafluoroprop-1-ene and its binary blends, Energy. 91 (2015) 386–392. doi:10.1016/j.energy.2015.08.037.

[523] S. Kondo, K. Takizawa, K. Tokuhashi, Effects of temperature and humidity on the flammability limits of several 2L refrigerants, J. Fluor. Chem. 144 (2012) 130–136. doi:10.1016/j.jfluchem.2012.08.004.

[524] C. Mateu-Royo, A. Mota-Babiloni, J. Navarro-Esbrí, Semi-empirical and environmental assessment of the low GWP refrigerant HCFO-1224yd(Z) to replace HFC-245fa in high temperature heat pumps, Int. J. Refrig. (2021). doi:10.1016/j.ijrefrig.2021.02.018.

[525] H. Yan, L. Ding, B. Sheng, X. Dong, Y. Zhao, Q. Zhong, W. Gong, M. Gong, H. Guo, J. Shen, Performance prediction of HFC, HC, HFO and HCFO working fluids

for high temperature water source heat pumps, Appl. Therm. Eng. 185 (2021) 116324. doi:10.1016/j.applthermaleng.2020.116324.

[526] J. Wu, Y. Zhou, An equation of state for fluoroethane (R161), Int. J. Thermophys. 33 (2012) 220–234. doi:10.1007/s10765-011-1151-3.

[527] Y. Higashi, R. Akasaka, Measurements of Thermodynamic Properties for R1123 and R1123 + R32 Mixture, 16th Int. Refrig. Air Cond. Conf. (2016) 2283-1–10.

[528] N. Sakoda, Y. Higashi, Measurements of PvT Properties, Vapor Pressures, Saturated Densities, and Critical Parameters for cis -1-Chloro-2,3,3,3-tetrafluoropropene (R1224yd(Z)), J. Chem. Eng. Data. 64 (2019) 3983–3987. doi:10.1021/acs.jced.9b00374.

[529] X. Chen, K. Liang, Z. Li, Y. Zhao, J. Xu, H. Jiang, Experimental assessment of alternative low global warming potential refrigerants for automotive air conditioners application, Case Stud. Therm. Eng. 22 (2020) 100800. doi:10.1016/j.csite.2020.100800.

[530] IPCC, Climate Change 2013: The Physical Science Basis. Contribution of Working Group I to the Fifth Assessment Report of the Intergovernmental Panel on Climate Change, 2013.

[531] C.G. Albà, I.I. Alkhatib, L.F. Vega, F. Llovell., US provisional Application No. 63/406,114 WO 2024/057105 A1 patent, 2024.

[532] D. Luo, A. Mahmoud, F. Cogswell, Evaluation of Low-GWP fluids for power generation with Organic Rankine Cycle, Energy. 85 (2015) 481–488. doi:10.1016/j.energy.2015.03.109.

[533] F. Pardo, G. Zarca, A. Urtiaga, Effect of feed pressure and long-term separation performance of Pebax-ionic liquid membranes for the recovery of difluoromethane (R32) from refrigerant mixture R410A, J. Memb. Sci. 618 (2021) 118744. doi:10.1016/j.memsci.2020.118744.

[534] Y.J. Kim, K.H. Simmrock, AZEOPERT: An expert system for the prediction of azeotrope formation—I. Binary azeotropes, Comput. Chem. Eng. 21 (1997) 93–111. doi:10.1016/0098-1354(95)00249-9.

[535] Z. Meng, H. Zhang, M. Lei, Y. Qin, J. Qiu, Performance of low GWP R1234yf/R134a mixture as a replacement for R134a in automotive air conditioning systems, Int. J. Heat Mass Transf. 116 (2018) 362–370. doi:10.1016/j.ijheatmasstransfer.2017.09.049.

[536] G. Li, Performance evaluation of low global warming potential working fluids as R134a alternatives for two-stage centrifugal chiller applications, Korean J. Chem. Eng. 38 (2021) 1438–1451. doi:10.1007/s11814-021-0785-5.

[537] A. Mota-Babiloni, C. Mateu-Royo, J. Navarro-Esbrí, Á. Barragán-Cervera, Experimental comparison of HFO-1234ze(E) and R-515B to replace HFC-134a in heat pump water heaters and moderately high temperature heat pumps, Appl. Therm. Eng. 196 (2021) 117256. doi:10.1016/j.applthermaleng.2021.117256.

[538] E. Askar, V. Schröder, T. Schmid, M. Schwarze, Explosion characteristics of

mildly flammable refrigerants ignited with high-energy ignition sources in closed systems, Int. J. Refrig. 90 (2018) 249–256. doi:10.1016/j.ijrefrig.2018.04.009.

[539] A. Mota-Babiloni, P. Makhnatch, R. Khodabandeh, J. Navarro-Esbrí, Experimental assessment of R134a and its lower GWP alternative R513A, Int. J. Refrig. 74 (2017) 680–686. doi:10.1016/j.ijrefrig.2016.11.021.

[540] P. Makhnatch, A. Mota-Babiloni, A. López-Belchí, R. Khodabandeh, R450A and R513A as lower GWP mixtures for high ambient temperature countries: Experimental comparison with R134a, Energy. 166 (2019) 223–235. doi:10.1016/j.energy.2018.09.001.

[541] C. Booten, S. Nicholson, M. Mann, O. Abdelaziz, Refrigerants: Market Trends and Supply Chain Assessment. Technical Report NREL/TP-5500-70207, 2020.

[542] T. Ohm, S. Myung, W. Jang, S. Yu, A comparison of refrigerant management policies and suggestions for improvement in South Korea, J. Mater. Cycles Waste Manag. 19 (2017) 631–644. doi:10.1007/s10163-015-0455-y.

[543] J. del Estado, Ley 6/2018, de 3 de julio, de Presupuestos Generales del Estado para el año 2018., Boletín Of. Del Estado. BOE-A-2018 (2018) 66621–67354.

[544] H. Tyagi, P.R. Chakraborty, S. Powar, A.K. Agarwal, Solar Energy systems, challanges, and opprtunities, Springer, 2020. doi:10.1007/978-981-15-0675-8.

[545] A. Mitra, The Taguchi method, Wiley Interdiscip. Rev. Comput. Stat. 3 (2011) 472–480. doi:10.1002/wics.169.

[546] D.C. Montgomery, G.C. Runger, Foldovers of 2k-p resolution IV experimental designs, J. Qual. Technol. 28 (1996) 446–450. doi:10.1080/00224065.1996.11979702.

[547] A. Kabul, Ö. Kizilkan, A.K. Yakut, Performance and exergetic analysis of vapor compression refrigeration system with an internal heat exchanger using a hydrocarbon, isobutane (R600a), Int. J. Energy Res. 32 (2008) 824–836. doi:10.1002/er.1396.

[548] D.M. Steinberg, 7 Robust design: Experiments for improving quality, Handb. Stat. 13 (1996) 199–240. doi:10.1016/S0169-7161(96)13009-1.

[549] L. Huwang, C.F.J. Wu, C.H. Yen, The idle column method: Design construction, properties and comparisons, Technometrics. 44 (2002) 347–355. doi:10.1198/004017002188618545.

[550] M. Direk, A. Kelesoglu, A. Akin, Drop-in Performance Analysis and Effect of IHX for an Automotive Air Conditioning System with R1234yf as a Replacement of R134a, Strojniški Vestn. - J. Mech. Eng. 63 (2017) 314–319. doi:10.5545/sv-jme.2016.4247.

[551] C. Mateu-Royo, J. Navarro-Esbrí, A. Mota-Babiloni, M. Amat-Albuixech, F. Molés, Thermodynamic analysis of low GWP alternatives to HFC-245fa in high-temperature heat pumps: HCFO-1224yd(Z), HCFO-1233zd(E) and HFO-1336mzz(Z), Appl. Therm. Eng. 152 (2019) 762–777. doi:10.1016/j.applthermaleng.2019.02.047.

[552] A. Mota-Babiloni, J. Navarro-Esbrí, V. Pascual-Miralles, Á. Barragán-Cervera, A. Maiorino, Experimental influence of an internal heat exchanger (IHX) using R513A and R134a in a vapor compression system, Appl. Therm. Eng. 147 (2019) 482–491. doi:10.1016/j.applthermaleng.2018.10.092.

[553] Electricity price statistics - Statistics Explained.

[554] Electricity prices around the world | GlobalPetrolPrices.com.

[555] Institue for European Enviromental Policy (IEEP), Tax on Fluorinated Greenhouse Gases in Spain, (2014) 1–9.

[556] Y.-R. Li, M.-T. Du, C.-M. Wu, S.-Y. Wu, C. Liu, Potential of organic Rankine cycle using zeotropic mixtures as working fluids for waste heat recovery, Energy. 77 (2014) 509–519. doi:10.1016/j.energy.2014.09.035.

[557] J. Radulovic, N.I. Beleno Castaneda, On the potential of zeotropic mixtures in supercritical ORC powered by geothermal energy source, Energy Convers. Manag. 88 (2014) 365–371. doi:10.1016/j.enconman.2014.08.048.

[558] B. Zühlsdorf, W. Meesenburg, T.S. Ommen, J.E. Thorsen, W.B. Markussen, B. Elmegaard, Improving the performance of booster heat pumps using zeotropic mixtures, Energy. 154 (2018) 390–402. doi:10.1016/j.energy.2018.04.137.

[559] B. Yu, D. Wang, C. Liu, F. Jiang, J. Shi, J. Chen, Performance improvements evaluation of an automobile air conditioning system using CO2-propane mixture as a refrigerant, Int. J. Refrig. 88 (2018) 172–181. doi:10.1016/j.ijrefrig.2017.12.016.

[560] B.O. Bolaji, Theoretical analysis of the energy performance of three low global warming potential hydro-fluorocarbon refrigerants as R134a alternatives in refrigeration systems, Proc. Inst. Mech. Eng. Part A J. Power Energy. 228 (2014) 56–63. doi:10.1177/0957650913507252.

[561] T. Goto, T. Usui, T. Yoshimura, Y. Yamada, Study of decomposition of R-1132(E) as ultra-low GWP refrigerants, Int. J. Refrig. 163 (2024) 71–77. doi:10.1016/j.ijrefrig.2024.04.013.

[562] Z. Yang, H. Liu, X. Wu, Theoretical and experimental study of the inhibition and inert effect of HFC125, HFC227ea and HFC13I1 on the flammability of HFC32, Process Saf. Environ. Prot. 90 (2012) 311–316. doi:10.1016/j.psep.2011.09.009.

[563] R.J. Bellair, L. Hood, Comprehensive evaluation of the flammability and ignitability of HFO-1234ze, Process Saf. Environ. Prot. 132 (2019) 273–284. doi:10.1016/j.psep.2019.09.033.

[564] A. Mota-Babiloni, J. Navarro-Esbrí, Á. Barragán, F. Molés, B. Peris, Theoretical comparison of low GWP alternatives for different refrigeration configurations taking R404A as baseline, Int. J. Refrig. 44 (2014) 81–90. doi:10.1016/j.ijrefrig.2014.04.015.

[565] A. Mota-Babiloni, J. Navarro-Esbrí, B. Peris, F. Molés, G. Verdú, Experimental evaluation of R448A as R404A lower-GWP alternative in refrigeration systems, Energy Convers. Manag. 105 (2015) 756–762. doi:10.1016/j.enconman.2015.08.034.

Annex

In this annex of Mr. Carlos Albà's thesis, the figures and tables labeled with the following letters correspond to specific chapters:

- A: Represents material from **Chapter 4**, focusing on the thermodynamic and ANN-based characterization of single-component refrigerants and mixtures of diverse nature.
- B: Corresponds to **Chapter 5**, assessing the impact of lubricant leaks into the performance of 4th generation refrigerant R513A.
- C: Corresponds to **Chapter 6**, covering the rapid screening of emerging eco-friendly refrigerants in single-stage vapor compression refrigeration cycles, along with a drop-in evaluation based on 4E criteria.
- D: Linked to **Chapter 7**, which involves the modeling of advanced VCRC-based cycle configurations using statistical methods, 4E analysis, and LCA methodologies to identify optimal compounds for industrial use.
- E: Refers to the main outcomes of **Chapter 8**, including flammability predictions generated by an ANN approach and a 4E assessment to identify suitable CO_2-based blends for low-temperature applications.

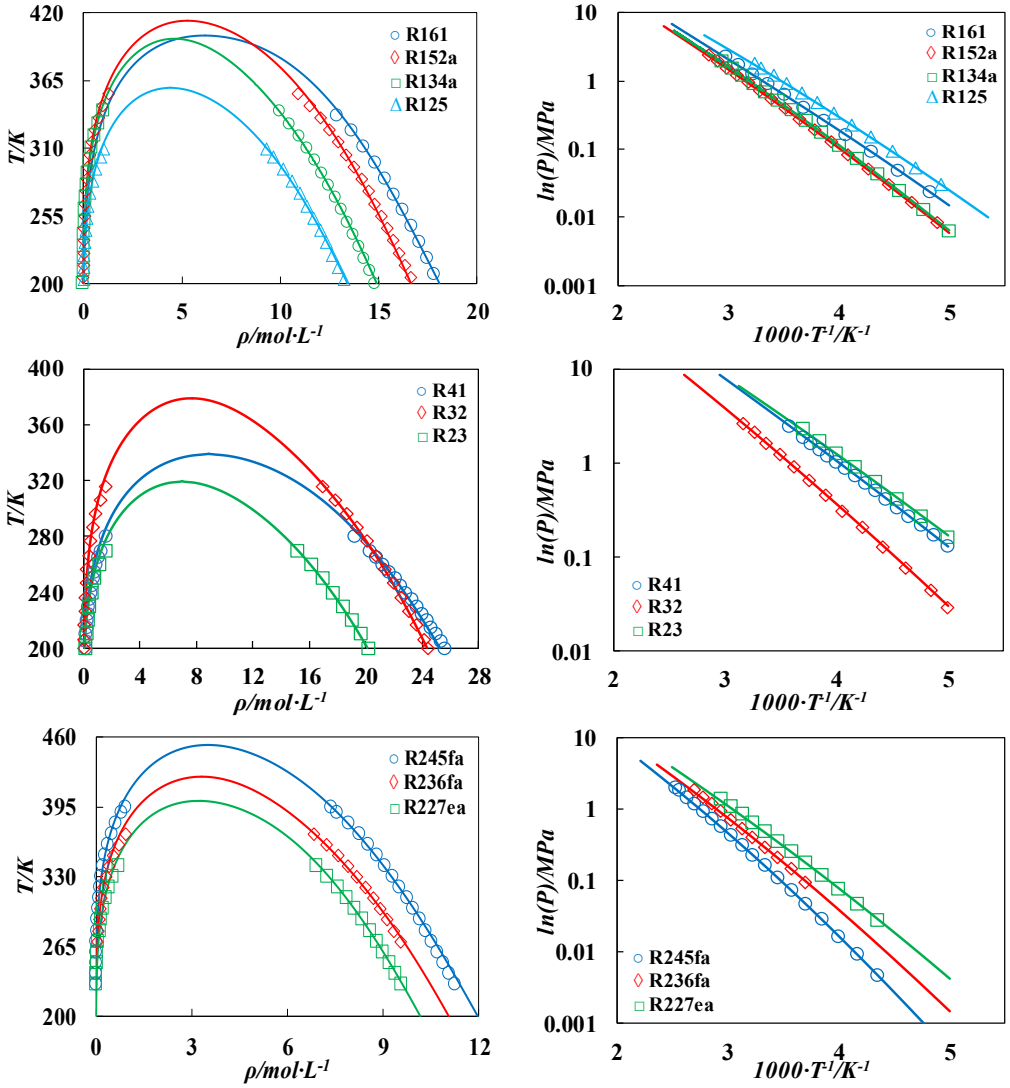

Figure A1. *Vapor pressure (right), and coexisting densities (left) for 3rd generation refrigerants, with polar soft-SAFT EoS (solid lines), compared to experimental data [1,2] (symbols).*

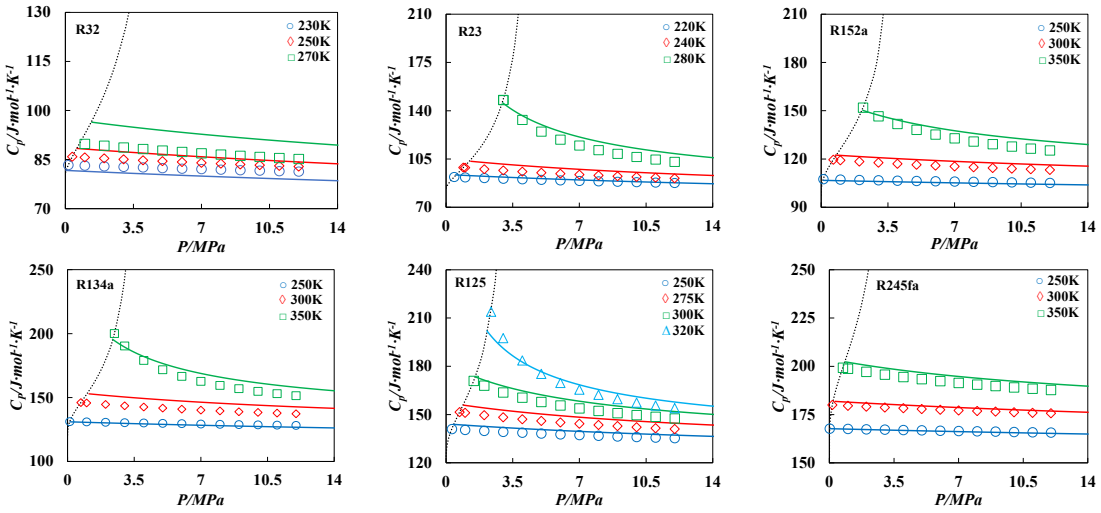

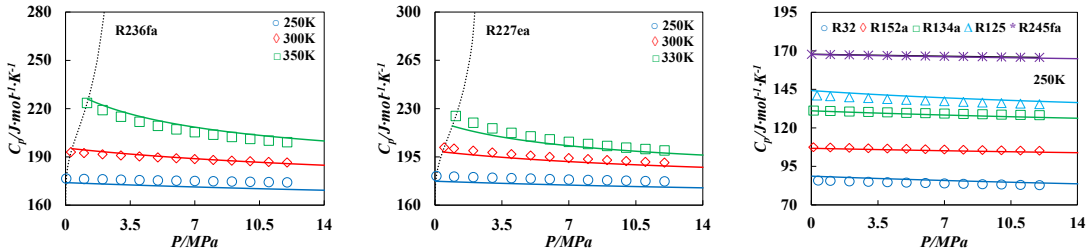

Figure A2. *Isobaric heat capacities of 3rd generation refrigerants predicted with polar soft-SAFT EoS (solid lines), compared to experimental data [1,3-5] (symbols).*

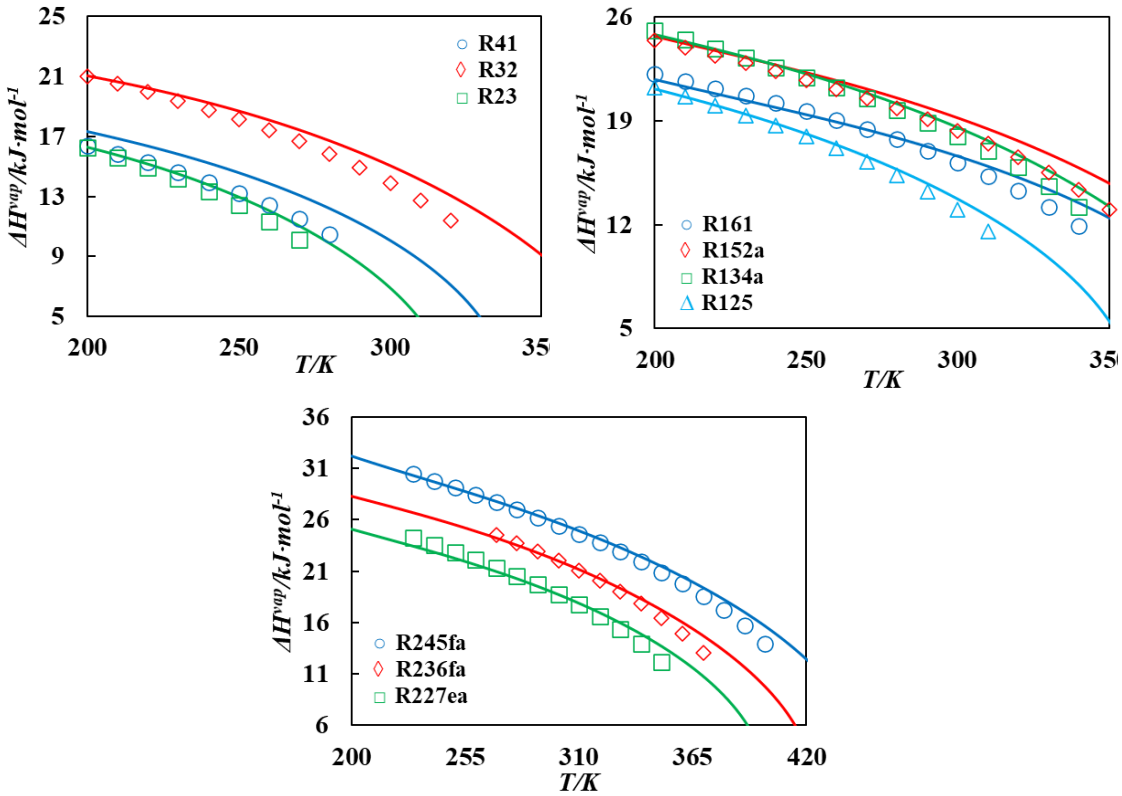

Figure A3. *Enthalpy of vaporization of 3rd generation refrigerants predicted with polar soft-SAFT EoS (solid lines), compared to experimental data [1] (symbols).*

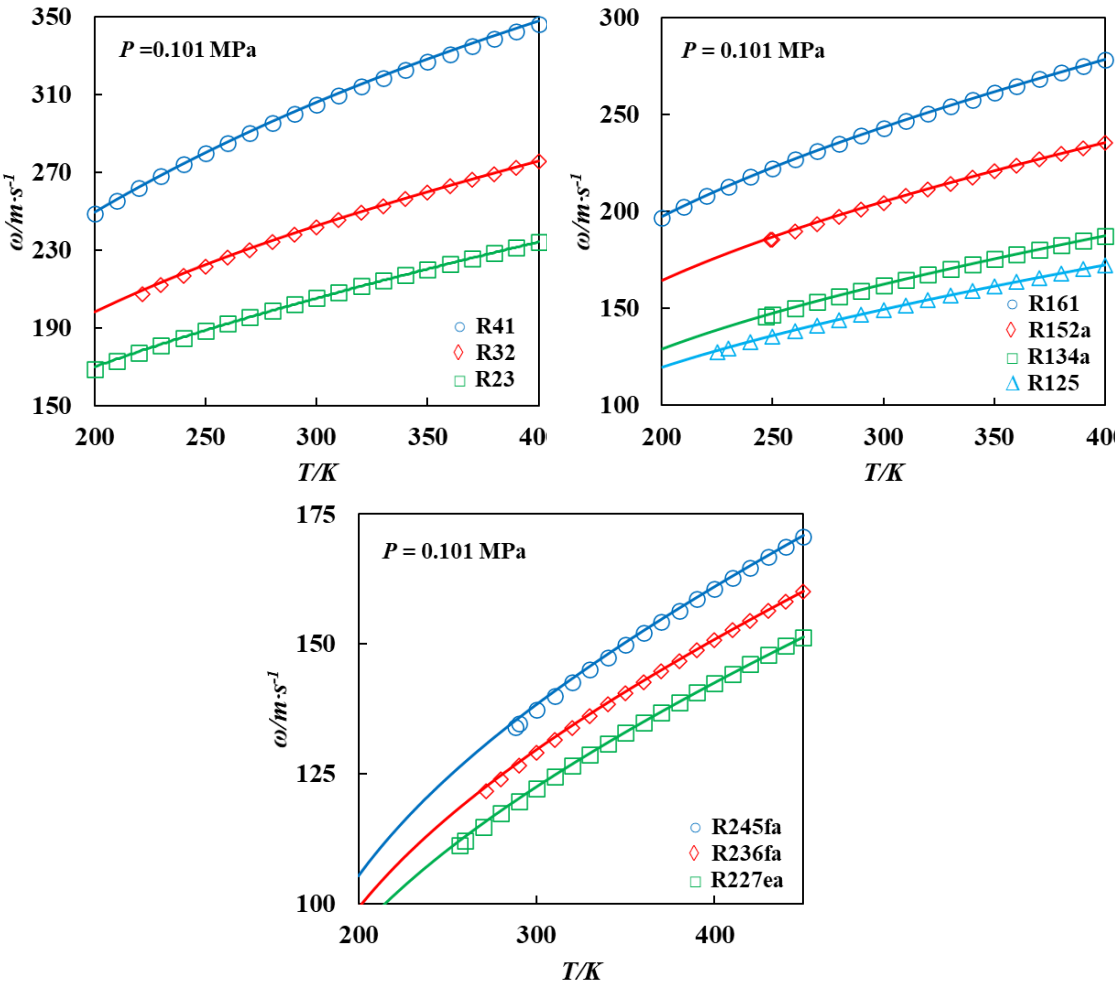

Figure A4. *Speed of sound of 3rd generation refrigerants predicted with polar soft-SAFT EoS (solid lines), compared to experimental data [1] (symbols).*

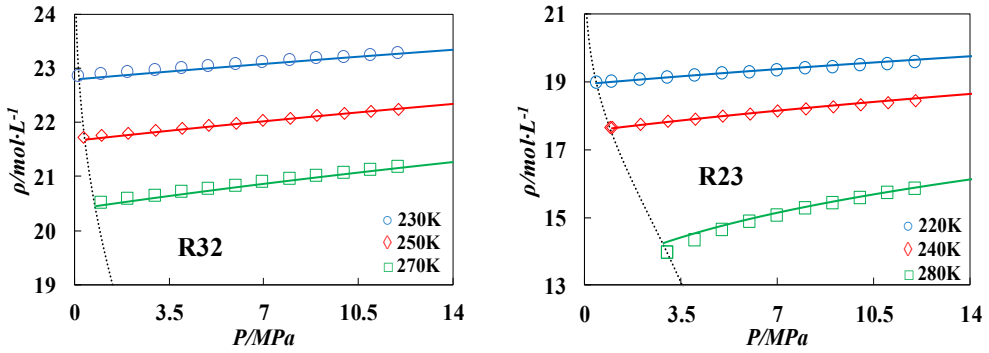

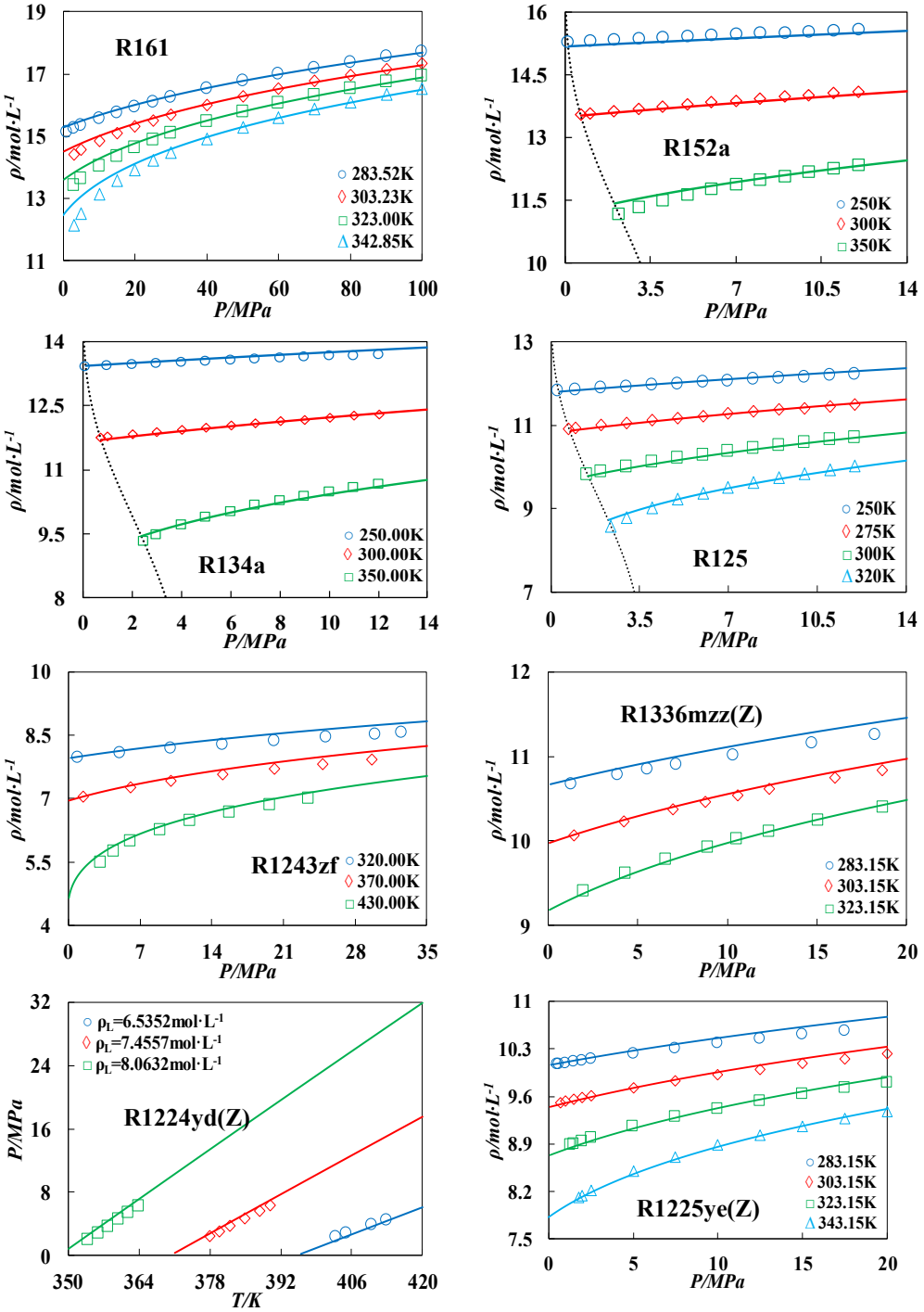

Figure A5. *Single-phase density of 3rd and 4th generation refrigerants predicted with polar soft-SAFT EoS (solid lines), compared to experimental data [1,6-10] (symbols).*

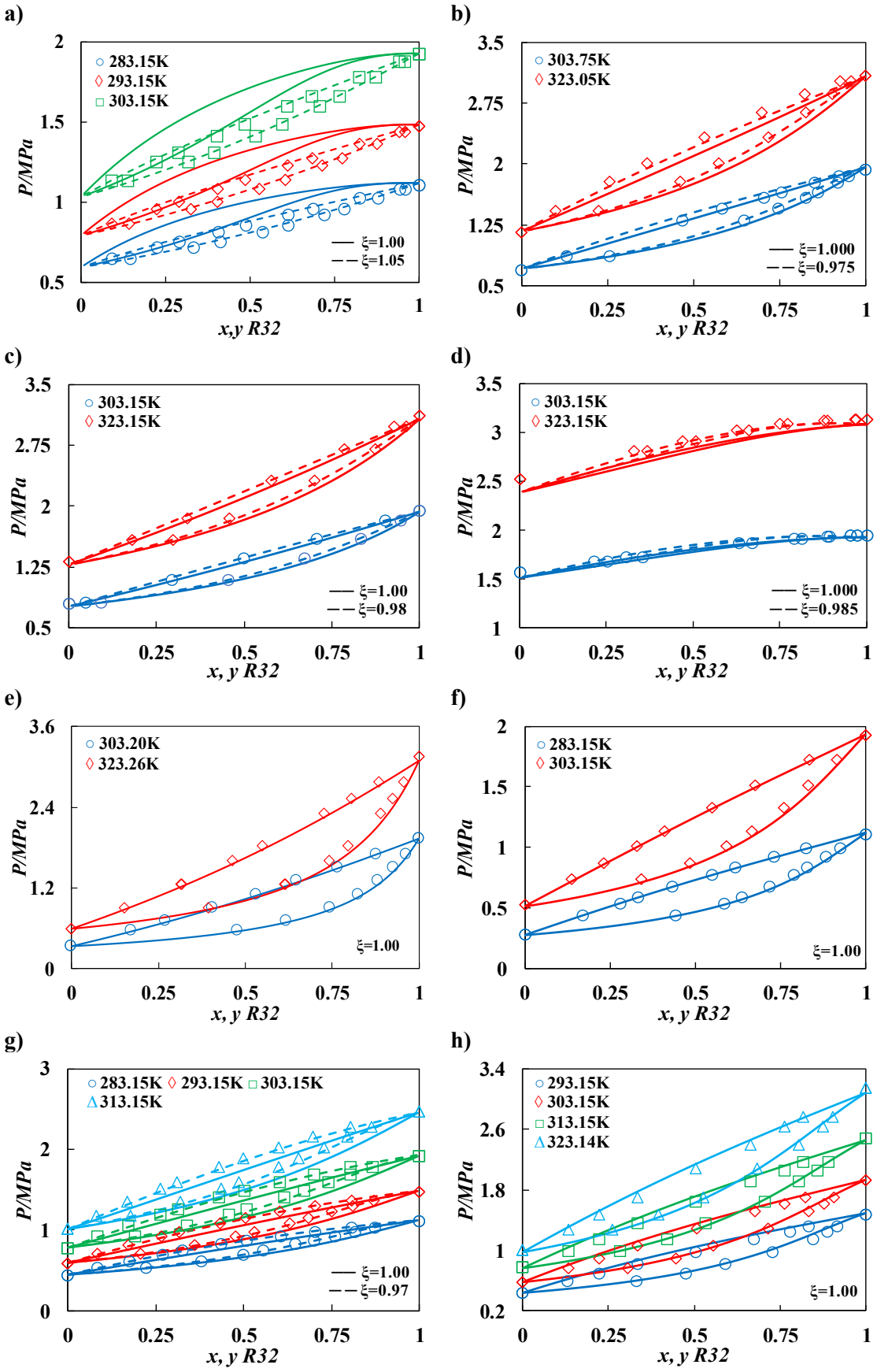
a)
283.15K
293.15K
303.15K
ξ=1.00
ξ=1.05
P/MPa
x,y R32
b)
303.75K
323.05K
ξ=1.000
ξ=0.975
P/MPa
x, y R32
c)
303.15K
323.15K
ξ=1.00
ξ=0.98
P/MPa
x, y R32
d)
303.15K
323.15K
ξ=1.000
ξ=0.985
P/MPa
x, y R32
e)
303.20K
323.26K
ξ=1.00
P/MPa
x, y R32
f)
283.15K
303.15K
ξ=1.00
P/MPa
x, y R32
g)
283.15K
293.15K
303.15K
313.15K
ξ=1.00
ξ=0.97
P/MPa
x, y R32
h)
293.15K
303.15K
313.15K
323.14K
ξ=1.00
P/MPa
x, y R32

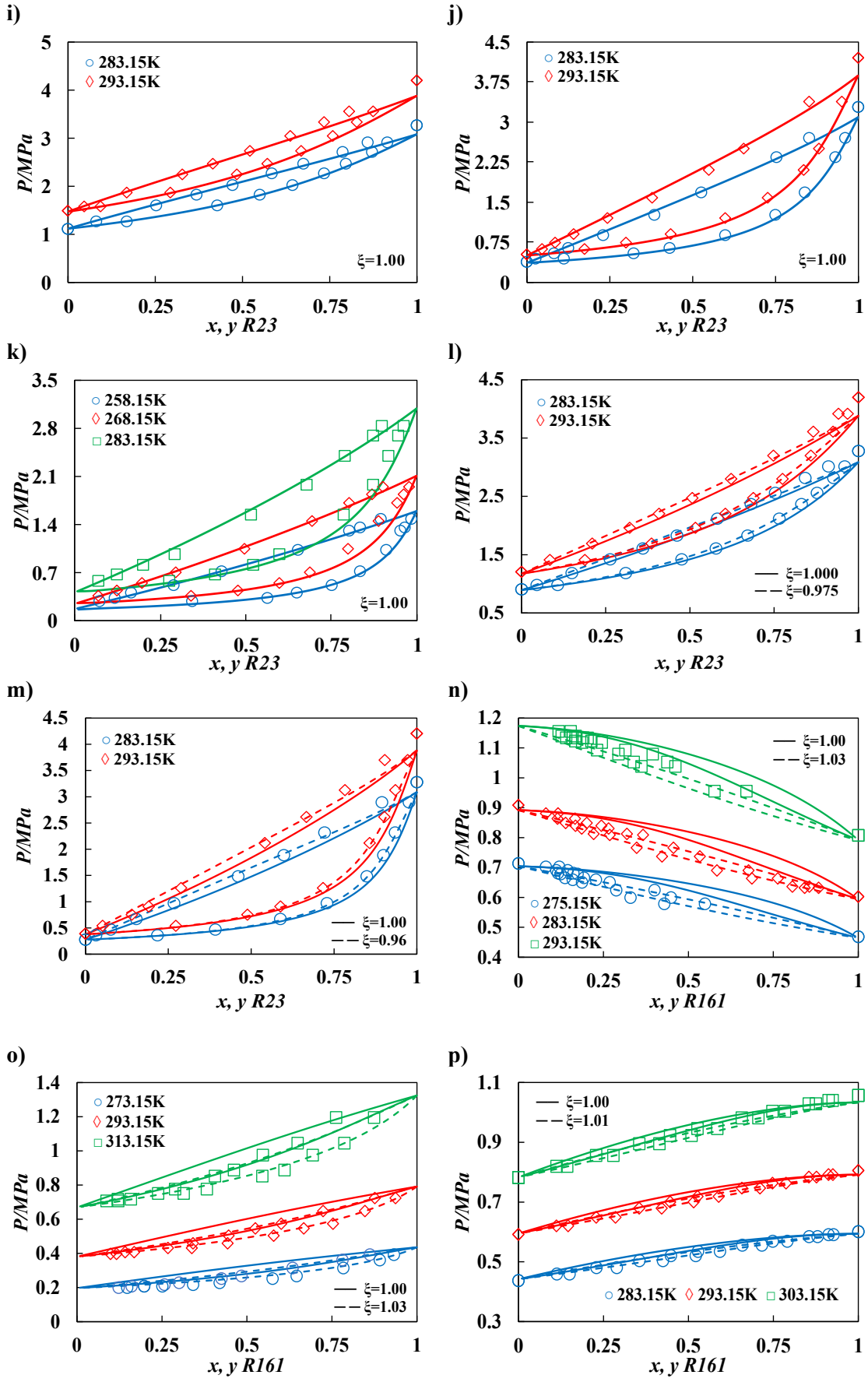
i)
283.15K
293.15K
ξ=1.00
P/MPa
x, y R23
j)
283.15K
293.15K
ξ=1.00
P/MPa
x, y R23
k)
258.15K
268.15K
283.15K
ξ=1.00
P/MPa
x, y R23
l)
283.15K
293.15K
ξ=1.000
ξ=0.975
P/MPa
x, y R23
m)
283.15K
293.15K
ξ=1.00
ξ=0.96
P/MPa
x, y R23
n)
ξ=1.00
ξ=1.03
275.15K
283.15K
293.15K
P/MPa
x, y R161
o)
273.15K
293.15K
313.15K
ξ=1.00
ξ=1.03
P/MPa
x, y R161
p)
ξ=1.00
ξ=1.01
283.15K
293.15K
303.15K
P/MPa
x, y R161

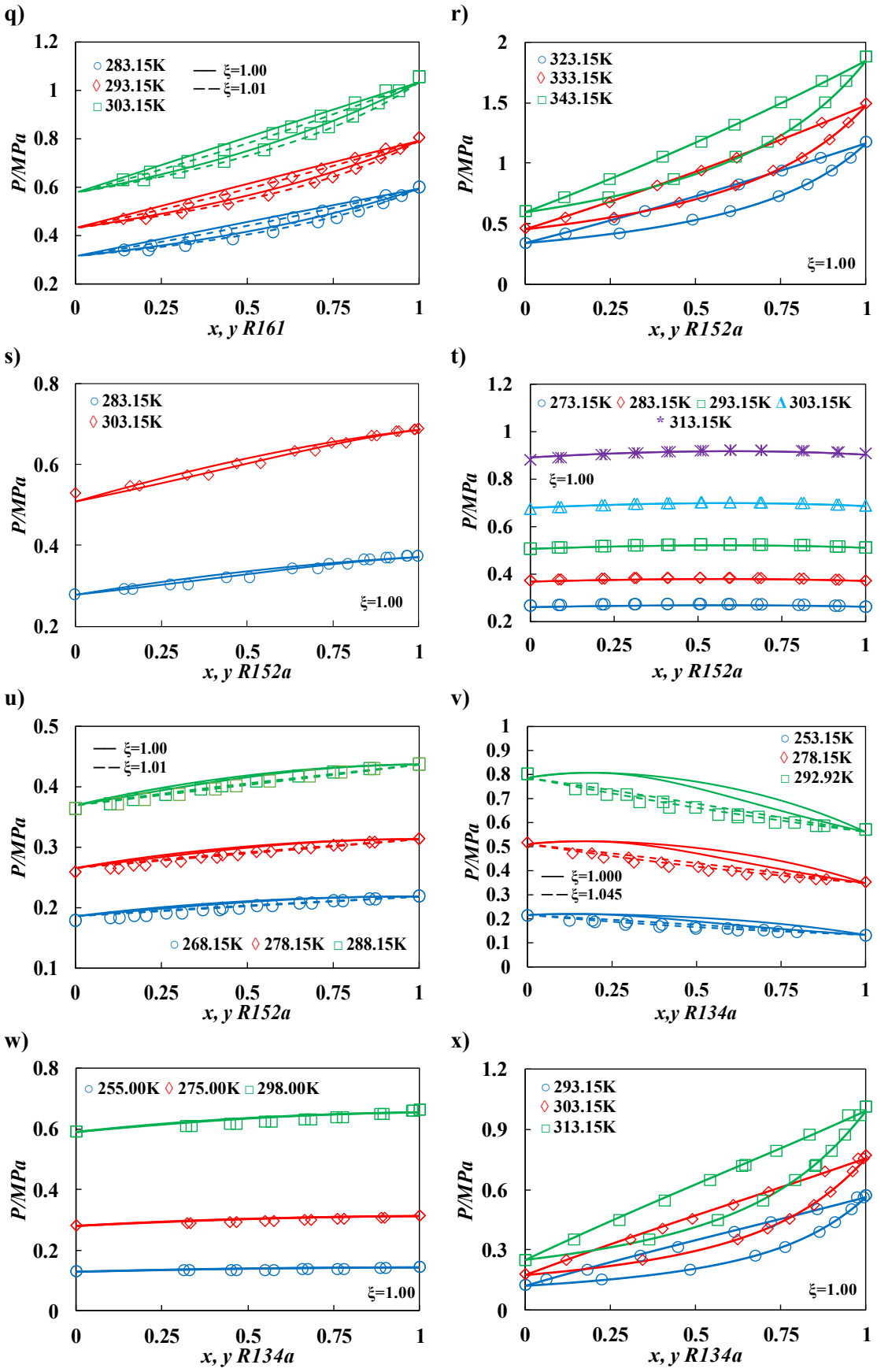
q)
283.15K
293.15K
303.15K
ξ=1.00
ξ=1.01
P/MPa
x, y R161
r)
323.15K
333.15K
343.15K
ξ=1.00
P/MPa
x, y R152a
s)
283.15K
303.15K
ξ=1.00
P/MPa
x, y R152a
t)
273.15K 283.15K 293.15K 303.15K
313.15K
ξ=1.00
P/MPa
x, y R152a
u)
ξ=1.00
ξ=1.01
268.15K 278.15K 288.15K
P/MPa
x, y R152a
v)
253.15K
278.15K
292.92K
ξ=1.000
ξ=1.045
P/MPa
x,y R134a
w)
255.00K 275.00K 298.00K
ξ=1.00
P/MPa
x, y R134a
x)
293.15K
303.15K
313.15K
ξ=1.00
P/MPa
x, y R134a

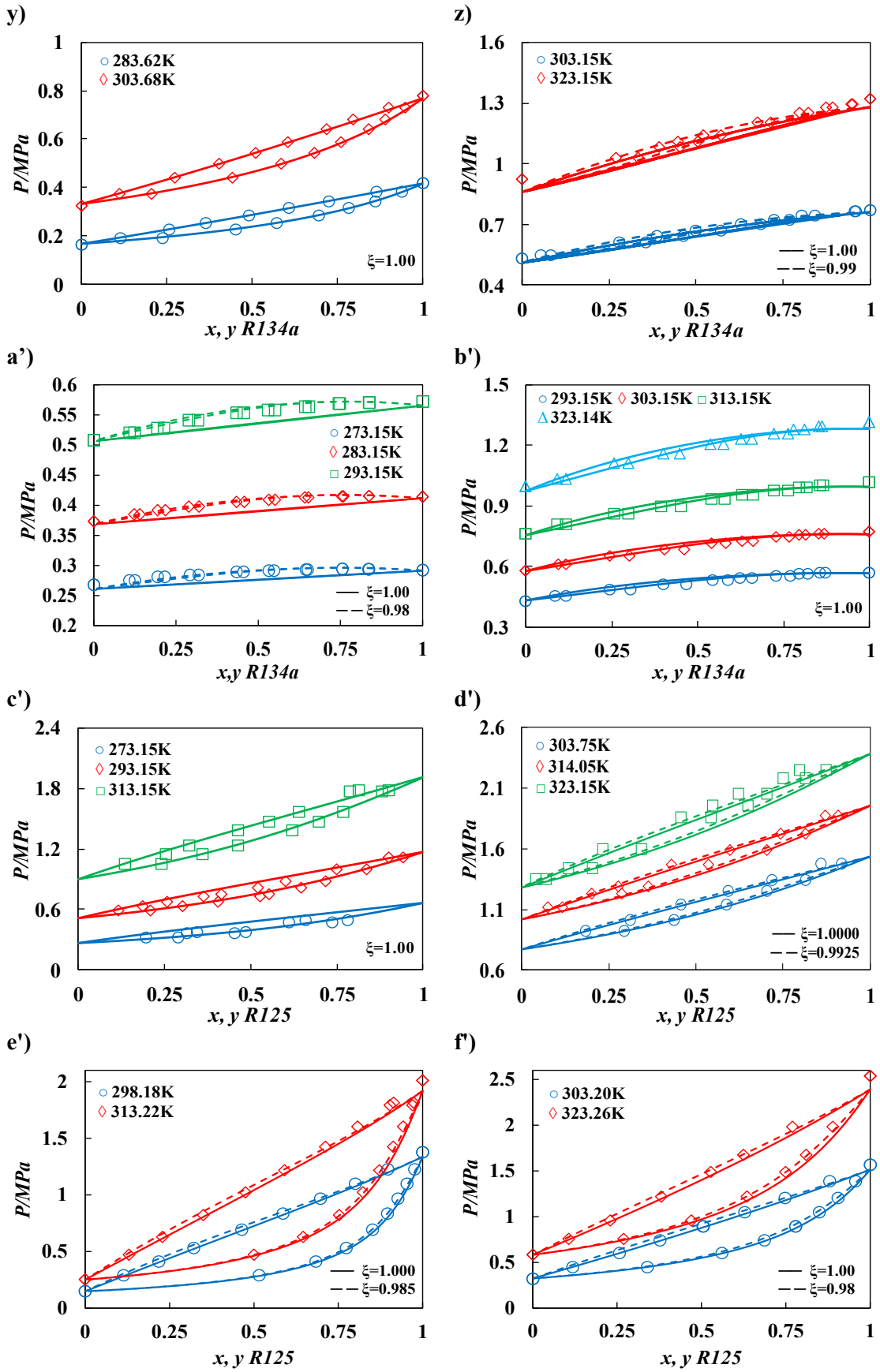
y)
283.62K
303.68K
ξ=1.00
P/MPa
x, y R134a
z)
303.15K
323.15K
ξ=1.00
ξ=0.99
P/MPa
x, y R134a
a')
273.15K
283.15K
293.15K
ξ=1.00
ξ=0.98
P/MPa
x,y R134a
b')
293.15K
303.15K
313.15K
323.14K
ξ=1.00
P/MPa
x, y R134a
c')
273.15K
293.15K
313.15K
ξ=1.00
P/MPa
x, y R125
d')
303.75K
314.05K
323.15K
ξ=1.0000
ξ=0.9925
P/MPa
x, y R125
e')
298.18K
313.22K
ξ=1.000
ξ=0.985
P/MPa
x, y R125
f')
303.20K
323.26K
ξ=1.00
ξ=0.98
P/MPa
x, y R125

g')

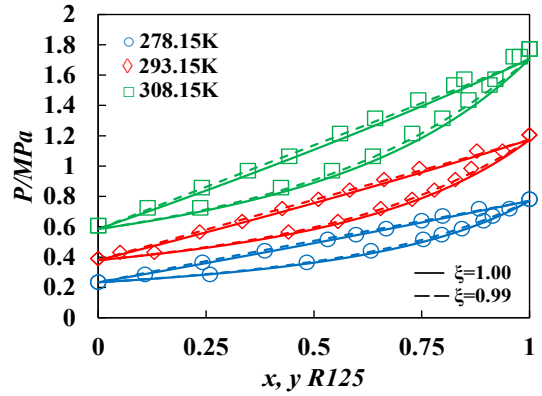
278.15K
293.15K
308.15K
ξ=1.00
ξ=0.99
P/MPa
x, y R125

h')

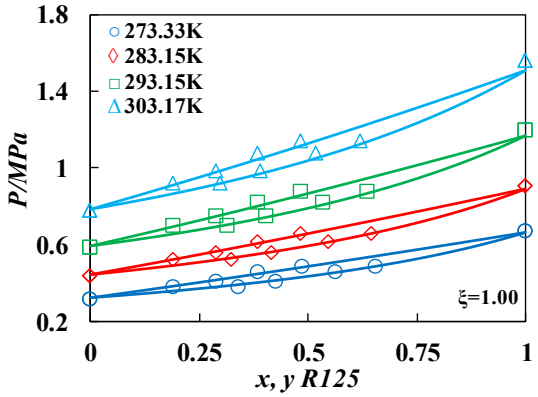
273.33K
283.15K
293.15K
303.17K
ξ=1.00
P/MPa
x, y R125

i')

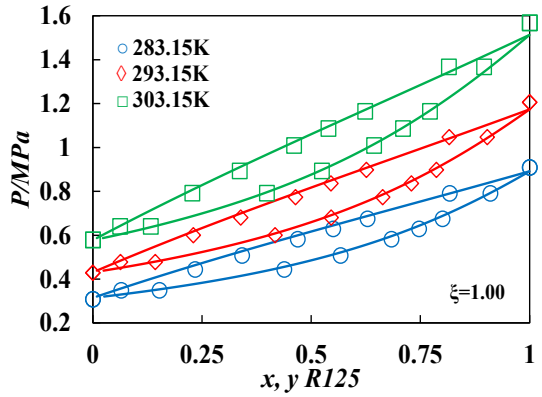
283.15K
293.15K
303.15K
ξ=1.00
P/MPa
x, y R125

j')

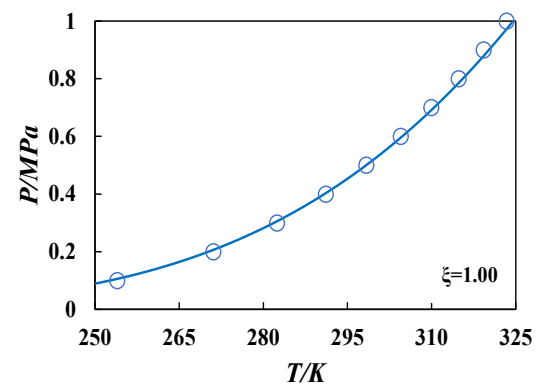
ξ=1.00
P/MPa
T/K

k')

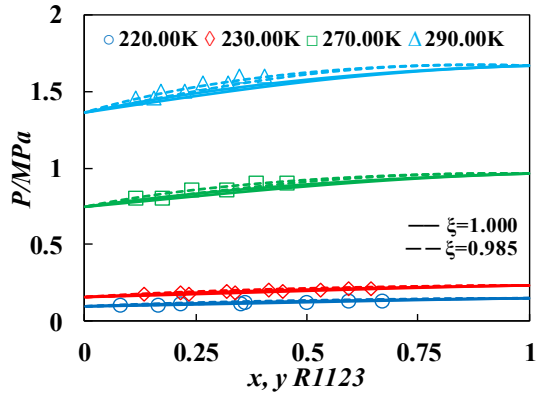
220.00K
230.00K
270.00K
290.00K
ξ=1.000
ξ=0.985
P/MPa
x, y R1123

l')

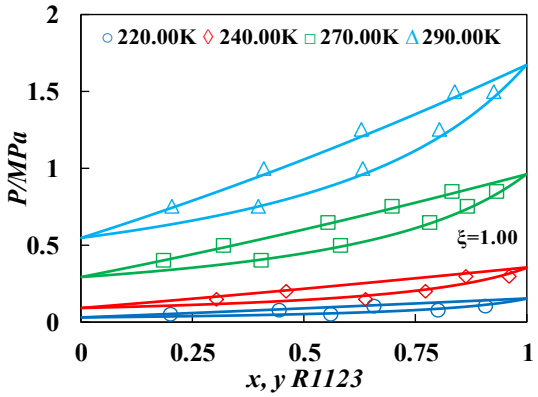
220.00K
240.00K
270.00K
290.00K
ξ=1.00
P/MPa
x, y R1123

m')

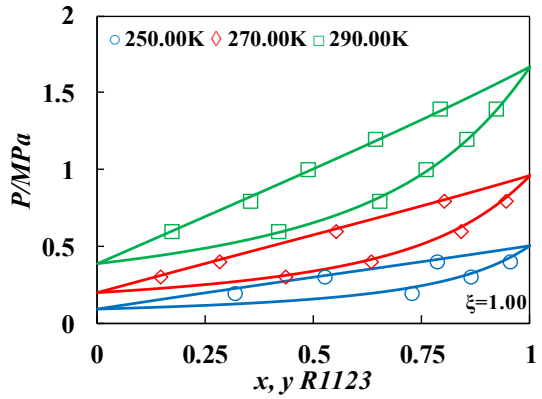
250.00K
270.00K
290.00K
ξ=1.00
P/MPa
x, y R1123

n')

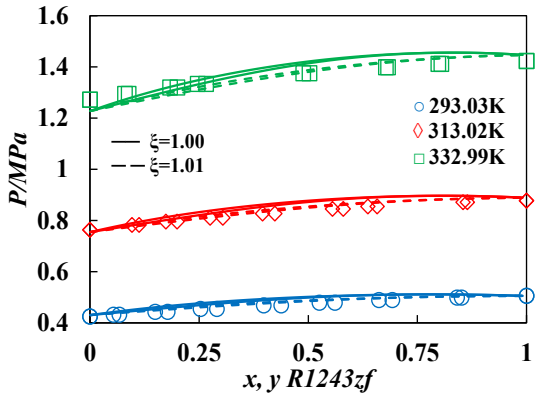
293.03K
313.02K
332.99K
ξ=1.00
ξ=1.01
P/MPa
x, y R1243zf

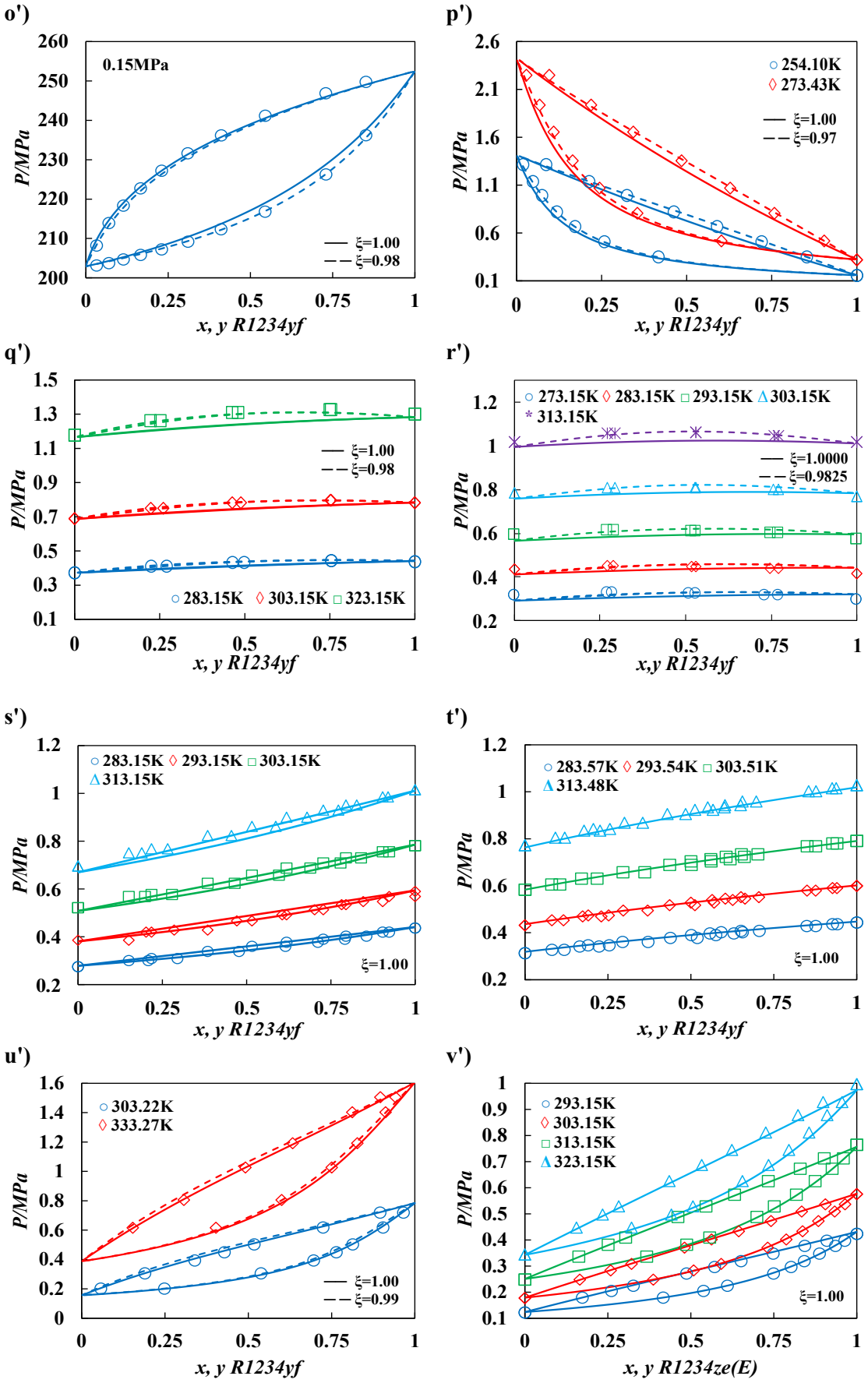
o')
0.15MPa
ξ=1.00
ξ=0.98
P/MPa
x, y R1234yf
p')
254.10K
273.43K
ξ=1.00
ξ=0.97
P/MPa
x, y R1234yf
q')
ξ=1.00
ξ=0.98
283.15K
303.15K
323.15K
P/MPa
x, y R1234yf
r')
273.15K
283.15K
293.15K
303.15K
313.15K
ξ=1.0000
ξ=0.9825
P/MPa
x,y R1234yf
s')
283.15K
293.15K
303.15K
313.15K
ξ=1.00
P/MPa
x, y R1234yf
t')
283.57K
293.54K
303.51K
313.48K
ξ=1.00
P/MPa
x, y R1234yf
u')
303.22K
333.27K
ξ=1.00
ξ=0.99
P/MPa
x, y R1234yf
v')
293.15K
303.15K
313.15K
323.15K
ξ=1.00
P/MPa
x, y R1234ze(E)

Figure A6. *VLE of refrigerants binary blends for* ***a)*** *R32+R161,* ***b)*** *R32+R152a ,* ***c)*** *R32+R134a,* ***d)*** *R32+R125,* ***e)*** *R32+R236fa,* ***f)*** *R32+R227ea,* ***g)*** *R32+R1234yf,* ***h)*** *R32+R1234ze(E),* ***i)*** *R23+R32,* ***j)*** *R23+R152a,* ***k)*** *R23+R134a,* ***l)*** *R23+R125,* ***m)*** *R23+R227ea,* ***n)*** *R161+R125,* ***o)*** *R161+R227ea,* ***p)*** *R161+R1234yf,* ***q)*** *R161+R1234ze(E),* ***r)*** *R152a+R245fa,* ***s)*** *R152a+R227ea,* ***t)*** *R152a+R1243zf,* ***u)*** *R152a+R1234ze(E),* ***v)*** *R134a+R161,* ***w)*** *R134a+R152a,* ***x)*** *R134a+R245fa,* ***y)*** *R134a+R236fa,* ***z)*** *R134a+R227ea,* ***a')*** *R134a+R1243zf,* ***b')*** *R134a+R1234ze(E),* ***c')*** *R125+R152a,* ***d')*** *R125+R134a,* ***e')*** *R125+R245fa,* ***f')*** *R125+R236fa,* ***g')*** *R125+R227ea,* ***h')*** *R125+R1234yf,* ***i')*** *R125+R1234ze(E),* ***j')*** *R227ea+R1234ze(E),* ***k')*** *R1123+R32,* ***l')*** *R1123+R1234yf,* ***m')*** *R1123+R1234ze(E),* ***n')*** *R1243zf+R1234ze(E),* ***o')*** *R1234yf+R41,* ***p')*** *R1234yf+R23,* ***q')*** *R1234yf+R152a,* ***r')*** *R1234yf+R134a,* ***s')*** *R1234yf+R227ea,* ***t')*** *R1234yf+R1234ze(E),* ***u')*** *R1234yf+R1233zd(E), and* ***v')*** *R1234ze(E)+R245fa. Symbols are experimental data and lines polar soft-SAFT calculations.*

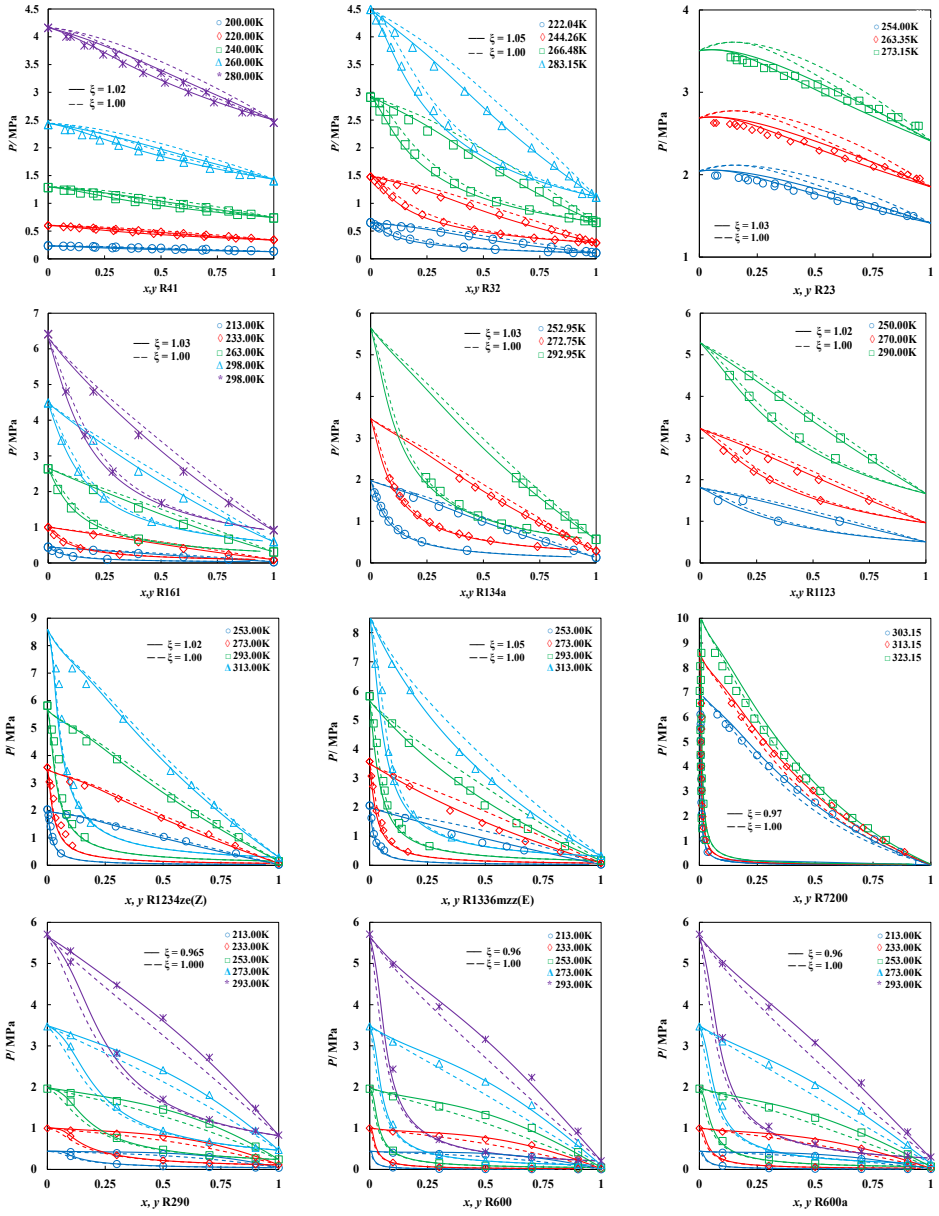

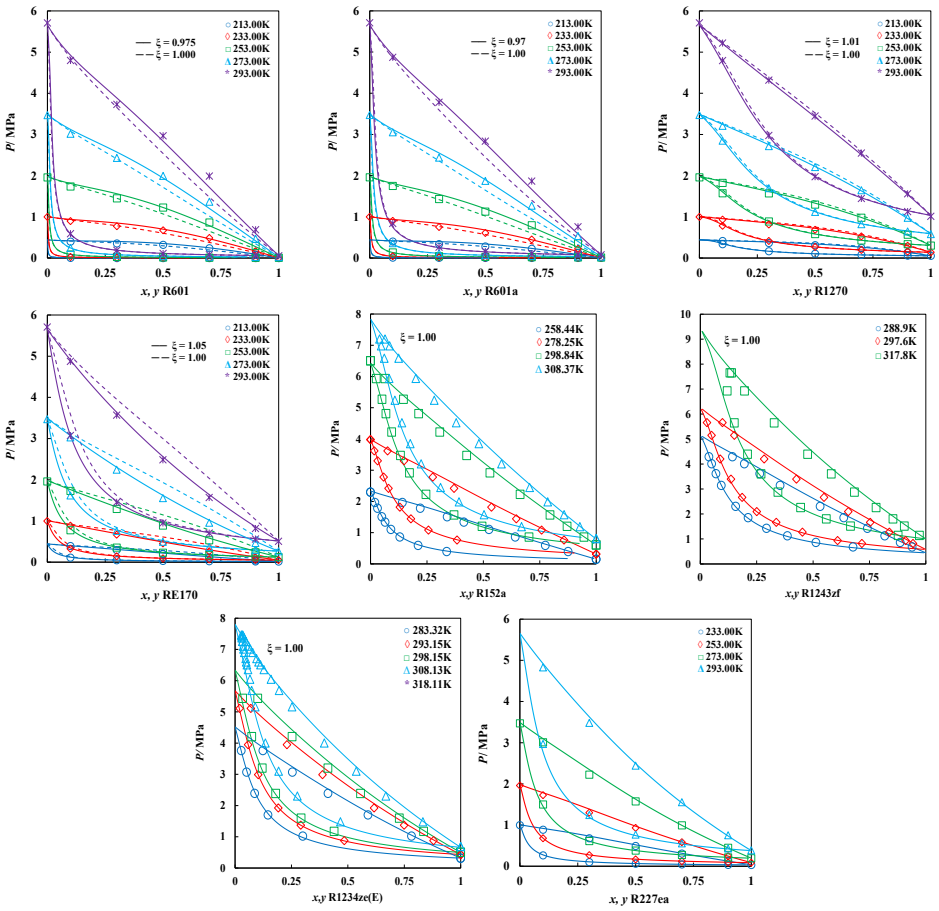

Figure A7. *VLEs for CO_2-based binary mixtures. Symbols correspond to experimental data, solid lines to fitted characterizations, and dashed lines to polar soft-SAFT predictions (ξ_{ij} =1.00).*

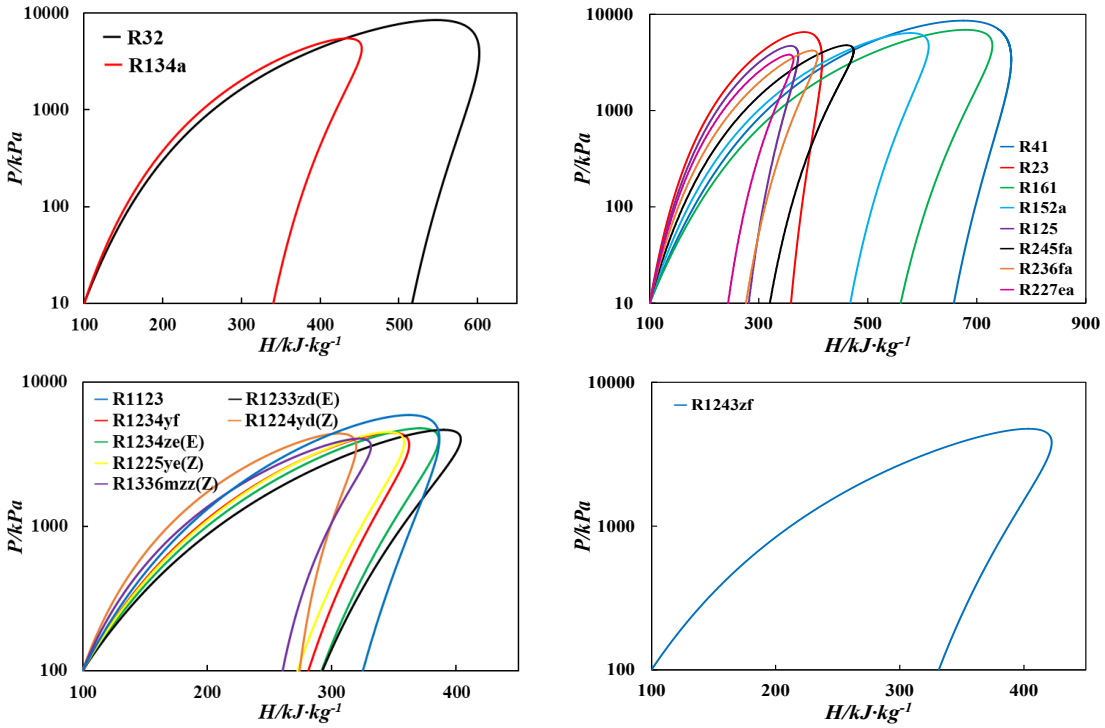

Figure A8. *Polar soft-SAFT predicted PH diagrams.*

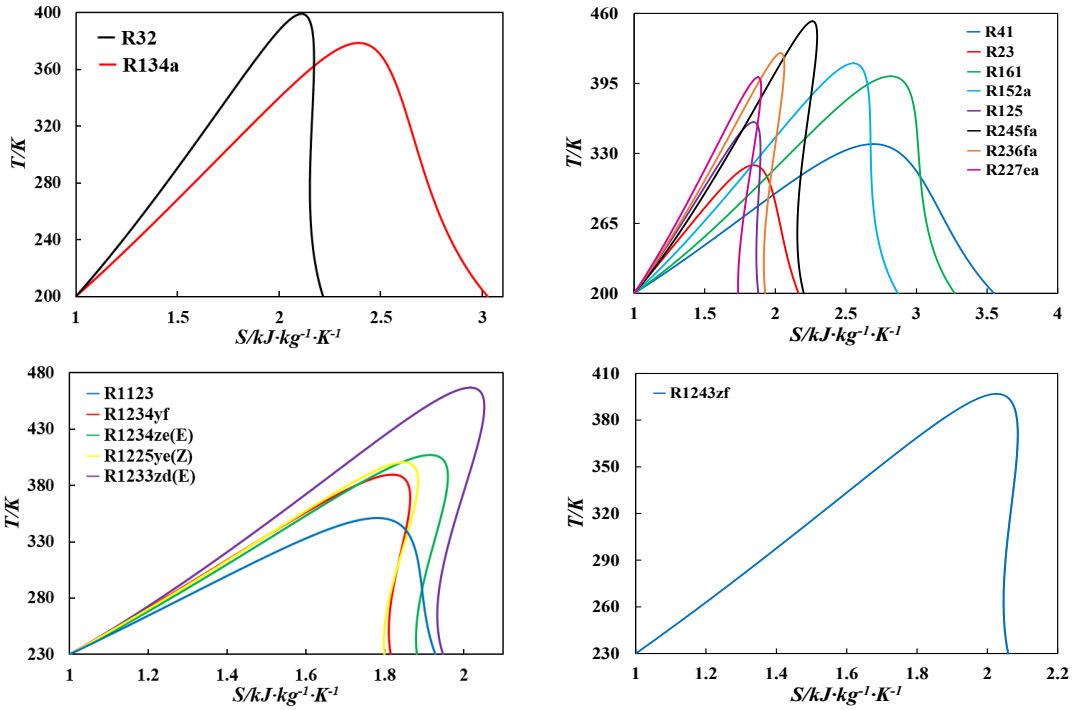

Figure A9. *Polar soft-SAFT predicted TS diagrams.*

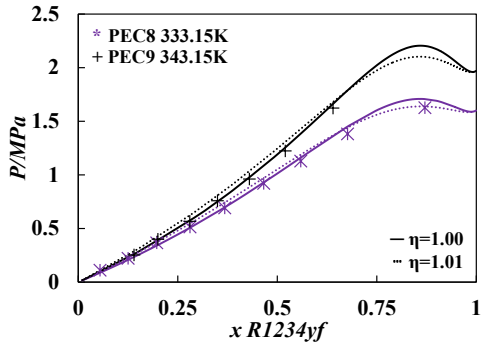

Figure B1. *Pressure-composition diagram of the blends formed by a mixture of R1234yf and* ***a)*** *PEC8 at 333.15K (magenta asterisks)* ***b)*** *PEC9 at 343.15K (black plusses).*

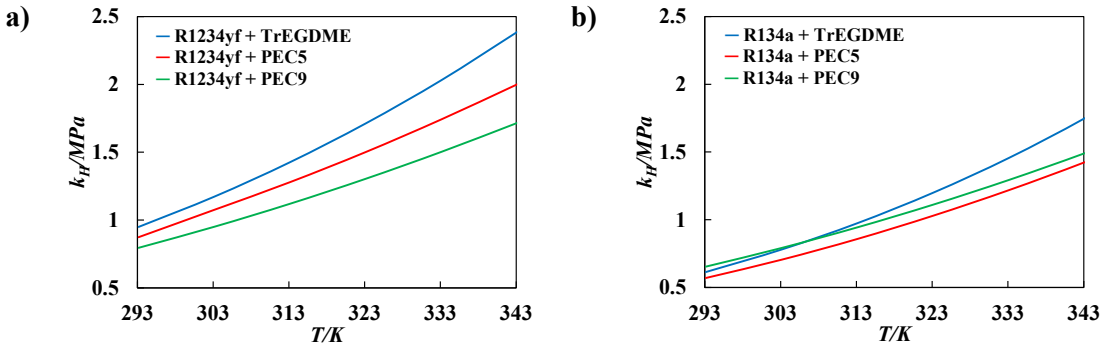

Figure B2. *Henry's law constants calculated by polar soft-SAFT as a function of temperature for* ***a)*** *R1234yf and* ***b)*** *R134a, in TrEGDME (blue), PEC5 (red) and PEC9 (green).*

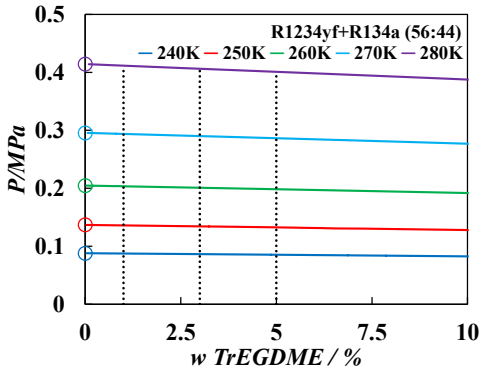

Figure B3. *Soft-SAFT liquid phase equilibria prediction of the ternary mixture R1234yf, R134a and lubricant TrEGDME at 240K (blue), 250K (red), 260K (green), 270K (light blue) and 280K (magenta). Circles represent the soft-SAFT predictions regarding R1234yf+R134a binary mixtures at the corresponding temperatures.*

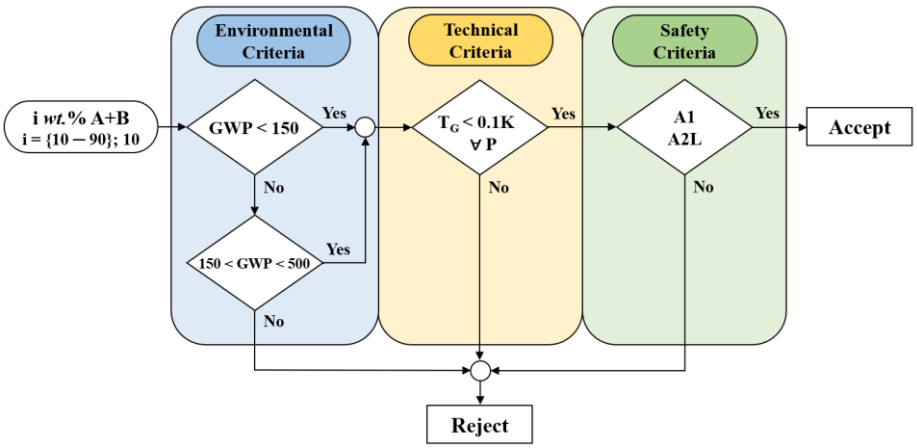

Figure C1. *Initial screening criteria for blend selection based on environmental, technical, and safety criteria.*

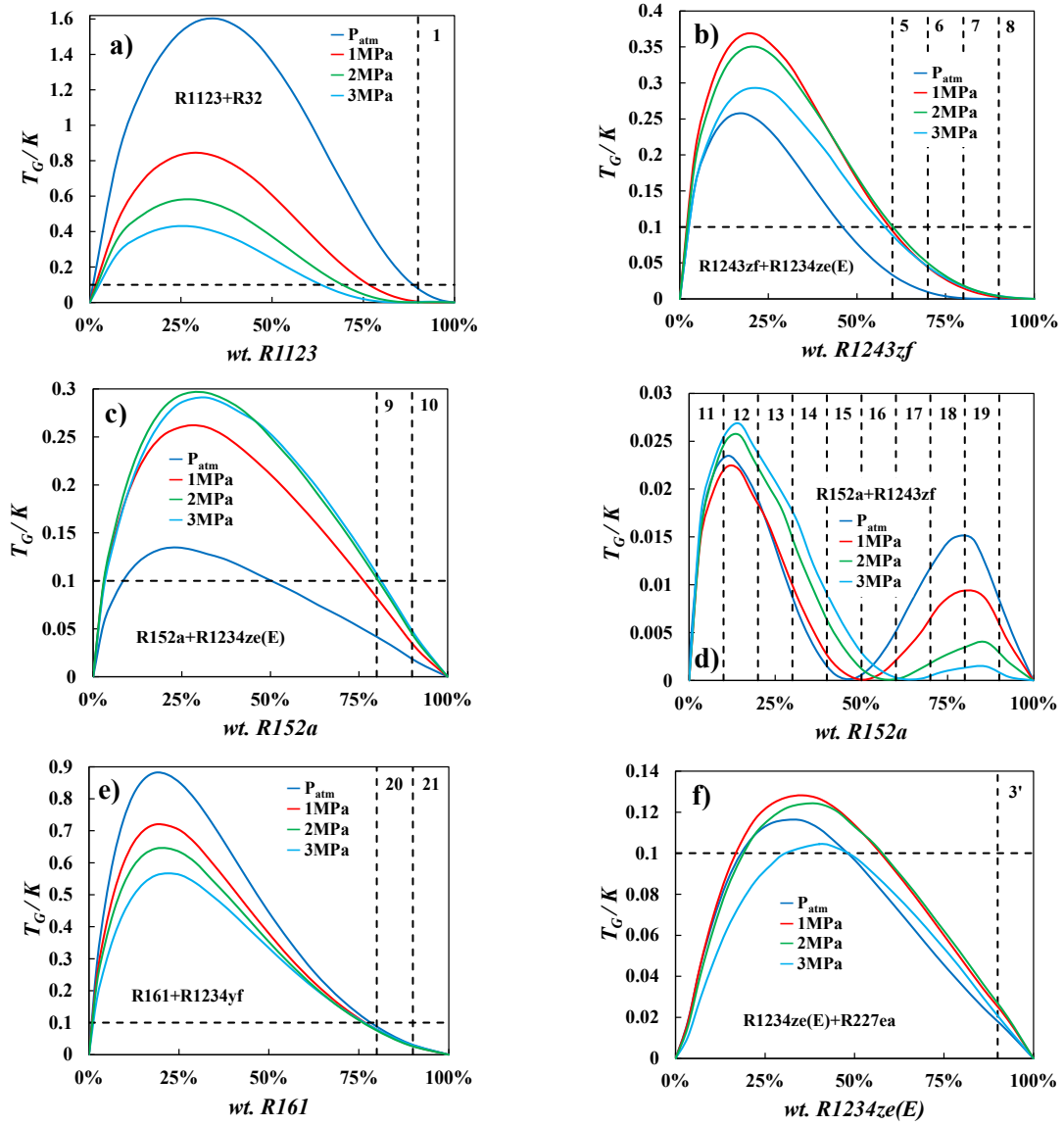

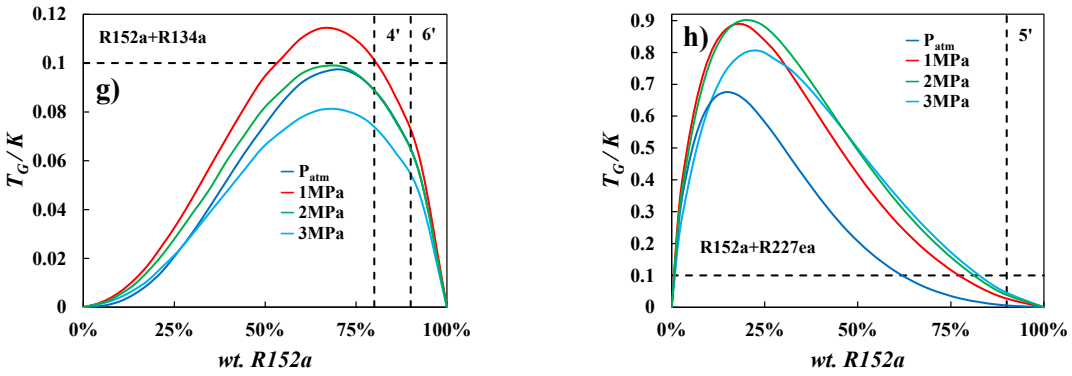

Figure C2. *Glide temperature as a function of the mass fraction for binary blends in* ***Table 6.1*** *as well as* **Figure *C1*** *with* ***a)*** *R1123 + R32,* ***b)*** *R1243zf + R1234ze(E),* ***c)*** *R152a + R1234ze(E),* ***d)*** *R152a + R1243zf,* ***e)*** *R161 + R1234yf,* ***f)*** *R1234ze(E) + R227ea,* ***g)*** *R152a + R134a and* ***h)*** *R152a + R227ea. Lines are polar soft-SAFT calculations.*

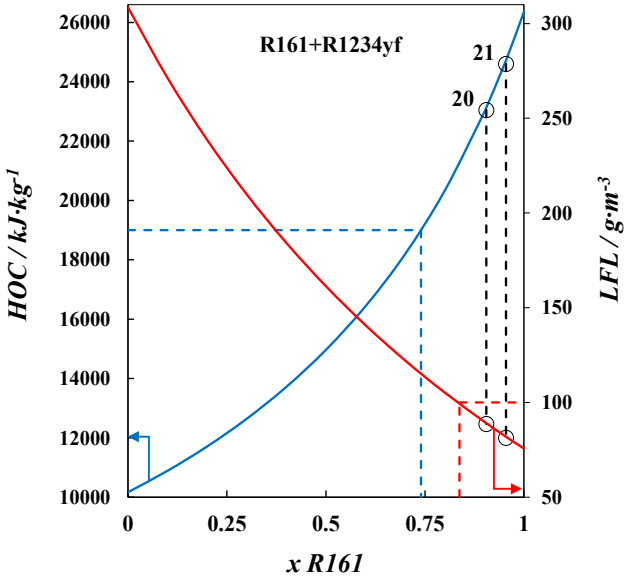

Figure C3. *Heat of combustion (left y -axis) and low flammability level (right y -axis) as a function of the mole fraction of A3 compound R161 within the binary mixture with R1234yf. Enthalpies of formation of pure fluids at 298K are taken from [11,12] while LFL data from [13].*

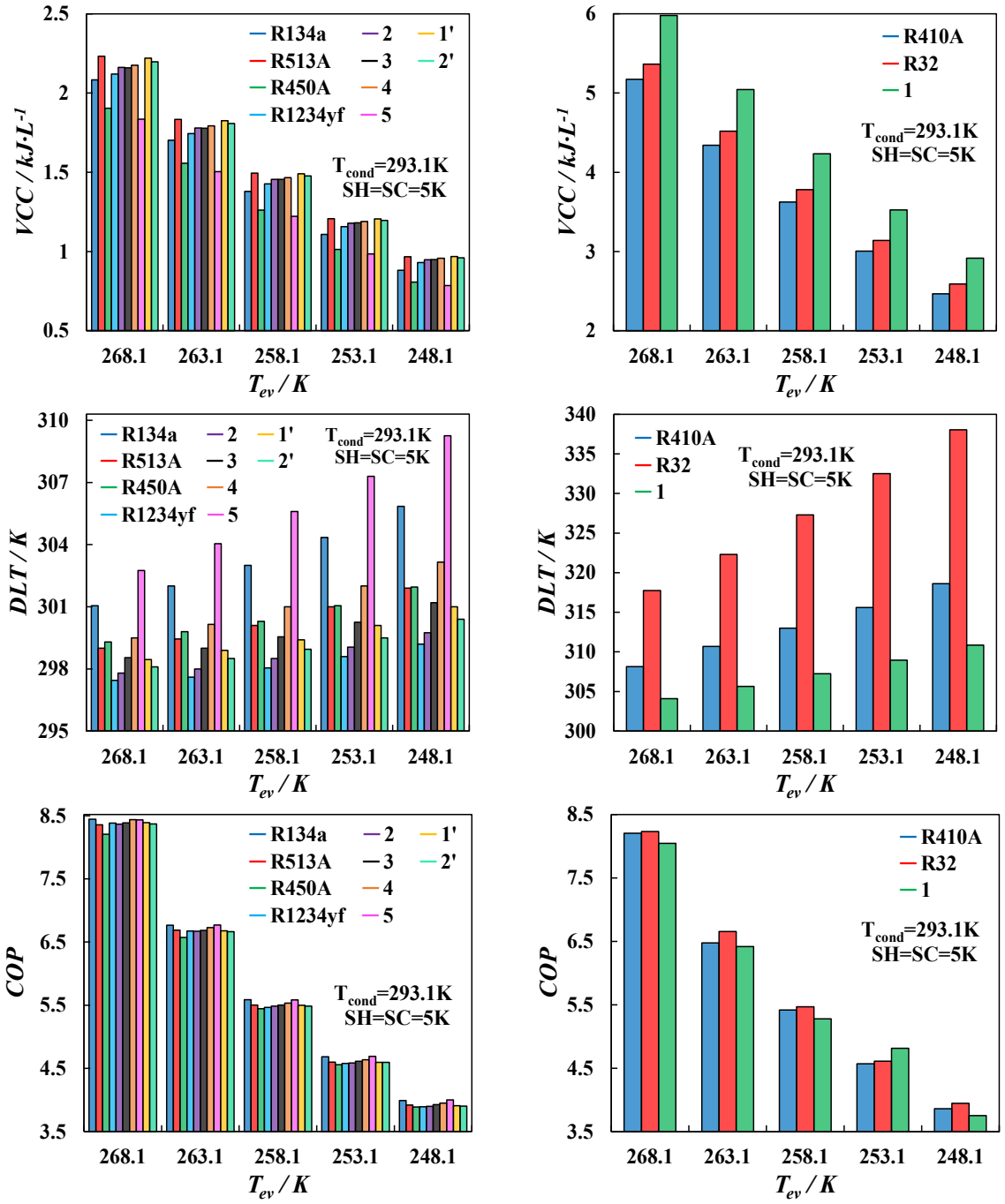

Figure C4. *Drop-in KPIs for promising drop-in replacements blends for R134a (left), and R410A (right) as a function of different outlet evaporator temperature.*

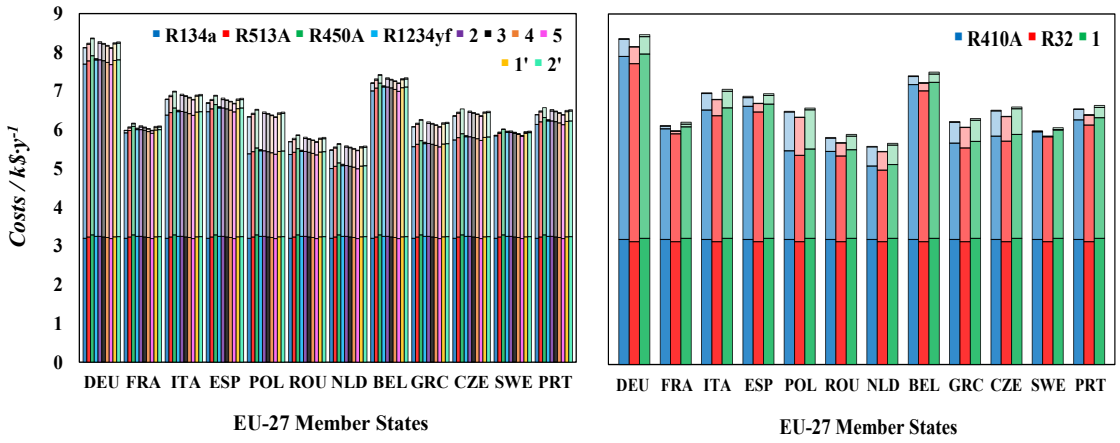

Figure C5. *Economic analysis for most promising alternatives for R134a (left) and R410A (right), for the selected EU-27 countries (top-12, > 85% of total population) sorted by population.*

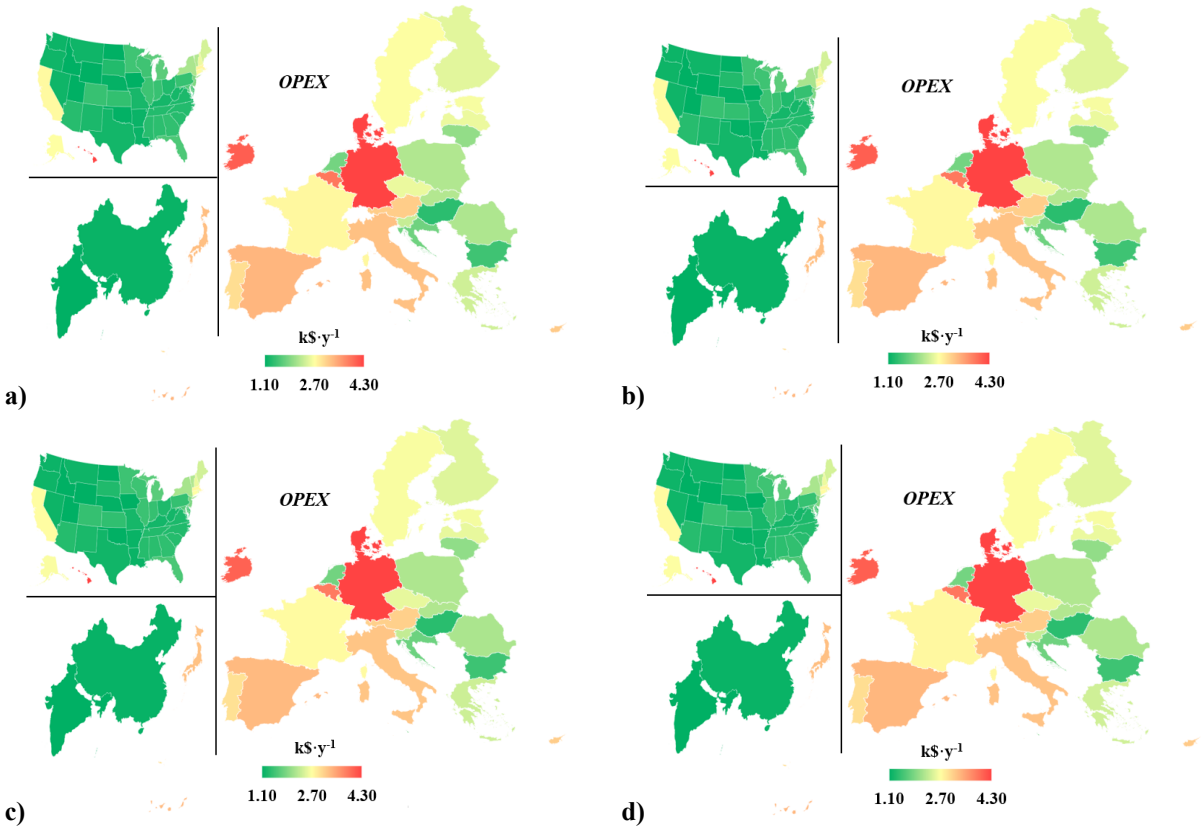

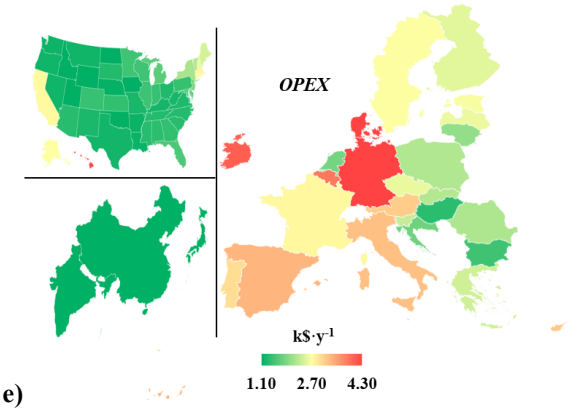

Figure C6. *OPEX costs of examined drop-in refrigerants:* ***a-c)*** *2-4, and* ***d-e)*** *1'-2'.*

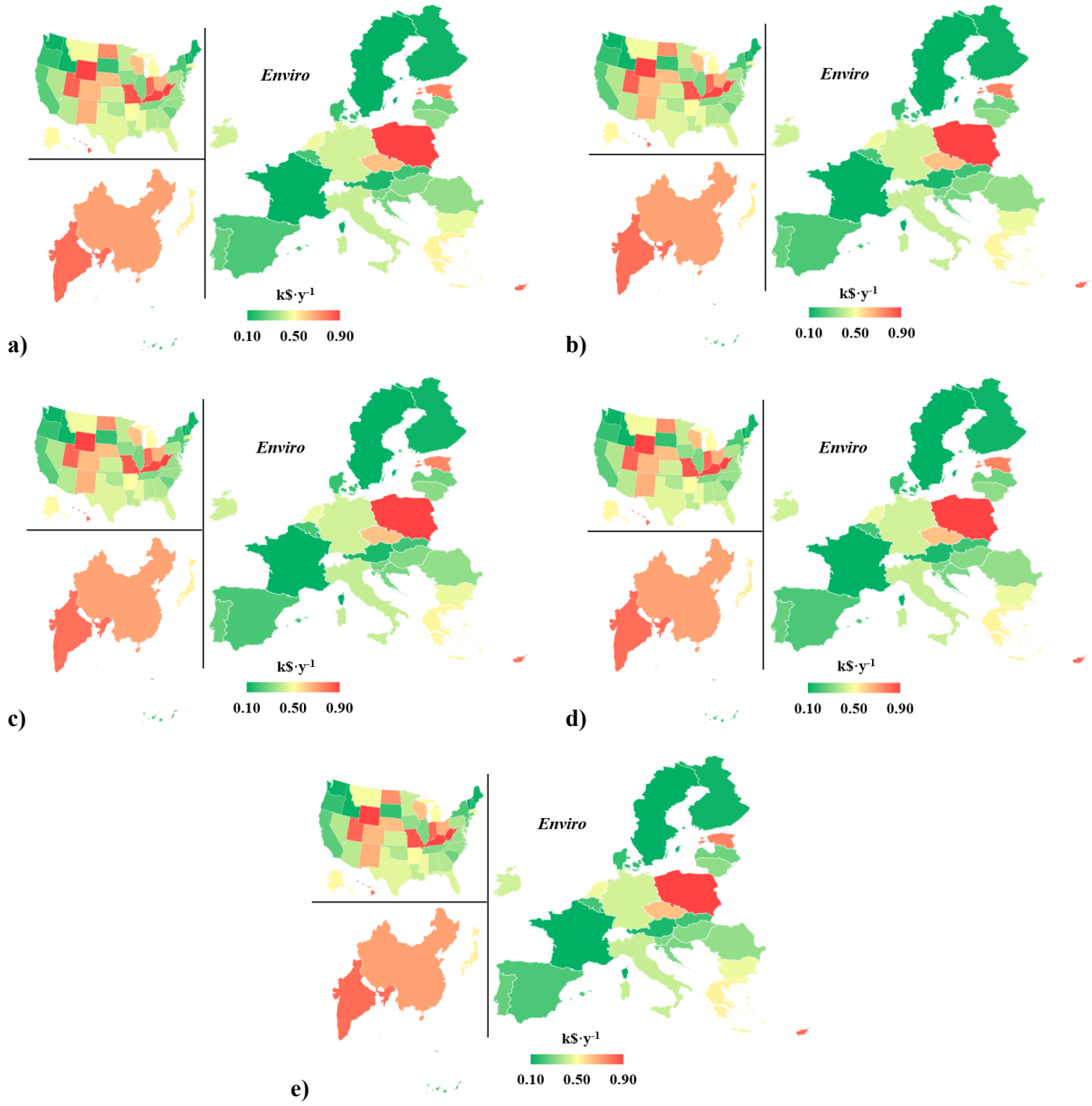

Figure C7. *Environmental costs of examined drop-in refrigerants:* ***a-c)*** *2-4, and* ***d-e)*** *1'-2'.*

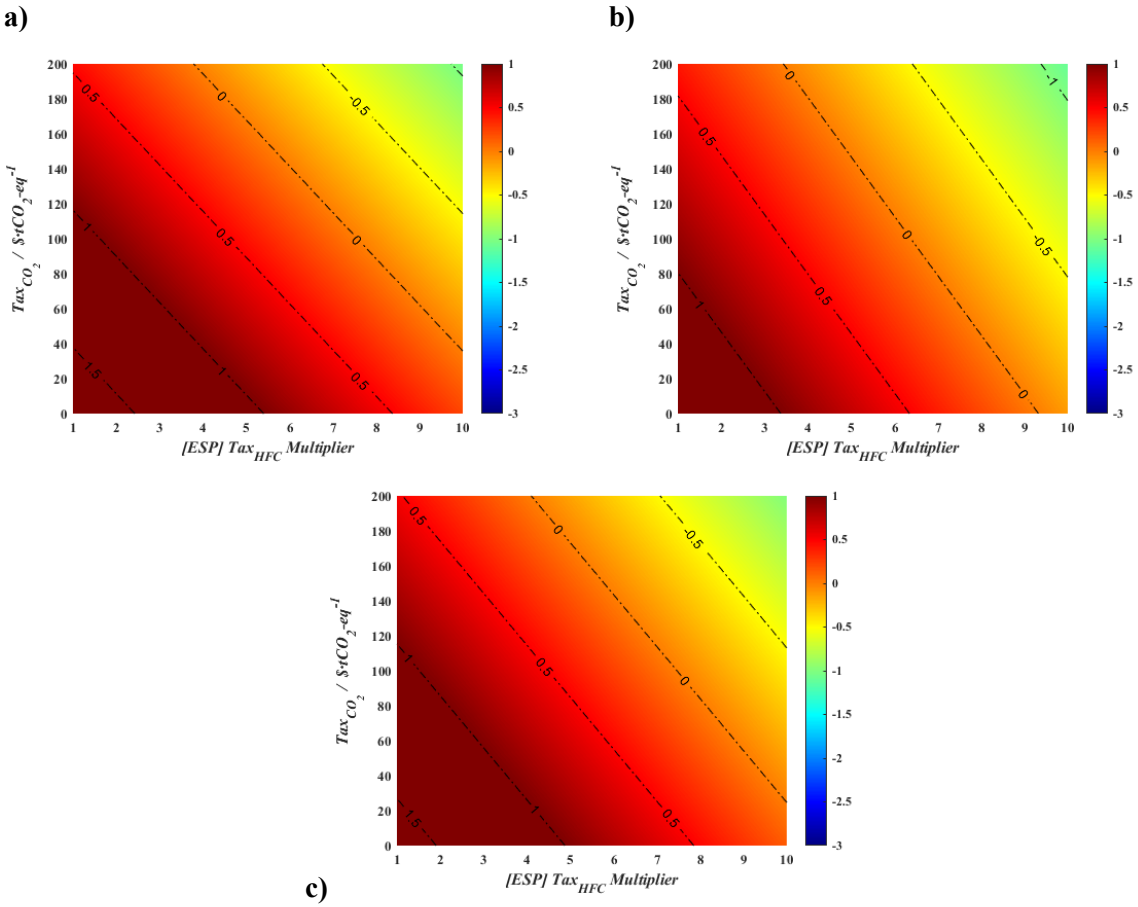

Figure C8. *Sensitivity analysis on replacing R134a by* ***a)*** *2,* ***b)*** *1', and* ***c)*** *2'.*

A	B	C	D	E	F	G
(A)	3	2	5	4	7	6
	(B)	1	6	7	4	5
		(C)	7	6	5	4
			(D)	1	2	3
				(E)	3	2
					(F)	1
						(G)

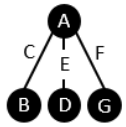

a)

b)

$$A + BC + DE + FG$$
$$B + AC + DF + EG$$
$$C + AB + AE + EF + DG$$
$$D + BF + CG$$
$$E + AD + CF + BG$$
$$F + BD + CE + AG$$
$$G + AF + BE + CD$$

Figure D1. *Taguchi's $L_8(2^7)$ orthogonal array with **a)** triangular table and **b)** alias structure.*

a)

I+ABCE+BCDF+ACDG+ADEF+BDEG+ABFG+CEFG
***A**+BCE+ABCDF+CDG+DEF+ABDEG+BFG+ACEFG*
***B**+ACE+CDF+ABCDG+ABDEF+DEG+AFG+BCEFG*
***C**+ABE+BDF+ADG+ACDEF+BCDEG+ABCFG+EFG*
***D**+ABCDE+BCF+ACG+AEF+BEG+ABDFG+CDEFG*
***E**+ABC+BCDEF+ACDEG+ADF+BDG+ABEFG+CFG*
***F**+ABCEF+BCD+ACDFG+ADE+BDEFG+ABG+CEG*
***G**+ABCEG+BCDFG+ACD+ADEFG+BDE+ABF+CEF*
***AB**+CE+ACDF+BCDG+BDEF+ADEG+FG+ABCEFG*
***AC**+BE+ABDF+DG+CDEF+ABCDEG+BCFG+AEFG*
***AD**+BCDE+ABCF+CG+EF+ABEG+BDFG+ACDEFG*
***AE**+BC+ABCDEF+CDEG+DF+ABDG+BEFG+ACFG*
***AF**+BCEF+ABCD+CDFG+DE+ABDEFG+BG+ACEG*
***AG**+BCEG+ABCDFG+CD+DEFG+ABDE+BF+ACEF*
***BD**+ACDE+CF+ABCG+ABEF+EG+ADFG+BCDEFG*
***ABD**+CDE+ACF+BCG+BEF+AEG+DFG+ABCDEFG*

b)

Exp	A	B	C	D	E	F	G	AB	AC	AD	AE	AF	AG	BD	ABD
1	-1	-1	-1	-1	-1	-1	-1	1	1	1	1	1	1	1	-1
2	1	-1	-1	-1	1	-1	1	-1	-1	-1	1	-1	1	1	1
3	-1	1	-1	-1	1	1	-1	-1	1	1	-1	-1	1	-1	1
4	1	1	-1	-1	-1	1	1	1	-1	-1	-1	1	1	-1	-1
5	-1	-1	1	-1	1	1	1	1	-1	1	-1	-1	-1	1	-1
6	1	-1	1	-1	-1	1	-1	-1	1	-1	-1	1	-1	1	1
7	-1	1	1	-1	-1	-1	1	-1	-1	1	1	1	-1	-1	1
8	1	1	1	-1	1	-1	-1	1	1	-1	1	-1	-1	-1	-1
9	-1	-1	-1	1	-1	1	1	1	1	-1	1	-1	-1	-1	1
10	1	-1	-1	1	1	1	-1	-1	-1	1	1	1	-1	-1	-1
11	-1	1	-1	1	1	-1	1	-1	1	-1	-1	1	-1	1	-1
12	1	1	-1	1	-1	-1	-1	1	-1	1	-1	-1	-1	1	1
13	-1	-1	1	1	1	-1	-1	1	-1	-1	-1	1	1	-1	1
14	1	-1	1	1	-1	-1	1	-1	1	1	-1	-1	1	-1	-1
15	-1	1	1	1	-1	1	-1	-1	-1	-1	1	-1	1	1	-1
16	1	1	1	1	1	1	1	1	1	1	1	1	1	1	1

Figure D2. *2^{7-3} fractional factorial design **a)** alias structure and **b)** inherent matrix. Note that in the matrix structure, columns designate only the first term of the corresponding alias row.*

Exp	A	B	C	D	E	F	G	AB	AC	AD	AE	AF	AG	BD	ABD	COP	VCC / kJ·L^{-1}	η_{II} / %
1	-1	-1	-1	-1	-1	-1	-1	1	1	1	1	1	1	1	-1	6.17	1.23	38.1
17	1	-1	-1	-1	-1	-1	-1	-1	-1	-1	-1	-1	-1	1	1	7.74	1.54	32.8
18	-1	1	-1	-1	-1	-1	-1	-1	1	1	1	1	1	-1	1	7.66	1.29	32.4
19	1	1	-1	-1	-1	-1	-1	1	-1	-1	-1	-1	-1	-1	-1	9.96	1.61	61.7
20	-1	-1	1	-1	-1	-1	-1	1	-1	1	1	1	1	1	-1	6.29	1.26	53.3
21	1	-1	1	-1	-1	-1	-1	-1	1	-1	-1	-1	-1	1	1	7.86	1.57	33.0
22	-1	1	1	-1	-1	-1	-1	-1	-1	1	1	1	1	-1	1	7.78	1.32	47.6
23	1	1	1	-1	-1	-1	-1	1	1	-1	-1	-1	-1	-1	-1	10.08	1.63	61.9
94	-1	-1	-1	1	-1	-1	-1	1	1	-1	1	1	1	-1	1	7.39	1.24	45.2
95	1	-1	-1	1	-1	-1	-1	-1	-1	1	-1	-1	-1	-1	-1	9.23	1.54	38.8
96	-1	1	-1	1	-1	-1	-1	-1	1	-1	1	1	1	1	-1	9.14	1.29	73.9
12	1	1	-1	1	-1	-1	-1	1	-1	1	-1	-1	-1	1	1	11.81	1.60	72.5
97	-1	-1	1	1	-1	-1	-1	1	-1	-1	1	1	1	-1	1	7.50	1.26	60.4
98	1	-1	1	1	-1	-1	-1	-1	1	1	-1	-1	-1	-1	-1	9.35	1.57	39.0
99	-1	1	1	1	-1	-1	-1	-1	-1	-1	1	1	1	-1	-1	9.26	1.32	89.1
100	1	1	1	1	-1	-1	-1	1	1	1	-1	-1	-1	1	1	11.93	1.63	72.8
59	-1	-1	-1	-1	-1	-1	1	1	1	1	1	1	-1	1	-1	6.20	1.25	53.3
60	1	-1	-1	-1	-1	-1	1	-1	-1	-1	-1	-1	1	1	1	7.82	1.55	33.1
61	-1	1	-1	-1	-1	-1	1	-1	1	1	1	1	-1	-1	1	7.69	1.31	47.7
62	1	1	-1	-1	-1	-1	1	1	-1	-1	-1	-1	1	-1	-1	10.04	1.62	62.0
63	-1	-1	1	-1	-1	-1	1	1	-1	1	1	1	-1	1	-1	6.31	1.28	68.5
64	1	-1	1	-1	-1	-1	1	-1	1	-1	-1	-1	1	1	1	7.94	1.58	33.3
7	-1	1	1	-1	-1	-1	1	-1	-1	1	1	1	-1	-1	1	7.81	1.34	62.9
65	1	1	1	-1	-1	-1	1	1	1	-1	-1	-1	1	-1	-1	10.15	1.64	62.3
108	-1	-1	-1	1	-1	-1	1	1	1	-1	1	1	-1	-1	1	7.41	1.26	60.4
109	1	-1	-1	1	-1	-1	1	-1	-1	1	-1	-1	1	-1	-1	9.30	1.55	39.1
110	-1	1	-1	1	-1	-1	1	-1	1	-1	1	1	-1	1	-1	9.17	1.31	89.2
111	1	1	-1	1	-1	-1	1	1	-1	1	-1	-1	1	1	1	11.88	1.61	72.9
112	-1	-1	1	1	-1	-1	1	1	-1	-1	1	1	-1	-1	1	7.53	1.28	75.6
14	1	-1	1	1	-1	-1	1	-1	1	1	-1	-1	1	-1	-1	9.42	1.58	39.3
113	-1	1	1	1	-1	-1	1	-1	-1	-1	1	1	-1	1	-1	9.28	1.34	104.3
114	1	1	1	1	-1	-1	1	1	1	1	-1	-1	1	1	1	12.00	1.64	73.1

Exp	A	B	C	D	E	F	G	AB	AC	AD	AE	AF	AG	BD	ABD	COP	VCC / kJ·L^{-1}	η_{II} / %
52	-1	-1	-1	-1	-1	1	-1	1	1	1	1	-1	1	1	-1	6.17	1.24	22.9
53	1	-1	-1	-1	-1	1	-1	-1	-1	-1	-1	1	-1	1	1	7.79	1.54	33.0
54	-1	1	-1	-1	-1	1	-1	-1	1	1	1	-1	1	-1	1	7.66	1.30	17.2
55	1	1	-1	-1	-1	1	-1	1	-1	-1	-1	1	-1	-1	-1	10.01	1.61	61.9
56	-1	-1	1	-1	-1	1	-1	1	-1	1	1	-1	-1	1	1	6.28	1.26	38.1
6	-1	1	1	-1	-1	1	-1	-1	1	-1	-1	1	-1	1	-1	7.91	1.57	33.2
57	-1	1	1	-1	-1	1	-1	-1	1	1	1	-1	1	-1	1	7.77	1.32	32.4
58	1	1	1	-1	-1	1	-1	1	1	-1	-1	1	-1	-1	-1	10.12	1.63	62.1
115	-1	-1	-1	1	-1	1	-1	1	1	-1	1	-1	1	-1	1	7.38	1.24	30.0
116	1	-1	-1	1	-1	1	-1	-1	-1	1	-1	1	-1	-1	-1	9.27	1.54	39.0
117	-1	1	-1	1	-1	1	-1	-1	1	-1	1	-1	1	-1	1	9.13	1.30	58.7
118	1	1	-1	1	-1	1	-1	1	-1	1	-1	1	-1	1	-1	11.85	1.61	72.8
119	-1	-1	1	1	-1	1	-1	1	-1	-1	1	-1	1	-1	1	7.50	1.27	45.2
120	1	-1	1	1	-1	1	-1	-1	1	1	-1	1	-1	-1	-1	9.39	1.57	39.2
15	-1	1	1	1	-1	1	-1	-1	-1	-1	1	-1	-1	1	1	9.25	1.32	73.9
121	1	1	1	1	-1	1	-1	1	1	1	-1	1	-1	1	-1	11.97	1.63	73.0
38	-1	-1	-1	-1	-1	1	1	1	1	1	1	-1	-1	1	-1	6.19	1.26	38.1
39	1	-1	-1	-1	-1	1	1	-1	-1	-1	-1	1	1	1	1	7.86	1.55	33.3
40	-1	1	-1	-1	-1	1	1	-1	1	1	1	-1	-1	-1	1	7.68	1.32	32.5
4	1	1	-1	-1	-1	1	1	1	-1	-1	-1	1	1	-1	-1	10.08	1.62	62.3
41	-1	-1	1	-1	-1	1	1	1	-1	1	1	-1	-1	1	-1	6.31	1.28	53.3
42	1	-1	1	-1	-1	1	1	-1	1	-1	-1	1	1	1	1	7.98	1.58	33.5
43	-1	1	1	-1	-1	1	1	-1	-1	1	1	-1	-1	-1	1	7.80	1.34	47.7
44	1	1	1	-1	-1	1	1	1	1	-1	-1	1	1	-1	-1	10.20	1.64	62.5
9	-1	-1	-1	1	-1	1	1	1	1	-1	1	-1	-1	-1	1	7.41	1.26	45.2
73	1	-1	-1	1	-1	1	1	-1	-1	1	-1	1	1	-1	-1	9.35	1.55	39.3
74	-1	1	-1	1	-1	1	1	-1	1	-1	1	-1	-1	1	-1	9.16	1.32	74.0
75	1	1	-1	1	-1	1	1	1	-1	1	-1	1	1	1	1	11.93	1.62	73.1
76	-1	-1	1	1	-1	1	1	1	-1	-1	1	-1	-1	1	-1	7.52	1.29	60.4
77	1	-1	1	1	-1	1	1	-1	1	1	-1	1	1	-1	-1	9.47	1.58	39.5
78	-1	1	1	1	-1	1	1	-1	-1	-1	1	-1	-1	1	1	9.28	1.34	89.1
79	1	1	1	1	-1	1	1	1	1	1	-1	1	1	1	-1	12.05	1.64	73.3

Exp	A	B	C	D	E	F	G	AB	AC	AD	AE	AF	AG	BD	ABD	COP	VCC / kJ·L^{-1}	η_{II} / %
66	-1	-1	-1	-1	1	-1	-1	1	1	1	-1	1	1	1	-1	6.31	1.26	23.9
67	1	-1	-1	-1	1	-1	-1	-1	-1	-1	1	-1	-1	1	1	7.88	1.56	33.6
68	-1	1	-1	-1	1	-1	-1	-1	1	1	-1	1	1	-1	1	7.80	1.32	18.2
69	1	1	-1	-1	1	-1	-1	1	-1	-1	1	-1	-1	-1	-1	10.09	1.63	62.5
70	-1	-1	1	-1	1	-1	-1	1	-1	1	-1	1	1	1	-1	6.43	1.29	39.0
71	1	-1	1	-1	1	-1	-1	-1	1	-1	1	-1	-1	1	1	8.00	1.59	33.8
72	-1	1	1	-1	1	-1	-1	-1	-1	1	-1	1	1	-1	1	7.92	1.35	33.4
8	1	1	1	-1	1	-1	-1	1	1	-1	1	-1	-1	-1	-1	10.21	1.65	62.7
101	-1	-1	-1	1	1	-1	-1	1	1	-1	-1	1	1	-1	1	7.53	1.27	30.9
102	1	-1	-1	1	1	-1	-1	-1	-1	1	1	-1	-1	-1	-1	9.36	1.56	39.6
103	-1	1	-1	1	1	-1	-1	-1	1	-1	-1	1	1	1	-1	9.28	1.32	59.7
104	1	1	-1	1	1	-1	-1	1	-1	1	1	-1	-1	1	1	11.94	1.63	73.4
13	-1	-1	1	1	1	-1	-1	1	-1	-1	-1	1	1	1	-1	7.64	1.29	46.1
105	1	-1	1	1	1	-1	-1	-1	1	1	1	-1	-1	-1	1	9.48	1.59	39.8
106	-1	1	1	1	1	-1	-1	-1	-1	-1	-1	1	1	1	-1	9.40	1.35	74.8
107	1	1	1	1	1	-1	-1	1	1	1	1	-1	-1	-1	1	12.06	1.65	73.6
24	-1	-1	-1	-1	1	-1	1	1	1	1	-1	1	-1	1	-1	6.34	1.28	39.1
2	1	-1	-1	-1	1	-1	1	-1	-1	-1	1	-1	1	1	1	7.95	1.57	33.9
25	-1	1	-1	-1	1	-1	1	-1	1	1	-1	1	-1	-1	1	7.83	1.34	33.5
26	1	1	-1	-1	1	-1	1	1	-1	-1	1	-1	1	-1	-1	10.17	1.64	62.9
27	-1	-1	1	-1	1	-1	1	1	-1	1	-1	1	-1	-1	-1	6.45	1.31	54.3
28	1	-1	1	-1	1	-1	1	-1	1	-1	1	-1	1	1	1	8.07	1.60	34.1
29	-1	1	1	-1	1	-1	1	-1	-1	1	-1	1	-1	-1	1	7.94	1.37	48.6
30	1	1	1	-1	1	-1	1	1	1	-1	1	-1	1	-1	-1	10.29	1.66	63.1
87	-1	-1	-1	1	1	-1	1	1	1	-1	-1	1	-1	-1	1	7.55	1.29	46.2
88	1	-1	-1	1	1	-1	1	-1	-1	1	1	-1	1	-1	-1	9.44	1.57	39.9
11	-1	1	-1	1	1	-1	1	-1	1	-1	1	-1	-1	1	-1	9.31	1.34	74.9
89	1	1	-1	1	1	-1	1	1	-1	1	-1	1	1	1	1	12.02	1.64	73.7
90	-1	-1	1	1	1	-1	1	1	-1	-1	1	-1	1	-1	-1	7.67	1.31	61.4
91	1	-1	1	1	1	-1	1	-1	1	1	-1	1	-1	-1	1	9.56	1.60	40.1
92	-1	1	1	1	1	-1	1	-1	-1	-1	1	-1	1	-1	1	9.42	1.37	90.1
93	1	1	1	1	1	-1	1	1	1	1	-1	1	1	1	1	12.13	1.66	73.9

Exp	A	B	C	D	E	F	G	AB	AC	AD	AE	AF	AG	BD	ABD	COP	VCC / kJ·L^{-1}	η_{II} / %
31	-1	-1	-1	-1	1	1	-1	1	1	1	-1	-1	1	1	-1	6.30	1.27	8.7
32	1	-1	-1	-1	1	1	-1	-1	-1	-1	1	1	-1	1	1	7.92	1.57	33.8
3	-1	1	-1	-1	1	1	-1	-1	1	1	-1	-1	1	-1	1	7.80	1.33	3.0
33	1	1	-1	-1	1	1	-1	1	-1	-1	1	1	-1	-1	-1	10.14	1.63	62.7
34	-1	-1	1	-1	1	1	-1	1	-1	1	-1	-1	1	1	-1	6.42	1.29	23.8
35	1	-1	1	-1	1	1	-1	-1	1	-1	1	1	-1	1	1	8.04	1.59	34.0
36	-1	1	1	-1	1	1	-1	-1	-1	1	-1	-1	1	-1	1	7.91	1.35	18.2
37	1	1	1	-1	1	1	-1	1	1	-1	1	1	-1	-1	-1	10.26	1.65	63.0
80	-1	-1	-1	1	1	1	-1	1	1	-1	-1	-1	1	-1	1	7.52	1.27	15.7
10	1	-1	-1	1	1	1	-1	-1	-1	1	1	1	-1	-1	-1	9.41	1.57	39.8
81	-1	1	-1	1	1	1	-1	-1	1	-1	-1	-1	1	1	-1	9.27	1.33	44.5
82	1	1	-1	1	1	1	-1	1	-1	1	1	1	-1	1	1	11.98	1.63	73.6
83	-1	-1	1	1	1	1	-1	1	-1	1	1	-1	1	-1	1	7.64	1.30	30.9
84	1	-1	1	1	1	1	-1	-1	1	-1	-1	1	-1	-1	-1	9.53	1.59	40.0
85	-1	1	1	1	1	1	-1	-1	-1	1	1	-1	1	1	-1	9.39	1.35	59.6
86	1	1	1	1	1	1	-1	1	1	-1	-1	1	-1	1	1	12.10	1.65	73.8
45	-1	-1	-1	-1	1	1	1	1	1	1	-1	-1	-1	1	-1	6.33	1.29	23.9
46	1	-1	-1	-1	1	1	1	-1	-1	-1	1	1	1	1	1	8.00	1.58	34.1
47	-1	1	-1	-1	1	1	1	-1	1	1	-1	-1	-1	1	1	7.82	1.35	18.3
48	1	1	-1	-1	1	1	1	1	-1	-1	1	1	1	-1	-1	10.21	1.64	63.1
5	-1	-1	1	-1	1	1	1	1	-1	1	-1	-1	-1	1	-1	6.45	1.31	39.1
49	1	-1	1	-1	1	1	1	-1	1	-1	1	1	1	1	1	8.12	1.60	34.3
50	-1	1	1	-1	1	1	1	-1	-1	1	-1	-1	-1	-1	1	7.94	1.37	33.4
51	1	1	1	-1	1	1	1	1	1	-1	1	1	1	-1	-1	10.33	1.66	63.3
122	-1	-1	-1	1	1	1	1	1	1	-1	-1	-1	-1	1	1	7.55	1.29	31.0
123	1	-1	-1	1	1	1	1	-1	-1	1	1	1	1	-1	-1	9.48	1.58	40.1
124	-1	1	-1	1	1	1	1	-1	1	-1	-1	-1	-1	1	-1	9.30	1.35	59.7
125	1	1	-1	1	1	1	1	1	-1	1	1	1	1	1	1	12.06	1.64	73.9
126	-1	-1	1	1	1	1	1	1	-1	-1	1	-1	-1	1	-1	7.66	1.32	46.2
127	1	-1	1	1	1	1	1	-1	1	1	-1	1	1	-1	-1	9.60	1.60	40.3
128	-1	1	1	1	1	1	1	-1	-1	-1	1	-1	-1	1	1	9.42	1.37	74.9
16	1	1	1	1	1	1	1	1	1	1	1	1	1	1	1	12.18	1.66	74.1

Figure D3. *Regressed responses for the full-factorial 2^7 design. Markers in yellow represent the 2^{7-3} fractional factorial design.*

							C							
1	**2**	**3**	**4**	**5**	**6**	**7**	**8**	**9**	**10**	**11**	**12**	**13**	**14**	**15**
(1)	3	2	5	4	7	6	9	8	11	10	13	12	15	14
	(2)	1	6	7	4	5	10	11	8	9	14	15	12	13
		(3)	7	6	5	4	11	10	9	8	15	14	13	12
			(4)	1	2	3	12	13	14	15	8	9	10	11
				(5)	3	2	13	12	15	14	9	8	11	10
					(6)	1	14	15	12	13	10	11	8	9
						(7)	15	14	13	12	11	10	9	8
							(8)	1	2	3	4	5	6	7
								(9)	3	2	5	4	7	6
									(10)	1	6	7	4	5
										(11)	7	6	5	4
											(12)	1	2	3
												(13)	3	2
													(14)	1

Factors	C assigned
dS'	1
A'	1, 2, 3
B'	1, 4, 5
C'	1, 8, 9
D'	1, 14, 15
A'B'	6, 7
A'C'	10, 11
A'D'	12, 13
B'C'	12, 13
B'D'	10, 11
C'D'	6, 7

Figure D4. *Triangular table for Taguchi's $L_{16}(2^{15})$ considering main-factors and second-order interactions.*

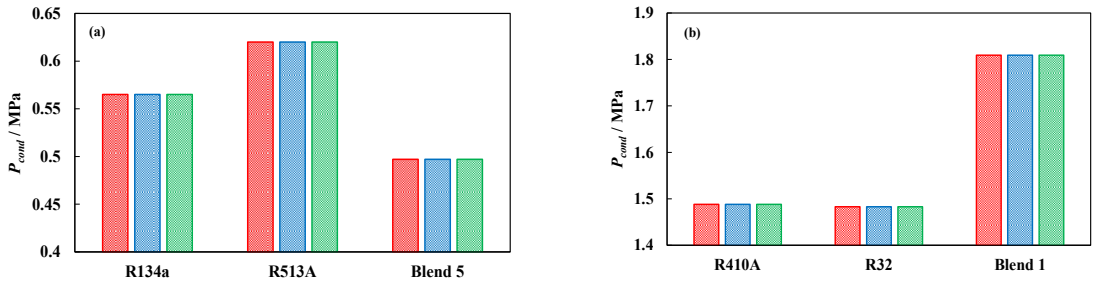

Figure D5. *Drop-in compatibility of designer blends 1 and 5 for replacing **(a)** commercial R134a, and **(b)** R410A, compared to commercial alternatives R513A and R32 based on P_{cond} considering operation in SS-VCRC (red bars replicated in **Figure 6.9**), LL/SL-HX VCRC (blue bars), and TS-VCRC (green bars).*

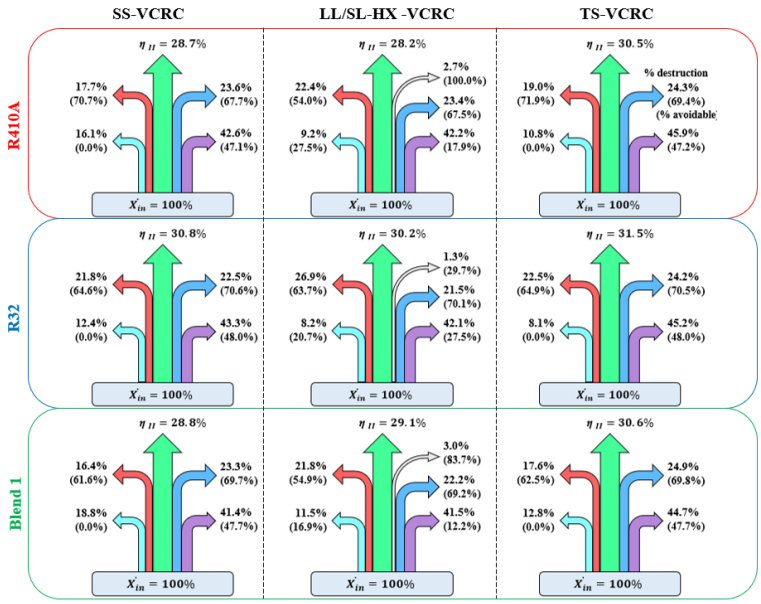

Figure D6. *Exergy destruction distribution for R410A and its replacements in the three cooling cycle configurations, with overall η_{II}% (light green), compressor ED% (blue), evaporator ED% (purple),*

condenser ED% (red), EEV (teal), and HX (grey). Note the numbers in brackets are the percentage of avoidable exergy destruction.

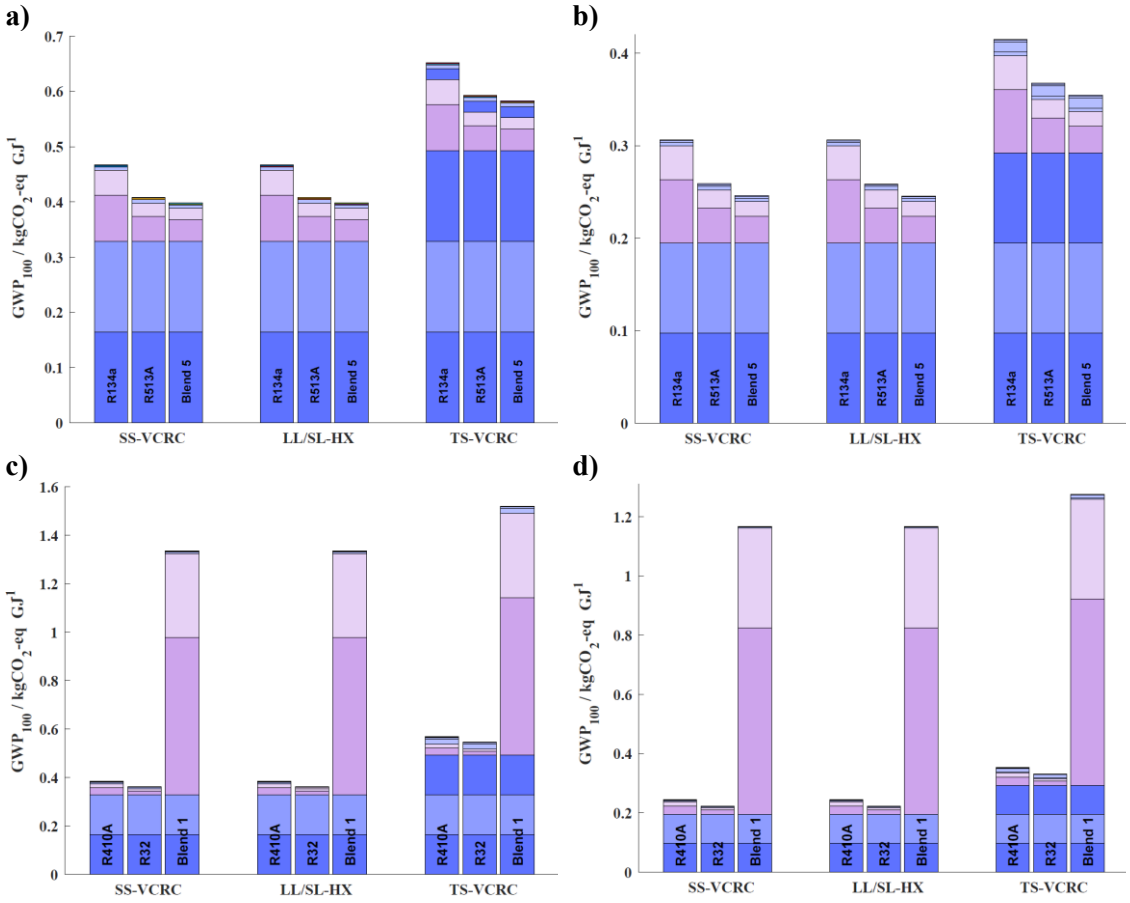

Figure D7. *Zoom LCA for contributions < 0.5kgCO₂-eq·GJ⁻¹ within* ***Figure 7.15*** *in order to replacing R134a in* ***a)****2021, and* ***b)****2050, and R410A in* ***c)****2021, and* ***d)****2050.*

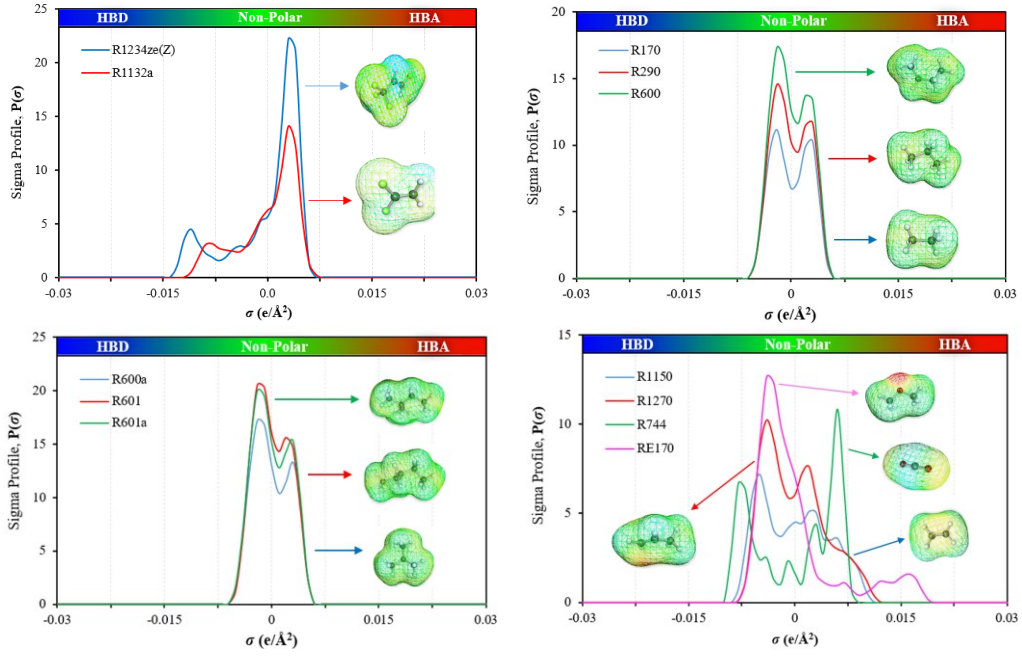

Figure E1. *σ-profiles of the single-component refrigerants used to predict the NFI. See additional σ-profiles in* ***Figure 4.6***.

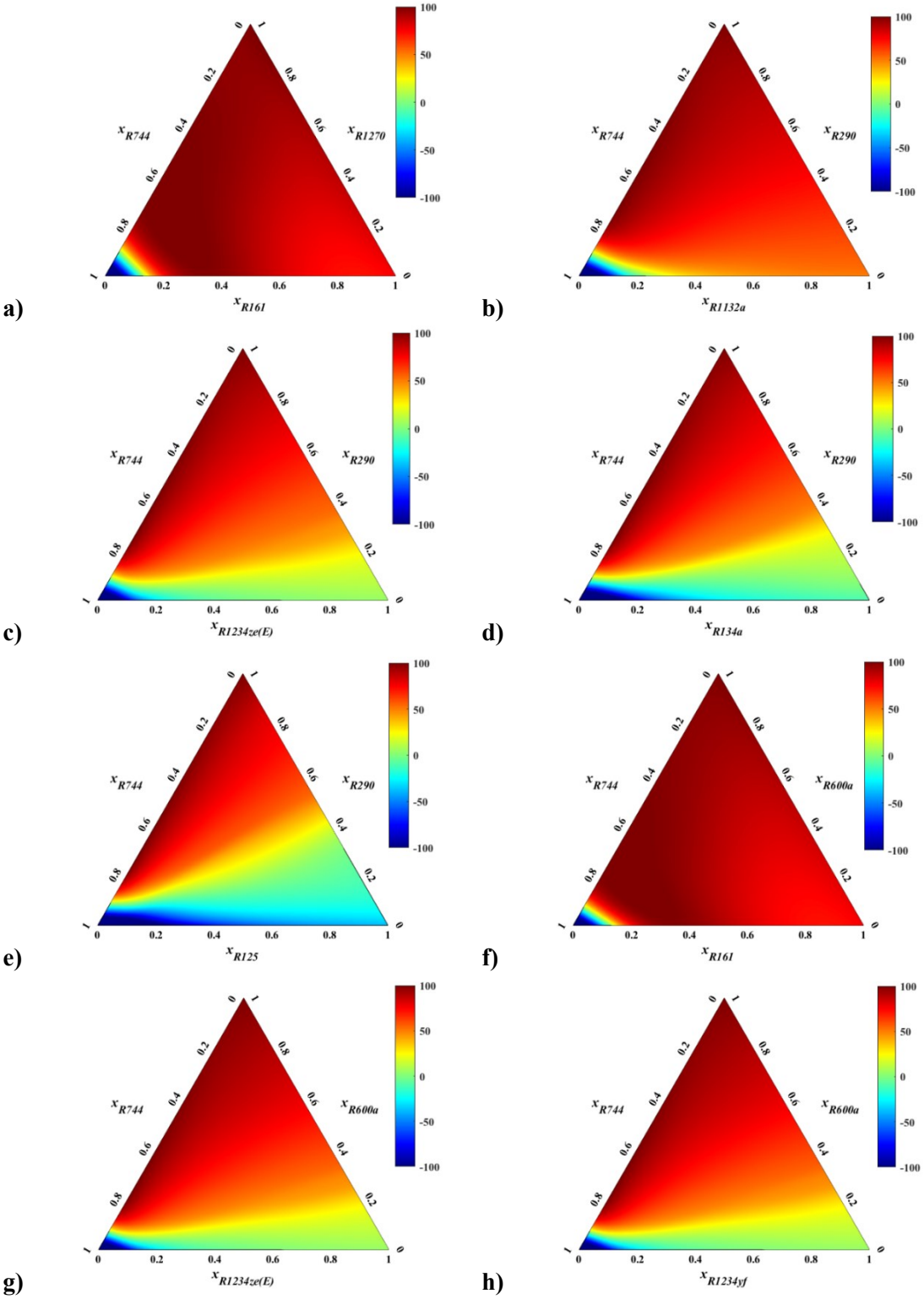

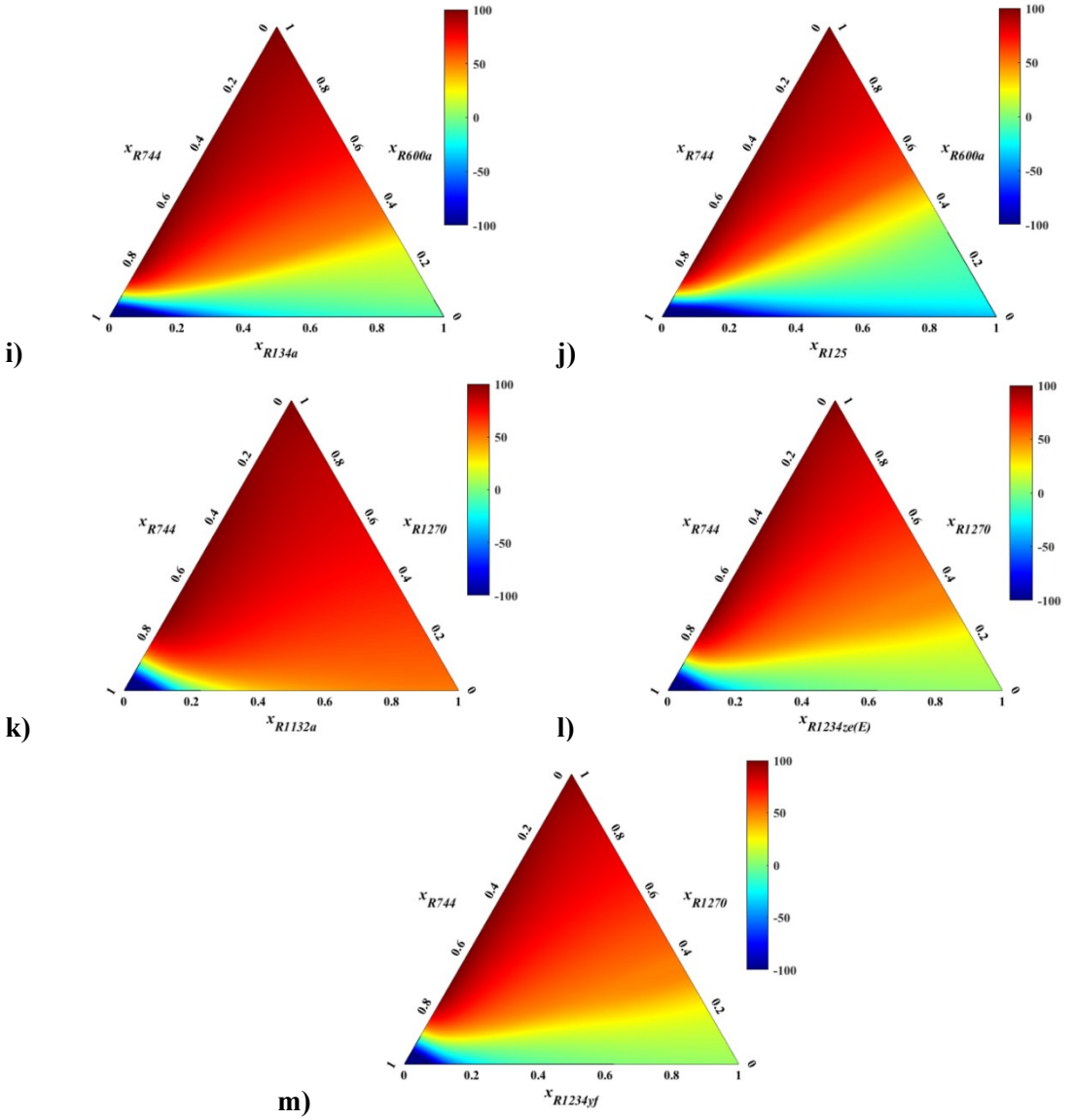

Figure E2. *Ternary contour plots generated by multitask ANN, depicting predictions of NFI for various CO_2 blends, including* ***a)*** *R1270 + R161,* ***b)*** *R290 + R1132a,* ***c)*** *R290 + R1234ze(E),* ***d)*** *R290 + R134a,* ***e)*** *R290 + R125,* ***f)*** *R600a + R161,* ***g)*** *R600a + R1234ze(E),* ***h)*** *R600a + R1234yf,* ***i)*** *R600a + R134a,* ***j)*** *R600a + R125,* ***k)*** *R1270 + R1132a,* ***l)*** *R1270 + R1234ze(E), and* ***m)*** *R1270 + R1234yf.*

Table A1. *Input dataset for ANN with molar mass and COSMO-RS molecular refrigerants.*

Compound	M_w / g.mol^{-1}	S_2	S_3	S_4	S_5	S_6
R41	34.03	0.0000	0.0118	0.0205	0.0053	0.0158
R32	52.02	0.0000	0.0208	0.0061	0.0246	0.0064
R23	70.01	0.0070	0.0062	0.0065	0.0536	0.0000
R161	48.06	0.0000	0.0079	0.0336	0.0112	0.0169
R152a	66.05	0.0000	0.0210	0.0186	0.0219	0.0107
R134a	102.03	0.0022	0.0146	0.0108	0.0599	0.0023
R125	120.02	0.0082	0.0046	0.0155	0.0695	0.0000
R245fa	134.05	0.0039	0.0170	0.0137	0.0741	0.0015
R236fa	152.04	0.0082	0.0074	0.0165	0.0879	0.0000
R227ea	170.03	0.0080	0.0029	0.0254	0.0792	0.0000
R1123	82.02	0.0018	0.0065	0.0233	0.0496	0.0002
R1243zf	96.05	0.0001	0.0186	0.0178	0.0627	0.0000
R1234yf	114.04	0.0003	0.0124	0.0268	0.0636	0.0000
R1234ze(E)	114.04	0.0038	0.0103	0.0216	0.0684	0.0000
R1225ye(Z)	132.03	0.0040	0.0055	0.0290	0.0705	0.0000
R1336mzz(Z)	164.06	0.0062	0.0067	0.0324	0.0860	0.0000
R1233zd(E)	130.49	0.0038	0.0087	0.0296	0.0725	0.0000
R1224yd(Z)	149.49	0.0035	0.0046	0.0375	0.0725	0.0000
R116	138.01	0.0005	0.0117	0.0210	0.0093	0.0000

Table A2. *Output dataset for ANN with polar soft-SAFT molecular parameters.*

Compound	$\mu \cdot 10^{-30}$ / C·m§	x_p	m	$m\sigma^3$ / Å^3	$m\varepsilon/k_B$ / K
R41	6.174	0.500	1.371	53.886	247.191
R32	6.598	0.750	1.376	59.300	226.352
R23	5.500	0.900	1.397	65.723	206.616
R161	6.470	0.330	1.577	79.427	366.337
R152a	7.545	0.500	1.662	87.925	336.223
R134a	6.865	0.700	1.813	97.145	307.304
R125	5.214	0.900	1.887	102.728	311.544
R245fa	5.167	0.800	2.479	123.041	488.611
R236fa	6.611	0.900	2.056	132.772	354.454
R227ea	4.857	1.000	2.131	139.787	406.382
R1123	5.737	0.800	1.527	81.171	267.683
R1243zf	8.169	0.500	1.904	111.215	323.680
R1234yf	6.708	0.700	1.740	118.350	333.384
R1234ze(E)	4.803	0.750	2.044	114.028	416.976
R1225ye(Z)	6.038	0.800	2.077	118.066	358.075
R1336mzz(Z)	10.641	0.600	1.806	157.011	353.254
R1233zd(E)	3.812	0.800	2.331	129.835	542.191
R1224yd(Z)	5.637	0.850	2.278	135.025	461.067

Table A3. *ANN weights and bias for the links between neurons in the input layer, and neurons in the 1st hidden layer.*

		Neurons in input layer (i)						Neuron bias (b_{ij})
		M_w	S_2	S_3	S_4	S_5	S_6	
Neurons in 1st hidden layer (j)	μ_1	0.0199	759.393	-221.629	-53.3194	-28.989	-55.8245	-0.945
	μ_2	0.0599	273.925	29.648	31.886	44.855	-1.577	-10.543
	μ_3	-0.00879	219.773	-202.017	-46.3872	19.301	-10.375	0.764
	μ_4	0.0668	-691.009	-127.769	103.573	3.469	-59.979	-5.633
	μ_5	0.000495	127.437	-3.887	-45.675	-30.769	337.681	1.913
	μ_6	0.00394	800.905	-15.216	93.798	57.655	-72.769	-8.912
	μ_7	-0.0315	521.543	330.952	22.345	1.337	146.780	-3.278
	μ_8	0.0449	-207.964	-48.581	80.760	2.153	-99.433	-2.484
	μ_9	0.0220	538.290	-139.335	-95.831	-40.209	-4.413	-0.301
	x_{p1}	0.0437	59.978	-134.377	-172.845	3.124	49.577	-0.0166
	x_{p2}	-0.0382	119.168	88.579	139.689	41.318	7.879	-1.839
	x_{p3}	-0.0139	-388.942	91.501	-16.887	-26.252	33.729	2.668

Table A4. *ANN weights and bias for the links between neurons in the HL1, and neurons in the 2HL.*

		Neurons in 2nd hidden layer (k)			
		H_1	H_2	H_3	H_4
Neurons in 1st hidden layer (j)	μ_1	-0.0196	0.0292	0.0132	-0.0759
	μ_2	-0.0186	-0.0014	-0.0313	0.0094
	μ_3	0.0869	0.0084	-0.0862	0.0653
	μ_4	-0.0445	0.0294	-0.0162	-0.0631
	μ_5	0.0471	-0.0016	0.0625	-0.0085
	μ_6	-0.0603	-0.0115	0.0047	-0.0019
	μ_7	-0.0109	-0.0379	0.0722	0.0284
	μ_8	-0.1219	-0.0184	-0.0273	-0.0020
	μ_9	-0.0359	-0.0017	0.0258	-0.0207
	x_{p1}	0.0020	0.0144	-0.0121	-0.0206
	x_{p2}	-0.0001	0.0076	-0.0503	-0.1121
	x_{p3}	0.0300	0.0151	0.0457	-0.0402
Neuron bias (b_{jk})		0.0973	-0.0019	0.0408	0.0209

Table A5. *ANN weights and bias for the links between neurons in the output layer, and neurons in HL1/2.*

		Neurons in output layer (O)				
		$\mu \cdot 10^{-30}$	x_p	m	$m\sigma^3$	$m\varepsilon/k_B$
Neurons in 1st hidden layer (j)	μ_1	11.898	-	-	-	-
	μ_2	-0.114	-	-	-	-
	μ_3	-8.478	-	-	-	-
	μ_4	-1.612	-	-	-	-
	μ_5	-1.039	-	-	-	-
	μ_6	-3.692	-	-	-	-
	μ_7	-0.111	-	-	-	-
	μ_8	1.618	-	-	-	-
	μ_9	4.457	-	-	-	-
	x_{p1}	-	-0.524	-	-	-
	x_{p2}	-	-0.804	-	-	-
	x_{p3}	-	-0.482	-	-	-
Neurons in 2nd hidden layer (k)	H_1	-	-	-100.481	1358.022	-42068.548
	H_1	-	-	411.074	-8831.445	178751.003
	H_1	-	-	119.880	-2067.174	51621.750
	H_1	-	-	226.605	-4999.385	96884.334
Neuron bias (b_{jo})		2.699	0.889	2.073	102.779	430.899

Table A6. *Developed ANN's weights and biases for bubble temperature predictions at 1MPa.*

	Hidden Layer 1											
	H_1	**H_2**	**H_3**	**H_4**	**H_5**	**H_6**	**H_7**	**H_8**	**H_9**	**H_{10}**	**H_{11}**	**H_{12}**
S_1-S_{13}	0	0	0	0	0	0	0	0	0	0	0	0
S_{14}	-0.2331	-0.5394	-0.0761	-0.0678	-0.3805	0.2526	-0.2954	-0.2368	0.1390	0.4358	0.0728	-0.0318
S_{15}	0.0247	-0.3573	0.1613	0.1702	-0.3891	-0.2758	0.0790	0.1078	-0.1421	-0.1844	0.2287	-0.3559
S_{16}	0.1396	-0.4863	-0.4088	-0.4766	-0.0739	-0.6236	-0.0847	0.3738	-0.5763	-0.3209	0.0300	0.1159
S_{17}	0.4352	-0.9045	0.1163	-0.1661	0.2446	-0.2543	0.0924	-0.0324	0.4334	0.0996	-0.1617	0.2720
S_{18}	0.2161	-0.1153	0.0507	-0.0975	0.1315	-0.0310	0.5402	0.4202	0.3468	-0.4191	0.4300	-0.0041
S_{19}	-0.0762	0.0136	0.1653	-0.0431	0.3091	-0.4775	0.1078	0.3361	0.2466	-0.0259	0.3292	-0.2167
S_{20}	-0.1456	0.2593	0.3014	0.2546	0.2887	0.0735	-0.0197	0.4509	-0.1251	0.7506	-0.5544	-0.1779
S_{21}	0.1722	0.1690	-0.3360	0.2916	-0.1832	0.2620	-0.3666	0.0022	-0.8911	0.1874	-0.1342	-0.1543
S_{22}	0.1547	-0.8243	-0.2502	-0.4403	0.2537	0.2793	0.0460	0.2799	0.3497	0.9832	-0.2822	-0.3518
S_{23}	0.1923	-0.5296	-0.1653	0.3590	0.4106	0.1851	0.5730	-0.0880	-0.4273	0.7688	-0.1578	0.1691
S_{24}	0.0184	0.0074	-0.2067	-0.1639	0.0186	-0.2504	-0.2068	0.1662	-0.1599	-0.0175	0.2913	-0.1099
S_{25}	-0.1698	-0.6254	0.3045	0.0425	-0.4294	0.3428	-0.2892	0.0959	0.1072	-0.2464	-0.1428	0.0017
S_{26}	0.0747	-0.0596	-0.3118	-0.1201	-0.1783	-0.7094	-0.2810	-0.3146	0.0685	-0.5250	-0.0927	0.5852
S_{27}	0.0234	0.4419	-0.3389	-0.2552	-0.0958	0.1494	0.3737	0.0989	0.1083	0.3243	-0.3931	0.4257
S_{28}	-0.2608	1.0421	0.2050	0.2031	-0.2651	0.4885	-0.1157	0.3521	0.5107	0.1148	0.5302	-0.2627
S_{29}	-0.3793	1.1658	0.2706	-0.2823	0.3222	0.1095	0.0125	-0.3368	-0.0059	-0.6704	0.1660	-0.4228
S_{30}	0.0869	1.0411	0.4062	0.1266	0.1190	0.1540	0.4822	-0.1966	0.5387	-0.0731	-0.2933	0.0214
S_{31}	0.1153	0.7855	0.2061	-0.2803	0.2191	0.1617	-0.0031	-0.1059	0.8424	-0.0936	-0.2131	-0.1692
S_{32}	-0.6807	0.5509	-0.1647	-0.0995	-0.1525	-0.3828	-0.1032	0.4348	-0.6107	-0.2607	0.1755	-0.1257
S_{33}	-0.2974	0.0307	-0.5600	-0.1646	0.1291	-0.2182	-0.3520	-0.3976	0.3070	-0.0396	-0.7628	0.0592
S_{34}	-0.3527	-0.4498	-0.1790	-0.5109	0.1559	0.0786	0.0724	-0.2640	0.4617	-0.0403	-0.7295	0.3535
S_{35}	0.7053	0.2900	-0.4432	0.2110	0.0197	0.1242	0.0244	0.1297	0.2027	-1.0634	-0.0903	0.1482
S_{36}	0.0422	0.8203	0.6891	0.1376	-0.3271	0.5067	0.0327	0.0053	-0.0909	0.0375	0.9891	-0.2119
S_{37}	0.2495	-0.0838	-0.0251	-0.2619	0.2063	-0.0905	0.3259	0.1513	-0.2979	0.6455	0.1358	-0.0812
S_{38}	0.3898	-0.0681	-0.8570	-0.0459	-0.1700	-0.2160	0.4440	0.0135	-0.5903	-0.0438	-0.3485	-0.1631
S_{39}	-0.2006	-0.8081	-0.2712	-0.2426	0.2110	0.7081	0.3008	0.0867	-0.1482	0.4996	-0.4339	-0.4642
S_{40}	0.0374	-0.2642	-0.0993	0.4388	-0.2191	0.6547	0.3915	0.0814	-0.3668	-0.0193	0.2324	-0.1975
S_{41}	0.0453	-0.2563	-0.1679	0.0277	-0.1363	0.4566	-0.1372	-0.2434	-0.5656	-0.1017	-0.1196	-0.0114
S_{42}	0.3952	-0.4043	0.3388	-0.0746	-0.0754	0.4583	0.4186	0.1141	-0.2899	0.1864	-0.1990	-0.6017
S_{43}	-0.3639	0.0552	0.2826	0.3991	0.2445	-0.4861	0.4166	0.3076	-0.2024	0.3626	-0.2088	0.2530
S_{44}	-0.2105	0.1227	0.2170	0.2061	0.1947	-0.0925	-0.1706	0.5312	-0.0074	0.3014	0.2731	0.3957
S_{45}	0.0410	-0.1403	-0.0931	0.2790	0.2396	-0.4742	-0.3542	0.1234	-0.3707	-0.2562	0.2218	-0.3625
S_{46}	-0.3278	0.1633	0.0813	-0.1466	-0.1276	-0.2673	0.0501	0.4279	0.2274	0.3970	-0.2484	0.0197
S_{47}	0.2945	-0.0049	-0.0298	-0.4136	-0.3032	-0.3992	0.1404	0.3809	-0.4847	-0.0213	-0.0937	0.3359

S_{48}	-0.2633	-0.3008	0.1464	-0.2849	0.1320	-0.3931	-0.3550	0.2695	0.0489	0.3980	-0.0734	0.2647
S_{49}	0.1574	0.0069	0.4587	0.0636	-0.0462	-0.0977	-0.2074	0.1056	-0.4255	0.2997	0.3814	-0.1581
S_{50}	0.2859	0.1344	0.4367	-0.0059	-0.4384	-0.2620	-0.0530	0.5756	-0.5402	0.4305	0.0541	0.3494
$S_{51\text{-}61}$	0	0	0	0	0	0	0	0	0	0	0	0
b_{1a}	1.5107	1.6777	1.2499	1.0947	1.0022	-0.8613	0.7822	0.3899	-0.3760	-0.5766	-0.3325	0.0384

Hidden Layer 1 (Continuation)

	H_{13}	**H_{14}**	**H_{15}**	**H_{16}**	**H_{17}**	**H_{18}**	**H_{19}**	**H_{20}**	**H_{21}**	**H_{22}**	**H_{23}**	**H_{24}**
S_1-S_{13}	0	0	0	0	0	0	0	0	0	0	0	0
S_{14}	-0.3581	0.3395	-0.1097	0.3523	0.2526	-0.2268	0.0969	-0.1997	0.2150	0.0675	-0.1984	0.0316
S_{15}	-0.2696	0.0699	0.1581	-0.2131	0.2505	-0.4951	0.3170	0.2935	-0.1286	0.0172	-0.1684	0.2647
S_{16}	-0.5203	0.1569	-0.1137	0.4225	0.3446	0.3856	-0.0974	0.3423	-0.2468	0.4505	0.4707	-0.1373
S_{17}	0.0222	0.0020	-0.3270	-0.2889	0.2497	-0.6302	0.1432	0.2309	0.3377	0.2638	-0.0063	0.3830
S_{18}	0.3165	-0.6012	-0.5335	0.0161	-0.4185	0.4196	-0.3529	-0.1637	0.2652	0.6683	0.0922	-0.0996
S_{19}	0.0294	0.2871	-0.0988	0.2715	0.0958	-0.1066	-0.2741	-0.2337	0.2806	0.4978	-0.0765	-0.1634
S_{20}	-0.1682	0.0870	-0.0046	0.5471	0.2709	-0.5027	0.5738	-0.1799	-0.0692	0.2542	-0.4883	-0.0380
S_{21}	0.3471	0.4638	0.2485	0.0134	-0.1999	0.1260	-0.0955	-0.3323	0.1568	0.1390	0.1736	-0.3431
S_{22}	0.0998	0.3589	0.4537	0.1684	-0.4138	-0.3110	-0.3551	-0.5201	0.3964	0.1728	0.0809	0.3040
S_{23}	-0.3369	0.1521	-0.4813	0.4848	0.0372	-0.5178	-0.2453	-0.0850	0.5673	0.2924	0.3762	-0.0483
S_{24}	-0.2345	-0.1305	-0.4956	-0.1066	-0.7842	0.1499	0.2819	0.2042	0.6824	0.3177	0.5432	-0.2563
S_{25}	0.0213	-0.0089	-0.6641	0.0352	0.3223	-0.4507	0.0086	0.2087	0.3338	0.5643	0.0223	-0.3780
S_{26}	0.2389	0.0558	0.0581	0.1556	0.9400	0.0400	-0.3323	0.1411	-0.1867	0.3536	-0.0619	-0.0297
S_{27}	0.2723	-0.1801	0.3448	-0.3357	0.1560	0.3242	-0.4085	0.1392	-0.0530	-0.2990	-0.1676	-0.0465
S_{28}	-0.2837	0.4067	0.0222	-0.1558	-0.2276	0.1485	-0.2488	0.0385	-0.3523	0.4309	-0.4419	0.2456
S_{29}	0.6094	-0.0190	-0.4977	-0.0843	-0.4231	-0.0009	0.1514	-0.2327	-0.0073	0.7351	-0.4637	-0.1588
S_{30}	0.2696	0.2932	-0.1207	-0.0006	-0.5144	0.2973	0.0556	-0.0163	-0.2601	0.2306	-0.5128	-0.2209
S_{31}	0.2013	0.7306	-0.7219	-0.1579	-0.1008	-0.4393	-0.7691	0.1865	-0.0602	1.1365	-0.0798	-0.5858
S_{32}	0.0503	0.2223	-0.2940	0.3676	-0.4595	0.3428	-0.1803	0.2252	-0.3685	0.0951	0.0410	-0.4460
S_{33}	-0.4234	0.2820	-0.8591	-0.0538	-0.0470	0.0481	0.0444	0.3373	-0.6405	0.3737	-0.2245	-0.1072
S_{34}	0.2234	0.2445	-0.3669	0.2360	0.5941	0.0534	0.1215	0.0837	-0.1090	-0.2040	-0.2658	-0.1756
S_{35}	0.3179	0.5087	0.4100	0.5091	0.5895	0.0401	0.3129	0.3715	0.3365	0.0039	0.6982	0.0981
S_{36}	-0.3001	0.5481	-0.4108	-0.2152	-0.0335	-0.3016	0.4171	0.0381	0.8126	0.9561	-0.5639	-0.1942
S_{37}	-0.3286	-0.7027	-0.2683	-0.3137	-0.1634	-0.1217	-0.0782	0.0723	0.4809	0.9232	-0.5086	-0.1322
S_{38}	0.5845	-0.2037	0.2656	0.5917	-0.1933	0.4836	-0.0184	-0.2321	-0.2329	0.2385	0.3876	-0.6792
S_{39}	0.3232	0.0991	-0.4248	-0.0460	0.2720	-0.4380	0.1820	0.4167	-0.1673	-0.4087	0.0298	-0.6207
S_{40}	0.1308	0.4152	0.2077	0.0035	-0.0625	-0.0625	-0.2415	-0.2045	-0.3325	-0.2277	0.3929	-0.5581
S_{41}	-0.4077	-0.1800	0.0590	0.1479	-0.4428	0.0629	0.3426	0.1826	-0.0129	0.4534	0.4624	0.0872
S_{42}	-0.1242	-0.2833	-0.0652	-0.6626	-0.3932	0.2009	0.0687	0.1312	-0.1372	0.2927	-0.2374	0.0387

S_{43}	0.1236	0.4770	0.1272	0.2167	0.0812	-0.0770	0.5458	0.3575	-0.4515	-0.5844	0.0802	0.2890
S_{44}	-0.0480	0.1632	0.5813	0.2511	-0.1971	0.2956	0.0832	-0.4842	-0.4173	-0.0500	-0.0147	0.2044
S_{45}	0.2943	-0.0583	-0.1434	0.0094	0.3532	-0.1870	0.2753	-0.0189	-0.2467	-0.2223	0.1100	-0.3104
S_{46}	-0.1790	-0.1023	-0.1243	-0.4095	0.0268	-0.2426	0.0856	0.2968	-0.3926	-0.5308	-0.2784	-0.3526
S_{47}	0.2532	-0.4094	0.2643	-0.1267	-0.4308	0.3356	0.4367	0.0242	0.2059	-0.4498	-0.1477	0.1184
S_{48}	0.4076	0.4630	-0.2229	-0.0493	-0.1884	-0.1052	0.5301	-0.2152	-0.0352	-0.6125	-0.3202	-0.1287
S_{49}	0.1020	-0.1001	0.6116	0.3849	-0.0853	0.1191	-0.0341	0.3509	-0.3308	-0.2002	0.3543	0.2946
S_{50}	0.1697	0.5540	0.1687	0.2892	-0.4215	-0.2347	0.5562	-0.4985	-0.3680	0.1063	0.1747	0.3899
$S_{51\text{-}61}$	0	0	0	0	0	0	0	0	0	0	0	0
b_{1a}	0.0334	0.1267	-0.4496	0.4556	0.4332	-0.6590	0.8263	-0.9195	1.2594	1.4498	-1.3311	1.4925

	Hidden Layer 2									
	HH_1	**HH_2**	**HH_3**	**HH_4**	**HH_5**	**HH_6**	**HH_7**	**HH_8**	**HH_9**	**HH_{10}**
H_1	-0.5886	-0.4072	-0.2735	-0.4008	-0.1462	0.0408	0.3436	-0.3061	-0.0186	-0.0337
H_2	0.9066	0.2608	1.2577	0.4537	-0.4527	0.3583	0.5876	0.7534	-0.2698	-0.9103
H_3	0.6463	0.1395	0.3933	0.4168	0.6172	0.1009	-0.4063	0.5207	0.3198	-0.9599
H_4	-0.0392	-0.0244	0.1272	0.4815	0.5123	0.2804	0.0583	0.4570	0.5935	0.5030
H_5	-0.0066	-0.4832	-0.0565	0.2645	0.4450	-0.1670	0.4080	-0.2524	-0.4837	-0.7014
H_6	0.8074	0.5377	-0.6617	-0.6523	0.3195	-0.2419	0.3909	0.0532	0.3925	-1.1164
H_7	-0.0529	0.4727	-0.2538	0.0973	-0.1915	0.0368	0.2164	-0.3074	-0.4219	-0.3426
H_8	-0.1079	-0.0128	-0.4493	0.2969	-0.0495	0.4892	0.1655	-0.0037	-0.1115	0.3147
H_9	0.7371	0.4015	-0.1966	0.4029	-0.6607	-0.6577	-0.3737	1.0285	-0.2553	-0.4540
H_{10}	0.0178	-0.3270	-0.4563	0.2548	-0.2206	0.0016	-0.7347	0.2654	0.1444	-0.3319
H_{11}	0.0814	0.2159	0.3691	0.3647	-0.8869	0.0775	-0.4578	-0.2477	0.1619	0.3571
H_{12}	0.0671	0.4702	0.2821	0.6025	-0.2991	0.0221	-0.4788	0.5580	0.0713	0.3261
H_{13}	0.0602	0.2942	0.4367	-0.2810	0.7852	0.5411	0.6801	0.0266	-0.1663	0.4394
H_{14}	-0.1192	-0.3935	0.1694	0.3037	0.7782	-0.6964	0.0514	-0.0750	0.3796	0.4070
H_{15}	0.3098	0.0936	0.0400	0.4008	-0.1237	0.1732	-0.7728	-0.5909	0.3664	1.1588
H_{16}	0.1064	-0.0122	-0.3655	0.3546	0.2187	-0.2697	0.3634	-0.6625	-0.4995	0.7245
H_{17}	0.7531	0.4517	-0.3002	0.2312	0.8205	0.8501	-0.1196	0.3160	-0.1067	0.7319
H_{18}	0.4230	0.0050	0.9796	-0.3311	-0.1754	-0.0337	0.2336	-0.0691	0.5105	-0.0524
H_{19}	-0.1434	0.0441	-0.4334	-0.4186	0.3958	0.3642	0.3847	0.1589	-0.4281	-0.1334
H_{20}	0.4702	-0.1774	0.5920	0.3904	0.3625	0.1114	0.0302	0.2241	0.1357	0.4117
H_{21}	-0.0701	-0.0298	0.3221	0.4292	-0.6207	-0.4195	0.2664	-0.4393	-0.2050	-0.1258
H_{22}	0.3773	-0.2849	0.3546	-0.4730	-0.8670	0.4545	-0.5192	0.3358	0.5229	-1.6212
H_{23}	-0.6336	-0.5285	0.3503	0.0560	0.3000	-0.6036	0.1004	-0.9269	-0.2815	0.8815
H_{24}	-0.3386	-0.0280	-0.5386	0.2248	-0.1547	-0.1420	-0.9343	0.3995	0.1746	0.4838
b_{2a}	1.4302	1.4622	1.2040	1.0851	1.0712	-0.7502	-0.4746	0.5209	0.2759	0.0570

	Hidden Layer 2 (Continuation)									
	HH_{11}	**HH_{12}**	**HH_{13}**	**HH_{14}**	**HH_{15}**	**HH_{16}**	**HH_{17}**	**HH_{18}**	**HH_{19}**	**HH_{20}**
H_1	-0.2559	0.6276	-0.0799	0.3817	0.4917	0.0088	0.0809	-0.3697	0.4924	0.3741
H_2	-0.3032	-0.1476	0.0823	-0.0735	-0.3839	-1.3958	0.2933	-0.2537	-0.4138	0.5109
H_3	-0.0489	0.2805	0.7189	0.3970	-0.3576	0.5429	0.0761	-0.1451	-0.8077	0.2008
H_4	-0.2041	-0.1821	0.0235	-0.1944	-0.0609	-0.5764	0.2321	-0.4184	-0.5215	-0.3755
H_5	0.4549	0.1703	-0.1708	-0.0830	0.2666	-0.1333	-0.1003	-0.1413	0.2442	-0.3613
H_6	0.0212	0.0566	-0.4506	0.5427	-0.2388	-0.2239	-0.2216	0.3234	-0.5370	0.1651
H_7	0.1567	0.0843	-0.7083	-0.0185	0.3154	0.4351	0.3515	0.2177	0.0452	-0.1959
H_8	0.4435	0.4992	0.2655	0.1631	-0.4630	0.0215	0.2320	-0.1493	0.0430	0.4554
H_9	-0.2241	0.0304	0.4028	-0.3990	-0.0765	0.4658	0.6436	-0.1686	0.3230	-0.2394
H_{10}	-0.3038	-0.0712	0.2858	0.1988	-0.1498	1.0817	-0.0474	-0.2205	0.5257	0.0171
H_{11}	0.2577	-0.1988	0.5448	0.1649	-0.3522	-0.4233	0.7599	0.7320	0.5943	-0.1327
H_{12}	-0.5768	0.5860	0.2319	0.4896	0.4414	0.0074	-0.1932	-0.3272	-0.2207	0.0226
H_{13}	-0.0931	-0.5258	0.6403	0.5043	0.1466	-0.1437	-0.6457	-0.4451	-0.3620	0.3288
H_{14}	-0.2454	0.4659	0.8824	-0.2064	-0.3621	0.3891	-0.0453	-0.0452	-0.3639	-0.2905
H_{15}	0.2957	0.7381	-0.5091	-0.1815	0.4931	0.2957	-0.5581	0.5844	-0.0777	-0.2389
H_{16}	0.2611	-0.2451	0.6484	-0.3149	-0.4962	-0.5680	-0.7262	0.0011	-0.5600	0.1165
H_{17}	-0.5036	0.4480	0.5147	-0.1900	-0.0127	0.1981	0.6427	-0.2573	0.5220	-0.0673
H_{18}	-0.4766	-0.4133	0.4288	-0.0748	-0.1731	-0.9692	-0.9475	0.1360	0.1209	0.3539
H_{19}	0.0904	-0.3326	0.2066	0.3378	0.4287	0.3740	0.4362	-0.5192	-0.5790	0.3698
H_{20}	0.0747	-0.1648	0.2478	0.3552	-0.3083	0.7008	0.1781	-0.0383	-0.0253	0.4093
H_{21}	-0.0173	0.6307	0.3062	0.1045	0.3127	-0.0522	0.2492	-0.7275	-0.4823	-0.5121
H_{22}	0.4719	0.5887	0.4156	-0.5208	-0.0324	-1.1947	-0.2457	-0.3583	0.3416	-0.6549
H_{23}	-0.0118	-0.0582	0.1609	-0.6760	-0.4149	0.1304	-0.1830	0.1963	-0.1531	-0.5377
H_{24}	-0.6603	0.0074	-0.1536	0.0738	0.0227	0.1483	0.1989	0.2714	-0.4525	0.3677
b_{2a}	-0.2109	0.2898	0.2901	0.5917	0.8397	0.7898	-1.0035	-1.1477	1.3681	1.4967

Table A7. *Developed ANN's weights and biases for dew temperature predictions at 1MPa.*

	Hidden Layer 1											
	H_1	**H_2**	**H_3**	**H_4**	**H_5**	**H_6**	**H_7**	**H_8**	**H_9**	**H_{10}**	**H_{11}**	**H_{12}**
S_1-S_{13}	0	0	0	0	0	0	0	0	0	0	0	0
S_{14}	0.2673	0.0975	-0.3968	0.5232	-0.1251	0.1430	0.3806	0.2961	-0.2968	-0.2405	-0.4743	0.0742
S_{15}	0.1889	0.2685	-0.3376	0.2666	0.3949	-0.1577	0.1762	0.0027	0.4932	-0.2172	-0.4782	-0.4397
S_{16}	0.3775	-0.3724	0.0265	0.0675	0.3123	0.0115	0.3900	-0.2034	0.2883	-0.0091	-0.4749	0.2352
S_{17}	0.2219	-0.2909	-0.2775	-0.7812	-0.2035	0.8164	-0.1866	-0.0162	0.3157	-0.3952	-0.0874	-0.1929
S_{18}	-0.2088	-0.0627	-0.2689	-0.0045	0.4533	0.3580	0.3643	-0.3722	-0.1683	0.1083	0.8837	-0.3544
S_{19}	0.2790	0.2060	-0.2269	-0.2574	-0.1583	-0.5750	0.3137	0.4344	-0.7742	-0.2886	0.2362	-0.9336
S_{20}	-0.2043	-0.0338	-0.4219	0.5180	-0.3774	0.2169	0.2778	0.2288	-0.2865	0.1100	-0.1533	-0.7861
S_{21}	0.0123	0.2429	0.1366	-0.0279	-0.1292	0.1176	-0.2752	0.0909	-0.4526	0.5208	0.2691	0.8210
S_{22}	0.0503	-0.1304	0.2870	-1.4017	-0.3260	0.3181	0.3471	-0.1187	0.7464	0.3946	-0.9408	-0.7093
S_{23}	-0.0707	0.0806	-0.0523	1.1031	-0.1459	-0.3031	0.2672	-0.3941	0.9289	0.5620	0.4252	-0.7662
S_{24}	0.3406	0.0029	-0.1349	0.8730	0.1414	-0.4741	-0.0815	-0.3620	1.0231	0.5932	-0.4666	-0.3549
S_{25}	0.2264	-0.0955	-0.2347	0.1986	-0.1469	-0.1840	0.2641	-0.1582	1.0027	0.5740	-0.2769	-0.6960
S_{26}	0.4090	-0.4133	0.3796	0.4124	0.1478	-0.2080	0.3474	0.4174	0.8071	0.4400	0.3549	-0.6271
S_{27}	-0.3783	-0.0842	0.0764	-1.2133	0.1538	0.0074	-0.4003	-0.0590	0.0972	0.3566	-0.2078	-0.2639
S_{28}	0.2133	0.4633	0.2394	0.3732	-0.2510	-0.8122	0.0806	0.2897	-0.0369	-0.2632	0.6889	1.1692
S_{29}	-0.2327	0.4507	-0.1119	-0.3818	-0.1289	-0.2762	0.1447	-0.2709	0.0143	-0.4331	0.2901	0.6410
S_{30}	0.0168	0.1260	0.1173	-0.8236	-0.2574	-0.8628	-0.1709	-0.1410	0.8451	0.5249	0.5741	-0.1010
S_{31}	0.1074	-0.1044	0.3443	0.7116	0.0966	-1.2925	-0.2793	-0.6744	0.5704	0.5963	1.1867	1.0744
S_{32}	-0.0900	-0.0796	-0.2048	-0.0686	0.3979	-0.4044	0.2023	-0.3517	-0.0121	0.2459	-0.3204	0.4190
S_{33}	0.0196	-0.0027	0.3039	0.1547	0.2449	0.0304	-0.0267	-0.0373	0.1019	0.3206	-0.4159	0.2499
S_{34}	0.0232	0.5186	0.3250	0.3942	0.3044	-0.2388	-0.2580	0.1021	-0.4457	-0.3839	0.3459	0.1496
S_{35}	0.3588	0.0026	0.3064	-0.7602	0.0481	-0.2484	0.4312	0.0812	-0.6589	-0.4474	0.8109	-0.4343
S_{36}	-0.0912	0.0682	0.0206	-0.2333	0.1141	0.1318	0.1639	-0.5776	0.3805	-0.3109	0.4830	-0.0831
S_{37}	0.0982	0.4747	0.1022	0.6759	0.4006	-0.2957	-0.1944	0.3223	1.2339	0.2405	-0.1477	-0.0444
S_{38}	0.3315	-0.1309	0.3177	-0.6075	0.2332	-0.4104	-0.2097	0.2470	1.0031	0.5171	-0.6071	0.1623
S_{39}	-0.1047	-0.1829	-0.1749	0.2936	-0.4099	-0.1397	-0.1597	-0.2520	0.3166	0.1460	-0.7578	0.9325
S_{40}	0.2784	-0.3545	0.3219	0.2715	-0.0649	0.2781	0.1878	-0.4528	0.1096	0.2564	-0.1001	-0.2206
S_{41}	0.1675	0.1532	0.0756	0.4078	-0.3648	-0.1769	0.1305	0.1454	0.3533	0.3064	0.0933	-0.6014
S_{42}	-0.2820	0.2399	-0.4127	0.0858	-0.2284	0.0690	-0.0021	-0.5083	0.3353	-0.0036	-0.0645	-0.1461
S_{43}	0.2366	-0.0594	-0.2686	-0.0316	-0.0225	0.0294	-0.2080	-0.1043	0.4063	0.4324	-0.2253	-0.1270
S_{44}	-0.3972	0.2133	0.0023	-0.3578	0.3341	0.0128	0.3898	0.0438	0.1172	0.1948	-0.3700	-0.3249
S_{45}	0.4542	0.2074	-0.1226	0.1924	0.4374	0.2719	0.1994	0.2599	0.6162	0.3598	-0.4618	0.0033
S_{46}	-0.1138	-0.5171	0.2282	-0.1875	-0.3088	0.3326	-0.2212	0.1175	0.1934	0.0542	-0.0820	0.0427
S_{47}	-0.3480	0.3472	0.1352	-0.1015	0.1649	0.0753	-0.1478	0.1920	0.1429	-0.1121	-0.4136	-0.4085

S_{48}	-0.0886	0.0604	-0.3658	0.3882	-0.0571	0.3125	-0.0668	0.4655	0.3177	-0.3494	-0.5107	-0.5272
S_{49}	0.4513	-0.0690	0.2342	0.4396	-0.2716	0.1163	0.3203	0.1006	0.3286	-0.3672	-0.1019	0.0082
S_{50}	-0.2459	-0.2650	0.0722	0.0856	0.0400	0.1444	0.1580	-0.2594	0.1963	0.4088	0.2422	-0.0618
$S_{51\text{-}61}$	0	0	0	0	0	0	0	0	0	0	0	0
b_{1b}	-1.5392	-1.2915	1.2879	-1.6357	0.9278	-0.9344	-0.6830	-0.5465	0.3555	0.4976	0.2836	-0.0746

Hidden Layer 1 (Continuation)											
	H_{13}	**H_{14}**	**H_{15}**	**H_{16}**	**H_{17}**	**H_{18}**	**H_{19}**	**H_{20}**	**H_{21}**	**H_{22}**	**H_{23}**
S_1-S_{13}	0	0	0	0	0	0	0	0	0	0	0
S_{14}	-0.0428	-0.0116	-0.2505	0.6208	0.2712	-0.0019	0.1583	0.1874	0.0894	-0.0002	-0.4492
S_{15}	-0.0197	-0.1098	0.1888	0.2353	-0.0087	0.3329	-0.3017	-0.3370	-0.3870	0.0104	0.3717
S_{16}	0.2062	-0.6635	0.2942	-0.1249	0.1195	-0.1062	0.3110	-0.2999	0.1025	0.2707	-0.2579
S_{17}	-0.4448	0.1912	0.1085	0.4178	0.5850	-0.2622	0.6710	-0.0916	0.1355	-0.3926	0.0928
S_{18}	-0.8137	-0.7802	-0.4066	-0.0521	0.3359	-0.3592	1.5146	0.2900	0.0952	0.3538	0.0557
S_{19}	-0.2152	0.4302	-0.1856	0.0292	-0.3628	0.3879	-0.1926	0.4283	0.6548	0.1748	-0.0684
S_{20}	-0.1234	0.1629	-0.4009	-0.3249	-0.6144	-0.0797	-0.0599	0.5651	0.4524	0.1985	-0.3123
S_{21}	0.1083	-0.4692	0.0587	-1.8675	0.4165	0.2344	0.2060	0.3232	0.8723	-0.3430	-0.0480
S_{22}	0.5846	0.2590	-0.0210	-1.1417	-0.3321	0.7159	-0.3097	0.3931	0.7963	0.2155	-0.2692
S_{23}	1.1965	0.6793	0.2147	-1.2650	-0.4159	-0.2812	-0.3765	0.4326	-1.2848	0.0486	0.1652
S_{24}	1.0073	1.1294	0.2103	-0.4557	-0.6010	-0.1943	-0.5241	0.4412	-0.9068	-0.2801	0.3530
S_{25}	0.4721	0.4651	-0.4972	-0.4503	0.1725	0.0211	-0.8974	-0.3203	-0.1326	-0.1302	-0.3007
S_{26}	0.4210	-0.2802	-0.4364	-0.4506	0.3754	0.2634	-0.6551	-0.2595	-0.3565	-0.3370	-0.3428
S_{27}	-0.1345	1.1154	0.5024	0.5445	-0.4600	0.8114	-0.6484	-0.3941	-0.5349	0.3821	0.1066
S_{28}	-0.4274	0.5625	0.5440	0.0021	-0.3785	-0.2584	0.9316	0.6140	-0.9238	0.2013	-0.3742
S_{29}	-0.1358	1.8226	0.1141	0.5728	-0.0589	0.3869	0.3068	0.6151	-0.3560	-0.3119	0.3059
S_{30}	0.3944	3.0136	-0.2516	0.4752	-1.0158	0.4103	-0.2226	0.4510	0.0810	-0.2705	0.2529
S_{31}	-0.1617	1.0660	0.1893	-1.1843	-0.0877	-0.8223	1.0772	0.0359	-0.2422	-0.3503	-0.0037
S_{32}	-0.5344	1.1234	-0.1515	-0.9347	-0.7425	-0.1865	-0.4947	-0.3050	-0.1030	0.0212	-0.1998
S_{33}	-0.3407	1.5907	0.3607	-0.2720	-0.9030	-0.3949	-0.6448	-0.3088	0.4226	0.1677	0.2822
S_{34}	0.1904	0.5987	-0.4962	-1.2722	-0.2115	0.2703	-0.3777	0.1978	-0.2478	-0.3467	0.1465
S_{35}	-0.3919	0.2122	-0.0932	-0.4696	0.3339	0.1191	0.1592	-0.1403	-0.0303	-0.2043	0.2738
S_{36}	-0.1829	0.1825	0.0815	-0.3674	-0.3547	0.2406	0.9438	0.0333	0.1017	-0.3143	0.0941
S_{37}	0.6632	0.1292	0.3269	-0.1209	-0.0876	0.1262	0.2218	0.1339	-0.6327	0.0772	0.1192
S_{38}	0.4104	0.6616	-0.0789	-0.3644	0.2175	0.8752	-0.6842	0.1442	-0.7337	0.2028	0.3998
S_{39}	-0.3247	-0.1919	-0.1565	-0.4421	0.5457	0.7598	-0.0191	-0.2901	-0.6226	-0.1923	0.3483
S_{40}	0.7861	0.5847	0.2623	-0.1219	0.1258	0.1444	-0.5749	-0.1851	0.4802	-0.1934	0.3859
S_{41}	0.2613	0.3329	-0.0370	0.0287	0.4127	0.1652	-0.0355	-0.2747	-0.4654	-0.0630	-0.0382
S_{42}	0.5557	-0.6605	-0.2914	-0.1871	-0.0621	-0.1112	0.1041	-0.0568	-0.5090	-0.2070	-0.4041

S_{43}	0.6282	-0.3993	0.1645	0.4304	0.0371	-0.3480	-0.5544	0.0723	-0.2975	-0.0777	0.2202
S_{44}	-0.0274	-0.5364	-0.2224	0.5918	0.0729	-0.4082	-0.3337	-0.1777	0.0375	0.0443	-0.0815
S_{45}	0.2467	-0.8944	0.3443	0.2956	-0.2445	-0.3799	-0.3171	0.4359	0.0740	0.1945	0.3226
S_{46}	0.6172	-0.4619	-0.0670	0.5392	0.1553	-0.1084	0.1574	-0.0511	0.1975	-0.3400	-0.3776
S_{47}	0.6732	-0.8737	-0.0985	0.3398	-0.1815	-0.2767	-0.0827	0.5335	-0.4830	0.1868	-0.0323
S_{48}	0.4052	-0.7508	-0.2729	0.3443	0.3682	-0.3598	-0.2700	0.1413	0.1342	-0.4097	-0.2474
S_{49}	0.3354	-0.8931	-0.0471	0.0809	0.2445	0.0106	0.1074	0.1002	0.2651	-0.3002	-0.0653
S_{50}	0.6168	-0.4549	0.0895	0.3280	0.1138	-0.0999	-0.3564	-0.1287	-0.3513	-0.3494	-0.2215
S_{51-61}	0	0	0	0	0	0	0	0	0	0	0
b_{1b}	-0.5117	1.1114	-0.4367	0.6559	0.6265	-0.7880	0.9909	1.0569	1.4448	1.3920	-1.4736

	Hidden Layer 2														
	HH_1	**HH_2**	**HH_3**	**HH_4**	**HH_5**	**HH_6**	**HH_7**	**HH_8**	**HH_9**	**HH_{10}**	**HH_{11}**	**HH_{12}**	**HH_{13}**	**HH_{14}**	**HH_{15}**
H_1	0.0964	0.4225	0.0738	0.1337	-0.2609	0.2993	-0.3470	-0.6247	0.3080	0.4428	0.5472	-0.6468	0.4686	0.3321	0.4310
H_2	-0.4059	0.5555	0.1478	0.2736	0.1014	0.1175	0.1396	0.3730	0.3443	0.3143	-0.2816	-0.1137	-0.2336	0.2674	-0.2610
H_3	0.1889	-0.1656	0.3911	0.5333	0.2751	0.5020	-0.2515	-0.4052	0.5358	-0.4962	0.3571	0.2245	0.5285	0.5008	0.2578
H_4	1.2162	-0.5344	0.7352	0.1292	-1.1046	0.2916	0.9429	0.0402	0.6309	0.0170	0.1590	1.9338	0.6372	-0.1412	-0.8315
H_5	-0.0997	-0.2341	0.6492	0.0313	0.2999	0.0537	0.5415	0.3419	0.2408	-0.2260	0.0230	0.2293	-0.3149	0.4242	-0.8068
H_6	-0.8134	0.4758	-0.2353	0.4191	0.8071	0.7958	-0.8534	0.3699	-0.4502	-0.1348	-0.1981	-0.7651	0.0235	-0.3251	-0.0949
H_7	0.3401	0.0107	0.1155	-0.5393	0.3506	0.3617	0.5364	-0.1985	-0.2946	0.2481	-0.3766	0.3613	-0.2208	-0.3978	0.3349
H_8	-0.4861	-0.3017	-0.5057	-0.4059	0.0734	0.4953	-0.0710	-0.7742	0.7610	-0.0784	0.3277	-0.2166	-0.3469	0.3993	-0.3979
H_9	-0.0204	-0.4334	0.0349	-0.2923	-0.8738	-0.0405	0.3775	0.0624	-1.6137	-0.4928	0.6277	0.4110	0.3104	0.5191	0.4733
H_{10}	-0.7898	0.0460	0.3901	0.1605	0.0830	-0.1555	0.3890	0.4448	-0.8562	-0.0664	0.3540	0.2482	0.7375	-0.4328	0.2210
H_{11}	0.8988	-0.2227	0.4788	-0.3859	0.3165	-1.0587	0.6573	-0.8278	0.5227	-0.6637	-0.2125	0.9791	0.7427	0.3030	-0.0720
H_{12}	-0.2946	-0.5312	0.4096	-0.2912	0.0616	-0.1701	0.1640	0.5711	1.8807	0.3690	0.8250	1.2548	-0.1473	0.0916	-0.2498
H_{13}	0.4076	0.0594	0.1260	-0.0770	-0.7381	0.6703	0.2192	0.7314	-0.7791	-0.1082	-0.8018	1.1793	0.0641	-0.2169	-0.4467
H_{14}	-0.9769	-0.2076	0.4482	0.3513	0.1306	-1.3406	-0.3118	0.5557	-2.7645	0.6065	-0.1227	-0.2261	0.8118	0.3938	-0.1087
H_{15}	-0.0691	0.3866	-0.1679	-0.0994	-0.2585	0.4288	-0.3898	-0.5641	-0.4141	0.1115	-0.6092	0.2729	-0.1612	-0.1350	-0.2283
H_{16}	0.6675	0.4710	0.2150	-0.6249	0.5026	0.8355	0.6683	0.3355	-0.6807	0.6515	-0.3221	-1.6042	-0.4816	-0.0139	0.0282
H_{17}	0.6009	-0.1259	-0.3311	-0.3675	0.2362	0.0200	0.6049	-0.6990	0.4736	-0.3070	-0.4632	0.9239	0.0313	-0.1073	-1.5651
H_{18}	-1.4339	0.1673	-0.1175	-0.5309	0.5649	-0.3654	-0.1318	-0.5571	0.1190	0.3581	-0.6972	-0.1958	0.5096	0.4181	-0.1973
H_{19}	0.8314	0.2799	0.4320	-0.4947	1.0124	-1.2680	-0.5745	-0.6985	1.9130	0.0417	0.9769	-0.4252	-0.1334	0.3532	0.0883
H_{20}	-0.1623	-0.0294	-0.0057	-0.2091	-0.7296	0.2885	-0.3768	0.0449	-0.5321	-0.4920	0.1207	-0.1470	0.6185	-0.2181	-1.1787
H_{21}	-0.4976	-0.0168	-0.5189	0.3295	1.1038	0.0376	-0.5608	-0.8084	-1.6102	0.1602	-0.3973	-0.6267	-0.0218	0.3241	-0.2137
H_{22}	0.0359	0.1549	-0.1449	-0.4575	-0.1244	0.0294	-0.6418	-0.0317	0.0966	0.1019	0.1022	0.0868	-0.4169	0.3636	-0.0925
H_{23}	-0.5187	0.5931	0.5012	-0.0219	0.6446	0.0449	0.0411	-0.3064	-0.0170	-0.0132	-0.3452	0.1122	-0.2150	-0.3143	0.0886
b_{2b}	-1.5453	-1.3790	-1.0331	-0.8728	0.5054	-0.3717	0.1495	0.1681	0.2665	0.4078	0.5732	-0.8098	1.1160	1.3525	1.5250

Table B1. *Detailed thermodynamic evaluation of the VCRC illustrated in Section 5.4.*

Operating Point	***Evap*^{out}**	***Comp*^{out}**	***Cond*^{out}**
Degrees of Freedom	3 (2 phases)	4 (1 phase)	3 (2 phases)
Fixed Variables	x^{HFC}, x^{HFO}, T_{evap}	x^{HFC}, x^{HFO}, P_{cond}, S	x^{HFC}, x^{HFO}, T_{cond}
Obtained Variables	P_{evap}	DLT	P_{cond}

*Superheating and Subcooling of 2.5 K are applied

Table C1. *Shortlisted 4th generation refrigerants based on their environmental and safety impact.*

ASHRAE Designation	IUPAC Name	GWP_{100}*	ODP†	Toxicity‡	Flammability‡
Accepted based on environmental and safety criteria					
R1123	1,1,2-trifluoroethene	0.005	0	A	2L
R1234yf	2,3,3,3-tetrafluoroprop-1-ene	0.501	0	A	2L
R1234ze(E)	trans-1,3,3,3-tetrafluoroprop-1-ene	1.370	0	A	2L
R1225ye(Z)	cis-1,2,3,3,3-pentafluoroprop-1-ene	0.344	0	NA+	NA+
R1336mzz(Z)	cis-1,1,1,4,4,4-hexafluoro-2-butene	2.080	0	A	1
R1233zd(E)	trans-1-chloro-3,3,3-trifluoroprop-1-ene	3.880	0.00024	A	1
R1224yd(Z)	cis-1-chloro-2,3,3,3-tetrafluoroprop-1-ene	< 1	0.00023	A	1
Benchmark refrigerants					
R32	Difluoromethane	771	0	A	2L
R134a	1,1,1,2-tetrafluoroethane	1530	0	A	1

*GWP values from [14] for R1224yd(Z) and IPCC AR6 WGI Chapter 7 for remaining agents.
†ODP values from [15-17].
‡ ASHRAE rating from [16-20].
+ASHRAE official classification have not been published, yet generally regarded as mildly toxic and non-flammable.

Table C2. *Technical KPIs.*

Compound	NBP / K	P_{cond} / MPa	ρ_V / kg·m^{-3}	c_p / kJ·kg^{-1}·K^{-1}	RE / kJ·kg^{-1}	COP
R32	221.07	1.78	19.21	2.27	275.05	7.68
R134a	247.04	0.69	12.57	1.58	160.02	7.73
R1123	212.10	2.13	41.14	1.80	131.35	7.05
R1234yf	243.11	0.72	15.80	1.60	126.49	7.48
R1234ze(E)	252.91	0.53	10.70	1.43	141.27	7.65
R1225ye(Z)	254.30	0.53	11.98	1.39	123.72	7.53
R1336mzz(Z)	304.34	0.09	1.82	1.21	137.28	7.63
R1233zd(E)	290.90	0.14	2.57	1.24	165.02	8.04
R1224yd(Z)	288.33	0.16	3.16	1.22	146.46	7.63

Compound	COP	η_{II} / %	TEWI / tCO_2	$TEWI_d$ / tCO_2	$TEWI_i$ / tCO_2
R32	7.68	80.05	18.04	1.84	16.20
R134a	7.73	80.59	23.16	7.07	16.09
R1123	7.05	73.48	17.66	0.02	17.64
R1234yf	7.48	78.03	16.62	0.00	16.62
R1234ze(E)	7.65	79.79	16.25	0.00	16.25
R1225ye(Z)	7.53	78.52	16.53	0.02	16.51
R1336mzz(Z)	7.63	79.68	16.24	0.01	16.23
R1233zd(E)	8.04	83.85	15.49	0.03	15.46
R1224yd(Z)	7.63	79.57	16.24	0.01	16.23

Table C3. *Designed blends rejected on basis of high flammability, shown in* ***Figure 6.8****.*

ID	Blend	*wt.*%[±]	GWP	T_G / K[*]
Study A				
9	R152a + R1234ze(E)	80.0	111	0.048
10		90.0	124	0.026
11	R152a + R1243zf	10.0	15	0.023
12		20.0	28	0.019
13		30.0	42	0.010
14		40.0	56	0.002
15		50.0	69	0.000
16		60.0	83	0.004
17		70.0	97	0.010
18		80.0	111	0.016
19		90.0	124	0.011
20[§]	R161 + R1234yf	80.0	3	0.099
21[§]		90.0	4	0.040
Study B				
5'	R152a + R227ea	90.0	459	0.010
6'	R152a + R134a	90.0	254	0.052

[±]The mass fraction for the 1st component in the blend
[*]Obtained at atmospheric pressure (0.1 MPa).
[§] ASHRAE Safety Group A3.

Table C4. *Criteria established to discretize the response (i) in* ***Figure 6.10*** *for R134a and R410A drop-ins.*

$$\frac{i_X - i_{R134a,R410A}}{i_{R134a,R410A}}$$

Rating	*NBP*	P_R	ρ_V	*PPTR*
5	< (-0.7)%	< (-5.9)%	> 15.9%	< (-0.5)%
4	(-0.7) – (-0.3)%	(-5.9) – (-4)%	12.5 – 15.9%	(-0.5) – 0%
3	(-0.3) – 0.2%	(-4) – 0%	(-2.5) – 12.5%	0 – 0.6%
2	0.2 – 0.7%	0 – 1%	(-7.5) – (-2.5)%	0.6 – 1.5%
1	> 0.7%	> 1%	< (-7.5)%	> 1.5%

Rating	*RE*	*COP*	η_{II}
5	> 10%	> 1%	> 1%
4	0 – 10%	0.5 – 1%	0.2 – 1%
3	(-5.3) – 0%	(-0.5) – 0.5%	(-0.5) – 0.2%
2	(-15) – (-5.3)%	(-2.5) – (-0.5)%	(-2.4) – (-0.5)%
1	< (-15)%	< (-2.5)%	< (-2.5)%

Table C5. *Parameters, definitions, and their corresponding values.*

Parameter	Definition	Value	Source
L	Annual leakage rate	12.5%	[21]
m	Refrigerant charge load	2.5 kg for A1 refrigerants 1.2 kg for A2L refrigerants	UL60335-2-89 regulation and BOE-2019

n	System operating life	15 years	[22-24]
α	Recovery factor	70%	[25]
E_a	System energy consumption	System and refrigerant-dependent, in kWh·y^{-1}	Polar soft-SAFT
β	Indirect emission factor	PRC: 0.5374 kgCO_2-eq·kWh^{-1} USA: 0.4239 kgCO_2-eq·kWh^{-1} EU-27: 0.2839 kgCO_2-eq·kWh^{-1} Japan: 0.4658 kgCO_2-eq·kWh^{-1} India: 0.7082 kgCO_2-eq·kWh^{-1}	[26]
ω_c	Net cycle compressor's work	Refrigerant-dependent, in kJ·kg^{-1}	Polar soft-SAFT
η_s	Compressor isentropic efficiency	85%	This thesis
CC	Cooling capacity	10 kW	[27]
$\dot{m}_{air}$	Auxiliary fluid (air) mass flow in the evaporator	1 kg·s^{-1}	This thesis
$\dot{m}_{CW}$	Auxiliary fluid (cooling water) mass flow in the condenser	1 kg·s^{-1}	This thesis
RE	Refrigeration effect	Refrigerant-dependent, in kJ·kg^{-1}	Polar soft-SAFT
AOT	Annual operation time	8760 h·y^{-1}	This thesis
ϕ	Maintenance factor	1.06	[28-31]
i	Annual interest rate	14%	[28-31]
U_{evap}	Evaporator heat transfer coefficient	0.3 kW·m^{-2}·K^{-1}	This thesis
U_{cond}	Condenser heat transfer coefficient	3 kW·m^{-2}·K^{-1}	This thesis
T_0	Dead-state temperature	288.15 K	This thesis
$T_{PP,ev}$	Pinch point temperature difference in the evaporator	5 K	This thesis
$T_{PP,cond}$	Pinch point temperature difference in the condenser	5 K	This thesis
α_{el}	Average or unit cost of electricity	PRC: 0.088 \$·kWh^{-1} USA: 0.113 \$·kWh^{-1} EU-27: 0.241 \$·kWh^{-1} Japan: 0.247 \$·kWh^{-1} India: 0.080 \$·kWh^{-1}	[32-34]
c_{CO_2}	Unit cost of CO_2 avoided - NGCC	PRC: 0.099 \$·kgCO_2-eq^{-1} USA: 0.089 \$·kgCO_2-eq^{-1}	[28,35]

		EU-27: 0.097 \$·kgCO_2-eq^{-1} Japan: 0.087 \$·kgCO_2-eq^{-1} India: 0.087 \$·kgCO_2-eq^{-1}	
RP	Retail price of raw materials	R32: 17.79 \$·kg^{-1} R152a: 15.9 \$·kg^{-1} R134a: 12.9 \$·kg^{-1} R227ea: 73.9 \$·kg^{-1} R1123: 100.0 \$·kg^{-1} R1243zf: 35.0 \$·kg^{-1} R1234yf: 80.5 \$·kg^{-1} R1234ze(E): 60.0 \$·kg^{-1} R513A: 64.4 \$·kg^{-1} R450A: 33.4 \$·kg^{-1} R410A: 31.1 \$·kg^{-1}	[36-41]
Tax_{HFC}	Enforced HFC tax in Spain	R32: 11.05 \$·kg^{-1} R152a: 0 \$·kg^{-1} R134a: 23.39 \$·kg^{-1} R125: 57.25 \$·kg^{-1} R227ea: 52.67 \$·kg^{-1} R410A: 34.14 \$·kg^{-1}	[42]
Tax_{CO_2} $(EU-ETS)$	Carbon tax on direct emissions according to the EU emissions Trading System	49.7 \$·tCO_2-eq^{-1}	[43]
Tax_{CO_2} (SWE)	Carbon tax on direct emissions in Sweden	137.2 \$·tCO_2-eq^{-1}	[43]
Th_{SS} ρ_{SS}	Stainless-Steel thickness Stainless-Steel density	0.0005 m 9850 kg·m^{-3}	This thesis
Th_{Al} ρ_{Al}	Aluminum thickness Aluminum density	0.00025 m 2730 kg·m^{-3}	This thesis
$\dot{W_{fan}}$	Electric power for fans and blowers	0.1 kW	This thesis
U_{HX}	HX heat transfer coefficient	1000 W·m^{-2}·K^{-1}	[44]
ε^{HX}	Intercooler effectiveness	60%	This thesis (Chapter 7.2)

Table D1. *Factorial effect and significance order for COP, VCC, and η_{II}.*

		A	B	C	D	E	F	G	AB	AC	AD	AE	AF	AG	BD	ABD
COP	**Level [-1]**	7.728	7.795	8.741	8.046	8.731	8.790	8.774	8.606	8.799	8.720	8.801	8.787	8.787	8.721	8.787
	Level [+1]	9.871	9.804	8.858	9.553	8.868	8.809	8.825	8.993	8.800	8.880	8.798	8.812	8.812	8.878	8.812
	Delta	2.143	2.010	0.118	1.506	0.136	0.019	0.051	0.388	0.001	0.160	0.003	0.026	0.024	0.156	0.024
	Rank	1	2	8	3	7	13	9	4	14	5	15	10	12	6	11
VCC	**Level [-1]**	1.304	1.423	1.441	1.441	1.445	1.456	1.451	1.452	1.454	1.454	1.454	1.454	1.454	1.453	1.453
	Level [+1]	1.602	1.483	1.465	1.465	1.461	1.451	1.455	1.455	1.452	1.452	1.452	1.452	1.453	1.453	1.453
	Delta	0.298	0.060	0.024	0.024	0.015	0.005	0.003	0.003	0.003	0.002	0.002	0.002	0.001	0.000	0.000
	Rank	1	2	4	14	3	8	5	7	13	10	9	12	6	11	15
η_{II}	**Level [-1]**	0.479	0.393	0.462	0.419	0.534	0.538	0.462	0.451	0.538	0.540	0.463	0.462	0.538	0.452	0.538
	Level [+1]	0.522	0.608	0.539	0.582	0.467	0.463	0.540	0.550	0.463	0.461	0.538	0.539	0.463	0.550	0.464
	Delta	0.043	0.215	0.077	0.163	0.067	0.075	0.078	0.099	0.075	0.079	0.075	0.077	0.075	0.098	0.074
	Rank	15	1	8	2	14	10	6	3	11	5	9	7	12	4	13

Table D2. *ANOVA results and contribution ratios on **a)** COP, **b)** VCC, and **c)** η_{II}.*

	SS=MS	C_i / %	F	p	Order
A	18.370	41.235	9.824	0.007	1
B	16.155	36.264	7.966	0.014	2
C	0.055	0.124	0.017	0.897	8
D	9.074	20.369	3.581	0.079	3
E	0.075	0.167	0.023	0.880	7
F	0.001	0.003	0.000	0.983	13
G	0.010	0.023	0.003	0.956	9
AB	0.601	1.348	0.191	0.668	4
AC	0.000	0.000	0.000	0.999	14
AD	0.102	0.230	0.032	0.860	5
AE	0.000	0.000	0.000	0.997	15
AF	0.003	0.006	0.001	0.978	10
AG	0.002	0.005	0.001	0.979	12
BD	0.097	0.219	0.031	0.863	6
ABD	0.000	0.000	0.000	0.979	11
Σ	44.548	100			

	SS	C_i / %	F	p	Order
A	0.355	94.584	244.47	0.000	1
B	0.015	3.874	0.564	0.465	2
C	0.002	0.599	0.084	0.776	4
D	0.000	0.000	0.000	0.996	14
E	0.002	0.620	0.087	0.772	3
F	0.000	0.010	0.001	0.971	8
G	0.001	0.250	0.035	0.854	5
AB	0.000	0.012	0.002	0.968	7
AC	0.000	0.002	0.000	0.987	13
AD	0.000	0.006	0.001	0.977	10
AE	0.000	0.008	0.001	0.975	9
AF	0.000	0.004	0.001	0.981	12
AG	0.000	0.027	0.004	0.952	6
BD	0.000	0.005	0.001	0.979	11
ABD	0.000	0.000	0.000	1.000	15
Σ	0.376	100			

	SS	C_i / %	F	p	Order
A	0.008	1.245	0.176	0.681	15
B	0.184	30.542	6.156	0.026	1
C	0.024	3.931	0.573	0.462	8
D	0.107	17.728	3.017	0.104	2
E	0.018	2.983	0.430	0.522	14
F	0.022	3.727	0.542	0.474	10
G	0.024	4.026	0.587	0.456	6
AB	0.039	6.530	0.978	0.339	3
AC	0.022	3.715	0.540	0.474	11
AD	0.025	4.179	0.611	0.448	5
AE	0.023	3.755	0.546	0.472	9
AF	0.024	3.941	0.574	0.461	7
AG	0.022	3.699	0.538	0.475	12
BD	0.038	6.381	0.954	0.345	4
ABD	0.022	3.619	0.526	0.480	13
Σ	0.603	100.00			

Table D3. *Suggested Taguchi's OAs for three-level and four factor systems.*

Taguchi OA	Fits by degrees of freedom?	Factors confounded with 2-order interactions?	Associated loss of orthogonality?
$L_4(2^3)$	No	-	-
$L_8(2^7)$	No	-	-
$L_9(3^4)$	Yes	Yes	No
$L_{12}(2^{11})$	No	-	-
$L_{16}(2^{15})$	Yes	No	Yes
$L_{18}(2^1 \cdot 3^7)$	Yes	Yes	No
$L_{25}(5^6)$	Yes	Yes	Yes
$L_{27}(3^{13})$	Yes	No	No

* Other non-considered designs of higher runs: $L_{32}(2^{31})$, $L_{36}(2^{11} \cdot 3^{12})$, $L_{54}(2^1 \cdot 3^{25})$

Table D4. *Positive and negative ideal distances, TOPSIS coefficients, and ranking of high-efficient experiences.*

#	D_i^+	D_i^-	C_i	Rank
1'	0.0078	0.0311	0.7992	5
2'	0.0040	0.0347	0.8956	3
3'	0.0073	0.0316	0.8131	4
4'	0.0040	0.0347	0.8956	2
5'	0.0385	0.0002	0.0062	16
6'	0.0167	0.0219	0.5669	6
7'	0.0226	0.0159	0.4127	11
8'	0.0202	0.0184	0.4768	9
9'	0.0220	0.0166	0.4301	10
10'	0.0001	0.0385	0.9971	1
11'	0.0197	0.0188	0.4881	8
12'	0.0169	0.0217	0.5625	7
13'	0.0356	0.0032	0.0831	14
14'	0.0324	0.0065	0.1665	12
15'	0.0362	0.0026	0.0673	15
16'	0.0328	0.0061	0.1576	13
$\gamma_{EWM} = 0.17 \cdot \gamma_{COP} + 0.16 \cdot \gamma_{VCC} + 0.67 \cdot \gamma_{\eta_{UI}}$				

Table D5. *Factors for estimating cycle total cost.*

Parameter	Definition	Value	Source
β	Indirect emission factor	0.2839kgCO_2-eq·kWh^{-1}	[26]
U_{HX}	HX heat transfer coefficient	1000 W·m^{-2}·K^{-1}	[44]
$T_{PP,evap}$	Evaporator's pinch point temperature difference	$10K$	[44]
$\dot{m}_{evap}$	Evaporator's air flow	$0.75kg \cdot s^{-1}$	[44]
α_{el}	Average or unit cost of electricity	0.241\$·kWh^{-1}	[44]
c_{CO_2}	Unit cost of CO_2 avoided - NGCC	0.087\$·kgCO_2-eq^{-1}	[44]

Table D6. *Technical performance for the evaluated working fluids and cooling cycles.*

	R134a			R513A			Blend 5		
	SS-VCRC	LL/SL-HX	TS-VCRC	SS-VCRC	LL/SL-HX	TS-VCRC	SS-VCRC	LL/SL-HX	TS-VCRC
***VCC* / kJ·L^{-1}**	1.702	1.717	1.707	1.833	1.861	1.839	1.504	1.512	1.507
***P_{cond}* / MPa**	0.565	0.565	0.565	0.620	0.620	0.620	0.497	0.497	0.497
***DLT* / K**	302.0	314.4	301.5	299.5	311.6	299.1	304.1	316.5	303.7
COP	6.768	6.809	7.052	6.688	6.772	6.967	6.769	6.803	7.003
η_{II} / %	31.25	31.58	33.21	30.83	31.29	32.05	31.31	31.41	32.59
	R410A			**R32**			**Blend 1**		
	SS-VCRC	LL/SL-HX	TS-VCRC	SS-VCRC	LL/SL-HX	TS-VCRC	SS-VCRC	LL/SL-HX	TS-VCRC
***VCC* / kJ·L^{-1}**	4.341	4.335	4.349	4.519	4.453	4.522	5.044	5.084	5.054
***P_{cond}* / MPa**	1.488	1.488	1.488	1.483	1.483	1.483	1.809	1.809	1.809
***DLT* / K**	310.8	323.4	309.7	322.3	335.4	321.6	305.7	317.7	305.0
COP	6.477	6.465	6.798	6.656	6.559	6.816	6.419	6.456	6.700
η_{II} / %	28.69	28.19	30.49	30.81	30.15	31.49	28.77	29.04	30.62

Table D7. *Exergy mapping for evaluated working fluids and cooling cycles including input, and output exergy, and produced, total destroyed, avoidable destroyed, and unavoidable destroyed per equipment in each cycle.*

	R134a			R513A			Blend 5		
$\dot{\chi}$ / kW	SS-VCRC	LL/SL-HX	TS-VCRC	SS-VCRC	LL/SL-HX	TS-VCRC	SS-VCRC	LL/SL-HX	TS-VCRC
Input	1.47747	1.46873	1.2102	1.27792	1.26956	1.21665	1.26793	1.26755	1.21765
Output	0.6090	0.6030	0.40193	0.39401	0.39723	0.38993	0.39705	0.39816	0.39678
Produced-Comp	1.263	1.265	1.210	1.278	1.269	1.217	1.268	1.268	1.218
Produced-Cond	0.052	0.046	0.052	0.053	0.060	0.053	0.048	0.051	0.048
Produced-EEV	1.864	1.812	3.743	2.124	2.048	4.245	1.699	1.659	3.429
Produced-Evap	0.557	0.557	0.557	0.558	0.921	0.558	0.558	0.857	0.558
Produced-HX	-	0.003	-	-	0.006	-	-	0.008	-
Destroyed-Comp	0.2143	0.2034	0.2078	0.2173	0.2078	0.2188	0.2093	0.2025	0.2104
Destroyed -Cond	0.1457	0.1814	0.1441	0.1401	0.1734	0.1392	0.1563	0.1928	0.1547
Destroyed -EEV	0.1153	0.0573	0.0631	0.1330	0.0687	0.0751	0.1108	0.0614	0.0611
Destroyed -Evap	0.3932	0.3933	0.3933	0.3935	0.3936	0.3936	0.3945	0.3946	0.3946
Destroyed -HX	-	0.0304	-	-	0.0288	-	-	0.0181	-
Unavoidable-Comp	0.0652	0.0620	0.0699	0.0670	0.0630	0.0664	0.0631	0.0582	0.0682
Unavoidable -Cond	0.0660	0.0704	0.0651	0.0645	0.0855	0.0647	0.0580	0.0750	0.0558
Unavoidable -EEV	0.1153	0.0410	0.0631	0.1330	0.0507	0.0751	0.1108	0.0435	0.0611
Unavoidable -Evap	0.2054	0.2056	0.2056	0.2058	0.3395	0.2058	0.2066	0.3173	0.2067
Unavoidable -HX	-	0.0047	-	-	0.0056	-	-	0.0078	-
Avoidable-Comp	0.1491	0.1413	0.1378	0.1503	0.1448	0.1523	0.1462	0.1443	0.1422
Avoidable -Cond	0.0798	0.1110	0.0789	0.0756	0.0879	0.0745	0.0983	0.1178	0.0990
Avoidable -EEV	0.0000	0.0163	0.0000	0.0000	0.0179	0.0000	0.0000	0.0179	0.0000
Avoidable -Evap	0.1877	0.1877	0.1878	0.1877	0.0541	0.1878	0.1879	0.0773	0.1880
Avoidable -HX	-	0.0257	-	-	0.0232	-	-	0.0103	-
	R410A			**R32**			**Blend 1**		

$\dot{\chi}$ / kW	SS-VCRC	LL/SL-HX	TS-VCRC	SS-VCRC	LL/SL-HX	TS-VCRC	SS-VCRC	LL/SL-HX	TS-VCRC
Input	1.32141	1.32387	1.25811	1.30013	1.3254	1.25881	1.33575	1.33815	1.27267
Output	0.37907	0.37321	0.38362	0.40061	0.39958	0.39636	0.38431	0.38864	0.38975
Produced-Comp	1.321	1.324	1.258	1.300	1.325	1.259	1.336	1.338	1.273
Produced-Cond	0.044	0.060	0.043	0.046	0.045	0.046	0.049	0.058	0.049
Produced-EEV	3.818	3.661	7.499	3.595	3.488	7.105	4.666	4.414	9.110
Produced-Evap	0.558	0.867	0.558	0.557	0.775	0.557	0.557	0.934	0.557
Produced-HX	-	-0.003	-	-	0.007	-	-	0.006	-
Destroyed-Comp	0.2226	0.2228	0.2129	0.2023	0.1993	0.2083	0.2220	0.2107	0.2198
Destroyed -Cond	0.1668	0.2130	0.1658	0.1959	0.2493	0.1943	0.1561	0.2071	0.1557
Destroyed -EEV	0.1515	0.0878	0.0947	0.1117	0.0757	0.0699	0.1792	0.1089	0.1132
Destroyed -Evap	0.4015	0.4013	0.4012	0.3896	0.3899	0.3900	0.3941	0.3942	0.3942
Destroyed -HX	-	0.0257	-	-	0.0117	-	-	0.0287	-
Unavoidable-Comp	0.0718	0.0724	0.0651	0.0594	0.0595	0.0615	0.0673	0.0648	0.0664
Unavoidable -Cond	0.0488	0.0980	0.0466	0.0693	0.0906	0.0682	0.0599	0.0933	0.0584
Unavoidable -EEV	0.1515	0.0637	0.0947	0.1117	0.0601	0.0699	0.1792	0.0905	0.1132
Unavoidable -Evap	0.2122	0.3293	0.2119	0.2026	0.2825	0.2029	0.2062	0.3460	0.2063
Unavoidable -HX	-	0	-	-	0.0082	-	-	0.0047	-
Avoidable-Comp	0.1508	0.1505	0.1478	0.1429	0.1398	0.1468	0.1547	0.1459	0.1534
Avoidable -Cond	0.1179	0.1151	0.1191	0.1266	0.1587	0.1261	0.0962	0.1138	0.0973
Avoidable -EEV	0.0000	0.0241	0.0000	0.0000	0.0156	0.0000	0.0000	0.0184	0.0000
Avoidable -Evap	0.1893	0.0720	0.1893	0.1870	0.1073	0.1871	0.1879	0.0482	0.1879
Avoidable -HX	-	0.0257	-	-	0.0035	-	-	0.0240	-

Table D8. *TEWI direct, indirect, and total contributions for the evaluated working fluids and cycle configurations deployed in PRC, US, and EU.*

TEWI / tCO_2-eq	R134a			R513A			Blend 5		
	SS-VCRC	LL/SL-HX	TS-VCRC	SS-VCRC	LL/SL-HX	TS-VCRC	SS-VCRC	LL/SL-HX	TS-VCRC
Direct	7.0688	7.0688	7.0688	3.1103	3.1103	3.1103	0.0023	0.0023	0.0023
Indirect-PRC	104.33	103.71	100.13	105.58	104.28	101.36	104.31	103.81	100.84
Indirect-US	82.30	81.82	78.99	83.29	82.26	79.96	82.29	81.89	79.55
Indirect-EU	55.12	54.79	52.90	55.78	55.09	53.55	55.11	54.84	53.27
Total-PRC	111.40	110.78	107.20	108.69	107.39	104.47	104.32	103.81	100.84
Total-US	89.37	88.89	86.06	86.40	85.37	83.07	82.29	81.89	79.55
Total-EU	62.19	61.86	59.97	58.89	58.20	56.66	55.11	54.84	53.28
TEWI / tCO_2-eq	R410A			R32			Blend 1		
	SS-VCRC	LL/SL-HX	TS-VCRC	SS-VCRC	LL/SL-HX	TS-VCRC	SS-VCRC	LL/SL-HX	TS-VCRC
Direct	10.4590	10.4590	10.4590	1.7670	1.7670	1.7670	0.1837	0.1837	0.1837
Indirect-PRC	109.03	109.22	103.87	106.09	107.67	103.60	110.00	109.37	105.39
Indirect-US	86.01	86.16	81.94	83.69	84.93	81.73	86.78	86.28	83.14
Indirect-EU	57.60	57.70	54.87	56.05	56.88	54.73	58.11	57.78	55.68
Total-PRC	119.49	119.68	114.33	107.86	109.43	105.37	110.18	109.55	105.57
Total-US	96.47	96.62	92.40	85.46	86.70	83.49	86.96	86.46	83.32
Total-EU	68.06	68.16	65.33	57.82	58.65	56.50	58.30	57.96	55.86

Table D9. *TAC and its components (CAPEX, OPEX, Enviro, SET) for the evaluated working fluids and cycle configurations deployed in PRC, US, and EU.*

Cost / k$.y^{-1}	R134a			R513A			Blend 5		
	SS-VCRC	LL/SL-HX	TS-VCRC	SS-VCRC	LL/SL-HX	TS-VCRC	SS-VCRC	LL/SL-HX	TS-VCRC
CAPEX	3.199	3.208	4.026	3.230	3.238	4.077	3.192	3.214	4.038
OPEX-PRC	1.139	1.132	1.093	1.153	1.138	1.107	1.139	1.133	1.101
OPEX-US	1.468	1.459	1.409	1.485	1.467	1.426	1.467	1.460	1.419
OPEX-EU	3.113	3.094	2.987	3.150	3.111	3.024	3.112	3.097	3.009
Enviro -PRC	0.689	0.602	0.581	0.697	0.605	0.588	0.688	0.602	0.585
Enviro-US	0.488	0.475	0.458	0.494	0.477	0.464	0.488	0.475	0.461
Enviro -EU	0.356	0.318	0.307	0.361	0.320	0.311	0.356	0.318	0.309
Set-up *-PRC*	0.0062	0.0062	0.0062	0.0309	0.0309	0.0309	0.0104	0.0104	0.0104
Set-up *-US*	0.0062	0.0062	0.0062	0.0309	0.0309	0.0309	0.0104	0.0104	0.0104
Set-up *-EU*	0.0174	0.0174	0.0174	0.0309	0.0309	0.0309	0.0104	0.0104	0.0104
TAC-PRC	5.033	4.948	5.706	5.110	5.012	5.802	5.030	4.960	5.734
TAC-US	5.162	5.148	5.899	5.240	5.213	5.997	5.158	5.160	5.928
TAC-EU	6.686	6.638	7.338	6.772	6.700	7.442	6.671	6.640	7.366
Cost / k$.y^{-1}	**R410A**			**R32**			**Blend 1**		
	SS-VCRC	LL/SL-HX	TS-VCRC	SS-VCRC	LL/SL-HX	TS-VCRC	SS-VCRC	LL/SL-HX	TS-VCRC
CAPEX	3.212	3.250	4.051	3.157	3.206	4.013	3.236	3.268	4.087
OPEX-PRC	1.190	1.192	1.134	1.158	1.175	1.131	1.201	1.194	1.150
OPEX-US	1.534	1.536	1.461	1.493	1.515	1.457	1.547	1.539	1.483
OPEX-EU	3.253	3.259	3.099	3.165	3.212	3.091	3.282	3.263	3.144
Enviro -PRC	0.720	0.633	0.602	0.700	0.624	0.601	0.726	0.634	0.611
Enviro -US	0.510	0.500	0.475	0.497	0.493	0.474	0.515	0.500	0.482
Enviro -EU	0.372	0.335	0.318	0.362	0.330	0.317	0.376	0.335	0.323
Set-up *-PRC*	0.0149	0.0149	0.0149	0.0041	0.0041	0.0041	0.0463	0.0463	0.0463
Set-up *-US*	0.0149	0.0149	0.0149	0.0041	0.0041	0.0041	0.0463	0.0463	0.0463
Set-up *-EU*	0.0312	0.0312	0.0312	0.0066	0.0066	0.0066	0.0463	0.0463	0.0463
TAC-PRC	5.137	5.091	5.802	5.019	5.010	5.749	5.209	5.143	5.895
TAC-US	5.271	5.302	6.002	5.150	5.217	5.948	5.344	5.353	6.098
TAC-EU	6.868	6.875	7.499	6.691	6.754	7.428	6.940	6.913	7.600

* Note that the TAC for the SS-VCRC is corroborated according to **Figure 6.12**.

Table D10. *Enthalpy of formation for all assessed compounds targeted in the synthetic routes detailed in* ***Eqs. D1a-f****.*

Compound	$\Delta_f^0 H$ / $kJ \cdot mol^{-1}$	Ref	Compound	$\Delta_f^0 H$ / $kJ \cdot mol^{-1}$	Ref
R32	-450.7	[45]	$CH_2Cl-CH_2-CCl_3$	-208.7	[48]
R125	-1100.4	a	$CH_2Cl-CHCl-CCl_3$	-232.1	[47]
Ethylene	52.5	[45]	R1123	-498.0	b
HCl	-92.3	[46]	R1234yf	-813.3	[49]
HF	-273.3	[46]	R1234ze(E)	-779.9	[50]
CCl_4	-96.0	[45]	R1243zf	-614.2	[51]
CH_2Cl_2	-95.5	[45]	$CF_2=CF_2$	-658.6	[45]
$CH_2F-CHF-CF_3$	-24.4	[47]	$CCl_2=CCl_2$	-12.4	[45]
$CF_3-CHF-CH_2Cl$	-22.9	[47]	$CF_3-CH=CHCl$	-25.4	[47]

a Prediction of Standard Enthalpy of Formation by a QSPR Model

b atct.anl.gov/Thermochemical%20Data/version%201.128/species/?species_number=502

Table D11. *2021 LCA for R134a, R513A, and Blend 5 as possible drop-ins in SS, LL/SL-HX and TS-VCRCs.*

	SS-VCRC			LL/SL-IHX			TS-VCRC		
	R134a	**R513A**	**5**	**R134a**	**R513A**	**5**	**R134a**	**R513A**	**5**
E, Compression	27.8431	28.1772	27.8386	27.6786	27.8291	27.7032	26.7216	27.0507	26.9117
ReE, Leakages	7.8196	3.4420	0.0028	7.8196	3.4420	0.0028	7.8196	3.4420	0.0028
E, Air Compressor	7.4038	7.7556	7.7556	7.4038	7.7556	7.7556	7.4038	7.7556	7.7556
CW	2.7674	2.7726	2.7674	2.7649	2.7674	2.7653	2.7499	2.7550	2.7533
E, CW Pump	1.9562	1.9562	1.9562	2.0451	2.0451	1.8845	1.9562	1.9562	1.9562
E, Air Blow	1.8845	1.8845	1.8845	1.8845	1.8845	1.8845	1.8845	1.8845	1.8845
ReE, End-of-Life	1.2511	0.5507	0.0005	1.2511	0.5507	0.0005	1.2511	0.5507	0.0005
MP, Compressor	0.1644	0.1644	0.1644	0.1644	0.1644	0.1644	0.1644	0.1644	0.1644
MP, Air Compressor	0.1644	0.1644	0.1644	0.1644	0.1644	0.1644	0.1644	0.1644	0.1644
MP, Compressor +1	0.0000	0.0000	0.0000	0.0000	0.0000	0.0000	0.1644	0.1644	0.1644
ReP, Leakages	0.0836	0.0450	0.0387	0.0836	0.0450	0.0387	0.0836	0.0450	0.0387
ReP, Closed Cycle	0.0446	0.0240	0.0206	0.0446	0.0240	0.0206	0.0446	0.0240	0.0206
MP, SS of Tanks	0.0000	0.0000	0.0000	0.0000	0.0000	0.0000	0.0203	0.0203	0.0203
MP, SS HEs	0.0067	0.0068	0.0067	0.0065	0.0066	0.0065	0.0067	0.0067	0.0067
MP, Al HEs	0.0021	0.0021	0.0021	0.0020	0.0020	0.0020	0.0021	0.0021	0.0021
MP, CW Pump	0.0019	0.0019	0.0019	0.0019	0.0019	0.0019	0.0019	0.0019	0.0019
GWP_{100}	**51.3932**	**46.9475**	**42.6042**	**51.3150**	**46.6828**	**42.3949**	**50.4391**	**45.9880**	**41.8479**

E: Electricity, ReE: Refrigerant Emissions, CW: Cooling Water, MP: Material Production, ReP: Refrigerant Production

Table D12. *2021 LCA for R410A, R32, and Blend 1 as possible drop-ins in SS, LL/SL-HX and TS-VCRCs.*

	SS-VCRC			LL/SL-IHX			TS-VCRC		
	R410A	**R32**	**1**	**R410A**	**R32**	**1**	**R410A**	**R32**	**1**
E, Compression	29.0968	28.3138	29.3563	29.1476	28.7332	29.1881	27.7209	27.6481	28.1252
ReE, Leakages	11.5275	3.9404	0.3963	11.5275	3.9404	0.3963	11.5275	3.9404	0.3963
E, Air Compressor	7.9774	7.4038	7.1820	7.9774	7.4038	7.1820	7.9774	7.4038	7.1820
CW	2.7871	2.7748	2.7911	2.7880	2.7814	2.7885	2.7656	2.7644	2.7718
E, CW Pump	2.0451	1.9562	1.9562	1.9562	1.9562	1.9562	1.4227	1.9562	1.9562
E, Air Blow	1.8845	1.8845	1.8845	1.8845	1.8845	1.8845	1.8845	1.8845	1.8845
ReE, End-of-Life	1.8444	0.6305	0.0634	1.8444	0.6305	0.0634	1.8444	0.6305	0.0634
MP, Compressor	0.1644	0.1644	0.1644	0.1644	0.1644	0.1644	0.1644	0.1644	0.1644
MP, Air Compressor	0.1644	0.1644	0.1644	0.1644	0.1644	0.1644	0.1644	0.1644	0.1644
MP, Compressor +1	0.0000	0.0000	0.0000	0.0000	0.0000	0.0000	0.1644	0.1644	0.1644
ReP, Leakages	0.0290	0.0154	0.6499	0.0290	0.0154	0.6499	0.0290	0.0154	0.6499
ReP, Closed Cycle	0.0155	0.0082	0.3466	0.0155	0.0082	0.3466	0.0155	0.0082	0.3466
MP, SS of Tanks	0.0000	0.0000	0.0000	0.0000	0.0000	0.0000	0.0203	0.0203	0.0203
MP, SS HEs	0.0065	0.0064	0.0066	0.0065	0.0063	0.0065	0.0065	0.0064	0.0066
MP, Al HEs	0.0020	0.0020	0.0020	0.0020	0.0020	0.0020	0.0020	0.0020	0.0020
MP, CW Pump	0.0019	0.0019	0.0019	0.0019	0.0019	0.0019	0.0019	0.0019	0.0019
GWP_{100}	**57.5464**	**47.2667**	**44.9657**	**57.5091**	**47.6926**	**44.7948**	**55.7114**	**46.7753**	**43.9001**

E: Electricity, ReE: Refrigerant Emissions, CW: Cooling Water, MP: Material Production, ReP: Refrigerant Production

Table D13. *2050 LCA for R134a, R513A, and Blend 5 as possible drop-ins in SS, LL/SL-HX and TS-VCRCs.*

	SS-VCRC			LL/SL-IHX			TS-VCRC		
	R134a	**R513A**	**5**	**R134a**	**R513A**	**5**	**R134a**	**R513A**	**5**
ReE, Leakages	7.8196	3.4420	0.0028	7.8196	3.4420	0.0028	7.8196	3.4420	0.0028
E, Compression	1.6486	1.6684	1.6484	1.6389	1.6478	1.6404	1.5822	1.6017	1.5935
ReE, End-of-Life	1.2511	0.5507	0.0005	1.2511	0.5507	0.0005	1.2511	0.5507	0.0005
E, Air Compressor	0.4384	0.4592	0.4592	0.4384	0.4592	0.4592	0.4384	0.4592	0.4592
CW	0.2817	0.2824	0.2817	0.2814	0.2817	0.2815	0.2794	0.2801	0.2799
E, CW Pump	0.1158	0.1158	0.1158	0.1211	0.1211	0.1116	0.1158	0.1158	0.1158
E, Air Blow	0.1116	0.1116	0.1116	0.1116	0.1116	0.1116	0.1116	0.1116	0.1116
MP, Compressor	0.0974	0.0974	0.0974	0.0974	0.0974	0.0974	0.0974	0.0974	0.0974
MP, Compressor +1	0.0000	0.0000	0.0000	0.0000	0.0000	0.0000	0.0974	0.0974	0.0974
MP, Air Compressor	0.0974	0.0974	0.0974	0.0974	0.0974	0.0974	0.0974	0.0974	0.0974
ReP, Leakages	0.0685	0.0375	0.0290	0.0685	0.0375	0.0290	0.0685	0.0375	0.0290
ReP, Closed Cycle	0.0366	0.0200	0.0155	0.0366	0.0200	0.0155	0.0366	0.0200	0.0155
MP, SS HEs	0.0037	0.0037	0.0037	0.0036	0.0036	0.0036	0.0037	0.0037	0.0037
MP, SS of Tanks	0.0000	0.0000	0.0000	0.0000	0.0000	0.0000	0.0111	0.0111	0.0111
MP, Al HEs	0.0018	0.0019	0.0018	0.0018	0.0018	0.0018	0.0018	0.0018	0.0018
MP, CW Pump	0.0010	0.0010	0.0010	0.0010	0.0010	0.0010	0.0010	0.0010	0.0010
GWP_{100}	**11.9733**	**6.8891**	**2.8659**	**11.9684**	**6.8729**	**2.8533**	**12.0132**	**6.9286**	**2.9178**

E: Electricity, ReE: Refrigerant Emissions, CW: Cooling Water, MP: Material Production, ReP: Refrigerant Production

Table D14. *2050 LCA for R410A, R32, and Blend 1 as possible drop-ins in SS, LL/SL-HX and TS-VCRCs.*

	SS-VCRC			LL/SL-IHX			TS-VCRC		
	R410A	**R32**	**1**	**R410A**	**R32**	**1**	**R410A**	**R32**	**1**
ReE, Leakages	11.5275	3.9404	0.3963	11.5275	3.9404	0.3963	11.5275	3.9404	0.3963
E, Compression	1.7229	1.6765	1.7383	1.7259	1.7014	1.7283	1.6414	1.6371	1.6654
ReE, End-of-Life	1.8444	0.6305	0.0634	1.8444	0.6305	0.0634	1.8444	0.6305	0.0634
E, Air Compressor	0.4724	0.4384	0.4253	0.4724	0.4384	0.4253	0.4724	0.4384	0.4253
CW	0.2843	0.2827	0.2848	0.2844	0.2835	0.2844	0.2815	0.2813	0.2823
E, CW Pump	0.1211	0.1158	0.1158	0.1158	0.1158	0.1158	0.0842	0.1158	0.1158
E, Air Blow	0.1116	0.1116	0.1116	0.1116	0.1116	0.1116	0.1116	0.1116	0.1116
MP, Compressor	0.0974	0.0974	0.0974	0.0974	0.0974	0.0974	0.0974	0.0974	0.0974
MP, Compressor +1	0.0000	0.0000	0.0000	0.0000	0.0000	0.0000	0.0974	0.0974	0.0974
MP, Air Compressor	0.0974	0.0974	0.0974	0.0974	0.0974	0.0974	0.0974	0.0974	0.0974
ReP, Leakages	0.0280	0.0144	0.6303	0.0280	0.0144	0.6303	0.0280	0.0144	0.6303
ReP, Closed Cycle	0.0149	0.0077	0.3361	0.0149	0.0077	0.3361	0.0149	0.0077	0.3361
MP, SS HEs	0.0036	0.0035	0.0036	0.0035	0.0035	0.0036	0.0036	0.0035	0.0036
MP, SS of Tanks	0.0000	0.0000	0.0000	0.0000	0.0000	0.0000	0.0111	0.0111	0.0111
MP, Al HEs	0.0018	0.0018	0.0018	0.0018	0.0017	0.0018	0.0018	0.0018	0.0018
MP, CW Pump	0.0010	0.0010	0.0010	0.0010	0.0010	0.0010	0.0010	0.0010	0.0010
GWP_{100}	**16.3283**	**7.4191**	**4.3031**	**16.3261**	**7.4447**	**4.2928**	**16.3157**	**7.4869**	**4.3363**

E: Electricity, ReE: Refrigerant Emissions, CW: Cooling Water, MP: Material Production, ReP: Refrigerant Production

Table E1. *Developed ANN's weights and biases.*

	Hidden Layer 1													
	H_1	**H_2**	**H_3**	**H_4**	**H_5**	**H_6**	**H_7**	**H_8**	**H_9**	**H_{10}**	**H_{11}**	**H_{12}**	**H_{13}**	**H_{14}**
S_1														
S_2	0	0	0	0	0	0	0	0	0	0	0	0	0	0
S_3	0	0	0	0	0	0	0	0	0	0	0	0	0	0
S_4	0	0	0	0	0	0	0	0	0	0	0	0	0	0
S_5	0	0	0	0	0	0	0	0	0	0	0	0	0	0
S_6	0	0	0	0	0	0	0	0	0	0	0	0	0	0
S_7	0	0	0	0	0	0	0	0	0	0	0	0	0	0
S_8	0	0	0	0	0	0	0	0	0	0	0	0	0	0
S_9	0	0	0	0	0	0	0	0	0	0	0	0	0	0
S_{10}	0	0	0	0	0	0	0	0	0	0	0	0	0	0
S_{11}	0	0	0	0	0	0	0	0	0	0	0	0	0	0
S_{12}	0	0	0	0	0	0	0	0	0	0	0	0	0	0
S_{13}	0	0	0	0	0	0	0	0	0	0	0	0	0	0
S_{14}	0.8458	-2.8818	-1.0014	1.0280	0.0565	-2.4029	-1.8018	2.8284	-1.3958	-2.6598	-1.2253	1.5103	-2.4375	-0.4681
S_{15}	-0.2075	0.5565	-0.4336	-0.3225	0.8986	-1.4568	0.0141	-0.5083	-0.6832	-0.9620	0.0730	-0.5960	-0.7045	-0.3797
S_{16}	-0.0420	-0.9716	0.1980	0.2326	0.4817	-0.5778	0.1160	-0.1190	-0.2024	-0.8362	-0.4973	0.3534	-0.0101	-0.2451
S_{17}	-0.1242	-0.6831	-0.3918	0.0612	0.4498	0.9127	0.3810	0.1004	-0.1382	0.0039	-0.2620	0.4858	0.0129	0.3271
S_{18}	-0.2648	0.7208	0.0489	-0.4739	0.3182	-0.9774	-0.4748	0.6585	-0.0579	0.1070	0.3020	0.0031	-0.2046	-0.0182
S_{19}	0.5436	-0.2822	0.1789	0.0545	-0.3789	0.3121	0.2268	-0.1822	-0.0223	-1.0864	0.2265	-0.1448	-0.6931	-0.1322
S_{20}	-0.0544	-0.1080	-0.2226	0.1345	-0.2125	0.8676	0.1626	-0.4861	0.3767	0.2059	-0.4288	0.0671	0.2071	0.0781
S_{21}	-0.1340	0.1226	-0.0720	-0.1219	0.1343	-0.6544	-0.3892	-0.1006	0.3139	0.4365	-0.2181	-0.0986	0.5160	0.0535
S_{22}	0.3013	-0.0026	0.3618	0.1885	-0.4095	0.7669	0.2337	0.0294	-0.8519	-0.8500	0.9069	0.0183	-0.5814	0.0328
S_{23}	0.0989	-0.7800	0.3459	0.1297	-0.4147	0.8101	-0.1587	-0.3154	-0.0937	0.6298	-1.1329	0.5140	0.0257	0.2170
S_{24}	0.0783	0.3142	-0.4355	-0.0218	-0.0870	-0.6036	-0.0510	-0.1005	0.7059	0.6007	0.2707	-0.4815	0.0817	-0.2435
S_{25}	-0.3056	1.3469	-0.0593	-0.0752	0.0691	-0.4876	-0.3930	0.2413	-0.6005	0.5594	1.0563	-0.3262	0.2841	0.0201
S_{26}	-0.6668	-0.5203	0.1390	0.1239	0.0474	0.4045	0.0559	0.1043	-0.6262	1.6126	-0.4221	0.4299	0.3607	-0.0431
S_{27}	0.3305	-0.0070	-0.1061	0.2185	0.0385	0.3718	0.0391	-0.0966	0.1564	-1.2582	0.5244	-0.0936	-0.0046	0.1240
S_{28}	-0.1911	0.2889	-0.1037	0.0308	-0.3479	-0.7942	-0.3377	0.2884	-0.0728	0.5285	-0.5527	-0.1052	0.3868	-0.0964
S_{29}	-0.7246	-0.3970	-0.3013	0.1151	-0.5175	-0.3552	0.4574	0.1324	-0.5002	2.5340	0.2442	0.0971	0.3455	-0.5602
S_{30}	-0.0133	0.4186	0.5083	0.2190	0.3684	1.0784	-0.5578	-0.2062	-0.6011	-1.1690	0.4780	0.2896	0.0142	0.8000

S_{31}	0.3900	-0.2749	0.0112	-0.4003	0.2787	-0.1079	0.0516	0.0322	0.8641	-0.8075	-0.8632	-0.1145	0.0146	-0.0451
S_{32}	0.3012	0.1685	-0.3948	0.0012	-0.2608	-0.3707	0.3654	-0.5010	0.3648	0.0772	0.2757	-0.2886	-0.0134	-0.5134
S_{33}	-0.3695	0.2555	0.3861	0.3996	0.1019	0.7585	-0.3733	-0.1764	-0.4813	-0.0184	0.2333	0.1530	0.2254	0.6138
S_{34}	0.1128	-0.5109	-0.0800	-0.5002	0.3694	-0.6640	0.3490	0.5210	0.2498	-0.2953	-0.1726	0.0795	-0.3850	-0.2771
S_{35}	0.1812	0.7339	-0.1567	0.1618	-0.2162	-0.2073	-0.1199	-0.3285	-0.1126	-0.0944	0.4139	-0.1916	0.1889	-0.1669
S_{36}	-0.4721	-0.6985	0.2856	0.2656	0.1084	0.5206	-0.0305	-0.2051	0.1354	0.7381	-0.5957	0.1159	0.5055	0.3921
S_{37}	0.2246	0.4807	-0.3618	-0.5902	0.2549	-0.6401	0.1568	0.5597	-0.1226	-0.9058	0.8417	0.0656	-0.3964	-0.0706
S_{38}	0.0929	0.0432	0.1408	0.2417	-0.0592	-0.1697	-0.0024	-0.3407	-0.0637	0.2076	-0.4002	-0.0228	-0.0229	-0.2159
S_{39}	0.2257	-1.1726	0.4945	0.2524	-0.0465	0.8416	0.2879	-0.5317	0.9494	0.2598	-0.8329	-0.0505	0.0145	0.2459
S_{40}	0.6905	0.2610	-0.1590	-0.2942	-0.0081	0.2651	0.2368	0.0789	0.1985	-1.6810	0.8810	0.0659	-0.5303	0.1440
S_{41}	0.4459	-0.3950	0.3738	-0.1648	0.3883	-0.9344	-0.1096	-0.0361	-0.9516	-0.6250	-1.0354	0.7487	-0.4512	0.0779
S_{42}	0.2501	0.1639	0.6585	-0.4493	-0.0411	-1.0826	-0.8020	0.3601	-0.7561	-0.5254	-1.1717	-0.1687	-0.3834	-0.3302
S_{43}	-0.7899	0.6348	0.1914	0.6987	-0.5303	-0.4871	0.3696	0.0225	0.3617	-0.2846	0.1156	0.3481	-0.3268	-0.6428
S_{44}	0.6794	-0.7828	-0.0959	-0.1586	0.7576	-0.4573	0.1760	-0.6900	-0.0469	-0.7902	-0.5326	-0.7873	0.4142	-0.0299
S_{45}	0.2992	0.4066	0.2741	-0.6989	-0.6230	-0.1659	0.5104	0.1735	-0.0891	0.4978	0.0956	0.2860	-0.3166	0.3128
S_{46}	-0.4264	-0.0579	0.2603	0.4627	0.6417	0.1776	-0.2646	0.4489	0.5059	0.2361	0.3559	0.5683	-0.1049	-0.2904
S_{47}	0.0468	-0.0539	-0.7060	0.2142	-0.0446	-0.5711	0.3175	-0.1118	-0.4560	0.0912	-0.2672	-0.4591	-0.1369	-0.3181
S_{48}	-0.6722	-0.2767	0.5550	-0.0732	0.6714	-0.7642	-0.0076	0.5971	0.1949	-0.1274	0.2126	0.4536	-0.3957	-0.2523
S_{49}	-0.9666	0.2498	-0.0633	0.7506	0.1629	0.3114	1.2805	0.0397	-0.3651	-0.0011	0.2802	0.5257	0.5121	0.7068
S_{50}	0.2117	4.8667	-6.7478	5.8320	-4.7707	-0.8295	6.7468	5.7124	8.0412	0.2563	5.8112	5.9861	1.3188	-7.6719
S_{51}	0	0	0	0	0	0	0	0	0	0	0	0	0	0
S_{52}	0	0	0	0	0	0	0	0	0	0	0	0	0	0
S_{53}	0	0	0	0	0	0	0	0	0	0	0	0	0	0
S_{54}	0	0	0	0	0	0	0	0	0	0	0	0	0	0
S_{55}	0	0	0	0	0	0	0	0	0	0	0	0	0	0
S_{56}	0	0	0	0	0	0	0	0	0	0	0	0	0	0
S_{57}	0	0	0	0	0	0	0	0	0	0	0	0	0	0
S_{58}	0	0	0	0	0	0	0	0	0	0	0	0	0	0
S_{59}	0	0	0	0	0	0	0	0	0	0	0	0	0	0
S_{60}	0	0	0	0	0	0	0	0	0	0	0	0	0	0
S_{61}	0	0	0	0	0	0	0	0	0	0	0	0	0	0
b_1	0.1353	-2.2195	-0.1200	-3.2270	1.4274	1.6435	0.5930	-0.5451	2.4942	-2.4254	-3.1677	-0.7024	-0.9291	-0.0244

Table E2. *TOPSIS weights for the 4E, and technical KPIs.*

KPIs	DLT	P_{cond}	VCC	$\dot{m}$	COP	$\sum \dot{X}_d$	η_{II}	TEWI	TAC
ω/%	4.95	41.12	40.31	13.62	19.14	23.14	21.10	19.14	17.47

Eqs. D1. *Synthetic routes for a) R1234yf, b) R1234ze(E), c) R1243zf, d) R125, e) R32, and f) R1123.*

$$\boldsymbol{a})\ CH_2Cl-CHCl-CCl_3(0.729kg)+4HF(0.270kg)\rightarrow R1234yf(1kg)+5HCl\ @\ 200-365ºC;0.5179kWh\cdot MJ^{-1}$$

$$CH_2Cl-CH_2-CCl_3(0.719kg)+Cl_2(0.281kg)\rightarrow CH_2Cl-CHCl-CCl_3(1kg)+HCl\ @\ 25ºC;1.2196kWh\cdot MJ^{-1}$$

$$CCl_4(0.846kg)+CH_2=CH_2(0.154kg)\rightarrow CH_2Cl-CH_2-CCl_3(1kg)\ @\ 100ºC;0.8105kWh\cdot MJ^{-1}$$

$$\boldsymbol{b})\ CF_3-CH=CHCl(0.867kg)+HF(0.133kg)\rightarrow R1234ze(E)\ (1kg)+HCl;4.4703kWh\cdot MJ^{-1}$$

$$2CH_2F-CHF-CF_3(0.786kg)+2HCl(0.214kg)\rightarrow CF_3-CHF-CH_2Cl+CHCl=CH-CF_3(1kg)+3HF;3.7996kWh\cdot MJ^{-1}$$

$$CH_2=CH-CF_3(0.717kg)+F_2(0.283kg)\rightarrow CH_2F-CHF-CF_3\ (1kg);5.1328kWh\cdot MJ^{-1}$$

$$CH_2Cl-CH_2-CCl_3(0.752kg)+3HF(0.248kg)\rightarrow CH_2=CH-CF_3(1kg)+4HCl;0.5521kWh\cdot MJ^{-1}$$

$$CCl_4(0.846kg)+CH_2=CH_2(0.154kg)\rightarrow CH_2Cl-CH_2-CCl_3(1kg);0.8105kWh\cdot MJ^{-1}$$

$$\boldsymbol{c})\ CH_2Cl-CH_2-CCl_3\ (0.752kg)+3HF(0.248kg)\rightarrow CH_2=CH-CF_3(1kg)+4HCl\ @\ 225-250ºC;0.5521kWh\cdot MJ^{-1}$$

$$CCl_4(0.846kg)+CH_2=CH_2(0.154kg)\rightarrow CH_2Cl-CH_2-CCl_3(1kg)\ @\ 100ºC;0.8105kWh\cdot MJ^{-1}$$

$$\boldsymbol{d})\ CCl_2=CCl_2(0.624kg)+5HF(0.376kg)\rightarrow R125(1kg)+4HCl;6.7173kWh\cdot MJ^{-1}$$

$$\boldsymbol{e})\ CH_2Cl_2(0.679kg)+2HF(0.320kg)\rightarrow R32(1kg)+2HCl;0.1534kWh\cdot MJ^{-1}$$

$$\boldsymbol{f})\ CF_2=CF_2(0.980kg)+H_2(0.020kg)\rightarrow R1123\ (1kg)@\ 300-750ºC;2.2837kWh\cdot MJ^{-1}$$

Eqs. E1. *Low Flammability Level (LFL) of CO_2-based blends*

$$LFL_M=\frac{100}{\sum_i\frac{A_i}{LFL_i'}}$$

$$LFL_i'=\frac{\left(100-LFL_M'-(1-\overline{K})\cdot\frac{\sum_{p=1}^{k}B_k}{\sum_{i=1}^{n}A_i}\cdot LFL_M'\right)}{(100-LFL_M')}\cdot LFL_i$$

$$LFL[g\cdot m^{-3}]=\frac{1000\cdot LFL_M[\%\ mole]}{V_m[SAFT\ @298K,1bar]}\cdot M_w$$

References of the Annex

[1] E.W. Lemmon, M.L. Huber, M.O. McLinden, NIST standard reference database 23: reference fluid thermodynamic and transport properties-REFPROP. Gaithersburg, USA: National Institute of Standards and Technology, Standard Reference Data Program; 2013. Version 9.1., (2013).

[2] I.H. Bell, J. Wronski, S. Quoilin, V. Lemort, Pure and Pseudo-pure Fluid Thermophysical Property Evaluation and the Open-Source Thermophysical Property Library CoolProp, Ind. Eng. Chem. Res. 53 (2014) 2498–2508. doi:doi.org/10.1021/ie4033999.

[3] Y. Liu, X. Zhao, S. Lv, H. He, Isobaric Heat Capacity Measurements for R1234yf from 303 to 373 K and Pressures up to 12 MPa, J. Chem. Eng. Data. 62 (2017) 1119–1124. doi:10.1021/acs.jced.6b00959.

[4] Y. Liu, X. Zhao, H. He, R. Wang, Heat Capacity of R1234ze(E) at Temperatures from 313 to 393 K and Pressures up to 10 MPa, J. Chem. Eng. Data. 63 (2018) 113–118. doi:10.1021/acs.jced.7b00713.

[5] Y. Liu, X. Zhao, Measurement of the heat capacity of R1233zd(E), Int. J. Refrig. 86 (2018) 127–132. doi:10.1016/j.ijrefrig.2017.11.015.

[6] H. Qi, D. Fang, K. Gao, X. Meng, J. Wu, Compressed Liquid Densities and Helmholtz Energy Equation of State for Fluoroethane (R161), Int. J. Thermophys. 37 (2016) 55. doi:10.1007/s10765-016-2061-1.

[7] M.O. Mclinden, R. Akasaka, Thermodynamic Properties of cis-1,1,1,4,4,4-Hexafluorobutene [R-1336mzz(Z)]: Vapor Pressure, (p, ρ, T) Behavior, and Speed of Sound Measurements and Equation of State, (2020). doi:10.1021/acs.jced.9b01198.

[8] G. Di Nicola, J. Steven Brown, L. Fedele, M. Securo, S. Bobbo, C. Zilio, Subcooled liquid density measurements and PvT measurements in the vapor phase for 3,3,3-trifluoroprop-1-ene (R1243zf), Int. J. Refrig. 36 (2013) 2209–2215. doi:10.1016/j.ijrefrig.2013.08.004.

[9] Y. Higashi, N. Sakoda, Measurements of PvT Properties, Saturated Densities, and Critical Parameters for 3,3,3-Trifluoropropene (HFO1243zf), J. Chem. Eng. Data. 63 (2018) 3818–3822. doi:10.1021/acs.jced.8b00452.

[10] J.S. Brown, L. Fedele, G. Di Nicola, S. Bobbo, G. Coccia, Compressed Liquid Density and Vapor Phase PvT Measurements of cis -1,2,3,3,3-Pentafluoroprop-1-ene (R1225ye(Z)), J. Chem. Eng. Data. 60 (2015) 3333–3340. doi:10.1021/acs.jced.5b00562.

[11] D. Calleja-Anta, L. Nebot-Andres, R. Cabello, D. Sánchez, R. Llopis, A3 and A2 refrigerants: Border determination and hunt for A2 low-GWP blends, Int. J. Refrig. 134 (2022) 86–94. doi:10.1016/j.ijrefrig.2021.11.012.

[12] S. Kondo, A. Takahashi, K. Tokuhashi, A. Sekiya, Y. Yamada, K. Saito, Theoretical calculation of heat of formation for a number of moderate sized fluorinated compounds, J. Fluor. Chem. 117 (2002) 47–53. doi:10.1016/S0022-1139(02)00167-7.

[13] B.O. Bolaji, Theoretical analysis of the energy performance of three low global warming potential hydro-fluorocarbon refrigerants as R134a alternatives in refrigeration systems, Proc. Inst. Mech. Eng. Part A J. Power Energy. 228 (2014) 56–63. doi:10.1177/0957650913507252.

[14] L. Fedele, S. Bobbo, M. Scattolini, C. Zilio, R. Akasaka, HCFO refrigerant cis-1-chloro-2,3,3,3 tetrafluoropropene [R1224yd(Z)]: Experimental assessment and correlation of the liquid density, Int. J. Refrig. 118 (2020) 139–145. doi:10.1016/j.ijrefrig.2020.06.001.

[15] S. Eyerer, F. Dawo, J. Kaindl, C. Wieland, H. Spliethoff, Experimental investigation of modern ORC working fluids R1224yd(Z) and R1233zd(E) as replacements for R245fa, Appl. Energy. 240 (2019) 946–963. doi:10.1016/j.apenergy.2019.02.086.

[16] E.W. Lemmon, M.L. Huber, M.O. McLinden, NIST standard reference database 23: reference fluid thermodynamic and transport properties (REFPROP), version 9.1, National Institute of Standards and Technology, Standard reference data program., (2010). http://www.nist.gov/srd/upload/REFPROP9.pdf.

[17] HoneyWell's Genetron Properties software, HoneyWell's Genetron Properties software (version 1.4), 2010.

[18] J. Yang, L. Gao, Z. Ye, Y. Hwang, J. Chen, Binary-objective optimization of latest low-GWP alternatives to R245fa for organic Rankine cycle application, Energy. 217 (2021) 119336. doi:10.1016/j.energy.2020.119336.

[19] Z. Yang, B. Feng, H. Ma, L. Zhang, C. Duan, B. Liu, Y. Zhang, S. Chen, Z. Yang, Analysis of lower GWP and flammable alternative refrigerants, Int. J. Refrig. 126 (2021) 12–22. doi:10.1016/j.ijrefrig.2021.01.022.

[20] X. Wu, C. Dang, S. Xu, E. Hihara, State of the art on the flammability of hydrofluoroolefin (HFO) refrigerants, Int. J. Refrig. 108 (2019) 209–223. doi:10.1016/j.ijrefrig.2019.08.025.

[21] D. Cowan, J. Gartshore, I. Chaer, C. Francis, G. Maidment, Real Zero - Reducing refrigerant emissions and leakage, in: Proc. Inst. Refrig., 2010: p. 16. https://www3.epa.gov.

[22] M. Karampour, S. Sawalha, State-of-the-art integrated CO2 refrigeration system for supermarkets: A comparative analysis, Int. J. Refrig. 86 (2018) 239–257. doi:10.1016/j.ijrefrig.2017.11.006.

[23] P. Makhnatch, R. Khodabandeh, The role of environmental metrics (GWP, TEWI, LCCP) in the selection of low GWP refrigerant, in: Energy Procedia, 2014: pp. 2460–2463. doi:10.1016/j.egypro.2014.12.023.

[24] R. Llopis, D. Calleja-Anta, A. Maiorino, L. Nebot-Andrés, D. Sánchez, R. Cabello, TEWI analysis of a stand-alone refrigeration system using low-GWP fluids with leakage ratio consideration, Int. J. Refrig. 118 (2020) 279–289. doi:10.1016/j.ijrefrig.2020.05.028.

[25] AIRAH, Methods of calculating Total Equivalent Warming Impact (TEWI) 2012, 2012.

[26] carbonfootprint.com - International Electricity Factors, (2020).

[27] H. Tyagi, P.R. Chakraborty, S. Powar, A.K. Agarwal, Solar Energy systems, challanges, and opprtunities, Springer, 2020. doi:10.1007/978-981-15-0675-8.

[28] A.H. Mosaffa, L.G. Farshi, C.A. Infante Ferreira, M.A. Rosen, Exergoeconomic and environmental analyses of CO2/NH3 cascade refrigeration systems equipped with different types of flash tank intercoolers, Energy Convers. Manag. 117 (2016) 442–453. doi:10.1016/j.enconman.2016.03.053.

[29] M. Navidbakhsh, A. Shirazi, S. Sanaye, Four E analysis and multi-objective optimization of an ice storage system incorporating PCM as the partial cold storage for air-conditioning applications, Appl. Therm. Eng. 58 (2013) 30–41. doi:10.1016/j.applthermaleng.2013.04.002.

[30] R. Roy, B.K. Mandal, Thermo-economic Assessment and Multi-Objective Optimization of Vapour Compression Refrigeration System using Low GWP Refrigerants, in: 2019 8th Int. Conf. Model. Simul. Appl. Optim., IEEE, 2019: pp. 1–5. doi:10.1109/ICMSAO.2019.8880390.

[31] M.S. Turgut, O.E. Turgut, Comparative investigation and multi objective design optimization of R744/R717, R744/R134a and R744/R1234yf cascade rerfigeration systems, Heat Mass Transf. Und Stoffuebertragung. 55 (2019) 445–465. doi:10.1007/S00231-018-2435-Y/FIGURES/14.

[32] Electricity price statistics - Statistics Explained.

[33] Electricity prices around the world | GlobalPetrolPrices.com.

[34] Electric Power Monthly - U.S. Energy Information Administration (EIA).

[35] L. Irlam, Global costs of carbon capture and storage 2017 Update, 2017.

[36] X. Chen, K. Liang, Z. Li, Y. Zhao, J. Xu, H. Jiang, Experimental assessment of alternative low global warming potential refrigerants for automotive air conditioners application, Case Stud. Therm. Eng. 22 (2020) 100800. doi:10.1016/j.csite.2020.100800.

[37] A. Ustaoglu, B. Kursuncu, A. Metin Kaya, H. Caliskan, Analysis of vapor compression refrigeration cycle using advanced exergetic approach with Taguchi and

ANOVA optimization and refrigerant selection with enviroeconomic concerns by TOPSIS analysis, Sustain. Energy Technol. Assessments. 52 (2022) 102182. doi:10.1016/j.seta.2022.102182.

[38] R. Ciconkov, Refrigerants: There is still no vision for sustainable solutions, Int. J. Refrig. 86 (2018) 441–448. doi:10.1016/J.IJREFRIG.2017.12.006.

[39] G. Kosmadakis, C. Arpagaus, P. Neofytou, S. Bertsch, Techno-economic analysis of high-temperature heat pumps with low-global warming potential refrigerants for upgrading waste heat up to 150 °C, Energy Convers. Manag. 226 (2020) 113488. doi:10.1016/j.enconman.2020.113488.

[40] C. Arpagaus, F. Bless, M. Uhlmann, J. Schiffmann, S.S. Bertsch, High temperature heat pumps: Market overview, state of the art, research status, refrigerants, and application potentials, Energy. 152 (2018) 985–1010. doi:10.1016/j.energy.2018.03.166.

[41] GeneralGas.

[42] J. del Estado, Ley 6/2018, de 3 de julio, de Presupuestos Generales del Estado para el año 2018., Boletín Of. Del Estado. BOE-A-2018 (2018) 66621–67354.

[43] Carbon Pricing Dashboard | Up-to-date overview of carbon pricing initiatives.

[44] C.G. Albà, I.I.I. Alkhatib, F. Llovell, L.F. Vega, Hunting sustainable refrigerants fulfilling technical, environmental, safety and economic requirements, Renew. Sustain. Energy Rev. 188 (2023) 113806. doi:10.1016/j.rser.2023.113806

[45] Chase, M.W., Jr., NIST-JANAF Themochemical Tables, Fourth Edition, J. Phys. Chem. Ref. Data, Monograph 9, 1998, 1-1951.

[46] Cox, J.D.; Wagman, D.D.; Medvedev, V.A., CODATA Key Values for Thermodynamics, Hemisphere Publishing Corp., New York, 1984, 1.

[47] Aspen Properties software.

[48] Kolesov, V.P.; Tomareva, E.M.; Shostakovskii, V.M.; Nefedov, O.M.; Skuratov, S.M., Standard enthalpy of formation of 1,1-dichlorocyclopropane, J. Phys. Chem., 1970, 44, 865-867.

[49] V.I. Babushok, D.R.J. Burgess, D.K. Kim, M.J. Hegetschweiler, G.T. Linteris, Modeling of combustion of fluorine-containing refrigerants, 2021. doi:10.6028/NIST.TN.2170.

[50] A.W. Ray, P. Weidner, A. Bodi, B. Sztáray, The Vagabond Fluorine Atom: Dissociative Photoionization of trans -1,3,3,3-Tetrafluoropropene, J. Phys. Chem. A. 124 (2020) 3738–3746. doi:10.1021/acs.jpca.0c01804.

[51] Kolesov, V.P.; Martinov, A.M.; Skuratov, S.M., Standard enthalpies of formation of 1,1,1-trifluoropropene, Zh. Fiz. Khim., 1967, 41, 913-91.